PHD THESIS - INVESTIGATIONS AND IMPLEMENTATIONS OF SUPERCONDUCTING QUANTUM ARCHITECTURES

Ilya Antonov

Royal Holloway and Bedford New college,
University of London

Thesis submitted to
The University of London
for the degree of
Doctor of Philosophy
May, 2023.

Abstract

This thesis presents a series of experimental investigations into superconducting artificial atoms. The central element of the devices is the Josephson junction, and its dual counterpart the quantum phase slip junction that operates by the coherent tunneling of flux quanta. Circuits embedding these elements are designed, simulated and tested at cryogenic temperatures to explore fundamental quantum phenomena, new materials and new devices more robust against decoherence.

The main text is divided into four sections covering: the generation of single photons using a transmon qubit with the main work developing the fabrication and measurement protocols for a time-resolved readout of the source's correlation functions; the investigation into a new type of dipole qubit that promises to improve flux noise sensitivity through the symmetric modification of a standard flux qubit's geometry - a proposal of a Hamiltonian that can match experiment data is given, and a detailed analysis on the potential energy landscape and transition amplitudes is performed; the coherent quantum phase slip qubit realised in TiN opens the window to the fabrication of compact quantum circuits using nanowires, while the demonstration of its readout through a capacitively coupled resonator offers design and material flexibility in the future studies of these dual devices; the twin coherent phase slip qubit is an interesting attempt at creating a distributed network supporting flux quanta, which is assigned an initial model that attempts to describe its rich experimental spectrum.

Supplementing the main text is a sizeable, self-contained appendix tasked with reminding the reader of the relevant superconducting and quantum theory, collected from a variety of literature, as well as walking through the more involved proofs and fabrication steps used in the realisation of all of the devices.

This work will be of most use for researchers working hands on with superconducting qubits in the lab, looking to capture the essential quantum optics theory required for the design and measurement of novel quantum structures.

Contents

Declaration of Authorship I

Acknowledgements II

Thesis motivation and overview III

1 Single photon source 1

1.1 Two level systems in superconductors 4

1.1.1 LC oscillator 4

1.1.2 The Cooper pair box qubit 5

1.1.3 Transmon qubit 8

1.2 Interacting with a qubit 10

1.2.1 Driving 10

1.2.2 Scattering 11

1.2.3 Emission spectrum 12

1.2.4 Qubit evolution 16

1.3 Noise and decoherence 18

1.3.1 Characterising noise 18

1.3.2 Types of decoherence 18

1.3.3 Sources of noise 21

1.4 Design 23

1.4.1 Operating energies 23

1.4.2 Transmission line design 26

1.4.3 Coupling to the transmission line 26

1.4.4 Holes penetrating the ground planes 27

1.4.5 Final design 28

1.5 Fabrication 30

1.5.1 Processing steps 30

1.5.2 Calibration 32

1.5.3 Result 34
1.6 Experiment 35
1.6.1 General measurement principles 35
1.6.2 Qubit spectrum 40
1.6.3 Rabi oscillations 42
1.6.4 Coherent and incoherent emission 44
1.6.5 Relaxation of qubit 45
1.6.6 Time resolved photon signal 46
1.7 Conclusion 55

2 Superconducting twin qubit **56**
2.1 Theory 61
2.1.1 Modelling the qubit 61
2.1.2 Stability regions 64
2.1.3 Anharmonic Josephson potentials 68
2.1.4 Energy spectrum 70
2.1.5 Transition matrix elements 72
2.1.6 Qubit asymmetry 73
2.2 Design 74
2.2.1 Operating energies 74
2.2.2 Transmission line design 75
2.2.3 Coupling to the transmission line 75
2.2.4 Flux loop areas 76
2.2.5 Final design 76
2.3 Fabrication 78
2.3.1 Processing steps 78
2.3.2 Result 80
2.4 Measurement 82
2.4.1 Qubit spectrum 82
2.4.2 Rabi oscillations 87
2.4.3 Resilience to noise 87
2.5 Conclusion 89

3 Coherent quantum phase slip qubit **90**
3.1 Theory 94
3.1.1 Coherent quantum phase slip 94

3.1.2 Coherent quantum phase slip qubit 96
3.1.3 Readout resonator 99
3.1.4 Driving 110
3.2 Design 114
3.2.1 Operating energies 114
3.2.2 Resonator design 116
3.2.3 Coupling system to the resonator 117
3.2.4 Final design 119
3.3 Fabrication 122
3.3.1 Processing steps 122
3.3.2 Result 124
3.4 Experiment 125
3.4.1 Resonator characterisation 125
3.4.2 Qubit spectrum 127
3.4.3 Qubit-resonator coupling 130
3.5 Conclusion 133

4 Coherent quantum phase slip twin qubit 135

4.1 Theory 137
4.1.1 Modelling the qubit 137
4.2 Design 139
4.2.1 Operating energies 139
4.2.2 Distribution along resonator 141
4.2.3 Final design 141
4.3 Fabrication 143
4.4 Experiment 144
4.4.1 Qubit spectrum 144
4.4.2 Transmission experiments 147
4.5 Conclusion 149

5 Summary and outlook 150

A Appendix theory 155

A.1 Superconductivity for artificial atoms 156
A.1.1 Cooper pair condensation 156
A.1.2 Meissner effect 157

A.1.3 Typical length scales in superconductors 158
A.1.4 Phase quantisation 158
A.1.5 Josephson Junction 160
A.1.6 Charge basis 165
A.1.7 Drude model 166
A.2 Simple systems 169
A.2.1 Transmon qubit 169
A.2.2 Unitary transformation of a 2-level system 171
A.2.3 Dipole coupling between 2-level system and microwave field 172
A.2.4 Unitary transformation of driven 2-level system 174
A.2.5 Dynamics of a driven qubit system 175
A.2.6 Two tone spectroscopy on a 3-level system 178
A.2.7 Decay in system due to phase noise 181
A.3 Microwave transmission lines 184
A.3.1 Classical transmission line equations 184
A.3.2 Quantised transmission line equations 186
A.3.3 Reflection in transmission lines 194
A.3.4 Noise in transmission lines 195
A.3.5 Emission rate into transmission lines 199
A.3.6 Dipole source voltage scattering 201
A.3.7 Dipole source power spectrum 203
A.4 Resonator 207
A.4.1 Classical resonator equations 207
A.4.2 Quality factor of resonator 210
A.4.3 Quantisation of fields in the resonator 215
A.4.4 Resonator mode shift due to coupling 217
A.5 Twin qubit 219
A.5.1 Phase operator for the twin qubit 219
A.5.2 Potential energy 219
A.5.3 Triple point 222
A.5.4 Degeneracy point 223
A.5.5 Transition matrix elements 223
A.6 Coherent quantum phase slip qubit 225
A.6.1 Qubit-resonator system 225
A.6.2 Unitary transformation of a qubit-resonator system 227

A.6.3 Unitary transformation of driven qubit-resonator system 228

A.6.4 Solving qubit-resonator master equation 230

A.6.5 Inductive coupling to resonator 233

A.7 Generic quantum formalism 236

A.7.1 Pauli matrices 236

A.7.2 Unitary transformations 237

A.7.3 The master equation 239

A.7.4 Perturbation theory 247

A.7.5 Comment on Poisson brackets 249

A.8 Generic maths formalism 251

A.8.1 Fourier transform definition 251

A.8.2 Wiener-Khinchin theorem for evaluating power spectral density . . 252

A.8.3 Lorentzian fit 254

A.8.4 Fourier transform of exponential decay 254

A.8.5 Distortion of exponential decay by VNA 255

A.8.6 Change of integration limits 256

B Appendix fabrication **258**

B.1 Lithography basics 259

B.1.1 Wet etching 260

B.1.2 Resist coating 260

B.1.3 Exposure 260

B.1.4 Development 263

B.1.5 Deposition 263

B.1.6 Liftoff 264

B.1.7 Covering substrate with material layer 264

B.1.8 Etching 265

B.1.9 Bonding 266

B.2 Josephson junction fabrication 267

B.2.1 Tilting deposition of Josephson junctions (JJs) 267

B.2.2 Manhattan deposition of JJs 268

B.3 Coplanar capacitance heuristic 269

B.4 Transmon photon source fabrication 270

B.4.1 Wafer cleaning and Aluminum (Al) layer 270

B.4.2 Layer 1: Coplanar waveguides 270

B.4.3 Layer 2: JJ 271
B.4.4 Layer 3: Patches 272
B.5 Twin qubit fabrication 273
B.5.1 Wafer cleaning 273
B.5.2 Layer 1: Coplanar waveguides 273
B.5.3 Layer 2: JJ 273
B.6 CQPS qubit fabrication 275
B.6.1 Layer 1: Coplanar waveguides 275
B.6.2 Layer 2: Constrictions 275

C Appendix experiment **277**
C.1 Dilution refrigerator 278
C.2 Data acquisition program 282
C.2.1 Program structure 283
C.2.2 Performance 284

D Glossary **286**
Acronyms 286
Constants 289
Symbols 290

Declaration of Authorship

I, Ilya Antonov, confirm that the work presented in this thesis is my own. Where information has been derived from other sources, I confirm that this has been indicated in the work.

Acknowledgements

This thesis was written over a unique period of world events, and it was the fortuitous combination granted from the creator that all experimental results were completed and summarised in this manuscript. The individuals that I have most to thank for the end result are:

- Oleg Astafiev for being an experienced supervisor opening up the opportunity to work in the progressive field of superconducting qubits, seeding the research directions, assisting in theory and publication preparation;
- Rais Shaikhaidarov for invaluable day-in day-out help in the laboratory office and clean room and well as informal support in my step by step journey throughout the years;
- Artem Shesterikov, Jacob Dunstan and Kyung Ho for support in the lab, presentations and informal discussions, forming the core of our group;
- Teresa Hönigl-Decrinis for helping onboard me at the start of PhD and creating the baseline of experimental procedures and equipment setup that was heavily utilised in my research;
- Multiple visiting students from MIPT including Yulia, Alexandra that offered both scientific collaboration in the laboratory and social events that kept up the spirit of the team;
- Thank you to Royal Holloway, and the National Physical Laboratory for supporting my PhD project financially, and providing the extra curricular environment for a comfortable place to work in. I would especially like to thank Alexander Tzalenchuk for coordinating the administrative side of the PhD and for maintaining positive encouragement in prioritising commitments and development;
- My dad for keeping me directed, focused and motivated throughout the roller-coaster years and offering ample opportunity for side projects and experience in the scientific domain and all the years committed to my growth in all aspects of life;
- My family: brother, mother and sister for providing the happy and warm environment that helped me stay on focus in research and pursue a healthy and fulfilling time as a PhD. For their belief and relentless support that I treasure very very much.
- My wife for completing me, and all the consequences thereof.

Thesis motivation and overview

Recent years have seen a significant push in quantum technology, with weekly updates of *innovative* or *next-generation* discoveries manifesting under the collective term - 2nd Quantum Revolution[1]. The 1st Quantum Revolution occurred at the equator of the last century, bringing about the transistor in 1947 [1], laser in 1958 [2] and semiconductor materials, most notably germanium and silicon, which underpin modern digital technology such as computers, mobile phones, internet, smart watches. And although microscopically they are described by quantum physics, it is their macroscopic interaction with the environment that drives their operation.

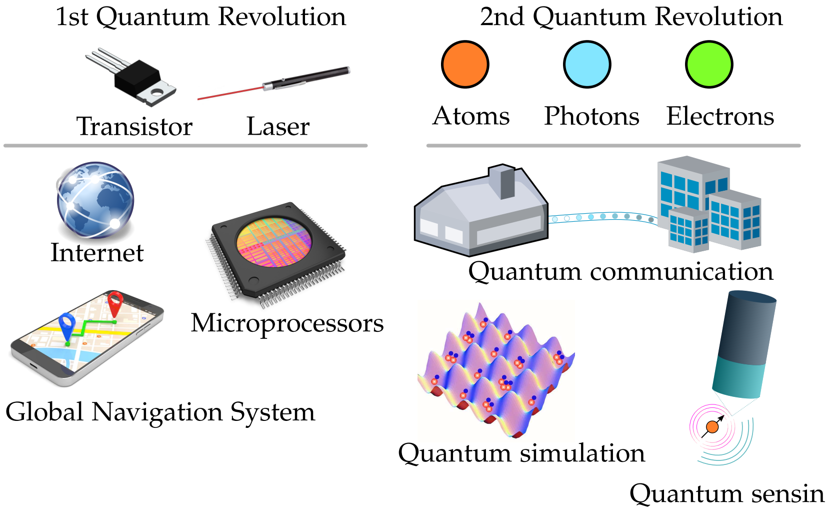
1st Quantum Revolution
Transistor
Laser
Internet
Microprocessors
Global Navigation System
2nd Quantum Revolution
Atoms
Photons
Electrons
Quantum communication
Quantum simulation
Quantum sensing

Figure 1: The two quantum revolutions: **1st Quantum revolution** involved the bulk control of photons (laser) and electrons (transistor), which underpin most of modern day technology; **2nd Quantum revolution** involves the ability to control individual particles and will bring forth devices utilising quantum effects such as entanglement and superposition to go beyond classical operation limits.

The 2nd Quantum Revolution is marked by increasing engineering capability of controlling individual quantum particles and states, starting with the demonstration of the JJ in 1962 [3] and atomic clocks in 1955 [4], which have defined the metrological standards for time and voltage. The next pivotal year was 1982, with the experimental demonstration of entanglement [5] and Feynman's seminal paper on the possibility of efficiently simulating quantum systems with a quantum processor [6]. With this momentum, the field has expanded to into the following directions of research and development [2]:

---

[1] Here we refer to the public understanding of Quantum Revolution, in terms of the chronology that the technologies came to consumer markets.

- **Quantum Computation:** new paradigm of computing using quantum states to run algorithms exponentially faster than on classical computers [7], Fourier Transform [8, 9], prime factorisation [10], database search [11] and more recently in applications to machine learning [12, 13]. These algorithms use the quantum analogous of AND, NOT, COPY gates required for a universal computation machine, but also quantum logic for creation and manipulation of intermediate states [14];
- **Quantum Simulation:** predicting behaviour of $\sim 10^{23}$ objects in nuclear, atomic and chemical systems [6], that would be impractical for classical computers even for cases with modest degrees of freedom. Quantum simulators can be programmed to simulate any local quantum system [14] and have been applied to study many-body dynamics [15] the Hubbard model [16] amongst others [17, 18, 19];
- **Quantum Communication:** realisation of a quantum network for the distribution of information between quantum nodes (with their own internal memory [20, 21, 22, 23]) via photons [24, 25] and teleportation [26, 27], as well as the demonstration of encrypted quantum channels [28, 29] sensitive to eavesdropping [30, 31, 32, 33];
- **Quantum Sensing:** detectors using the sensitivity of quantum states to electric [34, 35, 36], magnetic [37, 38, 39, 40, 41], air pressure [42], chemical presence [43] and gravitational waves [44] for ultra high resolution probes [45];
- **Quantum Imaging:** super resolution of objects beyond standard diffraction limits [46, 47], enhancing contrast [48, 49], underwater imaging [50], imaging from behind corners [51], constructing 3D images [52] to name just a few [53];

Investments reflect the belief in the revolutionary effect of these technologies: European Quantum Flagship - allocation of €2b over 2018-2028, financing 5000 researchers, and making it the biggest flagship after the Graphene and Human Brain project[3]; UK National Quantum Technologies Program - £315m allocation in 2018, with encouragement to spread awareness within businesses and industry bodies and raise a generation of undergraduates, technicians, apprenticeship level and PhDs to boost UK's prominence in the field[4]; U.S. National Quantum Initiative Act - $1.2 billion allocation in 2018 to double down on quantum research. Interest from technology giants [5], defence companies [6] and academic institution has given wide span for niche research to explore and exploit the new quantum phenomena as part of this 2nd Quantum Revolution.

---

[2] UK Quantum Technology Hub, Annual Report 2014–15 (2015)

[3] European Quantum Flagship

Superconducting artificial atoms

All these quantum systems require addressable atoms with a discrete energy level structure, whose transitions are accompanied by the release and absorption of quantum packets of energy - photons. The study of such photon-atom interaction is collectively referred to as quantum optics. There are a number of systems that provide such quantum levels: cold trapped ions that are cooled and manipulated using laser irradiation [54, 55]; quantum dots in which single electrons are confined to potential wells, and voltage manipulations are used to control their spin [56, 57]; computation based on nuclear magnetic resonance utilising the spins of thousands of atoms [58, 59, 60], neutral atoms [61] and photons [62].

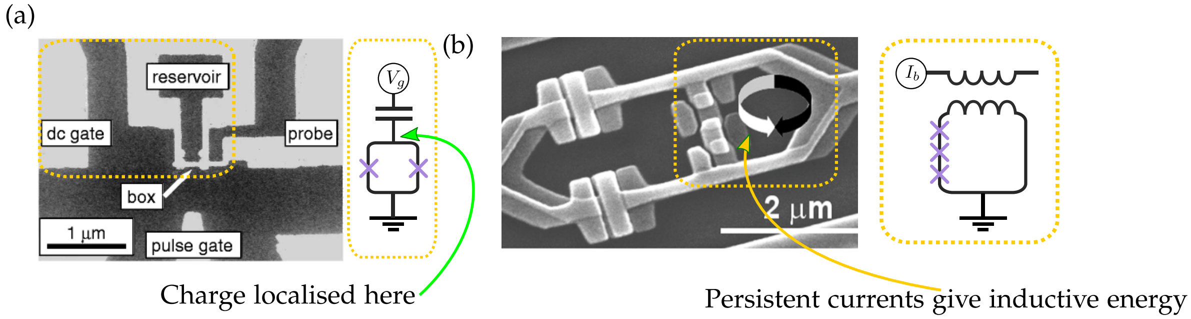

Figure 2: The pioneering superconducting artificial atoms: **(a)** CPB, whose quantised states arise from charge localisation on island (SEM image taken from [63]); **(b)** Flux qubit, whose quantised states arise from persistent currents in the superconducting loop (SEM image taken from [64]). Highlighted in yellow is the part that corresponds to the circuit diagram. Purple crosses denote JJ, that allow the tunnelling of CP and are essential for the establishment of a quantised energy system.

Proposed at the end of the century where artificial atoms based on superconducting materials. Superconductors provide dissipation-free electric circuits with long range coherence and quantum states associated with macroscopic parameters, making them a promising choice for preparing, manipulating and maintaining quantum states. The μm-sized devices are fabricated by depositing layers of aluminum on top of silicon wafers and the operation frequencies are in the GHz (microwave) range. The Cooper pair box [65] and flux qubits [66] were demonstrated experimentally in 1999 [63, 64], their energy states arising from electron localisation on isolateed islands and persistent currents in superconducting loops (see Fig. 2).

---

[4] House of Commons, Science and Technology Committee, Quantum technologies Twelfth Report of Session 2017–19

[5] Google, IBM and Microsoft developing big teams and infrastructure for their in-house realisation of quantum processors.

[6] UK already taking orders for quantum technology components.

With time, superconducting qubits have come to dominate the field of quantum computation - both Google's 72 qubit and IBM's 50 qubit quantum processors (see Fig. 3) are based of the transmon qubit and have the following qualities:

- Can be batch-fabricated using standardised nanotechnology techniques in the semiconductor industry [67], leveraging the industrial infrastructure that has enabled production of modern electronics for decades;
- Can have their qubit blocks designed with controllable characteristics: energy profile, relaxation rate, coupling strength to external environment. In contrast to quantum technology based off natural atoms, where the parameters are fixed by nature, these qubits can be fine tuned to give a greater variety of implementations for specific environments, and can also be tuned in situ by electric and magnetic fields, allowing for dynamic reconfiguration;
- Have their signals confined to propagating along a 1-D TL, as opposed to dispersive emission into 3D-space as is the case with natural atoms and trapped ions (see Fig. 1.1) resulting in much stronger interaction with the control systems;
- Compatible with abundant microwave circuitry allowing large scale integration;
- Operate at temperatures $\leq 1\,\mathrm{K}$ for thermal noise to be lower than the GHz energies characteristic of these systems (as a general rule, thermal energy at $1\,\mathrm{K}$ is equivalent to $20\,\mathrm{GHz}$).

Fundamental research into superconducting atoms has gone further to demonstrate the functionality of: a MOSFET transistor [25, 68, 69] - where a control field was used to pass or block a probe field at a different frequency; multiplexer [70] - two input signals mixed to controllably generate a single output signal; serial bus [71] and amplifier [72], expanding the available modules of the future quantum computing platform.

Most of the functionality can be attributed to the strong interaction of superconducting artificial atoms with microwaves, that allows for regimes inaccessible with natural atoms

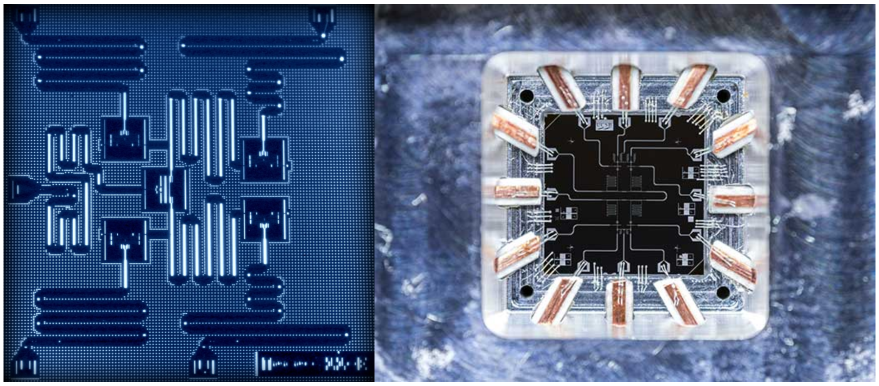

Figure 3: Earlier quantum computer prototypes of the **(Left)** IBM 5 qubit experience and **(Right)** Google Transmon that realise the qubits with Al blocks printed on a 2D wafer - much in the same way as is done in modern computer chips.

[69, 73, 74]. The results of this has been the manipulation of single photons[75], quantum amplification [72] and quantum wave mixing, the likes of which has never measured in other quantum optics systems [70, 76].

Outline of thesis

This thesis describes four fundamental investigations on superconducting artificial atoms (see Fig. 4) taking each device through the design, fabrication and experimental characterisation stages:

- Chapter 1 looks at the realisation of a transmon single photon source - a fundamental building block for using photons as information carriers in quantum networks and integrated experiments. The goal is to develop a platform for making and characterising this device in preparation for more complex correlation measurements. This chapter will introduce the common theory of superconducting qubits, the technical know-how of their fabrication and experimental characterisation;

- Chapter 2 investigates a new type of qubit with a symmetric geometry in an attempt of decreasing sensitivity to flux noise and improving coherence times of a regular flux qubit. This section involves more simulation and theoretical description of the device and will be useful for one looking to propose original designs with unique Hamiltonian;

- Chapter 3 investigates a qubit based on the coherent phase slip - the tunneling of flux across a superconductor, dual to the tunneling of a CP across an insulator. This paves the way for investigations of the coherent quantum phase slip under the influence of strong magnetic fields, helping its establishment as a fundamental superconducting quantum circuit element like the JJ;

- In Chapter 4 a symmetrised geometry is applied to the CQPS qubit to, once again, use symmetry to counteract flux noise.

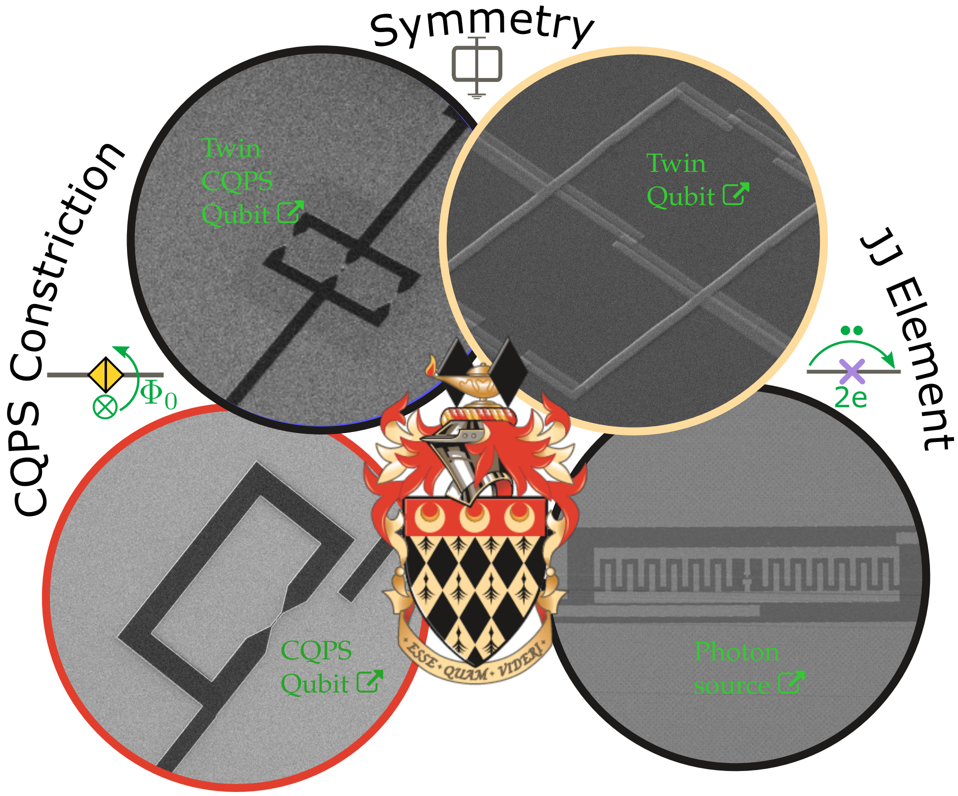

Figure 4: Preview of the devices investigated in the thesis. These devices are interlinked by either their geometrical features or the quantum element central to their operation - the JJ or CQPS constrictions. These structures could serve as fundamental quantum blocks for integration into more complex systems.

Theory immediately relevant to each chapter is introduced in short introductory sections. More thorough theoretical derivations, not always covered in books and papers, are broken down in the Appendix, which also describes the fabrication technology and low temperature experimental techniques.

I hope the thesis will be accessible to new students embarking on their master and PhD projects and serve as an introductory read to this broad and exciting field of superconducting artificial atoms.

Chapter 1

Single photon source

Single photon sources have been well studied in the optical domain [77, 78, 79] and have recently been demonstrated in superconducting cavity resonators [80, 81, 82, 83] and Transmission lines (TLs) [75, 84]. Superconducting photon sources have capitalised on the strong photon-atom coupling that can achieve 90% efficiency [69, 72] compared to 12% in natural atoms [85, 86, 87] to showcase the routing of single photons with 99% fidelity [25] and transmitting quantum information at the individual photon level [83].

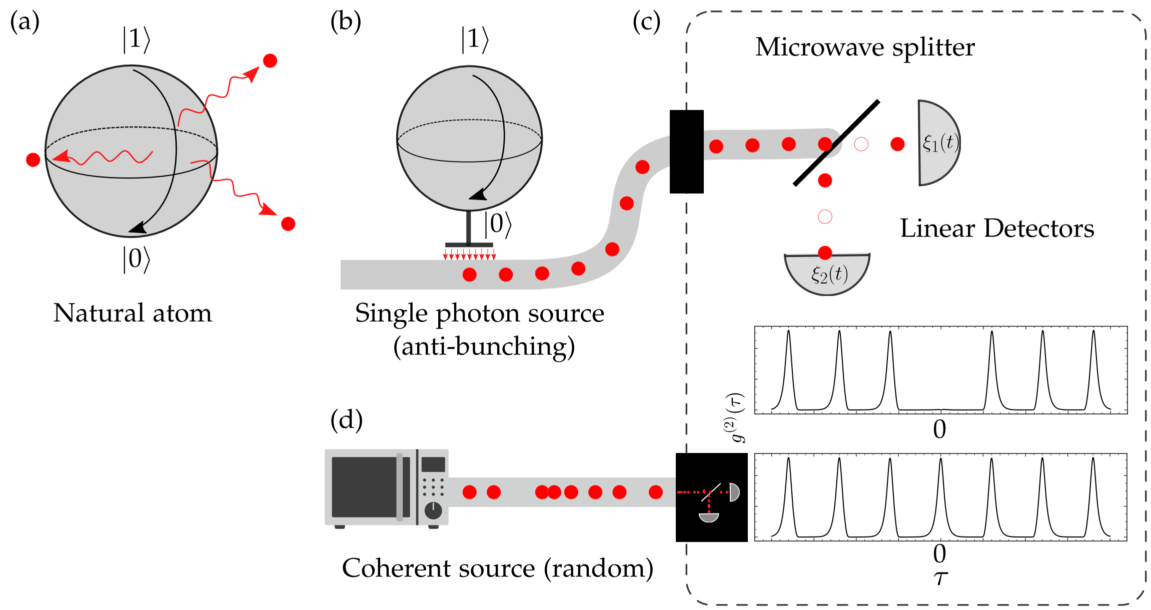

Figure 1.1: Emissions by a quantum system during a state transition: **(a)** Trapped ion - radiation is spread over the solid sphere in 3D-space; **(b)** Superconducting artificial atoms exemplify strong coupling to 1D microwave TLs, and there is a smaller proportion of non-radiative emission; **(c)** To prove that the atom is indeed generating periodic single photons, the emitted voltage needs to be passed through a microwave beam splitter and the $g^{(2)}(\tau = 0) = 0$ shown by evaluating the correlation function across these detectors; **(d)** A coherent source will have $g^{(2)}(\tau = 0) \neq 0$ as photons come in bunches which allows simultaneous clicks on both detectors.

A photon source can be realised by a 2-level system, where a transition $|1\rangle \rightarrow |0\rangle$ is accompanied by the emission of a single photon of energy $\hbar\omega_{01}$ (see Fig. 1.1). Periodic excitations can be tuned to emit single photons for an average photon number $\bar{n} \equiv 1$ on demand.

However the average photon number alone will not differentiate a single photon source from a low intensity classical field with $\bar{n} \equiv 1$. What will differ are their probability distributions: coherent light sources such as a laser have a Poissonian distribution with variance $\Delta n^2 = \bar{n}$; classical thermal sources follow super-Poissoninan statistics with $\Delta n > \bar{n}$ (bunching) [88], while single photon sources follow sub-Poissonian statistics $\Delta n < \bar{n}$ (anti-bunching), due to the arrival of photons at fixed time intervals at the detectors (see

Fig. 1.1 (c)).

Usually these statistics are built up using non-linear detectors that produce a *click* every time a photon is incident on them and associated with the number operator ($n = \langle a^\dagger a \rangle$). However the energy of a microwave photon ($300\,\mathrm{MHz} \leq \omega/2\pi \leq 300\,\mathrm{GHz}$) is 5 orders of magnitude smaller and no efficient single photon detectors exist (although progress is being made [89]). The linear detectors that are available record the voltage quadratures associated with operators $\xi(t) \propto \langle ia - ia^\dagger \rangle$. And although these detectors add substantial noise, their phase resolution allows a different way of probing the quantum nature of light through correlation functions

$$\begin{cases} g^{(1)}(\tau) = \int dt\, [\xi_1^*(t)\xi_2(t-\tau)]\,, \\ g^{(2)}(\tau) \int dt\, [\xi_1(t)^*\xi_1^*(t-\tau)\xi_2(t-\tau)\xi_2(t)]\,, \end{cases}$$

using the time-resolved voltages $\xi_1(t), \xi_2(t)$ on the branches of a beam splitter in a Hanbury-Brown Twiss setup [46] (see Fig. 1.1 (c)). $g^{(1)}(\tau)$ captures the ability of the photon to interfere with itself [90], while the distinct absence of peak at $g^{(2)}(\tau = 0)$ would represent the impossibility of simultaneous photon detection onto the two detector branches for a truly single photon source [91].

A robust fabrication and experimental platform needs to be developed in preparation for these non-trivial measurements in a noisy environment. Following a general introduction to superconducting systems (Sec. 1.1) the work of this chapter concentrates on preparing these protocols with local fabrication and measurement facilities, beginning with the design (Sec. 1.4) and fabrication (Sec. 1.5) of the flux-tuneable single photon source. The source undergoes preliminary characterisation (Sec. 1.6) and a readout scheme with supporting software package (C.2.1) is developed for the future measurement of $g^{(1)}(\tau)$ and $g^{(2)}(\tau)$ correlations.

1.1 Two level systems in superconductors

1.1.1 LC oscillator

The most basic superconducting 2-level system can be made from a standard LC oscillator (see Fig. 1.2 (a)) with energy oscillating between that stored by the charge Q on the capacitor ($Q^2/2C$) and energy in the inductor ($\partial_t Q^2/2L$). Being in the superconducting state, the harmonic oscillator dissipates no energy, has a fundamental mode $\omega_r = 1/\sqrt{LC}$ and has evenly spaced energy levels, which can be quantum manipulated by driving the system with microwaves at frequencies $\sim \omega_r$.

However an LC oscillator is impractical for quantum manipulations as an excitation from $|0\rangle \underset{\omega_r}{\longrightarrow} |1\rangle$ would bring about an uncontrollable ladder of further excitations (they do have use as an auxiliary circuit element in Ch. 3).

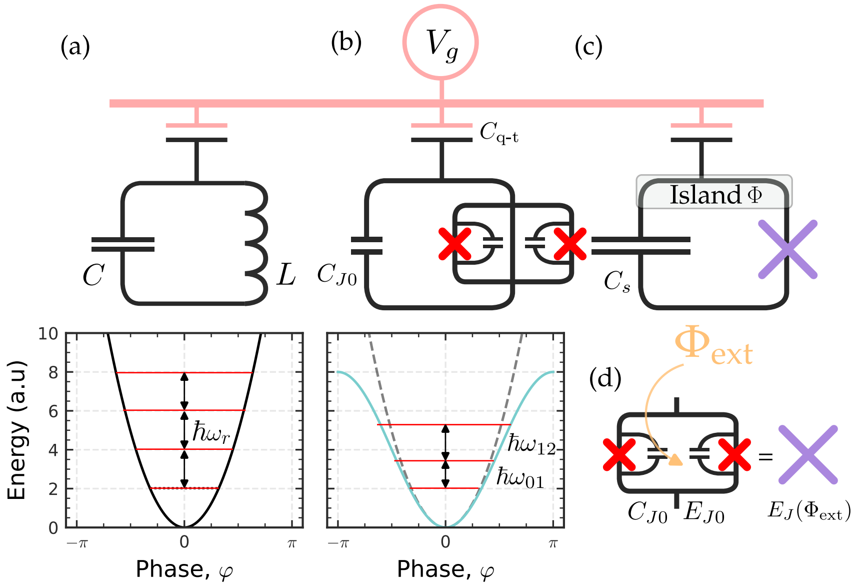
(a)
(b)
(c)
V_g
$C_{\text{q-t}}$
Island Φ
C
L
C_{J0}
C_s
Energy (a.u)
10
8
6
4
2
0
$\hbar\omega_r$
$-\pi$
0
π
Phase, φ
$\hbar\omega_{12}$
$\hbar\omega_{01}$
$-\pi$
0
π
Phase, φ
Φ_{ext}
(d)
=
C_{J0}
E_{J0}
$E_J(\Phi_{\text{ext}})$

Figure 1.2: Progression from a superconducting LC oscillator to a transmon qubit. **(a)** Circuit and equal spaced energy levels of an LC resonator; **(b)** CP box achieves energy level anharmonicity by using a non-linear inductor - the JJ. This defines a computational subspace in its lower energy levels; **(c)** A transmon adds a large shunt capacitor (C_s) that decreases its sensitivity to charge. The state of the system is controlled with external voltage (V_g) supplied via the coupling capacitor ($C_{\text{q-t}}$) and external flux (Φ_{ext}); **(d)** A DC-SQUID consisting of two JJ interrupting a superconducting loop - it is usually represented as a single flux-tuneable JJ.

1.1.2 The Cooper pair box qubit

The solution is to restrict the system to the lowest energy levels by including a non-linear element to break the harmonicity of the system, while maintaining the dissipationless environment required for superconducting circuit. The Josephson junction (JJ) [3] (whose properties are summarised in A.1.5) is just that element with a non-linear inductance and energy

$$L_J = \frac{\Phi_0}{2\pi}\frac{1}{I_c\cos(\varphi)}, \qquad E_J = E_{J0}\left(1-\cos(\varphi)\right).$$

The phase (φ) of the junction corresponds to the phase difference between the macroscopic condensate wavefunctions of the two superconductors it connects and I_c is the maximal current of tunneling Cooper pair (CP) that it can pass without dissipation.

The resulting structure (see Fig. 1.2 (b)) is known as a Cooper pair box (CPB), and consists of a small Aluminum (Al) island connected to a superconducting reservoir through a JJ on one side and biased through a gate capacitance ($C_{\text{q-t}}$) on the other. The two energy scales characterising the system are:

- The charging energy $E_C = e^2/2C_\Sigma$ gained when an electron jumps into the CPB;
- The Josephson energy $E_{J0} = \Phi_0 I_c/2\pi$ gained when a CP tunnels across the JJ.

Evaluation of the system's Hamiltonian is given in A.2.1, which is expressed through the CP number ($\hat{N}$) and phase ($\hat{\varphi}$) operators

$$H_q = 4E_C\left(\hat{N}-N_{\text{ext}}\right)^2 - E_J\cos\left(\hat{\varphi}\right), \tag{1.1.1}$$

and where $N_{\text{ext}} = C_{\text{q-t}}V_g/2e$ is the charge induced on the transmon island by the external voltage through capacitor through the gate capacitor.

A modification of the CPB is to *split* the JJ in order to have another degree of control over the qubit using an external magnetic field (see Fig. 1.2 (d)). A.1.5.3 shows that this parallel JJ structure is equivalent to a single JJ with a flux-controlled Josephson energy

$$E_J\left(\Phi_{\text{ext}}\right) = E_{J0}\times 2\left|\cos\left(\frac{\pi\Phi_{\text{ext}}}{\Phi_0}\right)\right|.$$

The flux-dependent E_J gives an additional magnetic flux handle (Φ_{ext}) for controlling the qubit, in addition to the externally induced charge (N_{ext}). In all further equations the external flux argument will be dropped for brevity $E_J\left(\Phi_{\text{ext}}\right) \to E_J$.

To proceed, the charge basis $\{|N\rangle\}$ is used, where eigenstates such as $|N=0\rangle$ and $|N=1\rangle$ correspond to 0 and 1 CPs on the island. To express Hamiltonian (1.1.1) in the charge basis, one makes use of the following representation of charge and phase operators $e^{\pm i\hat{\varphi}} = \sum_N |N \pm 1\rangle \langle N|$ and $\hat{N} = \sum_N N\,|N\rangle\langle N|$ (refer to A.1.6)

$$
\begin{aligned}
H_q &= E_C\left(\hat{N} - N_{\text{ext}}\right)^2 - E_J \cos\left(\hat{\varphi}\right) \\
&= \sum_n \left[E_C (N - N_{\text{ext}})^2 |N\rangle\langle N| - \frac{E_J}{2}\left(|N+1\rangle\langle N| + |n-1\rangle\langle N| \right) \right] \\
&= \begin{array}{c} \\ \langle -2| \\ \langle -1| \\ \langle 0| \\ \langle 1| \\ \langle 2| \end{array}
\begin{array}{ccccc}
|-2\rangle & |-1\rangle & |0\rangle & |1\rangle & |2\rangle \\
E_C(-2-N_{\text{ext}})^2 & -E_J/2 & 0 & 0 & 0 \\
-E_J/2 & E_C(-1-N_{\text{ext}})^2 & -E_J/2 & 0 & 0 \\
0 & -E_J/2 & E_C(N_{\text{ext}})^2 & -E_J/2 & 0 \\
0 & 0 & -E_J/2 & E_C(1-N_{\text{ext}})^2 & -E_J/2 \\
0 & 0 & 0 & -E_J/2 & E_C(2-N_{\text{ext}})^2
\end{array},
\end{aligned}
\tag{1.1.2}
$$

which can be numerically solved to find the eigenstates ($|\psi_i\rangle = \sum_N a_N |N\rangle$) and eigenenergies ($E_i = \hbar\omega_i$) as shown in Fig. 1.3 as functions of the external biases ($N_{\text{ext}}, \Phi_{\text{ext}}$).

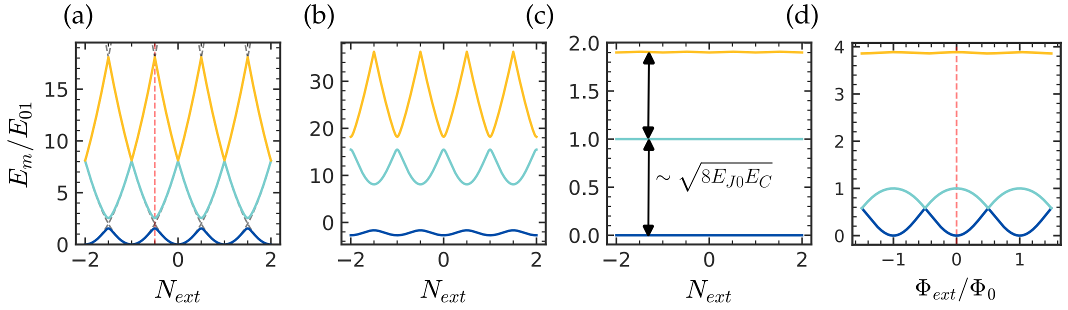

Figure 1.3: Eigenenergies of (1.1.2) for different ratios E_{J0}/E_C at different $N_{\text{ext}}, \Phi_{\text{ext}}$ biases: **(a)** $E_{J0}/E_C = 1$, $\Phi_{\text{ext}} = 0$ which corresponds to a CPB; **(b)** $E_{J0}/E_C = 10$, $\Phi_{\text{ext}} = 0$; **(c)** $E_{J0}/E_C = 100$, $\Phi_{\text{ext}} = 0$ which corresponds to a transmon - the large shunt capacitance (C_s) of the transmon lowers charge sensitivity, but also reduces anharmonicity. In this regime the first transition energy $\hbar\omega_{01} = \sqrt{8E_{J0}E_C} - E_{J0}$ [92] ; **(d)** $E_{J0}/E_C = 100$, $N_{\text{ext}} = 0.5$. Energies are given in units of first transition energy. Vertical dashed lines mark the degeneracy points of minimal sensitivity: $\Phi_{\text{ext}}/\Phi_0 = 0$ and $N_{\text{ext}} = 0.5$.

The non-harmonic energy contribution of the JJ in (1.1.1) brings about an asymmetry between the transitions - performing an excitation $|0\rangle \to |1\rangle$ would not involuntarily cause $|1\rangle \to |2\rangle$. This restricts the computational space to the lowest energy levels (see Fig. 1.2 (b)).

Next to degeneracy points ($N_{\text{ext}} = N + 1/2, N \in \mathbb{Z}$, see dashed line in Fig. 1.3 (a)) the system is least sensitive to charge fluctuations, and the eigenstates of the system are dominated by two charge states (highlighted by the box in Fig. 1.4). The Hamiltonian can be truncated to the ✥ matrix element in (1.1.2)

$$H_q = \begin{pmatrix} -\varepsilon/2 & -\Delta/2 \\ -\Delta/2 & \varepsilon/2 \end{pmatrix}, \tag{1.1.3}$$

where $\varepsilon = \left(E_C N_{\text{ext}}^2 - E_C(1+N_{\text{ext}})^2\right) = -E_C\left(1+2N_{\text{ext}}\right)$, $\Delta = E_J$. This generic 2×2 matrix can be trivially solved to find eigenstates and eigenenergies (refer to A.2.2)

$$\begin{aligned} E_g &= \frac{\Delta E}{2}. \qquad |g\rangle = \begin{pmatrix} \cos(\theta/2) \\ -\sin(\theta/2) \end{pmatrix}, \\ E_e &= -\frac{\Delta E}{2}, \quad |e\rangle = \begin{pmatrix} \sin(\theta/2) \\ \cos(\theta/2) \end{pmatrix}, \\ \Delta E &= \sqrt{\varepsilon^2 + \Delta^2}, \qquad \tan(\theta) = \frac{\Delta}{\varepsilon}. \end{aligned} \tag{1.1.4}$$

Hence at the working point, the CPB defines a 2-level system, which can release a photon of frequency $\omega_q = \Delta E/\hbar$ during a transition.

1.1.3 Transmon qubit

The CPB has a large charging energy ($E_C = e^2/2C_\Sigma, C_\Sigma = 2C_{J0}$) due to the small capacitance (C_{J0}) of the JJ, and hence has a strong response to charge fluctuations in the environment. This causes two problems:

- It necessitates the inclusion of a voltage gate next to the CPB in order to maintain the system in the charge sweet spot (see dashed line in Fig. 1.3);
- It introduces decoherence to the system which can destroy a quantum state in a matter of nanoseconds (more detail on this is given in Sec. 1.3).

To minimise sensitivity to charge noise, a transmon qubit with a large shunt capacitor was proposed [92] and implemented [93] as shown in Fig. 1.2 (c). This decreases the charging energy by increasing the capacitance parallel to the JJs to $2C_{J0} + C_s$ and thereby increasing the E_{J0}/E_C ratio. The net effect is the *flattening* out of the energy bands as seen in Fig. 1.3 (b,c). The flatter bands arise from the participation of more CP states in the eigenstates of the system, with individual one having less of a contribution (see Fig. 1.4 (a)).

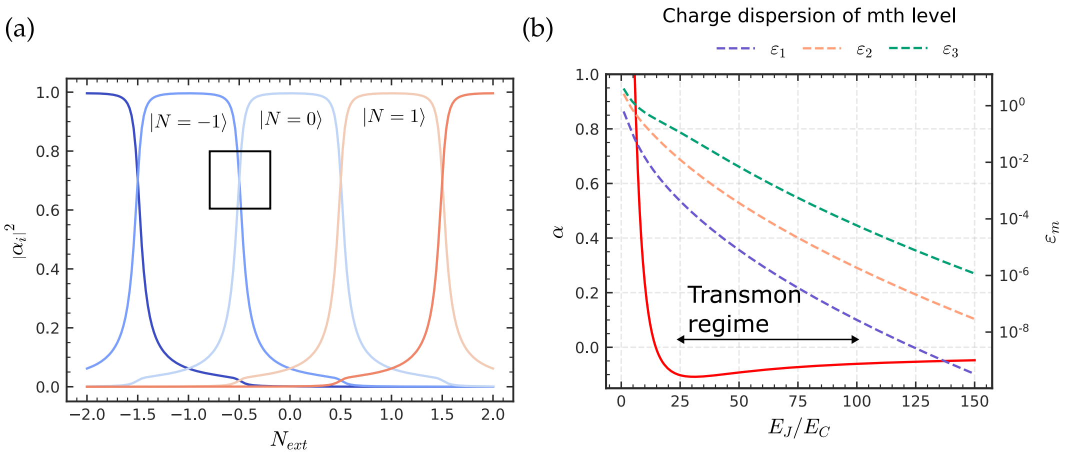

Figure 1.4: **(a)** Contributions of components $a_N |N\rangle$ to the system's ground state ($|g\rangle = \sum_N a_N |N\rangle$). At $N_{\text{ext}} = N + 1/2, N \in \mathbb{Z}$ (highlighted box), it becomes more favourable to reduce the systems energy by crossing over to a new charge state that becomes dominant for the next period. $E_{J0}/E_C = 10$ and $\Phi_{\text{ext}} = 0$ is used; **(b)** Charge dispersion quantified by $\varepsilon_m = (E_m(N_{\text{ext}} = 0.5) - E_m(N_{\text{ext}} = 0))/E_{10}$ compared with anharmonicity $\alpha = (E_{21} - E_{10})/E_{10}$ for a range of E_{J0}/E_C values. In the transmon regime $20 \leq E_{J0}/E_C \leq 100$.

A CPB operating at theoretical limits showed a benchmark decoherence time $T_2^* = 325\,\text{ps}$ [94] which was boosted to to $T_2^* \sim 1.75\,\mu\text{s}$ in the first experimental transmon realisation [93]. The relaxation time $T_1 \sim 1\,\mu\text{s}$ remained unchanged indicating that a source of pure dephasing was suppressed (see Sec. 1.3). This makes it the more suitable choice for the realisation of a photon source, as there is a higher degree of control over its quantum state, and indeed the transmon design was used in previous superconducting photon sources [75, 80, 81, 82, 83, 84].

The constraining effect is that the big shunt capacitor (C_s) causes a drop in anharmonicity, quantified by $\alpha = (E_{21} - E_{10})/E_{10}$, reverting back to the LC circuit where there will be a state leakage out of the $\{|0\rangle, |1\rangle\}$ subspace that prevents the application of fast control pulses [92]. Ideally the transition frequencies should differ by $\sim 100\,\text{MHz}$ to ensure that they are above the minimal bandwidth resolution of microwave electronics. The trade off between anharmonicity and charge sensitivity is shown in Fig. 1.4 (b), where charge dispersion is shown to decrease exponentially, preventing linear noise contributions from affecting qubit transition frequency, while anharmonicity decreases as a power law. The equilibrium spot for the transmon is the $E_{J0}/E_C \in [20, 100]$ range.

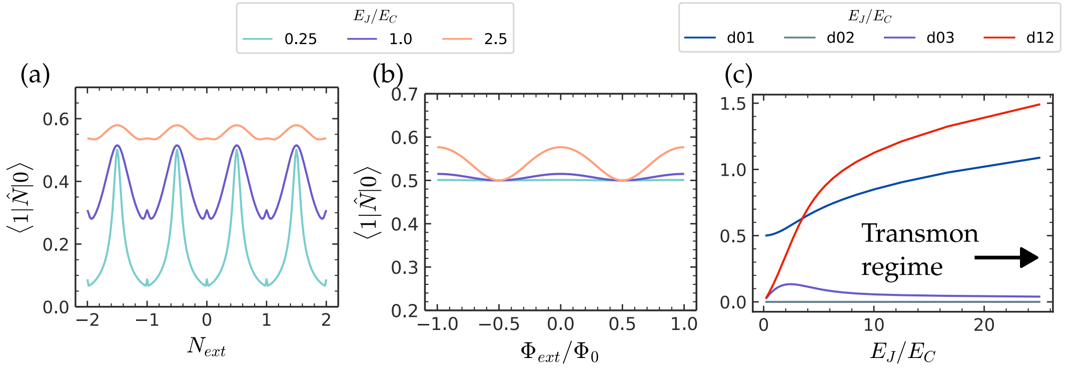

Figure 1.5: **(a-b)** Transition matrix element ($\langle 1|\,\hat{N}\,|0\rangle$) of (1.1.5) under different biases and different E_{J0}/E_C ratios. As expected, the transition is strongest near the working point ($N_{\text{ext}} = 0.5$), where there is a tendency for the state to oscillate between the neighbouring charge states (see Fig. 1.4). At larger E_{J0}/E_C ratios this gets washed out, as the state superposition contains more charge states; **(c)** Different transition elements at different E_{J0}/E_C ratios, showing the improvement of $|0\rangle \leftrightarrow |1\rangle$ and $|1\rangle \leftrightarrow |2\rangle$ transitions as one moves from the CPB into the transmon regime.

The other unexpected benefit of the transmon, is that it enhances transitions between its charge states. To see this, one evaluates the matrix element associated with a transition between states $|i\rangle$ and $|j\rangle$

$$\text{Transition energy} = \langle i|\, 2e\hat{N}\frac{C_{\text{q-t}}}{C_\Sigma}V_g\,|j\rangle \propto \langle i|\,\hat{N}\,|j\rangle \tag{1.1.5}$$

where the operator $\left(2e\hat{N}/C_\Sigma\right) C_{\text{q-t}}V_g$ quantifies the interaction between the external voltage and qubit through the coupling capacitance (refer to A.2.3). Fig. 1.5 (b) shows how the first and second transitions get stronger, while double excitations such as $|0\rangle \rightarrow |2\rangle$ are restricted. So while protected from low frequency charge fluctuations, the transmon remains highly polarisable to high frequency electric fields that drive resonant state transitions.

1.2 Interacting with a qubit

Microwaves are used to interact with the transmon qubit - incoming microwave modes influence the motion of the atom (driving, V_{mw}), while outgoing modes carry energy away (emission, V_{sc}). There are different mechanisms for such *scatterings* to occur, which is quantified in the analysis below.

1.2.1 Driving

The TL is characterised by a capacitance (c) and inductance (l) per unit length, impedance $Z = \sqrt{l/c}$ and propagation speed $v = 1/\sqrt{lc}$ (refer to A.3). The driving field

$$V_{\text{mw}}(x,t) = V_{\text{mw}} e^{i(kx-\omega t)} \tag{1.2.1}$$

with amplitude V_{mw} and frequency ω (wavevector $k = \omega/v$) is of greatest interest when it matches the transition frequency of the transmon ($\omega \sim \omega_q$) and induces $|0\rangle \leftrightarrow |1\rangle$ transitions. Each such event involves the tunneling of CPs to and from its isolated island, and a subsequent charge redistribution in the TL in response to the new electrostatic potential (see Fig. 1.6). This two-way interaction across the coupling capacitor is modelled with a drive Hamiltonian derived in A.2.3

$$H_{\text{mw}} = \text{Re}\left[\hat{\vartheta}\right] V_{\text{mw}} = \hbar\Omega\cos(\omega t)\sigma_x, \tag{1.2.2}$$

where the dipole operator and dipole amplitude are

$$\hat{\vartheta}(t) = \vartheta e^{-i\omega t}\sigma_x, \qquad \vartheta = e\frac{C_{\text{q-t}}}{C_\Sigma}, \tag{1.2.3}$$

or equivalently the driving amplitude[1]

$$\Omega = \frac{1}{\hbar}\vartheta V_{\text{mw}}. \tag{1.2.4}$$

Each is useful in different contexts:

- The dipole operator ($\hat{\vartheta}$) captures the *locking* of the transmon onto the frequency of the driving field and creating coherent state transitions under its influence. The effect of these transitions is a time-varying charge dipole experienced by the TL, which ultimately gives rise to the interaction Hamiltonian (1.2.2);

---

[1] A more rigorous derivation gives $\Omega = \frac{1}{\hbar}\left[e\frac{C_{\text{q-t}}}{C_\Sigma}\right]\left(\frac{E_J}{2E_C}\right)^{1/4} V_{\text{mw}}$, with the numerical factor evaluating ~ 1 in the transmon regime [92].

- The dipole amplitude (ϑ) will be implicit in measurable quantities such as the relaxation rate (Γ_1, see A.3.5) and is determined by the specifics of individual samples;
- The driving amplitude (Ω) will be a useful quantity when working with Hamiltonians, since it has the natural units of frequency and is called the Rabi frequency.

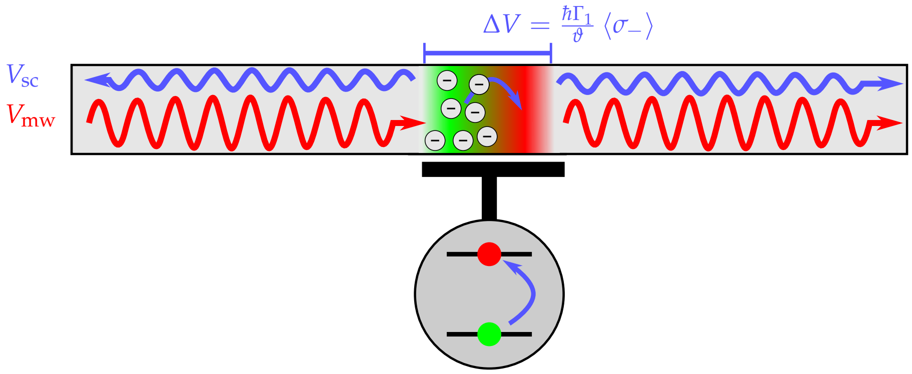
$\Delta V = \frac{\hbar\Gamma_1}{\vartheta}\langle\sigma_-\rangle$
V_{sc}
V_{mw}

Figure 1.6: Interaction between a capacitively coupled transmon and an incident driving field V_{mw}. The stimulated transitions in the transmon are mirrored by a corresponding charge redistribution in the TL, whose second derivative generates a localised voltage difference (ΔV). This additional *source* term in the wave equation (1.2.6) leads to the scattering of another voltage field V_{sc}. Because the rate of transitions will be set by the drive, this scattered voltage will occur at the same frequency. From the perspective of the TL, the transmon acts like a localised charge dipole.

1.2.2 Scattering

Apart from characterising the driving (1.2.2) that influences the motion of qubit, the dipole operator ($\hat{\vartheta}$) also characterises the emission process - voltage scattering into the TL travelling symmetrically in both directions (see Fig. 1.6). As seen in (1.2.3) $\hat{\vartheta}(t)$ represents the effective charge induced in the TL, and so its first time derivative ($l\partial_t\left\langle\hat{\vartheta}(t)\right\rangle$) is the induced flux change and $l\partial_{tt}\left\langle\hat{\vartheta}(t)\right\rangle$ is the voltage it generates in the TL.

Here the dipole approximation is made (from which the operator gets its name), in which the interaction is treated as occurring at a single point on the TL ($x = 0$). This is a motivated assumption, since the characteristic size of the qubit will be $\sim 15\,\mu$m (see Sec. 1.4) which is negligibly small compared to the $\lambda \sim 30\,$mm wavelength of a GHz driving field, giving a voltage source at the location of the qubit

$$V_{\text{source}} = l\partial_{tt}\left\langle\hat{\vartheta}(t)\right\rangle\delta(x). \tag{1.2.5}$$

The total voltage in the TL will then satisfy the inhomogenous 1D wave equation, with source term (1.2.5)

$$\partial_{xx}V(x,t) - \frac{1}{v^2}\partial_{tt}V(x,t) = l\partial_{tt}\left\langle\hat{\vartheta}\right\rangle\delta(x), \tag{1.2.6}$$

and is shown in A.3.6 to have a solution $V(x,t) = V_{\mathrm{sc}}(x,t) + V_{\mathrm{mw}}(x,t)$, where $V_{\mathrm{mw}}(x,t)$ is exactly the driving term (1.2.1), while

$$V_{\mathrm{sc}}(x,t) = il\frac{\omega^2\vartheta}{k}\left\langle\sigma_-\right\rangle e^{ik|x|-\omega t}, \tag{1.2.7}$$

is the particular solution determined by the dipole source. Introducing the relaxation rate of the atom into the TL due to voltage noise (refer to A.3.5)

$$\Gamma_1(\omega_q) = \frac{\vartheta^2\omega_q Z_0}{\hbar}, \tag{1.2.8}$$

with an industry standard microwave line impedance $Z_0 = 50\,\Omega$. (1.2.7) can then be rewritten in the following form[2]

$$V_{\mathrm{sc}}(x,t) = i\frac{\hbar\Gamma_1}{\vartheta}\left\langle\sigma_-\right\rangle e^{ik|x|-i\omega t}. \tag{1.2.9}$$

This scattering is coherent or Rayleigh scattering, occurring at the frequency of the driving field, and one can understand this as the locking of the emission field to the driving field through an intermediate qubit. It is proportional to $\langle\sigma_-\rangle$, which is projection of the 2-level state onto the equatorial plane of the Bloch sphere (refer to A.2.5.1) and thus an indication of the superposition state of the atom.

1.2.3 Emission spectrum

The scattered voltage (1.2.9) gives rise to a power spectrum of the atom's spontaneous emission (refer to A.8.2)

$$\begin{aligned} S(\omega) &= \frac{1}{Z_0}\int_{-\infty}^{\infty} d\tau\left[\langle V_{\mathrm{sc}}(\tau)V_{\mathrm{sc}}^*(0)\rangle_{ss}\, e^{-i\omega\tau}\right] \\ &= \hbar\omega\Gamma_1\int_{-\infty}^{\infty} d\tau\left[\langle\sigma_-(\tau)\,\sigma_+(0)\rangle_{ss}\, e^{-i\omega\tau}\right], \end{aligned} \tag{1.2.10}$$

where ss denotes the stationary state $\langle\sigma_-(\tau)\,\sigma_+(0)\rangle_{ss} = \lim_{t\to\infty}\langle\sigma_-(\tau)\sigma_+(0)\rangle$. Evaluation of these terms is involved and [88] or [95] shows how it can be decomposed into coherent and incoherent components (refer to A.3.7)

$$S(\omega) = S_{\mathrm{coh}}(\omega) + S_{\mathrm{inc}}(\omega),$$

by presenting $\sigma_i(t) = \langle\sigma_i\rangle_{ss} + \Delta\sigma_i(t)$ as a steady state mean value with random fluctuations.

---

[2] Direct substitution $il\frac{\omega^2\vartheta}{k} = il\Gamma_1\frac{\hbar\omega}{\vartheta k Z_0} = il\frac{\hbar\Gamma_1}{\vartheta}\frac{v}{Z_0} = i\frac{\hbar\Gamma_1}{\vartheta}\frac{l/\sqrt{lc}}{\sqrt{l/c}} = i\frac{\hbar\Gamma_1}{\vartheta}$.

The steady state value $\langle\sigma_i\rangle_{ss}$ is completely specified by the driving field, maintains a constant value and results in coherent emission at the frequency of the drive

$$\begin{aligned} S_{\text{coh}}(\omega) &= \hbar\omega\Gamma_1 \int_{-\infty}^{\infty} d\tau \left[e^{i(\omega-\omega_q)\tau} \langle\sigma_-\rangle_{ss} \langle\sigma_+\rangle_{ss} \right] \\ &= \hbar\omega\Gamma_1 \frac{1}{2}\frac{\Upsilon^2}{(1+\Upsilon^2)^2}\delta(\omega-\omega_q), \end{aligned} \tag{1.2.11}$$

where $\Upsilon = \sqrt{2}\Omega/\Gamma_1$.

On the other hand, fluctuations $\Delta\sigma_i(t)$ are present even in the absence of a drive ($\Omega = 0$) due to the relaxation processes $\sim \Gamma_1$

$$\begin{aligned} S_{\text{inc}}(\omega) &= \hbar\omega\Gamma_1 \int_{-\infty}^{\infty} d\tau \left[e^{i(\omega-\omega_q)\tau} \langle\Delta\sigma_-(\tau)\Delta\sigma_+(0)\rangle_{ss} \right] \\ &= \hbar\omega\Gamma_1 \int_{-\infty}^{\infty} d\tau\, e^{i(\omega-\omega_q)\tau} \\ &\qquad \frac{1}{4}\frac{\Upsilon^2}{1+\Upsilon^2} e^{-\Gamma_1\tau/2} \\ &\qquad -\frac{1}{8}\frac{\Upsilon^2}{(1+\Upsilon^2)^2}\left(1-\Upsilon^2+(1-5\Upsilon^2)\frac{\Gamma_1/4}{\delta}\right) e^{-(\frac{3\Gamma_1}{4}-\delta)\tau} \\ &\qquad -\frac{1}{8}\frac{\Upsilon^2}{(1+\Upsilon^2)^2}\left(1-\Upsilon^2+(1-5\Upsilon^2)\frac{\Gamma_1/4}{\delta}\right) e^{-(\frac{3\Gamma_1}{4}+\delta)\tau} \end{aligned} \tag{1.2.12}$$

where $\delta = \sqrt{(\Gamma_1/4)^2 - \Omega^2}$. (1.2.12) contains three Fourier transforms (FTs), which can be transformed into three Lorentzians by simple parameter substitution (refer to A.3.7.1). Under a strong drive ($\Omega \gg \Gamma_1$ stronger than the relaxation rate of the atom) $\delta \approx i\Omega$ is an imaginary number, resulting in a shift of the Lorentzian peaks to the sides in an effect known as the Mollow triplet [96] demonstrated in Fig. 1.7:

- The central peak has width $\Gamma/2$;
- Side peaks have width $3\Gamma/4$.

For a final evaluation of the total powers, (1.2.10) is integrated over the full frequency spectrum (thereby almost reverting the FT see A.8.1)

$$\begin{aligned} P_{\text{total}} &= \int_{-\infty}^{\infty} \frac{d\omega}{2\pi}\, S(\omega) \\ &= \hbar\omega\Gamma_1 \int_{-\infty}^{\infty} \frac{d\omega}{2\pi} \int_{-\infty}^{\infty} d\tau \left[\langle\sigma_-(\tau)\sigma_+(0)\rangle_{ss}\, e^{i\omega\tau} \right] \\ &= \hbar\omega\Gamma_1 \frac{1-\langle\sigma_z\rangle_{ss}}{2} \underbrace{\int \frac{1}{2\pi} \int e^{i\omega\tau}\, d\tau d\omega}_{=1} \\ &= \hbar\omega\Gamma_1 \frac{1-\langle\sigma_z\rangle_{ss}}{2} \end{aligned} \tag{1.2.13}$$

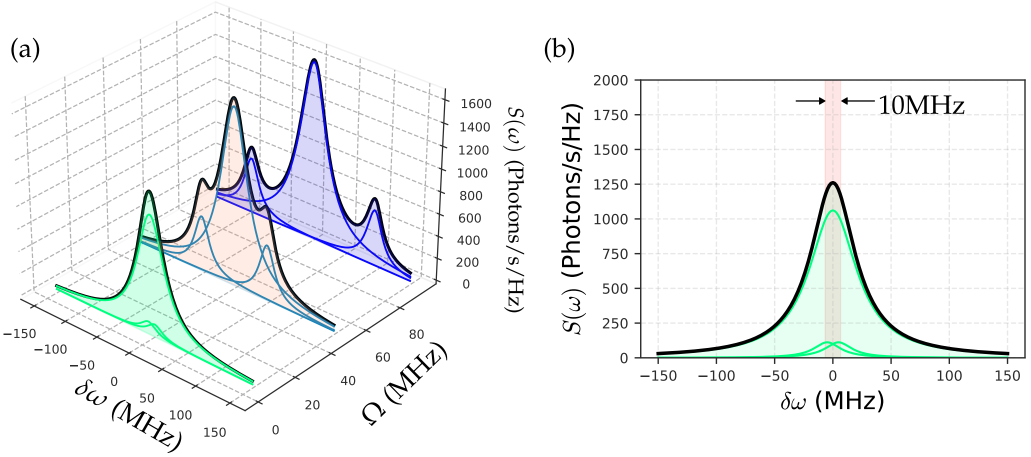

Figure 1.7: **(Left)** Simulation of incoherent scattering components of (1.2.12), showing the growth of side peaks under stronger drives. Black lines are the total power from all 3 *peaks*; **(Right)** Comparison of emission spectra of coherent (red) and incoherent (green) emission under a weak drive. Coherent power (1.2.11) is artificially spread over a 10 MHz bandwidth of an imaginary device taking the spectra. Even with such a bandwidth, incoherent emission is much stronger at resonance (which would be measured experimentally on a finite-bandwidth Vector Network Analyser (VNA). All simulations performed with $\Gamma_1 = 5\,\text{MHz}, \omega_q = 10\,\text{GHz}$.

where the identity $\langle\sigma_-(\tau)\sigma_+(0)\rangle = (1 - \langle\sigma_z(\tau)\rangle)/2$ is used [88] and likewise for (1.2.11)

$$\begin{aligned} P_{\text{coherent}} &= \int_{-\infty}^{\infty} d\omega\ S_{\text{coh}}(\omega) \\ &= \hbar\omega\Gamma_1 \langle\sigma_-\rangle_{ss} \langle\sigma_+\rangle_{ss}\,. \end{aligned} \tag{1.2.14}$$

Summarising the final results with reference to Fig. 1.8:

- **Total power** $\propto (1 - \langle\sigma_z\rangle_{ss})/2$ is proportional to the excited state population. It is split between coherent and incoherent emission;

- **Coherent emission (Rayleigh scattering)** $\propto \langle\sigma_+\rangle_{ss}\langle\sigma_-\rangle_{ss}$ occurs at the frequency of the driving field and is associated with the transmon state in the equatorial plane, $\langle\sigma_\pm\rangle = (\langle\sigma_x\rangle \mp i\langle\sigma_y\rangle)/2$ (refer to A.2.5),

  $$P_{\text{coherent}} = \hbar\omega_q\Gamma_1 \langle\sigma_+\rangle_{ss}\langle\sigma_-\rangle_{ss} \qquad \Rightarrow \qquad P^{\text{Max}}_{\text{coherent}} = \frac{\hbar\omega_q\Gamma_1}{8}. \tag{1.2.15}$$

  The phase of the driving field is mapped onto an angle φ in the equatorial plane (see Fig. 1.8) which evolves deterministically and scatters a phase-locked voltage

  $$V_{\text{coherent}}(t) = |V_{\text{coherent}}(t)|\,e^{i\varphi(t)}.$$

  The atom absorbs a photon and reemits it as the same frequency - a consequence of conservation of energy. It is usually ultra narrow, and in experiments its measured bandwidth will be limited by the resolution of the measuring device.

- **Incoherent emission (Raman scattering)** $\propto (1-\langle\sigma_z\rangle_{ss})/2 - \langle\sigma_+\rangle_{ss}\langle\sigma_-\rangle_{ss}$ is associated with the relaxation of the qubit, $|1\rangle \to |0\rangle$ and for a weak drive has a Lorentzian-like spectrum (refer to A.3.7.1)

$$S(\omega) = \hbar\omega\Gamma_1 \frac{1}{4}\frac{\Upsilon^2}{1+\Upsilon^2}\frac{\Gamma/2}{(\Gamma/2)^2+\delta\omega^2} \tag{1.2.16}$$

with a Full width at half maximum (FWHM) of $\Delta\omega = \Gamma_1/2$, typically on the order of a few MHz. The power emitted as incoherent radiation is the total power (1.2.14) minus the power that is emitted as coherent radiation (1.2.15)

$$P_{\text{incoherent}} = \hbar\omega_q\Gamma_1\Big(\frac{1-\langle\sigma_z\rangle}{2} - \langle\sigma^+\rangle\langle\sigma^-\rangle\Big) \quad \Rightarrow \quad P^{\text{Max}}_{\text{incoherent}} = \frac{\hbar\omega_q\Gamma_1}{2}. \tag{1.2.17}$$

With no projection onto the equatorial plane ($\langle\sigma_x\rangle$ and $\langle\sigma_y\rangle$ components), phase coherence with the driving field is lost in the scattered voltage.

$$V_{\text{incoherent}}(t) = |V_{\text{incoherent}}(t)|\, e^{i\varphi_{\text{random}}}.$$

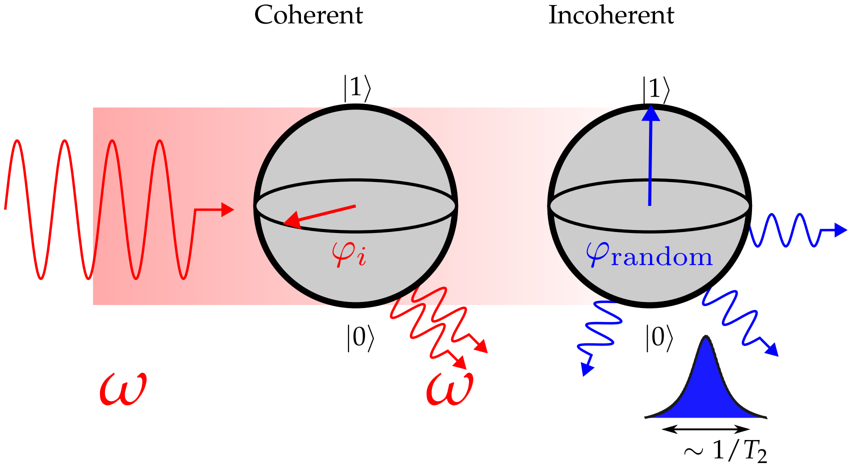

Figure 1.8: **(Left)** A driving field ω will stimulate re-emission at the same frequency, for the *components* of the qubit in the equatorial plane during steady stage driving. Phase evolution is deterministic and governed by the Bloch equations (see A.2.5); **(Right)** Under the presence of dissipation, there will be tendency of the qubit to undergo fluctuations, which add a frequency uncertainty to the emission spectrum, on the rate of $\sim 1/T_2$. Maximal incoherent emission will occur when the qubit has no projection onto the equatorial plane and $\langle\sigma_-\rangle = 0$, which will occur once during a driving cycle (see Fig. A.4 (b)).

1.2.4 Qubit evolution

Having considered the scattering and emission features in Sec. 1.2, here analysis is extended to a system under external drive that will determine expectation values such as $\langle \sigma_z \rangle, \langle \sigma_- \rangle$ by combining Hamiltonians from (1.1.4) and (1.2.2) into a full description

$$H = H_q + H_{\text{mw}} = -\frac{\hbar\omega_q}{2}\sigma_z + \hbar\Omega\cos(\omega t)\,\sigma_x.$$

Applying a convenient unitary transformation that preserves expectation values and a Rotating wave approximation (RWA) that ignores energy-non-conserving processes (refer to A.2.4)

$$H = \frac{\hbar}{2}\begin{pmatrix} -\delta\omega & \Omega \\ \Omega & \delta\omega \end{pmatrix},$$

where $\delta\omega = \omega - \omega_q$. Combined with the von-Neumann equation for the evolution of the system's state in the density matrix formalism (A.7.10) and representing dissipation and decoherence processes through the Linbland operator (refer to A.7.3 and Sec. 1.3)

$$\partial_t \rho = -\frac{i}{\hbar}[H,\rho] + \mathcal{L}(\rho), \qquad \mathcal{L}(\rho) = \begin{pmatrix} \Gamma_1\rho_{11} & -\Gamma_2\rho_{01} \\ \Gamma_2\rho_{10} & -\Gamma_1\rho_{11} \end{pmatrix},$$

one has a system of equations to solve for the density matrix components $\rho_{00}, \rho_{01}, \rho_{10}, \rho_{11}$. This can be done analytically[3] for the stationary state, by setting $\partial_t\rho = 0$ and requiring that ρ describes a physical state $\rho_{ij} = \rho_{ji}$ and $\rho_{11} = 1 - \rho_{00}$ (since $\mathrm{Tr}\{\rho\} = 1$, see A.7.3). The solution found using the same approach as shown in A.6.4, is a general result that can be applied to any driven 2-level system

$$\rho = \begin{pmatrix} 1 - \frac{\Gamma_2\Omega^2}{2\left(\Gamma_1\left(\Gamma_2^2+\delta\omega^2\right)+\Gamma_2\Omega^2\right)} & \frac{\Gamma_1\Omega(\delta\omega+i\Gamma_2)}{2\left(\Gamma_1\left(\Gamma_2^2+\delta\omega^2\right)+\Gamma_2\Omega^2\right)} \\ \frac{\Gamma_1\Omega(\delta\omega-i\Gamma_2)}{2\left(\Gamma_1\left(\Gamma_2^2+\delta\omega^2\right)+\Gamma_2\Omega^2\right)} & \frac{\Gamma_2\Omega^2}{2\Gamma_1\left(\Gamma_2^2+\delta\omega^2\right)+\Gamma_2\Omega^2} \end{pmatrix}.$$

This equation allows evaluation of the expectation values of the relaxation operator, already seen in Sec. 1.2.2.

$$\langle \sigma_- \rangle = \mathrm{Tr}\{\sigma_-\rho\} = \rho_{01} = \frac{\Omega}{2\Gamma_2}\frac{i + \delta\omega/\Gamma_2}{1 + (\delta\omega/\Gamma_2)^2 + \Omega^2/\Gamma_1\Gamma_2}.$$

Taking the ratio of the incident field V_{mw} and the scattered field V_{sc} (1.2.9) (see Fig. 1.6)

$$t = 1 - r = 1 - \frac{V_{\text{sc}}}{V_{\text{mw}}} = 1 - r_0\frac{1 + i\delta\omega/\Gamma_2}{1 + (\delta\omega/\Gamma_2)^2 + \Omega^2/\Gamma_1\Gamma_2}, \tag{1.2.18}$$

gives the analytical expression for the complex transmission ratio. As a reminder:

---

[3] Numerically it can be done with a library such as Qutip [97].

- $\delta\omega$ is the detuning of the drive from the qubit's resonance;
- Ω is the strength of the drive quantifed by (1.2.4);
- Γ_1 is the depolarisation rate from the qubit to the TL quantified by (1.2.8) and motivated in Sec. 1.3;
- $\Gamma_2 = \Gamma_1/2 + \Gamma_\varphi$ is the total dephasing rate, bounded by the relaxation rate (Γ_1) and any additional pure dephasing (Γ_φ) in the system (refer to Sec. 1.3);
- $r_0 = \Gamma_1/2\Gamma_2$ is an effective reflection coefficient, which sometimes has a prefactor η quantifying non-radiative emission.

A convenient measure of how strongly the qubit interacts with the drive is the power extinction caused by the destructive interference of V_{mw} and V_{sc} in the output line, and at exact resonance ($\delta\omega = 0$) it reads

$$1 - |t|^2 = \frac{\Gamma_1^2}{2\Gamma_1\Gamma_2 + 2\Omega^2}.$$

It will approach 100% for strong interaction, and is maximised in the absence of pure dephasing when $\Gamma_2 = \Gamma_1/2$.

1.3 Noise and decoherence

The qubit systems described in Sec. 1.1 expose two degrees of freedom ($N_{\text{ext}}, \Phi_{\text{ext}}$) for external control. But these degrees of freedom also open up the system to charge and flux noise in the environment. Such noise can arise from microscopic charge Two level systems (TLS), moving vortices, magnetic field fluctuations, quasiparticle poisoning, macroscopic circuit interference, and it will interfere with the analytical evolution of the quantum state. This phenomenon is called decoherence and is quantified by coherence rates ($\Gamma_1 = T_1^{-1}, \Gamma_2 = T_2^{-1}$) that have already made their appearance in the text.

The amount of literature dedicated to the study of noise in superconducting systems goes far beyond the scope of this work. Summarised below are the main concepts [98] and sources of noise and what affect they have on superconducting qubits. This knowledge will be relevant in the design, fabrication, and measurement preparation of the quantum circuits.

1.3.1 Characterising noise

In general a noise source is quantified by its operator $\hat{\lambda}$ that can couple to the system either longitudinally

$$\hat{\lambda} \propto \sigma_z,$$

an example would be coupling to the CP number operator ($\hat{N}$) of a charge qubit, or traversaly

$$\hat{\lambda} \propto \sigma_{x,y}$$

an example would be the coupling to a transition operator (σ_-). Its spectral density (refer to A.8.2)

$$S_\lambda(\omega) = \int dt \left\langle \hat{\lambda}(0)\hat{\lambda}(t) \right\rangle e^{-i\omega t},$$

quantifies a noise sources tendency to absorb ($\omega > 0$) and emit ($\omega < 0$) energy quanta with respect to qubit. For example, noise with no correlation ($\left\langle \hat{\lambda}(t)\hat{\lambda}(0) \right\rangle = \delta(t)$) produces a uniform spectrum at all frequencies.

1.3.2 Types of decoherence

Noise gives rise to the following types of types of decoherence:

- **Depolarisation** is quantified by a rate $\Gamma_1 = T_1^{-1}$ describing the tendency of system to relax to the ground energy state. The rate is given by Fermi's golden rule for a transition[4] (A.3.40)

$$\Gamma_1 = \frac{1}{\hbar^2}\left|\langle g|\,\frac{\partial H}{\partial\hat{\lambda}}\,|e\rangle\right|^2 S_\lambda(\omega_q).$$

This rate depends on noise that couples traversaly and promotes an energy exchange (σ_x for a qubit system or $a + a^\dagger$ for a resonator[5]). Also, the rate is determined by the power spectral density at the qubit frequency $S_\lambda(+\omega_q)$, meaning it is noise close to the qubit frequency that contributes the most to this mechanism. For multiple decay mechanism the rates add up ($\Gamma_1 = \sum_i \Gamma_1^i$).

- **Pure Dephasing** is quantified by a rate Γ_φ and describes the gradual quantum phase loss due to stochastic unitary evolution. A noise source that couples linearly (σ_z in a qubit, or $a^\dagger a$ in resonator) has the effect of temporaly varying its transition energy by $\delta E = \hbar\delta\omega(t)$ resulting in unitary evolution of the form

$$U(t) = \exp\left[i\hbar\left(\frac{1}{2}\omega_q\sigma_z + \delta\omega(t)\sigma_z\right)\right] = U_0(t)e^{i\delta\varphi(t)}, \quad \delta\varphi(t) = \frac{1}{\hbar}\int_0^t d\tau\delta E(\tau). \tag{1.3.1}$$

Over a characteristic time period T_φ this random phase accumulation will result in the gradual loss of phase information producing some form of decay $\left\langle e^{i\delta\varphi(t)}\right\rangle \sim e^{-t\Gamma_\varphi} \sim e^{-t^2\Gamma_\varphi^2}$ where the specifics will depend on the spectral density of the noise source ($S(\omega)$) discussed below. Unlike depolarisation, dephasing is a non-dissipative process with no energy exchange with the environment.

Any change to the qubit's energy will bring about dephasing, and thus noise at all frequencies will contribute - broadband noise. When the spectral density in a quantum system is measured, it is universally found that the level of noise increases with decreasing frequency

$$S(\omega) \propto 1/\omega^\alpha, \quad \alpha \sim 1, \tag{1.3.2}$$

irrespective of the system being observed, be it flux and charge qubits, JJs, superconductors, bulk metals or semiconductors. This noise is known to be a persistent problem in quantum measurements as it is hard to filter out with band filters because of its low frequency. Furthermore, the sources may not have time to relax to the ground state between successive measurements.

It remains an unsolved problem to provide a theory explaining the universal shape of (1.3.2). It has been attributed to supercurrent fluctuations [99], excess charge, and phase flipping due to interactions with TLS and phonons [100, 101], jumping of charges between localised normal metal states and superconductor [102], adsorbed molecular Oxygen (O_2) [103]. But on the assumption that each noise is Gaussian and ensemble averaging over all of the noise sources [104] it is shown in A.2.7 that

---

[4] In fact (1.2.8) arises directly from this with a noise spectral density $S(\omega) = 2Z_0\hbar\omega$.

[5] Otherwise the $\langle g|\,\frac{\partial H}{\partial\hat{\lambda}}\,|e\rangle$ term would evaluate to zero.

$$\left\langle e^{i\delta\varphi(t)}\right\rangle = \exp\left(-\Gamma_\varphi^2 t^2\right), \qquad \Gamma_\varphi^2 = \frac{S_{EE}(\omega=0)}{2\hbar^2}, \tag{1.3.3}$$

leads to a decay, whose rate depends on the system's energy fluctuations from noise source low frequencies $S_{EE}(0 \ll \omega_q)$ [99, 63].

- **Dephasing** is quantified by the rate $\Gamma_2 = T_2^{-1}$ and represents the effect of all decoherence processes on the phase of the qubit. It is commonly used as an indicator of the time scale over which a superconducting qubit remains viable for quantum information.

In addition to the loss of phase coherence by pure dephasing, depolarisation also wipes away phase information (refer to A.2.5), since information about the qubits orientation in the x-y plane is lost. The effect of both is most accurately felt by the effect on the off diagonal components of the density matrix

$$\langle\sigma_x\rangle = e^{-t\Gamma_1}e^{-t^2\Gamma_\varphi^2},$$

which can be approximated if $\Gamma_1 \gg \Gamma_\varphi$ [98, 105]

$$\langle\sigma_x\rangle = e^{-t\Gamma_2}, \qquad \Gamma_2 \sim \frac{1}{2}\Gamma_1 + \Gamma_\varphi. \tag{1.3.4}$$

At the optimal working point where the qubit is least sensitive to fluctuations of the control parameters[6], the low frequency noise vanishes to first order [106, 107], setting $\Gamma_\varphi = 0$. This gives a formal argument of why qubit manipulations should be done in that regime.

There are a number of experiments that can approximate the dephasing time T_2:

$$T_2^* < T_{2\text{E}} \sim T_{2\text{R}}, \tag{1.3.5}$$

related to Ramsay (T_2^*) measurements [98] , echo ($T_{2\text{E}}$) and driven measurement ($T_{2\text{R}}$) [108]. Ramsay measurements are sensitive to 1/f noise, which can be mitigated in echo measurements by reversing evolution and refocusing coherent dephasing errors, meaning $T_{2E} > T_2^*$. Driven evolution will generally produce a longer decay time $T_{2\mathrm{R}} > T_2^*$, due to better quantum coherence in the oscillating basis [98].

---

[6] For example for a transmon at the working point $dE/d\Phi_{\text{ext}} = 0$.

1.3.3 Sources of noise

There are a number of noise sources that contribute longitudinally and traversaly to decoherence. Microscopic TLS account for the majority of the noise sources. They are systems that can be represented by two local minima at bias ε separated by energy barrier Δ coupling the two states

$$H_{\mathrm{TLS}} = -\frac{\varepsilon}{2}\sigma_z - \frac{\Delta}{2}\sigma_x,$$

and thus can be described in the same way as qubits, with hybridised levels of energy $\sqrt{\varepsilon^2 + \Delta^2}$ (refer to (1.1.3)). Their states transition correspond to a fluctuation of a physical quantity such as charge, current or spin, which can contribute to both types of decoherence:

- Assuming a log-uniform distribution of the tunnel splitting (density $\propto 1/\Delta$), or that hopping times are distributed in an exponentially broad domain, it has been shown that a bath of TLS produce 1/f noise [101, 102, 109] and hence contribute to pure dephasing (1.3.3);
- At higher frequencies TLS couple traversaly to the qubit by interacting with its electromagnetic field [110] across elements such as the JJ or capacitors. Any losses the TLS experiences in the process, such as phonon emission, lead to a loss of quantum information from the system through depolarisation (relaxation), and hence T_1 is affected [111, 112].

A non-exhaustive list of common sources of noise in superconducting circuits.

- **Charge noise** (impacts Γ_1, Γ_φ) is predominantly a TLS phenomenon attributed to the hopping of electrons between localised traps [92]. It can couple both traversaly and longitudinally [113, 114], and is considered the most dominant source of decoherence;
- **Amorphous materials** (host TLS) in the substrate [115], oxide layers [116, 117, 118] and JJs themselves [119]. The TLS can be in the form of dangling OH bonds [120], remnants of resist, absorbents, film stress, unpassivated surfaces or inadvertently grown structures during nanofabrication [120]. These dielectric materials dissipate electromagnetic energy and contribute directly to relaxation events [121];
- **Critical current** (impacts Γ_φ caused by TLS) inside a JJ the TLS are exposed to high electric fields and can couple strongly with the qubit [112, 122]. While this does not

necessarily cause decoherence, their switching between two states opens and closes transport channels for CPs which impacts the critical current hence the energy of the qubit, leading to dephasing [111, 123, 124]. In a typical JJ a couple of such fluctuators are present [125];

- **Shot noise** (impacts Γ_φ) exists due to discrete charges causing pulses of current and has a characteristic 1/f spectrum [102, 126];
- **Magnetic flux noise** (impacts Γ_φ) has been measured to contribute as 1/f noise and scale linearly with device dimensions [112]. It can be caused by hopping of surface spins [102, 121], adsorbed molecular O_2 [103], jumping of electrons with different spin orientations [92], spin fluctuations in magnetic defects [127]. Generally the spectral density of flux noise $S_{\Phi\Phi} = (10^{-6}\Phi_0)^2/f$ [103, 128] is much weaker than the spectral density for charge $S_{QQ} = (10^{-4}e)^2/f$ for charge noise [129], making it a secondary concern when looking to improve qubit coherence;
- **Quasiparticles** (impact Γ_1) are free electrons appearing from the break up CP by infrared light that enters the experimental system. They lead directly to relaxation [130] and are usually addressed with shielding [131] or using normal metal to trap quasiparticles in a potential well away from the superconducting circuit [132].

1.4 Design

The design of a photon source based on the transmon qubit described in Sec. 1.1.3 takes the following constraints:

- Energies of the system should be within the 2-12 GHz range of the laboratory microwave equipment, which is discussed in more detail in Sec. 1.6.1;
- The lithographical procedure (refer to B.1) cannot reliably make JJ smaller than $100 \times 100\,\mathrm{nm}^2$;
- Al structures defining the transmon and readout circuit, will expel magnetic field once they become superconducting at $T < 1.4\,\mathrm{K}$, and should have perforation to avoid the formation of randomised flux vortices;
- The microwave TL on the chip must match the standard $Z_0 = 50\,\Omega$ impedance of the TLs and to avoid reflections (refer to A.3.3).

1.4.1 Operating energies

Putting the corresponding variables into the TLS Hamiltonian (1.1.4) gives transition energies $\hbar\omega_q = \Delta E = \sqrt{(E_C/2)^2 + E_J(\Phi)^2}$ that are evaluated for different E_C and E_{J0} to find the combinations compatible with the 2-12 GHz frequency window of the measurement equipment, shown as the red region in Fig. 1.9. To satisfy the anharmonicity condition, Fig. 1.5 indicates that work should be done in the $E_{J0}/E_C < 100$ regime. Given the variability of E_{J0} values in the fabrication process, the targeted energies were $E_C/\hbar = 0.2\,\mathrm{GHz}$ and $E_{J0}/\hbar = 30\,\mathrm{GHz}$ to be in the middle of the frequency window.

1.4.1.1 Realising the charging energy

The charging energy ($E_C = e^2/2C_\Sigma$) is determined by the two parallel capacitors isolating the island (see Fig. 1.2 (c))

$$C_\Sigma = C_\mathrm{s} + C_\text{q-t}.$$

The shunting capacitor (C_s) is realised by an interdigitated structure (see Fig. 1.10) with capacitance

$$C_s = c \times N \times (W + L)\,,$$

where $c = 0.85 \times 10^{-10}\,\mathrm{F/m}$ is the capacitance per unit length of coplanar structures of Silicon (Si) (refer to B.3), N is the number of *fingers* and W, L are their dimensions.

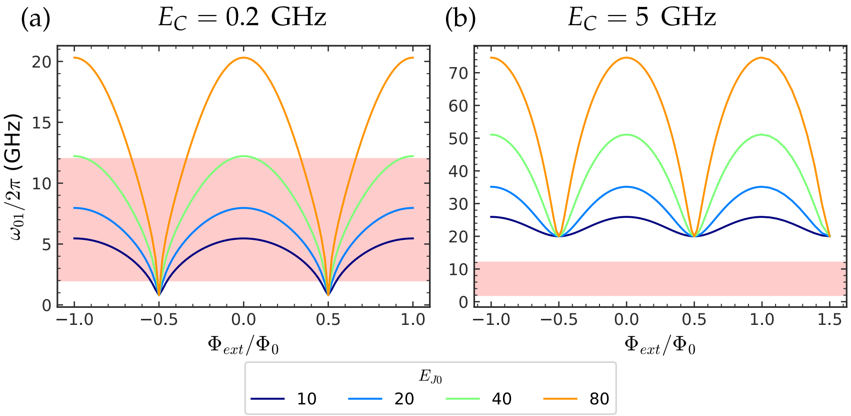

Figure 1.9: Simulation of transition energies allows assessment of the size of the shunt capacitor and size of JJ to fall within the 2-12 GHz frequency range of laboratory equipment. **(a)** Simulation for $E_C/\hbar = 0.2$ GHz; **(b)** Simulation for $E_C/\hbar = 5$ GHz.

Likewise, the contribution from the coupling capacitor

$$C_{\text{q-t}} = c \times L_{\text{q-t}},$$

depends on its interface length ($L_{\text{q-t}}$). It is going to be much smaller than C_s and so will not be considered.

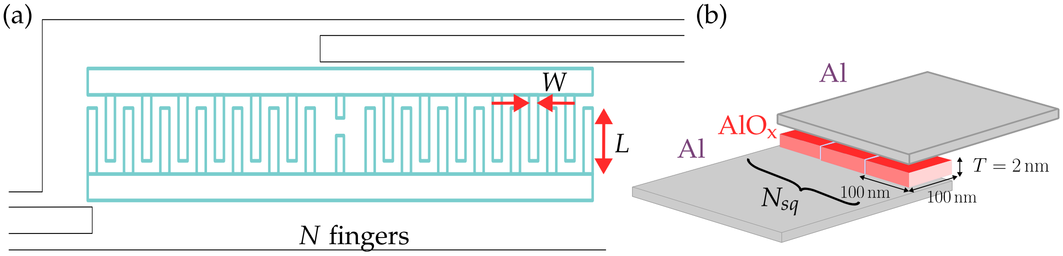

Figure 1.10: **(a)** Geometry of an interdigitated capacitor, of N fingers each with dimensions $W \times L$; **(b)** Geometry of the JJ, where the defining feature is the size of the Aluminum Oxide (AlO$_x$) *overlap* between the bulk superconductors.

1.4.1.2 Realising the Josephson energy

The energy of a JJ ($E_{J0} = \Phi_0 I_c/2\pi$) is determined by its critical current (I_c) which is derived from Bardeen-Cooper-Schrieffer theory (BCS) Ambegaokar-Baratoff formula [133] (refer to A.1.5)

$$I_c R_n = \frac{\pi\Delta(T)}{2e} \tanh\left(\frac{\Delta(T)}{2k_b T}\right),$$

for a superconducting energy gap of $\Delta(T)$ and normal resistance R_n of the JJ. In the limit

$T \to 0$ this reads $I_c R_n = \frac{\pi\Delta(0)}{2e}$ so that

$$E_{J0} = \Phi_0 I_c \frac{1}{2\pi} = \frac{h}{2e}\frac{\pi\Delta(0)}{2eR_n}\frac{1}{2\pi} = \frac{R_q}{R_\square/N_{\rm sq}}\frac{\Delta(0)}{2}, \tag{1.4.1}$$

which scales linearly with the amount of $N_{\rm sq}$ squares on the JJ interface (see Fig. 1.10). Here $R_q = h/4e^2 = 6.484\,\mathrm{k\Omega}$, $\Delta = 3.1 \times 10^{-23}\,\mathrm{J}$ is the superconducting energy gap for Al and $R_\square$ is the sheet resistance of the Al-AlO$_{\rm x}$-Al layer which depends on the oxidation conditions under which the oxide layer AlO$_{\rm x}$ is formed (see Tab. 1.2).

It is inevitable that the JJs produced in the DC-SQUID loop (see Fig. 1.2 (d)) will have a degree of asymmetry, leading to a more complex form of the effective Josephson energy (A.1.20). Taking an expected 5% asymmetry, it is found that this shifts the transition energy by few hundred MHz (see Fig. 1.11), but has no effect on the periodicity. It does however causes an increase in flux sensitivity, which can be ignored to first order when working at degeneracy points.

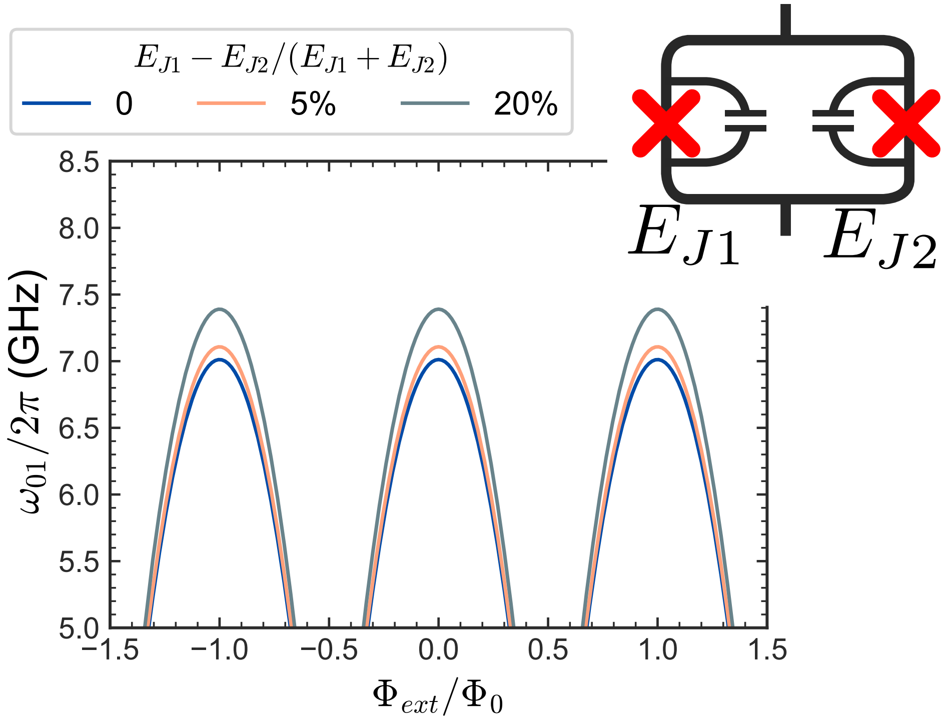

Figure 1.11: Effect of asymmetry between the JJs, making up the flux-tuneable DC-SQUID (inset), on the ω_{01} transition energy.

1.4.2 Transmission line design

The dimensions of the TL need to be chosen to match the impedance $Z_0 = 50\,\Omega$ of the laboratory equipment and minimise the reflections occurring at their interface (refer to A.3.3). This can be simulated with extensive packages such as `Comsol`, but for the non-complex design an online tool [134] is used that takes the dimensions shown in Fig. 1.12 - Si wafer thickness $T_w \sim 20\,\mathrm{mm}$ and relative permittivity $\varepsilon_r = 11.7$ to evaluate the impedance using elliptical integrals [135]. This indicates that the TL must have a width $W_c = 20\,\mu\mathrm{m}$ and have a gap of $W_g = 12\,\mu\mathrm{m}$ with the ground planes.

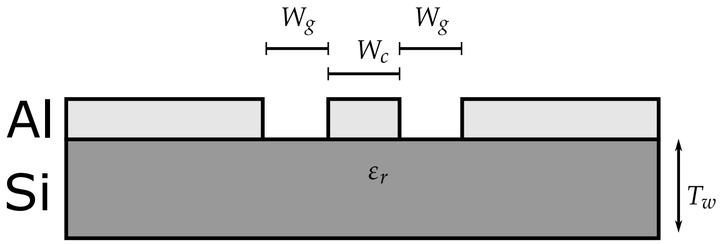

Figure 1.12: Geometrical parameters for the TL - in places where TL the broadens for the contact pads the impedance must also be matched [134].

1.4.3 Coupling to the transmission line

The photon relaxation rate to the output line must be much larger that any dephasing processes, since they cause the untraceable evolution of the off-diagonal elements of the density matrix (refer to A.2.5.4 and A.7.3), which affect the phase of the emitted photon [25]. Formally the design must achieve:

$$\Gamma_1 \gg \Gamma_\Phi.$$

for the photon be be released quicker than the atom has time to decohere. This is achieved by coupling the transmon strongly to the 1D continuum of the TL by using a large capacitor that maximises the dipole moment of the atom ϑ (1.2.3) and correspondingly the relaxation rate Γ_1 (1.2.8).

Separate controls and emission lines are used for driving the qubit and reading out photon signals respectively, as was done in [75, 84] to block the strong driving field from leaking into the readout line. Every $|1\rangle \rightarrow |0\rangle$ relaxation event will emit radiation into the control line (Γ_1^c) emission line (Γ_1^e) or via some other non-radiative (from the perspective of laboratory equipment) channel (Γ_1^n). To maximise the likelihood of emitting photons into the output line Γ_1^e must be dominant. Writing out the voltage scattering amplitude

(1.2.9) in a form that will expose the coupling capacitances $C_{\text{q-tc}}$ and $C_{\text{q-te}}$ of the control and emission lines with respectively

$$\begin{cases} x < 0: & V_{\text{q=tc}}(x,t) = il\frac{\omega^2}{k}C_{\text{q-tc}}V_{\text{qubit}}\left\langle\sigma^-\right\rangle e^{-ikx-i\omega t}, \\ x > 0: & V_{\text{q-te}}(x,t) = il\frac{\omega^2}{k}C_{\text{q-te}}V_{\text{qubit}}\left\langle\sigma^-\right\rangle e^{ikx-i\omega t}. \end{cases}$$

This implies a power distribution into the input and output lines proportional to the square of the capacitance ratio:

$$\text{Ratio} = \left|\frac{V_{\text{q-te}}(0,t)}{V_{\text{q-tc}}(0,t)}\right|^2 \approx \frac{C^2_{\text{q-te}}}{C^2_{\text{q-tc}}}.$$

This motivates a design in which the coupling of the qubit to the output line is significantly greater than coupling to the input line. A ratio of 60 was used, for $\geq 99\%$ emission to the output line (see the final design in Fig. 1.14).

1.4.4 Holes penetrating the ground planes

Al has a superconducting transition temperature of $T_c = 1.2\,\text{K}$ and enters a superconducting state in the 13 mK environment of the dilution refrigerator where the experiment is performed. Flux will be expelled from its interior, with a boosted magnetic field concentration at the edges as a consequence of the Meissner effect [136] (see Fig. 1.13 (a)). This field may be very large due to the sizes of the ground planes, and beyond a critical limit, it becomes energetically favourable for certain locations in the ground plane to go into normal state and thus allow the tunnelling of a single flux Φ_0 to form trapped vortices [137].

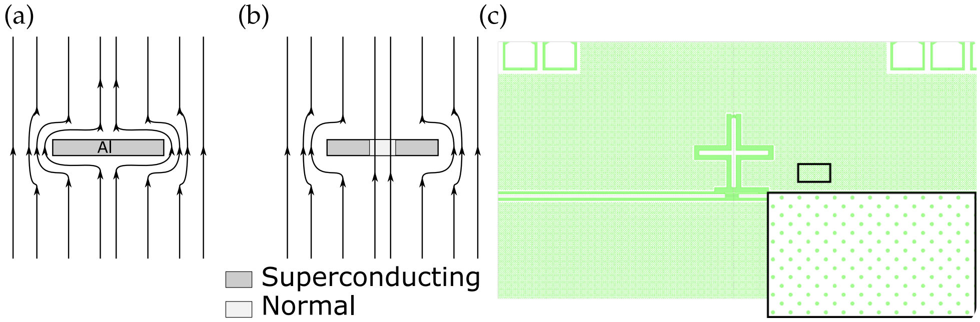

Figure 1.13: Cross section of a transmon device in a magnetic field: **(a)** Expulsion of magnetic field from bulk of superconductor; **(b)** It is energetically favourable for regions of Al to go to normal state, and pass through a unit of flux. This creates a flux vortex that will impact the magnetic environment of the surroundings; **(c)** Perforating the Al ground plan with holes, reduces the jumping of magnetic field.

This jumping of field in the environment of the qubit, leads to additional impracticality of measurements involving a change in magnetic field. By perforating the ground plane with additional holes, magnetic field concentrations such as this are prevented from building up (see Fig. 1.13 (b,c)).

1.4.5 Final design

The design shown in Fig. 1.14 features the parameters shown in Tab. 1.1. Included on the top of design are test structures - standalone JJ with large contact pads, that are used to test the Room temperature (RT) resistance and asses E_{J0} through (1.4.1).

Table 1.1: Summary design parameters for transmon photon source.

Design parameter	**Values**
ω_q	6.9 GHz
$E_{J0}/\hbar$	30 GHz
$E_C/\hbar$	0.154 GHz
Gap of CPW (W_g)	12 μm
Width of CPW (W_c)	20 μm
Input coupling (C_{q-tc})	4 μm
Output coupling (C_{q-te})	300 μm
Meanders	$N = 25$, $L = 40\,\mu\text{m} \times W = 10\,\mu\text{m}$
JJ	100 nm × 100 nm
Z_0	50 Ω

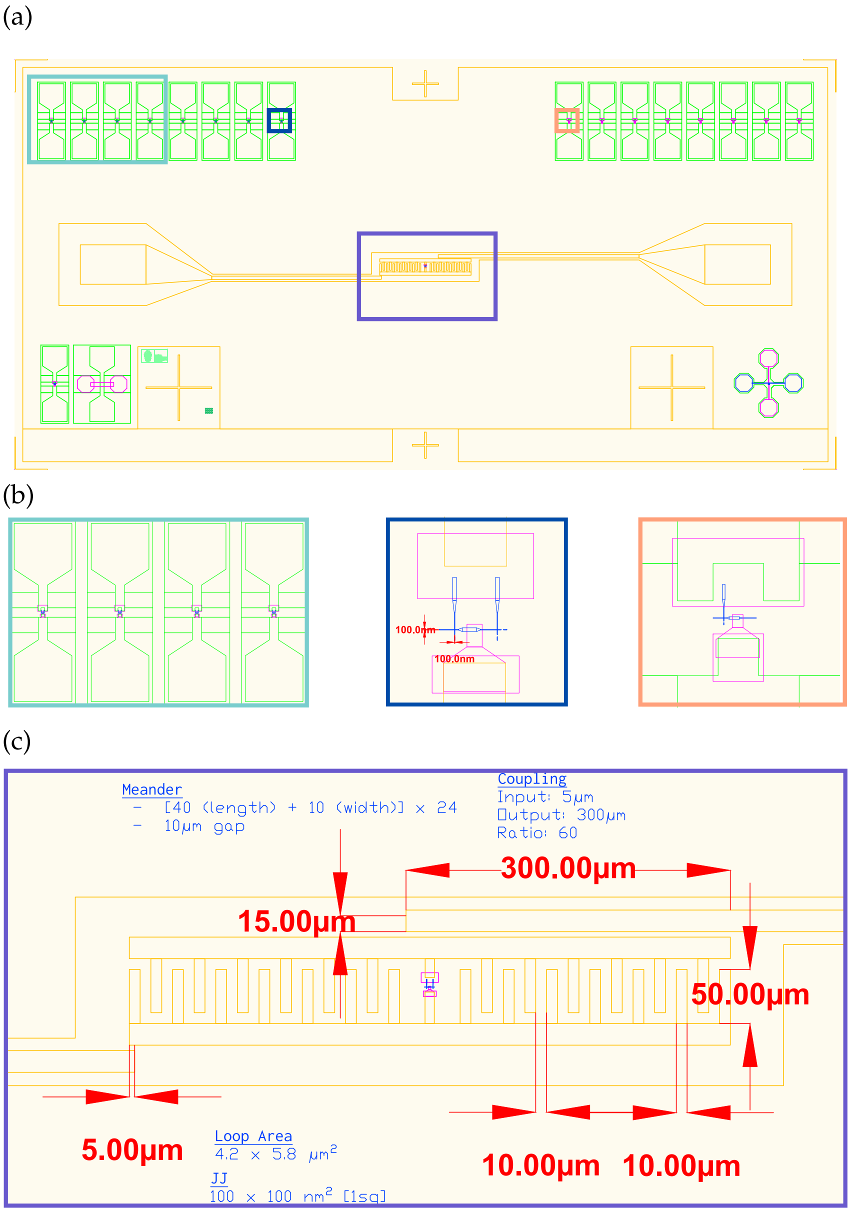
(a)
(b)
100.0nm
100.0nm
(c)
Meander
- [40 (length) + 10 (width)] x 24
- 10μm gap
Coupling
Input: 5μm
Output: 300μm
Ratio: 60
300.00μm
15.00μm
50.00μm
5.00μm
Loop Area
4.2 x 5.8 μm²
JJ
100 x 100 nm² [1sq]
10.00μm
10.00μm

Figure 1.14: **(a)** Complete chip design with photon source located in the opening between the ground planes. TLs lead from the transmon to large contact pads - they will be used to bond the chip to a Printed circuit board (PCB) that will connect to laboratory equipment; **(b)** Test samples were positioned on the top of the sample chips. The JJ geometry was identical to the one in the real structure. Large contact pads on the test samples allow one to monitor the RT $R_\square$ over the course of fabrication. **(c)** Close up of the photon source - note the asymmetric control and emission line couplings of length 5 μm ($C_{\text{q-tc}}$) and 300 μm ($C_{\text{q-te}}$).

1.5 Fabrication

The design from Sec. 1.4 is fabricated using multi-layer electron beam lithography, in which the sample chip is covered with resist, exposed with an electron beam that will harden or soften its polymer chains and developed to wash off shorter ones. This produces a mask through which material can be deposited or the underlying layers can be etched. Refer to B.1 for full detail of lithography techniques and B.4 for the detailed fabrication steps - what will follow is their summary.

1.5.1 Processing steps

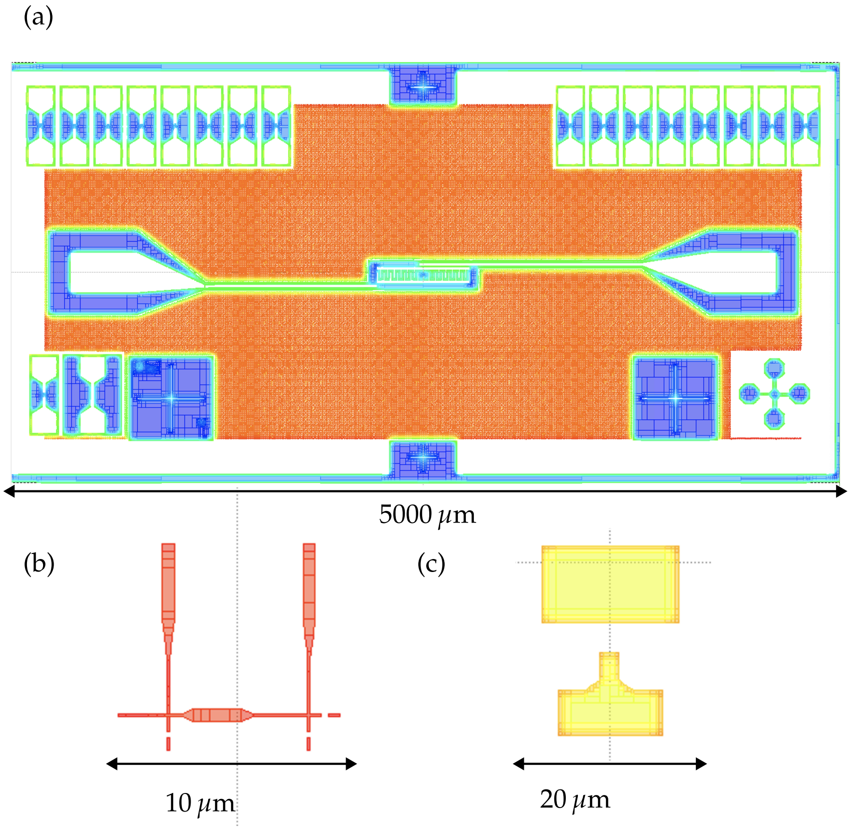

Figure 1.15: Colour coded proximity correction to the designed structures of Fig. 1.14: **(a)** Layer 1 - bulky structures with dose factor ranging from 0.74 (blue) to 1.5 (red); **(b)** Layer 2 - JJ have a very high relative dose due to the 100 nm dimensions where proximity correction applies an additional dose to compensate for the lower dwell time in that region; **(c)** Layer 3 - Patches clearly demonstrate additional dose applied to their edges compared to their bulk.

- **Proximity correction:** Each electron-beam pattern undergoes proximity correction in order to account for the finite width and backscattered electrons of the electron beam, which assigns different doses depending on the *bulkiness* of a feature (refer to B.1.3.2). These doses are colour coded in Fig. 1.15 for each of the design layers.

- **Wafer preparation:** Si is cleaned with Hydrogen fluoride (HF) before fabrication begins to etch away the top layer on Si, which contains TLS [138] (refer to Sec. 1.3.3). Immediately after, the cleaned wafer is loaded into an evaporator and pumped to vacuum to avoid reoxidation. 100 nm of Al is evaporated to fully cover the surface in preparation for the next step.

- **Layer 1:** The surface is covered in resist (`ARP6200 9%`) and exposed in an Electron beam lithographer (EBL) according to the doses shown in Fig. 1.15 (b). This softens the resist, which is washed away by a developer (`ARP 600-546`). All the uncovered Al is etched away (`MF319`), leaving only the structures of the TL, interdigitated capacitor and perforated ground plane.

  Because the bulky structures do not require great accuracy, the exposure on EBL can be performed using a high current of 100 nA which optimises the speed of exposure to ~ 10 minutes.

- **Layer 2:** For realising the JJ, a strip of Al is deposited, oxidised, and then a second layer is deposited on top to get the Al-AlO$_x$-Al structure shown in Fig. 1.10. The Manhattan method of deposition is used (refer to B.2.2), in which evaporation is performed at perpendicular angles to improve JJ uniformity and avoid artifact JJ structures that can be a source of decoherence (refer to Sec. 1.3.3).

  As this layer involves deposition of a material into narrow holes in the mask, two resists are used to achieve an undercut (refer to B.1.4 and B.1.6) that ensures that the deposited material dose not form a continuous film that is hard to liftoff. The fine $100 \times 100\,\text{nm}^2$ sizes of the JJ require a more accurate electron-beam lithography at 2 nA.

- **Layer 3:** Layer 1 and layer 2 lithographies result in structures that are disconnected from one another (see Fig. B.9) and this final patching layer produces galvanic connection between them, free of contamination or oxide layers, which would act as additional JJs in the system. It is typically the most error prone stage of the fabrication, since contamination of the etching gas, inadequate etching, or thin patches, lead to deteriorated or even broken contact pads (see Fig. 1.16). Deposition of patches is performed with continuous rotation, to ensure that the patch is not broken at the edge of the JJ.

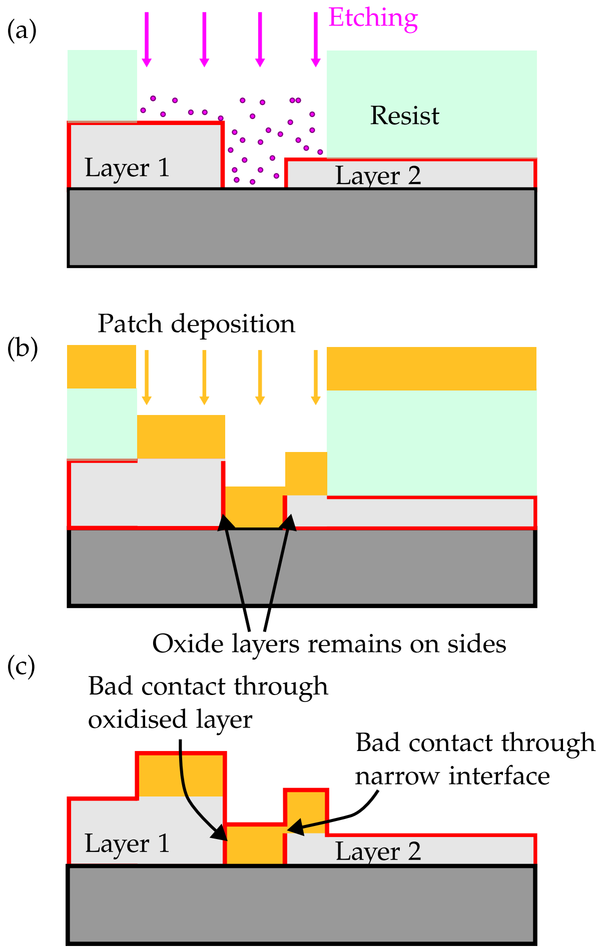
(a)
Etching
Resist
Layer 1
Layer 2
(b)
Patch deposition
Oxide layers remains on sides
(c)
Bad contact through
oxidised layer
Bad contact through
narrow interface
Layer 1
Layer 2

Figure 1.16: Example of thin patching failing to connect layer 1 and layer 2 structures: **(a)** Patch window is opened in EBL resist, which is then hardened by baking. AlO_x layers are etched away with plasma; **(b)** Deposition of patch layer aims to connect the two structures; **(c)** The patch film may break at edges if patch layer is too thin leading to poor contact and potential failure of the structure.

1.5.2 Calibration

A lot of factors contributed to the properties of fabricated samples, especially the Josephson energy E_{J0} (1.4.1) which was sensitive to the resistance of the JJ:

- Scaling of the JJ structures in the X-Y directions due to astigmatism effects in the EBL;
- Different resistances of the $100 \times 100\,\mathrm{nm}^2$ JJ under different oxidation conditions;
- Increase of the JJ resistance when cooled for the experimental environment;
- Oxidation pressure and time;
- Purity of evaporated Al;

- Specifics of the Si wafer being fabricated on - the surface layer could be riddled with impurities.

Table 1.2: Resistance measurements taken on batches of test samples.

Parameter	**Value**
$R_\square$ Dynamic-20 sccm	6.7 kΩ
$R_\square$ Static-0.4mBar	17 kΩ
$R_\square$ Static-0.25mBar	12.17 kΩ
$R_\square$ Static-0.1mBar	10.67 kΩ
Resistance cooling scaling	1.1
Scaling of JJ compared to design (X direction)	1.04
Scaling of JJ compared to design (Y direction)	1.05

These parameters were statistically calibrated using the test samples positioned on the top of the design chips (see Fig. 1.14). Over 100 readings were taken for each of the conditions in Tab. 1.2. Dimension measurements were made on a `Zeiss Orion Nanofab` Focused ion beam (FIB) [139], and compared against the design values to get the X-Y scaling. Resistance measurements were done with a standard I-V current probe and normalised against a 100 nm × 100 nm JJ. The inevitable scaling of resistance at low temperatures was gauged from earlier experiments, by measuring of the JJ at RT and taking its ratio with the resistance used to fit experimental results.

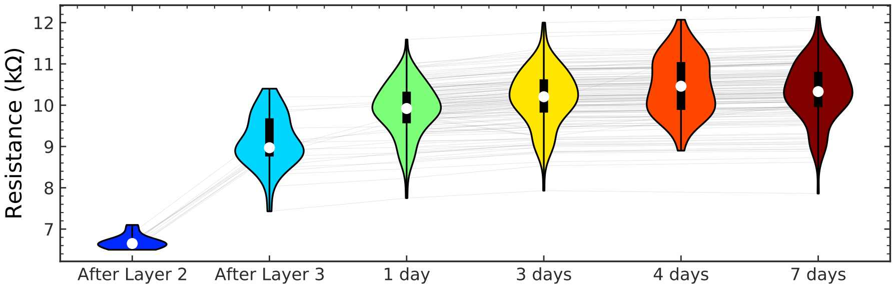

Figure 1.17: Violin plot of resistance measurement made on test JJs under 0.1 mBar oxidation over a week after their deposition. The light lines connect measurements made on the same JJ, showing that most followed a similar oxidation trend, reaching saturation after a couple of days. The average resistance increase between the measurement periods where: 36% → 8% → 3% → 3% → −1%. White dots indicate the mean, while the black boxes the upper and lower quartiles.

Furthermore, time-sampled resistance measurements of the test structures during the process of fabrication and up until the loading into the cryostat (see Fig. 1.17) showed the drift in resistance, as oxidation processes continue to occur. Patch deposition done in layer 3 (refer to B.4.4) increased JJ resistance by $\sim 40 \pm 8\%$ because of the annealing process that occurs during the baking of the resist. Following the completion of fabrication, the resistance increases from 8.8 kΩ to 10.2 kΩ just by the sample lying in the laboratory and reaches saturation in 3-4 days. This should be factored in since sample are not immediately loaded into the vacuum environment of the cryostat after fabrication.

1.5.3 Result

Results of fabrication are presented in Fig. 1.18. Certain structures closer to the edges of the chip, where the resist liquid builds up forming an edge bead [140] were subject to flaking. The undercut in those regions was too shallow and the Al deposited through the mask would form a continuous film, latching onto the top resist layer (see Fig. B.4). These flakes have the potential of short circuiting the smaller structures, and distorting the electric fields in the JJ regions.

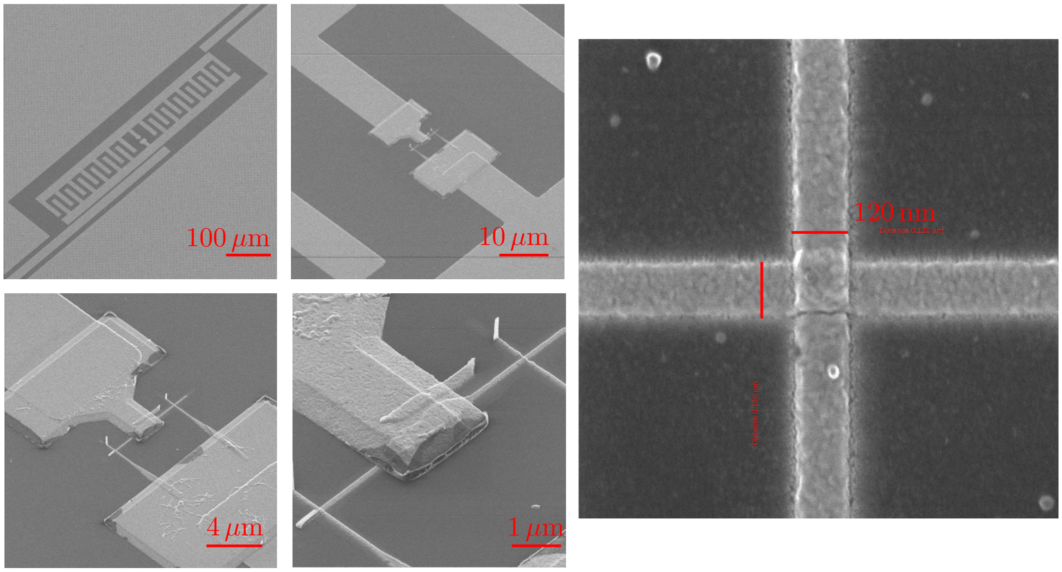

Figure 1.18: Transmon single photon source at different magnifications. Image taken from an angle on an FIB, allowing the resolution of sub-nanometer structures. Al patches visible on the lower images connect the structures made in two separate lithography steps. A close up on the edge of the structures, reveals *cliffs* on the ends of the thin *crosses* characteristic of a shallow undercut. The JJ overlap seen in the bottom right image shows the graininess of the Al, comparable to the size of the junction itself.

1.6 Experiment

The following section will present results for two geometrically-similar photon sources: **(A)** Fabricated in Japan; **(B)** Designed and fabricated in Sec. 1.4. First however, the general measurement principles that apply to these and all subsequent measurements performed in the thesis are covered.

1.6.1 General measurement principles

1.6.1.1 Sample mounting

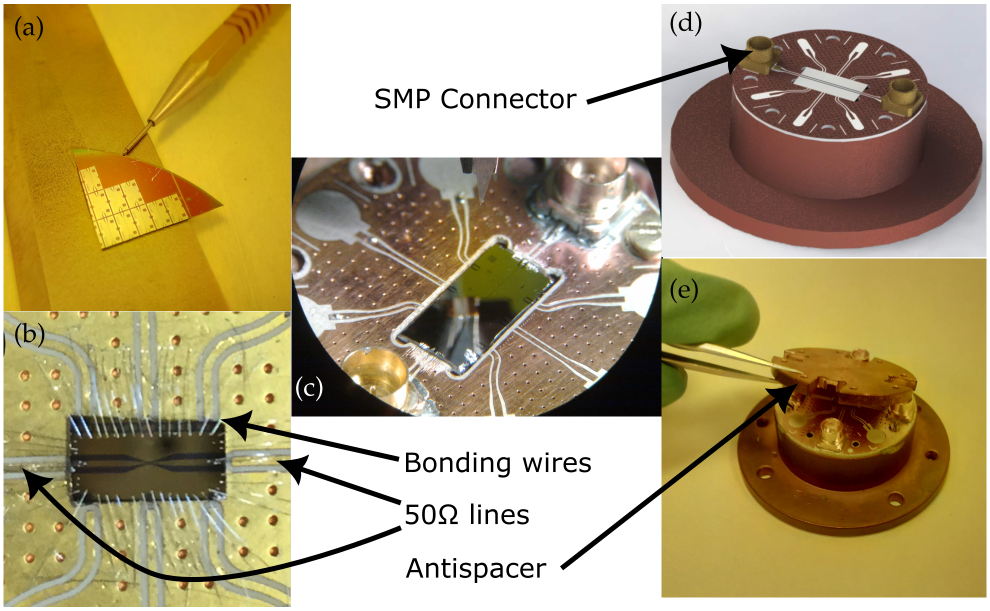

Figure 1.19: Mounting of the sample onto a PCB: **(a)** Isolating the fabricated chip by splitting wafer with a diamond cutter. As splitting occurs along crystalline axes, it was important for the samples to be aligned with the guiding edges of the wafer; **(b)** The TL on the chip is connected to the $Z_0 = 50\,\Omega$ TL on the PCB and likewise for the ground plane; **(c)** Old-gen PCB partially bonded chip; **(d)** Sample holder without the lid showing connection to SubMiniature push-on (SMP) connectors; **(e)** Mounting of chip onto the sample holder and covering with an antispacer.

Figure 1.19 shows the chip mounting procedure. Once a chip is fabricated, care is taken to ground against static voltage buildups that have damaged samples in the past. The wafer with the sample is dissected into individual chips using a diamond tip pen after which a chip will naturally split along the crystalline axis of the Si wafer. Electrically neutral varnish is used to mount the sample onto a PCB which provides the interface to the SubMiniature version A (SMA) electronics through its SMP connectors.

The ground planes and TL of the samples are bonded with $25\,\mu$m Al wires using a

`7KE West Bond machine` [141] to the corresponding elements on the PCB as shown in Fig. 1.19 (b). The ground planes must always be at the same potential, to prevent parasitic modes between them. An antispacer is put onto the PCB to dampen parasitic resonances by physically constraining the enclosure of the qubit (see Fig. 1.19 (e)).

1.6.1.2 Sample loading

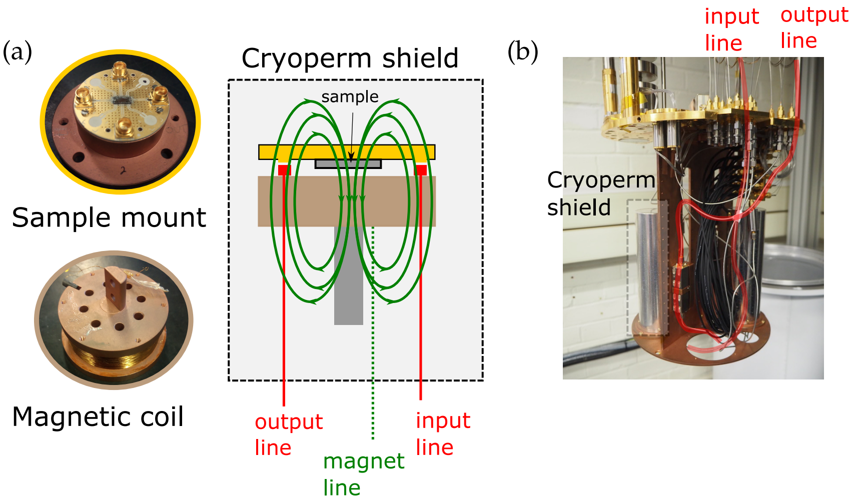

Figure 1.20: **(a)** Sample holder (yellow) mounted on top of a copper magnet stand (brown) and placed inside a cryoperm shield. Here green lines indicate the magnetic field generated by the coil and incident perpendicularly onto the sample; **(b)** Sample positioned on the cold 13 mK stage of cryostat.

The device is enclosed in a copper package, and positioned inside a 4000-turn superconducting solenoid passing mA current and producing a field of $B_{\text{ext}} \sim 1.5\,\text{G/mA}$, perpendicular to the plane of the sample (see Fig. 1.20 (a)) and is driven by a `Yokogawa 7651` DC source . The structure is covered by a cryoperm shield and tightly screwed onto the 13 mK stage of `Bluefors` dilution refrigerator (see Fig. 1.20 (b)). The cryoperm is a Nickel (Ni) alloy with a crystalline structure that has a very high magnetic susceptibility - its magnetic domains align in a way that channels the external magnetic flux through its bulk, which protects the interior.

At these temperature the Al material becomes superconducting and the experiment runs below the level of thermal excitation $k_b T \ll \hbar\omega_q$ that could interfere with the $\sim 1\,\text{GHz}$ transition frequencies of the qubit. The process of cooling down is described in C.1. Radiation cans were mounted on each stage of the refrigerator to block radiation that could create quasiparticles (refer to Sec. 1.3.3).

1.6.1.3 SMA components

Although the setup of individual experiments in this thesis varied, the common elements of the measurement circuitry are summarised below and depicted schematically in Fig. 1.21.

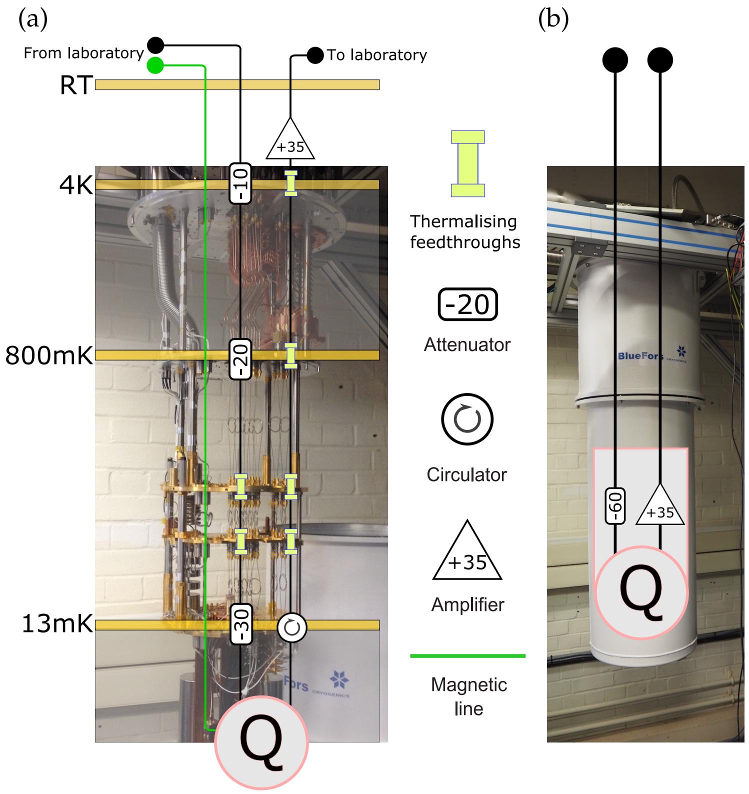

Figure 1.21: **(a)** Temperature stages of the cryostat, showing attenuator, isolator and amplifier positions. **(b)** In forthcoming diagrams, this will be represented by a 60 dB input attenuation and +35 dB output line amplification. The cryostat is sealed and the cooldown procedure described in C.1 is run.

Interaction with superconducting elements is done with microwaves, whose frequency band 100 MHz-20 GHz, covers the typical energies of these systems. These microwaves are guided to and from the system via TLs with a standard $Z_0 = 50\,\Omega$ impedance. There is an ample industry of laboratory equipment and components (microwave generators, connecting cables, power splitters, attenuators, etc) from different providers, that can be assembled together like Lego blocks into flexible experimental schemes through standardised SMA connectors:

- **Wiring elements**: The cryostat is equipped with semi-rigid coaxial cables with a characteristic impedance of $Z_0 = 50\,\Omega$. From RT to the still stage, the cables are stainless steel (UT-85-SS) as stainless steel has low heat conduction. From the still stage to the mixing chamber stage, both Niobium (Nb) and Niobium Titanium (NbTi) cables are used. When they are superconducting ($< 10\,\mathrm{K}$), they have a very low thermal conductivity but a high electrical conductivity. On each stage, the outer conductor of the cables are thermally anchored using panel mounted bulk head feed throughs.

Anything with poor thermal contact will only be able to emit its internal energy via black body radiation (the can is evacuated preventing convective heat loss) which could stall the base temperature at 800 mK during cooldown.

- **VNA**: `Rohde and Schwartz ZNB20` generates microwaves at frequency ω for driving the system on its output port. It tracks the signal in the output line at the same frequency ω, evaluating the amplitude and phase shifts of its input and output signals: $t = V_{\text{in}}/V_{\text{out}}$. The VNA thus measures the transmission amplitude described by (1.2.18).

- **Spectrum analyser (SPA)** `Anritsu MS2830A` [142] is used to monitor the emission spectra $S(\omega)$ described in Sec. 1.2.3. Selecting a suitable Radio bandwidth (RBW) and Video band width (VBW) is important to locate weak signals and minimise spectrum distortions.

- **Microwave generator** `Rohde and Schwartz SNB 100A` is an additional microwave source, used commonly in two-tone measurements described in Sec. 3.1.3.4 and A.2.6. To combine microwaves from the generator and VNA, a `Minicircuit ZFRSC-183-S+` power divider is used.

- **Cold temperature amplifiers** `Low noise factory LNF_LNC1_12A` is the first amplifier positioned on the output line after the isolator on the 4 K stage of the fridge (see Fig. 1.21). These amplifiers have low power dissipation and do not heat up their environment. These amplifiers are also ultra low noise, which is important because at this stage qubit emissions are the weakest and are sensitive to any Signal to noise ratio (SNR) deterioration (discussed in detail in Sec. 1.6.6.3).

- **Room temperature amplifiers/filters** Radio frequency (RF) amplifiers include `Minicircuit ZVA-183G-S+`, `Atlantic Microwave AOX-040120` and `Low noise factory LNF-LNR1_15A` and Direct current (DC) amplifiers include `Minicircuit ZFL-500LN+,ZHL-6A+`. In the output line, a wide band of frequencies is amplified, with the total power $P = \int S(\omega)d\omega$ potentially saturating at these amplifiers. Strategically placed filters will attenuate non-important parts of the spectrum and increase the amount of amplification that can be done on the useful signal.

- **Attenuators** are placed on the input lines to match the laboratory powers larger than $-60\,\mathrm{dBm}$ to powers of qubit processes $\hbar\omega\Gamma_1 \sim -140\,\mathrm{dBm}$ (using $\omega \sim 10\,\mathrm{GHz}$ and $\Gamma_1/2\pi \sim 1/100\,\mathrm{ns}$ in (1.2.13)). Additionally, they perform the important function of thermalising the black body radiation travelling down the TLs.

  With dB defined as $\mathrm{dB} = 10\log\left(P_a/P_B\right)$, a 10 dB attenuator will divide the temperature noise by a factor of 10. Coming in from room temperature, 20 dB of attenuation was required in order to lower the radiation to a temperature $< 4\,\mathrm{K}$ of the top plate. The same procedure applies further down the line as well.

- **Pulse generator (PG)** `Keysight 81160A` is used in conjunction with a chopper to cut a continuous driving field (input line) into pulses of length Δt for Rabi oscillation measurements or to cut a continuous emission field (output line) and expose VNA or SPA to selected *windows* for averaging. The custom chopper is made from `Marki M80420LS` mixers `Minicircuit ZFRSC- 42-S+` power divider and `Minicircuit SLP-1200+` low pass filter.

- **Current source** `Yokogawa GS200` is used to pass a constant current through a superconducting solenoid next to the sample, and controls the biasing flux as described in (2.2.1).

- **Isolator** `Quinstar isolator` acts as an asymmetric attenuator that applies a 20 dB attenuation to signals going *against* its orientation. Placing it on the readout line blocks unwanted feedback from the cold temperature amplifier (see above), realising the condition described in Sec. 1.2.1 of only a single incident field from the input line driving the qubit. It operates on the principle of polarising the electro-magnetic field of incident microwaves and rotating them as they pass through a ferrite material. Forward propagating waves pass through with a small attenuation, whereas microwaves incident in the reverse direction undergo a polarisation that is dissipated by a resistive vane.

- **Digitiser** `ADQ214 SP` measures voltage ($V(t)$) with a resolution of 2.5 ns in time and $\sim 0.13\,\mathrm{mV}$ in amplitude. Whereas the SPA and VNA perform averaging, to collect a signal over the bandwidth used for the measurements, the digitiser measures genuine time resolved signals, allowing for correlation statistics (refer to Sec. 1.2.3) to be evaluated.

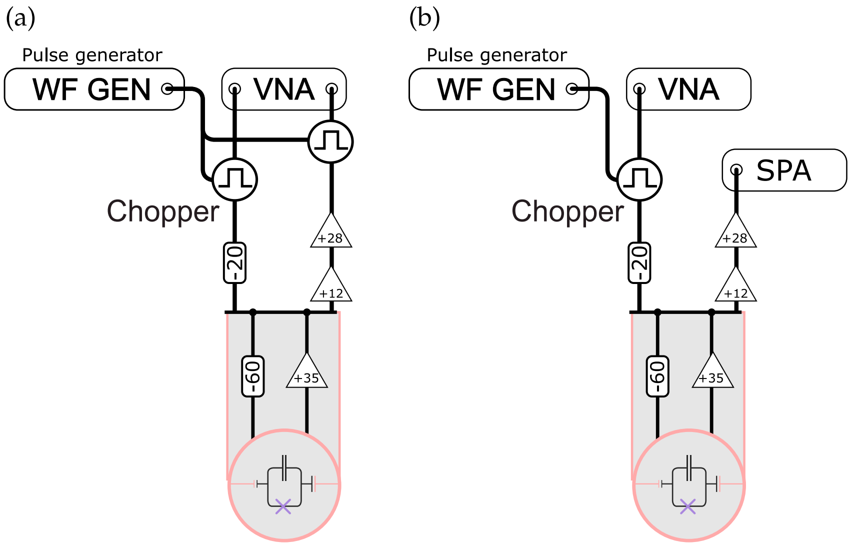

Figure 1.22: **(a)** Setup for transmission measurements with VNA. When there was no need for chopping the signal, the chopper was left in an *open* state by sending very long positive pulses from the PG; **(b)** Setup for power spectrum measurements with SPA.

1.6.2 Qubit spectrum

The energy spectrum of the transmon ($\Delta E(\Phi)$) is mapped by performing transmission measurements. As per (1.2.18) the transmission of microwaves through the system depends on the detuning of the driving field frequency (ω) from the transition frequency of the qubit ($\omega_q = \Delta E(\Phi)/\hbar$). To detect the qubit the driving field is swept at different magnetic fields biases ($B = \Phi/A_{\text{JJ-transmon}}$) to produce a 2D-series of transmission amplitudes ($t(\omega, \Phi)$) that peak on resonance of the driving field with the qubit $|0\rangle \leftrightarrow |1\rangle$ transition.

The VNA is used to both produce the driving field from one of its ports (which is connected to the input line) and to receive the signal from the system on its other port (see Fig. 1.22 (a)). The raw results ($t_{\text{raw}}(\omega, \Phi)$) are normalised by the average transmission, to account for the systematic frequency-dependent transmission bias loss in the circuitry

$$t(\omega, \Phi) = \frac{t_{\text{raw}}(\omega, \Phi)}{\int d\Phi' t_{\text{raw}}(\omega, \Phi')}, \tag{1.6.1}$$

and displayed in Fig. 1.23.

Fitting is performed using (1.1.4) determining E_C and E_{J0} that are used as tuning parameters. Results from **Photon Source B** differ from the designed parameters in Tab. 1.1. Although the charging energy (E_C) that depends on the capacitor network, is consistent, the Josephson energy (E_{J0}) is very small, corresponding to a resistance of 54 kΩ/1.1 at RT (1.1 is the increase in the JJ resistance at cold temperature due to the charge carrier

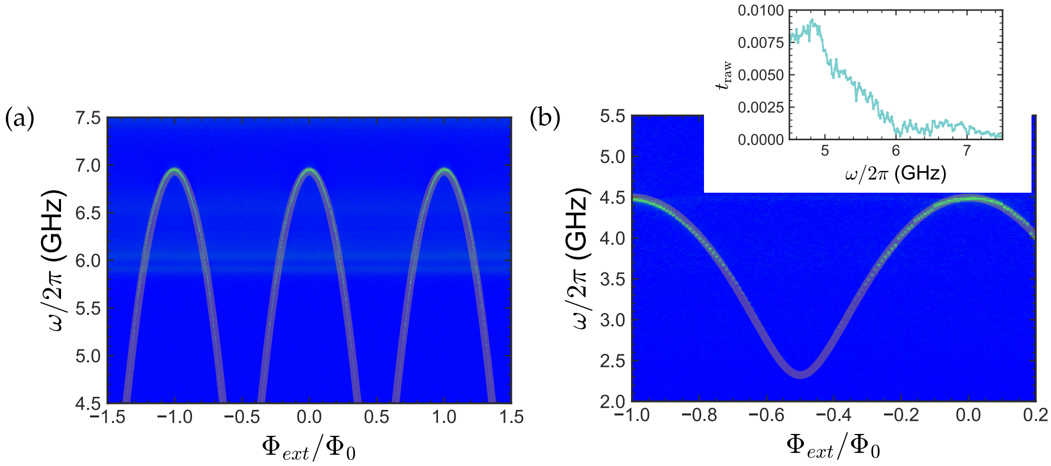

Figure 1.23: Spectra showing the resonant frequency of the transmon (ω_q) at different bias fluxes $\Phi \equiv I_{\text{bias}}$. These transmission spectra are fitted with E_C and E_J values. **(a)** Transmon A spectrum and fitting with $E_C/\hbar = 0.16\,\text{GHz}$ and $E_{J0}/\hbar = 30\,\text{GHz}$; **(b)** Transmon B spectrum and fitting with $E_C/\hbar = 0.32\,\text{GHz}$ and $E_{J0}/\hbar = 2.80\,\text{GHz}$. Inset shows one of the raw transmission profiles - they are normalised out in (1.6.1) to bring out the transmon-specific features.

depopulation from the conduction band). From this it is concluded that this was a highly resistive sample with a dirty contact - it is hard to micromanage the purity of every contact and inevitably there will be contaminated samples in every fabricated batch.

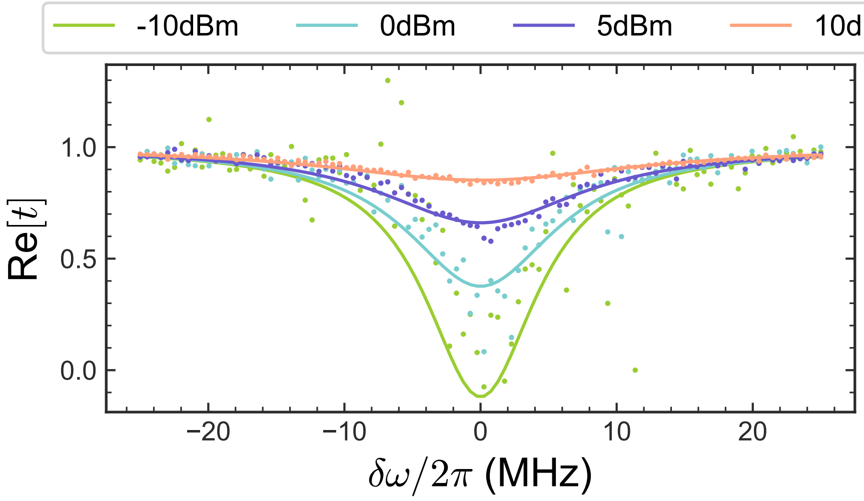

Figure 1.24: Transmission measurements for **Photon Source A**, showing the real parts of the transmission coefficient (Re[t]) for a range of driving powers (Ω) fitted with the (1.2.18). When the incident field is resonant with the transmon ($\delta\omega = 0$), transmission is minimised, as the coherent driving and scattering fields undergo destructive interference - this effect is strongest with weak driving fields. From fits, a relaxation rate of $\Gamma_1/2\pi \approx 20\,\text{MHz}$ and total decoherence rate of $\Gamma_2/2\pi \approx 8\,\text{MHz}$ are estimated.

The transmission profile at degeneracy point ($\Phi \sim 0$) for **Photon Source A** is shown in Fig. 1.24. This is known as the working point of a qubit, since it a point of minimal curvature with respect to the magnetic field, and hence the transition energy (ΔE) will be most robust to magnetic field noise (refer to Sec. 1.3.2). The weakest driving configuration are fitted with (1.2.18) to extract the relaxation rate of the transmon $\Gamma_1/2\pi \approx 20\,\text{MHz}$ which corresponded to an emission time for a single photon of $1/\Gamma_1 \sim 50\,\text{ns}$.

1.6.3 Rabi oscillations

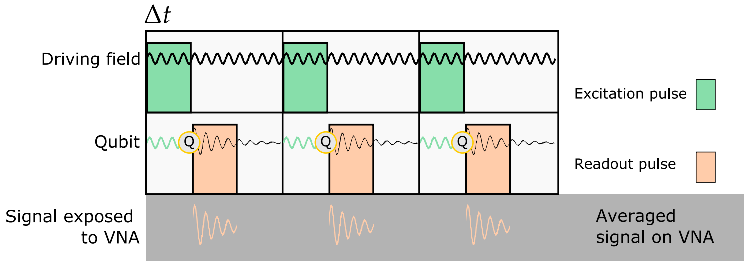

Figure 1.25: Rabi oscillation pulse procedure. The atom is driven for a time Δt after which a window is opened using a chopper, allowing the VNA to measure the average emission from the atom. Many repetitions will allow one to statistically infer the state of the atom.

Rabi oscillation are run to calibrate the excitation pulse for exciting the transmon $|0\rangle \rightarrow |1\rangle$. A resonant microwave pulse ($\omega = \omega_q$) of amplitude Ω applied for a time Δt rotates the ground state around the Bloch sphere, leading to oscillations with a period $T = 2\pi/\Omega$ under unitary evolution $U = e^{-i\Omega\Delta t/2\sigma_x}$ (refer to A.2.4)

$$\begin{aligned} |\psi\rangle = U|0\rangle &= \cos\left(\frac{\Omega\Delta t}{2}\right)|0\rangle + i\sin\left(\frac{\Omega\Delta t}{2}\right)|1\rangle \Rightarrow \\ \Rightarrow \rho &= \frac{1}{2}\begin{pmatrix} 1+\cos(\Omega\Delta t) & \underbrace{-i\sin(\Omega\Delta t)}_{\diamond} \\ i\sin(\Omega\Delta t) & 1-\cos(\Omega\Delta t) \end{pmatrix}, \end{aligned} \tag{1.6.2}$$

which the VNA would register by tracking the scattered signal $V_{\text{sc}} \propto \langle\sigma_-\rangle = \rho_{01}$ (see Sec. 1.2.2), which will be seen as a phase shifted sinusoidal oscillations highlighted in (1.6.2). Under the presence of decoherence, the oscillations will additionally decay at rate $\Gamma_2/2\pi \sim 1/T_{2R}$ (refer to A.2.5 and Sec. 1.3.2), giving a net expected signal

$$V_{\text{sc}}(\Delta t) \propto \sin(\Omega\Delta t)e^{-i\Delta t/T_{2R}}. \tag{1.6.3}$$

Rabi oscillation measurements are done using a VNA and two choppers (see Fig. 1.22 (a) and Fig. 1.25). The VNA is tuned to the qubit frequency, while a PG creates pulses of width Δt that *chops* the driving field from the VNA into excitation pulses. On the output line, the VNA accumulates a multitude of emission signals from identical quantum state preparations over its internal time period of 0.2 s.

To locate the best Rabi oscillation regime of minimal noise (greatest amplitude and contrast) and best decoherence times (T_{2R}), a number of experimental parameters were swept, demonstrated below for **Photon Source B**:

- **Frequency of the drive:** It was found that driving exactly at the frequency of the qubit produced skewed Rabi oscillations. It was best in this case to measure slightly at the side 4.48 GHz (see Fig. 1.26 (a)).

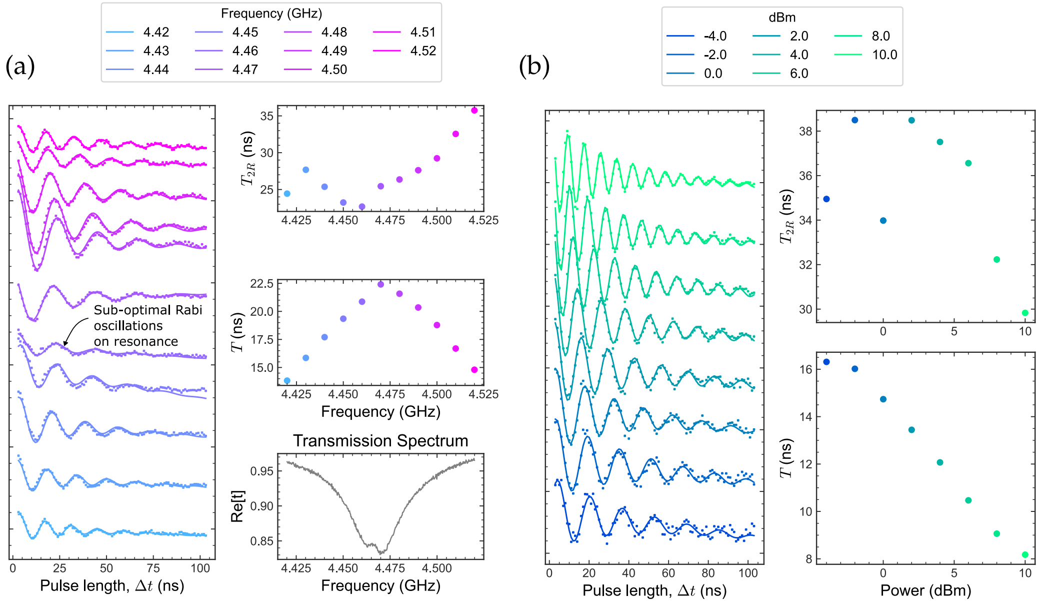

Figure 1.26: **(a)** A frequency sweep shows that maximal Rabi amplitude as achieved at a 0.01 MHz detuning from the transmon frequency. Driving on resonance resulted in the over-driving of the system, weakening the emission contrast. **(b)** The power sweep shows that the contrast of Rabi oscillations was maximised for stronger powers, but stronger powers also decreased T_{2R}.

- **Power of the drive:** Strong drives would lead to the splitting of the qubit transition energy, meaning that side frequencies around the original qubit frequency would be preferable (see Fig. 1.26 (b)). The contrast of oscillations was maximised with increasing drive, but it also lead to shorter decoherence times. A compromise was found at an input power of -10 dBm;

- **Repetition frequency:** The faster the sequence shown in Fig. 1.25 was repeated, the larger the average signal collected by the VNA its measurement period would be. A 10 MHz $\equiv$ 100 ns repetition period was chosen, which ensured that any leftover excitation following the drive would have enough time to decay ($T_1 = 1/\Gamma_1 \sim 50\,\mathrm{ns}$ found in Sec. 1.6.2) before the next sequence was started.

Under optimal conditions, the π-pulse was found to be $\Delta t_\pi \equiv T/2 = 12.2\,\mathrm{ns}$ for a -10 dBm input power to **Photon Source A** (see Fig. 1.27). Decoherence would be occurring during the driving pulse itself, so its length is limited to $\Delta t_\pi / T_{2R} < 1$ so that the preparation of the qubit occurred fast enough to not interfere with the qubit relaxation dynamics.

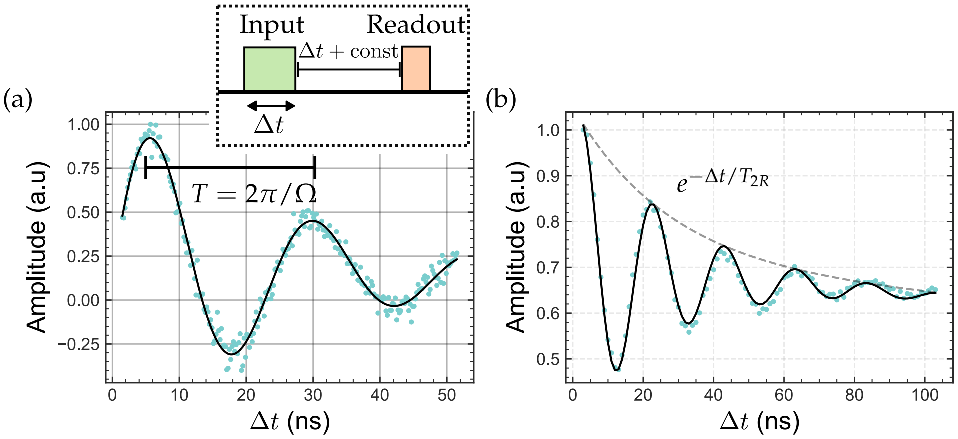

Figure 1.27: Fits made with (1.6.3). **(a)** Optimal Rabi oscillations for **Transmon A**: $\Delta t_\pi = T/2 = 12.2\,\mathrm{ns}$ and $T_{2R} = 25\,\mathrm{ns}$. **(b)**: Optimal Rabi oscillations for **Transmon B**, with $\Delta t_\pi = 13.6\,\mathrm{ns}$ and $T_{2R} = 20\,\mathrm{ns}$. Inset shows the pulse sequence used in the experiment - the output readout bucket had a time delay to match the time it took the excitation signal to propagate through the system.

1.6.4 Coherent and incoherent emission

Figure 1.22 (b) setup was used to have the SPA track emission power in a span of frequencies $\omega_q \pm 25\,\mathrm{MHz}$ around the qubit. This is a measurement of $S(\omega)$ introduced in Sec. 1.2.3, and will differentiate between coherent emission $\propto \langle \sigma_- \rangle = \rho_{10}$ and incoherent emission $\propto 1 - \langle \sigma_z \rangle / 2$. The full power of incoherent emission is spread out over a frequency range $\Delta\omega \sim \Gamma_1$ (1.2.16), and hence has a weak intensity. A large RBW of 2 MHz was set on the SPA to raise the aggregated incoherent signal above the noise level of the SPA.

One can distinguish two frequency profiles in Fig. 1.28. There are the bright coherent peaks at $\delta\omega = 0$ which is the coherent emission measured with Rabi oscillation in the previous section. There is also a broad incoherent profile, maximised, when the qubit is rotated into the excited state $|1\rangle$ in accordance with (1.2.17). Taking a cross-section at $\Delta t_\pi = 12\,\mathrm{ns}$ to better show the emission spectrum, one can clearly identify the narrow coherent peak, whose narrowness is limited by the 2 MHz measurement bandwidth, and broad incoherent signal with width $\Gamma_1/2\pi \approx 20\,\mathrm{MHz}$.

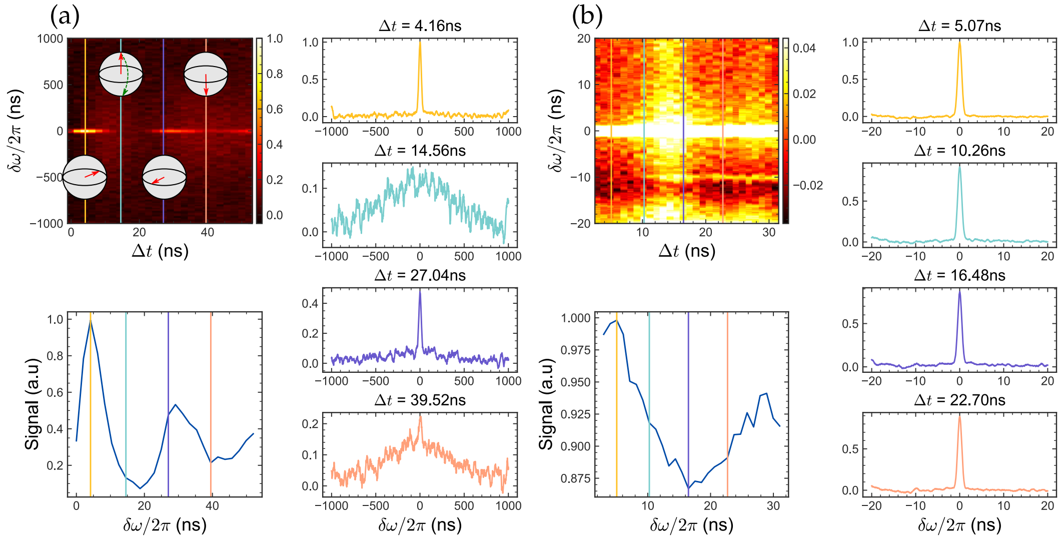

Figure 1.28: **(a) Photon Source A** showed both the coherent emission, seen as Rabi oscillations at $\delta\omega = 0$, and the broad incoherent peak maximised at $\Delta t_\pi = 14.56\,\text{ns}$ and seen as broad red patches. Note how the coherent signal width is limited by the 2 MHz RBW set on the SPA. An overlay of the qubit state depicts the origin of coherent and incoherent emissions at the different moments in time; **(b) Photon Source B** showed how weak incoherent emission could be - under a lot of averaging, it was still barely resolvable against the noise level.

Noticeably, there are missing order coherent oscillations in Fig. 1.28 (a), which occurs because no chopping was performed on the output line, with the SPA registering both qubit emission and driving pulses. The extra incident power shifts the amplitude of the Rabi oscillations by a constant offset, masking the oscillation minima.

1.6.5 Relaxation of qubit

To measure T_1, decay of the signal $\propto (1 - \langle\sigma_z\rangle)$ is monitored after the qubit has been excited by a π-pulse and shifting a 40 ns-wide readout bucket to expose the VNA to different stages of the relaxation process as shown by the inset in Fig. 1.29. There is going to be some degree of distortion in measuring the decay in this way, since the finite 40 ns size will not be the signal at a delay time t, but the average in the period $[t - 20\,\text{ns}, t + 20\,\text{ns}]$, however A.8.5 shows that this will not be significant.

In a single read, the VNA will accumulate the resultant signal from over 100 such cycle repetitions, and output a single point corresponding to the bucket delay (t). The decay profile is summarised Fig. 1.29, and is fitted with a decay time $T_1 \sim 40\,\text{ns}$ in close alignment to the $\Gamma_1 = T_1^{-1}$ fitted in Sec. 1.6.4.

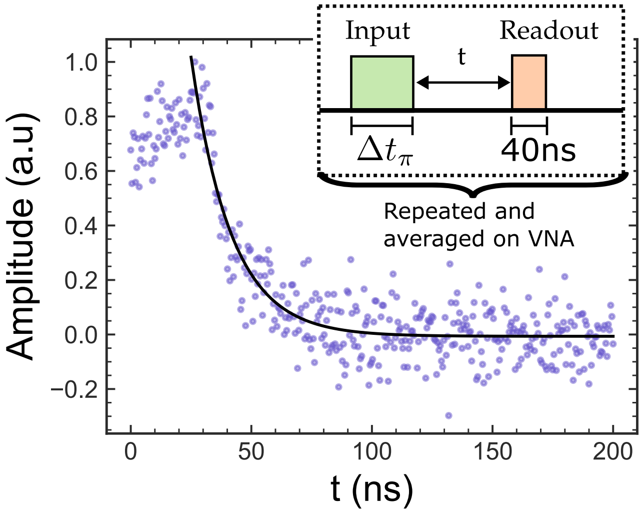

Figure 1.29: The output signal from the system is chopped into a window, which is shifted over time to map out the decay. After being excited by the π-pulse, the state decays over a characteristic time $T_1 \sim 40\,\text{ns}$. Inset shows the pulse sequence, with fixed input and readout pulses - the delay was swept to map out the full relaxation spectrum.

1.6.6 Time resolved photon signal

In Sec. 1.6.5 the relaxation of the transmon was mapped by using the average signal value in readout buckets, from which the temporal evolution of the signal was reconstructed. In order to measure the $g^{(1)}(\tau), g^{(2)}(\tau)$ correlation functions, one cannot work with such averages, and genuine time resolved signals need to be collected in order to capture the interference effects between consecutive photons.

In this section such time-resolved data is acquired by sampling the voltage field with a 400 MHz digitiser:

- A homodyne detection setup is developed to shift the signal carried by the GHz frequency that the qubit emits at, into a range than can be sampled by the digitiser;
- Emphasis is placed on making the readout protocol as efficient as possible;
- Emphasis is placed on increasing the SNR of the acquired signal.

The latter two points are necessary to have good efficiency of future correlation evaluation, which historically has involved terabytes of data and 30+ hour acquisition times [81]. This section will explain the non-trivial experimental setup given in Fig. 1.30, Fig. 1.31 and follow up with some time-resolved power measurements.

1.6.6.1 Digitiser setup

The digitiser at the end of the microwave circuitry was a 400MHz Analogue to digital converter (ADC) [143] placed in a PXIe crate [144]. It was connected via a fast `PCIe-8375` fibre-optic cable [145] to the laboratory computer on which data processing was made (see Fig. 1.30). Fast data transfer is supported by the fibre optic cable, and fast data processing is realised by the custom `C++-CUDA-Python` library running atop a `Quadro P6000` `Graphical processing unit (GPU)` [146]. Its 3840 cCUDE cores are used to speed up data processing speed by x4 times, ensuring that the limiting factor in measurements was the readout speed of the digitiser (refer to C.2 for a description of the program).

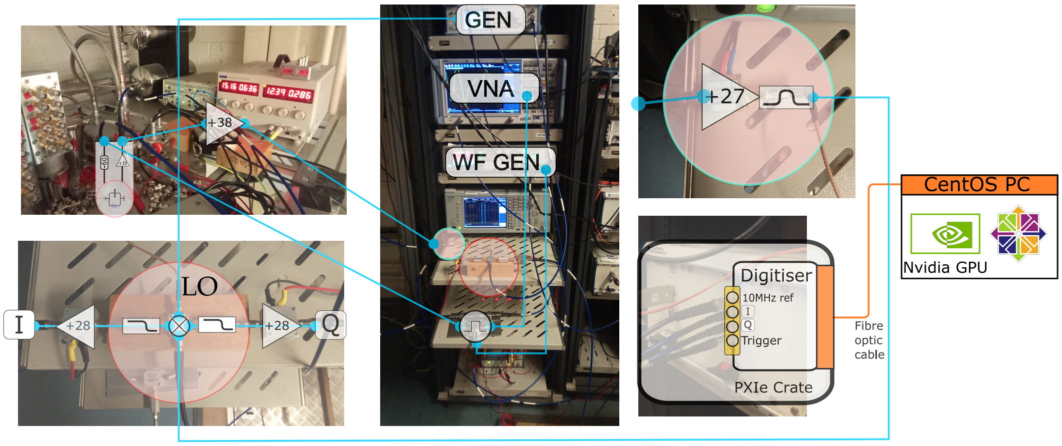

Figure 1.30: Annotated laboratory setup for digitiser measurements with highlighted generator, VNA and PG, IQ-mixer (red circle) and digitiser inputs. The digitiser is connected via a fibre-optic cable to a workstation with a 24 GB GPU. Both the data transfer via a fibre optic cable, and fast processing of data on the GPU, ensured that there was no processing bottleneck in the potentially long measurements. The corresponding schematic is in Fig. 1.31.

1.6.6.2 Homodyning

The digitiser is limited to a 400 MHz sampling rate, and therefore to register the profile of the GHz photon signals homodyne down conversion of the signal needs to be performed. The output line is connected to a IQ-mixer [147], where mixing occurs with a phase locked signal at the same frequency as the drive, supplied by a synchronised generator (see Fig. 1.30). Considering the signal to consist of a complex envelope $\xi(t)$ carried by a wave at the frequency of the qubit (ω_q)

$$V(t) = \xi(t)e^{-i\omega t_q},$$

the mixer will output two quadratures of the envelope, I and Q, which together reconstruct the signal envelope without the high frequency carrier wave component

$$\xi(t) = I_{\xi}(t) + iQ_{\xi}(t). \tag{1.6.4}$$

1.6.6.3 Signal propagation through system

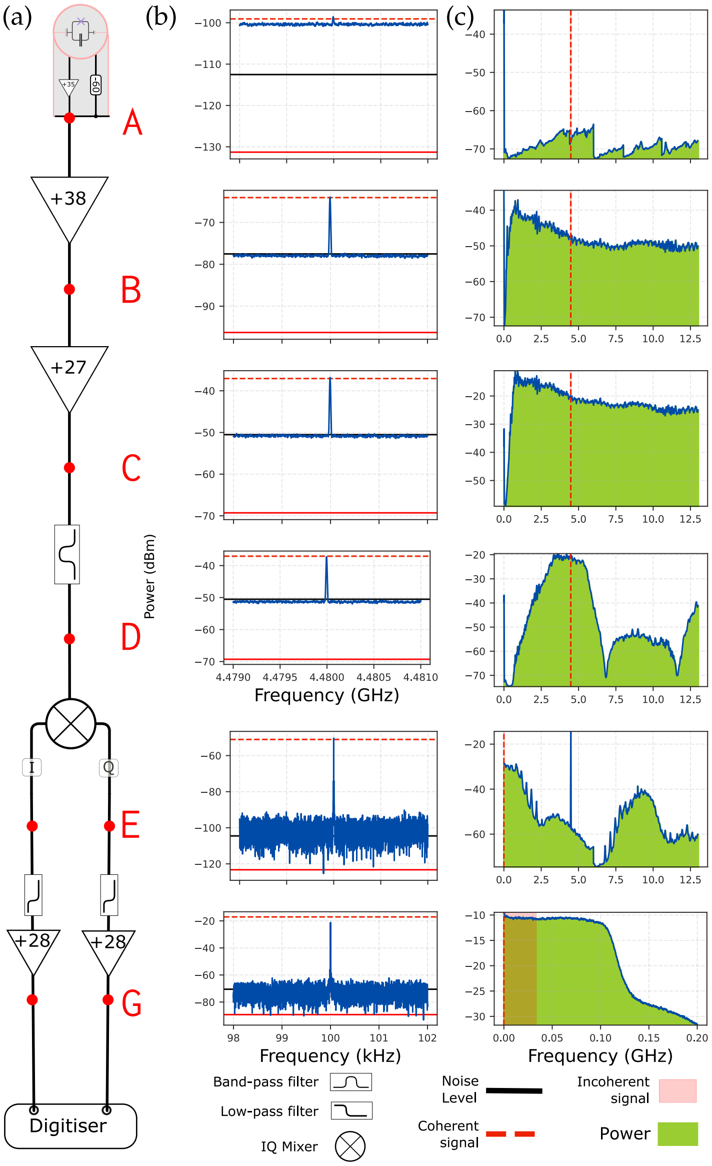

Figure 1.31: Monitoring of photon signal as it propagates through the readout system. **(a)** Microwave circuit components; **(b)** Spectrum centered on the coherent signal; **(c)** Wide spectrum capturing coherent and incoherent signal as well as background noise. The expected values of the coherent, incoherent and noise spectra at different stages in the output line are shown with solid red, dashed red and black lines respectively, with numerical values presented in Tab. 1.4. The corresponding laboratory setup is shown in Fig. 1.30.

The signal originates from the transmon photon source with a frequency $\omega_q \sim 7\,\mathrm{GHz}$ and relaxation time $T_1 \sim 40\,\mathrm{ns}$ measured in Sec. 1.6.5. Thus the coherent signal strength is $\hbar\omega_q/8T_1 = -139\,\mathrm{dBm}$ while the incoherent signal strength $\hbar\omega_q/2T_1 = -133\,\mathrm{dBm}$ spread over a frequency range $\sim \Gamma_1$ (refer to Sec. 1.2.3).

Table 1.3: Summary of the gain and noise contribution from different components on the qubit readout line (see Fig. 1.31). A microwave component will always have internal temperature noise $\propto k_bT$, plus operational noise quantified by its noise figure (F).

Component	Gain (dB)	Noise Figure	Temperature	Position in circuit
`Quinstar Isolator 4-12 GHz` [148]	-0.8		13 mK	Before A
`Low Noise Factory LNF-LNC-12A` [149]	39		5.5 K	Before A
`Amplifier ZVA-183G-S+` [150]	38	3	290 K	A-B
`Amplifier AOX Series` [151]	27	4	290 K	B-C
`Marki IQ Mixer` [147]	-7		290 K	D-E
`Minicircuit ZFL-500LN+ Amplifier`	28	2.9	290 K	E-G

For the components positioned in the output line that amplify and modify this signal (summarised in Tab. 1.3 and shown in Fig. 1.31) the important parameters are:

- **Gain (G):** which indicates how much it amplifies an input signal $\Xi_0 \propto \xi_0^2$

$$\Xi_1 = G \times \Xi_0 \qquad\qquad \Xi_1^{\mathrm{dBm}}, = \Xi_0 + G^{\mathrm{dB}}. \tag{1.6.5}$$

- **Operating temperature (T):** each component of resistance R has a noise spectrum $S(\omega) = 2hfR/(1-e^{-hf/k_bT})$ (refer to A.3.4 using $Z = R$), which, in the limit $hf \ll k_bT$, yields the classical Johnson-Nyquist noise[7]

$$S(\omega) = 2Rk_bT,$$

  with the white noise spectrum arising from the thermal agitation of conduction electrons and holes [152]. Hence each component will produce internal noise proportional to its operating temperature

$$\mathcal{N} \propto k_bT\Delta f, \tag{1.6.6}$$

  where Δf is the collection bandwidth.

---

[7] $\lim_{hf\ll k_bT} S(\omega) = 2hfR(1-(1-hf/k_bT+\mathcal{O}((hf/k_bT)^2)))^{-1} \approx 2hfR/(hf/k_bT) = 2Rk_bT$. In the electrical engineering convention it is the sum of positive and negative frequencies that is quoted $S(\omega)+S(\omega) = 4Rk_bT$, which is more commonly seen.

- **Noise figure (F):** which quantifies the SNR deterioration caused by the component. To understand this value, consider a component with gain G_1 and internal noise $\mathcal{N}_1 = k_b T_1 \Delta f$ arising from Johnson-Nyquist noise (1.6.6) due to its temperature T_1, that amplifies an input signal Ξ_0 with noise $\mathcal{N}_0 = k_b T_0 \Delta f$. The output noise is then

  $$\mathcal{N}_1^{\text{out}} = G_1(\mathcal{N}_0 + \mathcal{N}_1) = G_1 k_b \Delta f (T_0 + T_1), \tag{1.6.7}$$

  giving a change in the SNR of

  $$\frac{\text{SNR}_0}{\text{SNR}_1} = \frac{\Xi_0 / k_b \Delta f T_0}{G_1 \Xi_0 / G_1 k_b \Delta f (T_0 + T_1)} = 1 + \frac{T_1}{T_0},$$

  which is quoted through a noise figure

  $$F_1 = 20 \log_{10}\left(1 + \frac{T_1}{T_0}\right) \geq 0.$$

  For a second component in this chain

  $$\mathcal{N}_2^{\text{out}} = G_2(\mathcal{N}_1^{\text{out}} + \mathcal{N}_2) = G_1 G_2 k_b \Delta f \left(T_0 + T_1 + \frac{T_2}{G_1}\right),$$

  and the SNR

  $$\frac{\text{SNR}_0}{\text{SNR}_2} = \frac{\Xi_0 / k_b \Delta f T_0}{G_1 G_2 \Xi_0 / G_1 G_2 k_b \Delta f (T_0 + T_1 + T_2/G_1)} = \frac{T_0 + T_1 + T_2/G_1}{T_0} = 1 + \frac{T_1}{T_0} + \frac{T_2}{T_1 G_1},$$

  resulting in a noise figure $F_{\text{total}} = F_1 + (F_2 - 1)/G_1$ for the chain. With more components

  $$G_{\text{total}}^{\text{dB}} = G_1^{\text{dB}} + G_2^{\text{dB}} + G_3^{\text{dB}} \cdots \qquad F_{\text{total}} = F_1 + \frac{F_2 - 1}{G_1} + \frac{F_3 - 1}{G_1 G_2} + \cdots \tag{1.6.8}$$

  (1.6.8) shows that the noise figure and gain of the lower components is most important, since their noise figures are less affected by further amplification, while their gains suppress the noise deterioration further up the chain. Furthermore, although the argument was made using Johnson-Nyquist noise, the noise figure may be lower or higher than the actual temperature of the component e.g. a component with a noise figure $F = 3$ at 290 K introduces less noise than the expected 290 K temperature.

The signal spectra are measured at different locations **A, B, C, D, E, G** in the readout circuit. Plots in Fig. 1.31 compare the actual measurements to the expected ones using (1.6.5), (1.6.7) and the component parameters from Tab. 1.3, while the numerical results are presented in Tab. 1.4.

Table 1.4: Propagation of photon signal through the RT readout line. Refer to Fig. 1.31 (a) for the component positions. Total power was assessed by taking the integral $\int df S(f)$ of the wide spectra in Fig. 1.31 (c). Different RBW where used for the narrow and wide spectra.

Position	Coherent (dBm)	Incoherent (dBm)	Noise (dBm)	Total Power (dBm)	RBW for (b)	RBW for (c)
A	-99	-131	-112	-59	10 kHz	10 MHz
B	-64	-96	-77	-35	10 kHz	10 MHz
C	-37	-69	-50	-8	10 kHz	10 MHz
D	-37	-69	-50	-17	10 kHz	10 MHz
E	-51	-123	-104	-27	1 Hz	10 MHz
G	-17	-89	-70	-20	1 Hz	1 MHz

Band pass and low pass filters were strategically placed to cut off noisy parts of the amplified spectrum, which ensured that the total power ($\Delta f S(\omega)$) incident on the components does not exceed their saturation values. To maintain the best SNR, noisy amplifiers were positioned at the latter stages of the output line, so that their internal noise underwent minimal subsequent amplification as argued by (1.6.8).

1.6.6.4 DC filtering

The digitiser will eventually register the amplified photon signal in combination with noise[8]

$$\xi(t) = \xi_0 \sqrt{G_{\text{total}}} \qquad V_{\text{noise}}(t) = \sqrt{S(f)\Delta f Z_0}, \tag{1.6.9}$$

where Δf is the bandwidth of the final DC filter, $Z_0 = 50\,\Omega$ is the impedance of the digitiser, and $S(f)$ is the noise spectral density in the last graph in Fig. 1.31. The measured values are presented Tab. 1.5.

Table 1.5: The relative SNR of the photon signal depends on the bandwidth of the filter Δf. The 14-bit, 2.2 Vpp digitiser gives an amplitude reading in *codes*, where 1 code $\equiv$ 0.14 mV. Results are shown below for **Photon Source A** (because fewer amplifiers were used, the powers are weaker than described in the text).

	Δf (MHz)	**Power** (dBm)	**Amplitude** (V)	**Amplitude** (Codes)	**SNR**
$\xi(t)$		-50 dBm	0.001	7	
$V_{\text{noise}}(t)$	15	-9 dBm	0.1	700	$\frac{1}{100}$
	48	-2 dBm	0.2	1500	$\frac{1}{200}$
	98	0 dBm	0.3	2200	$\frac{1}{300}$

Using a narrower filter improves the SNR, however the narrower bandwidth will also distort the exponential decay whose frequency span would be on the order of $\Gamma_1/2\pi \sim 20$ MHz (see Fig. 1.32). A compromise was set at a 98 MHz DC filter for measurements.

---

[8] From rearrangement of $P = V^2/R$.

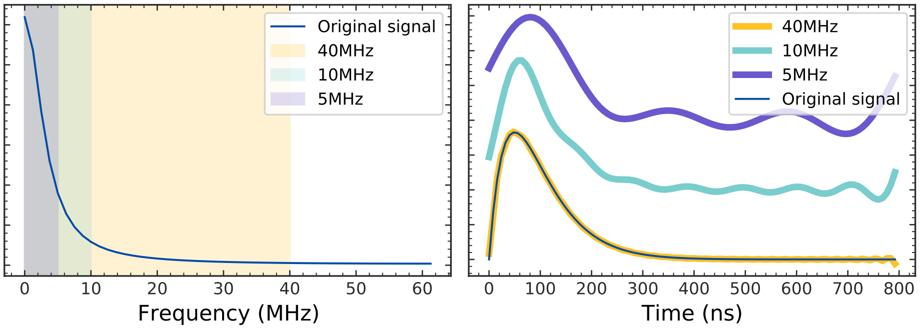

Figure 1.32: Filters of bandwidth Δf =5,10,40 MHz distort an exponential decay signal, but improve the SNR. **(Left)** Filter effect is evaluated by taking a FT of the exponential decay signal (dark blue) and cutting away frequencies outside the filter span (coloured areas); **(Right)** The corresponding time domain signals after filters cut away certain frequencies. Tighter filtering introduces bigger distortions.

1.6.6.5 Selecting excitation pulse

As measured in Sec. 1.6.3, an input power of -10 dBm would excite the qubit with a π-pulse of length $\Delta t_\pi \sim 10$ ns. It was important to engineer this excitation pulse to avoid distortions - just as the exponential decay of the photon signal was subject to distortion from the DC filter (see Fig. 1.32), so too would be the excitation pulse that leaks into the output line.

This would have the effect of leaving a *trail* of the excitation pulse long after it has been turned off. Programming the PG to deliver a Gaussian pulse instead of a purely square one reduced such leakage following the DC filter, due to a narrower frequency band required for their synthesis. This was experimentally verified in Fig. 1.33 (a,b). Furthermore a pulse-width measurement showed that it was better to avoid short pulses which suffered from greater distortion (see Fig. 1.33 (c,d)).

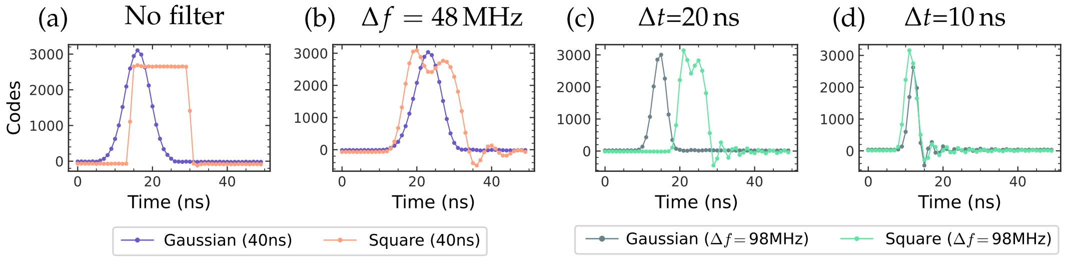

Figure 1.33: Comparison of experimentally measured square and Gaussian excitation pulses using the digitiser: **(a)** No filtering; **(b)** $\Delta f = 48$ MHz DC filter placed before digitiser - not how little it effects the temporal shape of the Gaussian pulse; **(c)** Pulses of length $\Delta t = 20$ ns; **(d)** Pulses of length $\Delta t = 10$ ns. The latter two measurements show that short pulses will lead to an oscillation *leakage* even after the main part of the signal has been complete.

1.6.6.6 Power measurements

Summarising the experimental details for performing time resolved power measurements:

- The readout line shown in Fig. 1.31 is setup for catching the signals;
- A 48 MHz DC filter will be placed right before the digitiser to improve the SNR while maintaining a non-distorted photon signal (see Sec. 1.6.6.4);
- Gaussian pulses will be used to apply the π-pulse ($\Delta t_\pi = 10 - 20\,\text{ns}$) to prepare the transmon in the excited state, fast enough to not interfere with the qubit dynamics, but slow enough to prevent leakage signal distortion (see Sec. 1.6.6.5).
- Measurements are made on **Photon Source A**, whose operating energy of $\sim$7 GHz fell inside the recommended 6GHz-12GHz of the Marki IQ-mixer [147] used for heterodyning (see Sec. 1.6.6.2).
- To ensure that the source with a characteristic relaxation time of $T_1 \sim 40\,\text{ns}$ (refer to Sec. 1.6.2) returned to its ground state, the pulse sequence was repeated every 250 ns.

A custom library (refer to C.2) was used to evaluate the instantaneous power emitted by the atom into the output line via a parallelised summation of the time resolved quadratures (1.6.4), and subtracting the average trace when no excitation take place for systematic error normalisation. Due to presence of noise, the measured quadratures has some noise components $I_\mathcal{N}(t), Q_\mathcal{N}(t)$:

$$I(t) = I_\xi(t) + I_\mathcal{N}(t)$$
$$Q(t) = Q_\xi(t) + Q_\mathcal{N}(t)$$

meaning that the evaluated power

$$\begin{aligned}\langle P(t)\rangle &= \frac{1}{Z_0}\frac{1}{N_\text{repetitions}}\sum_{i=0}^{N_\text{repetitions}}\left[I_i(t)^2 + Q_i(t)^2\right]\\ &= \frac{1}{Z_0}\frac{1}{N_\text{repetitions}}\sum_{i=0}^{N_\text{repetitions}}\left[\underbrace{I_{\xi,i}(t)^2 + Q_{\xi,i}(t)^2}_{\xi_i^*(t)\xi_i(t)} + \underbrace{I_{\mathcal{N},i}(t)^2 + Q_{\mathcal{N},i}(t)^2}_{V_\text{noise}^*(t)V_\text{noise}(t)} + I_{\mathcal{N},i}(t)Q_{\xi,i}(t) + I_{\xi,i}(t)Q_{\mathcal{N},i}(t)\right]\\ &= \frac{\langle\xi^*(t)\xi(t)\rangle}{Z_0} + S(f)\Delta f + \langle\text{cross terms}\rangle\end{aligned} \tag{1.6.10}$$

contains the following components

- The average photon signal $\langle\xi^*(t)\xi(t)\rangle$ following (1.6.4);

- The random background noise, $S(f)\Delta f$ following (1.6.9). With the SNR$\sim$ 100 after DC filters have been applied (see Sec. 1.6.6.4), $N_{\text{repetitions}} \geq 1000$ will be required in order to distinguish the single photon signal;

- The cross terms will statistically average out as they do not have any correlation.

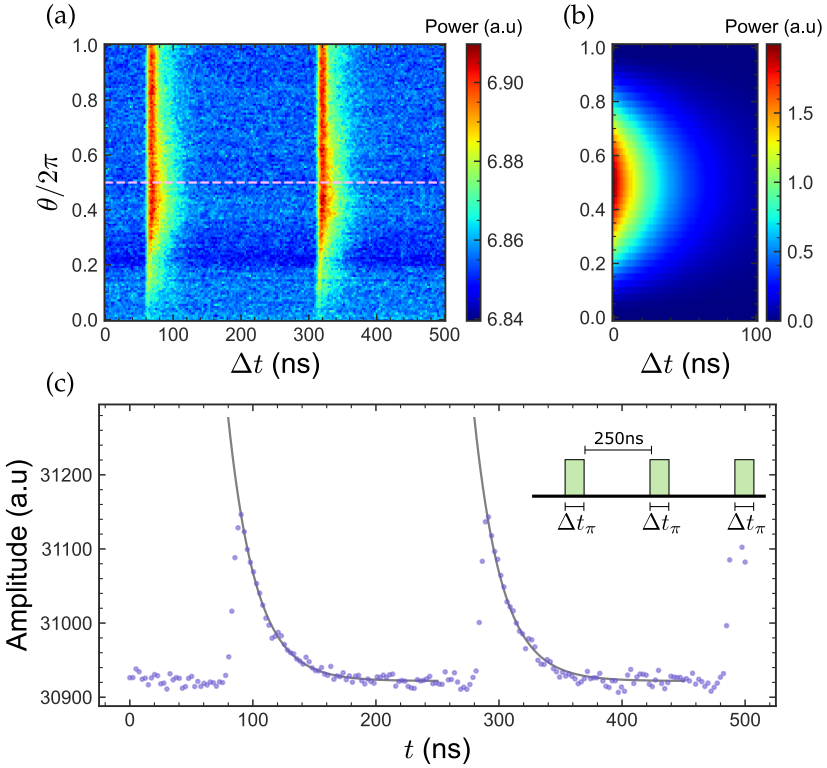

Figure 1.34: **(a)** Time-resolved power following (1.6.10) with varied excitation pulse lengths $\theta = \Omega t$. $N_{\text{repetitions}} \sim 10^7$; **(b)** Simulated power evolution following an excitation pulse according to (1.6.11); **(c)** Single power trace at $\theta = \pi \Rightarrow \Delta t = \Delta t_\pi$ with an exponential decay best fit e^{-t/T_1} (shown in pink in (a)). The pulses are repeated with a periodicity of 250 ns, which is much greater that the decay time of $T_1 = 33$ ns

Increasing the power of the drive (Ω), and hence the rotation angle $\theta = \Omega t$, one can track the population of the excited state $\rho_{11} \propto 1 - \cos(\theta)$ as a change in the maximum power from which the exponential decays start

$$P(\theta) \equiv \frac{\hbar\omega_q\Gamma_1}{2}\Big(1 - \cos(\theta)\Big)e^{-t/T_1}. \tag{1.6.11}$$

The time resolved signal of the absolute power culminating the investigation is presented in Fig. 1.34, where the relaxation time of **Photon Source A** is again confirmed to be T_1 =33 ns.

1.7 Conclusion

The outcome of this section has been the establishment of design, fabrication and measurement protocols for the further investigation on superconducting photon sources. The photon source was fabricated had a decay time of around 50 ns that could be manipulated by individual $\pi-$pulses, with further parameters presented in Tab. 1.6.

Table 1.6: Extracted parameters for the two photon sources investigated in this chapter.

Parameter	**Photon Source A**	**Photon Source B**
ω_q	6.95 GHz	4.48 GHz
$E_C/\hbar$	0.16 GHz	0.32 GHz
$E_{J0}/\hbar$	30 GHz	2.80 GHz
Γ_1	20 MHz	20 MHz
$T_2 \sim T_{2R}$	33-40 ns	40 ns
T_1	33 ns	40 ns

The next step will be the addition of a beam splitter at the low temperature stages, which will be realised with a microwave bi-directional coupler, in order to have the setup of Fig. 1.1. This will allow the measurement of $g^{(1)}(\tau)$ and $g^{(2)}(\tau)$ correlation functions using the optimised Photon source library (PSL) library for fast readout and processing of the data-heavy measurements.

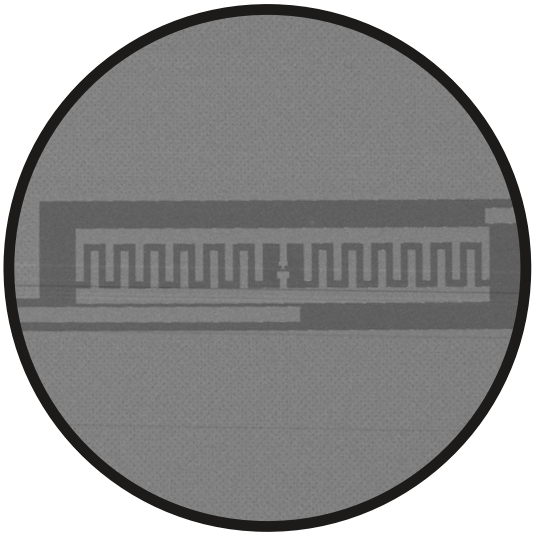

Chapter 2

Superconducting twin qubit

One of the limitations when operating superconducting qubits are their relatively short coherence times (T_2) beyond which quantum information becomes lost (see Fig. A.5). Since the first superconducting charge qubit was proposed and demonstrated in 1999 $T_2 = 2\,\mathrm{ns}$ [63], there has been ongoing research into increasing coherence times, to the $T_2/\tau_{\text{operation}} \geq 10,000$ threshold for running quantum algorithms [153, 154]. Most recently state-of-the art transmons show a benchmark value of $T_2 = 0.3\,\mathrm{ms}$ [155], still short of the $T_2 = 5500\,\mathrm{s}$ on trapped ions [156].

Large decoherence comes as a result of the macroscopic size of superconducting qubits, which couples them to a multitude of charge and flux noise sources in their local environment. Sec. 1.3 summarised the mechanisms that bring about decoherence, notably that noise sources close to the qubit frequency induce depolarisation (relaxation) with characteristic rate $\Gamma_1 = T_1^{-1} \propto S(\omega \sim \omega_q)$, and low frequency noise sources result in pure dephasing with characteristic rate $\Gamma_\varphi \propto S(\omega \sim 0)$.

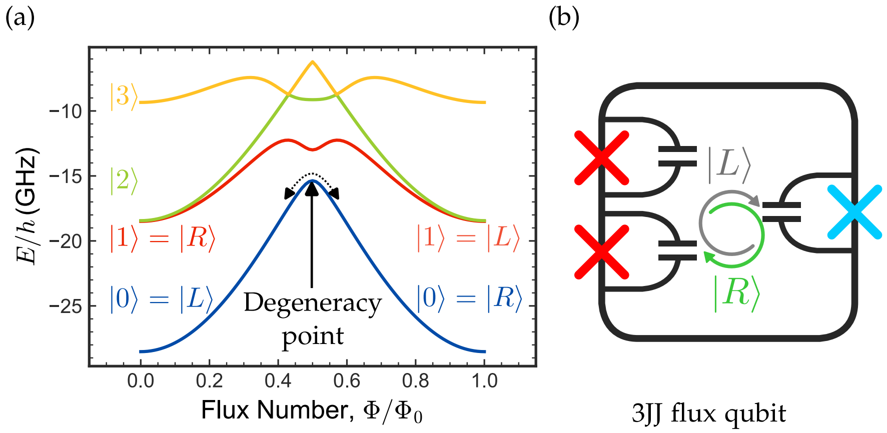

Figure 2.1: **(a)** Energy level of a 3-Josephson junction (JJ) flux qubit [157]. The qubit is best protected at the degeneracy point against magnetic field variations that changes the energy level structure; **(b)** Standard flux qubit circuit diagram showing JJs and their internal shunt capacitances. The superposition of persistent current states ($|L\rangle$, $|R\rangle$) readjusts to ensure flux quantisation and is equally weighted at the degeneracy point.

In flux qubits [66, 157] magnetic noise is the dominant contributor to decoherence [158]. For a standard 3-JJ flux qubit the transition frequency is described by a 2-level system (refer to A.2.2)

$$\hbar\omega_{01} = \hbar\sqrt{\varepsilon^2 + \Delta^2}, \tag{2.0.1}$$

where $\hbar\varepsilon = 2I_p(\Phi - n\Phi_0/2), n \in \mathbb{Z}$ is the energy bias controlled by external flux (Φ) and Δ is the tunneling energy between two persistent current states. Magnetic flux noise ($\delta\Phi$) induces variations in the energy bias ($\delta\varepsilon$), which to second order changes the transition frequency of the qubit $\delta\omega_q = \frac{\varepsilon}{\omega_q}\delta\varepsilon + \frac{1}{2}\frac{\Delta^2}{\omega^3}\delta\varepsilon^2 + \mathcal{O}(\delta\varepsilon^3)$[1], contributing to pure dephasing (Γ_φ) through longitudinal coupling. Operating the devices at the degeneracy point (see Fig. 2.1) protects to first order from these fluctuations [107] and reaches the regime $1/T_2 \sim 1/2T_1$ where depolarisation processes become the limiting factor for coherence [117, 158].

A number of fabrication and experimental techniques have protected from or minimised the noise sources introduced in Sec. 1.3.3, helping flux qubits progress from initial coherence times of 20 ns in 2003 [64] to 10 μs in 2011 [130], 80 μs in 2019 [105]:

- Treatment of wafers remove noisy Two level systems (TLS) in the amorphous layers in vicinity of the qubit [121, 159, 160]. B.1.1 shows this can be done with Hydrogen fluoride (HF) [161];
- Proper cleaning of wafer after development to remove resist residue that introduces hydroxides into JJ tunnel barriers and can cause atomic diffusion of the contaminants left on the surface [162]. An Oxygen (O_2) plasma descum procedure described in B.1.4 can be used for this;
- Annealing the sample at Room temperature (RT), which was experimentally shown to remove TLS [98]. Partial annealing occurred as a side effect of resist baking at 160^oC;
- Decoupling the qubit from the readout environment using 2D [112, 163, 164] and 3D resonators [165, 166], which only allow a narrow bandwidth of frequency channels to interact with the qubit (refer to Sec. 3.1.3 for a detailed overview);
- Running controllable growth of crystalline Al_2O_3 during the oxidation step (refer to B.2.1) of the JJ [167] as it has fewer defects that the usual amorphous Aluminum Oxide (AlO_x);
- Depositing the substrate layers using molecular-beam epitaxy instead of sputtering and moving to materials with thinner oxide layers such as superconducting nitrides [168];
- Adding normal metal quasiparticle traps to remove *hot* electrons out of the superconductor [169];
- Coating sample boxes with epoxy resin [156], and using a combination of rf-filters and isolators on the experimental lines to limit infra-red photon coming down from the RT stages [112] (see Sec. 1.6.1.3 for the cryogenic line setup);

---

[1] Taylor expansion of $\omega_{01} = \sqrt{\varepsilon^2 + \Delta^2}$ to second order.

- Using superconducting and cryoperm shielding to protect qubit from external magnetic fields (refer to Sec. 1.6.1.2);
- Improving vacuum to limit adsorption of O_2 which contributes 1/f magnetic noise [103]. Experiments are run at 10^{-6} mBar, which is several orders of magnitude above the ideal limit of 10^{-9} mBar.

The other approach to boosting coherence times, is to directly change the Hamiltonian of the circuit through new design elements that reduce coupling to persistent noise sources [170]:

- Decreasing the size off the JJs to statistically limit the number of uncontrollable TLS in the AlO_x layer [111, 171];
- Reducing the area of the JJ loops, to decrease the linking of magnetic field through $\Phi = BA$, whose variation will fluctuate the qubit's energy (2.0.1);
- **Charge qubits:** The transmon studied in Ch. 1 came from the shunting of a Cooper pair box (CPB) with a very large capacitor, that suppressed the effect of charge fluctuations by lowering the charging energy (E_C) [92]. Similar approaches were taken in designing the Gatemon [172] and C-shunt qubit [173]. This can further be extended by engineering the capacitor shape to decrease electric field concentration near the lossy metal-substrate and substrate-vacuum interfaces [109, 112, 174, 175];
- **Flux qubits:** As discussed above, with dominant Josephson and inductance energies ($E_J, E_L \gg E_C$) flux qubits are sensitive to magnetic fields and stray currents. Adding a 4th junction results in an easier-to-tune qubit due to the broader parameter range from the additional E_J contribution [176], while adding a shunting inductor decreases E_L [177, 178].

This part of the thesis will discuss an alternative flux-qubit topology that aims to counterbalance global flux noise variations. A chain of 15 such *twin* qubits was used in a coplanar waveguide to demonstrate flux-tuneable transmission of microwaves [179] (see Fig. 2.2 (a)). It caught the attention as a way of increasing the decoherence times through symmetry - usually a fluctuation of the magnetic field would lead to circulating current around the superconducting loop, disrupting the quantum state of the system.

An addition of a second loop shown in Fig. 2.2 (b) can be a way of balancing such effects out, since both of the symmetric loops would respond equally to the change of bias and circulating currents on the peripheral branches would undergo some form of

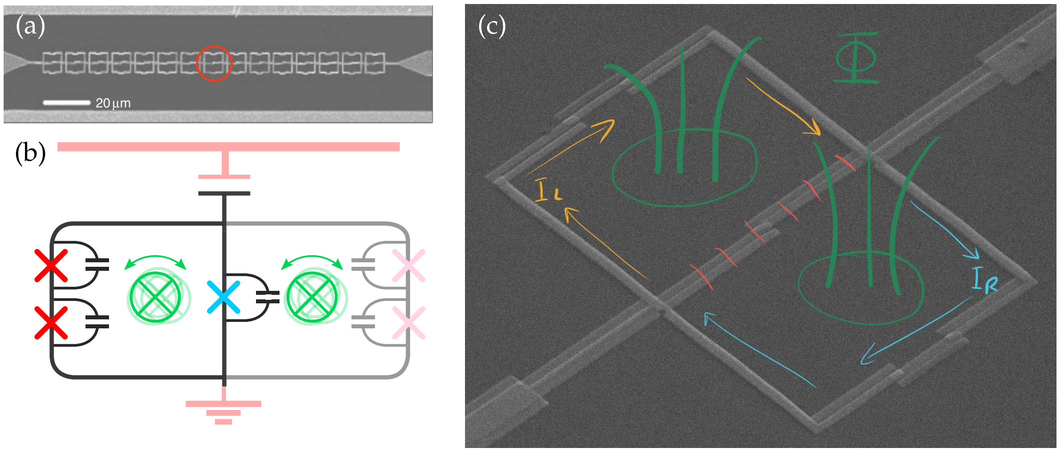

Figure 2.2: **(a)** Original chain of twin qubits on which the device from this section is based. Image from [179]; **(b)** Geometry of a 3-JJ flux qubit (dark) and proposal to make a symmetrical loop across the central JJ (light); **(c)** Artistic rendition of how the symmetrical loop will feel the same flux fluctuations, and the two counter currents flowing in the branches interfering in the middle branch.

cancellation in the middle branch (see Fig. 2.2 (c)). The circuit also has the potential of delocalising the ground state across the richer network, making it less sensitive to local perturbations [180].

This chapter describes measurements on one of these *twin* qubits - a symmetrical pair of superconducting loops, with two JJs in each, joined by a common JJ. Global magnetic flux variations should not affect the qubit as much, due to symmetrical compensation by the supercurrents circulating the loops. It begins by the mapping out the Hamiltonian and energies of the system to show the interesting regimes the devices can operate in (Sec. 2.1). The device is designed (Sec. 2.2) fabricated (Sec. 2.2.5) and characterised to compare it with the theoretical predictions made (Sec. 2.4).

2.1 Theory

This section will introduce the Hamiltonian used to model the twin qubit and perform an analysis of the implied features of the device: transition matrix elements between its different energy states; stability diagram under external flux biasing; shape of the Josephson potential that the qubit state resides in.

2.1.1 Modelling the qubit

The qubit in Fig. 2.3 will be treated in a lumped element model, since the individual element are much smaller than the microwaves they interact with $\lambda \sim$ cm. The 3 islands will be assigned a state (φ_i, N_i) describing the superconducting phase and number of Cooper pairs (CPs) that they isolate. The Hamiltonian $H = T + U$ should express the energy of the system through suitable quantum operators $\hat{\varphi}, \hat{N}$.

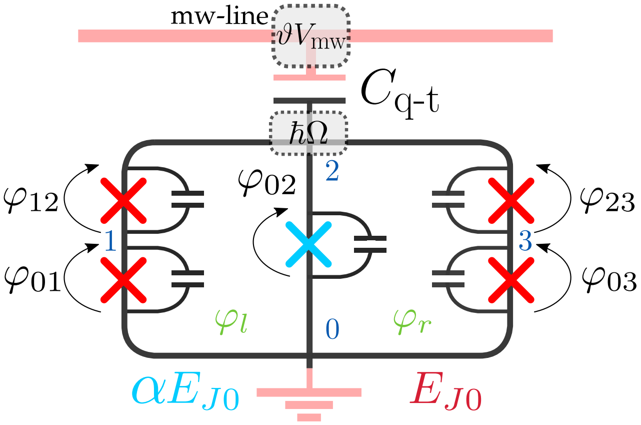

Figure 2.3: Schematic diagram of the twin qubit elements. The *twin* qubit is a symmetrical arrangement of two individual flux qubits [66] sharing the central JJ. The central JJ (blue) is different from the outside ones (red) by a factor α. Across each JJ is its self capacitance from its finite size. The system defines 3 islands for CP to reside on, which are labelled by their number occupation ($\vec{N} = |N_1, N_2, N_3\rangle$) and phases across its junctions (φ_{ij}) where i and j are the island indices. External flux biases introduce additional phases φ_l, φ_r in the left and right loops.

- **Charging energy (T):** Each JJ has capacitance C_{ij}, where i and $j \in \{0, 1, 2, 3\}$ are island numbers. The corresponding capacitance matrix, derived by writing equations of the form $Q_1 = C_{01}(V_1 - 0) - C_{12}(V_2 - V_1)$, is

$$\mathbf{C} = \begin{pmatrix} C_{01} + C_{12} & -C_{12} & 0 \\ -C_{12} & C_{12} + C_{02} + C_{23} + C_{\text{q-t}} & -C_{23} \\ 0 & -C_{23} & C_{03} + C_{23} \end{pmatrix}. \tag{2.1.1}$$

The outer JJs are identical $C_{01} = C_{12} = C_{03} = C_{23} = C$, while the central junction has an asymmetry α and a coupling capacitance $C_{\text{q-t}}$. Since the typical size of the JJs $\sim 100\,\text{nm}$ is much smaller that the size of the gate capacitor $\sim 10\,\mu\text{m}$, $C_{\text{q-t}} \ll C$ and the total capacitance of the central junction $\approx \alpha C$. The capacitance matrix (2.1.1) is simplified to

$$\mathbf{C} = C\hat{\mathbf{C}} \quad \text{where} \quad \hat{\mathbf{C}} = \begin{pmatrix} 2 & -1 & 0 \\ -1 & 2+\alpha & -1 \\ 0 & -1 & 2 \end{pmatrix}. \tag{2.1.2}$$

The capacitance matrix couples charges on the islands $\vec{Q} \equiv 2e\vec{N} = 2e\{N_1, N_2, N_3\}$ with their potentials $\vec{V} = \{V_1, V_2, V_3\}$ through

$$2e\vec{N} = \mathbf{C}\vec{V}.$$

The interaction of the CPs, carrying a charge $\vec{Q} = 2e\vec{N}$, and potentials on their respective islands is the electrostatic energy of the system $\vec{Q}\vec{V}$ and gives rise to the kinetic energy term of the Hamiltonian:

$$T = \vec{Q}^T\vec{V} = 4CE_C\vec{N}^T\hat{\mathbf{C}}^{-1}\vec{N}. \tag{2.1.3}$$

◎ **Josephson Energy (U):** Each JJ contributes $E_{Jij}\big(1 - \cos(\varphi_{ij})\big)$ to the potential energy of the system. The loops are biased by an external magnetic field, which can be accounted for as externally induced phases in the left (φ_l) and right (φ_r) loops (see Fig. 2.3). Therefore $\varphi_{01} + \varphi_{12} - \varphi_{02} = -\varphi_l$ and $\varphi_{02} - \varphi_{32} - \varphi_{03} = -\varphi_r$ are the phase-bounding conditions due to flux quantisation (refer to A.1.4). The potential energy of the full device is then

$$\begin{aligned} U =& E_{J0}\big[4 + \alpha - \alpha\cos\varphi_{02} - \cos\varphi_{01} - \cos\varphi_{03} \\ & - \cos(\varphi_{02} - \varphi_{01} - \varphi_l) - \cos(\varphi_{02} - \varphi_{03} + \varphi_r)\big]. \end{aligned} \tag{2.1.4}$$

The system's Hamiltonian is a combination of (2.1.3) and (2.1.4)

$$\begin{aligned} H &= T + U \\ &= 4CE_C\vec{N}^T\hat{\mathbf{C}}^{-1}\vec{N} + 4E_{J0} + \alpha E_{J0} \\ &- \frac{\alpha E_{J0}}{2}\big(e^{i\varphi_{02}} + e^{-i\varphi_{02}}\big) - \frac{E_{J0}}{2}\big(e^{i\varphi_{01}} + e^{-i\varphi_{01}}\big) - \frac{E_{J0}}{2}\big(e^{i\varphi_{03}} + e^{-i\varphi_{03}}\big) \\ &- \frac{E_{J0}}{2}\big(e^{i\varphi_{02} - i\varphi_{01} - i\varphi_l} + e^{-i\varphi_{02} + i\varphi_{01} + i\varphi_l}\big) \\ &- \frac{E_{J0}}{2}\big(e^{i\varphi_{02} - i\varphi_{03} + i\varphi_r} + e^{-i\varphi_{02} + i\varphi_{03} - i\varphi_r}\big). \end{aligned} \tag{2.1.5}$$

(2.1.5) is represented in the charge basis $\{|N_1, N_2, N_3\rangle\}$ where state $|-1, 0, 1\rangle$ would correspond to a CP occupation of -1, 0 and 1 on islands 1, 2 and 3. Using the relationships in Tab. 2.1 and dropping constant energy terms, the Hamiltonian will have a matrix representation

$$
\begin{aligned}
H_{|n_1,N_2,N_3\rangle} = \sum_{N_1,N_2,N_3} & U(N_1, N_2, N_3)\,|N_1, N_2, N_3\rangle\,\langle N_1, N_2, N_3| \\
& - \frac{\alpha E_{J0}}{2}\Big[\,|N_2 - 1\rangle\,\langle N_2| + |N_2 + 1\rangle\,\langle N_2|\,\Big] \otimes \mathbb{I}_{1,3} \\
& - \frac{E_{J0}}{2}\Big[\,|N_1 - 1\rangle\,\langle N_1| + |N_1 + 1\rangle\,\langle N_1|\,\Big] \otimes \mathbb{I}_{2,3} \\
& - \frac{E_{J0}}{2}\Big[\,|N_3 - 1\rangle\,\langle N_3| + |N_3 + 1\rangle\,\langle N_3|\,\Big] \otimes \mathbb{I}_{1,2} \\
& - \frac{E_{J0}}{2}\Big[e^{-i\varphi_l}\,|N_1 - 1, N_2 + 1\rangle\,\langle N_1, N_2| + e^{+i\varphi_l}\,|N_1 + 1, N_2 - 1\rangle\,\langle N_1, N_2|\,\Big] \otimes \mathbb{I}_3 \\
& - \frac{E_{J0}}{2}\Big[e^{+i\varphi_r}\,|N_2 + 1, N_3 - 1\rangle\,\langle N_2, N_3| + e^{-i\varphi_r}\,|N_2 - 1, N_3 + 1\rangle\,\langle N_2, N_1|\,\Big] \otimes \mathbb{I}_1,
\end{aligned}
$$

shown in Fig. 2.4, which will be different for different values of the biasing fluxes (φ_r, φ_l).

Table 2.1: Representations in the charge basis. Kinetic terms $T(N_1, N_2, N_3)$ naturally fall on the diagonal axis of the matrix. The phase-dependent terms $U(\varphi_1, \varphi_2, \varphi_3, \varphi_{\text{ext}})$ are represented using the procedure in Sec. A.5.1.

$4CE_C\vec{N}^T\hat{\mathbf{C}}^{-1}\vec{N}$	$\begin{cases} \sum_{N_1,N_2,N_3} \mathbf{U}(N_1, N_2, N_3)\,\|N_1, N_2, N_3\rangle\,\langle N_1, N_2, N_3\| \\ \mathbf{U}(N_1, N_2, N_3) = 4CE_C\begin{pmatrix} N_1 & N_2 & N_3 \end{pmatrix}\hat{\mathbf{C}}^{-1}\begin{pmatrix} N_1 \\ N_2 \\ N_3 \end{pmatrix} \end{cases}$
$\cos(\varphi_{0i}) = \frac{1}{2}\left(e^{i\varphi_{0i}} + e^{-i\varphi_{0i}}\right)$	$\begin{cases} e^{i\varphi_{0i}} = \sum_{N_i}\|N_i + 1\rangle\,\langle N_i\| \\ e^{-i\varphi_{0i}} = \sum_{N_i}\|N_i - 1\rangle\,\langle N_i\| \end{cases}$
$\cos(\varphi_{0i} - \varphi_{0k}) = \frac{1}{2}\left(e^{i\varphi_{0i} - i\varphi_{0k}} + e^{-i\varphi_{0i} + i\varphi_{0k}}\right)$	$e^{i(\varphi_{0i} - \varphi_{0k})} = \Big[\sum_{N_i}\|N_i + 1\rangle\,\langle N_i\|\Big] \otimes \Big[\sum_{N_k}\|N_k - 1\rangle\,\langle N_k\|\Big]$

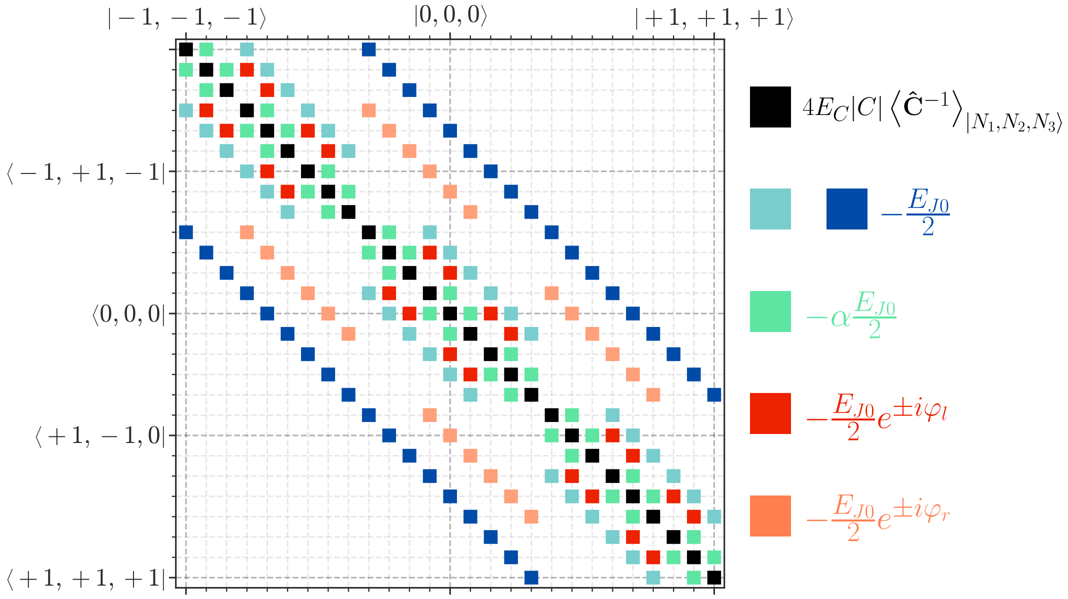
$|-1,-1,-1\rangle$
$|0,0,0\rangle$
$|+1,+1,+1\rangle$
$\langle -1,+1,-1|$
$\langle 0,0,0|$
$\langle +1,-1,0|$
$\langle +1,+1,+1|$
$4E_C|C|\left\langle \hat{C}^{-1} \right\rangle_{|N_1,N_2,N_3\rangle}$
$-\frac{E_{J0}}{2}$
$-\alpha\frac{E_{J0}}{2}$
$-\frac{E_{J0}}{2}e^{\pm i\varphi_l}$
$-\frac{E_{J0}}{2}e^{\pm i\varphi_r}$

Figure 2.4: Hamiltonian in the CP-basis representation for 3-CP-states-per-island (27 system states). Black squares denote the kinetic terms that all fall on the main diagonal. Blue and green squares denote simple off-diagonal terms distributed symmetrically about the main diagonal, arising from terms such as $\cos(\varphi_{02})$. Pink and red blue squares have an additional flux dependence ($e^{i\varphi_l}, e^{i\varphi_r}$) arising from terms such as $\cos(\varphi_{02} - \varphi_{01} - \varphi_l)$.

2.1.2 Stability regions

Figure 2.5 (a) shows the energetically-favourable minimal value of the potential energy $U_{\text{min}}(\varphi_l, \varphi_r) = \min_{\varphi_{01},\varphi_{12},\varphi_{03}}(U)$ of (2.1.4) as a function of the external phases, done through numerical evaluation. Collectively, the figures demonstrate that there are hexagonal cells centered at $\varphi_l = 2\pi F_L$ and $\varphi_r = 2\pi F_R$ where $F_L, F_R \in \mathbb{Z}$.

Energetically favourable configurations with the *stable* flux states are denoted with $|F_L F_R\rangle$. For example, $|00\rangle$ denotes the favourable state of the system in the cell centered at $\varphi_l = 0$ and $\varphi_r = 0$. Moving through a boundary of this cell results in a new *stable* flux configuration, which is labelled in Fig. 2.5 (a) for four of the cells. The following sections will investigate the features of this potential in more detail.

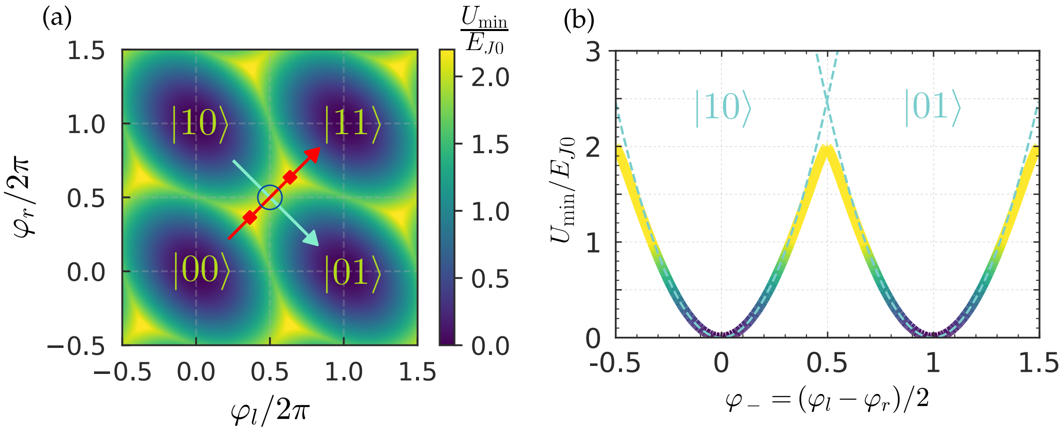

Figure 2.5: **(a)** The minimal value of the Josephson potential is plotted as a function of externally induced phase in the left (φ_l) and right (φ_r) loops. The stable flux configurations are denoted as $|00\rangle$, $|01\rangle$, $|10\rangle$, and $|11\rangle$. When the loops are symmetrically biased, in the case of a uniform global magnetic field and identical loop areas, the potential takes values along the red arrowed line. The triple points are marked by red squares - they terminate the $|01\rangle - |10\rangle$ degeneracy line; **(b)** Energies along the blue line. The coloured curve is the minimised potential and the dashed curves are parabolic approximations for $|01\rangle$ and $|10\rangle$ flux configurations.

2.1.2.1 Potential wells

Considering now the properties of the Josephson potential in cells centered at $\{\varphi_l/2\pi, \varphi_r/2\pi\} = \{F_L, F_R\}$. The minimal values of the Josephson potential can be found from $\partial U/\partial\varphi_{ij} = 0$ (the complete steps are shown in A.5.2). Differentiating with respect to φ_{01} and φ_{03} and applying the phase-bounding conditions in the loops

$$\begin{aligned}\varphi_{01} = \varphi_{12} &= \frac{\varphi_{02} - \varphi_l}{2} + \pi F_L,\\ \varphi_{03} = \varphi_{32} &= \frac{\varphi_{02} + \varphi_r}{2} - \pi F_R.\end{aligned}$$

where $F_L, F_R \in \mathbb{Z}$ index the flux state in the left and right loops. The minimised Josephson potential reads

$$\begin{aligned}U_{\min}(F_L, F_R) = E_{J0}\Big[4 + \alpha - 2(-1)^{F_L}\cos\left(\frac{\varphi_{02} - \varphi_l}{2}\right)\\ - 2(-1)^{F_R}\cos\left(\frac{\varphi_{02} + \varphi_r}{2}\right) - \alpha\cos\varphi_{02}\Big].\end{aligned} \tag{2.1.6}$$

which in turn allows a minimisation in φ_{02}

$$\begin{aligned}\frac{\partial U}{\partial\varphi_{02}} = (-1)^{F_L}\sin\left(\frac{\varphi_{02} - \varphi_l}{2}\right) +\\ (-1)^{F_R}\sin\left(\frac{\varphi_{02} + \varphi_r}{2}\right) + \alpha\sin\varphi_{02} \equiv 0.\end{aligned} \tag{2.1.7}$$

This condition is equivalent to the Kirchhoff's law for currents that flow in the loops of the device. Expansion in first order results in

$$\varphi_{02} \approx \frac{\varphi_l - \varphi_r - 2\pi(F_L - F_R)}{2(1+\alpha)}. \tag{2.1.8}$$

Substituting (2.1.8) into (2.1.6), and expanding up to second order around the center of the cells, gives a good approximation to the shape of the potentials. The blue curve in Fig. 2.5 (b) shows the potential along the blue line ($\varphi_+ = \pi$, $\varphi_+ = (\varphi_l + \varphi_r)/2$) minimised in all φ_{ij}. Two blue parabolic curves are taken from the series expansion of $U_{\min}$ with the left parabola taken for $F_L = 0$, $F_R = 1$ (state $|01\rangle$) and the right one for $F_L = 1$, $F_R = 0$ (state $|10\rangle$). This approximation is equivalent to the replacement of the JJs by linear inductances that do not have a periodic phase dependence. The parabolic approximations are accurate for the center of the cells, deviating from the exact calculations only at boundary of the cell ($\varphi_l/2\pi \sim 0.5$).

2.1.2.2 Triple point

Figure 2.5 (a) also identifies a *triple-point* (φ_T, red squares) where energies of three configurations are degenerate such that $U(F_L, F_R) = U(F_L, F_R + 1) = U(F_L + 1, F_R)$.

- Using (2.1.6) and (2.1.7) to minimise $U(0,0)$, it is found that $\varphi_{02} = 0$ and, therefore, $U_{\min}(0,0)/E_{J0} = 4 - 4\cos(\varphi_T/2)$;
- Similarly the condition for minimal $U(0,1)$ is found to be $\sin(\varphi_{02}/2) = \sin(\varphi_T/2)/\alpha$ and $U_{\min}(1,0)/E_{J0} = 4 - 2\sin^2(\varphi_T/2)/\alpha$.

The condition $U_{\min}(0,0) = U_{\min}(0,1) = U_{\min}(1,0)$ results in the solution (refer to A.5.3)

$$\varphi_T = 2\arccos(\sqrt{1+\alpha^2} - \alpha).$$

For $\alpha = 1$, $\varphi_T/2\pi \approx 0.36$ and the total length of the degeneracy $|01\rangle - |10\rangle$ line has an analytical value $\Delta\varphi_l/2\pi = \Delta\varphi_r/2\pi \approx 0.28$.

2.1.2.3 Phase distribution

Figure 2.6 (a-c) show the associated phase distributions across the central (φ_{02}) left ($\varphi_{01} + \varphi_{12}$) and right ($\varphi_{03} + \varphi_{32}$) arms when the potential is minimised. Note that $\varphi_{01} = \varphi_{12}$ and $\varphi_{03} = \varphi_{32}$ as it is expected that the same current flows in junctions situated sequentially on a branch, and $I_{ij} = I_{cij}\sin\varphi_{ij}$ where I_{cij} is the critical current across junction ij.

The abrupt change of the phase by 2π at the boundaries of the cells corresponds to a flux quantum (Φ_0) jumping in or out of the loops:

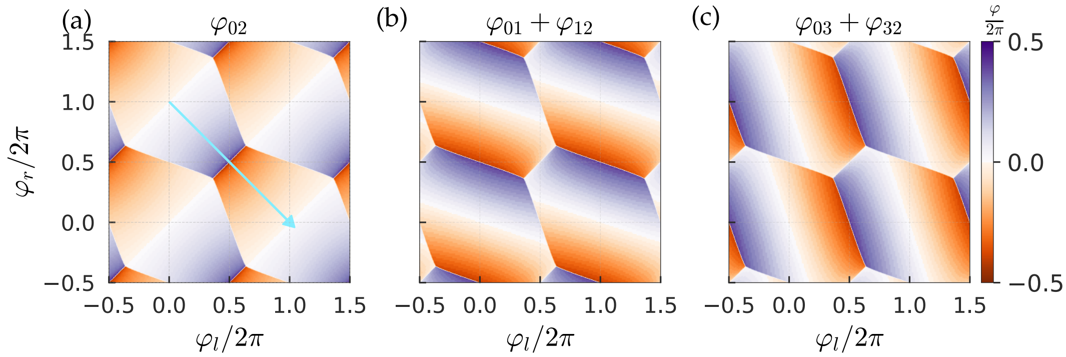

Figure 2.6: Stability diagrams of the system: **(a, b, c)** show phases φ_{02}, $\varphi_{01}+\varphi_{12}$, and $\varphi_{03}+\varphi_{32}$. The abrupt phase change by $\sim 2\pi$, indicated by the blue arrow, corresponds to a flux quantum jumping through the central junction.

- Motion along the blue line in Figure 2.6 (a) is a trajectory of a flux quantum jumping from the right loop directly into the left loop with phase across the central junction (φ_{02}) abruptly jumping from -π to π;
- Varying φ_l at fixed φ_r (e.g. $\varphi_r = 0$) results in the phase jump in the left shoulder of the structure when the total phase ($\varphi_{01}+\varphi_{12}$) flips from $-\pi$ to π close to $\varphi_l = \pi + 2\pi F_L$ (see Fig. 2.6 (b)). This corresponds to movement of a flux quantum into the left loop;
- Similarly, a flux quantum movement occurs into the right loop close to $\varphi_r \approx \pi + 2\pi F_R$. The flux in the right branch ($\varphi_{03}+\varphi_{32}$) is flipped from $-\pi$ to π (see Fig. 2.6 (c)).

2.1.3 Anharmonic Josephson potentials

Next consider the Josephson potential in the φ_{ij} space at fixed φ_l and φ_r, in particular the symmetric point $\varphi_l = \pi$ and $\varphi_r = \pi$ on the boundary of cells $\{0,1\}$ and $\{1,0\}$ where states $|01\rangle$ and $|10\rangle$ are degenerate (see the blue circle in Fig. 2.5).

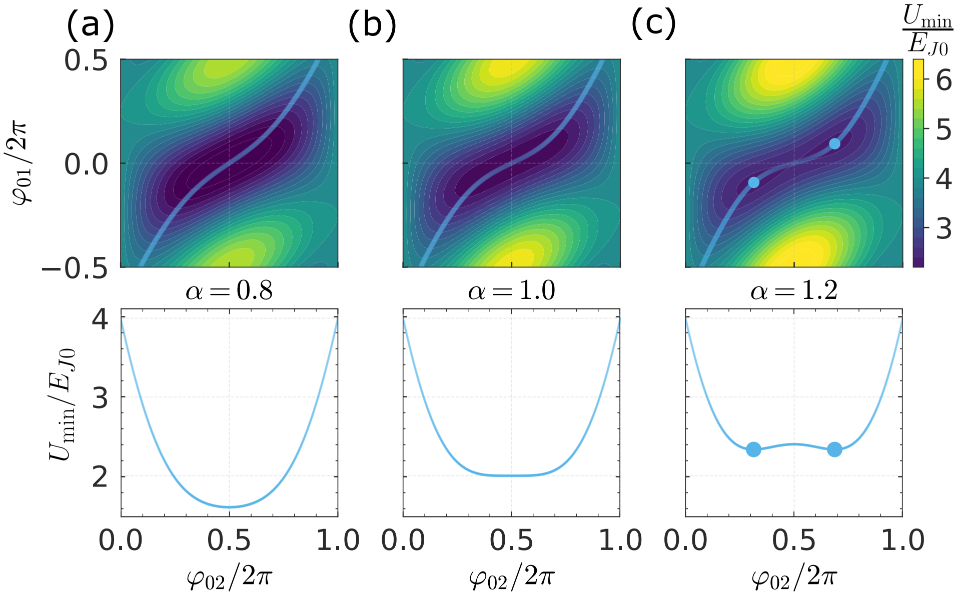

Figure 2.7: Potential minimum at the degeneracy point ($\varphi_l = \pi, \varphi_r = \pi$). The plots show 2D Josephson potential (2.1.9) in φ_{02}-φ_{01} coordinates and 1D potentials (2.1.10) along the minimum as a function of φ_{02} (light blue line) for: **(a)** $\alpha = 0.8$; **(b)** $\alpha = 1.0$; **(c)** $\alpha = 1.2$. A double well emerges for $\alpha > 1.0$ (light blue points).

Because the potential is a function of three independent variables (φ_{01}, φ_{02}, and φ_{03}), for visualisation on a 2D plot the number of variables is reduced by excluding φ_{03} through minimisation. A.5.4 shows that $\varphi_{03} = \varphi_{32} = (\varphi_{02} \mp \pi)/2$ and so

$$\min_{\varphi_{03}}(U) = E_{J0}[4 + \alpha - \alpha \cos \varphi_{02} - \cos \varphi_{01} \mp 2 \sin \frac{\varphi_{02}}{2} + \cos(\varphi_{02} - \varphi_{01})]. \tag{2.1.9}$$

Figure 2.7 (a-c) show $\min_{\varphi_{03}}(U)$ for three different α parameters ($\alpha = 0.8$, $\alpha = 1.0$, and $\alpha = 1.2$). All phases are defined on a 2π interval, however for clarity φ_{02} is shifted along the x axis from $[-\pi; \pi]$ to $[0; 2\pi]$ to center on the potential minimum. The 2π-phase flip from $\varphi_{02} = -\pi \rightarrow \pi$ along the blue line in Fig. 2.6 (accompanied by a flux quantum jump) now corresponds to $\varphi_{02} = \pi - 0 \rightarrow \pi + 0$.

To follow the potential along the minimum trajectory shown in light blue lines, another minimisation of (2.1.9) is performed, this time with respect to φ_{01} for $\varphi_{01} = \varphi_{12} = (\varphi_{02} \pm \pi)/2$ finding

$$\min_{\varphi_{03}, \varphi_{02}}(U) = E_{J0}[4 + \alpha - \alpha \cos \varphi_{02} \mp 4 \sin \frac{\varphi_{02}}{2}]. \tag{2.1.10}$$

The bottom plots of Fig. 2.7 show the potential $U(\varphi_{02})/E_{J0} = \min_{\varphi_{03},\varphi_{01}} U/E_{J0}$ along the light blue trajectories of the corresponding 2D plot. One can see that the potential has a minimum (or minima) in the vicinity of $\varphi_{02} = \pi$, which will be labelled as a deviation $\delta\varphi_{02} = \varphi_{02} - \pi$

$$\min_{\varphi_{01},\varphi_{03}} (U) \approx E_{J0} \left[4 + \alpha + \alpha \cos \delta\varphi_{02} - 4 \cos \frac{\delta\varphi_{02}}{2} \right]. \tag{2.1.11}$$

When $\delta\varphi_{02}$ is small, both terms are approximated by parabolas, where the first term behaves as if it were classical linear inductance. To gauge the effect of α on the shape of the potential minima, a series expansion up to second order gives $U \approx E_{J0}[2\alpha + (1-\alpha)(\delta\varphi_{02}^2)/2]$:

- ◎ (a) $\alpha < 1$: the potential is anharmonic but with a nonzero second order curvature at the center;
- ◎ (b) $\alpha = 1.0$: corresponds to the case when the second order of the potential at the minimal point is completely suppressed, in contrast to the three and four-junction flux qubits where the potential well would have already split into two;
- ◎ (c) $\alpha > 1$: the potential curvature at $\delta\varphi_{02} = 0$ becomes negative and the potential shape turns to a double well.

The values of the potential minima can be found by a final differentiation of (2.1.11) with respect to φ_{02}

$$\min_{\varphi_{01},\varphi_{03},\varphi_{02}} (U) \approx 2 \sin \frac{\delta\varphi_{02}}{2} \big(1 - \alpha \cos \frac{\delta\varphi_{02}}{2}\big),$$

resulting in two minima positions depending of α:

$$\begin{cases} \varphi_{02} = \pi, & \alpha \leq 1 \\ \varphi_{02} = \pi \pm 2 \arccos \dfrac{1}{\alpha}, & \alpha > 1. \end{cases}$$

When $\alpha > 1$, the potential has two minima at $\varphi_{02} = \pi \pm \varphi$, where $\varphi = 2\arccos(1/\alpha)$, these are indicated with blue dots in Fig. 2.7. If the phase is mapped back into the $[-\pi;\pi]$ range, then $\varphi_{02} \approx -\pi + \varphi$ and $\varphi_{02} \approx \pi - \varphi$. This means that with small φ, the jump of the system from one well to another is accompanied by change of the phase by nearly 2π and therefore a jump of a flux quantum through the middle junction.

2.1.4 Energy spectrum

2.1.4.1 Truncation of matrix

Having investigated the features of the potential, evaluation of the full energies (E_{N_1,N_2,N_3}) of the eigenstates ($|N_1, N_2, N_3\rangle$) using the matrix representation (2.1.1) is performed. To decide on the number of states for the simulation, a sufficiently complete system state of 19 interacting CPs was taken, which was them methodically truncated[2].

The deviation of the energy spectra calculated for different number of included CP-states is shown in Fig. 2.8. With $n = 9$ CP-states the system is almost as good as with the complete system state. This truncation was used for all further simulations.

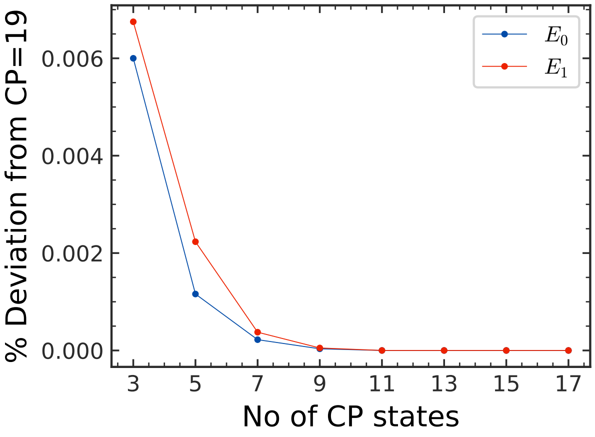

Figure 2.8: The energy levels for state $|0\rangle$ (blue) and $|1\rangle$ (red) were simulated for different numbers of interacting CP and compared to the simulation with 19 CP. Consistency is reached for simulations with 9 CP.

2.1.4.2 Energy spectrum

Figure 2.9 shows the ground-to-excited state transition energies of the qubit under local phase biases $E_{01}(\varphi_l, \varphi_r) = E_1 - E_0$. The eigenenergies ($E_i$) were evaluated by constructing the matrix (2.1.1) for every combination of phase biases and using a sparse matrix evaluator to compute the eigenvalues.

In the ideal case of symmetric bias ($\varphi_l = \varphi_r$) and away from the symmetric point ($\varphi_l = \varphi_r = \pi$) the transition energy varies slowly with the global magnetic field, demonstrating the flat curve I in Fig. 2.9 (c). In the perpendicular directions to $\varphi_+ = (\varphi_l + \varphi_r)/2$ = const, attributed to events when the system undergoes completely anticorrelated fluctuations in

---

[2] Further increase of the number of states does not improve the accuracy of calculations, since those state would have a large charging energy and would not participate in the qubits dynamics.

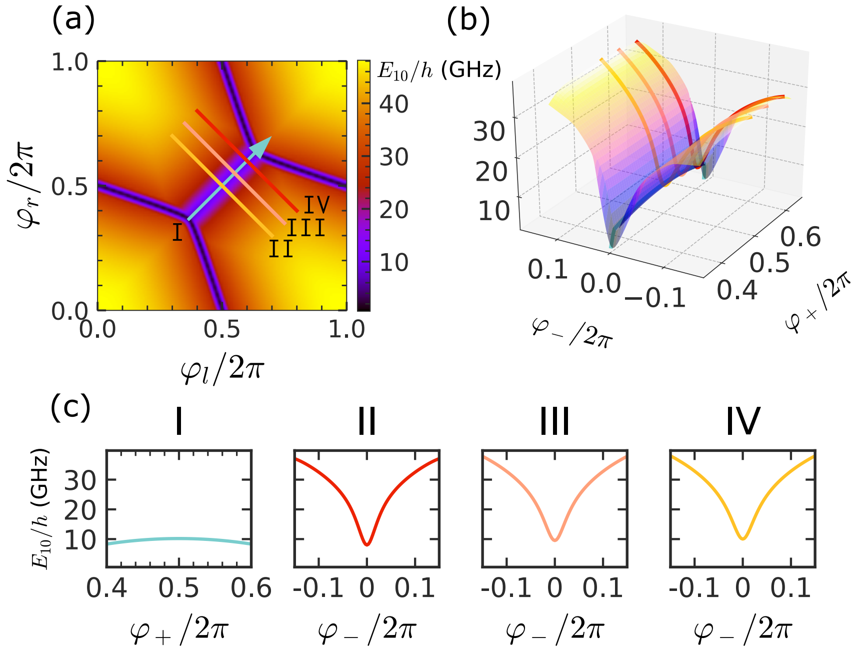

Figure 2.9: Energies of ground-to-excited state transitions. **(a-b)** Transition energies as functions of external phase biases $\varphi_l, \varphi_r, \varphi_+ = (\varphi_l + \varphi_r)/2, \varphi_- = (\varphi_l - \varphi_r)/2$; **(c)** Transition energies along lines denoted I, II, III and IV. Curve I shows the transition energy as a function of the global magnetic flux, which increases with φ_+. Curves II, III, and IV show the transition energy as a function of the difference in magnetic fluxes, denoting local flux fluctuations. The qubit is much better protected against the global field fluctuations as curve I has a much smaller curvature.

the two loops such as a spin flip, energy bands have a steep gradient demonstrated by the curves II, III, IV in Fig. 2.9 (c).

Numerically calculated curvatures at $\varphi_l = \varphi_r = \pi$ for local and global fields are $\hbar^{-2}\partial^2 E_{10}/\partial\varphi_-^2 \approx -380\ \mathrm{GHz}/\Phi_0^2$ and $\hbar^{-2}\partial^2 E_{10}/\partial\varphi_+^2 \approx 4 \times 10^4\ \mathrm{GHz}/\Phi_0^2$ correspondingly. This confirms that although in first order there is no sensitivity to both global and local flux noise, in the second order the qubit is much better protected against the global fluctuations. The local noise can be produced by spin fluctuations due to jumping electrons explored in Sec. 1.3.3. Local flux sensitivity can be reduced in expense of anharmonicity by increasing the junction shunting capacitances [130].

2.1.5 Transition matrix elements

Transition matrix elements represent the *amplitude* of the induced potential on island 2, under a system transition $|j\rangle \leftrightarrow |i\rangle$ (refer to A.5.5)

$$d_{ij} = \langle i|\, \hat{V}_2 \,|j\rangle \equiv \frac{2E_C}{e(1+\alpha)} \langle i|\, [\hat{n}_1 + 2\hat{n}_2 + \hat{n}_3]\, |j\rangle \,. \tag{2.1.12}$$

The transitions between energy levels are shown in the top row of Fig. 2.10 and their magnitude (2.1.12) is on the bottom rows for two mutually perpendicular sweeps of the biasing fields.

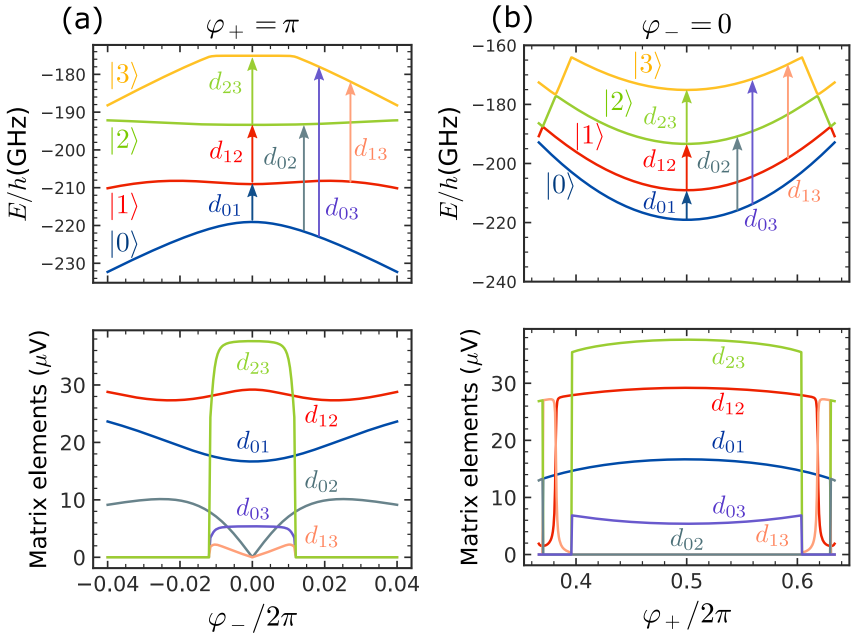

Figure 2.10: Energies of the system and the corresponding transition matrix elements. **(a)** As a function of the local magnetic flux deviations with $\varphi_+ = \pi$ perpendicular to the $|01\rangle$-$|10\rangle$ degeneracy line; **(b)** As a function of the global magnetic flux bias with $\varphi_- = 0$.

The general rule for transitions is that all elements are nonzero close to the degeneracy point ($\varphi_- = 0$). However along the degeneracy line there are clear selection rules:

- The transitions between even-odd ($|k\rangle \leftrightarrow |k+1\rangle$) and odd-even states ($|k\rangle \leftrightarrow |k+3\rangle$) characterised by $\{d_{01}, d_{12}, d_{23}, d_{03}\}$ are allowed;
- The transitions between even-even or odd-odd states are prohibited $\{d_{02} = d_{13} = 0\}$;

In contrast with a flux qubit for which $d_{02} = 0$ strictly at the degeneracy point ($\Phi_0/2$), for a twin qubit it happens for a wide magnetic flux interval.

2.1.6 Qubit asymmetry

Figure 2.11 compares the transition spectra for a qubit under flux biases φ_l, $\eta\varphi_r$ to its two loops under symmetric ($\eta = 1$) and asymmetric cases. Asymmetry is expected to be in the range of $\eta \leq 1.02$ based on the precision of fabrication (refer to Sec. 2.3).

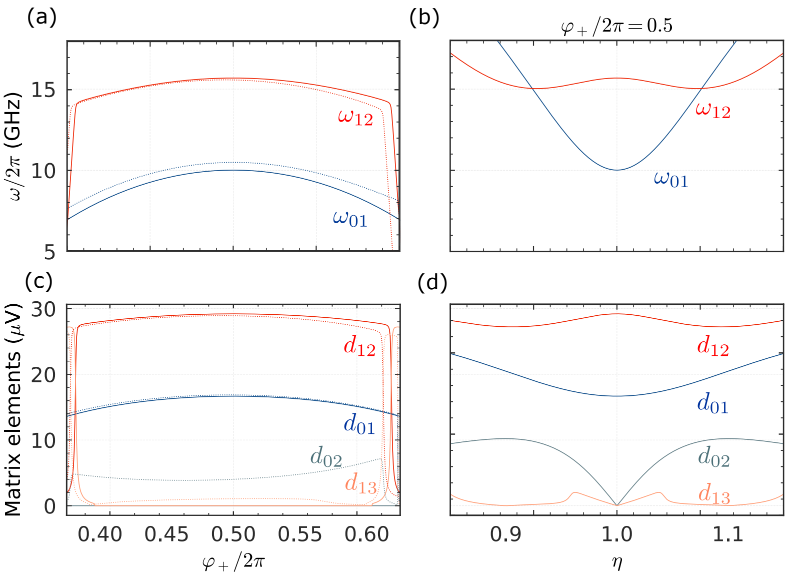

Figure 2.11: Effect of loop asymmetry on the qubit spectrum. **(a, c)** The transition frequencies and dipole matrix elements for symmetric, $\eta = 1$ (solid lines), and asymmetric, $\eta = 1.02$ (dashed lines), qubits. The curves are periodic in Φ_0. **(b, d)** Effect of qubit asymmetry (η) on the transition frequencies and dipole matrix elements at $\varphi_+ = \pi$. Transitions that are forbidden under perfect symmetry, $|0\rangle \leftrightarrow |1\rangle$ (d_{01}) and $|1\rangle \leftrightarrow |3\rangle$ (d_{13}), can be reintroduced when symmetry between the two loops is broken.

A small asymmetry has a minor effect on the transition energies, as seen by the vanishing derivative of ω_{01} and ω_{12} at $\eta = 1$ in Fig. 2.11 (b). However dipole matrix elements determining the selection rules are strongly affected, immediately reintroducing the transition between even-even (d_{02}) and odd-odd (d_{13}) states. Upon perfect symmetry of the two loops, the $|1\rangle \rightarrow |3\rangle$ transitions matrix element $\langle 1|H|3\rangle$ would vanish, creating a dark state transition.

This shows that the operational range of the qubit lies approximately from 0.43 to 0.57 of Φ_0, where the α-junction is in the superposed 0-π state [181]. Away from that range the transition frequency ω_{12} diverges (see Fig. 2.11 (a)).

2.2 Design

The design of a twin qubit based off Fig. 2.3 has additional requirements to that of the transmon photon source (Sec. 1.4):

- Achieve the most symmetrical realisation to approach the $\eta = 1$ limit;
- Fabricate multiple qubits with a varied central junction asymmetry α, to increase the yield of devices within the operable parameter range.

2.2.1 Operating energies

Based on the eigenenergies (E_i) and resulting transition frequencies ($\hbar\omega_{ij} = E_i - E_j$) of Hamiltonian (2.1.1), the required E_C, E_{J0}, α are chosen to land in the 2-12 GHz window of the microwave electronics. Figure 2.12 demonstrates how both the first (ω_{01}) and second (ω_{12}) transitions fall comfortably in this window with $E_C \sim 5$ GHz and $E_{J0} \sim 90$ GHz for a wide range of junction asymmetries $\alpha \in [1, 1.3]$.

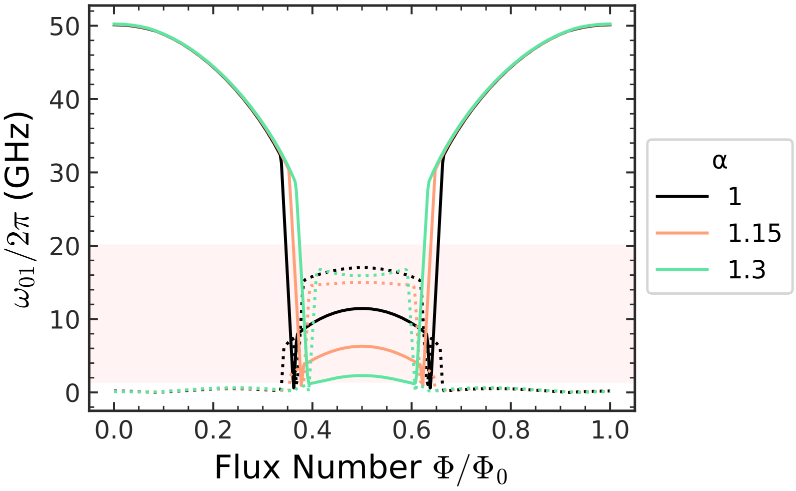

Figure 2.12: Simulation of transition frequencies ω_{01} (solid) and ω_{12} (dotted) using (2.1.1) with $E_C = 5$ GHz and $E_{J0} = 90$ GHz designed to fall into the frequency range 2-20 GHz. The asymmetry of the central JJ for the 3 plot pairs is scaled from $\alpha = 1.0, 1.15, 1.3$.

For the transmon (Ch. 1) charging energy (E_C) and Josephson energy (E_{J0}) depended on different elements of the circuit - the shunt capacitor and JJ dimensions respectively. In the flux qubit, both energies are determined through the dimension of the JJ alone:

- $E_c = e^2/2C$: The absence of a large shunt capacitor means that for the flux qubit the self capacitance of its JJ sets the charging energy for the system. With reference to

Fig. 1.10, the JJ can be modelled as a parallel plate capacitor with capacitance

$$C = \frac{\varepsilon_r \varepsilon_0 A}{T},$$

for an overlap area of A and an $\mathrm{AlO_x}$ layer of thickness $T \approx 2\,\mathrm{nm}$ with $\varepsilon_r = 11.7$;

- E_{J0} would be determined from the sheet resistance $R_\square$ and the size of the JJ in N_{sq} through (1.4.1).

Hence, while E_C is determined by the absolute area of the overlap, E_{J0} is determined by the overlaps length-to-width ratio, allowing for both conditions to be optimised independently. A JJ with dimensions $A = 800 \times 200\,\mathrm{nm}^2$ ($N_{\mathrm{sq}} = 4$) and sheet resistance $R_\square = 6700\,\mathrm{k}\Omega$ would result in $E_C = 2.75\,\mathrm{GHz}$ and $E_{J0} = 82\,\mathrm{GHz}$, consistent with the targeted values of the simulation performed in Fig. 2.12. To attain the required sheet resistance, calibration Tab. 1.2 is referenced for which is was found that `Dynamic-20sccm` should be used for JJ oxidation.

2.2.2 Transmission line design

The design was subject to the same impedance matching constraint of $Z_0 = 50\,\Omega$ as the transmon photon source. Using the same tools as in Sec. 1.4.2 a central width of $W_c = 240\,\mu\mathrm{m}$ and gap width of $W_g = 130\,\mu\mathrm{m}$ was simulated for the coplanar Transmission line (TL).

Due to the limited fabrication equipment available at the time of these experiments, the ground planes and contact pads were fabricated in a different layer to the qubits and central section of the TL. As seen in the final design of Fig. 2.13, placement space was limited and a narrower-than-usual TL with an impedance $Z \sim 100\,\Omega$ had to be used. It is expected that due to its short length it can be treated as a point object minimising the effect of this mismatch.

2.2.3 Coupling to the transmission line

A T-shaped capacitor is needed to provide a big enough coupling strength between the qubit and TL. Guided by the $c = 0.85 \times 10^{-10}\,\mathrm{F/m}$ capacitance heuristic (refer to B.3) a capacitor of $10\,\mu\mathrm{m}$ was used.

2.2.4 Flux loop areas

The samples were designed with multiple qubit coupled to the same TL, across which the central junction asymmetry (α) was varied. This carried the convenience of being able to load and measure up to 8 qubits during a single experimental run (a typical cooldown and warmup cycle would last a few weeks) thus being robust to fabrication defects if some qubits where to fail.

The qubits were biased by a magnetic field that is generated by a superconducting solenoid (see Fig. 1.20). Parameters of the solenoids are

$$L_{\text{Cell-T}} = 1.65\,\text{G/mA},$$
$$L_{\text{Cell-A}} = 1.56\,\text{G/mA}.$$

The superconducting loops of area A_{loop} exhibit flux periodicity, as they adjust their phases to maintain flux quantisation which would be seen experimentally as a periodicity in the biasing current

$$I_{\Phi_0} = \frac{1}{L_{\text{Cell}}}\frac{\Phi_0}{A_{\text{loop}}}. \tag{2.2.1}$$

In order to avoid an overlap of multiple qubit spectra (see how even 3 overlapping spectra in Fig. 2.12 would make it hard to identify individual qubits), one had to stagger the area of their superconducting loops (A_{loop}). Ranging the areas of the loops between 18-35 μm^2 would ensure that the smallest qubit has a period of $\sim 0.73\,\text{mA}$ and largest $\sim 0.40\,\text{mA}$ so that there are no overlaps within the first period.

2.2.5 Final design

The design of Fig. 2.13 features the parameters shown in Tab. 2.2.

Table 2.2: Summary design parameters for twin qubit.

Design parameter	Values
$E_c/\hbar$	2.75 GHz
$E_{J0}/\hbar$	82 GHz
JJ	200 nm × 400 nm
α	1-1.3 across the qubits
T-shaped coupling	10 μm
A_{loop}	18-35 μm^2

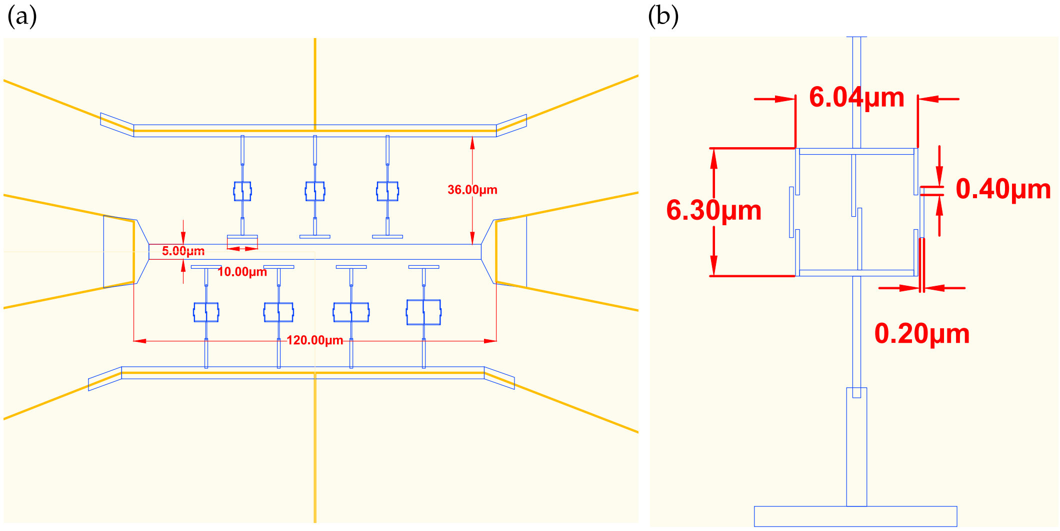

Figure 2.13: Two magnifications of the capacitively coupled twin qubit (blue) placed into the opening between pre-fabricated ground planes (gold) seen in **(a)**. As multiple qubits are coupled to the same TL, different flux-penetrating areas are used identify the qubits in experiment through their different periodicities. On the close up of the twin qubits **(b)** one can observe the *straddled* strips that will be deposited through in order to create the JJ overlap using shadow evaporation (see B.2.1).

2.3 Fabrication

The large structures that did not require high precision such as the ground planes, contact pads for bonding, and the bulk of the TL (see Fig. 2.14 (a)) are fabricated using photolithography and a pre-fabricated mask. The qubits, coupling capacitors and TL in their vicinity are made using Electron beam lithographer (EBL) lithography. The full recipe is described in B.5.

2.3.1 Processing steps

- **Wafer preparation:** An undoped Silicon (Si) wafer (whose main purpose is to support the qubit structure) is used so that there is no free charge flow out of the qubit. It is cleaned from physical debris and organics using acetone and O_2 plasma.

- **Layer 1:** Photolithography (refer to B.1.3.1) is performed, depositing a Gold (Au) pattern defined by a prefabricated mask in Fig. 2.14. The clean Si wafer is covered with two layers of photo resist, `LOR5B` and `S1813`. Next, the mask is pressed against the wafer and placed in a box with a mercury lamp for 4 minutes.

  The Ultra violet (UV) photons break the polymer chains in the resist in the areas admitted by the mask, with an accuracy of $4\,\mu$m limited by the wavelength of the mercury source ($\lambda \approx 436$ nm). Care must be taken to ensure that the resist is evenly spread and that the chip is free from debris to avoid distortion effects on the projected pattern.

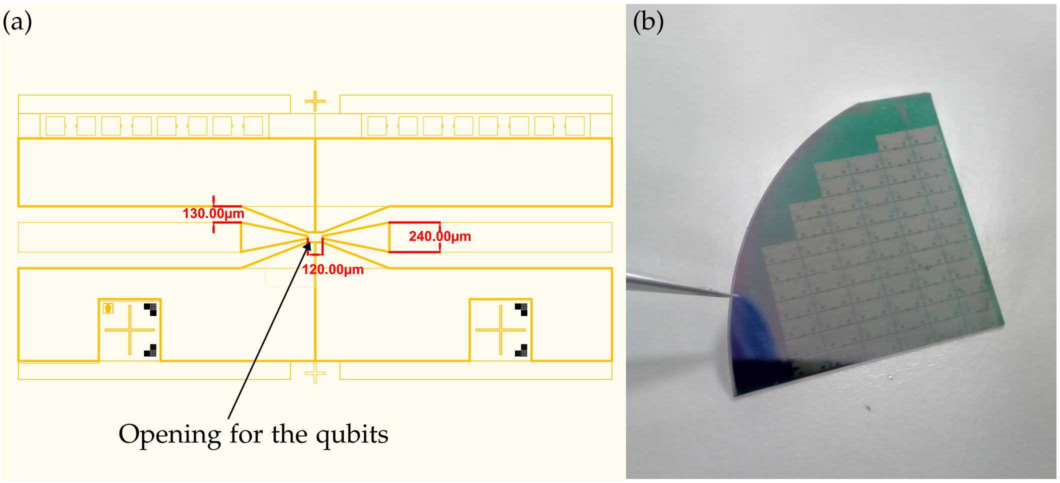

Figure 2.14: **(a)** Design of the photomask with an opening in the ground planes where the structures will be placed; **(b)** Array of ground plane structures is made, in preparation for multiple attempts of fabricating the twin qubits.

Development in `MF319` creates a mask with an undercut (see Fig. B.4) through which Au will be deposited onto the wafer. A 10 nm layer of Nickel (Ni) is thermally evaporated for adhesion followed by 80 nm of Au. After liftoff in `MF-1165` remover, the resulting pattern looks like Fig. 2.14 (b).

- **Layer 2:** involves the more precise 200 nm × 400 nm JJ structures, the pattern for which is traced out using an EBL (refer to B.1.3.2). Deposition of the central section of TL and the qubits is performed using a shadow evaporation technique, with the tilting of the chip at $\alpha = 12^\circ$ (refer to B.2). The deposition is done in Plassys `MEB550S`. The system is pumped to 5×10^{-7} mBar to remove any remnant particles that could affect the oxidation process.

  Initially the sample is tilted and a first 20 nm layer of Aluminum (Al) is deposited through the mask and allowed to cool. After this, a continuous flow of O_2 is admitted to the chamber through a mass flow controller tuned to 20 sccm, oxidising the first layer of Al. After 10 minutes oxidation is stopped, the chamber is evacuated again and the second 30 nm layer of Al is deposited on top of the AlO_x with a reverse angle of 12°.

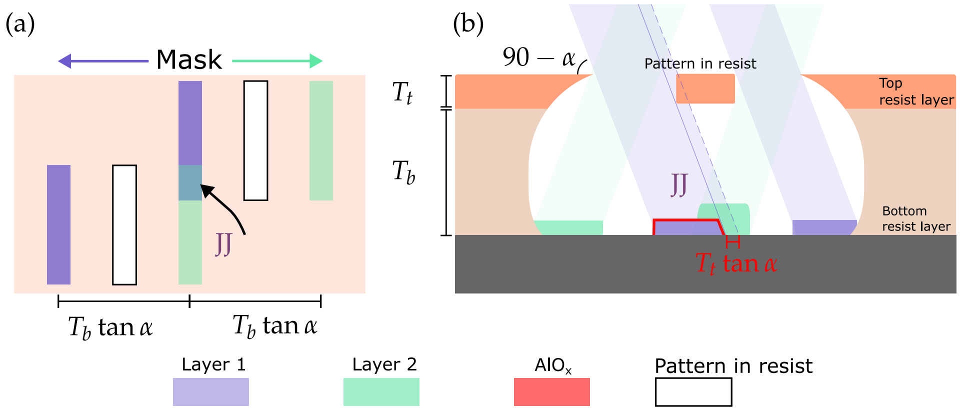

Figure 2.15: **(a)** A mask pattern for fabrication of JJ using shadow evaporation - deposition under an angle α will create an overlap under the resist of thickness T_b between the two sequentially deposited Al layers. The mask holes will need to be positioned at a distance $2T_b \tan(\alpha)$; **(b)** Cross section of the undercut resist that opens up a central region where the overlap occurs. With a top resist thickness of T_t, the deposited patterns will be shortened by $T_t \tan(\alpha)$.

Fig. 2.15 shows how given a target position for the JJ, the windows are moved correspondingly to the left and right by $T_b \tan(\alpha)$ and elongated by $T_t \tan(\alpha)$ to ensure that deposition at an angle α preserves the dimensions when the overlap is made. For $T_b = 600$ nm and $T_t = 100$ nm and 12° the required shift is 150 nm which is taken into account in the design (see Fig. 2.13).

Angles shallower than 12° should not be used in order to keep the separation between neighbouring windows $\geq 100\,\mathrm{nm}$ and prevent the caving-in of the resist during and post development.

Contact between the qubits and ground planes does not require a 3rd patching layer as was needed for the transmon (see Fig. 1.16) because the Au does not oxidise and good galvanic contact can be achieved without any etching.

2.3.2 Result

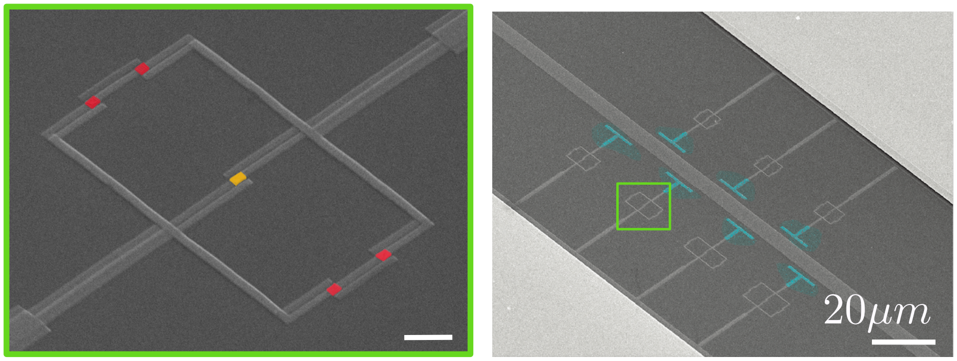

Figure 2.16: **(a)** Scanning electron microscope (SEM) image of the *twin* qubit. The Al-AlO$_x$-Al JJs are highlighted in red and yellow. φ_l and φ_r are phases induced in the left and right loops by an external magnetic field; **(b)** Each of the qubits is coupled to the TL with a T-shaped capacitor (light blue); **(c)** Optical image of the experimental sample. There are large Au ground planes and contacts (gold), with the Al transmission and qubit structures in the middle of the chip (beige). **(d)** A dark field optical image of the central opening containing 7 qubits depicting the finer structure.

The completed samples are shown in Fig. 2.16. The coplanar TL with impedance $Z_0 \sim 50\,\Omega$ runs to the opening between the ground planes in the center of the chip, where the central section of the TL and qubits reside. The qubits are coupled to the TL through T-shaped capacitors. An external magnetic field is applied to change magnetic flux linked through the almost-identical loops. Using a test sample on the same chip, the resistance of the $400 \times 200\ \mathrm{nm}^2$ JJ was measured to be $R = 1.6\,\mathrm{k\Omega}$ which is consistent with the sheet resistance of $R_{\square} = 6700\,\mathrm{k}\Omega$ expected under the chosen oxidation conditions from Tab. 1.2.

Fig. 2.16 (d) shows an image taken with dark field microscopy showing up the more finer details. Unlike with usual brightfield microscopy, the sample is illuminated only with oblique light rays (see Fig. 2.17) and unless they are scattered they do not make it to the objective lens. This greatly reduces the low frequency DC component that causes high exposure in Fig. 2.16 (c), and enhances contrast in specimens that are not well imaged under normal illumination, showing up scattering features such as outlines, edges and boundaries.

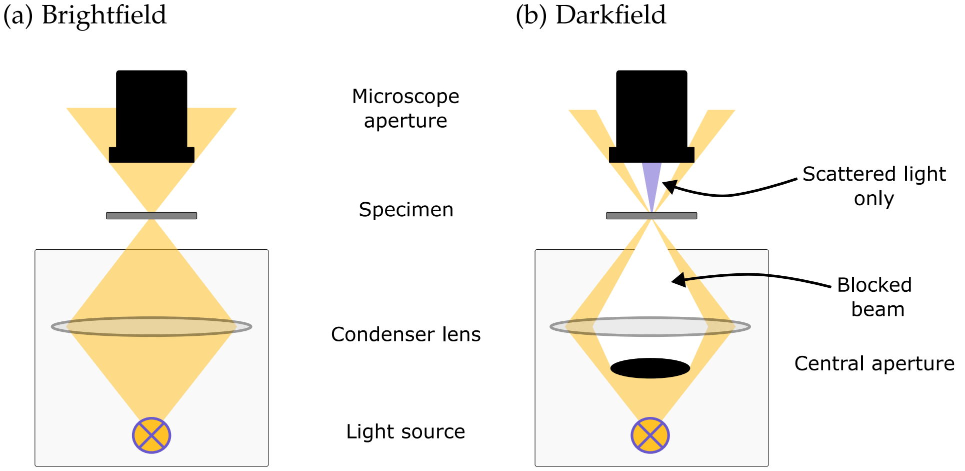
(a) Brightfield
(b) Darkfield
Microscope aperture
Specimen
Condenser lens
Light source
Scattered light only
Blocked beam
Central aperture

Figure 2.17: Comparison of two different microscopy techniques. **(a)** Usually one shines and focuses light directly at the specimen, resulting in an image on a highly illuminated light background, such as Fig. 2.16 (c); **(b)** With dark field microscopy a central aperture blocks all but only the most oblique light from reaching the sample. Light that isn't scattered is blocked off by a secondary aperture, and thus only light which has interacted by scattering or diffraction with the sample features will make it to the objective lens of the microscope.

2.4 Measurement

The primary goal is to study the operation of the qubit in the vicinity of a double degeneracy point ($\Phi_0/2$) and fit it with the model simulated in Sec. 2.1.4. The sample is mounted on a holder at the 13 mK stage of a dilution refrigerator and shielded. The output line components are exactly the same as described in Sec. 1.6.1. Two setups are connected for taking the spectrum and Rabi oscillation measurements as shown in Fig. 2.18.

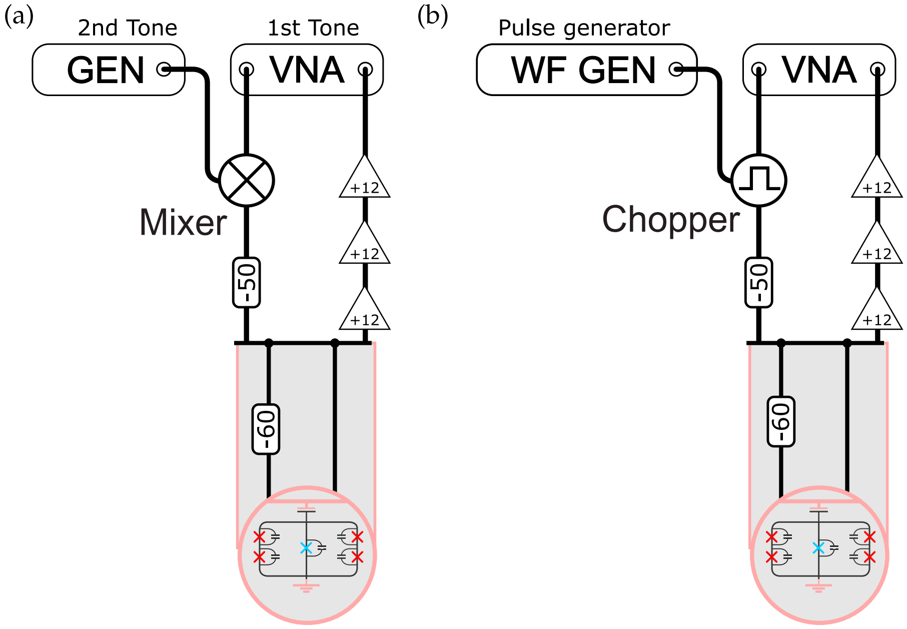

Figure 2.18: **(a)** Setup for transmission and two-tone measurements. A mixer combines the Vector Network Analyser (VNA) and generator signals at RT, and feeds them down the TL to the qubit; **(b)** Setup for Rabi oscillation measurements. No output chopper was used to avoid attenuating the weak coherent signal from the system.

2.4.1 Qubit spectrum

The energy spectrum of the *twin* qubit is found by measuring transmission of coherent waves while sweeping the biasing magnetic flux. Prior to all of the characterisation measurements of the qubit, the background spectrum is taken with the qubit detuned to a very low energy. Every subsequent measurement is corrected by subtracting this background transmission profile (1.6.1).

2.4.1.1 ω_{01} transition

The $|0\rangle \leftrightarrow |1\rangle$ transition is mapped with a VNA which measures the transmission of signal ω_{VNA} through the system. Away from resonance the signal passes through the circuit without any interaction with the qubit so that the transmission is close to 100%. Only near resonance ($\omega_{\text{VNA}} \approx \omega_{01}$) does the qubit exchange photons with the driving field as it evolves between the ground and excited states. The qubit emits a wave that is in antiphase with the driving field (refer to Sec. 1.2.2) so that the destructive interference in the output line results in a transmission dip (see Fig. 2.19).

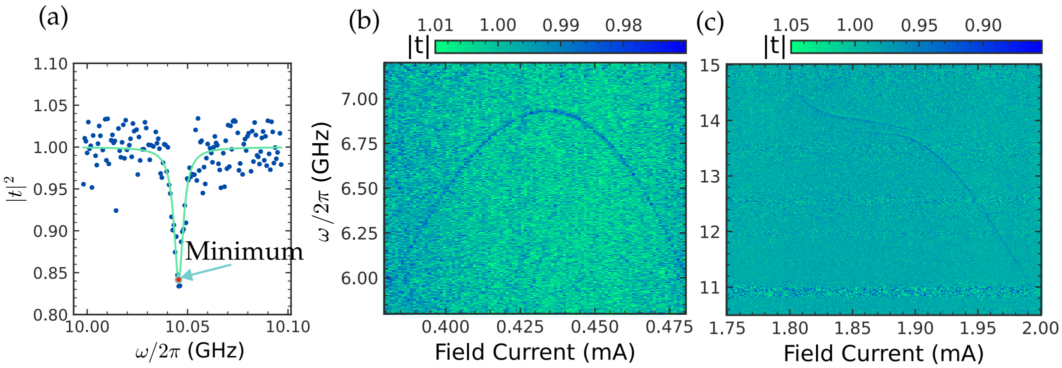

Figure 2.19: **(a)** The power transmission coefficient ($|t|^2$) for the $|0\rangle \leftrightarrow |1\rangle$ transition, taken in the weak driving limit. The width ($\Delta\omega$) gives an indication of the coherence time $T_2^{-1} = \Gamma_2$, while the dip position maps out the qubit energy; **(b)** Transmission spectrum at small magnetic fields; **(c)** Transmission spectrum at large magnetic fields where the signal starts distorting significantly.

In the weak driving limit ($\Omega \approx 0$) transmission through the system (1.2.18) becomes

$$t = 1 - r = 1 - r_0 \frac{1 + i\delta\omega/\Gamma_2}{1 + (\delta\omega/\Gamma_2)^2}, \tag{2.4.1}$$

with $r_0 = \eta\Gamma_1/2\Gamma_2$ giving the maximal extinction of the signal when $\delta\omega = 0$. The extinction of $\sim 70\,\%$ measured in Fig. 2.19 (a) indicates that there is a combination of

- Large pure dephasing (Γ_φ), in which case $\Gamma_2 = \frac{\Gamma_1}{2} + \Gamma_\varphi >> \Gamma_1$;
- Large non-radiative emission quantified by η.

Expanding (2.4.1) to get the absolute transmission profile

$$|t|^2 = \frac{\delta\omega^2 \mathrm{r0}^2}{\Gamma 2^2 \left(\frac{\delta\omega^2}{\Gamma 2^2} + 1\right)^2} + \frac{\mathrm{r0}^2}{\left(\frac{\delta\omega^2}{\Gamma 2^2} + 1\right)^2} - \frac{2\mathrm{r0}}{\frac{\delta\omega^2}{\Gamma 2^2} + 1} + 1 = 1 - 2r_0 \frac{1}{1 + (\delta\omega/\Gamma_2)^2} + \mathcal{O}(r_0^2), \tag{2.4.2}$$

on can recognise an inverted Lorentzian with Full width at half maximum (FWHM) of[3]

$$\Delta\omega = 2\Gamma_2,$$

directly giving an approximation for the decoherence rate (Γ_2) of the qubit.

The dip is fit with $\Gamma_2/2\pi \approx 3.5\,\text{MHz}$. Repeated measurements at different magnetic fields, move the position of the dip and map out the qubits ω_{01} spectrum (see Fig. 2.19 (b)). Such transmission spectra are only visible in the vicinity of external flux bias $\Phi \sim \Phi_0/2$, where the low curvature of transition energies with respect to the magnetic field allows for stable measurements to be taken. As the magnetic field increases further, the energy spectrum at degeneracy becomes more and more distorted, and eventually disappears out of range (see Fig. 2.19 (c)).

2.4.1.2 ω_{12} transition

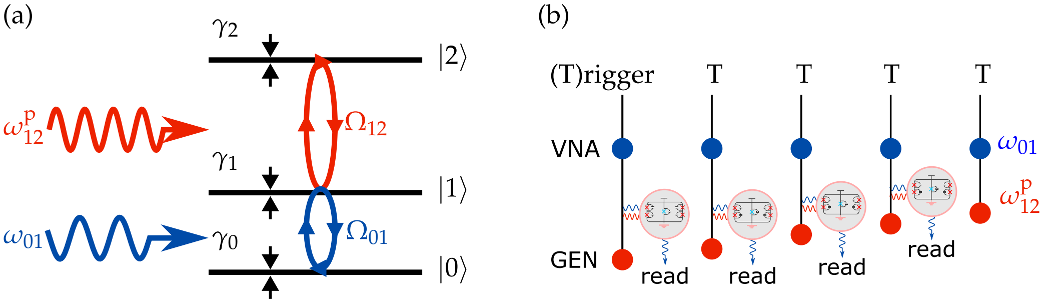

Figure 2.20: **(a)** Driving of a 3 level system using a control tone that populates $|1\rangle$ (ω_{01}) and a probe tone (ω_{12}^{p}) that searches for the $|1\rangle \leftrightarrow |2\rangle$ transition; **(b)** Depiction of measurement procedure, where a VNA and generator are triggered simultaneously to send both pulses to the qubit. The VNA *sits* on the first transition, noting deviations from the steady state that occur when the generator's probe tone is resonant with the second transition $\omega_{12}^{p} \sim \omega_{12}$.

The $|1\rangle \leftrightarrow |2\rangle$ transition (ω_{12}) is mapped using spectroscopy with two tones (see Fig. 2.20). The network analyser sends in a control signal at ω_{01} found in Sec. 2.4.1.1, while an additional generator sweeps a second frequency (ω_{12}^{p}) which are combined with a mixer at RT (see Fig. 2.18 (a)). In order for the tones to be fired and measured simultaneously, the generator and VNA are triggered by the same 10 MHz clock.

A thorough explanation of how this combination detects higher transitions is given in A.2.6. Qualitatively it can be understood that whenever the second tone from the generator hits the $|1\rangle \rightarrow |2\rangle$ transition ($\omega_{12}^{p} = \omega_{12}$) the qubit undergoes a ladder of excitations,

---

[3] The generic Lorentzian has distribution $A\left(\frac{\gamma^2}{\gamma^2+\delta\omega^2}\right) = A\left(\frac{1}{1+(\delta\omega/\gamma)^2}\right)$, which reaches half-maximum at $\delta\omega = \pm\gamma$. It has a FWHM of $\Delta\omega = 2\gamma$ (refer to A.8.3).

$|0\rangle \xrightarrow{\omega_{01}} |1\rangle \xrightarrow{\omega_{12}} |2\rangle$, depopulating states $|0\rangle$ and $|1\rangle$. Because of this depopulation the control signal at ω_{01} is modified and monitoring it on the VNA indirectly identifies ω_{12}. The power of the control signal ($\Omega_{01} = -10\,\mathrm{dBm}$) is set much weaker that the probe ($\Omega_{12} = 5\,\mathrm{dBm}$) since we want to detect the smallest difference to the control probe transmission, which is less sensitive if there are many photons in the TL.

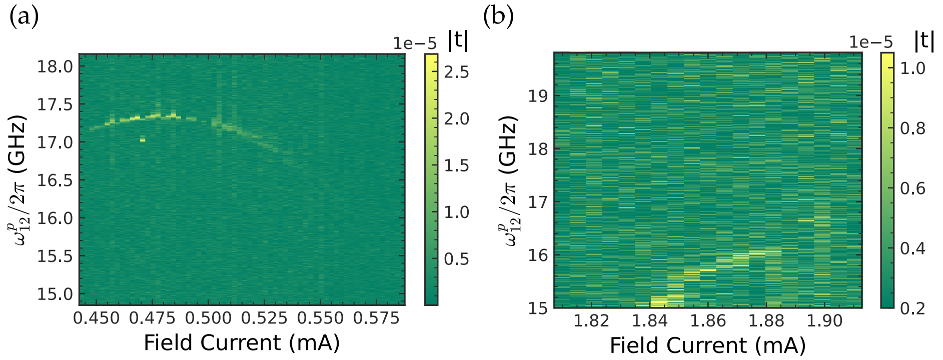

Figure 2.21: Two tone measurements searching for ω_{12} transitions. As it is the control tone (ω_{01}) that is being monitored on the VNA, the y-axis is ω_{12}^{p} but the *z-values* read out are those of ω_{01}. Second tone measurements are more suspect to noise, as they rely on the control tone to be as close to ω_{01} as possibly, which is not trivial given its field variation. Note how weaker the absolute amplitude ($|t|$) is compared to the single tone. **(a)** Signal at low magnetic field; **(b)** The signal is smeared at large magnetic fields.

The measurements of the second transition in Fig. 2.21 were less contrasting, than the equivalent measurements of ω_{01} (Fig. 2.19), since errors in assessing the *true* position of ω_{01} would propagate into only a partial population of $|1\rangle$, reducing the potency of subsequent $|1\rangle \rightarrow |2\rangle$ transitions.

2.4.1.3 Full transition spectrum

The transmission minima measured in Fig. 2.20 and Fig. 2.21 are handpicked and collected in Fig. 2.22. For both of the transitions, readings get more uncertain at larger magnetic fields, which can be explained by a combination of two effects:

- Because $\Phi \propto I_{\mathrm{solenoid}}$, the finite stability and accuracy of current through the solenoid loops results in amplified magnetic field fluctuations at larger I_{solenoid};
- Flux vortices start to penetrate the superconducting arms of the qubit following the argument given in Sec. 1.4.4, leading to instability in the local magnetic field.

Because of a small asymmetry in the loops due to defects during the fabrication (see

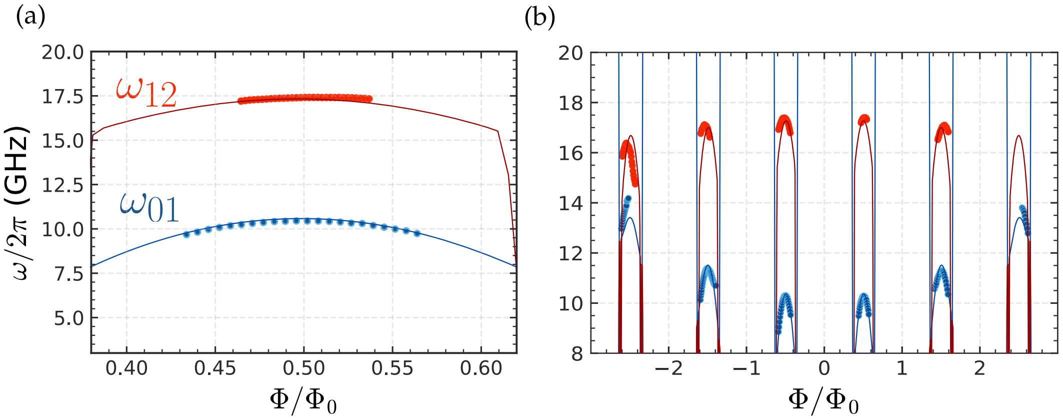

Figure 2.22: Spectrum of the *twin* qubit: **(a)** The resonance frequencies (ω_{01}) in the vicinity of $\Phi_0/2$ (blue points). The transition frequencies ω_{12} (red) are obtained in a two-tone measurement. **(b)** The spectrum measured in a wide flux bias range. Experimental data (circles) are compared with simulations (solid lines) for ω_{01} (blue) and ω_{12} (red). Asymmetry in the flux penetrating the left and right loops results in the gradual change of transition frequencies with every Φ_0 period: ω_{01} creeps up, while ω_{12} creeps down, breaking the usual periodicity seen in flux qubits.

Fig. 2.16) the actual fluxes felt by the loop are different as the global flux (Φ) is swept:

$$\begin{cases} \varphi_l = \Phi/2\pi, \\ \varphi_r = \eta\Phi/2\pi, \end{cases}$$

where $\eta = \varphi_r/\varphi_l$ quantifies the asymmetry. This results in a gradual change of the resonant frequency at larger magnetic fields. This effect is captured when fitting all the results simultaneously by numerically finding the eigenvalues of (2.1.5) with $E_{J0}/h = 91.0\,\text{GHz}$, $E_C/h = 13.5\,\text{GHz}$, $\alpha = 1.023$ and $\eta = 1.011$, shown by the solid blue (ω_{01}) and red (ω_{12}) curves.

The photon emission rate is estimated using relationship $\Gamma_1 = (d_{01}C_{\text{q-t}})^2\omega Z_0/\hbar$ (refer to Sec. 1.2.2) and found that the previously estimated value ($\Gamma_1/2\pi \sim 2\Gamma_2/2\pi = 6\,\text{MHz}$ from fitting transmission dip in Sec. 2.4.1.1) can be obtained if using a coupling capacitance $C_{\text{q-t}} = 6$ fF, which is very reasonable for the designed coupling capacitor geometry.

2.4.2 Rabi oscillations

Measuring Rabi oscillations is another method of getting a feel for a qubits coherence time, which will be an optimistic estimate of $T_2 \leq T_{2R}$ (see (1.3.5)). The setup for Rabi oscillations is shown in Fig. 2.18 (b) and the pulse sequence in Sec. 1.6.3. The first degeneracy point in magnetic field is selected and the ω_{01} transition is driven with a fixed power of 0 dBm.

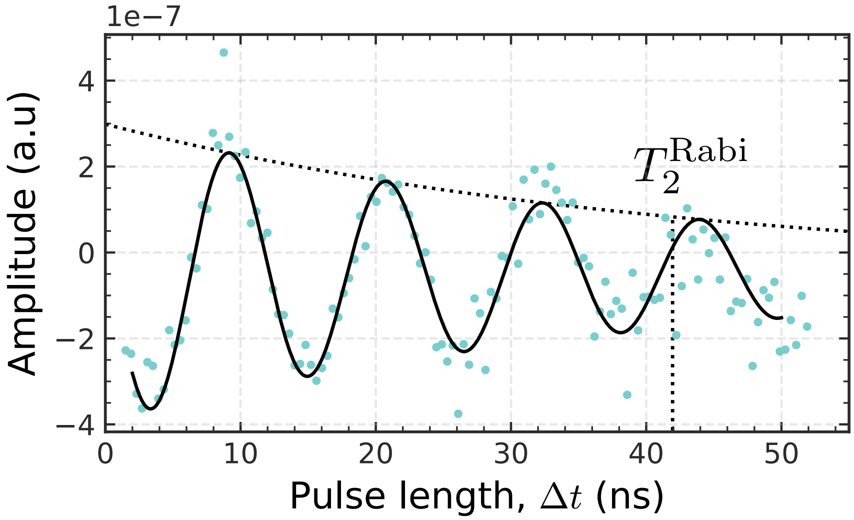

Figure 2.23: Rabi oscillations taken at the first degeneracy point by driving the qubit with resonant microwaves pulses for fixed time periods Δt. The decoherence time of $T_{2R} = 42\,\mathrm{ns}$ is extracted from the decay envelope $e^{-\Delta t/T_{2R}}$ of oscillations (dotted black line).

The oscillations decay with characteristic time T_{2R} = 42 ns, consistent with the decoherence time taken earlier from the transmission fitting (Sec. 2.4.1.1) $\Gamma_2/2\pi = 3.8\,\mathrm{MHz}$.

2.4.3 Resilience to noise

- **Global flux noise:** At the *twin* qubit's degeneracy points the curvature is $(-550 \pm 10)\,\mathrm{GHz}/\Phi_0^2$. It is substantially smaller than for 3-JJ and capacitively-shunted flux qubits with similar JJ parameters [68, 182, 183] where the curvature is of the order of $10^5\ \mathrm{GHz}/\Phi_0^2$. The qubit is now experimentally shown to be robust to global flux noise supporting the prediction made in Fig. 2.9.

- **Local flux noise:** There is also the possibility for local magnetic sources affecting loops independently or in an anticorrelated fashion. The latter could be produced by spin fluctuations on the metallic surfaces as explained in Sec. 1.3.3. Figure 2.24 demonstrates the effect on the transition energy ω_{01} at the degeneracy point under random and anticorrelated flux noise in the two loops run using Monte Carlo sampling. It is shown that even fluctuations on the order of $0.01\,\Phi_0$ add longitudinal noise to the qubit, and the symmetrised loops are not able to compensate for this.

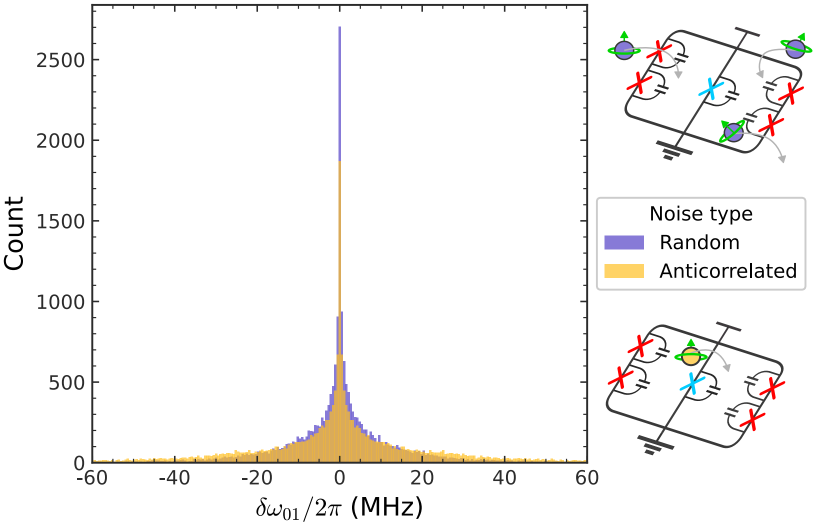

Figure 2.24: Deviation of the first transition energies $\delta\omega_{01}$ at the degeneracy point under random ($\delta\Phi_L \perp\!\!\!\perp \delta\Phi_R$) and anticorrelated ($\delta\Phi_L = -\delta\Phi_R$) flux noises in the two loops of the qubit. The fluctuations were sampled from a Gaussian distribution $\sim N\left(0, 0.001^2\right)$ in units of Φ_0 over 10,000 runs, which resulted in tens-of-MHz deviations of the transition energy. Schematic shows how spin fluctuators can move between the loops to give rise to the two types of noise.

2.5 Conclusion

This chapter has characterised and performed detailed analytical analysis of the double-loop system, revealing its properties and comparing experimental results with numerical simulations. At half-flux quantum bias of both loops, the qubit is protected against global and local magnetic field fluctuations with much less sensitivity to the global field in the second order ($(-550 \pm 10)\,\mathrm{GHz}/\Phi_0^2$) and exhibits high anharmonicity. The system selection rules allow even-odd transitions and prohibit transitions between even-even or odd-odd levels due to the symmetry of the device (see Fig. 2.10).

The measured energy level structure is well reproduced by the numerical model, meaning that important interactions and dynamics of the system have been accounted for. Experimental spectra (see Fig. 2.22) show the effect of loop asymmetry on the periodicity of the transition frequencies. Although the explicit study of asymmetric flux biasing has not been done, simulations demonstrate interesting regimes if one is able to *move* along the φ_- direction experimentally.

There was no improvement to $T_{2R} = 42\,ns$ times, due to the *twin* qubit being coupled directly to the TL, exposing the sample to poisoning from infrared radiation. Our group is working on improving the filtering inside the cryostat system to better isolate the qubit in a box with epoxy covering and closing off gaps for photons. When a subsequent repetition of the experiment is made, we will make sure to put the qubit in a resonator and investigate noise sensitivity in an isolated environment. Its sensitivity to local *perpendicular* noise could make it useful (see Fig. 2.24) as a gradiometer distinguishing between local variations of the magnetic field using the two loops as its sensor arms.

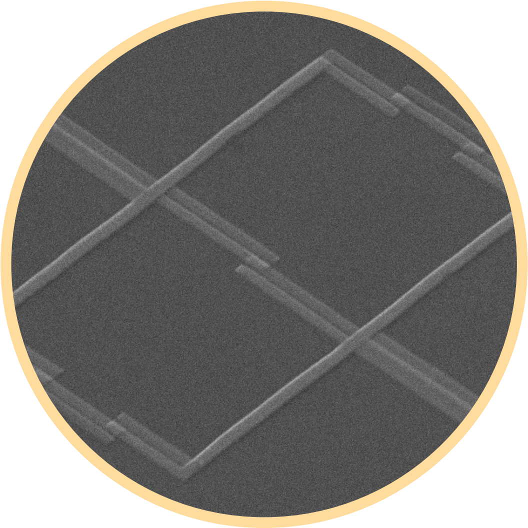

Chapter 3

Coherent quantum phase slip qubit

Quantum mechanics postulates a duality between magnetic flux and electric charge in superconducting devices [184]. The first demonstration of this duality was between the Aharonov-Bohm [185] and Aharonov-Casher [186] interference experiments, where in the former a charge picks up a phase when diffracting around magnetic flux and in the latter a fluxon picks up a phase when diffracting around a line of electric charge. Another example is how the tunneling of Cooper pair (CP) across an insulator in a Josephson junction (JJ) has an conjugate analogue of flux quanta Φ_0 tunneling across a superconductor in what is known as a Quantum phase slip junction (QPSJ), with a summary shown in Tab. 3.1.

Table 3.1: Duality between the JJ and QPSJ.

Josephson junction	Quantum phase slip junction
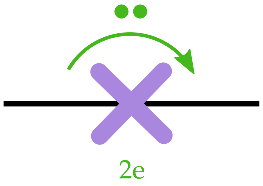	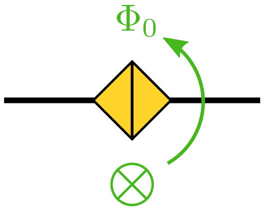
Tunnelling of CP	Tunnelling of flux quantum Φ_0
Defines CP states $\lvert N \rangle$ states	Defines flux state $\lvert F \rangle$
Josephson energy (E_J)	Phase slip energy (E_S)
Insulator	Superconductor
Current $= \partial_t Q$	Voltage $= \partial_t \Phi$

There are a number of reasons for exploring the potential of devices based on this duality. Lots of modern superconducting quantum systems are based on the JJ [170, 187] and as the industry begins to scale quantum processors into the thousands, reproducibility of individual junctions becomes an important factor. JJs have a reported 5-25% variability [188] and even when fabricated on a single chip, their resistances will differ spatially and temporally due to variable oxidation conditions during and post-fabrication (see Sec. 1.5.2 and Sec. 2.3.2).

While alternatives are being explored to bypass the shadow evaporation technique and minimise noisy metal-air interfaces [189], the inevitable presence of Two level systems (TLS) in the amorphous oxide layer (see Sec. 1.3.3) could ultimately set a limit to further fabrication optimisations. This leaves the experimental calibration of individual qubits to make them usable: locating the working point; tuning control pulses; characterising decay rates, with the industry already offering automated solution with machine learning protocols that can calibrate an array of quantum dot devices in around 40 minutes [190].

The QPSJ, on the other hand, can be realised by a narrow wire in a suitable high inductive material. If the 10 nm nanowire constrictions can be standardised, they might prove easier to fabricate and have a higher yield than their JJ counterparts. They fulfill all of the requirements of a JJ: introduce non-linearity into superconducting circuits; couple distinct quantum states facilitating their superposition for quantum manipulation; can be integrated and fabricated using existing coplanar techniques.

Research into QPSJ (see Fig. 3.1 (a,b)) is beginning to accelerate. Our group has used them to demonstrate quantised current steps $I_n = n2ef, n \in \mathbb{Z}$ from photon-assisted tunnelling of magnetic fluxes in Niobium Nitride (NbN) [191] analogous to the quantised voltage steps measured 50 years earlier on JJ arrays [192, 193]. Elsewhere they have been integrated into a CQUID - the dual analogue on the SQUID that is sensitive to local charge [194]; have been shown to operate as a transistor [195]; are starting to explore qubit applications [196, 197].

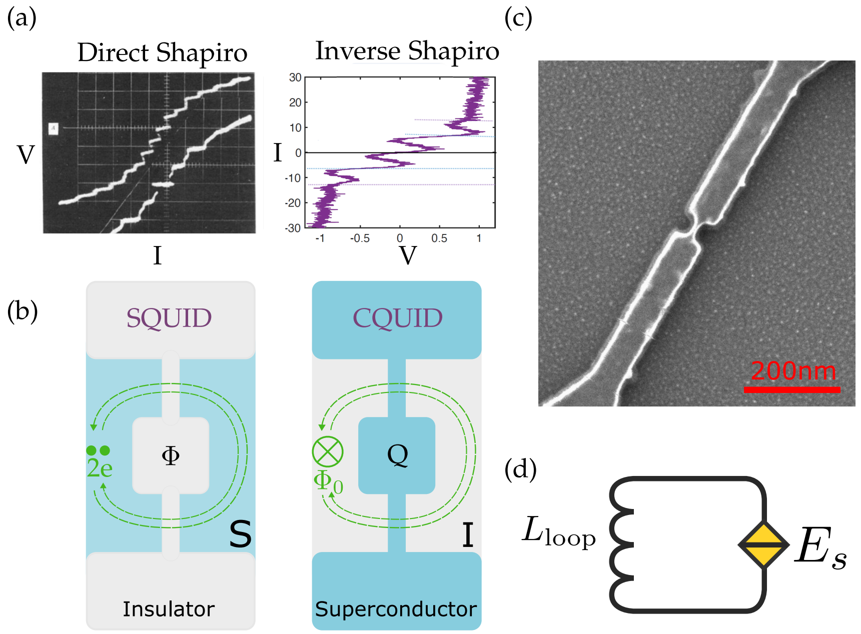

Figure 3.1: Overview of QPSJ progress: **(a)** Quantised voltage steps measured in 1963 on JJs and the dual quantised current steps measured by our group in 2021 on QPSJs (image adapted from [191]); **(b)** Comparison of the tunneling elements in a SQUID and CQUID (image adapted from [194]); **(c)** Realisation of a QPSJ with a narrow 20 nm constriction in Titanium Nitride (TiN) - there are no isolated islands and the whole structure is galvanically uninterrupted unlike the JJ; **(d)** Original proposal of the circuit of a CQPS qubit, consisting of a QPSJ shunted by an inductor. Both of the elements are made from the same high resistive material.

The original proposal of a qubit operating on the QPSJ was given by Mooij in 2005 [184, 198] (see Fig. 3.1 (d)) and was demonstrated first by Astafiev in Indium Oxide (InO_x) [199], and later by Peltonen in NbN [200, 201]. There are practical advantages of this qubit compared to its direct CP box counterpart (refer to Sec. 1.1):

- Absence of noise from TLS that reside in JJs barriers (see Sec. 1.3.3);
- Absence of charge noise, since the qubit has no isolated islands that could cause charge blockages and external charge buildup (see Fig. 3.1 (c));
- It shall also be seen that a qubit based on the QPSJ has very anharmonic transition frequencies, so fast excitation can be performed with no leakage of quantum information into the higher states.

This chapter extends the investigation of these qubits with a realisation in TiN, which is known to have a much smaller superconducting gap ($\Delta \sim 180\,\mu$eV) [194] compared to that of NbN ($\Delta \sim 1.6\,$meV) [202], making it more susceptible to thermal noise. However this material is pursued because TiN films are more robust against degradation, ensuring a more stable lifetime for the devices. This was evidenced from our experience with NbN films whose normal resistance would double over a few months (similar degradation was noticed in other investigations [203]). TiN also has one of the largest kinetic inductances because its films are closer to the SIS transition [194], allowing for a more compact realisation of the inductive element.

Furthermore, capacitive coupling to these qubits is demonstrated for the first time, as all previous investigations [199, 200, 201] have used inductive coupling. By galvanically decoupling the qubit from the resonator, the approach provides flexibility in material choice, design and fabrication techniques, and allows the independent study of Coherent quantum phase slip (CQPS) devices without less constraints put on the readout circuit.

The latest theory pertaining to QPSJ is presented in Sec. 3.1 which is contrasted to Thermally activated phase slips (TAPS) which have been studied for a number of decades, and the CQPS that is required for all of the interesting application in Fig. 3.1. The device is then designed (Sec. 3.2), fabricated (Sec. 3.3) and characterised (Sec. 3.4) to demonstrate an intermediate coupling regime with the readout resonator.

3.1 Theory

3.1.1 Coherent quantum phase slip

Phase slips were discovered when investigating miniaturisation of superconducting elements to approach the limit beyond which the finite size of CP would result in their localisation. It was found that in nanowires the superconducting order parameter $|\Psi| e^{i\varphi}, |\Psi| \propto \sqrt{n_{\mathrm{CP}}}$ could undergo a phase flip event ($\varphi \to \varphi \pm 2\pi$) though a temporary suppression of the local CP concentration (n_{CP}), without affecting the macroscopic state (see Fig. 3.2).

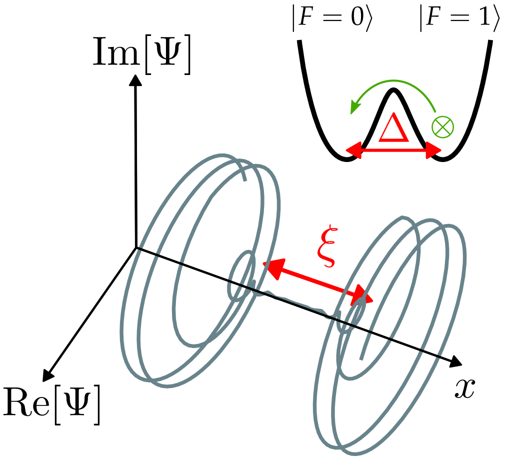

Figure 3.2: Variation of the superconducting order parameter $\Psi(x)$ along a length of a wire. Each *turn* of the helix corresponds to a phase change by 2π. The mechanism by which the phase slip occurs involves the temporal suppression of the order parameter's amplitude $|\Psi|$ which fluctuates over a few coherent lengths ($\sim \xi$) to zero, followed by a phase slip ($\varphi \to \varphi \pm 2\pi$). **Inset** shows how a phase slip event has an energy barrier Δ, whose height is related to suppression of the local CP concentration.

The resulting magnetic flux flow $\partial_t \Phi$ induces a voltage in the wire, which, for a finite time, develops an effective resistance $R \sim \partial_t \Phi / I_p$ well below T_c of the superconductor [204]. This event requires an input of the condensation energy $\sim \Delta$ (refer to A.1) in order to *break* the CP, which acts as a dynamic barrier for the phase slip event [205] (after the order parameter recovers to its initial value, this energy is also recovered). These events are called Quantum phase slip (QPS), and each one is associated with the tunnelling of a fictitious particle with a flux Φ_0 across the superconductor[1].

The first studies of phase slips occurred in the dissipative regime, where phase slip events were powered by thermal fluctuations close to the transition temperature T_c [206,

---

[1] Reminder that from A.1.4, $\varphi = \varphi_1 - \varphi_2$ is the phase difference across the JJ, which is related to the flux difference across the JJ $\varphi = \Phi 2\pi / \Phi_0$

207] and a wire with current I dissipated an energy $I\Phi_0$ for each phase slip. These kinds of phase lips are known as TAPS and have an exponential dependence on temperature $R_{\text{TAPS}} \propto \exp\left(-\Delta F/k_b T\right)$ [208].

However the TAPS mechanism failed to explain finite resistances at temperatures $T \ll T_c$ and the missing contribution was proposed to come from phase slips that occurred through quantum mechanical tunnelling [209]. These tunneling events could occur without dissipation [210], and multiple events at different location in the wire could even coherently interfere with each other [177]. Experiments have confirmed these coherent phase slips exist and that they are particularly strong in disordered, quasi-1D superconducting wires [204, 211, 212].

Where Bardeen-Cooper-Schrieffer theory (BCS) and Ginzburg-Landau equations fail for strongly disordered superconductors below T_c, the phase slip amplitude of a CQPS event across a short wire of width W can be derived from qualitative argumentation [204, 213, 214] assuming that:

- Individual CQPS occur around a single phase slip center of size $\xi = \sqrt{\xi_0 L_{\text{mean-free-path}}}$;
- The transition frequency $\omega_s = \Delta/\hbar$ is given by the condensation energy one needs to temporarily suppress in the tunneling process (see Fig. 3.2);
- Progressive scaling of the process amplitude $\propto \sqrt{L_s/\xi}$ with wire length (L_s) in units of ξ;
- Scaling prefactor taking into account damping in the tunneling process $\sim \sqrt{R_q/R_\xi}$ where $R_\xi \propto R_n \xi / W_s$ for normal state resistance R_n of wire segment of length ξ and width W_s and $R_q = h/4e^2$;
- An exponential factor $\exp\left(-aR_q/R_\xi\right)$ using BCS-Gorkov expressions for a dirty superconductor,

collectively giving an expression of the form

$$E_s = \Delta \sqrt{\frac{L_s}{\xi}\frac{R_q}{R_\xi}} \exp\left(-a\frac{R_q}{R_\xi}\right), \tag{3.1.1}$$

where $a \sim 0.36$ has been diffusive conductor [215]. The amplitude is maximised for materials with a short coherence length, however if the CP are too localised $\xi_{\text{loc}} < \xi$ (CP overlap is smaller that the dimensions of the device as shown in the design section Fig. 3.13) then superconductivity itself becomes suppressed [199]. The optimal condition for CQPS is when $\xi \approx \xi_{\text{loc}}$ which occurs close to the Superconductor-insulator transition (SIT) and requires material with a high kinetic inductance [194].

3.1.2 Coherent quantum phase slip qubit

The standard CQPS qubit circuit proposed by Mooij [216] is shown in Fig. 3.3. When constructing its Hamiltonian, we apriori know that the loop is going to be made from a highly inductive material with a large kinetic inductance L_k (refer to A.1.7) in addition to the geometrical inductance of the loop $L_{\text{geometric}}$.

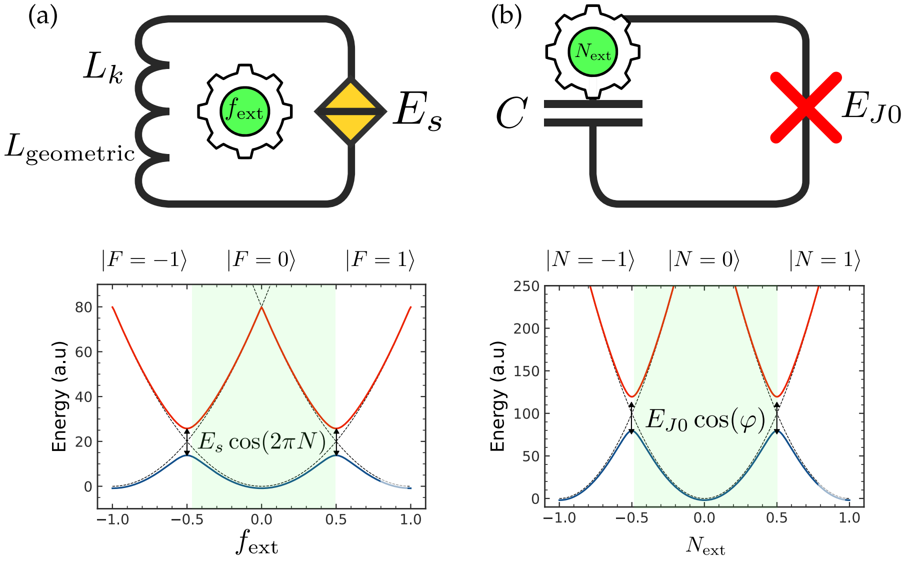
(a)
L_k
$L_{\text{geometric}}$
f_{ext}
E_s
(b)
N_{ext}
C
E_{J0}
$|F=-1\rangle$
$|F=0\rangle$
$|F=1\rangle$
Energy (a.u)
80
60
40
20
0
$E_s\cos(2\pi N)$
−1.0
−0.5
0.0
0.5
1.0
f_{ext}
$|N=-1\rangle$
$|N=0\rangle$
$|N=1\rangle$
Energy (a.u)
250
200
150
100
50
0
$E_{J0}\cos(\varphi)$
−1.0
−0.5
0.0
0.5
1.0
N_{ext}

Figure 3.3: Duality between **(a)** CQPS qubit and **(b)** Cooper pair box (CPB), showing their respective external degrees of control $f_{\text{ext}}, N_{\text{ext}}$. Both have conjugate circuit elements and both are dominated by a large quadratic dependence of their *natural* charge and flux states. A QPSJ lifts the degeneracy at $f_{\text{ext}} \sim 0.5$ by allowing change of fluxoid number in the loop through $E_s\cos(2\pi N) \sim |F\rangle\langle F+1| + |F+1\rangle\langle F|$ much like the JJ lifts the degeneracy by allowing tunnelling of CPs through $E_{J0}\cos(\varphi) \sim |N\rangle\langle N+1| + |N+1\rangle\langle N|$.

If a phase difference $\Delta\varphi$ is established across the inductive part of the device, a current

$$I = \left(\frac{\Delta\varphi}{2\pi}\Phi_0\right)\frac{1}{L_k}, \tag{3.1.2}$$

will circulate in the loop, linking a flux of $IL_{\text{geometric}}$. With the addition of an an external bias $\Phi_{\text{ext}} = f_{\text{ext}}\Phi_0$ the flux quantisation condition (refer to A.1.4) for the loop reads

$$\begin{aligned} 2\pi F &= \Delta\varphi + 2\pi f_{\text{ext}} + 2\pi\frac{IL_{\text{geometric}}}{\Phi_0} \\ \Rightarrow \Delta\varphi &= 2\pi f_{\text{ext}} - 2\pi F - \underbrace{\frac{L_{\text{geometric}}}{L_k}\Delta\varphi}_{\text{✥}\approx 0}, \end{aligned} \tag{3.1.3}$$

where $F \in \mathbb{Z}$ is the flux number. Because of the highly disordered materials utilised for CQPS qubits, the condition $L_k \gg L_{\text{geometric}}$[2] means that the trailing term ✥ can be ignored and the total inductance of the loop $\approx L_k$. The total energy from the circulating current (3.1.2) will then be

$$E = \frac{1}{2} I^2 L_k = \frac{\Phi_0^2}{2L_k}(F - f_{\text{ext}})^2, \tag{3.1.4}$$

which defines the parabolic lines in the energy spectrum of Fig. 3.3 (a). A phase slip couples the otherwise uninteracting states through an amplitude E_s, which lifts the degeneracy between two neighbouring flux states $|F\rangle$ and $|F+1\rangle$ around the degeneracy points (see Fig. 3.3 (a)).

A nice consequence of duality, is that at this stage the Hamiltonian of the system ends up being identical to CPB (see the circuit diagrams in Fig. 3.3 and refer to Sec. 1.1 for CPB) under the following substitutions:

$$\begin{array}{lcl}
N_{\text{ext}} & \to & f_{\text{ext}} = \Phi/\Phi_0 \\
\hat{N} & \to & \hat{F} \\
E_{J0}\cos(\hat{\varphi}) & \to & E_s \cos(2\pi\hat{N}) \\
E_C = \dfrac{e^2}{2C} & \to & E_L = \dfrac{\Phi_0^2}{2L}.
\end{array}$$

Performing the substitutions results gives the Hamiltonian of a CQPS qubit

$$\begin{aligned}
H_{\text{q}} &= E_L(\hat{F} - f_{\text{ext}})^2 - E_s \cos\left(2\pi\hat{N}\right), \\
&= E_L(\hat{F} - f_{\text{ext}})^2 - \frac{E_s}{2}\sum_F \Big[|F+1\rangle\langle F| + |F\rangle\langle F+1| \Big],
\end{aligned} \tag{3.1.5}$$

where the basis is of the flux states $\{|F\rangle\}$ instead of the CP basis $\{|N\rangle\}$ and where an identity between the CP number and flux states $e^{i2\pi\hat{N}} = \sum |F\rangle\langle F+1|$ is analogous to the identity between phase and charge states (refer to A.1.6).

In the vicinity of a degeneracy point $f_{\text{ext}} = (F + 1/2) \pm \delta f$, one can redefine the inductance energy in term of the energy difference between two neighbouring flux states $|F\rangle$ and $|F+1\rangle$

$$E_L(F+1-f_{\text{ext}})^2 - E_L(F - f_{\text{ext}})^2 = E_L(\mp 2\delta f) \Rightarrow E_\pm = \frac{\Phi_0^2}{L_k}(\mp\delta f)$$

where + and - correspond to two persistent currents of magnitude $I_p = \Phi_0/L_k$ circulating in opposite directions[3]. Written in the basis of these circulating currents, the qubit hamiltonian

---

[2] In Sec. 3.4.2 an inductance of $L_\square \approx 7\,\text{nH}$ is fit, which dominates any geometric inductance evaluated with the standard $L_{\text{geometric}} = \mu N^2 A/l$.

$$H_\mathrm{q} = I_p \begin{array}{cc} & \begin{array}{cc} |F\rangle & |F{+}1\rangle \end{array} \\ \begin{array}{c} \langle F| \\ \langle F{+}1| \end{array} & \begin{bmatrix} -\delta f & 0 \\ 0 & \delta f \end{bmatrix} \end{array} - \frac{1}{2} \begin{array}{cc} & \begin{array}{cc} |F\rangle & |F{+}1\rangle \end{array} \\ \begin{array}{c} \langle F| \\ \langle F{+}1| \end{array} & \begin{bmatrix} 0 & E_s \\ E_s & 0 \end{bmatrix} \end{array} = -I_p \delta\Phi \sigma_z - \frac{1}{2} E_s \sigma_x. \tag{3.1.6}$$

Transition between the two states can only be induced when $E_S \neq 0$, so detection of resonant qubit transitions is direct evidence of CQPS. In fact it was only with the first CQPS qubit that coherent flux tunneling was conclusively demonstrated, as transport-resistance measurements one could not distinguish their effect from standard Coulomb blockades in the wires [214].

The system next to the degeneracy point (3.1.6) can be recognised to describe a diagonalisable 2-level system (refer to A.2.2) with energy splitting and Hamiltonian

$$\Delta E = \hbar\omega_q = \sqrt{\varepsilon^2 + \Delta^2}, \qquad \varepsilon = -2 I_p \delta\Phi, \qquad \Delta = E_S, \qquad H_\mathrm{q} = -\frac{\Delta E}{2}\sigma_z \tag{3.1.7}$$

The eigenstates of the system will be the superposed neighbouring flux states $\{|F\rangle, |F+1\rangle\}$, physically corresponding to opposite current circulating in the loop

$$\begin{aligned} |g\rangle &= \cos(\theta/2)\,|F\rangle + i\sin(\theta/2)\,|F+1\rangle = \cos(\theta/2)\,|\circlearrowleft\rangle + i\sin(\theta/2)\,|\circlearrowright\rangle\,, \\ |e\rangle &= i\sin(\theta/2)\,|\circlearrowleft\rangle + \cos(\theta/2)\,|\circlearrowright\rangle\,. \end{aligned}$$

---

[3] This can be seen by the change of sign in the circulating current (3.1.2) from the $\pm\delta f$ variations of f_ext in (3.1.3).

3.1.3 Readout resonator

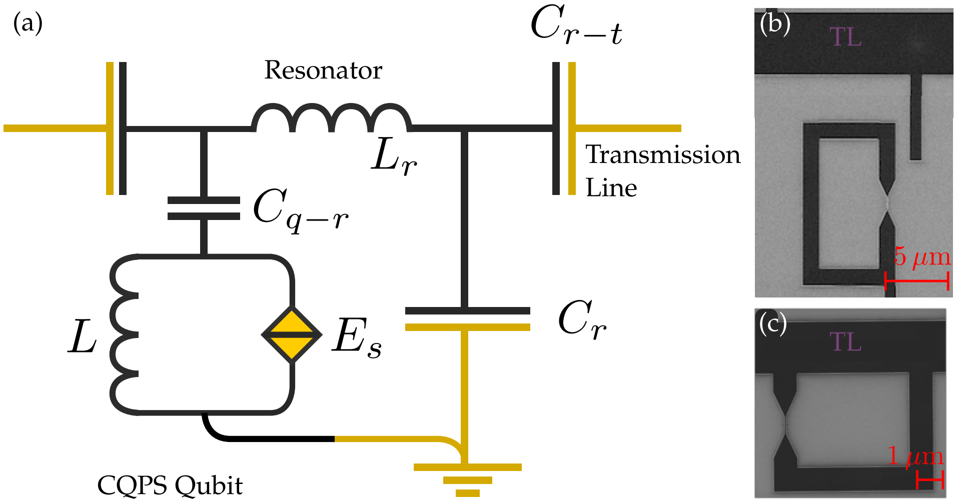

Figure 3.4: **(a)** Schematic of the $\lambda/2$ resonator capacitively coupled to the Transmission line (TL) and CQPS qubit. The resonator protects the qubit while being galvanically decoupled from it. Colours show the different materials that are used in the final design (see Sec. 3.2): Dark - TiN; Yellow - Gold (Au); **(b)** Realisation of capacitive coupling; **(c)** Realisation of inductive coupling.

In contrast to earlier experiments that have all used inductive coupling to CQPS qubits [199, 200, 201], readout was performed with a capacitively coupled resonator shown in Fig. 3.4. The qubit under investigation is galvanically decoupled from the readout circuit, which has the following advantages:

- It allows greater flexibility in modifying the qubit material independently of the readout circuit. While the latter is often made out of Aluminum (Al) in the same layer as the rest of the auxiliary circuit elements, the qubit material does not need to be superconducting. Inductive coupling on the other hand requires that the full readout line is in a superconducting state [217];
- The kinetic sheet inductance (refer to A.1.7)

$$L_{k,\square} = \frac{\hbar R_\square}{\pi \Delta} = 0.18 \frac{\hbar R_\square}{k_b T_c}, \tag{3.1.8}$$

  is determined by the field-dependent superconducting energy gap $\Delta(B)$, which opens up the possibility of studying the CQPS qubit systems in strong magnetic fields and probe near-quantum phase slip regimes in disordered film devices such as TiN, NbN, $\mathrm{InO_x}$ without affecting the properties of the Al readout circuit.
- Because there is no galvanic connection to the resonator, the qubit is protected from

hot electrons or quasiparticle diffusion from the readout circuitry that can dephase the qubit (see Sec. 1.3.3).

3.1.3.1 General resonator properties

A resonator is characterised by its resonance frequencies (refer to A.4.1)

$$f_m = mf_r \Leftrightarrow \omega_m = m\omega_r, \qquad m \in \mathbb{Z}_{\geq 1}, \tag{3.1.9}$$

where for a $\lambda/2$ LC resonator in see Fig. 3.4 the base frequency $f_r = v/\lambda = (1/\sqrt{lc})/2L$ depends on its length (L) capacitance (c) and inductance (l) per unit length.

Resonators were initially used in atomic physics to address the problem of weak interaction between photons and natural atoms. Placing an atom in an optical resonator and shining a laser at it allows the photons to reflect back and forth in a confined space, increasing the energy density and having more interaction with the atom to slowly *collect* or manipulate its quantum state over multiple passes [218] (see Fig. 3.5 (a)). The effect is to modify the interaction of the atom with the external environment in two ways depending on the resonance condition ($\delta_{q-r} = \omega_q - \omega_r$):

- $\delta_{q-r} \sim 0$: The seminal 1946 meeting by Purcell [219] noted that spontaneous emission from the confined atom is enhanced in proportion to the quality factor of the resonator (Q introduced below) and can be magnitudes of times larger compared to free space [220];

- $\delta_{q-r} \gg 1$: Complementary to this, a 1981 paper [221] demonstrated that a system inside a resonator has its spontaneous emission inhibited when the two are not in resonance. This can be understood by the resonator decoupling the atom from vacuum states (shown in A.3.5 and A.3.4 to enhance spontaneous emission), modifying the regular $Z_0 = 50\,\Omega$ impedance of the TL [222] to

  $$Z(\omega) = \frac{Z_0}{1 + \frac{(2\delta_{q-r})^2}{(\kappa)^2}},$$

  which in accordance with (A.3.37) will decrease the depolarisation rate when the qubit is detuned from the resonator [221, 223]. Stray photons do not pass through the resonator and the qubit can evolve in a noise free environment, demonstrating coherence times 5 orders of magnitudes higher than if it was coupled to a TL [222].

Thus the resonator can protect or stimulate the qubit - this effect is shown pictorially in

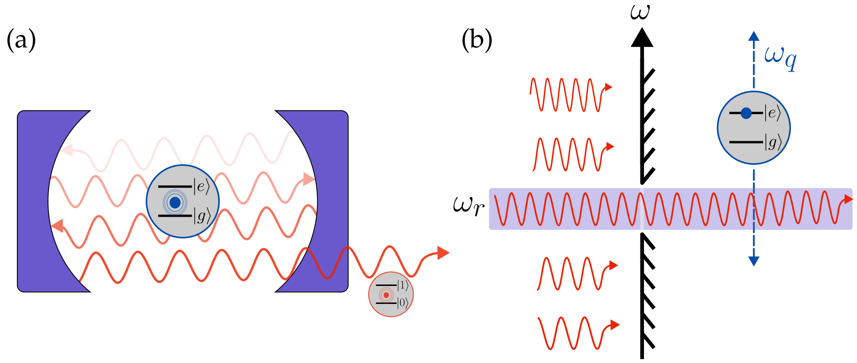

Figure 3.5: **(a)** Multiple interactions of reflecting photons with the atom allow them to *imprint* the state of the atom by the time they leak out, allowing much stronger coupling to be achieved compared to free space; **(b)** The resonator *filters* out photon at non resonant frequencies, decoupling the atom from vacuum fluctuations that cause depolarisation. If the atom is tuned to resonance ($\omega_q = \omega_r$) the opposite effect occurs, and the concentrated field promotes rapid decay.

Fig. 3.5 (b) and quantified through the quality factor (refer to A.4.2)

$$Q_m = \frac{\omega_m}{\kappa_m}, \qquad \kappa_m = \frac{\omega_m(2\omega_m Z_0 C_{\text{r-t}})^2}{\pi m} = \frac{4Z_0\omega^2 C_{\text{r-t}}^2}{mC_r}, \tag{3.1.10}$$

where m is the resonator mode and κ_m is the photon loss rate of the resonator capacitor ($C_{\text{r-t}}$) to a TL with standard impedance Z_0.

Initially used in the study of Rydberg atoms [224, 225] since 2004 resonators have found widespread adoption in the superconducting qubit community [164, 226]:

- The large voltage fields in superconducting resonators in combination with the close separation between qubit and resonator lines allows 100 times stronger coupling than with Rydberg atoms [225] and three orders of magnitude stronger that in atomic-microwave experiments [94] in regimes known as strong or ultra-strong coupling;
- Both the atom and resonator are fixed in place relative to each other, and hence do not suffer from temporal coupling fluctuations;
- It has become almost expected that all qubit readout is done through resonators, because of how well they protect from environmental noise, how straightforward it is to integrate with existing circuits, given the identical lithographical steps to qubit fabrication.

The quantisation of the resonator is shown in A.3.2 and written here for fundamental mode $\omega_{m=1} = \omega_r$

$$\begin{gathered} H_r = \hbar\omega_r\left(a^\dagger a + \frac{1}{2}\right) \\ a^\dagger a\,|n\rangle = n\,|n\rangle\,. \end{gathered} \tag{3.1.11}$$

Here $\hat{a}$ and $\hat{a}^\dagger$ are photon creation and annihilation operators acting on Fock photon states $\{|n\rangle\}$ describing n photons in the resonator (refer to Appendix).

3.1.3.2 Qubit-resonator coupling

To achieve coupling, the qubit is placed in the middle of a $\lambda/2$ resonator. The voltage operator of the coplanar resonator is expressed as (refer to A.4.3)

$$\hat{V}_r = V_m(x)(ia - ia^\dagger), \qquad V_m(x) = \begin{bmatrix} \sqrt{m}V_{r0}\cos\left(m\pi\frac{x}{L}\right), & m \text{ odd}, \\ \sqrt{m}V_{r0}\sin\left(m\pi\frac{x}{L}\right), & m \text{ even}, \end{bmatrix} \tag{3.1.12}$$

where $V_{r0} = \sqrt{\hbar\omega_r/C_r}$ is the resonator's zero-point voltage fluctuation amplitude. The coupling energy of the resonator-qubit system follows the same logic as in A.2.3:

$$H_{\text{int}} = \hat{V}_q C_{\text{q-r}} \hat{V}_r, \tag{3.1.13}$$

considering qubit voltage ($\hat{V}_q$) and resonator voltage ($\hat{V}_r$) across the coupling capacitance ($C_{\text{q-r}}$). The qubit voltage operator can be found by rewriting the qubit Hamiltonian of (3.1.5) into a form

$$H_{\text{q}} = E_L\left(\hat{F} - f_{ext}\right)^2 - E_S\cos(2\pi(\hat{N} + \delta N)), \tag{3.1.14}$$

that adds an induced charge δN along the QPSJ from the phase slip process. Then differentiating (3.1.14) wrt to this induced charge defines the voltage operator

$$\begin{aligned} \hat{V}_q &= \frac{1}{2e}\frac{\partial H_{\text{q}}}{\partial \delta N} \\ &= \frac{1}{2e}\frac{\partial}{\partial \delta N}\left(E_L(\hat{F} - f_{ext})^2 - E_S\cos(\hat{N} + \delta N)\right) \\ &= \frac{2\pi E_S}{2e}\sin(2\pi\hat{N}) = V_s\sin(2\pi\hat{N} + \delta N), \end{aligned} \tag{3.1.15}$$

where the phase slip voltage $V_s = 2\pi E_s/2e$ is introduced. In general the CQPS junction is shunted by an inductor, and the DC offset charge $\delta N = 0$ before any phase slips occur. Expressing (3.1.15) in the basis of flux states where $e^{i2\pi\hat{N}} = \sum|F+1\rangle\langle F|$ (refer how this was done in (3.1.5))

$$\hat{V}_q = \frac{V_s}{2}\sum_n\left[-i\,|F+1\rangle\langle F| + i\,|F\rangle\langle F+1|\right], \tag{3.1.16}$$

which motivates the qualitative understanding that the voltage operator couples two neighbouring fluxoid states $|F\rangle \leftrightarrow |F+1\rangle$ through the phase slip event. When truncated to two neighbouring flux states $|F\rangle$ and $|F+1\rangle$

$$\hat{V}_q = -\frac{V_s}{2}\sigma_y.$$

Collecting together (3.1.12), (3.1.16) into (3.1.13) gives

$$
\begin{aligned}
H_{\text{int}} &= \left(-\frac{V_s}{2}\sigma_y\right) C_{\text{q-r}} \left(V_m(ia - ia^\dagger)\right) \\
&= -\frac{1}{2}\frac{2\pi E_S C_{\text{q-r}} V_m}{2e}\sigma_y(ia - ia^\dagger) \\
&= -\hbar g \sigma_y (ia - ia^\dagger),
\end{aligned}
\tag{3.1.17}
$$

where the qubit-resonator coupling strength g is defined

$$
\hbar g = \frac{1}{2} V_s C_{\text{q-r}} V_m. \tag{3.1.18}
$$

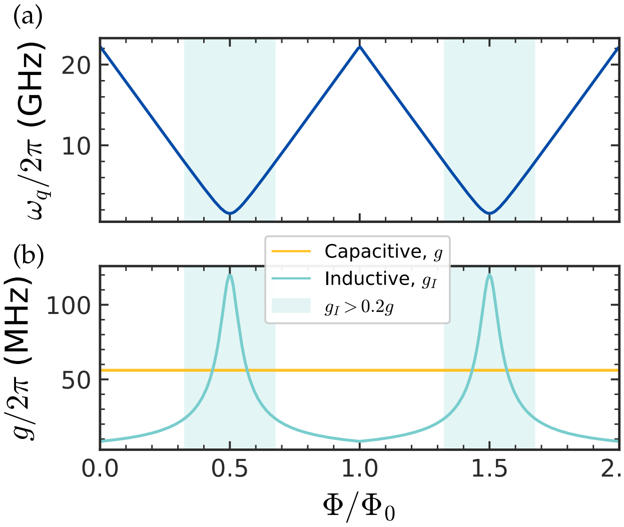

Figure 3.6: **(a)** Energy of a CQPS qubit as a function o the magnetic field $\Delta E(\Phi) = \hbar\omega_q$ evaluated with (3.1.7); **(b)** Comparison of inductive (blue, g_I, see A.6.5) and capacitive (yellow, g, see (3.1.18)) coupling strengths at different values of $\Delta E(\Phi)$. Inductive coupling strength peaks at the flux degeneracy points, getting substantially weaker away from it (region where qubit has good inductive coupling $g_I > 0.2g$ is shaded in blue). Experimentally this weak interaction makes it harder to detect the CQPS qubit away from the degeneracy point. Simulations were run for a resonator with realistic $C_r = 60\,\text{fF}, L_r = 1600\,\text{nH}, E_s/h = 1.5\,\text{GHz}$ values later found in experiment (see Sec. 3.4.1) and $M = 10\,\text{nH}$ (12 pH used in [199]).

Unlike inductive coupling where $g_I \propto M I_p I_r E_s/\Delta E$ (refer to A.6.5), the coupling strength does not depend on the qubit's energy ($\Delta E = \hbar\omega_q$). This is because capacitive coupling is traverse ($\propto \sigma_y$, see (3.1.17)), promoting a flux state exchange, in contrast to inductive coupling which is longitudinal ($\propto \sigma_z$, see (A.6.16)) that modifies the persistent current of the qubit directly. Hence the qubit should have uniform visibility across the whole energy spectrum as plotted in Fig. 3.6.

3.1.3.3 Qubit-resonator hybrid system

The full Hamiltonian includes the qubit H_q (3.1.7), resonator H_r (3.1.11) and interaction H_int (3.1.17) terms

$$H_\text{q-r} = -\frac{\hbar\omega_q}{2}\sigma_z + \underbrace{\hbar\omega_r(a^\dagger a + \frac{1}{2}) - \hbar g\sigma_y(ia - ia^\dagger),}$$

which can be turned into the more familiar Jaynes-Cummings Hamiltonian form [227] by moving to the interaction picture (refer to A.6.2) and removing energy non-conserving terms such as $\sigma_+ a^\dagger$ (double excitation) and $\sigma_- a$ (double relaxation) through the Rotating wave approximation (RWA)

$$H_\text{q-r} = -\frac{\hbar\omega_q}{2}\sigma_z + \hbar\omega_r(a^\dagger a + \frac{1}{2}) - \hbar g(\sigma_+ a + \sigma_- a^\dagger). \tag{3.1.19}$$

The CQPS qubit will interact with the resonator via the following energy-preserving transitions:

- Qubit absorbs a photon and transitions to the excited state: $|g,n\rangle \to |e,n-1\rangle$;
- Qubit relaxes to ground state and releases a photon into the resonator: $|e,n-1\rangle \to |g,n\rangle$.

(3.1.19) has an analytical solution derived in A.6.1, and for the n-th *excitation* manifold (n is number of resonator photons + ground (0) or excited (1) state of the qubit) the Hamiltonian (A.6.3)[4]

$$\frac{1}{\hbar}H_{q-r,n} = \begin{array}{c|cc} & |g,n\rangle & |e,n-1\rangle \\ \hline \langle g,n| & (n+\frac{1}{2})\omega_r - \frac{1}{2}\omega_q & g\sqrt{n} \\ \langle e,n-1| & g\sqrt{n} & (n+\frac{1}{2})\omega_r + \delta_{q-r} - \frac{1}{2}\omega_q \end{array}, \qquad \frac{1}{\hbar}H_{n=0} = \begin{array}{c|c} & |g,0\rangle \\ \hline \langle g,0| & -\frac{\hbar\delta_{q-r}}{2} \end{array},$$

has eigenvalues

$$E_{\pm,n\geq 1} = \frac{\hbar}{2}\left((2n+1)\omega_r - \omega_q \pm \Omega_n\right), \qquad E_{g,n=0} = -\frac{\hbar\delta_{q-r}}{2}, \tag{3.1.20}$$

and eigenstates

$$\begin{aligned} |-,n\rangle &= \cos(\theta_n/2)\,|g,n\rangle - \sin(\theta_n/2)\,|e,n-1\rangle \\ |+,n\rangle &= \sin(\theta_n/2)\,|g,n\rangle + \cos(\theta_n/2)\,|e,n-1\rangle \\ &|g,n=0\rangle\,, \end{aligned} \tag{3.1.21}$$

---

[4] Constant offset $-1/2\omega_q + 1/2\omega_r$ is reintroduced.

for a detuning $\delta_{q-r} = \omega_q - \omega_r$ between the qubit and resonator, $\Omega_n = \sqrt{\delta_{q-r}^2 + 4ng^2}$ and $\tan(\theta_n) = 2g\sqrt{n}/\delta_{q-r}$. These *excitation* manifolds are shown in Fig. 3.7 and the new eigenstates have a different share of qubit and photon components depending on θ_n. Three cases can be distinguished:

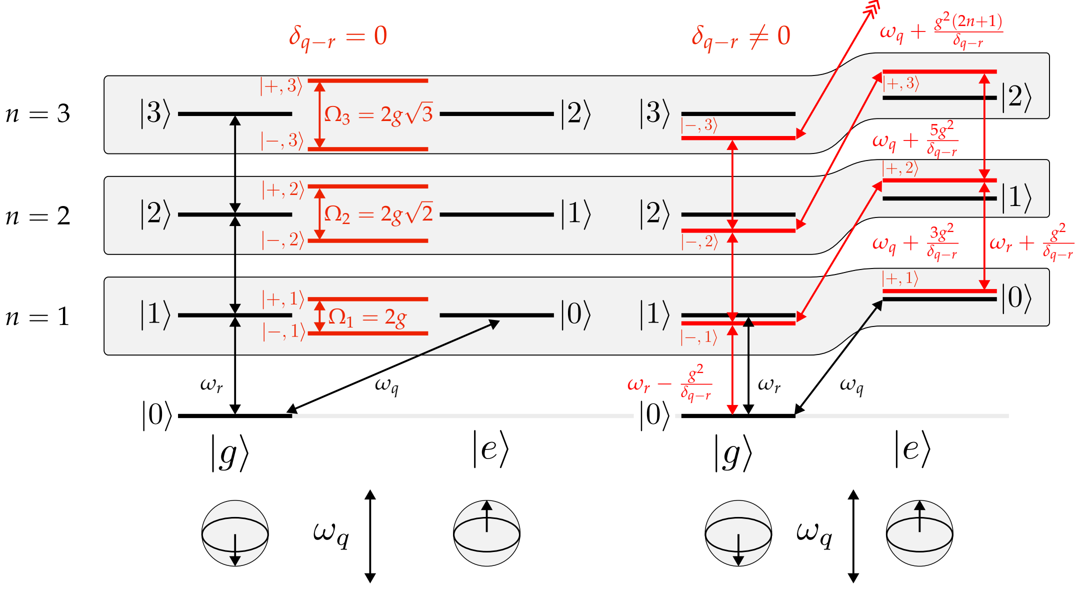
(a) Dressed state **(b)** Dispersive/Stark Shift

$\delta_{q-r} = 0$
$\delta_{q-r} \neq 0$
$n = 3$
$n = 2$
$n = 1$
$|3\rangle$
$|2\rangle$
$|1\rangle$
$|0\rangle$
$|+,3\rangle$
$|-,3\rangle$
$|+,2\rangle$
$|-,2\rangle$
$|+,1\rangle$
$|-,1\rangle$
$\Omega_3 = 2g\sqrt{3}$
$\Omega_2 = 2g\sqrt{2}$
$\Omega_1 = 2g$
ω_r
ω_q
$\omega_q + \frac{g^2(2n+1)}{\delta_{q-r}}$
$\omega_q + \frac{5g^2}{\delta_{q-r}}$
$\omega_q + \frac{3g^2}{\delta_{q-r}}$
$\omega_r + \frac{g^2}{\delta_{q-r}}$
$\omega_r - \frac{g^2}{\delta_{q-r}}$
$|g\rangle$
$|e\rangle$

Figure 3.7: Manifold states (shown in red and indexed by n) of the qubit-resonator system (native states shown in black) under different detunings $\delta_{q-r} = \omega_q - \omega_r$: **(a)** Dressed states when there is zero detuning ($\omega_r = \omega_q$), where degeneracy between states $|g,n\rangle, |e,n-1\rangle$ is lifted by the coupling g; **(b)** When there is a sizeable detuning, as per (3.1.27) the resonator frequency changes by $\pm g^2/\delta_{q-r}$ depending on the state of the qubit, while the qubit frequency changes by $(2n+1)g^2/\delta_{q-r}$ depending on the number of photons in the resonator.

- **No coupling:** setting $g = 0$ implies that the qubit and resonator do not interact with each other

$$\frac{1}{\hbar}H_{q-r,n} = \begin{array}{c c} & \begin{array}{cc} |g,n\rangle & |e,n-1\rangle \end{array} \\ \begin{array}{c} \langle g,n| \\ \langle e,n-1| \end{array} & \begin{bmatrix} (n+\frac{1}{2})\omega_r - \frac{1}{2}\omega_q & 0 \\ 0 & (n-\frac{1}{2})\omega_r + \frac{1}{2}\omega_q \end{bmatrix} \end{array}.$$

  The eigenstates correspond to the raw qubit-resonator states ($|g,n\rangle, |e,n-1\rangle$) whose total energy is the sum of of the qubit's and resonator's photon energies.

- **Resonant case:** Setting $\delta_{q-r} = 0$ puts the qubit at the same frequency as the resonator, allowing them to coherently exchange photons

$$\frac{1}{\hbar}H_{q-r,n} = \begin{array}{c|cc} & |g,n\rangle & |e,n-1\rangle \\ \hline \langle g,n| & n\omega_r & g\sqrt{n} \\ \langle e,n-1| & g\sqrt{n} & n\omega_r \end{array}.$$

In the weak drive limit with $n=1$, the resonant interaction *dresses* two manifold states $|\pm,1\rangle = |g,1\rangle \pm |e,0\rangle/\sqrt{2}$ with energy difference $\hbar\Omega_{n=1} = 2\hbar g$ (see Fig. 3.7 (a)). They will flip flop between each other in a process known as Rabi splitting - identical to the oscillations between two states in Sec. 1.6.3.

The excitation in this manifold can exist as an excited qubit ($|e\rangle$) and have decay rate Γ_1 (refer to Sec. 1.3.2)

$$|\langle e|\pm,1\rangle|^2 = \frac{1}{2}, \tag{3.1.22}$$

or in the cavity as a photon ($|n=1\rangle$) with decay rate κ (refer to A.4.2)

$$|\langle n=1|\pm,1\rangle|^2 = \frac{1}{2}, \tag{3.1.23}$$

and so the state will have an average decay rate of $(\Gamma_1+\kappa)/2$ (see Fig. 3.8).

◎ **Dispersive case** of large detuning $1 \ll \delta_{q-r}$, the angle $\theta_n \approx 2g\sqrt{n}/\delta_{q-r}$ and the eigenstates (3.1.21) resemble *mostly* qubit and *mostly* cavity states with only a small photonic component of magnitude $\sim g\sqrt{n}/\delta_{q-r}$

$$|-,n\rangle \approx |g,n\rangle - \underbrace{\frac{g\sqrt{n}}{\delta_{q-r}}|e,n-1\rangle}_{\text{photonic component}}, \quad |+,n\rangle \approx \underbrace{\frac{g\sqrt{n}}{\delta_{q-r}}|g,n\rangle}_{\text{photonic component}} + |e,n-1\rangle \tag{3.1.24}$$

resulting in a Stark shift of the resonator modes (see Fig. 3.7 (b)). For example, state $|-,1\rangle$ will have only a small contribution from the excited qubit state $|e,0\rangle$ scaling the decay rate Γ_1 for a total rate $\Gamma_1 + (g/\delta_{q-r})^2\kappa$. Likewise, eigenstate $|g,1\rangle$ decays at a rate $(g/\delta_{q-r})^2\Gamma_1 + \kappa$. These rates and relation to the new eigenstates of the system are shown in Fig. 3.8.

The amplitude $\Omega_n \approx \delta_{q-r} + 2ng^2/\delta_{q-r}$ also changes the resonator transition frequency from (3.1.20)

$$(\textbf{Stark shift}) \qquad \omega_r' = \frac{1}{\hbar}(E_{\pm,n} - E_{\pm,n-1}) = \omega_r \pm \frac{g^2}{\delta_{q-r}}, \tag{3.1.25}$$

which now depends on the state of the qubit, while the effective qubit frequency

$$\textbf{(Dispersive shift)} \qquad \omega_q' = \frac{1}{\hbar}(E_{+,n+1} - E_{-,n}) = \omega_q + \frac{(2n+1)g^2}{\delta_{q-r}}, \tag{3.1.26}$$

depends the number of photons in the resonator (these new frequencies are shown as red arrows in Fig. 3.7)[5].

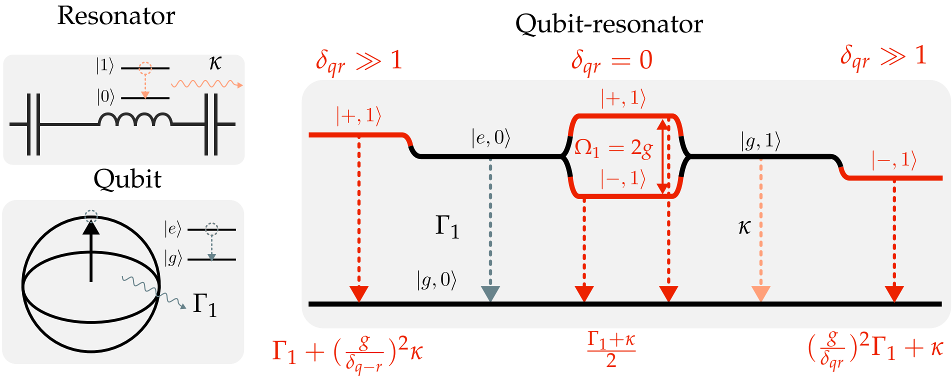
Resonator
$|1\rangle$
$|0\rangle$
κ
Qubit
$|e\rangle$
$|g\rangle$
Γ_1
Qubit-resonator
$\delta_{qr} \gg 1$
$\delta_{qr} = 0$
$\delta_{qr} \gg 1$
$|+,1\rangle$
$|e,0\rangle$
$|+,1\rangle$
$\Omega_1 = 2g$
$|-,1\rangle$
$|g,1\rangle$
$|-,1\rangle$
Γ_1
κ
$|g,0\rangle$
$\Gamma_1 + (\frac{g}{\delta_{q-r}})^2\kappa$
$\frac{\Gamma_1+\kappa}{2}$
$(\frac{g}{\delta_{qr}})^2\Gamma_1 + \kappa$

Figure 3.8: Relaxation mechanisms for manifold $n = 1$ states under the low photon population regime. The excitation can be lost via the relaxation of qubit $|e\rangle \rightarrow |g\rangle$ or emission of photon into the output line $|1\rangle \rightarrow |0\rangle$, with characteristic rates Γ_1 and κ respectively. Depending on the detuning (δ_{q-r}), the excitation in the manifold splits differently between an excited qubit state and a photon in the resonator leading to different decay rates (see (3.1.22), (3.1.23), (3.1.24)).

The full spectrum of the energy and transition frequencies at different detuning ($\delta_{q-r} = \omega_q(\Phi) - \omega_r$) is presented in Fig. 3.9 - these are the spectra shapes that one would expect to see in experiments.

3.1.3.4 Two-tone measurements

It is not trivial to measure the spectrum shown in Fig. 3.9 (b,c), as simply sweeping frequency as was done in Sec. 1.6.2 will not work - any non-resonant frequencies will be filtered out by the resonator. What will allow the mapping of the qubit are the effects in the dispersive limit

---

[5] An equivalent approach to arrive at (3.1.25), (3.1.26) is to apply an interaction picture transformation $U = \exp\left[\left(\hbar g(a\sigma^+ + a^\dagger\sigma^-\right) / \delta_{q-r}\right]$ on Hamiltonian (3.1.19) and expand to second order in powers of g/δ_{q-r}[164]

$$\begin{aligned} UH_{\text{q-r}}U^\dagger &\approx \hbar\omega_r a^\dagger a + \underbrace{\frac{\hbar}{2}\left(\omega_q + \frac{2g^2}{\delta_{q-r}}\left(a^\dagger a + \frac{1}{2}\right)\right)\sigma_z}_{\text{Stark + Lambda shift}} \\ &\approx \hbar\underbrace{\left(\omega_r + \frac{g^2}{\delta_{q-r}}\sigma_z\right)}_{\text{Dispersive shift}} a^\dagger a + \frac{\hbar}{2}(\omega_q + \frac{g^2}{\delta_{q-r}})\sigma_z \end{aligned} \tag{3.1.27}$$

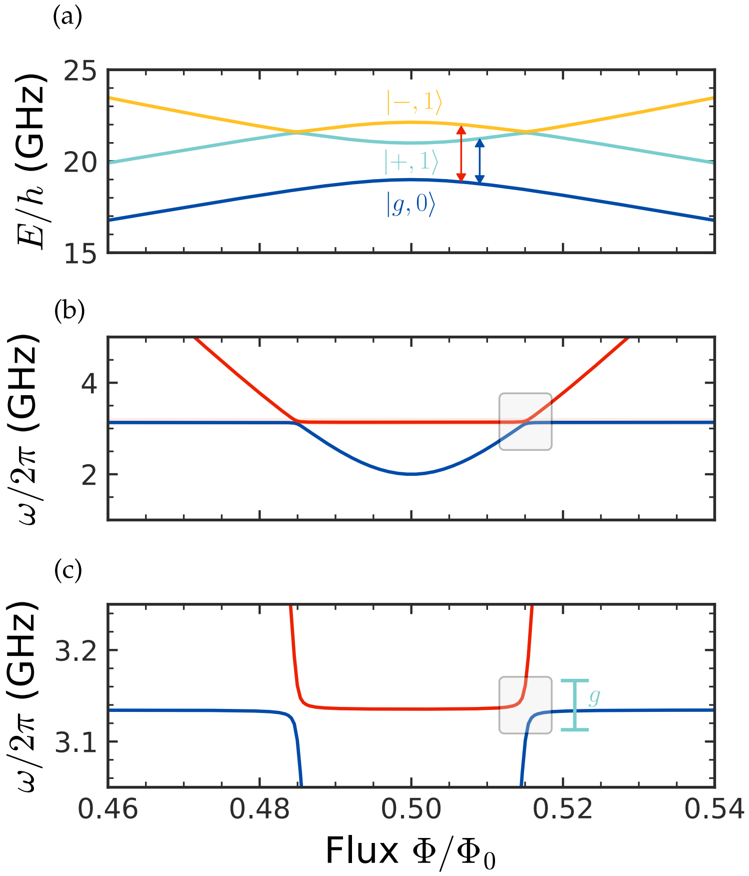

Figure 3.9: **(a)** First 3 states of a qubit-resonator system evaluated using (3.1.20); **(b)** Transition frequencies shown with arrows in (a) - there is an anticrossing (shown with grey square) where the energies of the qubit-resonator states become degenerate, leading to the creation of manifold states seen in Fig. 3.7; **(c)** Close up of the qubit-resonator degeneracy point, showing how the strength of the coupling g determines the size of the anticrossing.

- ◎ (3.1.26) **Stark and Lambda shifts**: photon-number-dependent shift of the qubit's transition frequency by $2g^2a^\dagger a/\delta_{q-r}$ (Stark shift) and a constant shift of g^2/δ_{q-r} due to vacuum resonator fluctuations (Lambda shift). This means that random fluctuations in the number of photons changes the qubit transition frequency, making the device more susceptible to additional shot noise in the resonator which dephases the qubit [222] (refer also to Sec. 1.3);

- ◎ (3.1.25) **Dispersive shift:** already seen in Fig. 3.7. The qubit *pulls* the cavity frequency by $\pm g^2/\delta_{q-r}$ depending on the qubit state.

The dispersive shift offers a way of searching for the qubit using two-tone spectroscopy [164] in the same way it was done for the twin qubit in Sec. A.2.6. One can monitor the change in amplitude of a control signal at $\omega_c = \omega_r \pm g^2/\delta_{q-r}$ that will be different for the

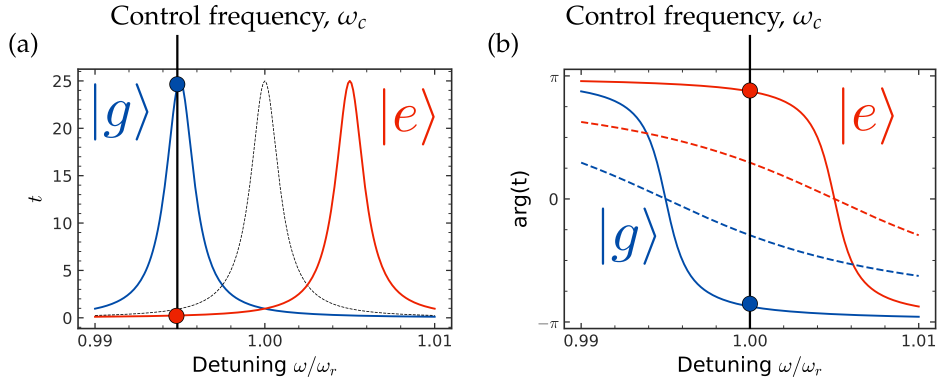

Figure 3.10: Two tone spectroscopy using a resonator, where a weak control tone (ω_c) is continuously monitored, while a probe field (ω) searches for the qubit: **(a)** There will be 2 transmission profiles for the control tone depending on the state of the qubit. A two tone measurement would consist of sitting on the frequency associated with the qubit's ground state ($\omega_c = \omega_r - g^2/\delta_{q-r}$), and checking for change of transmission in the control signal that indicates a $|e\rangle \leftrightarrow |g\rangle$ transition; **(b)** Monitoring can also be done at the resonator frequency $\omega_c = \omega_r$, in which case the phase of transmission will detect a qubit state change. Dotted lines indicate $\kappa \gg 1$ in which case the contrast of the measurement weaker (but still more resolvable that monitoring transmission amplitude).

two qubit states, which is good when the shift is greater than the linewidth of the cavity (κ, see Fig. 3.10 (a)). Alternatively, on can monitor the phase at the original resonance position ($\omega_c = \omega_r$) which differ by π depending on the qubit state, which is good when $g^2/\delta_{q-r} \ll \kappa$ (see Fig. 3.10 (b)).

Interestingly, the additional terms in (3.1.27) commute with the rest of the Hamiltonian, meaning that any measurements that are made will conserve photon number and qubit state making two tone spectroscopy a quantum non-demolition measurement [228].

3.1.4 Driving

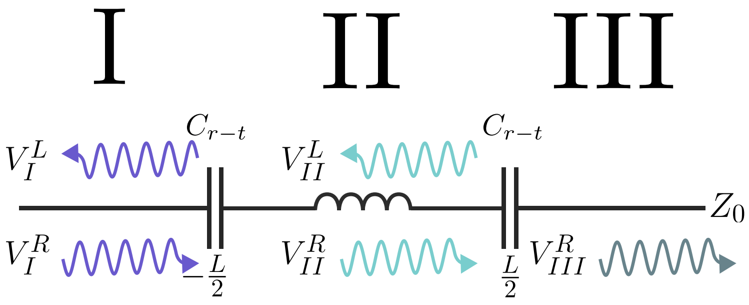

Figure 3.11: The resonator inside a TL will have voltage amplitudes defined in each of the 3 regions. Boundary conditions (BCs) at $x = \pm L/2$ are set to ensure continuity of voltage and continuity of current following Kirchhoff's laws. V_I^R is the driving field and V_{III}^R is the field in the output line, determined by the field in the resonator at the output capacitor $x = L/2$. The TL is assumed to be suitably terminated with Z_0 impedance. and not driven from the $\overset{\mathrm{L}}{\leftarrow}$.

3.1.4.1 Solving the steady state

Sec. 3.1.3 considered just the energy spectra of a qubit-resonator system, which can be probed with two tone measurements described in Sec. 3.1.3.4. However the probing itself will modify the state of the system, and needs to be accounted for by an additional driving term to Hamiltonian (3.1.19)

$$H = H_{\text{q-r}} + H_{\text{mw}}.$$

The interaction is quantified through the scattering of right-propagating drive wave $V_{\text{mw}}(x,t) = V_I^R \left(e^{ik(x+L/2)-i\omega t} + \text{h.c.}\right)$ which drives the resonator with a voltage field $\hat{V}_r$ (A.4) through the $C_{\text{r-t}}$ capacitor located as $x = -L/2$ (see Fig. 3.11). In direct analogy to (3.1.13) the energy from this drive[6]

$$\begin{aligned} H_{\text{mw}} &= V_{\text{mw}}(-L/2) C_{\text{r-t}} \hat{V}_r(-L/2) \\ &= V_I^R \left(e^{-i\omega t} + e^{i\omega t}\right) C_{\text{r-t}} \sqrt{m} V_{r0} (ia - ia^\dagger) \\ &= \hbar\Omega \left(ia - ia^\dagger\right) \left(e^{-i\omega t} + e^{i\omega t}\right), \end{aligned} \tag{3.1.28}$$

where similarly to Sec. 1.2.1 a driving amplitude

$$\hbar\Omega = \sqrt{m} V_I^R C_{\text{r-t}} V_{r0}, \tag{3.1.29}$$

is defined. A.6.2 shows how a unitary transformation and RWA can be applied to get a new Hamiltonian

---

[6] For $m = \text{odd}$ $\hat{V}(-L/2) \propto \sin(m\pi(-L/2)/L) \equiv \pm 1$ and $m = \text{even}$ $\hat{V}(-L/2) \propto \cos(m\pi(-L/2)/L) \equiv \pm 1$ (see A.4.3).

$$H = H_{\text{q-r}} + H_{\text{mw}} = -\frac{\hbar\delta_q}{2}\sigma_z + \hbar\delta_r a^\dagger a - \hbar g\left(a\sigma_+ + a^\dagger\sigma_-\right) - \frac{\hbar\Omega}{2}\left(ia - ia^\dagger\right), \tag{3.1.30}$$

where $\delta_q = \omega_q - \omega, \delta_r = \omega_r - \omega$ are the detunings of the qubit and resonator from the driving field. The system state evolving under Hamiltonian (3.1.30) and in the presence of dissipation is solved using the master equation formalism

$$\begin{gathered}\partial_t\rho = -\frac{i}{\hbar}\left(H,\rho\right) + \mathcal{L}\left[\rho\right],\\ \left\{\begin{aligned} -\frac{i}{\hbar}\left(H,\rho\right) =& i\frac{\delta_q}{2}\left[\sigma_z\rho - \rho\sigma_z\right] - i\delta_r\left[a^\dagger a\rho - \rho a^\dagger a\right]\\ &+ ig\left(a\sigma_+\rho - \rho a\sigma_+ + a^\dagger\sigma_-\rho - \rho a^\dagger\sigma_-\right)\\ &+ i\frac{i\Omega}{2}\left(a\rho - \rho a - a^\dagger\rho + \rho a^\dagger\right),\\ \mathcal{L}\left[\rho\right] =& \frac{\kappa}{2}\left(2a\rho a^\dagger - a^\dagger a\rho - \rho a^\dagger a\right)\\ &+ \frac{\Gamma_1}{2}\left(2\sigma_-\rho\sigma_+ - \sigma_+\sigma_-\rho - \rho\sigma_+\sigma_-\right)\\ &+ \frac{\Gamma_\varphi}{2}\left(\sigma_z\rho\sigma_z - \rho\right),\end{aligned}\right.\end{gathered} \tag{3.1.31}$$

with Linbland terms describing the dissipative processes happening in the qubit and resonator (refer to Sec. A.7.3):

- $L_r = \kappa(2a\rho a^\dagger - a^\dagger a\rho - \rho a^\dagger a)/2$ corresponds to jump operator $\sqrt{\kappa}a$ for finite rate of photon decay in the resonator (3.1.10);
- $L_q = \Gamma_1\left(2\sigma_-\rho\sigma_+ - \sigma_+\sigma_-\rho - \rho\sigma_+\sigma_-\right)/2 + \Gamma_\varphi(\sigma_z\rho\sigma_z - \rho)/2$ where Γ_1, Γ_φ are the relaxation and dephasing rates of the qubit corresponding to energy level fluctuation in qubit $\sqrt{\Gamma_\varphi}\sigma_z$ and spontaneous decay $\sqrt{\Gamma_1}\sigma^-$ (refer to Sec. 1.3).

A.6.4 solves (3.1.31) for the stationary state ($\partial_t\rho = 0$) in the qubit-resonator basis $\{|e,n\rangle, |g,n\rangle\}$ in the case of low photon number in the resonator ($n = 0$ and $n = 1$) and weak drive ($\mathcal{O}(\Omega^2) \to 0$) to find all the matrix elements ρ_{ij}

$$\rho = \begin{array}{c} \\ \langle g,0| \\ \langle g,1| \\ \langle e,0| \\ \langle e,1| \end{array} \begin{array}{cccc} |g,0\rangle & |g,1\rangle & |e,0\rangle & |e,1\rangle \\ \end{array}$$

$$\rho = \begin{array}{c|cccc} & |g,0\rangle & |g,1\rangle & |e,0\rangle & |e,1\rangle \\ \langle g,0| & 1-\rho_{11}-\rho_{22}-\rho_{33} & \rho_{01} & \rho_{02} & \rho_{03} \\ \langle g,1| & \rho_{10} & \rho_{11} & \rho_{12} & \rho_{13} \\ \langle e,0| & \rho_{20} & \rho_{21} & \rho_{22} & \rho_{23} \\ \langle e,1| & \rho_{30} & \rho_{31} & \rho_{32} & \rho_{33} \end{array}.$$

These elements can be used to evaluate the expectation value of the field in the resonator

$$\begin{aligned}\left\langle a^{\dagger}\right\rangle &= \mathrm{Tr}\left\{a\rho\right\} = \rho_{10} + \rho_{32} \\ &= \frac{-i\Omega/2}{\frac{g^2}{\delta_q + i\left(\frac{\Gamma_1}{2} + \Gamma_\varphi\right)} - \left(\delta_r + i\frac{\kappa}{2}\right)}\end{aligned} \tag{3.1.32}$$

3.1.4.2 Transmission profile

The analytical result of the resonator field in the stationary state (3.1.32) defines the expectation value of the voltage in the resonator at $x = L/2$ (see Fig. 3.11) according to (A.4.17) and will be[6]

$$\langle V(L/2)\rangle_{II} = \pm i V_{r0}\left(\langle a\rangle - \langle a^{\dagger}\rangle\right).$$

This field induces a charge on the coupling capacitors[7] $\langle Q\rangle = \langle V\rangle_{II} C_{\text{r-t}}$. The current leaking out the resonator is a time derivative of this charge

$$\begin{aligned}\langle I(L/2)\rangle_{III} &= \partial_t \langle Q\rangle \\ &= i V_{r0} C_{\text{r-t}}\left(\partial_t\langle a\rangle - \partial_t\langle a^{\dagger}\rangle\right) \\ &= i V_{r0} C_{\text{r-t}}\left(-i\omega_r\langle a\rangle - i\omega_r\partial_t\langle a^{\dagger}\rangle\right) \\ &= \omega_r V_{r0} C_{\text{r-t}}\left(\langle a\rangle + \langle a^{\dagger}\rangle\right),\end{aligned}$$

where the time evolution of the creation/annihilation operators ($a(t) = ae^{-i\omega_r t}, a^{\dagger}(t) = a^{\dagger}e^{i\omega_r t}$) is defined in the interaction picture (see (A.3.28)). Thus the voltage in the output line of characteristic impedance Z_0 will be

$$V^R_{III}(L/2) = I_{III}(L/2) \times Z_0 = \omega_r V_{r0} C_{\text{r-t}} Z_0\left(\langle a\rangle + \langle a^{\dagger}\rangle\right). \tag{3.1.33}$$

Subbing in the values of (3.1.29) and (3.1.32) into (3.1.33) will give

$$\begin{aligned}V^R_{III}(L/2) &= -i\frac{1}{2\hbar}\omega_r C^2_{\text{r-t}} Z V^R_I V_{r0}\left(\frac{1}{g^2/\delta'_q - \delta'_r} + \text{h.c.}\right) \\ &= -\frac{i}{2}V^R_I\frac{C^2_{\text{r-t}}\omega_r^2 Z}{C_r}\left(\frac{1}{g^2/\delta'_q - \delta'_r} + \text{h.c.}\right),\end{aligned}$$

where $\delta'_r = \delta_r + i\kappa/2$, $\delta'_q = \delta_q + i\Gamma_2$ and $\Gamma_2 = \Gamma_1/2 + \Gamma_\varphi$ has the same definition as in (1.3.4). The ratio of the original driving field with the scattered field will be the transmission coefficient of this system (see Fig. 3.11)

---

[7] More heuristically, one can think of the voltage in the resonator as inducing a displacement current $I \times Z_{r-t}$ where $Z_{r-t} = 1/i\omega C_{\text{r-t}}$ is the impedance of the coupling capacitors. In the output line with impedance Z_0 the voltage as a result of this current is $Z_0 I = iV_{r0}\left(\langle a\rangle - \langle a^{\dagger}\rangle\right)$

$$t_{r-t} = \frac{V^R_{III}}{V^R_I} = -\frac{i}{2}\frac{C^2_{\text{r-t}}\omega_r^2 Z}{C_r}\left(\frac{1}{g^2/\delta'_q - \delta'_r} + \text{h.c.}\right) = -i\frac{\kappa}{8}\left(\frac{1}{g^2/\delta'_q - \delta'_r} + \text{h.c.}\right), \quad (3.1.34)$$

where in the last step, the decay rate of the resonator (3.1.10) is substituted in.

3.2 Design

The device shown in Fig. 3.4 is fabricated under the same constraints as the transmon photon source (Sec. 1.4) and twin qubits (Sec. 2.2). The device has the following specifications:

- Narrow constrictions that would support a high rate of CQPS for strong qubit features. Together with inductive energy (E_L), E_s should give transition energies within the 2-12 GHz window of the experimental setup;
- Resonator harmonics should be in the 2-12 GHz window of the experimental setup;
- Capacitive coupling between qubit and resonator ($C_{\text{q-r}}$) should achieve the strong coupling regime $g > (\kappa + \Gamma_1)/2$ to ensure that qubit manipulations occur faster than the system relaxes to the ground state as per (3.1.18).

3.2.1 Operating energies

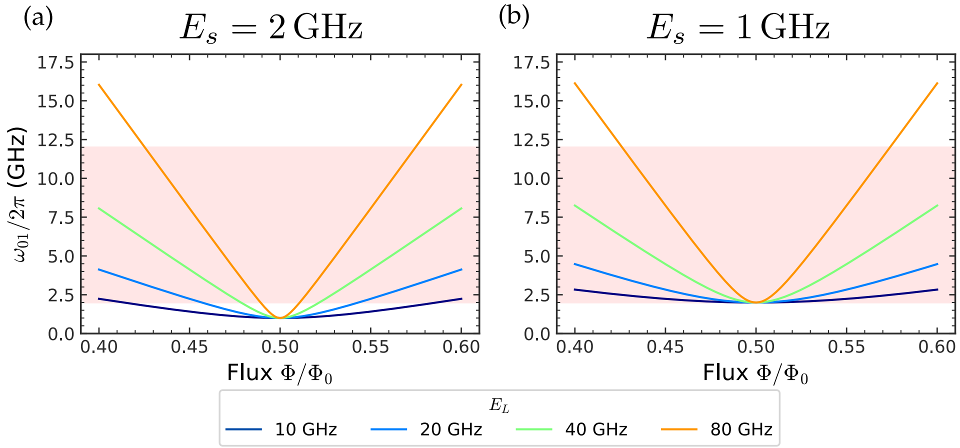

Figure 3.12: Simulation of the ω_{01} transition for a CQPS qubit with **(a)** $E_s = 2\,\text{GHz}$; **(b)** $E_s = 1\,\text{GHz}$. The value of E_s determines the *minimum* of the qubit spectrum, while E_L determines the *curvature* at the degeneracy point. Red bands indicate the 2-12 GHz operating band of the microwave setup.

The operating frequency ($\omega_{01} \equiv \omega_q$) for the $|0\rangle \leftrightarrow |1\rangle$ transition comes from numerically solving (3.1.5) for the different phase slip (E_s) and inductance energies (E_L). Running the simulation for a range of values in Fig. 3.12 shows that there is a large parameter range of E_L that will result in detectable devices. More importantly is to have $E_s \in [1\,\text{GHz}, 10\,\text{GHz}]$ to capture most of the qubit spectrum within the 2-12 GHz window.

3.2.1.1 Realising the QPSJ

Simply matching the E_s energies according to the empirical formula (3.1.1) will not guarantee success - one needs to realise a one-dimensional conduction channel with a width on the order of the coherence length ξ_0, which is $\sim 12\,\mathrm{nm}$ for TiN films (see Tab. A.1).

When the superconducting state in the wire is spatially homogenous (Al for example) the phase slips are delocalised along the wire, as opposed to an inhomogenous superconductor, where local phase slips occur preferentially at weak spots such as constrictions. The latter regime is targeted by using the highly disordered TiN, narrowing the amount of interaction channels to explore individual quantum phase slips. An example QPSJ connecting two superconducting leads via a nanowire of width $W_s \ll \xi$ and length $\xi \ll L_s$ is shown in Fig. 3.13.

With a band gap of $\Delta_{\mathrm{TiN}} = 1.784 T_c k_b = 2.95 \times 10^{-23}\,\mathrm{J}$ and normal resistance $R_{\square,\mathrm{TiN}} = 2\,k\Omega$, choosing constrictions $L_s = 50\,\mathrm{nm}$ long and $W_s = 8$-$16\,\mathrm{nm}$ wide will target E_s in the range of 2-10 GHz.

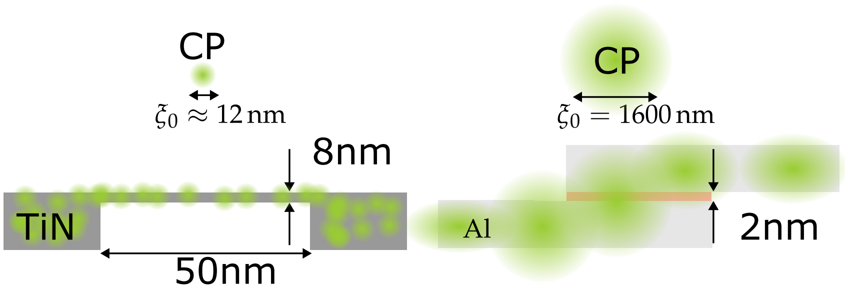

Figure 3.13: **(a)** Two superconducting electrodes are connected by a nanowire. The coherence length of CP in this disordered superconductor is small and the wavefunctions in the bulk of the conductors do not overlap, since the length of the constrictions is much longer than the coherence length $L_s \gg \xi_0 = 12\,\mathrm{nm}$; **(b)** JJ formed by two superconducting electrodes separated by an insulating barrier. The amplitudes of the wavefunctions decay within the barrier over a coherence length $\xi_0 = 1600\,\mathrm{nm}$, and the overlap provides coupling between them.

3.2.1.2 Realising inductive loop

The sheet kinetic inductance of TiN $L_{k,\square} \sim 2\,\mathrm{nH}$ (gauged from a number of experimental runs) is used to asses the required dimensions of the loop for the inductance energy ($E_L = \Phi_0^2/2L_{k,\square}N_{\mathrm{sq}}$, recall from Sec. 3.1.2 that geometric inductance is ignored) where N_{sq} is the number of squares of TiN along the perimeter of the loop.

Because the yield of constrictions from Sec. 3.2.1.1 is expected to be low, multiple qubits are included in the design to account for the failed QPSJ. To resolve their different spectra, the area (A) of the loops is staggered as in Sec. 2.2.4, to have different a flux number bias

($f_{\text{ext}} = B_{\text{ext}}A/\Phi_0$) from the magnetic field generated by the same coil as in Sec. 1.6.

Loop areas ranging from $A = 30\text{-}75\,\mu\text{m}^2$ with $N_{\text{sq}} = 30\text{-}40$ are chosen. A higher inductance energy (E_L) was favoured in order for the spectrum to be narrow and avoid strong overlap between the different qubit signals and to work with smaller magnetic fields (see Fig. 3.12). Furthermore, in order to have the continuum of CP states required to define flux states $\{|F\rangle\}$[8], the loops are grounded to allow the free flow of electrons to an from the system.

3.2.2 Resonator design

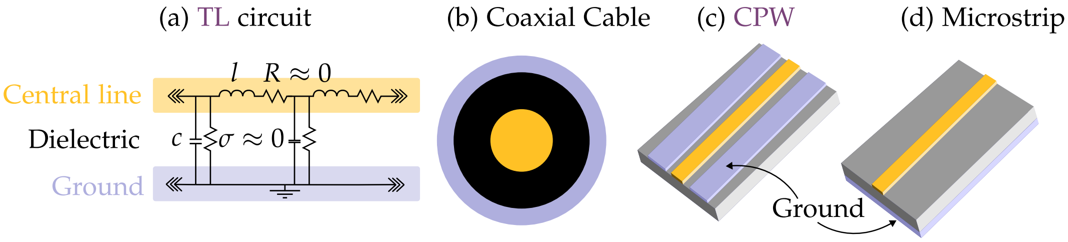
(a) TL circuit (b) Coaxial Cable (c) CPW (d) Microstrip

Figure 3.14: Realisation of a generic TL with central line and ground: **(a)** Circuit diagram of a TL under the dissipationless assumption that $R \approx 0, \sigma \approx 0$; **(b)** Realisation of circuit with coaxial cable; **(c)** Realisation of circuit with a Coplanar waveguide (CPW) on Si; **(d)** Realisation of circuit with a microstrip - it will require a ground beneath the substrate, complicating the fabrication procedure.

The resonator will be realised with a CPW [229], in which the central line and ground exist on the same plane (see Fig. 3.14) and will be fabricated from the same TiN material as the qubit. There is no strict constraint on the material used - it could equally have been made from Al or Au, however this would involve more lithography layers.

To achieve the 2-12 GHz resonator frequencies ($f_m = mv/2L$, see (3.1.9)) in TiN, with a high kinetic inductance and hence small propagation velocity ($v = 1/\sqrt{lc}$), will require a short resonator length (L). This actually allows for a compact design - a narrow bar in the center of a standard chip, without requiring a meander as would usually be the case (see for example [230, 231]).

With a known $L_{k,\square} \sim 2\,\text{nH}$ and capacitance per unit length $c = 0.85 \times 10^{-10}\,\text{F/m}$ a coplanar $\lambda/2$ resonator of TiN of length $L = 1140\,\mu\text{m}$ and width $W = 5\,\mu\text{m}$ will result in the necessary frequencies. The qubits are distributed around its center, where they would couple stronger to the even modes of the resonator (see Fig. 3.15). The impedance (A.3.5)

---

[8] Recall that charge ($\hat{Q} = 2e\hat{N}$) and flux ($\hat{\Phi} = \Phi_0\hat{f}$) are conjugate variables satisfying the commutation relation $[\hat{Q}, \hat{\Phi}] = i\hbar$ (refer to A.1.6), which implies the uncertainty relation $\Delta\Phi\Delta Q \geq \hbar/2$ - specifying a flux state necessarily creates infinite uncertainty in the charge state. Practically this means that charge should be free to *enter* and *leave* the system.

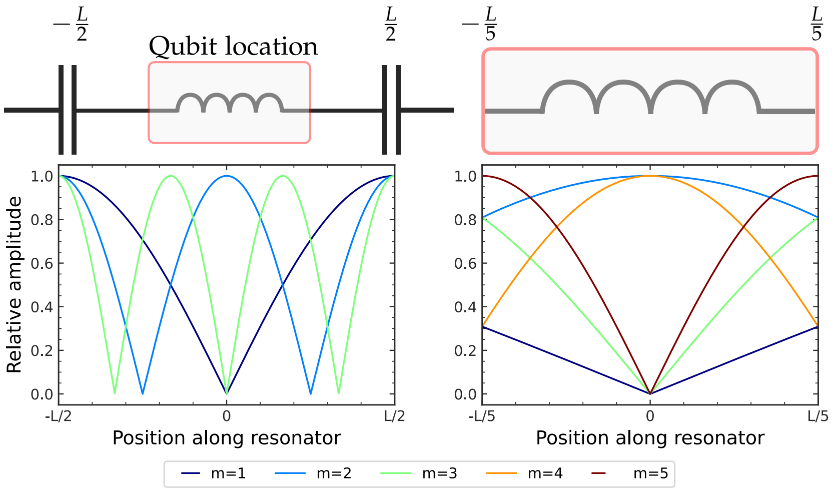

Figure 3.15: Voltage amplitudes ($V_m(x)$) of the different resonator modes defined by (A.4.18) compared to the location of the qubits: **(a)** Full resonator; **(b)** Central section. Even modes will couple strongest to the qubits by delivering the greatest voltage field, as a result of having antinodes in the center of the resonator.

of such a resonator will be

$$Z_r = \sqrt{\frac{L_r}{C_r}} = \sqrt{\frac{(L_{k,\square} \times L/W)}{L \times c}} \approx 3.3\,\mathrm{k}\Omega,$$

creating a strong impedance mismatch at the interface with the $Z_0 = 50\,\Omega$ TL. The strong reflection that results from this (refer to A.3.3) has the effects of:

- Reflecting all waves approaching the coupling capacitors at $x = \pm L/2$ (from both the resonator and TL sides), giving a net zero current in at this interface. This reflection limits the dissipation of power through photon decay;
- Fulfilling the precondition for the formation of the standing waves of the resonator modes seen in Fig. 3.15.

As seen from (A.4.15) any galvanic coupling between the central line of the resonator and the ground planes that gives a finite conductance $\sigma \neq 0$ leads to an internal resonator dissipation rate $\kappa_{\mathrm{internal}}$ that affects the total photon relaxation rate $\kappa = \kappa_{\mathrm{internal}} + \kappa_{\mathrm{external}}$. Furthermore, there must not be losses in the dielectric to prevent loss of energy into free space [232].

3.2.3 Coupling system to the resonator

Although in the experiment there are multiple qubits on the same resonator, only a single qubit coupling is considered (although it is possible to do a full multi-qubit treatment

[233]). At resonance between the resonator and qubit ($\delta_{q-r} = 0$) the hybrid qubit-resonator states ($|\pm, n\rangle$) decay with rates $\sim (\Gamma_1 + \kappa)/2$ (refer to (3.1.3.3)). To manipulate the quantum state faster than these decays, the coupling strength (g) must be stronger that these rates:

$$g \gg \kappa, \Gamma_1.$$

Fig. 3.16 shows simulations of the transmission profiles made with (3.1.34) - this is what is expected to be measured experimentally on the system at different driving frequencies and qubit biases. In the strong coupling regime ($g > \Gamma_1, \kappa$) two transmission peaks will be visible, corresponding to transitions between the two manifold states to the ground state and revealed as an anticrossing in the resonator signal (recall from Sec. 3.1.3.4 that the qubit state is inferred indirectly from the phase or amplitude response of the resonator). In the weak coupling regime ($g \sim \kappa < \Gamma_1$) the dominant decay rate of the manifold states will hide the Rabi splitting, giving a weaker anticrossing feature.

Revisiting the important rates of the qubit resonator system discussed in Sec. 3.1.3.2:

- $\Gamma_1 \sim 30\,\text{MHz}$ is the qubit relaxation rate defined by noise processes and $\Gamma_2 \approx \Gamma_1/2 + \Gamma_\varphi$ is the total dephasing rate of the qubit (refer to Sec. 1.3.2). It estimated from previous works with analogous structures [201] where $1/\Gamma_1 \sim 30\,\text{ns}$;
- $\kappa_m = 4Z_r C_{\text{r-t}}^2 \omega_m^2 / mC_r \sim 150\,\text{MHz}$ is the photon leakage rate out the resonator through the coupling capacitors ($C_{\text{r-t}}$, refer to A.4.2). It is estimated on the second resonator mode $m = 2$, by taking a $20\,\mu\text{m}$ interface length of the coupling capacitor (see Fig. 3.17 (d)) and a $f_r = 5\,\text{GHz}$ resonator with length $L = 1140\,\mu\text{m}$ and width $W = 5\,\mu\text{m}$ (taken from Sec. 3.2.2) from which $C_r = c \times L \approx 100\,\text{fF}$, $L_r = L_{k,\square} \times L/W \approx 1\,\text{mH}$ and $Z_r = \sqrt{L_r/C_r} \approx 3\,k\Omega$;
- $g = V_s C_{\text{q-r}} V_m / 2\hbar$ defined in (3.1.18) is the coupling strength that depends on the characteristic voltages of the resonator and qubit across their mutual coupling capacitor ($C_{\text{q-r}}$). The strength is a direct indicator of how quickly the resonator and qubit can exchange quantum information.

This gives an estimate assessment that $g \geq 100\,\text{MHz}$ is required to achieve the strong coupling regime. Evaluating (3.1.18) for a phase slip energy $E_s/\hbar = 1\,\text{GHz}$ and $C_{\text{q-r}} = c \times L_{C_{\text{q-r}}}$ one finds that $L_{C_{\text{q-r}}}$ can be on the order of $\sim 10\,\mu\text{m}$. This will be realised with *fingers*, coming perpendicularly off the resonator and overlapping with the loop of the qubit.

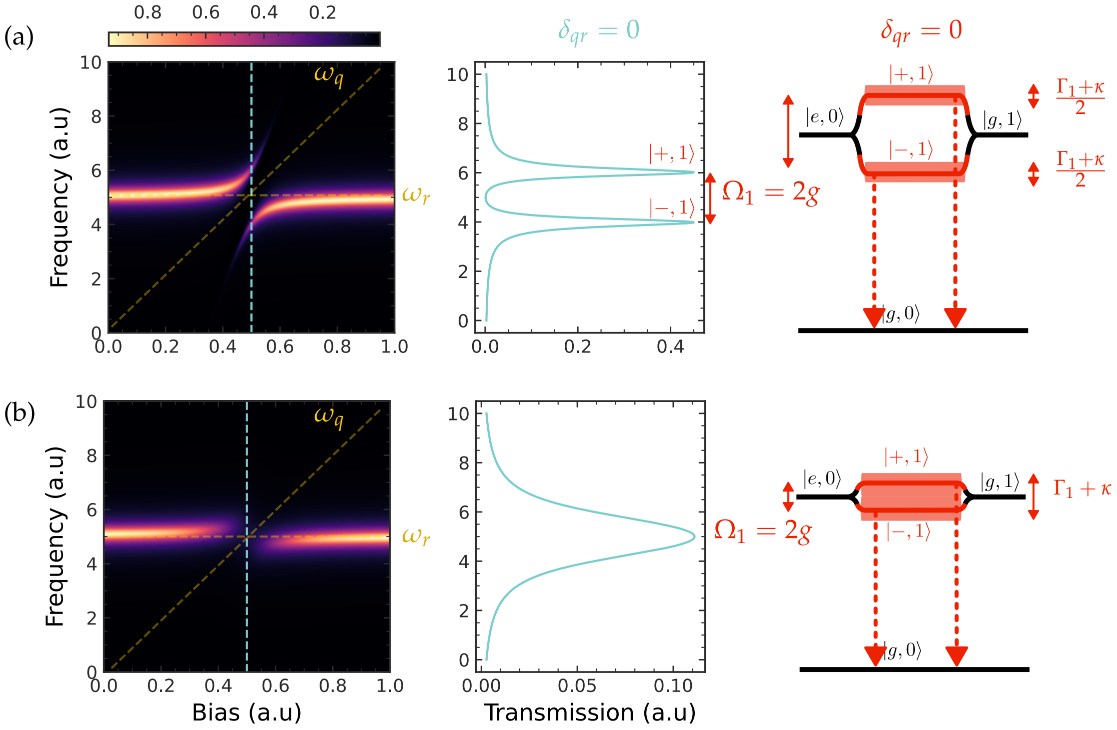

Figure 3.16: Qubit-resonator anticrossing due to formation of hybridised qubit-resonator states that would be detected when sweeping the bias and monitoring transmission at different frequencies. Simulations are run with (3.1.34) for different relaxation rate combinations, with the transmission cross sections (middle column) and eigenstates (right column) shown at $\delta_{q-r} = \omega_q - \omega_r = 0$: **(a)** Strong coupling regime with $g = 1, \Gamma_1 = 0.5, \kappa = 0.5$ which reveals the Rabi splitting of the level corresponding to the two transition from ground state into the first manifold $|0, g\rangle \leftrightarrow |\pm, 0\rangle$ (see Fig. 3.7 (a)); **(b)** Weak coupling regime with $g = 1, \Gamma_1 = 8, \kappa = 0.5$, in which the qubit decays before it has substantial time to interact with the resonator (equivalently the linewidth of the hybrid states shown in red highlight, is larger than the Rabi splitting $\Omega_1 = 2g$). The qubit will be harder to detect as the anticrossing energy gets *lost* in the transmission peak of the resonator.

3.2.4 Final design

The design shown in Fig. 3.17 features the parameters shown in Tab. 3.2. The loop areas are staggered to separate the qubits out in magnetic field. The TL and ground planes (shown in yellow in Fig. 3.17 (a)) will be made from Au, while the rest of the structure in blue will be etched out in TiN.

Table 3.2: Summary design parameters for CQPS qubit.

Design parameter	**Values**
ω_q	2-8 GHz
$E_s/\hbar$	1-10 GHz
$E_L/\hbar \Leftrightarrow I_p$	20-40 GHz $\Leftrightarrow$ 12-26 nA
Constriction	Widths (W_s): 8-13.5 nm, Length (L_s): 50 nm
Loop areas (A)	30-75 μm^2
N_{sq} in loops	30-40
Resonator	Width (W): 5 μm, Length (L): 1140 μm
C_r	$L \times c \sim 100$ fF
$C_{\text{q-r}}$	3 μm $\times c$
$C_{\text{r-t}}$	20 μm $\times c$

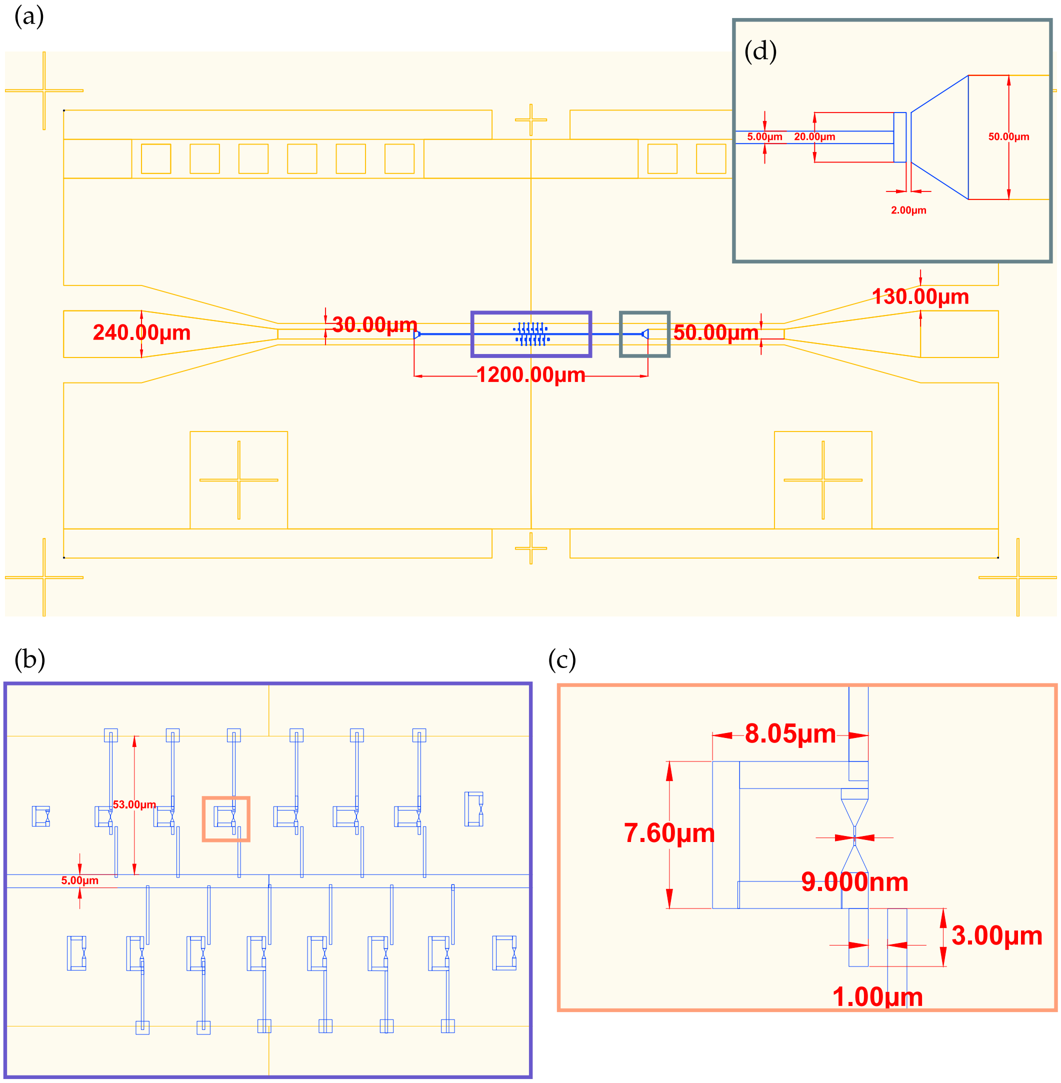
(a)
240.00μm
30.00μm
1200.00μm
50.00μm
130.00μm
(d)
5.00μm
20.00μm
50.00μm
2.00μm
(b)
53.00μm
5.00μm
(c)
8.05μm
7.60μm
9.000nm
3.00μm
1.00μm

Figure 3.17: **(a)** Complete chip design with multiple CQPS qubits capacitively coupled to a $\lambda/2$ resonator (blue), and clustered around its center. Given the statistics of successful constrictions, only a subset of the qubits would be operable; **(b)** Close up of the qubit array - staggered areas will spread the device spectra out during magnetic field sweeps; **(c)** Individual CQPS qubit, made fully from TiN. Coupling to the ground allows free exchange of CP during operation. The narrow constrictions ranged from 8-13.5 nm and the coupling capacitor ($C_{\text{q-r}}$) had a length $L_{C_{\text{q-r}}} = 3\,\mu$m; **(d)** Interface between resonator and TL with coupling capacitor $C_{\text{r-t}}$ having a length of $20\,\mu$m.

3.3 Fabrication

The substrate fabricated at Delft University was a 2-3 nm thick TiN film deposited on a Si(100) wafer using plasma-assisted Atomic layer deposition (ALD) [234, 235] (for comparison, a 20 nm film was used in [199] and 3 nm film in [200]). The film would vary from process to process, and the device was made using a wafer that has already demonstrated CQPS qubits. Using this initial wafer, recipe B.6 is executed.

3.3.1 Processing steps

- **Layer 1:** A pattern of the resonator, groundplanes and TLs for connecting to laboratory microwave measurement circuit is deposited using bilayer lithography. Titanium (Ti) is used as an adhesion layer, followed by 80 nm of Au;
- **Layer 2:** The constrictions of 10 nm are fabricated on the Electron beam lithographer (EBL). From the way that Proximity effect correction (PEC) applied to the qubit pattern (see Fig. 3.18) assigns the same dose to the narrow constrictions and bulkier structures surrounding it, one can infer that it there is an degree of hit-and-miss with the EBL being able to trace out the narrow line. With a pattern units of 0.05 nm (the stride with which the EBL produces electron shots), this constriction would receive around 200 shots across its width.

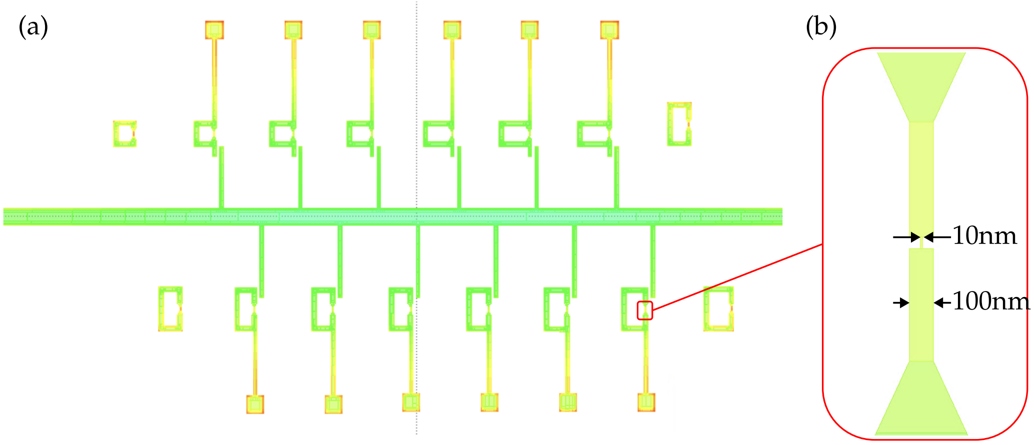

Figure 3.18: Proximity effect correction to the design shown in Fig. 3.17 showing the base dose ranging from 1.0-1.3. **(a)** Main design; **(b)** Close up of an individual constriction. Notice how the same dose is applied to the wide and narrow constrictions settings, due to reaching the limits of resolution supported by EBL and the `Beamer` software.

The resonator line and CQPS-qubits are patterned into a negative resist (`Ma-N2410` [236]) spun to a thickness of 50 nm, which acts as a mask for Reactive ion etching

(RIE) in Ar:CF$_4$ (1:10) plasma. The EBL is done in high resolution mode and a low 200 pA current. The negative resist is not removed after etching, as it protects the TiN structures from oxidation.

To confirm the success of etching, test TiN bars with dimensions $80 \times 20\,\mu\text{m}^2$ (4 squares) are fabricated on the same chip. A resistance of 200-300 Ω prior to etching should increase to 10 kΩ once the bars are etched out. Not all constrictions would be successful - images taken on a Focused ion beam (FIB) microscope show the mask failing for very narrow constrictions, with structures below 8 nm tending to collapse due to thin resist and the wet etching happening in the horizontal plane underneath the resist (see Fig. 3.19).

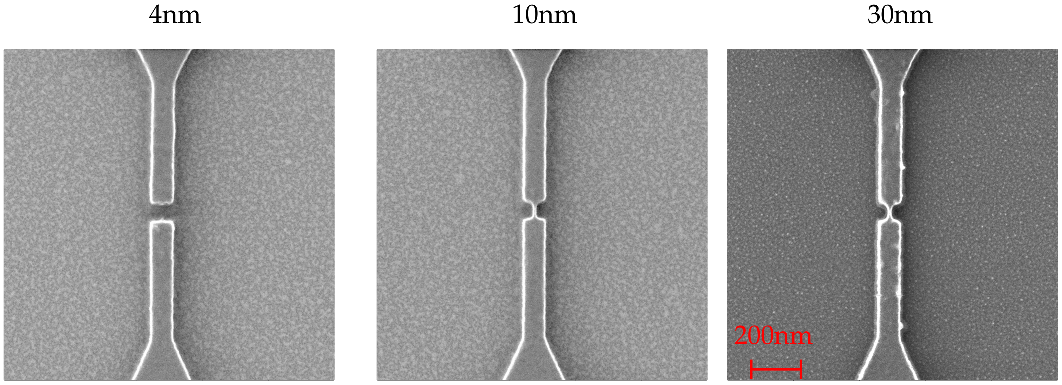

Figure 3.19: FIB images of constriction in CQPS qubits across which the phase slip occurs: 4 nm, 10 nm and 30 nm. These constrictions are a result of etching through a negative resist that below 10 nm would fail to protect the TiN underneath it, leading to had a low yield due to open circuits seen for the 4 nm case.

The resistances of the bars were monitored down to low temperatures, and it was found that the superconducting transition is approximately at $T_c \approx 1.2\,\text{K}$ and the normal sheet resistance is $R_\square = 2.07\,\text{k}\Omega$ (see Fig. 3.20) implying $L_{k,\square} \sim 2\,\text{nH}$ from (3.1.8), which is in the order of expected magnitude.

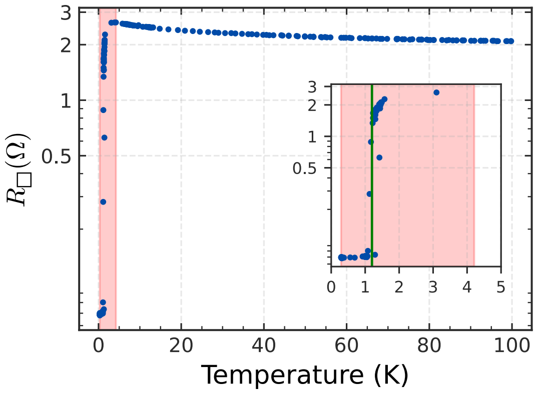

Figure 3.20: Sheet resistance of a 80 × 20 μm^2 TiN film bar monitored during cooldown in order to estimate the kinetic inductance $L_{k,\square}$ (refer to A.1.7) and superconducting transition temperature $T_c = 1.2$ K (shown in green). Inset shows the close up view of the transition region (red).

3.3.2 Result

Fig. 3.21 shows a batch of fabricated CQPS qubits according to the specification in Tab. 3.2. Isolated grains seen in the close up image of the constriction with weak inter-grain coupling could result in Coulomb blockade [234] which would prevent CQPS observation.

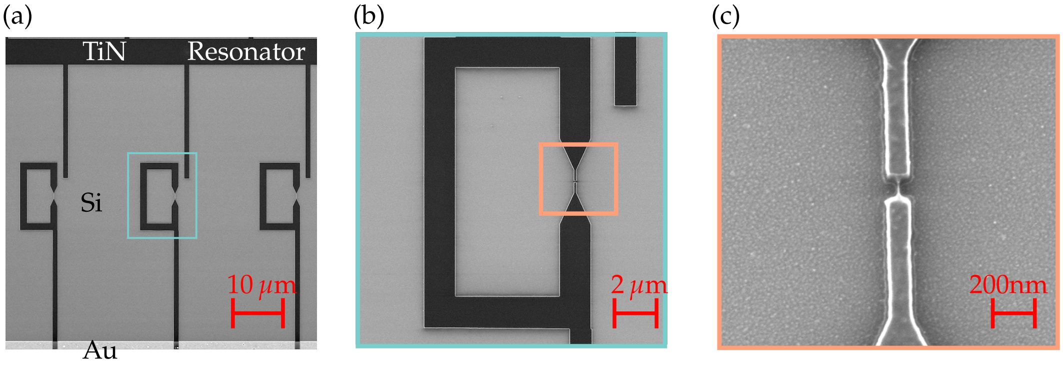

Figure 3.21: **(a)** FIB Micrograph of the CQPS qubits capacitively coupled via fingers ($C_{\text{q-r}}$) to the TiN resonator. Shown is the coupling capacitor with the resonator on top of the image and the grounding line running to the bottom ground plane. The three materials involved in the fabrication are labelled and correspond to dark (TiN), light (Au) and neutral (Silicon (Si)) colours; **(b)** Magnification of an individual qubit - the TiN from which it was cut is a 2-3 nm layer on top of the Si wafer; **(c)** Constriction in the qubit loop, across which the phase slip occurs.

3.4 Experiment

The experiment was performed using two techniques schematically demonstrated in Fig. 3.22: single-tone measurements that track transmission through the qubit-resonator system and which are described by (3.1.34); two-tone measurements that identify the qubit spectrum through it's back action on the resonator shown in Fig. 3.10. The sample is mounted and loaded as described in Sec. 1.6 - the 13 mK, environment ensures that TAPS will not be present during measurements.

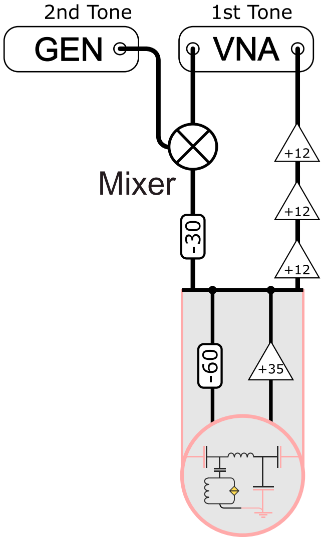

Figure 3.22: Experimental setup for two tone spectroscopy measurements of the CQPS qubit through a resonator.

3.4.1 Resonator characterisation

The $\lambda/2$ resonator is characterised by taking the transmission profile and finding the resonant modes (f_m) defined in (3.1.9). Standard transmission measurements with a Vector Network Analyser (VNA) give the complex microwave transmission through the resonator as a function of a probe frequency (f). They are fitted with (A.4.15), which in the limit off no internal loss ($\sigma = 0 \Leftrightarrow \kappa_{\text{internal}} = 0$) has a Lorentzian form (A.8.10)

$$|t(\omega)|^2 = A + B\frac{1}{1+\left(\frac{2\delta\omega}{\kappa}\right)^2}, \tag{3.4.1}$$

where A, B are a scalar offset and multiplier to account for systematic biases and $\delta\omega = \omega - \omega_m$ is the detuning from the m-th resonance.

The fitting of (3.4.1) to experimental data in Fig. 3.23 immediately identifies the quality factor of the m-th mode of the resonator ($Q_m = \omega_m/\kappa_m$) and extracted parameters are presented in Tab. 3.3. The visible peaks correspond to $m = 2,3,4,5$ with resonance frequencies $f_2 = 3.14\,\text{GHz}$, $f_3 = 5.12\,\text{GHz}$, $f_4 = 6.28\,\text{GHz}$, $f_5 = 7.95\,\text{GHz}$. The fundamental mode $f_1 \approx 1.58\,\text{GHz}$ falls outside the measurement equipment measurement range of 2-12 GHz. One may note that the harmonics do not follow the regularity expected from $f_m = mf_1$, which could not be accounted for at this stage.

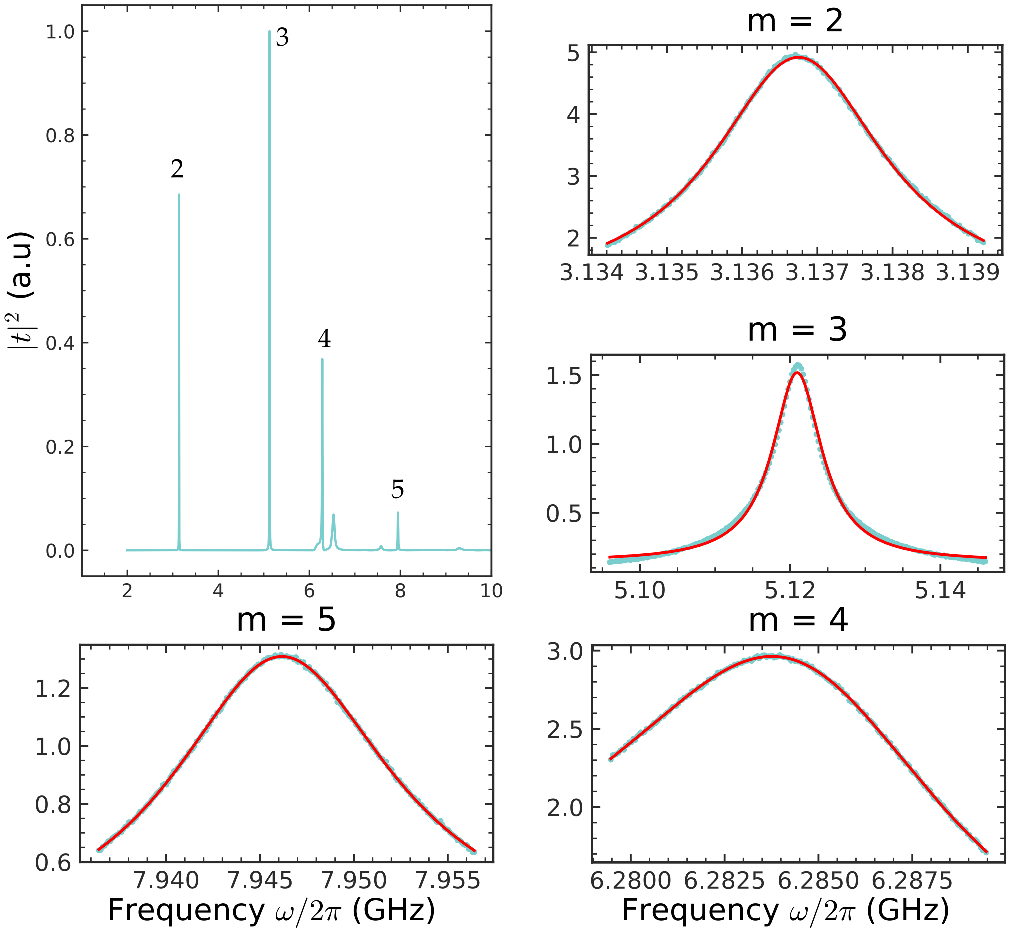

Figure 3.23: Fitting of resonator transmission spectra using (3.4.1), with 5 harmonics clearly visible in the 2-12 GHz range of the laboratory equipment. The linewidth (κ_m) and transmission amplitude varies for each of the harmonics, giving different quality factors for the different resonances.

The propagation velocity $v = 2Lf_1 \approx 3.57 \times 10^6\,\text{m/s}$ along the $W = 5\,\mu\text{m} \times L = 1140\,\mu\text{m}$ resonator with the standard capacitance per unit length $c = 0.85 \times 10^{-10}\,\text{F/m}$ implies:

- A sheet inductance[9] of $L_{k,\square} = Wl = W/v^2c \approx 5.6\,\text{nH}$ for the TiN material of the resonator;

---

[9] Direct analogy to sheet resistance $R_\square = \rho/T$ and resistance per unit length $R/L = \rho/WT$ from which $R_\square = WR/L$.

- A resonator impedance of $Z = \sqrt{l/c} \approx 3.3\,\mathrm{k}\Omega$;
- A coupling capacitance (from rearrangement of (3.1.10)) between the resonator and TL $C_{\text{r-t}} = \sqrt{\kappa_{m=2} C_{\text{r}} / 2Z} / \omega_r \sim 2\,\text{fF}$ for which the resonator total capacitance of $C_{\text{r}} = c \times L \sim 100\,\text{fF}$ was used.

Notably, these parameters agree with the estimates made in Sec. 3.2.2. The sheet inductance ($L_{k,\square}$) will also apply to the CQPS qubit that is made from the same TiN material as the resonator.

Table 3.3: Extracted resonator parameters for the different modes indexed by m. The resonator is assumed to have total capacitance $C_r = c \times L$.

Resonator mode m	f_m (GHz)	Q_m	$\kappa/2\pi$ (MHz)
2	3.14	1129	2.78
3	5.12	827	6.19
4	6.28	400	15.7
5	7.95	557	14.27

3.4.2 Qubit spectrum

The CQPS qubits are identified with two-tone spectroscopy measurements described in Sec. 3.1.3.4 using the setup in Fig. 3.22. The complex transmission (t) of a control tone on one of the harmonics ($f_c = f_m$) at $-25\,\text{dBm}$ power is monitored while sweeping an probe field (f) at $-5\,\text{dBm}$ power that *searches* for the qubit. The qubit state is mapped onto the phase of the control tone (see Fig. 3.10) to sense when the $|0\rangle \leftrightarrow |1\rangle$ transition is resonant, which indirectly maps out the qubit frequency spectrum.

Figure 3.24 (a) shows the response measured on $f_c = f_2 = 3.1\,\text{GHz}$. By sweeping the external magnetic field (B_{ext}) over a wide range, eight out of the twelve qubits are identified by their periodicity. The bright horizontal lines indicated are the resonator modes while the fits in Fig. 3.24 (b) are made using $\hbar\omega_q = \Delta E = \sqrt{(2I_p\delta\Phi)^2 + E_s^2}$ from (3.1.7) and summarised in Tab. 3.4. Because the coupling strength (g) varies with the position of the qubits on the resonator (see (3.1.18) and Fig. 3.15), some of the qubits are not visible on certain resonator modes. Fig. 3.24 (c) is a slice at the degeneracy point of one of the qubits, showing its linewidth. A Lorentzian fit (2.4.2) gives a relatively high decoherence rate $\Gamma_2/2\pi = 13.83\,\text{MHz}$ attributed to kinetic inductance fluctuations in the disordered TiN film [201], however it is still narrower than than for the CQPS qubits made on NbN (26 MHz [201]) and InO_x (260 MHz [199]).

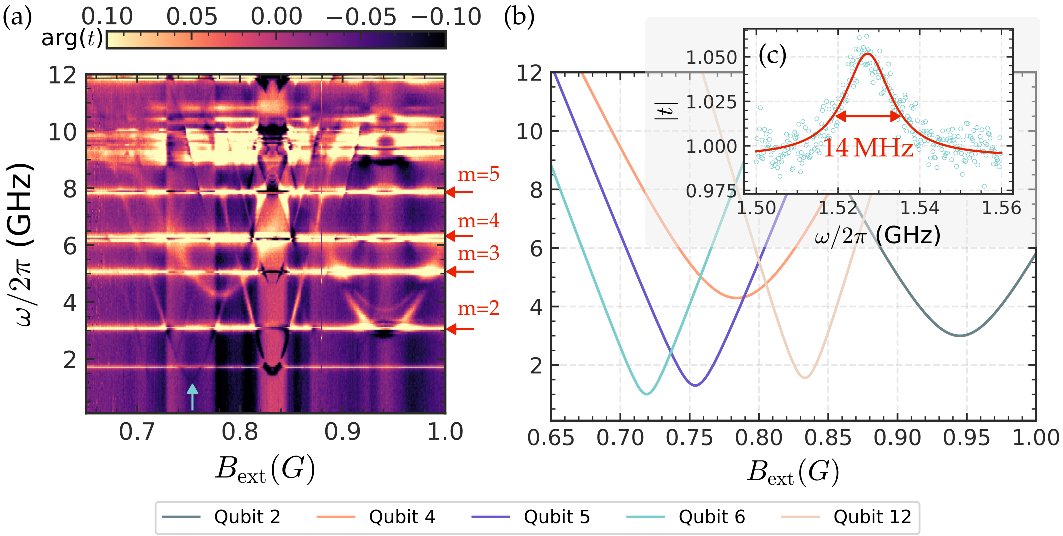

Figure 3.24: **(a)** Two-tone spectroscopy, where the phase of transmission (arg(t)) through the resonator at $f_2 = 3.14$ GHz is monitored while a probe drive (ω) and external field (B_{ext}) are independently swept. Strong phase variations in the resonator's transmission occur on qubit resonance ($\omega = \omega_q$), allowing the mapping of the qubit spectra; **(b)** Identified qubits are fitted with (3.1.7), taking into account their different periodicity due to their staggered areas; **(c)** Lorentzian fit (2.4.2) made to qubit 6 at its degeneracy point (blue arrow in (a)), with Full width at half maximum (FWHM) giving $\Gamma_2/2\pi = 13.83\,\text{MHz}$.

Normalising the fitted inductance of the CQPS loops ($L_k = \Phi_0/I_p$)[10] by the number of squares on their perimeters (see Tab. 3.2) results in $L_{k,\square} \approx 3.5 - 4\,\text{nH}$ which has good agreement with expected value from $L_{k,\square} = 0.18\hbar R_\square/k_b T_c \approx 3.1\,\text{nH}$, and the sheet inductance of 5.6 nH derived from resonator measurements (see Sec. 3.4.1). The larger values are attributed to variations in film thickness on the original TiN wafer, the wire width and roughness introduced during the fabrication process. The disagreement is reasonable given how close this disordered superconductor is to the SIT, where it is known that L_k diverges [199].

As for the phase slip energy (E_s), there is an order of magnitude agreement between experimental (Tab. 3.4) and theoretical estimations made with (3.1.1) using: $\xi_{0,\text{TiN}} \approx 12\,\text{nm}$ measured on the same TiN film [234]; $\Delta_{TiN} = 2.95 \times 10^{-23}$ J; $R_{\square,\xi} = R_\square W_s/\xi_{\text{TiN}}$ with $R_\square = 2.07\,\text{k}\Omega$ measured in Sec. 3.3; constriction dimensions from Tab. 3.2. Given that the tunneling process (illustrated in Fig. 3.2) is exponentially sensitive to width and material parameters, the variation in E_s is unexpectedly low and with no seeming dependence on the width of the constriction as predicted by (3.1.1). Working on the limit of EBL resolution, this could be a result of fabrication variations, or it can also indicate that CQPS are not localised to a single amplitude across these constrictions [200]. The multiple amplitudes would be added with a phase factor $E_s = \sum_j E_{s,j} \exp[i2\pi Q_j]$ [162], which depends on the charge distribution (Q_j) in the wire.

---

[10] As argued in Sec. 3.1.2, the total inductance of the system is mostly the kinetic inductance $L_\Sigma \approx L_k$.

Table 3.4: Table of parameters of detected CQPS qubits. Design parameters are shown to the left of the divider and the values fitted to experimental data to the right. The fitted inductance energy ($E_L = \Phi_0^2/2L_\Sigma$) defines the total loop inductance (L_Σ) and persistent current ($I_p = \Phi_0/L_\Sigma = 2E_L/\Phi_0$).

Qubit id	W (nm)	N_{sq}	Period (mA)	E_S (GHz)	E_L (GHz)	I_p (nA)	L_Σ (nH)
1	8.0	44	34.9	2.88	26.2	16.80	124
2	8.5	35	36.2	2.92	24.0	15.36	135
3	9.0	33	36.4	0.98	24.7	15.81	131
4	9.5	28	37.4	4.20	21.3	13.63	152
5	10.0	27	38.30	1.30	23.9	15.30	136
6	10.5	25	41.1	1.00	24.0	15.36	135
9	12.0	21	41.1	0.76	20.9	13.34	155
12	13.5	18	41.6	1.56	22.2	14.21	146

3.4.2.1 Multi-photon events

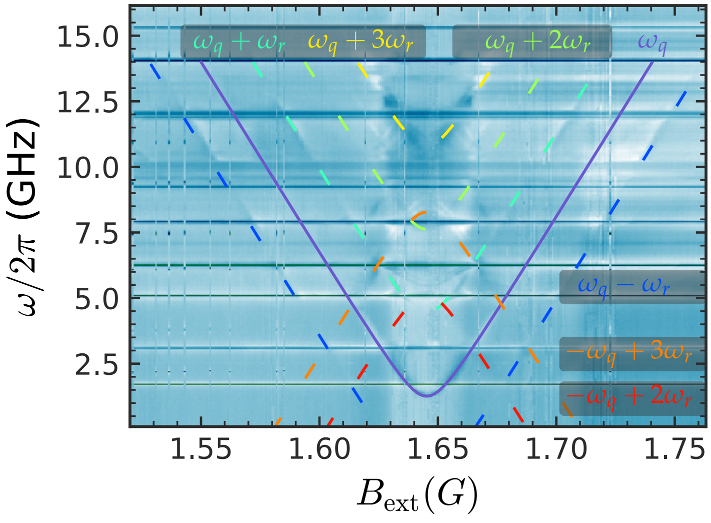

Figure 3.25: Spectra of qubit under a strong -10 dBm drive, with an attenuation of -83 dB inside the cryostat. The $\pm n = 3$ photon excitation processes are visible and traced out with dashed lines.

Multiple photon excitations [233] are visible when the system is subject to a strong input drive of -10 dBm (see Fig. 3.25). The simulated lines corresponds to $\pm\omega_\mathrm{q} \pm n\omega_\mathrm{r}, n \in 1, 2, 3$ and correspond to processes such as a double photon excitation and atom transition ($2\omega_r - \omega_q$). For the qubit characterisation measurements (see Fig. 3.24 and Fig. 3.26) the driving power is -25 dBm (30 times weaker), eliminating $n > 1$ processes and allowing for both $|n = 0\rangle, |n = 1\rangle$ and $\mathcal{O}(\Omega^2) \rightarrow 0$ approximations to be made in the analytical solution of the master equation (3.1.34).

3.4.3 Qubit-resonator coupling

The transitions frequency between hybridised qubit-resonator states $|\pm, n = 1\rangle$ described by (3.1.20)

$$\omega_{\pm,n=1} = (E_{+,n=1} - E_{-,n=1})/\hbar = \Omega_{n=1} = \sqrt{\delta_{q-r}^2 + 4g^2}, \tag{3.4.2}$$

is probed by monitoring the transmission of a weak single tone[11] close to resonator modes ($\omega \sim \omega_m$). Fig. 3.26 (a) demonstrates the case for the $m = 3$ resonator mode, which experiences an avoided crossing with the qubit when their energies become degenerate ($\delta_{q-r} = \omega_q - \omega_{m=3} \approx 0$). Using the qubit and resonator parameters found earlier, (3.4.2) fits the spectrum with $g/2\pi = 18.0\,\text{MHz}$ and is shown as dashed lines.

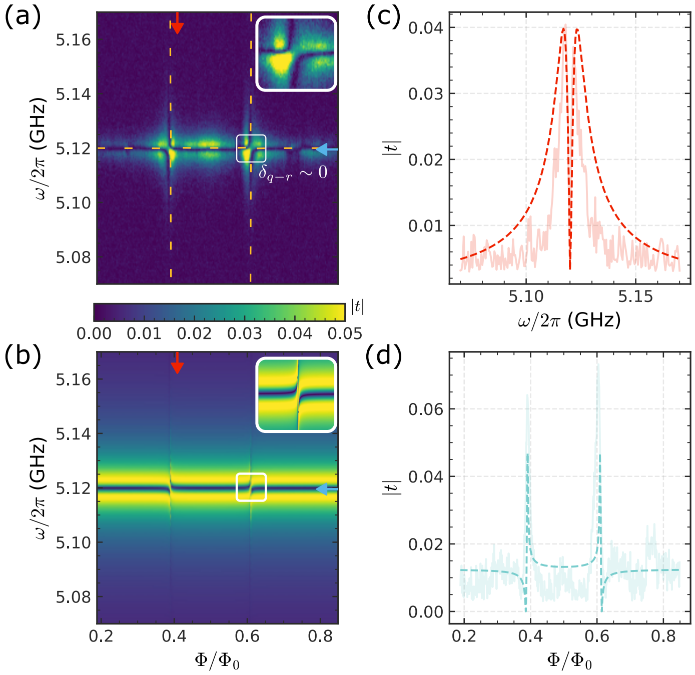

Figure 3.26: **(a)** Experimental spectrum of the qubit-resonator system of qubit 12 near the $m = 3$ resonator mode $\omega_{m=3} = 5.12\,\text{GHz}$. Transmission is modified whenever $\omega = \omega_{\pm,n=1}$ (seen a transmission dip), allowing to map the transition frequency in (3.4.2) with $g/2\pi = 18.0\,\text{MHz}$ (shown with orange dashed lines); **(b)** Simulation of the full transmission spectrum with using (3.4.3) that incorporates the qubit and resonator dissipation $\Gamma_2/2\pi = 13\,\text{MHz}, \kappa = 6.19\,\text{MHz}$. This describes the avoided crossing seen on the resonator signal around $\delta_{q-r} \sim 0$ shown in the insets; **(c,d)** Cross sections at the red and blue arrows demonstrate quantitative agreement between (a) and (b).

The master equation formalism introduced in Sec. 3.1.4 allows to fit not only the resonant transition $\omega_{\pm,n=1}$, but the full dispersive profiles that depend on the system's decoherence rates κ and Γ_2. Using and measured resonator decay rates $\kappa/2\pi = 2 - 14\,\mathrm{MHz}$ (refer to Tab. 3.3) and qubit dephasing rate $\Gamma_2/2\pi \sim 13.8\,\mathrm{MHz}$ (refer to Fig. 3.24), a degree of quantitative agreement with experimental results (see Fig. 3.26 (b)) can be achieved using the expanded form of (3.4.3)

---

[11] This validates working in the single excitation manifold $n = 1$.

$$t = -i\frac{\kappa}{8}\frac{2g^2\delta_q - 2\delta_q^2\delta_r - 2\Gamma_2^2\delta_r}{(\Gamma_2\kappa + g^2)^2 - 2g^2\delta_q\delta_r + \delta_q^2\left((\kappa)^2 + \delta_r^2\right) + \Gamma_2^2\delta_r^2}, \tag{3.4.3}$$

where, as a reminder, $\delta_q = \omega_q - \omega, \delta_r = \omega_r - \omega$ are the detunings from the probing tone. (3.4.3) captures the main features of the avoided crossing - the resonator resonance being interrupted when it is degenerate with the qubit frequency ($\delta_{q-r} = \omega_q - \omega_r = 0$) as well as the cross section profiles in Fig. 3.26 (c,d). Normalisation is performed for

- The $\sim 90\,\mathrm{dB}$ of attenuation on the input line and $\sim 90\,\mathrm{dB}$ amplification on the output line (see Fig. 3.22);
- The frequency dependent attenuation profile (see inset of Fig. 1.23).

The same procedure is applied to qubit 12 on the other resonator modes (see Fig. 3.27) and several other qubits, whose results are summarised in Tab. 3.5. The coupling strengths indicate that the system is operating in the intermediate coupling regime $g \sim \Gamma_2 > \kappa$, enough to suppress the resonator transmission peak at the center of the anticrossing [237] (see Fig. 3.26 (d)) and have the qubit-resonator dynamics be stronger than the relaxation rate of the resonator.

Table 3.5: Summary of fits to various qubit-resonator avoided crossings. Expected values are evaluated with (3.1.18), using the qubits energies in Tab. 3.4, resonator parameters in Tab. 3.3 and a coupling capacitor $C_{\text{q-r}} = 0.3\,\mathrm{fF}$ designed in Tab. 3.2.

Qubit	**Mode** m	$g/2\pi$ **expected** (MHz)	$g/2\pi$ **fitted** (MHz)
3	2	16.5	16.4
	3	2.5	2.6
	4	23.1	23.0
5	2	21.6	21.5
	3	8.0	7.8
6	2	16.0	16.0
	3	10.1	9.8
12	2	24.5	24.4
	3	18.3	18.0
	4	27.0	27.1
	5	34.3	33.8

(a) m=2

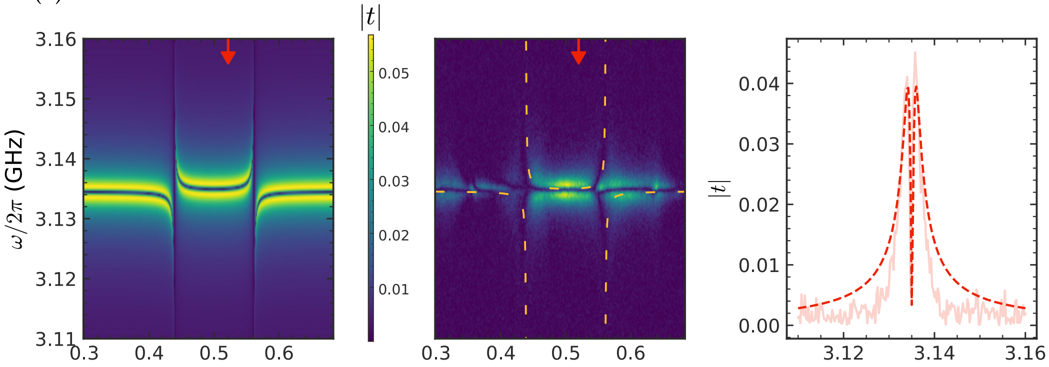

(b) m=4

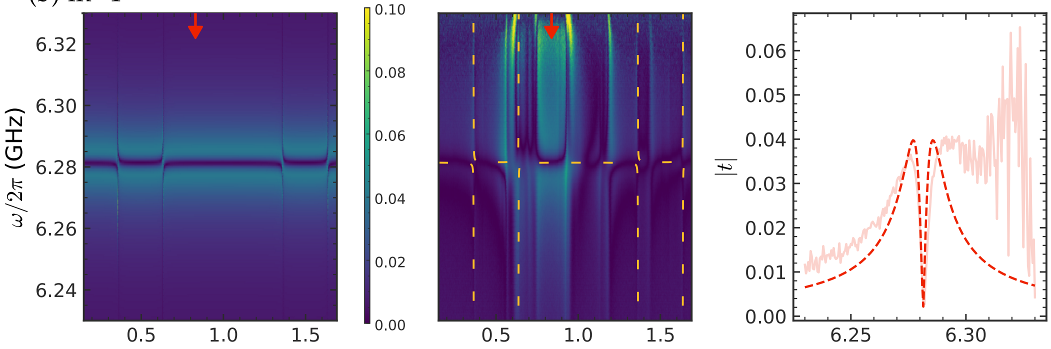

(c) m=5

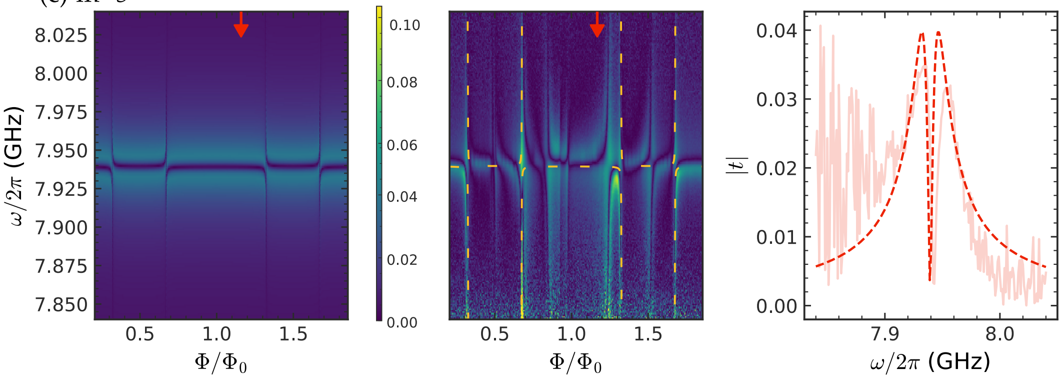

Figure 3.27: Measurements and simulated results for qubit 12 on the other resonator modes. (3.4.2) is used to fit: **(a)** $g = 24.4\,\mathrm{MHz}$; **(b)** $g = 27.0\,\mathrm{MHz}$; **(c)** $g = 34.3\,\mathrm{MHz}$ for modes $m = 2, 4$ and 5, summarised in Tab. 3.5. The middle and right columns simulate the full transmission profile using (3.4.3) with $\Gamma_2/2\pi = 13.8\,\mathrm{MHz}$ and: **(a)** $\kappa_{m=2} = 2.78\,\mathrm{MHz}$; **(b)** $\kappa_{m=4} = 15.7\,\mathrm{MHz}$; **(c)** $\kappa_{m=5} = 14.27\,\mathrm{MHz}$. The spectra are noisier for the higher resonator modes - as seen from (3.24) the signals from a multitude of qubits in the higher frequencies begin to overlap with one another.

3.5 Conclusion

Multiple CQPS qubits on TiN where fabricated and successfully characterised using a superconducting resonator made from the same material, providing confirmation of CQPS operation in yet another strongly disordered superconductor.

- Fitting of the qubit spectra demonstrated a moderate variation of the phase slip energy (E_s) without any seeming exponential consistency with their widths (see Tab. 3.4) as would be expected from theory. This could be a result of working at the limitation of EBL lithography when making the $W_s \sim 10\,\mathrm{nm}$ constrictions, or an indicator that the wires contain multiple locations where phase slips occur, resulting in constructive or destructive interference that brings in unaccounted for modulation to the phase slip energy;

- The inductance of TiN is evaluated from fitting the qubit spectra and resonator frequencies independently, both methods agreeing on a value $L_{k,\square} = 3.5 - 6\,\mathrm{nH}$, which is three times larger than the theoretically predicted value for TiN, but reasonable given its high disorder.

Collectively the uncertainties in phase slip energy and inductance show how much more standardisation work the QPSJ would require in order to become a direct competitor to the JJ.

A major novelty of the work was the first demonstration of capacitive coupling of CQPS qubit to the readout resonator.

- Decoupling from the readout circuit opens ups a greater variety of conditions in which to study CQPS devices, such as other high disorder materials and large magnetic fields that modify their properties, which is not possible with inductive coupling in which the resonator needs to remain superconducting;

- Furthermore, this provides flexibility in the realisation of the readout circuit - for example the ground plane,TL and resonator can be made from Al in the same layer as other circuit elements on the chip, bypassing the isotropic etching which leads to inevitable rounding of the structures (see Layer 2 in Sec. 3.3).

A full theory of the qubit resonator capacitive interaction is applied to experimental data in Fig. 3.26, and the intermediate coupling regime $g \sim \Gamma_2 > \kappa$ is reached. While the model of capacitive coupling (see (3.1.18)) predicts a uniform coupling strength (g) independent of the qubit's energy, there is no conclusive evidence of this and in fact the qubit visibility in Fig. 3.24 seems to get weaker away from the degeneracy point (however this could equally be due to the general broadening of the qubit's linewidth). A full assessment of this would explore the manifold states in measurements analogous to Sec. 3.4.3 where coupling can be used to fit the avoided crossings directly.

Given the outstanding contribution of JJ in the superconducting industry, we will continue to explore the CQPS as thoroughly as its JJ counterpart and to capitalise on dualities that make it less sensitive to certain types of noise or more natural to operate in certain environments. The TiN material studied has a high kinetic inductance, allowing for more compact elements, better stability than the films used in previous CQPS qubit experiments, and higher localisation of charge carriers which could make the devices less sensitive to charge noise. They also offer an alternative strategy for fabrication through controlled etching, that bypasses the artisinal step of JJ oxidation, and could potentially lay the bedrock for more easier and more reproducible batch fabrication of these devices.

It was after all exactly this *search for dualities* that resulted in the demonstration of the dual Coherent quantum interference device (CQUID) [194] and quantised current steps [191] which have all the potential of becoming foundational in metrology.

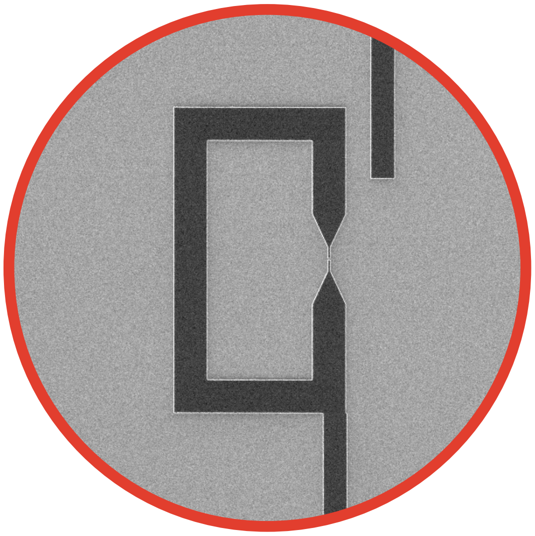

Chapter 4

Coherent quantum phase slip twin qubit

Just as Josephson junctions (JJs) have been embedded into numerous artificial quantum systems, their dual counterpart Coherent quantum phase slip (CQPS) constrictions are beginning to see wider implementation in quantum devices: CQPS qubits [198, 199, 200, 201] hybrid structures [197], CQPS-based transistor [238], CQPS quantum interference device [194].

This section proposes another device that extends the CQPS qubit (Ch. 3) in the same way that the twin flux qubit (Ch. 2) extended the flux qubit. In this system, instead of Cooper pairs (CPs) localised on islands and tunneling across JJs, it is flux quanta localised to loops and tunnel across Quantum phase slip junctions (QPSJs) (see grey localisation regions in Fig. 4.1). This work was done under the same motivations as the twin flux qubit (see Ch. 2), investigating the possibility of modifying device geometry to improve coherence times. The goal was to characterise and test the decoherence properties of such a qubit implementation.

This chapter gives a history of the device's evolution, and suggests a model for capturing the important features of this system (Sec. 4.1). The chip design aimed at achieving a *cleaner* transmission spectrum and calibrating the CQPS amplitude is presented (Sec. 4.2) and fabricated (Sec. 4.3). Spectroscopy measurements are used characterise the decoherence characteristics of initial samples and demonstrate limitations of the proposed model (Sec. 4.4).

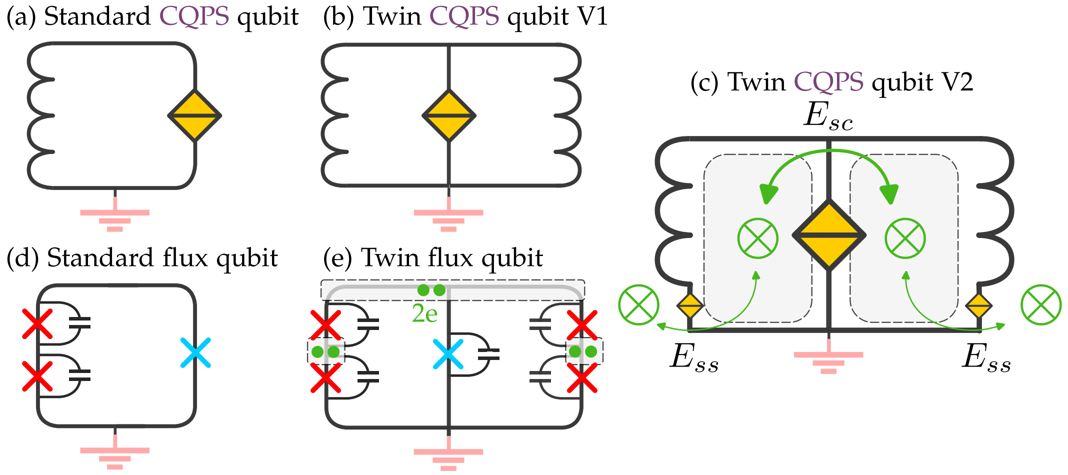
(a) Standard CQPS qubit
(b) Twin CQPS qubit V1
(c) Twin CQPS qubit V2
(d) Standard flux qubit
(e) Twin flux qubit

Figure 4.1: The CQPS twin qubit hierarchy **(a,b,c)** paralleling the evolution of a flux qubit **(d,e)**. The dashed grey areas indicate the respective CP and flux quanta localisation regions in both systems. The first symmetrical design of the CQPS qubit (b) did not provide a way of exchanging flux quanta with the environment, so additional QPSJ where added on its arms (c).

4.1 Theory

The twin CQPS qubit design went through a series of evolutions shown Fig. 4.1. Initially it was designed with a single constriction down the middle branch across which flux would tunnel during a phase slip event, paralleling the mirroring of the loop done for the twin flux qubit. However following a series of *null* experiments where no qubit features were identified, it was speculated that the system was too constrained in having only the flux trapped in the loops during cooldown (after which the loops become superconducting) available for exchange during qubit operations (see Fig. 4.1 (b)).

In the flux qubits, the system had access to a reservoir of CP through their connection to ground (see Fig. 4.1 (d, e)), which allows the islands to assume an occupation that optimally minimised energy under different conditions. In order to connect the twin CQPS qubit to an analogous reservoir of *flux quanta*, one needs to lower the barrier for external flux tunnelling by adding additional constrictions on the sidearms of the qubit. The final schematic incorporating this is shown in Fig. 4.1 (c).

4.1.1 Modelling the qubit

To construct a Hamiltonian for Fig. 4.1 (c), work is done in the basis of flux states $\{|F_L, F_R\rangle\}$ (where F_L and F_R the number of flux quanta in the left and right loops of the device) with operators:

$$\begin{cases} \hat{F}_L\,|F_L, F_R\rangle = f_L\,|F_L, F_R\rangle \\ \hat{F}_R\,|F_L, F_R\rangle = f_R\,|F_L, F_R\rangle\,. \end{cases}$$

The Hamiltonian contains:

- The inductive energy - the energy of the additional current in the loops that ensure flux quantisation (see (3.1.4)). Assuming that the loops have the same inductance L;

$$U = \frac{\Phi_0^2}{2L}\left((\hat{F}_L - f_{\text{ext,L}})^2 + (\hat{F}_R - f_{\text{ext,R}})^2\right);$$

- Energy of the CQPS events occurring across the middle and outer constrictions, in the exact same way it was done in (3.1.5). The former involves a flux exchange between the left and right loops ($|F_L, F_R\rangle \to |F_L \pm 1, F_R \mp 1\rangle$) and is given an amplitude E_{sc}, while the latter just a flux loss or gain from the environment ($|F_L, F_R\rangle \to |F_L \pm 1, F_R\rangle$) and is given an amplitude E_{ss}

$$\begin{aligned} T = &-\frac{E_{sc}}{2}\sum\left[|F_L, F_R\rangle\langle F_L+1, F_R-1| + \text{h.c.}\right] \\ &-\frac{E_{ss}}{2}\sum\left[|F_L, F_R\rangle\langle F_L+1, F_R| + |F_L, F_R\rangle\langle F_L, F_R+1| + \text{h.c.}\right]. \end{aligned}$$

The qubit Hamiltonian is thus

$$\begin{aligned} H_\text{q} &= T + U \\ &= \frac{\Phi_0^2}{2L}\left((\hat{F}_L - f_\text{ext,L})^2 + (\hat{F}_R - f_\text{ext,R})^2\right) \\ &- \frac{E_{sc}}{2}\sum\left[|F_L, F_R\rangle\langle F_L+1, F_R-1| + \text{h.c.}\right] \\ &- \frac{E_{ss}}{2}\sum\left[|F_L, F_R\rangle\langle F_L+1, F_R| + |F_L, F_R\rangle\langle F_L, F_R+1| + \text{h.c.}\right]. \end{aligned} \tag{4.1.1}$$

Fig. 4.2 visualises this Hamiltonian in matrix format, constructed for a 3-states-per-loop truncation. The energy spectrum arising from this Hamiltonian will be analysed in Sec. 4.4.1, where it will be directly compared to experimental results.

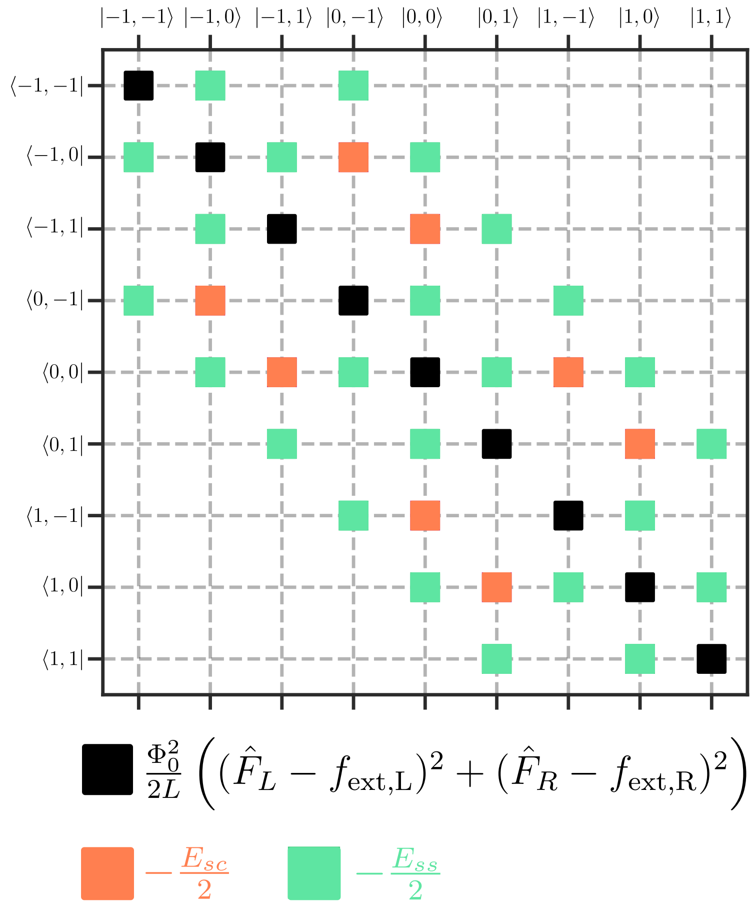
$|-1,-1\rangle$
$|-1,0\rangle$
$|-1,1\rangle$
$|0,-1\rangle$
$|0,0\rangle$
$|0,1\rangle$
$|1,-1\rangle$
$|1,0\rangle$
$|1,1\rangle$
$\langle -1,-1|$
$\langle -1,0|$
$\langle -1,1|$
$\langle 0,-1|$
$\langle 0,0|$
$\langle 0,1|$
$\langle 1,-1|$
$\langle 1,0|$
$\langle 1,1|$
$\frac{\Phi_0^2}{2L}\left((\hat{F}_L - f_\text{ext,L})^2 + (\hat{F}_R - f_\text{ext,R})^2\right)$
$-\frac{E_{sc}}{2}$
$-\frac{E_{ss}}{2}$

Figure 4.2: Visualisation of matrix for Hamiltonian (4.1.1). The left and right loops can exist in states $\{|F=-1\rangle, |F=0\rangle, |F=1\rangle\}$.

4.2 Design

This was an extension of the working CQPS qubit design, featuring qubits capacitively coupled to a $\lambda/2$ resonator (see Fig. 3.17) with the following modifications:

- Limit the number of qubits on a single chip and avoid the complex spectra of multiple qubits and their-cross talks through the common resonator line - this in part caused the multitude of anticrossing in Fig. 3.27 (b,c);
- Keep a number of single CQPS qubits in order to have something to calibrate against on the loaded chip.

4.2.1 Operating energies

As fabrication would be done on the same Titanium Nitride (TiN) material as in Ch. 3, there was confidence in getting the same I_p and E_s under identical fabrication conditions. A simulation using $E_{sc} = 2\,\text{GHz}$, $E_{ss} = 0.5\text{-}2\,\text{GHz}$ and $E_L \sim 10\text{-}30\,\text{GHz}$ (corresponding to $I_p = 3\text{-}10\,\text{nA}$) shows that the transitions are at the limits of the measurement window (see Fig. 4.3).

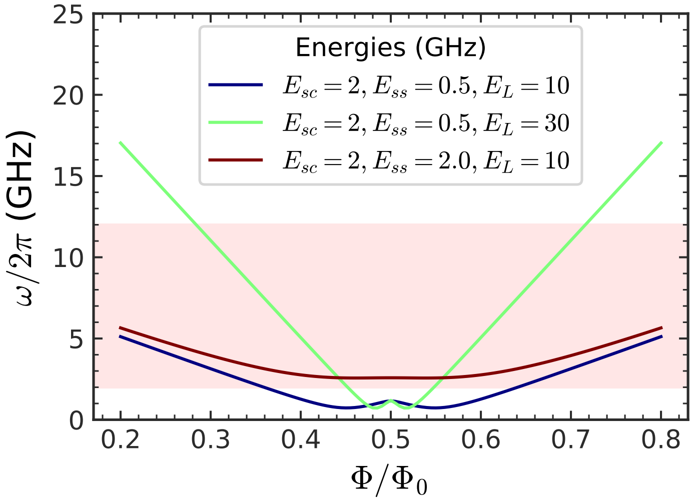

Figure 4.3: Simulation of the ω_{01} transition for a twin CQPS-qubit under different conditions. The phase slip amplitude of the side constrictions (E_{ss}) affects the position of the *minimum*. The parameters chosen will put the qubit's degeneracy point at the lower end of the 2-12 GHz measuring window.

- **Constrictions for E_s:** The single CQPS qubit fabricated in Ch. 3 showed that constriction with widths $\geq 10\,\text{nm}$ had a higher fabrication success rate. The E_s energies achieved varied substantially, so a consistent approach to maximise the number of successful qubits was taken, with a fixed 10 nm central constriction and 10-20 nm outer constrictions. The transition energy simulations in Fig. 4.3 show that the phase slip rate on these side arms (E_{ss}) has a big effect on the resulting energy spectrum, so this parameter is varied to *catch* the most suitable spectrum.

Working with these wider constrictions, the higher success rate allows to lower their number from 12 to 7 compared to the design in Fig. 3.17, which would result in a cleaner transmission spectrum;

- **Loop dimensions for $E_L \leftrightarrow I_p$:** The inductance of the TiN loop is found by integrating their inverse width (W) over the perimeter of the loop

$$L_\Sigma \sim L_{k,\square} \int dx \left[\frac{1}{W(x)}\right],$$

done by *unwrapping* the loop as shown in Fig. 4.4. For triangular sections given by $W(x) = (W_B - W_T)x/L + W_T$, where W_B is the base of the triangle, W_T is the top of the triangle and H is its height[1]

$$L_\Sigma = L_{k,\square} \frac{H}{W_B - W_T} [\ln(W_B) - \ln(W_T)] = \frac{H}{W_B - W_T} \ln(\frac{W_B}{W_T}).$$

Whether $L_\square = 2\,\text{nH}$ (theoretical) or $\approx 4\,\text{nH}$ (measured experimentally in Sec. 3.4.1) is used, the loop perimeters of the single CQPS design achieve $10 \leq E_L \leq 40\,\text{GHz}$. The loop areas, setting the periodicity, are also maintained from the previous run, and all that is required is to mirror them about the central constriction.

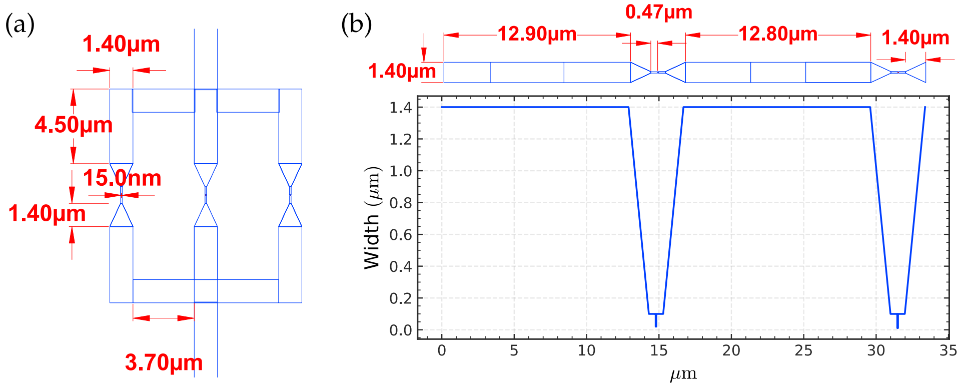

Figure 4.4: Evaluation of the kinetic inductance of CQPS qubit, performed by taking the qubit **(a)** and unrolling on of its loops into a linear geometry and performing numerical integration **(b)**.

---

[1] $\int_0^c \frac{1}{ax+b}dx = \left[\frac{\ln(ax+b)}{a}\right]_0^c$

4.2.2 Distribution along resonator

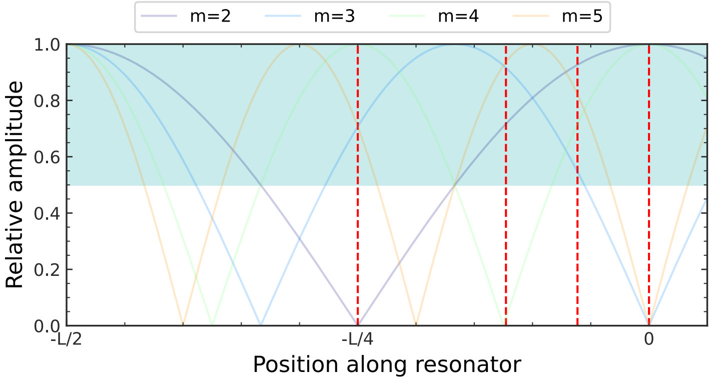

Figure 4.5: Strategic placement of qubits to interact with different resonator modes with amplitudes given by (A.4.18). For a resonator of length $L = 1440\,\mu$m qubits are placed at positions $285, 430, 500, 570\,\mu$m (shown in red dashed lines).

To differentiate qubits even better and prevent the overcrowding seen in Fig. 3.27 (b,c), they were strategically placed along the resonator to interact with different harmonics. The coupling factor defined in (3.1.13) is proportional to the resonator voltage amplitude (A.4.18) and will be zero on certain harmonics where the voltage field has a node (see Fig. 4.5). This means that during two-tone measurement, selection of the harmonic used for the first tone will filter out some of the qubits, giving a cleaner spectrum for analysis.

4.2.3 Final design

The design shown in Fig. 4.6 features the parameters compiled in Tab. 4.1. Two calibration samples with constriction widths 10 nm and 20 nm are included to provide a way for calibrating E_S and E_L for the twin CQPS qubits on the same chip.

Table 4.1: Summary design parameters for twin CQPS qubit, showing design and expected values. E_{ss}, E_{sc} will ultimately be determined by the specifics of fabrication, but according to (3.1.1) and with the given constriction sizes they will be in the GHz region.

Qubit	Area (μm^2) (Design)	Period (mA) (Expected)	Position (Design)	Missing harmonics (Expected)	Constriction (nm)	Outside Arms (nm)	E_L (GHz)	I_p (nA)
1	31.93	0.43	430 μm	4	12.5	10	20.0	12.8
2	37.20	0.37	570 μm	3, 5	12.5	12.5	19.6	12.6
3	41.23	0.34	430 μm	4	12.5	12.5	19.4	12.4
4	46.50	0.30	500 μm		12.5	15	19.5	12.4
5	50.53	0.27	500 μm		12.5	20	19.3	12.3
A	54.25	0.25	285 μm	2	12.5	NA	24	15.4
B	58.90	0.23	285 μm	2	20	NA	16	25.2

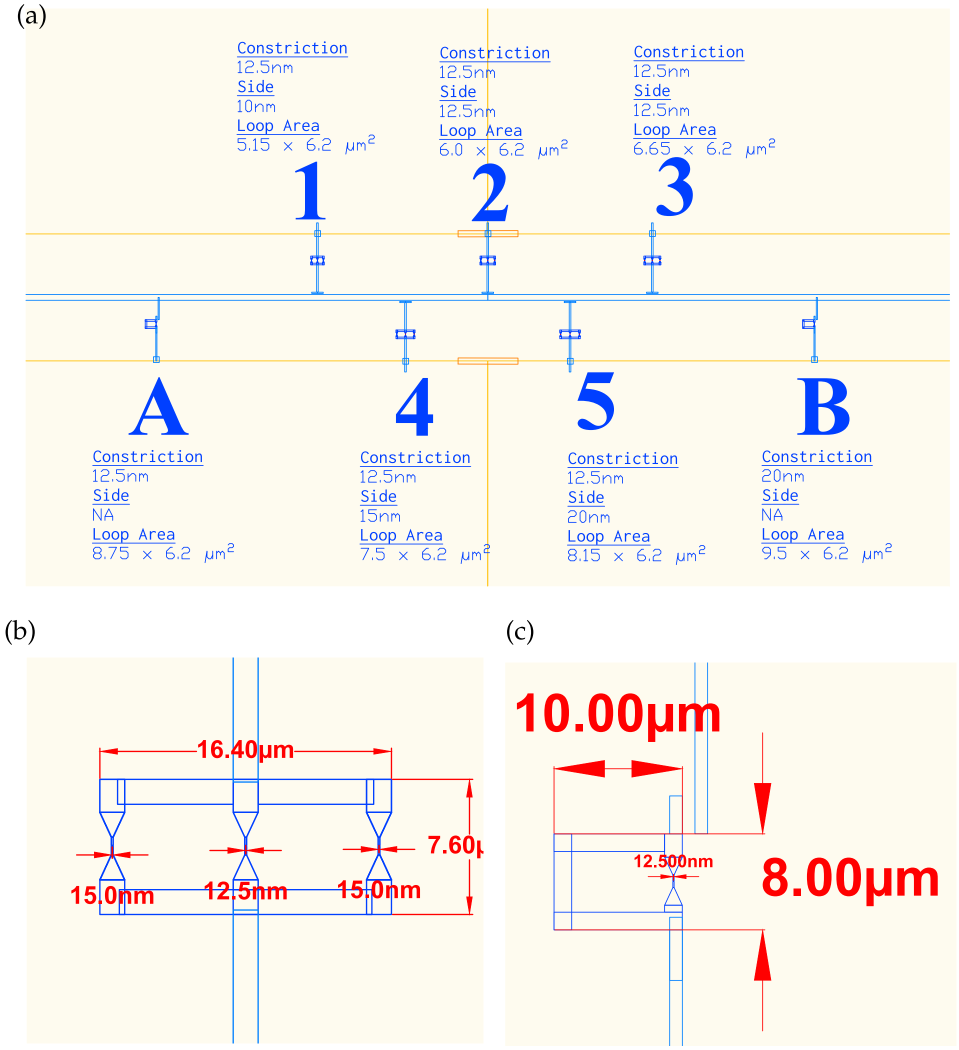
(a)
Constriction
12.5nm
Side
10nm
Loop Area
5.15 x 6.2 μm²
1
Constriction
12.5nm
Side
12.5nm
Loop Area
6.0 x 6.2 μm²
2
Constriction
12.5nm
Side
12.5nm
Loop Area
6.65 x 6.2 μm²
3
A
Constriction
12.5nm
Side
NA
Loop Area
8.75 x 6.2 μm²
4
Constriction
12.5nm
Side
15nm
Loop Area
7.5 x 6.2 μm²
5
Constriction
12.5nm
Side
20nm
Loop Area
8.15 x 6.2 μm²
B
Constriction
20nm
Side
NA
Loop Area
9.5 x 6.2 μm²
(b)
16.40μm
7.60μ
15.0nm
12.5nm
15.0nm
(c)
10.00μm
12.500nm
8.00μm

Figure 4.6: **(a)** Design of twin CQPS qubit array, staggered along the resonator to interact with certain harmonics. Coupling is performed with **T**-shaped capacitors of length $L_T = 10\,\mu$m and positioned $1\,\mu$m away from the resonator/Transmission line (TL); **(b)** Close up of individual twin CQPS qubit; **(c)** A single CQPS qubit is also loaded to help with calibration measurement with a known system already studied in

4.3 Fabrication

The fabrication steps are identical to the ones presented in Sec. 3.3. Images of the fabricated samples taken on the `Zeiss Orion Nanofab` Focused ion beam (FIB) [139] in Fig. 4.7 demonstrate the uncertainty in the size of the constrictions. The dimension of the constriction in the fabricated design varied from 10-25 nm.

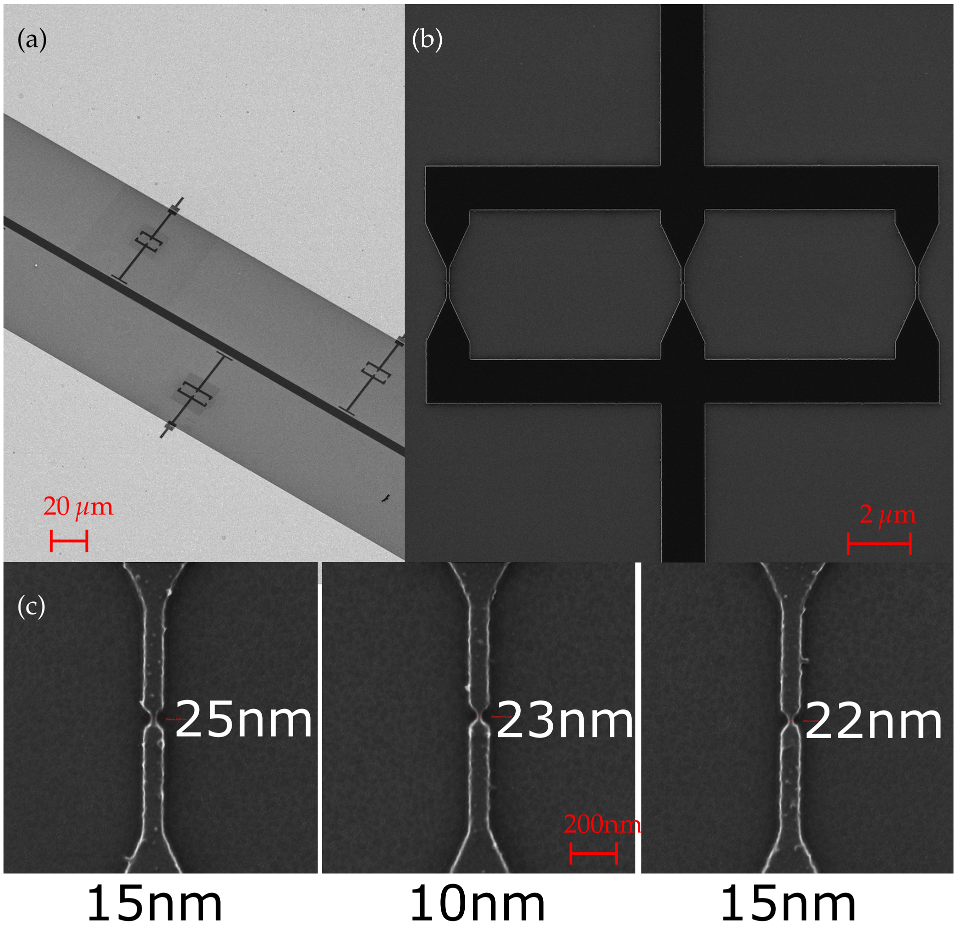

Figure 4.7: FIB images of the fabricated qubit based on the design in Tab. 4.1: **(a)** Large field; **(b)** Showing an individual qubit; **(c)** Closeups of the constrictions with measured sizes (white) compared to design ones (black).

4.4 Experiment

The experiment results shown below, are performed on single series of successfully fabricated twin CQPS qubits. They were coupled via the TL instead of the resonator, meaning direct transmission measurements were performed at the expense of greater noise in the system (see Fig. 4.8).

The optimised design with qubits staggered along the resonator described in Tab. 4.1 was not measured in time for the writing of the thesis - instead a set of 7 qubits with fixed 20 nm outer constrictions and inner constrictions ranging between 6-17 nm was measured.

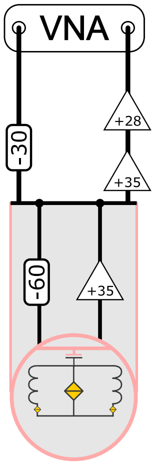

Figure 4.8: Experimental setup for measuring twin CQPS qubits coupled directly to a TL. Only the Vector Network Analyser (VNA) was required to take the spectroscopy data.

4.4.1 Qubit spectrum

Standard single tone transmission measurements (refer to Sec. 1.6.2) were performed using the experimental setup of Fig. 4.8. The transmission spectrum of Fig. 4.9 identifies a collection of different qubits, staggered with different repetition periods. Through careful extraction of these periods and the ratios of the design structures, 6 repetitive signals are identified and associated with the qubits in Tab. 4.2. Two of the qubits seem to have a failed central constriction (and example of such a failure was seen earlier in Fig. 3.19), combining the two distinct loops into a bigger area which increased their flux repetition period.

The broken constrictions would imply that these qubits should behave as a single CQPS qubit, with an adjusted phase slip amplitude

$$E_s = E_{ss} + e^{i\phi}E_{ss},$$

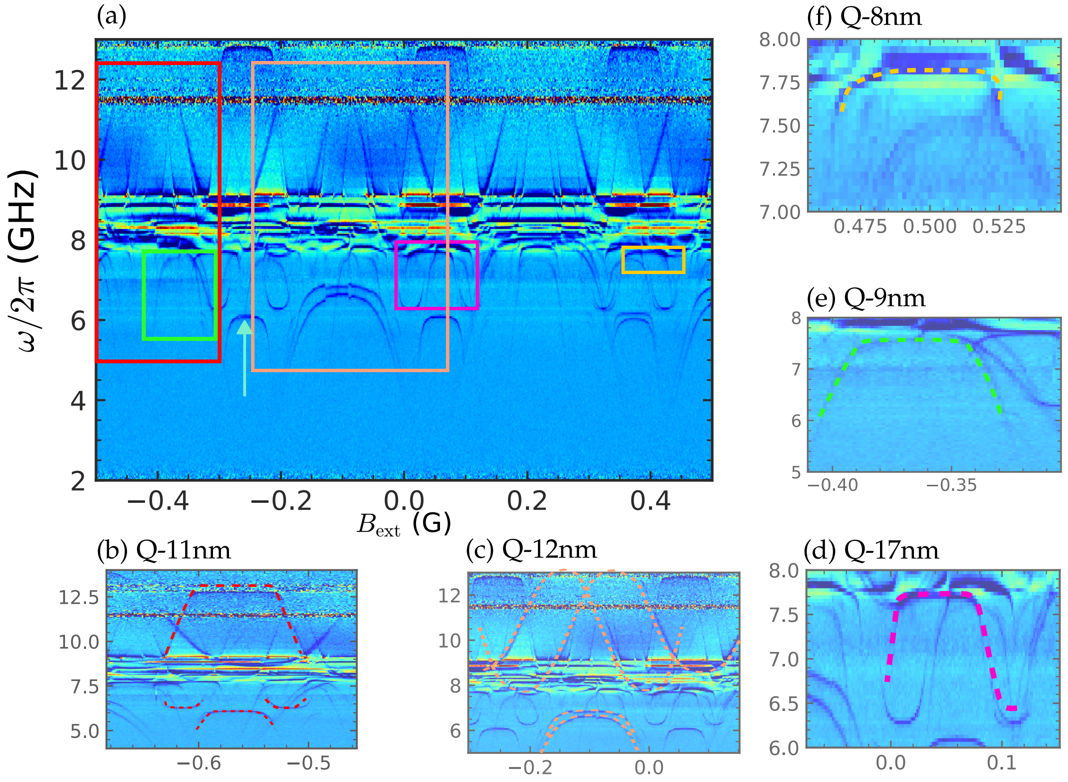

Figure 4.9: **(a)** Complex spectrum of the CQPS twin qubit. Coloured boxes indicate periodic patterns arising from the different qubits. The blue arrow indicates where transmission measurements where taken in Fig. 4.11; **(b)** Feature associated with the 11nm qubit; **(c)** 12 nm qubit; **(d)** 17 nm qubit; **(e)** 9 nm qubit; **(f)** 8 nm qubit.

where the complex phase (ϕ) depends on the charge distribution between the two outer junctions [194], in what can be approximated as a CQUID (see Fig. 3.1).

However neither of the features corresponding to these broken qubits (see Fig. 4.9 (e, f)) can be fit with the *parabolic-like* (3.1.1) even taking into account the possible constructive and destructive interference resulting from ϕ.

Table 4.2: Identified repetitive features are associated with twin CQPS qubits.

Pattern	Repetition Period (mA)	Associated Qubit	Design Loop Area (μm^2)	Loop squares
Q-8nm	0.093	10 - broken central constriction	47.56	53.39
Q-9nm	0.096	9 - broken central constriction	46.05	53.11
Q-11nm	0.206	7	40.99	42.35
Q-12nm	0.420	1	21.12	38.45
Q-17nm	0.228	6	37.44	42.15

More generally, none of the identified spectra can be described by the proposed theoretical models. The regimes expected from (4.10) and shown in Fig. 4.10 are:

(a) $E_L = 20, E_{sc} = 0.8, E_{ss} = 1.9\,\text{GHz}$: dominant tunnelling rate with the environment ($E_{ss} > E_{sc}$), where in the limiting case that $E_{sc} = 0$ there is no tunnelling between the two loops, the system devolves to two single CQPS qubits sharing a common central inductance line. Their energy levels would vary in tandem with the external field, and the transmission spectrum would look be a *doublet* of a CQPS qubit spectrum (see for example Fig. 3.24).;

(b) $E_L = 20, E_{sc} = 5.0, E_{ss} = 1.9\,\text{GHz}$: dominant tunnelling rate across the central constriction ($E_{ss} < E_{sc}$) leading to a double well at the degeneracy points ($\Phi = \Phi_0(2n+1), n \in \mathbb{Z}$);

(c) $E_{L-\text{left}} = 20, E_{L-\text{right}} = 30, E_{sc} = 5, E_{ss} = 1.9\,\text{GHz}$: asymmetrical left and right loop inductances ($E_{L-\text{left}} \neq E_{L-\text{right}}$). Unlike with the twin flux qubit, where tilted evaporation (refer to Sec. 2.3) resulted in loop asymmetry, here the symmetrical etching of both loops meant that the external flux in the two loops was identical, and the only potential asymmetry in inductance energy ($E_L = \Phi_0^2/2L_\Sigma$) was in the inductance of the two loops. Such as asymmetry primarily affects the $|1\rangle \leftrightarrow |2\rangle$ transition, leading to *sharp* features in the spectrum.

Neither of the aforementioned regimes were able to accurately fit the qubit spectra Fig. 4.9 (b-d) using typical values of $E_s \sim 0.1\text{-}5\,\text{GHz}$ and $E_L \sim 10\text{-}30\,\text{GHz}$ measured on the single CQPS qubit made on the same film (Sec. 3.4). This is an indication of the limitation of the proposed model, which does not capture important processes in the device.

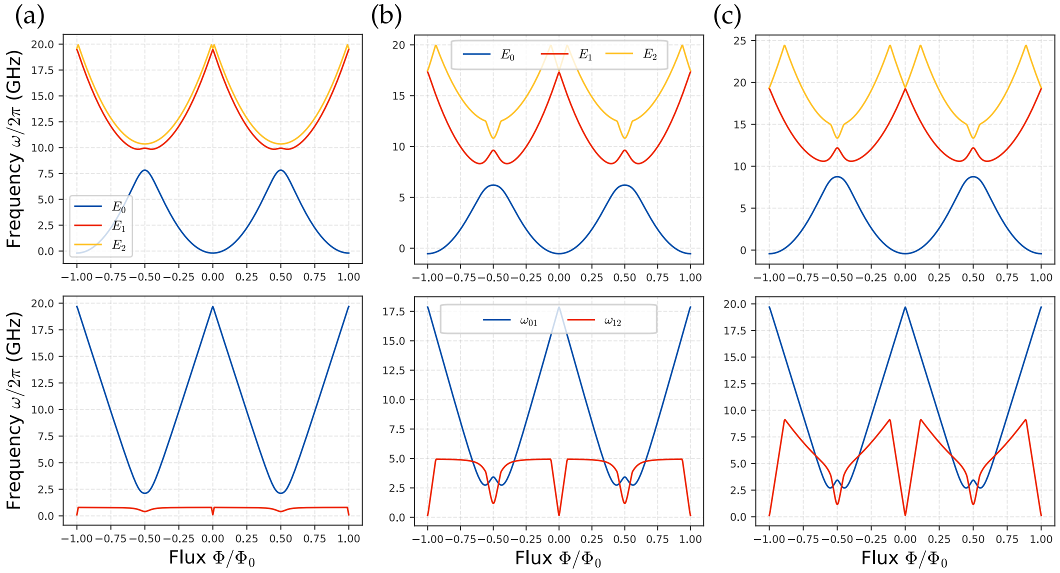

Figure 4.10: Energy spectra simulations from Hamiltonian (4.1.1): **(a)** Regime of single CQPS, when central constrictions has a low CQPS amplitude, preventing flux quanta exchange between the left and right loops ($E_L = 20, E_{sc} = 0.8, E_{ss} = 1.9\,\text{GHz}$); **(b)** Regime where the strong tunnelling across the central junction splits the energy minima of the excited states ($E_L = 20, E_{sc} = 5.0, E_{ss} = 1.9\,\text{GHz}$); **(c)** Regime of asymmetry of the inductance of the left and right loops which sharpens the transition frequency features. ($E_{L-\text{left}} = 20, E_{L-\text{right}} = 30, E_{sc} = 5, E_{ss} = 1.9\,\text{GHz}$).

4.4.2 Transmission experiments

Even though the energy spectrum of the twin CQPS qubit cannot be matched at this stage, it still defines a 2-level system that can be characterised with a transmission measurement. They are run for different powers at the position of the blue arrow in Fig. 4.9 (a) and fitted with the standard transmission profile of a 2-level system (1.2.18) to find the decoherence rates of the 11 nm qubit.

Fig. 4.11 shows fits to the real component of transmission and a qualitative match between the Smith charts. Prior to fitting, the measured transmission amplitudes were scaled by $10^{\text{amplification-bias}/20}$, where amplification-bias of 10 dB$\approx$ 3.16 comes from the net attenuation of the signal in the input line and amplification on output line (see Fig. 4.8 for reference). First $\Gamma_1 = 3\,\text{MHz}$ and $\Gamma_2 = 16\,\text{MHz}$ were fit for the weakest drive, where the driving term $\Omega \to 0$ was ignored. At subsequent powers, the driving amplitude (Ω^2) was increased at 5 dB increments for all further plots. With minor modifications the same set of parameters achieved a consistent set of fits.

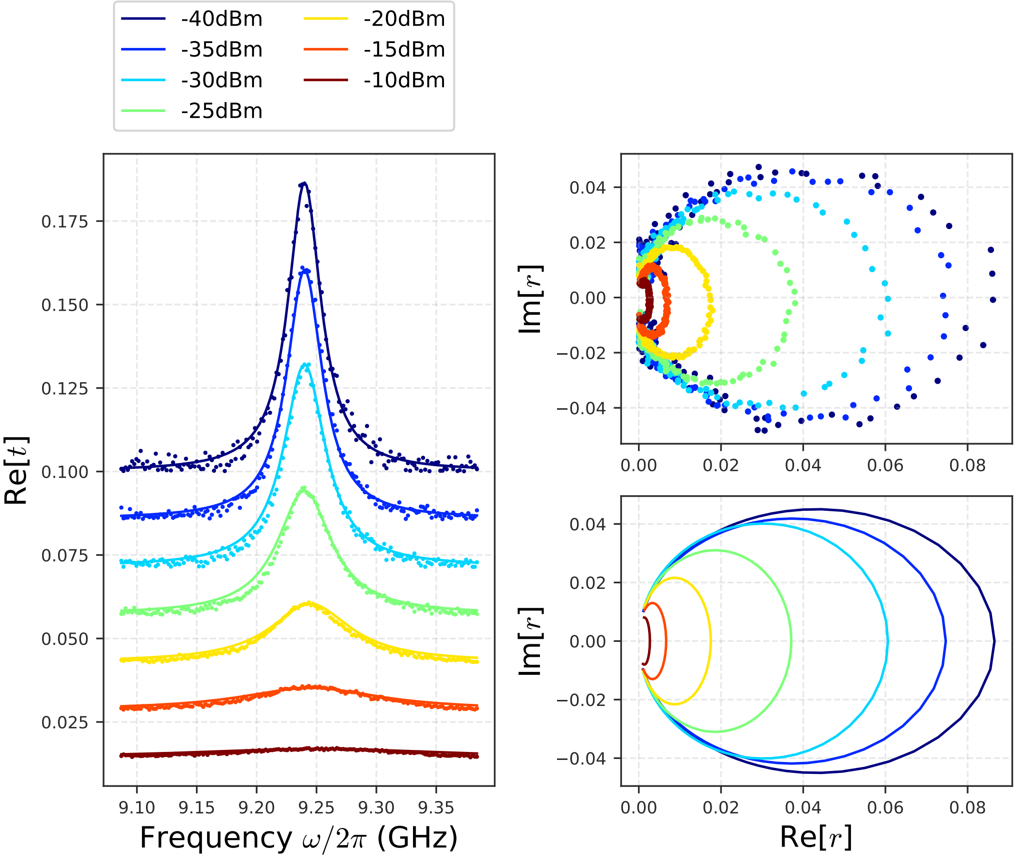

Figure 4.11: Fitting normalised transmission (t) and demonstration of Smith charts of raw data and simulations. At -40 dBm $\Gamma_1 = 3$ MHz and $\Gamma_2 = 16$ MHz a good quantitative and qualitative fit was achieved.

4.5 Conclusion

The result of this section has been the proposal and experimental realisation of the twin CQPS qubit and another step in exploring experimental regimes offered by the fundamental phase slip effect.

The obtained spectra are complex, partially due to the large number of qubits fabricated on the same resonator, but potentially undescribable by the proposed Hamiltonian (4.1.1). Nevertheless, a 2-level system has been successfully demonstrated in these devices by a clear set of transmission measurements (see Fig. 4.11) and promising relaxation rates. A more detailed experimental study using the design with staggered qubits and control qubits proposed in Sec. 4.2 will help with identifying qubits more clearly and explore the limitations of the theoretical model.

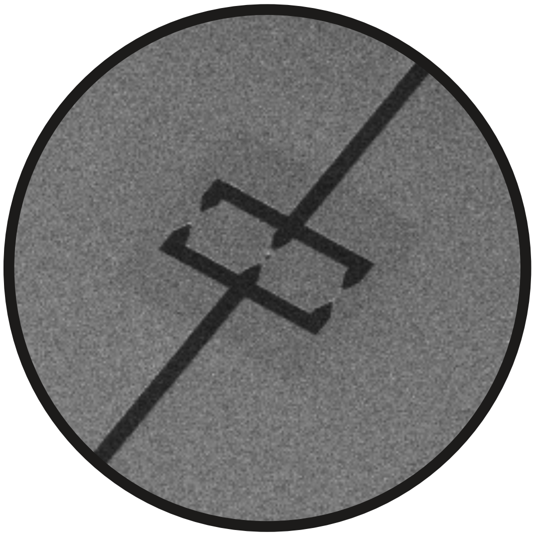

Chapter 5

Summary and outlook

This thesis has built on established works in a number of superconducting artificial atom domains. A project often began by recreating of a set of results, with the development of procedures for designing, fabricating and conducting experiments in house, after which an extension or variation was introduced to explore a specific regime or material. The result has been the creation of a robust experimental platform for future experiments in these domains.

Several experiments were performed. There is a natural link between each of the devices - they are all developed as quantum blocks utilising JJ and QPSJ as non-linear elements. Fabricated with similar lithographical techniques, and read out with a single experimental setup, this thesis showcased the tight overlaps that exist in this field of research. Running through the experiments individually:

◎ **Single photon source** was a classical example of recreating a system demonstrated in other laboratories. The work developed the know how-of making and characterising transmon single photon sources, with the greatest complication coming in the setting up of the readout line to detect GHz photons using a 400MHz digitiser. Careful construction of the readout line element by element, achieved optimal amplification of the weak photon signals, enough to take down their time-resolved relaxation profiles.

The end result of the work was the full pipeline from fabrication to the characterisation of a transmon source and a custom library written in `C++` and `Python` that leverages a 3840 core Graphical processing unit (GPU) for optimal evaluation of future correlation experiments. The next step will be to introduce a bidirectional coupler into the cryostat for making the first $g^{(1)}(\tau)$ and $g^{(2)}(\tau)$ correlation measurements;

- **Twin flux qubit** was a device designed by identifying that symmetry can reduce a flux qubits sensitivity to global magnetic field variations. The device was interesting to explore from a theoretical perspective as it exhibits an simple analytical potential that leads to abrupt state transitions corresponding to the tunnelling of flux quanta, and forbids certain level transitions that a flux qubit would normally allow. The proposed Hamiltonian is able to capture the essential mechanisms of interaction in the system and map out its energy spectrum with agreeable fittings. Lower-than usual curvature at the working point is the main argument for the qubit being more robust to magnetic variations, but a more direct head-to-head comparison with a flux qubit would give a more definitive answer.

  The main drawback of the qubit was its lack of periodicity in magnetic field even for asymmetries on the order of $\sim 1\%$ between the loops, although it could be argued that this allows a single qubit to dynamically span a wider energy range and allowing the possibility of multiple working points at significantly different frequencies.

  The device has the potential of being explored in the gradiometer regime, where the natural spatial extent of its two loops could be used to sense magnetic field gradients in micro-Kelvin environments;

- **CQPS qubit** stepped away from the convectional JJ and showcased a CQPS qubit whose mode of operation was determined by coherent flux tunnelling in and out of the loop. It was the first such qubit to be made from TiN and the 3rd one in disordered superconductors in general, giving support to the universality of the phenomenon and raising questions about the domain-specificity of theoretical estimations such as the kinetic inductance and E_s energies.

  This was also the first CQPS device to be read out through a capacitively coupled resonator. This is a big milestone, as the study of highly disordered superconductors necessarily brings in complications when dealing with their thin and unstable films. With the freedom of being able to make and design the readout circuit without galvanic coupling to the qubit, more materials can be studied for the qubit and peculiar regimes of high magnetic fields (which would not affect the Aluminum (Al) or Gold (Au) readout circuit) can be explored.

  It is still early to call, as to whether CQPS based devices will have impact beyond demonstration of fundamental physics. If anything, their unique fabrication process that uses a single etch instead of evaporation-oxidation-evaporation of JJs may end up being more standardised and less variative, paving the way for their mass implementation in superconducting devices.

- **Twin CQPS qubit** was an early attempt at exploring a network of coherently coupled flux spaces. Progress was made in understanding the need of coupling the system to a bath of fluxes - the equivalent procedure of connecting a charge qubit to a bath of CP to facilitate energy transitions, by adding QPSJ onto the sidearms of the device. When measured it defined a good 2-level computational space, responding coherently in transmission measurements. The energy structure taken by sweeping the field was more feature-rich than the proposed Hamiltonian managed to capture, so at the writing of this thesis it remains an open-ended investigation to understand the dynamics of this system.

  Should CQPS devices peak the communities interest, there will be an interest in coupling them among one another with mutual phase slip centers and experiments of a similar nature will grow in popularity. Furthermore, knowing that decoherence from charge source is much more dominating than decoherence from flux noise sources, one can expect more devices whose energies and interactions are defined and facilitated by flux states.

A summary of the Hamiltonians of the promising systems are presented in Tab. 5.1. Being defined in their own basis states, relevant to the underlying system, they define addressable multiple-level qubits that could one day define substitutable quantum blocks.

Table 5.1: Head on comparison of the models describing the novel qubits.

	Flux Twin Qubit	CQPS Twin Qubit	CQPS Qubit
System states	$\lvert N_1, N_2, N_3\rangle$ (charge)	$\lvert F_L, F_R\rangle$ (flux)	$\lvert F\rangle$ (flux)
Kinetic energy, T	$E_C C\vec{n}^T C^{-1}\vec{n}$	$E_L\left[(\hat{F}_L - f_{\text{ext,L}})^2 + (\hat{F}_R - f_{\text{ext,R}})^2\right]$	$E_L(\hat{F} - f_{ext})^2$
Potential energy, U	$\frac{E_J}{2}\sum \lvert N+1, N-1\rangle\langle N, N\rvert$	$E_{sc}\sum \lvert F_L, F_R\rangle\langle F_L+1, F_R-1\rvert + \text{cc.}$	$E_s\sum \lvert N\rangle\langle N+1\rvert + \text{cc.}$
		$E_{ss}\sum \lvert F_L, F_R\rangle\langle F_L+1, F_R\rvert + \dots$	

In conclusion of the thesis, I will reiterate the goal and title of the thesis - investigations and implementations of superconducting quantum architectures. The four pieces of work focused on the design and fabrication of novel quantum structures, guided by analysis of their microscopic models. Each device was a multi-level addressable qubit that we can begin to call quantum blocks.

I hope that the reader of the thesis has found it an understandable piece of work and can find inspiration for new ideas from the pages above.

List of Publications

The thesis is based on the work obtained for the following papers

- T. Hönigl-Decrinis et al. "Mixing of coherent waves in a single three-level artificial atom". In: *Physical Review A* 98.4 (Oct. 2018)
- I. V. Antonov et al. "Superconducting "twin" qubit". In: *Physical Review B* 102.11 (Sept. 2020)
- **In preparation:** Capacitive Coupling of Coherent Quantum Phase Slip Qubits to a Resonator;
- **In preparation:** Coherent quantum phase slip *twin* qubit

Other publications outside the scope of this thesis

- T J B M Janssen et al. "Operation of graphene quantum Hall resistance standard in a cryogen-free table-top system". In: *2D Materials* 2.3 (Aug. 2015), p. 035015
- M. Hegedüs et al. "Detection of black body radiation using a compact terahertz imager". In: *Applied Physics Letters* 117.23 (Dec. 2020), p. 231106
- Rais S. Shaikhaidarov et al. "Quantized current steps due to the a.c. coherent quantum phase-slip effect". In: *Nature* 608.7921 (Aug. 2022), pp. 45–49

Appendix A

Appendix theory

A.1 Superconductivity for artificial atoms

This appendix provides a surface-level overview of the main features of superconductivity necessary for work with superconducting circuits.

An accessible read preserving the main results in suggested in [242].

A.1.1 Cooper pair condensation

In a normal metal electrons move through an ionic lattice, with continuous collisions dissipating energy through Joule heating $\propto I^2R$. The discovery of superconductivity by Kamerlingh Onnes in 1911 [243] demonstrated the possibility of current transport without dissipation, which the Bardeen-Cooper-Schrieffer theory (BCS) explained by the pairing of normal electrons into a Cooper pair (CP) condensate at low enough temperatures [244].

CPs arise from the 2nd order interaction between electrons in a metal via phonons - vibrations of the atomic lattice [245]. This interaction is attractive, and electrons with opposite momentum[1] and spin near the Fermi surface (E_F) pair up to form a bosonic particle with an energy $2E_F - 2\Delta$ (see Fig. A.1 (a)) where [244]

$$2\Delta \approx 3.52 k_b T_c.$$

This condensation is energetically favourable, and locks normal electrons out of participation in transport at low temperatures ($k_b T \ll 2\Delta$). The 2Δ energy required to break a CP makes them highly resilient to scattering events making the overall quantum state very stable. The CPs exist in a single ground state, described by the superconducting order parameter [246]

$$\Psi(\vec{r}) = \sqrt{n_{\text{CP}}} e^{i\varphi(\vec{r})}, \tag{A.1.1}$$

which is a macroscopic, single-valued wavefunction of coordinates ($\vec{r}$), CP concentration (n_{CP}) and phase (φ). The size of a CP is the material-dependent coherence length (ξ_0) over which (A.1.1) persists outside the superconductor [246] (see Fig. A.1 (c)). Its finite value allows for interaction between closely spaced superconductors which is important for the operation of the Josephson junction (JJ) described in A.1.5. Typically the mean distance between the individual CPs is smaller than this coherence length [247].

---

[1] This may seem to imply counter-intuitively that the electrons travel in opposite directions, but because of continuous scattering a single CP does not necessarily consist of the same electrons and hence this movement does not result in the *grow* of a CP size.

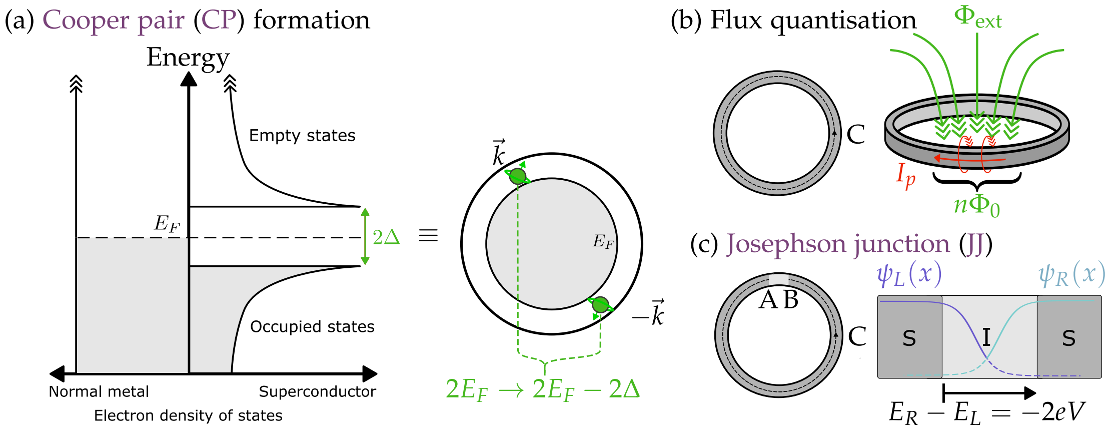
(a) Cooper pair (CP) formation

(b) Flux quantisation

(c) Josephson junction (JJ)

Figure A.1: **(a)** Energy occupation diagram for electrons in a superconductor and normal metal at $T = 0$, where states up to the Fermi energy (E_F) are filled. For a superconductor, the condensation of electrons into CPs is represented by putting the Fermi energy between the conduction (bottom) and valence (top) bands. Electrons in the conduction band are locked from participating in transport, as they have no free states to scatter into, and 2Δ of energy is required to excite an electron to the valence band - the energy required to break up a CP. On the right is the alternative representation showing how two electrons near the Fermi surface combine into a CP releasing the same energy 2Δ. Note that the CPs states are not represented in either diagram; **(b)** Flux quantisation in a loop is fulfilled by persistent currents (I_p) which *add* or *subtract* to the nearest flux quanta; **(c)** Leakage of wavefunctions of two superconductors across a gap in an SIS junction that realises the JJ. The wavefunction can persist outside a superconductor on the scale of the coherence length $\sim \xi_0$. The integration contours C are shown in (b) and (c) for a pure and an interrupted superconducting ring.

A.1.2 Meissner effect

It has been experimentally established that superconductors expel magnetic fields from their bulk when cooled below their transition temperature T_c [136]. This condition is ensured by circulating currents within a characteristic range $\sim \lambda_L$ of the superconductor's surface (the London penetration depth), which generate a magnetic field that exactly cancels out with the external one. Hence the length scale λ_L also determines the depth of penetration of the external magnetic field.

A.1.3 Typical length scales in superconductors

Table A.1: The typical coherence lengths (ξ_0) and penetration depths (λ_L) of various superconducting materials.

Material	ξ_0 (Coherence length)	λ_L (London penetration depth)
Al	1600 nm	16 nm
TiN	12 nm [234]	250-700 nm [160]
NbN	4 nm [202]	200-500 nm [248, 249]
InO_x	10-30 nm [250]	-
MoGe	$<$ 8 nm [204]	-

A.1.4 Phase quantisation

Phase quantisation in a superconductor arises from the necessity of the condensate wavefunction (A.1.1) to be single valued [137, 205]. It forces the phase difference ($\Delta\varphi$) across interruptions in a superconducting loop (see Fig. A.1 (c)) to have a tight coupling with the externally applied flux (Φ_{ext})

$$\Delta\varphi + \varphi_{\text{ext}} = 2\pi F, \qquad F \in \mathbb{Z}, \qquad \varphi_{\text{ext}} = 2\pi\frac{\Phi_{\text{ext}}}{\Phi_0},$$

where $\Phi_0 = h/2e$ is the flux quantum.

The following is a concise summary of the complete argument given in Feynman's lecture on superconductivity [251]:

Proof

1. The expression of electric current

$$I(x) \propto \nabla\varphi(x) - 2e\vec{A}(x)/\hbar, \tag{A.1.2}$$

is given by the gradient of the superconducting phase (φ) and the vector potential ($\vec{A}$) describing the external magnetic field.

2. Deep inside the superconductor and well inside the penetration depth (refer to Sec. A.1.2) the electric current is zero, in which case (A.1.2) reads

$$\nabla\varphi(x) = 2e\vec{A}(x)/\hbar. \tag{A.1.3}$$

3. Taking the integral of (A.1.3) along contours C shown in Fig. A.1 (b,c) in the center of the conductor

$$\underbrace{\oint_C dx[\nabla\varphi(x)]}_{\Delta\varphi} = \frac{2e}{\hbar}\underbrace{\oint_C dx[\vec{A}(x)]}_{\Phi}. \tag{A.1.4}$$

The integral of the vector potential is by definition the flux (Φ) encompassed by the contour, and the line integral of the gradient from one point to another is the difference of the condensate phase ($\Delta\varphi$) between the start and end points.

Depending on the contour, two conditions can be derived:

- If the contour is around a superconducting ring like in Fig. A.1 (b), the accumulated phase around the loop must be $\Delta\varphi = 2\pi n, F \in \mathbb{Z}$ in order for the condensate wavefunction (A.1.1) to be single valued, meaning (A.1.4) simplifies to

$$2\pi F = \frac{2e}{\hbar}\Phi \qquad \Rightarrow \qquad \Phi_0 F = \Phi = \Phi_{\text{ext}} + \Phi_{I_p} + \Phi_{\text{elements}}. \tag{A.1.5}$$

  Hence the total flux trapped inside the loop, which is a combination of:

  - Externally applied flux (Φ_{ext});
  - Flux created by circulating currents (Φ_{I_p});
  - Flux created by other circuit elements (Φ_{elements} - in an uninterrupted superconducting loop it would be zero),

  must be quantised in integer values of flux $\Phi_0 = h/2e$;

- If the contour passes through an interrupted superconductor like in Fig. A.1 (c), then integrating from A to B:

$$\oint_{A-B} dx[\nabla\varphi(x)] = \Delta\varphi,$$

  is the phase difference across the gap and

$$\oint_{A-B} dx[\vec{A}(x)] = \Phi_{\text{elements}},$$

  is approximately the flux across the interruption element. Taken together in (A.1.4) this relates the phase difference across the superconducting gap to the flux in the loop

$$\Delta\varphi = 2\pi\frac{\Phi_{\text{element}}}{\Phi_0}, \tag{A.1.6}$$

  which is a fundamental relation in superconducting circuits with JJs[2].

---

[2] Interestingly, differentiating (A.1.6) with respect to time $\partial_t\varphi = 2eV(t)/\hbar$ gives an alternative approach to showing the first Josephson relation in (A.1.7).

◎ Using the flux quantisation condition (A.1.5) and re-expressing (A.1.6) in a form that separates out $\Phi_{\text{element}} = n\Phi_0 - \Phi_{\text{ext}}$ into the externally applied flux and the number of flux quanta in the loop[3]

$$\Delta\varphi = 2\pi F - 2\pi\frac{\Phi_{\text{ext}}}{\Phi_0}$$

which couples the phase difference ($\Delta\varphi$) along interruptions in superconducting loops to the externally applied flux (Φ_{ext}) and flux quantisation number (F).

QED ☐

A.1.5 Josephson Junction

A JJ is a non-linear superconducting element realised by a SIS structure (see Fig. A.1 (c)), where the phase difference (φ) across the junction defines its inductance

$$L_J = \frac{\Phi_0}{2\pi}\frac{1}{I_c\cos(\varphi)},$$

and energy

$$E_{J0}(1-\cos(\varphi)), \qquad E_{J0} = \frac{\Phi_0 I_c}{2\pi} = \frac{R_q}{R_n/N_{\text{sq}}}\frac{\Delta(0)}{2},$$

through its resistance (R_n), dimensions (N_{sq}) and superconducting gap of the material (Δ). The JJ passes dissipationless current across gap when it is below the critical value

$$I_c R_n \approx= \frac{\pi\Delta(0)}{2e}.$$

A.1.5.1 Josephson relations

In 1962 Brian Josephson [3] concluded that if two superconductors were put in close vicinity of each other and connected via a weak link with dimensions $\sim \xi_0$ (see Fig. A.1 (c)) a zero-voltage tunnelling current (called a super-current) of CPs could flow across with a non-linear I-V relationship.

The phase difference (φ) across the JJ defines two relations characterising transport properties across the junction (also know as the Josephson relations)

$$\begin{cases} V = \dfrac{\hbar}{2e}\partial_t\phi, \\ I = I_c\sin(\varphi), \end{cases} \tag{A.1.7}$$

---

[3] This time flux created by circulating currents is neglected, as the interruption will limit the free current that can circulate in the loop, meaning $\Phi_{\text{element}} \gg \Phi_{I_p}$.

which can be motivated by the following arguments (the original paper [3] and extended literature such as [252] give the more thorough derivation):

Proof

1. The wavefunctions in the two superconductors (see Fig. A.1 (c)) will each fulfil their respective Schrödinger equation:

$$\begin{cases} i\hbar\partial_t\psi_L = H_L\psi_L, \\ i\hbar\partial_t\psi_R = H_R\psi_R, \end{cases} \tag{A.1.8}$$

   with eigenvalues E_L and E_R.

2. Expanding the Hamiltonians in (A.1.8) to include the effect of coupling (κ_{JJ}) across the gap $H_L = E_L |\psi_L\rangle\langle\psi_L| \to E_L |\psi_L\rangle\langle\psi_L| + \kappa_{JJ} |\psi_R\rangle\langle\psi_L|$

$$\begin{cases} i\hbar\partial_t\psi_L = E_L\psi_L + \kappa_{JJ}\psi_R \\ i\hbar\partial_t\psi_R = E_R\psi_R + \kappa_{JJ}\psi_L. \end{cases} \tag{A.1.9}$$

3. Inserting the condensate wavefunction (A.1.1) into (A.1.9) and separating out the real and imaginary components

$$\begin{aligned} i\hbar\partial_t n_{s,L}\frac{1}{2\sqrt{n_{s,L}}}e^{i\varphi_L} - \hbar\partial_t\varphi_L\sqrt{n_{s,L}}e^{i\varphi_L} &= E_L\sqrt{n_{s,L}}e^{i\varphi_L} + \kappa_{JJ}\sqrt{n_{s,L}}e^{i\varphi_R} \\ \sqrt{n_{s,R}}e^{i\varphi_R}\left(i\hbar\partial_t n_{s,R}\frac{1}{2n_{s,R}} - \hbar\partial_t\varphi_R\right) &= \sqrt{n_{s,R}}e^{i\varphi_R}\left(E_R + \kappa_{JJ}e^{-i\varphi_R+i\varphi_L}\right) \end{aligned} \Rightarrow \begin{cases} \hbar\partial_t n_{s,L} = 2\kappa_{JJ}\sqrt{n_{s,R}n_{s,L}}\sin(\varphi_R-\varphi_L) \\ \hbar\partial_t n_{s,R} = -2\kappa_{JJ}\sqrt{n_{s,R}n_{s,L}}\sin(\varphi_R-\varphi_L) \\ \hbar\partial_t\varphi_L = \kappa_{JJ}\cos(\varphi_R-\varphi_L) - E_L \\ \hbar\partial_t\varphi_R = \kappa_{JJ}\cos(\varphi_R-\varphi_L) - E_R \end{cases} \tag{A.1.10}$$

4. As the voltage drop (V) across the junction is the difference in energy of the right and left superconducting states

$$E_R - E_L = -2eV,$$

   taking the difference of last 2 equations of (A.1.10), one finds the first Josephson equation

$$\hbar(\partial_t\varphi_R - \partial_t\varphi_L) = -E_R + E_L = 2eV \qquad \Rightarrow \qquad V = \frac{\hbar}{2e}\partial_t\phi,$$

   relating the voltage across the junction to the time derivative of the phase ($\varphi = \varphi_R - \varphi_L$) across the junction. If no voltage is applied

$$h\partial_t(\varphi_R - \varphi_L) = 0 \quad \Rightarrow \quad \varphi_R - \varphi_L = \text{const},$$

then the top two equations of (A.1.10) imply a uniform flow of CP across the junction without any charge buildup

$$\partial_t n_{s,L} = -\partial_t n_{s,R}.$$

5. Assuming the same material and hence the same CP density ($n_{s,L} = n_{s,R} = n_s$) in both superconductors, the net current can be found from the top equation of (A.1.10)

$$I \propto \partial_t n_s = \frac{2\kappa_{JJ} n_s}{\hbar} \sin(\varphi_R - \varphi_L) \qquad \Rightarrow \qquad I = I_c \sin(\varphi), \tag{A.1.11}$$

which is the second Josephson equation, with a certain critical current density (I_c) that depends on the coupling strength (κ) and CP concentration (n_s). The full theory [252, 3, 133] gives a specific value for the critical current definition (shown in (A.1.17)).

QED ☐

A.1.5.2 JJs in practice

In superconducting circuits the most common way of realising the weak link is with an Aluminum (Al) JJ, which is easy to fabricate in laboratory conditions using a shadow evaporation technique (described in B.2). A dissipationless JJ can be represented through the circuit elements shown in Fig. A.2. Using the two Josephson relations (A.1.7), a number of useful formulas can be derived that characterise a JJ:

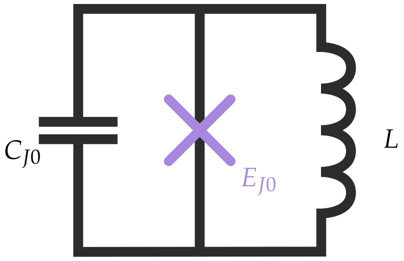

Figure A.2: Circuit representation of a JJ, including its finite size giving rise to self capacitance (C_{J0}), and a Josephson inductance (L_J) from (A.1.16). The presence of the shunt inductance and shunt capacitor has an effect when the JJ is embedded in a quantum circuit, giving rise to charge and inductive energy contributions.

- **The JJ energy** can be determined by taking an integral over the power dissipation IV occurring on it

$$\begin{aligned}\int_0^t dt[IV] &= \int_0^t dt\left[I_c \sin(\varphi)\frac{\Phi_0}{2\pi}\frac{d\varphi}{dt}\right] \\ &= \int_0^\varphi d\varphi[E_J \sin(\varphi)] \\ &= E_{J0}(1-\cos(\varphi)),\end{aligned} \tag{A.1.12}$$

where

$$E_{J0} = \frac{\Phi_0 I_c}{2\pi}. \tag{A.1.13}$$

◎ **The Josephson inductance** can be derived by considering a perturbation in the junction current (δ_I) caused by a flux perturbation (δ_φ). The Josephson equations of (A.1.7) read

$$I + \delta_I = I_c \sin(\varphi + \delta_\varphi) \quad \Rightarrow \quad \delta_I = I_c \cos(\varphi)\delta_\varphi, \tag{A.1.14}$$

and

$$V = \frac{\Phi_0}{2\pi}\left(\partial_t \varphi + \partial_t \delta_\varphi\right) = \frac{\Phi_0}{2\pi}\frac{\partial_t \delta_I}{I_c \cos(\varphi)}. \tag{A.1.15}$$

(A.1.15) and (A.1.14) express the Josephson inductance

$$L = V/\frac{dI}{dt} = V/\partial_t \delta_I = \frac{\Phi_0}{2\pi}\frac{1}{I_c \cos(\varphi)}. \tag{A.1.16}$$

◎ **The JJ critical current** introduced in (A.1.11) is derived from BCS theory [133]

$$I_c R_n = \frac{\pi \Delta(T)}{2e} \tanh\left(\frac{\Delta(T)}{2k_b T}\right), \tag{A.1.17}$$

for a superconducting energy gap of $\Delta(T)$ and normal resistance (R_n) of the JJ. Taking the limit of low temperature where $\lim_{T\to 0} \tanh\left(\Delta(T)/2k_b T\right) = 1$

$$I_c R_n \approx \frac{\pi \Delta(0)}{2e}. \tag{A.1.18}$$

◎ **The Josephson energy from physical JJ parameters** can be found by subbing in (A.1.18) into (A.1.13):

$$E_J = \frac{R_q}{R_n/N_{\text{sq}}}\frac{\Delta(0)}{2},$$

with $R_q = h/(2e)^2$. The wider the JJ is in squares (N_{sq}) the lower the resistance of the junction and the larger its Josephson energy.

A.1.5.3 Flux biased JJ

The DC-Superconducting interference device (SQUID) formed by two parallel JJs is equivalent to a single JJ with a controllable Josephson energy.

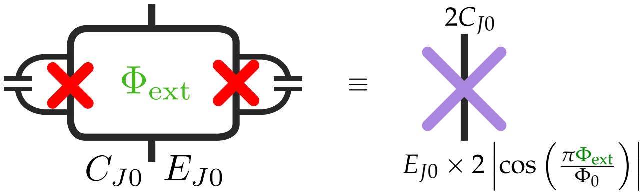
Φ_{ext}
C_{J0}
E_{J0}
$\equiv$
$2C_{J0}$
$E_{J0} \times 2\left|\cos\left(\frac{\pi\Phi_{\mathrm{ext}}}{\Phi_0}\right)\right|$

Proof

1. The two currents across the parallel JJs combine for a total current (A.1.7)

$$\begin{aligned} I &= I_{c1}\sin(\varphi_1) + I_{c2}\sin(\varphi_2) \\ &= 2I_c \sin(\frac{\varphi_1+\varphi_2}{2})\cos(\frac{\varphi_1-\varphi_2}{2})) \end{aligned} \tag{A.1.19}$$

   where $I_{c1} = I_{c2} \equiv I_c$ are the critical currents of the individual junctions.

2. The phase quantisation condition $\varphi_1 + \varphi_2 + \varphi_{\mathrm{ext}} = 2\pi F, F \in \mathbb{Z}$ (refer to A.1.4) introduces external flux into (A.1.19)

$$\begin{cases} I = 2I_c \left|\cos\left(\frac{\pi\Phi_{\mathrm{ext}}}{\Phi_0}\right)\right| \sin(\varphi), \\ \varphi = \frac{\varphi_1+\varphi_2}{2}. \end{cases}$$

3. Evaluation of the Josephson energy is made by taking the integral of the power being dissipated across a time period like in (A.1.12)

$$\begin{aligned} \int_0^t dt[IV] &= \int_0^t dt\left[2I_c\left|\cos\left(\frac{\pi\Phi_{\mathrm{ext}}}{\Phi_0}\right)\right|\sin(\varphi)\frac{\Phi_0}{2\pi}\frac{d\varphi}{dt}\right] \\ &= E_J(1-\cos(\varphi)), \end{aligned}$$

   where the external flux can now tune the effective energy

$$\begin{aligned} E_J\left(\Phi_{\mathrm{ext}}\right) &= \frac{\Phi_0 I_c}{2\pi} \times 2\left|\cos\left(\frac{\pi\Phi_{\mathrm{ext}}}{\Phi_0}\right)\right| \\ &= E_{J0} \times 2\left|\cos\left(\frac{\pi\Phi_{\mathrm{ext}}}{\Phi_0}\right)\right|. \end{aligned}$$

4. For an asymmetry $d = \frac{E_{J2}-E_{J1}}{E_{J1}+E_{J2}}$ between the JJs equivalent steps lead to

$$E_J(\Phi_{\text{ext}}) = \left[E_{J1}+E_{J2}\right]\left(1-\cos\left(\frac{\pi\Phi_{\text{ext}}}{\Phi_0}\right)\sqrt{1+d^2\tan^2\left(\frac{\pi\Phi}{\Phi_0}\right)}\right). \tag{A.1.20}$$

QED ☐

A.1.6 Charge basis

Sec. A.3.2 shows how $\hat{\Phi} = \Phi_0\hat{\varphi}/2\pi$ and $\hat{Q} = 2e\hat{N}$ are equivalent to the coordinate-momentum pair $(\hat{x}, \hat{p})$ (see Tab. A.2) - thus one can define a basis on charge states $\{|N\rangle\}$ of the transmon where N is the number of CPs on its island. The relevant identities for this basis are:

$$\left[\hat{N},\hat{\varphi}\right] = \frac{1}{2e}\left[\hat{Q},\hat{\Phi}\right]\frac{2\pi}{\frac{h}{2e}} = i, \quad \hat{N}\left|N\right\rangle = N\left|N\right\rangle, \quad e^{\pm i\varphi} = \sum_n \left|N\pm 1\right\rangle\left\langle N\right|. \tag{A.1.21}$$

Orthonormality of basis

Proof

The claim that $\{|N\rangle\}$ constitutes an complete and orthornormal basis follows from the identification of $\hat{N}$ with position operator $\hat{x}$ in Tab. A.2 by noting their analogous functions in a harmonic oscillator systems. It is known that the otherwise innumerable position operator has an approximate identity [253]

$$\mathbb{I} \approx \int dx\left|x\right\rangle\left\langle x\right|, \tag{A.1.22}$$

as well as the usual orthornormality relation

$$\langle x|x'\rangle = \delta(x-x'). \tag{A.1.23}$$

The discrete versions of (A.1.22) and (A.1.23) result in

$$\mathbb{I} = \sum_n \left|N\right\rangle\left\langle N\right|, \qquad \langle n|m\rangle = \delta_{n,m},$$

which are the conditions for the definition of a complete basis. QED ☐

Phase operator in charge basis Proof of $e^{\pm i\hat{\varphi}} = \sum_n |N \pm 1\rangle \langle N|$ proceeds as follows:

Proof

1. Derive the commutation relation between the number ($\hat{N}$) and the exponential phase ($e^{\pm i\hat{\varphi}}$) by using the commutation relation in (A.1.21)
$$\begin{aligned}\left[\hat{N}, e^{\pm i\hat{\varphi}}\right] &= \left[\hat{N}, \sum_{\alpha=0}^{\infty} \frac{(\pm i\hat{\varphi})^{\alpha}}{\alpha!}\right] = \sum_{\alpha=0}^{\infty} (\pm i)^{\alpha} \frac{\left[\hat{N}, \hat{\varphi}^{\alpha}\right]}{\alpha!} \\ &= \sum_{\alpha=0}^{\infty} (\pm i)^{\alpha} \frac{-\alpha i\hat{\varphi}^{\alpha-1}}{\alpha!} = \pm \sum_{\alpha=1}^{\infty} i^{\alpha-1} \frac{(\pm\hat{\varphi})^{\alpha-1}}{(\alpha-1)!} = \pm e^{\pm i\hat{\varphi}}.\end{aligned}$$

2. Operating with the number operator on state $e^{\pm i\hat{\varphi}} |N\rangle$ and using the commutation result
$$\begin{aligned}\hat{N}\left[e^{\pm i\hat{\varphi}} |N\rangle\right] &= \left[\pm e^{\pm i\hat{\varphi}} + e^{\pm i\hat{\varphi}}\hat{N}\right] |N\rangle \\ &= (N \pm 1)\left[e^{\pm i\hat{\varphi}} |N\rangle\right].\end{aligned}$$

3. Evidently, the exponential phase operator is a ladder operator for the $|N\rangle$ state:
$$e^{\pm i\hat{\varphi}} |N\rangle = |N \pm 1\rangle \qquad \Rightarrow \qquad e^{\pm i\varphi} = \sum_N |N \pm 1\rangle \langle N| .$$

QED □

A.1.7 Drude model

A superconducting material will have a sheet kinetic inductance of

$$L_{k,\square} = 0.18\frac{\hbar R_{\square}}{k_b T_c},$$

that depends on the normal state sheet resistance ($R_{\square}$) and superconducting transition temperature (T_c) of the material. It arises from the inertia of CP particles reacting with a phase delay to an applied electric field due to their finite mass and relaxation time.

Proof

1. Assume that the charge carriers (Q) start off with momentum $\vec{p}(t_0)$ and which have an average collision time τ. In the following time interval (dt) two things can happen under the influence of a random force ($\vec{f}(t)$):

- The charge carriers undergo a collision with probability dt/τ. Momentum will be randomised to ($\vec{g} = \vec{f}(t)dt$) with absolute kinetic energy $|\vec{g}|^2/2m = 3k_bT/2$ given by the equipartition theorem;
- The charge carriers do not undergo collision with probability $1 - dt/\tau$, emerging with original momentum and an impulse added by the external force ($\vec{f}(t)dt$).

The net momentum would thus be

$$\vec{p}(t_0 + dt) = \left(1 - \frac{dt}{\tau}\right)\left(\vec{p}(t_0) + \vec{f}(t)dt\right) + \frac{dt}{\tau}\vec{f}(t)dt.$$

2. Ignoring $\mathcal{O}(dt^2)$ and rearranging

$$\frac{d\vec{p}}{dt} = -\frac{\vec{p}(t)}{\tau} + \vec{f}(t). \tag{A.1.24}$$

3. Under the action of a time dependent electric field ($\vec{E}(t) = \mathrm{Re}\left[Q\vec{E}(\omega)e^{-i\omega t}\right]$), whose interaction with the charge (Q) supplies the force $\vec{f} = Q\vec{E}$, momentum will also oscillate at the same frequency (ω)

$$\vec{p}(t) = \mathrm{Re}\left[\vec{p}(\omega)e^{-i\omega t + \varphi}\right]. \tag{A.1.25}$$

4. Substitution of (A.1.25) into (A.1.24)

$$-i\omega\vec{p}(\omega) = -\frac{\vec{p}(\omega)}{\tau} - q\vec{E}(\omega). \tag{A.1.26}$$

5. A rearrangement of (A.1.26) to a form $\vec{I}(\omega) = \sigma(\omega)\vec{E}(\omega)$

$$\vec{I}(\omega) = -nq\frac{\vec{p}(\omega)}{m} = \frac{(nq^2/m)\vec{E}(\omega)}{1/\tau - i\omega},$$

allows one to read off

$$\sigma(\omega) = \sigma_1 - i\sigma_2 = \frac{nq^2\tau}{m(1+\omega^2\tau^2)} - i\frac{nq^2\omega\tau^2}{m(1+\omega^2\tau^2)}, \tag{A.1.27}$$

which is the Drude model expression for conductance - a semi-quantitative analogue to Ohm's law.

6. In a case of a superconductor there are no CP collisions, so $\tau \to \infty$. When irradiated by a microwave field of GHz frequency one has $\omega\tau \gg 1$, which leads to the domination of the second term in (A.1.27)

$$\sigma^{-1}(\omega) = (\sigma_1 - i\sigma_2)^{-1} = \frac{i}{\sigma_2}\left(1 - i\frac{\sigma_1}{\sigma_2}\right)^{-1} \xrightarrow[\sigma_2 \gg \sigma_1]{} \frac{i}{\sigma_2}\left(1 - i\frac{\sigma_1}{\sigma_2}\right) = \frac{\sigma_1}{\sigma_2^2} + \frac{i}{\sigma_2}.$$

7. The total impedance can thus be separated out into what can be associated as the resistance (R) and complex impedance ($Z\omega$)

$$Z(\omega) = \frac{L}{WT}\frac{1}{\sigma(\omega)} = \underbrace{\frac{L}{WT}\frac{\sigma_1}{\sigma_2^2}}_{R} + \underbrace{i\frac{L}{WT}\frac{1}{\sigma_2}}_{Z(\omega)}, \tag{A.1.28}$$

where L, T, W are the length, thickness and width of the wire.

8. The Mattis-Bardeen formula gives an expression for σ_2 through the normal state conductance of a superconducting wire σ_N [205] taken in the low temperature limit

$$\sigma_2 = \sigma_N \frac{\pi\Delta}{\hbar\omega}\tanh\left(\frac{\Delta}{2k_bT}\right) \xrightarrow[\lim T\to 0]{} \sigma_N\frac{\pi\Delta}{\hbar\omega},$$

and hence the second term in (A.1.28)

$$Z(\omega) = i\frac{L}{WT}\frac{1}{\sigma_N}\frac{\hbar\omega}{\pi\Delta} = i\omega L_K,$$

can be identified with the impedance caused by an inductor

$$L_k = \frac{L}{WT\sigma_N}\frac{\hbar}{\pi\Delta}. \tag{A.1.29}$$

The subscript k indicates that this is kinetic inductance, as it arises from the inertia of the CP in the wire.

9. Identifying $R_\square = \sigma_N T$ as the sheet resistance of the wire in the normal state, one gets an expression for the sheet kinetic inductance from (A.1.29)

$$L_{k,\square} = \frac{\hbar R_\square}{\pi\Delta} \approx 0.18\frac{\hbar R_\square}{k_bT_c},$$

where in the final step, energy gap in the low temperature limit can be expressed through the critical temperature of the material [205] $\lim_{T\to 0}\Delta(T) = 1.764k_bT_c$.

QED □

A.2 Simple systems

A.2.1 Transmon qubit

The Hamiltonian for a transmon qubit shown in Fig. 1.2 (c) is given by

$$H_{\mathrm{q}} = 4E_C\left(\hat{N} - N_{\mathrm{ext}}\right)^2 - E_J(\Phi_{\mathrm{ext}})\cos\left(\hat{\varphi}\right),$$
$$\begin{cases} E_C = \dfrac{(e)^2}{2C_\Sigma}, \qquad C_\Sigma = 2C_{J0} + C_s, \\ E_J(\Phi_{\mathrm{ext}}) = E_{J0} \times 2\left|\cos\left(\dfrac{\pi\Phi_{\mathrm{ext}}}{\Phi_0}\right)\right|, \end{cases}$$

where $N_{\mathrm{ext}} = C_{\text{q-t}}V_g/2e$ and Φ_{ext} are the two degrees of external control, $\hat{N} = \hat{Q}/2e$ is CP number operator and $\hat{\varphi}$ is the phase operator.

Proof

1. Following the standard convention, one must first write out the Lagrangian for the system
$$\mathcal{L} = K - U,$$
where the flux (Φ) on the isolated island (see Fig. 1.2 (c)) is used as the generalised coordinate.

2. The kinetic term will be associated with the time derivative of the generalised coordinate ($\partial_t\Phi \equiv V$) which can be associated with charging energy induced on the shunt (C_s) and JJ (C_{J0}) capacitors
$$K_1 = 2\frac{C_{J0}}{2}(\partial_t\Phi)^2 + \frac{C_s}{2}(\partial_t\Phi)^2 = \frac{C_\Sigma}{2}(\partial_t\Phi)^2,$$
with $C_\Sigma = 2C_{J0} + C_s$.

3. Another contribution to charging energy will come from the voltage source acting on the qubit through the coupling capacitor ($C_{\text{q-t}}$)
$$\begin{cases} K_2 = V_g \times Q_{\mathrm{qubit}} \\ Q_{\mathrm{qubit}} = C_{\text{q-t}} \times \partial_t\Phi \end{cases} \Rightarrow K_2 = V_g C_{\text{q-t}}\partial_t\Phi.$$

4. The potential energy comes from the JJ (refer to A.1.5 and A.1.5.3)

$$\begin{aligned} U &= E_J(\Phi_{\text{ext}})\left(\underbrace{1}_{\text{✥}} - \cos\left(2\pi\frac{\Phi}{\Phi_0}\right)\right) \\ &\equiv E_J(\Phi_{\text{ext}})\cos\left(2\pi\frac{\Phi}{\Phi_0}\right), \end{aligned}$$

   where redundant constant energy term ✥ is dropped, since one is only interested in transition energies between the levels.

5. The full Lagrangian of the system reads

$$\begin{aligned} \mathcal{L} &= K_1 + K_2 - U \\ &= \underbrace{\frac{C_\Sigma}{2}(\partial_t\Phi)^2 + V_g C_{\text{q-t}}\partial_t\Phi}_{K} + \underbrace{E_J\cos(\frac{2\pi}{\Phi_0}\Phi)}_{U}, \end{aligned} \tag{A.2.1}$$

   for the generalised coordinate (Φ). Note how the kinetic terms depend on the time derivative of the generalise coordinate, and potential energies on the coordinate itself.

6. The conjugate momentum is defined through the derivative of (A.2.1)

$$\frac{\partial\mathcal{L}}{\partial\partial_t\Phi} = C_\Sigma\partial_t\Phi + V_g C_{\text{q-t}} \equiv Q,$$

   which, from inspection, can be associated with an effective charge on the transmon island. The system coordinates Φ and Q constitute a conjugate pair which map onto quantum mechanical operators $\hat{\Phi}, \hat{Q}$ (refer to Tab. A.2 and A.1.6) with a commutation relation

$$\left[\hat{Q}, \hat{\Phi}\right] = i\hbar.$$

7. Expressing the resulting Hamiltonian

$$\begin{aligned} H_{\text{q}} &= \hat{Q}_J\partial_t\hat{\Phi} - \mathcal{L} \\ &= \frac{(\hat{Q}_J - C_{\text{q-t}}V_g)^2}{2C_\Sigma} - E_J\cos\left(2\pi\frac{\hat{\Phi}}{\Phi_0}\right). \end{aligned} \tag{A.2.2}$$

8. For readability, $N_{\text{ext}} = C_{\text{q-t}}V_g/2e$ is defined to be the number of CPs induced on the transmon island by the external voltage, and similarly $\hat{N} = \hat{Q}/2e$ the native CP

occupation of the transmon, which rearranges (A.2.2) to

$$H_{\mathrm{q}} = E_C\left(\hat{N} - N_{\mathrm{ext}}\right)^2 - E_J \cos\left(\hat{\varphi}\right),$$

$$\begin{cases} E_C = \dfrac{(2e)^2}{2C_\Sigma}, \qquad C_\Sigma = 2C_{J0} + C_s, \\ E_J = E_{J0} \times 2\left|\cos\left(\dfrac{\pi\Phi_{\mathrm{ext}}}{\Phi_0}\right)\right|, \end{cases}$$

where N_{ext} and Φ_{ext} are two degrees of external control.

QED □

A.2.2 Unitary transformation of a 2-level system

A 2-level system described by a Hamiltonian in basis of physical states $\{|0\rangle, |1\rangle\}$

$$H = -\frac{\varepsilon}{2}\sigma_z - \frac{\Delta}{2}\sigma_x$$

can be diagonalised through a unitary transformation to give a Hamiltonian

$$H' = -\frac{\Delta E}{2}\sigma_z,$$

with eigenvectors and eigenvalues of the ground (g) and excited (e) states

$$\begin{cases} E_g = -\dfrac{\Delta E}{2} & |g\rangle = \cos(\theta/2)\,|0\rangle - \sin(\theta/2)\,|1\rangle, \\ E_e = \dfrac{\Delta E}{2} & |e\rangle = \sin(\theta/2)\,|0\rangle + \cos(\theta/2)\,|1\rangle, \end{cases}$$

with energy splitting and angle

$$\Delta E = \sqrt{\varepsilon^2 + \Delta^2} \qquad \tan(\theta) = \frac{\Delta}{\varepsilon}.$$

Proof

1. Although the eigenvectors and eigenvalues of $H = -\frac{\varepsilon}{2}\sigma_z + -\frac{\Delta}{2}\sigma_x$ can be easily found manually, the more general approach is to apply a unitary transformation that would rotate the state representation to match the natural symmetry of the system. To see what rotation needs to be done, the Hamiltonian is factorised:

$$H = -\frac{\Delta E}{2}\left(\frac{\varepsilon}{\Delta E}\sigma_z + \frac{\Delta}{\Delta E}\sigma_x\right) = -\frac{\Delta E}{2}\left(\cos(\theta)\sigma_z + \sin(\theta)\sigma_x\right) \tag{A.2.3}$$

where $\Delta E = \sqrt{\varepsilon^2 + \Delta^2}$ and $\tan(\theta) = \Delta/\varepsilon$.

2. A unitary transformation $U_y(\theta/2) = \exp(i\theta/2\sigma_y)$, will rotate (A.2.3) about an axis perpendicular to both σ_x and σ_z. Using (A.7.2), the identities in (A.7.3) and noting that the transformation has no time dependence ($U\partial_t U^\dagger = 0$)

$$\begin{aligned}
H' = U_y H U_y^\dagger &= U_y(\theta/2)\left(\frac{\Delta E}{2}\left(\cos(\theta)\sigma_z + \sin(\theta)\sigma_x\right)\right)U^\dagger(\theta/2) \\
&= -\frac{\Delta E}{2}\left(\cos(\theta)\sigma_z U_y^\dagger(\theta/2)U_y^\dagger(\theta/2) + \sin(\theta)\sigma_x \underbrace{U_y^\dagger(\theta/2)U_y^\dagger(\theta/2)}_{U_y^\dagger(\theta)}\right) \\
&= -\frac{\Delta E}{2}\left(\cos(\theta)\sigma_z + \sin(\theta)\sigma_x\right)\underbrace{\left(\cos(\theta)\mathbb{I} - i\sin(\theta)\sigma_y\right)}_{U_y^\dagger(\theta)} \\
&= -\frac{\Delta E}{2}\left(\cos^2(\theta)\sigma_z + \sin(\theta)\cos(\theta)\sigma_x - i\sin(\theta)\cos(\theta)\sigma_z\sigma_y - i\sin^2(\theta)\sigma_x\sigma_y\right) \\
&= -\frac{\Delta E}{2}\left(\cos^2(\theta)\sigma_z + \sin(\theta)\cos(\theta)\sigma_x - i\sin(\theta)\cos(\theta)(-i\sigma_x) - i\sin^2(\theta)(i\sigma_z)\right) \\
&= -\frac{\Delta E}{2}\sigma_z.
\end{aligned}$$

3. The rotated eigenstates $|\psi'\rangle = U|\psi\rangle$ can now be expressed through states $|0\rangle, |1\rangle$ of the original Hamiltonian

$$|g\rangle = U_y(\theta/2)\,|0\rangle = \begin{pmatrix} \cos(\theta/2) & \sin(\theta/2) \\ -\sin(\theta/2) & \cos(\theta/2) \end{pmatrix}\begin{pmatrix} 1 \\ 0 \end{pmatrix} = \begin{pmatrix} \cos(\theta/2) \\ -\sin(\theta/2) \end{pmatrix}$$

and likewise

$$|e\rangle = \sin(\theta/2)\,|0\rangle + \cos(\theta/2)\,|1\rangle\,.$$

QED □

A.2.3 Dipole coupling between 2-level system and microwave field

A transmon driven by a microwave field with frequency ω acts like a dipole particle with charge

$$\vartheta = C_{\text{q-t}}V_{\text{qubit}},$$

and quantum operator

$$\hat{\vartheta}(t) = \vartheta e^{-i\omega t}\sigma_x.$$

If the voltage field has amplitude V_{mw} the Hamiltonian describing the driven system

$$H_{\text{mw}} = \text{Re}\left[\hat{\vartheta}(t)\right] V_{\text{mw}}.$$

Proof

1. Write out the charging energy in the qubit, due to the qubits innate (Q_{qubit}) and induced ($Q = V_{\text{mw}} C_{\text{q-t}}$) charges on the island (see Fig. 1.2 (b)):

$$\begin{aligned} \text{Electrostatic energy} &= \frac{Q_{\text{total}}^2}{2C_\Sigma} = \frac{\left[Q_{\text{qubit}} + Q\right]^2}{2C_\Sigma} \\ &= \frac{1}{2C_\Sigma}\left[Q_{\text{qubit}} + C_{\text{q-t}} V_{\text{mw}}\right]^2 \\ &= \frac{1}{2C_\Sigma}\left[Q_{\text{qubit}}^2 + \underbrace{2Q_{\text{qubit}} C_{\text{q-t}} V_{\text{mw}}}_{\text{✥}} + C_{\text{q-t}}^2 V_{\text{mw}}^2\right], \end{aligned} \tag{A.2.4}$$

   which can be seen as the energy in moving a CP using the voltage in Transmission line (TL).

2. Only ✥ in (A.2.4) is of interest for interaction, since it is the only term that links the qubit and microwave systems:

$$\begin{aligned} \text{Interaction energy} &= \frac{Q_{\text{qubit}}}{C_\Sigma} C_{\text{q-t}} V_{\text{mw}} \\ &= V_{\text{qubit}} C_{\text{q-t}} V_{\text{mw}}, \end{aligned} \tag{A.2.5}$$

   where the residual voltage from the charge on the qubit is defined as $V_{\text{qubit}} = Q_{\text{qubit}}/C_\Sigma$.

3. Casting the interaction energy (A.2.5) into a Hamiltonian by mapping the classical qubit voltage operator into a quantum mechanical one that describes the induced atomic transitions $|0\rangle \leftrightarrow |1\rangle$ by the driving field through excitation ($\sigma_+ = |1\rangle\langle 0|$) and relaxation ($\sigma_- = |0\rangle\langle 1|$) operators,

$$V_{\text{qubit}} \longrightarrow \hat{V}_{\text{qubit}} = V_{\text{qubit}} \sigma_x, \tag{A.2.6}$$

   where $\sigma_x = \sigma_- + \sigma_+$.

4. Evaluating (A.2.5) with the qubit operator (A.2.6) and incident driving field $V_{\text{mw}} = V_{\text{mw}}(0,t) = \text{Re}\left[V_{\text{mw}} e^{-i\omega t}\right]$ evaluated at $x = 0$ (see the homogenous solution in

(A.3.47)), the driven system is described by Hamiltonian

$$\begin{aligned} H_{\mathrm{mw}} &= \hat{V}_{\mathrm{qubit}} C_{\text{q-t}} V_{\mathrm{mw}} \\ &= \mathrm{Re}\left[\hat{\vartheta}(t)\right] V_{\mathrm{mw}}, \end{aligned} \tag{A.2.7}$$

in which $\hat{\vartheta}(t) = \vartheta e^{-i\omega t}\sigma_x$ is the dipole operator and $\vartheta = C_{\text{q-t}} V_{\mathrm{qubit}}$ is the dipole amplitude, whose interpretations are described in the main text.

QED ☐

A.2.4 Unitary transformation of driven 2-level system

A 2-level system, driven by a resonant field $V(t) = \hbar\Omega\cos(\omega t + \phi)$ has a Hamiltonian

$$H' = -\frac{\hbar\delta\omega}{2}\sigma_z - \frac{\hbar\Omega}{2}\Big(\sigma_x\cos\phi + \sigma_y\sin\phi\Big). \tag{A.2.8}$$

Proof

1. The following unitary transformation

$$U = e^{i\frac{\omega t}{2}\sigma_z},$$

is applied to the driven 2-level system Hamiltonian $H = -\hbar\omega_q\sigma_z/2 - \hbar\Omega\cos(\omega t)\,\sigma_x$ as described in Sec. A.7.2

$$\begin{cases} \quad H' = UHU^\dagger - i\hbar U\partial_t U^\dagger, \\ i\hbar U\partial_t U^\dagger = \dfrac{\hbar\omega}{2}\sigma_z, \\ UHU^\dagger = U\left[-\dfrac{\hbar\omega_q}{2}\sigma_z\right]U^\dagger - U\left[\dfrac{\hbar\Omega}{2}\left(e^{i\omega t}\sigma_x + e^{-i\omega t}\sigma_x\right)\right]U^\dagger \\ \qquad = -\dfrac{\hbar\omega_q}{2}\sigma_z - \dfrac{\hbar\Omega}{2}\left(\sigma_-(1+\underbrace{e^{-i2\omega t}}_{\text{✥}}) + \sigma_+(1+\underbrace{e^{i2\omega t}}_{\text{✥}})\right). \end{cases} \tag{A.2.9}$$

2. Applying the Rotating wave approximation (RWA), the fast oscillating terms ✥ with $2\omega t$ oscillating components are ignored, which is justified when the oscillation period (ω) is much faster than any transition in the system and hence does not lead to observable dynamics

$$H' = -\frac{\hbar\delta\omega}{2}\sigma_z - \frac{\hbar\Omega}{2}(\sigma_- + \sigma_+) = \frac{\hbar}{2}\begin{pmatrix} -\delta\omega & -\Omega \\ -\Omega & \delta\omega \end{pmatrix},$$

where $\delta\omega = \omega_q - \omega$ is the detuning of the driving field from the 2-level system.

3. In the case that driving is performed with a phase shift ϕ

$$\hbar\Omega\cos(\omega t + \phi)\sigma_x = \hbar\Omega\left(\cos(\omega t)\cos(\phi) - \sin(\omega t)\sin(\phi)\right)\sigma_x, \tag{A.2.10}$$

a repeat of procedure (A.2.9) with (A.2.10) results in $-\hbar\Omega\cos(\phi)\sigma_x/2$ for the cosine term and $-\hbar\Omega\sin(\phi)\sigma_y/2$ for the sine term, with a resulting Hamiltonian

$$H' = -\frac{\hbar\delta\omega}{2}\sigma_z - \frac{\hbar\Omega}{2}\Big(\sigma_x\cos\phi + \sigma_y\sin\phi\Big).$$

QED □

A.2.5 Dynamics of a driven qubit system

The dynamics of a resonantly driven ($\delta\omega = 0$) 2-level system under dissipation is found by solving the master equation (refer to Sec. A.7.3) with Hamiltonian (A.2.8)

$$\begin{cases} \partial_t\rho = -\dfrac{i}{\hbar}\left(H\rho - \rho H\right) + \mathcal{L}[\rho], \\ H = -\dfrac{\hbar\Omega}{2}\Big(\sigma_x\cos\phi + \sigma_y\sin\phi\Big), \\ \mathcal{L}[\rho] = \begin{pmatrix} \Gamma_1\rho_{11} & -\Gamma_2\rho_{01} \\ -\Gamma_2\rho_{10} & -\Gamma_1\rho_{11} \end{pmatrix}, \end{cases}$$

where Γ_1 quantifies depolarisation and Γ_2 total decoherence (refer to Sec. 1.3.2). One can solve directly for the expectation values of operators

$$\partial_t\langle\sigma_j\rangle = \mathrm{Tr}\left\{\partial_t\langle\sigma_j\rangle\right\} = \mathrm{Tr}\left\{-\frac{i}{\hbar}\sigma_j\big(H\rho - \rho H\big) + \sigma_j\mathcal{L}\right\},$$

and evaluate all the Pauli matrices

$$\begin{cases} \partial_t\langle\sigma_x\rangle = -i\dfrac{\Omega}{2}\mathrm{Tr}\left\{\big(\sigma_x\sigma_x\rho - \sigma_x\rho\sigma_x\big)\cos(\phi) + \big(\sigma_x\sigma_y\rho - \sigma_x\rho\sigma_y\big)\sin(\phi)\right\} + \mathrm{Tr}\left\{\sigma_x\mathcal{L}\right\} \\ \qquad\quad = \Omega\langle\sigma_z\rangle\sin(\phi) - \Gamma_2\langle\sigma_x\rangle, \\ \partial_t\langle\sigma_y\rangle = \Omega\langle\sigma_z\rangle\sin(\phi) - \Gamma_2\langle\sigma_y\rangle \\ \partial_t\langle\sigma_z\rangle = -\Omega\big(\langle\sigma_x\rangle\cos(\phi) + \langle\sigma_y\rangle\sin(\phi)\big) - \Gamma_1\langle\sigma_z\rangle + \Gamma_1. \end{cases}$$

The result can be rewritten in compact form known as the Bloch equation

$$\frac{d\vec{\sigma}(t)}{dt} = \mathbf{B}\vec{\sigma}(t) + \vec{b},$$

where

$$\mathbf{B} = \begin{pmatrix} -\Gamma_2 & 0 & \Omega\sin(\varphi) \\ 0 & -\Gamma_2 & \Omega\cos(\varphi) \\ -\Omega\sin(\varphi) & -\Omega\cos(\varphi) & -\Gamma_1 \end{pmatrix} \vec{b} = \begin{pmatrix} 0 \\ 0 \\ \Gamma_1 \end{pmatrix} \vec{\sigma} = \begin{pmatrix} \langle\sigma_x\rangle \\ \langle\sigma_y\rangle \\ \langle\sigma_z\rangle \end{pmatrix}. \tag{A.2.11}$$

A.2.5.1 The Bloch sphere

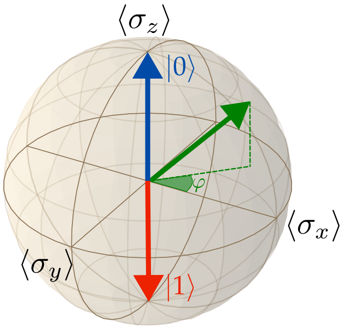

Figure A.3: Representation of the system state on a Bloch sphere, showing the ground (blue), excited (red) and arbitrary (green) system states. The state will evolve in accordance with (A.2.11).

Figure A.3 shows how different components of the vector $\vec{\sigma}$ in (A.2.11) can be represented on a Bloch sphere. Using (A.7.9), one can associate some common quantum states and their Bloch vector equivalents:

- **Ground state** $\rho_{00} = 1 \Leftrightarrow \vec{\sigma} = (0, 0, 1)$;
- **Excited state**: $\rho_{11} = 1 \Leftrightarrow \vec{\sigma} = (0, 0, -1)$;
- **Superposition state**: $\rho_{00} = \rho_{11} \Leftrightarrow \vec{\sigma} = (\cos(\varphi), \sin(\varphi), 0)$, where φ is the angle shown in Fig. A.3.

A.2.5.2 Evolution with no drive

An initial state $\vec{\sigma}(t = 0)$ is prepared using a controllable Rabi pulse, after which the drive is turned off and the system evolves according to (A.2.11) with $\Omega = 0$:

$$\frac{\partial\langle\vec{\sigma}\rangle}{\partial t} = \begin{pmatrix} -\Gamma_2 & 0 & 0 \\ 0 & -\Gamma_2 & 0 \\ 0 & 0 & -\Gamma_1 \end{pmatrix} \begin{pmatrix} \langle\sigma_x\rangle \\ \langle\sigma_y\rangle \\ \langle\sigma_z\rangle \end{pmatrix} + \begin{pmatrix} 0 \\ 0 \\ +\Gamma_1 \end{pmatrix} \quad \Rightarrow \begin{cases} \langle\sigma_x\rangle(t) = \langle\sigma_x(0)\rangle\, e^{-i\Gamma_2 t} \\ \langle\sigma_y\rangle(t) = \langle\sigma_y(0)\rangle\, e^{-i\Gamma_2 t} \\ \langle\sigma_z\rangle(t) = 1 - (1 - \langle\sigma_z\rangle\,(0))e^{-\Gamma_1 t}. \end{cases}$$

As seen $\langle\sigma_z\rangle$ slowly decays to $\langle\sigma_z\rangle$ = 1 - the ground state of the atom (see Fig. A.4 (a)).

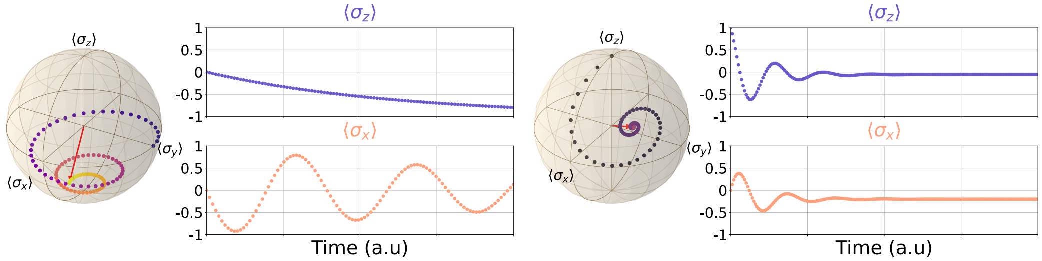
(a) No drive, $\Gamma_1 = 0.4, \Gamma_\varphi = 0.1$

(b) $\Omega = 2.0, \Gamma_1 = 0.4, \Gamma_\varphi = 0.1$

Figure A.4: Simulations of the Bloch equation (A.2.11) under different conditions: **(a)** Decay of an undriven system ($\Omega = 0, \Gamma_1 = 0.4, \Gamma_\varphi = 0.1$); **(b)** Driven system approaching a stationary state ($\Omega = 2, \Gamma_1 = 0.6, \Gamma_\varphi = 0.1$) shown in the interaction picture with Hamiltonian (A.2.8) to hide the natural qubit evolution $U = \exp[iH_q t/\hbar]$ seen in (a) as a precession around the sphere.

A.2.5.3 Evolution with drive

Evolution under a drive is numerically evaluated and shown in Fig. A.4 (b). The 2-level system approaches a stationary state ($\partial_t \rho = 0$) where counter-intuitively $\langle \sigma_x \rangle \neq 0$. This stationary state condition is commonly used to solve the master equation and determine measurable properties of the system.

A.2.5.4 Evolution under dissipation

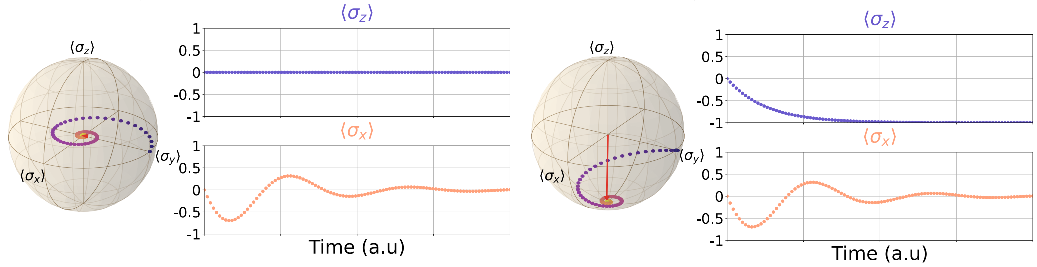
(a) $\Gamma_1 = 0, \Gamma_\varphi = 1$

(b) $\Gamma_1 = 2.0, \Gamma_\varphi = 0$

Figure A.5: Effect on depolarisation (Γ_1) and dephasing (Γ_φ) on the state of a non-driven qubit; **(a)** No depolarisation keeps the state in the equatorial plane ($\Gamma_1 = 0, \Gamma_\varphi = 1$) - slowly phase coherence is lost due to dephasing and ($\langle \sigma_x \rangle \to 0$); **(b)** Presence of depolarisation ($\Gamma_1 = 2, \Gamma_\varphi = 0$) leads to loss relaxation to the ground state ($\langle \sigma_z \to 0 \rangle$) but also leads to loss of coherence quantified by $\Gamma_2 = \Gamma_1/2 + \Gamma_\varphi$ as ($\langle \sigma_x \rangle \to 0$).

To see explicitly the effect of depolarisation (Γ_1) and dephasing (Γ_φ) from Sec. 1.3.2, two extreme cases of no depolarisation and no dephasing are compared in Fig. A.5. It can be seen that dephasing leads to loss of phase coherence, as $\langle \sigma_x \rangle$ containing information on the superposition of the system tends to zero, but does not affect the excitation state of the qubit ($\langle \sigma_z \rangle$) - such noise is non-dissipative.

On the other hand depolarisation brings about both a depolarisation of the qubit state

($\langle \sigma_z \rangle \to 0$) and causes loss of phase coherence, as the qubit naturally has less phase information as it becomes more localised in the ground state. This effect is quantified in the total decoherence rate ($\Gamma_2 = \Gamma_1/2 + \Gamma_\varphi$) due to depolarisation and dephasing effects.

A.2.6 Two tone spectroscopy on a 3-level system

Here it is shown how monitoring of a control tone $\omega_{01}^c \sim \omega_{01}$ on the $|0\rangle \leftrightarrow |1\rangle$ transition will help with identifying a $|1\rangle \leftrightarrow |2\rangle$ transition by sweeping a probe tone ω_{12}^p. This procedure allows the identification of higher order qubit transitions in a process known as two-tone spectroscopy. It is shown that small amplitudes should be used for the control tone in order to get the cleanest transition spectrum [70].

Proof

1. Starting with the Hamiltonian for a 3-level atom in its eigenstate basis $\{|0\rangle, |1\rangle, |2\rangle\}$

$$H_\mathrm{q} = \begin{pmatrix} E_0 & 0 & 0 \\ 0 & E_1 & 0 \\ 0 & 0 & E_2 \end{pmatrix} = \begin{pmatrix} E_1 - \hbar\omega_{01} & 0 & 0 \\ 0 & E_1 & 0 \\ 0 & 0 & E_1 + \hbar\omega_{12} \end{pmatrix}, \tag{A.2.12}$$

   where $\hbar\omega_{01} = E_1 - E_0$ and $\hbar\omega_{12} = E_2 - E_1$.

2. The control and probe field coupling states $|0\rangle \leftrightarrow |1\rangle$, $|1\rangle \leftrightarrow |2\rangle$ are written in matrix form as

$$H_\mathrm{int} = -\hbar\Omega_{01}\cos(\omega_{01}^c t) \begin{pmatrix} 0 & 1 & 0 \\ 1 & 0 & 0 \\ 0 & 0 & 0 \end{pmatrix} - \hbar\Omega_{12}\cos(\omega_{12}^p t) \begin{pmatrix} 0 & 0 & 0 \\ 0 & 0 & 1 \\ 0 & 1 & 0 \end{pmatrix}. \tag{A.2.13}$$

3. The total Hamiltonian ($H = H_\mathrm{q} + H_\mathrm{int}$) is a sum of (A.2.12), (A.2.13), written for convenience with complex exponentials,

$$\begin{aligned} H = & \begin{pmatrix} E_1 - \hbar(\omega_{01}^c - \delta\omega_{01}) & -\frac{\hbar\Omega_{01}}{2}\left(e^{i\omega_{01}^c t} + e^{-i\omega_{01}^c t}\right) & 0 \\ -\frac{\hbar\Omega_{01}}{2}\left(e^{i\omega_{01}^c t} + e^{-i\omega_{01}^c t}\right) & E_1 & -\frac{\hbar\Omega_{12}}{2}\left(e^{i\omega_{12}^p t} + e^{-i\omega_{12}^p t}\right) \\ 0 & -\frac{\hbar\Omega_{12}}{2}\left(e^{i\omega_{12}^p t} + e^{-i\omega_{12}^p t}\right) & E_1 + \hbar(\omega_{12}^p - \delta\omega_{12}) \end{pmatrix} \\ = & \begin{pmatrix} H_{00} & H_{01} & H_{02} \\ H_{10} & H_{11} & H_{12} \\ H_{20} & H_{21} & H_{22} \end{pmatrix}, \end{aligned} \tag{A.2.14}$$

where $\delta\omega_{01} = \omega^{c}_{01} - \omega_{01}, \delta\omega_{12} = \omega^{p}_{12} - \omega_{12}$ represent the detunings of the control and probe fields from the resonant frequencies of the atom.

4. Hamiltonian (A.2.14) governs the time evolution of the system state $|\psi\rangle = a_0 |0\rangle + a_1 |1\rangle + a_2 |2\rangle$ through the standard Schrödinger equation, which takes on the matrix form

$$\begin{pmatrix} H_{00} & H_{01} & H_{02} \\ H_{10} & H_{11} & H_{12} \\ H_{20} & H_{21} & H_{22} \end{pmatrix} \begin{pmatrix} a_0 \\ a_1 \\ a_2 \end{pmatrix} = i\hbar \begin{pmatrix} \partial_t a_0 \\ \partial_t a_1 \\ \partial_t a_2 \end{pmatrix}. \tag{A.2.15}$$

5. By applying a time dependent transformation

$$b_i = e^{i\phi_i(t)} a_i, \qquad i = 1, 2, 3,$$

one can rewrite (A.2.15) as

$$\begin{pmatrix} H_{11} - \hbar\partial_t\phi_0 & H_{01}e^{i\phi_{01}} & H_{02}e^{i\phi_{02}} \\ H_{10}e^{i\phi 10} & H_{11} - \hbar\partial_t\phi_1 & H_{12}e^{i\phi 12} \\ H_{20}e^{i\phi 20} & H_{21}e^{i\phi 21} & H_{22} - \hbar\partial_t\phi_2 \end{pmatrix} \begin{pmatrix} b_0 \\ b_1 \\ b_2 \end{pmatrix} = i\hbar \begin{pmatrix} \partial_t b_0 \\ \partial_t b_1 \\ \partial_t b_2 \end{pmatrix},$$

where $e^{i\phi_{kj}} = e^{i(\phi_k - \phi_j)}$. Setting

$$\phi_0 = \left(\frac{E_1}{\hbar} - \omega^{d}_{01}\right)t;\ \phi_1 = \frac{E_1}{\hbar}t;\ \phi_2 = \left(\frac{E_1}{\hbar} + \omega^{d}_{12}\right)t,$$

which effectively rotates the state vector components at the natural atomic evolution and detuning frequencies[4] will simplify Hamiltonian (A.2.14)

$$H = \begin{pmatrix} \hbar\delta\omega_{01} & -\frac{\hbar\Omega_{01}}{2} & 0 \\ -\frac{\hbar\Omega_{01}}{2} & 0 & -\frac{\hbar\Omega_{12}}{2} \\ 0 & -\frac{\hbar\Omega_{12}}{2} & -\hbar\delta\omega_{12} \end{pmatrix} + \underbrace{\begin{pmatrix} 0 & -\frac{\hbar\Omega_{01}}{2}e^{-i2\omega^{d}_{01}t} & 0 \\ -\frac{\hbar\Omega_{01}}{2}e^{i2\omega^{d}_{01}t} & 0 & -\frac{\hbar\Omega_{12}}{2}e^{-i2\omega^{d}_{12}t} \\ 0 & -\frac{\hbar\Omega_{12}}{2}e^{i2\omega^{d}_{12}t} & 0 \end{pmatrix}}_{\text{⌖}}.$$

6. In the RWA, one ignores the contribution from the fast rotating $2\omega^{c}_{01}, 2\omega^{p}_{12}$ in ⌖, since their oscillations will be averaged out at the time-scales of significant qubit dynamics

---

[4] The full unitary transformation applied:
$$U(t) = \exp\left[\frac{it}{\hbar}\left[(E_1 - \hbar\omega^{c}_{01})|0\rangle\langle 0| + (E_1|1\rangle\langle 1|) + (E_1 + \hbar\omega^{p}_{12})|2\rangle\langle 2|\right]\right]$$

(they correspond to energy non-conserving processes) resulting in

$$H \approx \frac{\hbar}{2} \begin{pmatrix} 2\delta\omega_{01} & -\Omega_{01} & 0 \\ -\Omega_{01} & 0 & -\Omega_{12} \\ 0 & -\Omega_{12} & -2\delta\omega_{12} \end{pmatrix}, \tag{A.2.16}$$

with $\omega_{01}^{c} = \omega_{01} + \delta\omega_{01}$ and $\omega_{12}^{p} = \omega_{12} + \delta\omega_{12}$. For various $\delta\omega_{ij} \approxeq 0$, certain energy levels in the rotated frame become degenerate in energy, and hybridised states forms with a splitting $\hbar\Omega$[5] as shown in Fig. A.6.

7. The density matrix of a 3 level atom

$$\rho = \begin{pmatrix} 1 - \rho_{11} - \rho_{22} & \rho_{01} & \rho_{02} \\ \rho_{10} & \rho_{11} & \rho_{12} \\ \rho_{20} & \rho_{21} & \rho_{22} \end{pmatrix},$$

evolves under Hamiltonian (A.2.16) with a Linbland term

$$\mathcal{L} = \begin{pmatrix} \Gamma_{01}\rho_{11} + \Gamma_{02}\rho_{22} & -\gamma_{01} & -\gamma_{02} \\ -\gamma_{01} & -\Gamma_{01}\rho_{11} + \Gamma_{12}\rho_{22} & -\gamma_{12} \\ -\gamma_{02} & -\gamma_{12} & -\Gamma_{02}\rho_{22} + \Gamma_{02}\rho_{22} \end{pmatrix},$$

that quantifies dissipation, according to the master equation (A.7.10). The typical linewidths of the energy levels is the sum of different decoherence rate e.g. $\gamma_0 \sim \gamma_{01} + \gamma_{02} + \Gamma_{01} + \Gamma_{12}$.

Solving for the stationary state ($\partial_t \rho = 0$), valid in the case of a continuous drive, can be done using `Mathematica` or `Qutip`. This determines the ρ_{ij} coefficients which fully characterises the state of the system.

8. Linking some earlier equations, transmission through the system is quantified

$$\begin{cases} (1.2.18) \quad t = 1 - r = 1 - \dfrac{V_{\mathrm{sc}}}{V_{\mathrm{mw}}} \\ (1.2.4) \quad \Omega = \dfrac{1}{\hbar}\vartheta V_{\mathrm{mw}} \\ (1.2.9) \quad V_{\mathrm{sc}} = i\dfrac{\hbar\Gamma_1}{\vartheta}\left\langle \sigma_- \right\rangle \end{cases} \Rightarrow t = 1 - i\frac{\Gamma_1}{\Omega}\left\langle \sigma_- \right\rangle,$$

and use the steady state solutions ρ_{ij} found in Step 7 to evaluate transmission of the

---

[5] For a 2-level system $H = \hbar\left(\begin{smallmatrix} 0 & -\Omega/2 \\ -\Omega/2 & 0 \end{smallmatrix}\right)$ has eigenenergies $\pm\hbar\Omega$ and hybrid eigenstates $\left(\,|0\rangle \mp |1\rangle\,\right)/\sqrt{2}$.

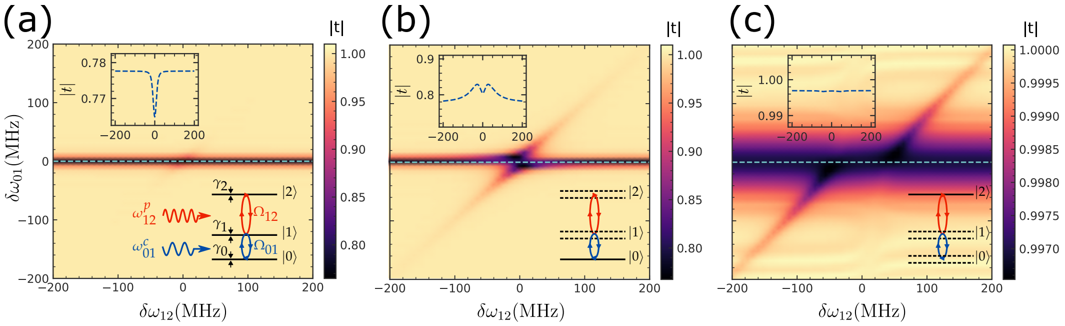

Figure A.6: Transmission of the control tone (ω^c_{01}) interacting with a 3-level atom subjected to $|0\rangle \leftrightarrow |1\rangle, |1\rangle \leftrightarrow |2\rangle$ drives of different strength - the goal is to identify the second transition i.e. $\delta\omega_{12} = 0$: **(a)** Weak driving ($\Omega_{01}, \Omega_{12} \ll \gamma_0, \gamma_1, \gamma_2$) of both the control and probe tones will preserve the original level structure. Inset shows the emission spectrum as a function of $\delta\omega_{12}$ - when the prove tone is resonant with the first transition ($\delta\omega_{01} = 0$, shown as dotted line in main graph), the dip in transmission accurately identifies the frequency of the second transition; **(b)** Strong drive of the probe tone ($\Omega_{12} \gg \gamma_1, \gamma_2$) will split levels $|1\rangle$ and $|2\rangle$, resulting in splitting along the $\delta\omega_{12}$ axis; **(c)** Strong drive of the control tone ($\Omega_{01} >> \gamma_1, \gamma_0$) must be avoided, or a complex emission spectrum will make it hard to identify the second transition.

control tone (ω^c_{01}) for which $\langle\sigma_-\rangle \equiv \langle\sigma_{01}\rangle = \rho_{01}$

$$t_{01} = 1 - i\frac{\Gamma_{01}}{\Omega_{01}}\rho_{01}. \tag{A.2.17}$$

9. Simulations of emission strengths (A.2.17) for different detunings ($\delta\omega_{ij}$) and Rabi amplitudes (Ω_{ij}) of the drives are presented in Fig. A.6. The best way to locate the $|1\rangle \leftrightarrow |2\rangle$ transition is to use control and probe tones with a small amplitude $\Omega_{01}, \Omega_{12} \ll \gamma_0, \gamma_1, \gamma_2$ shown in (a). A strong drive of the of the probe tone (ω^p_{12}) *searching* for transition will *split* the energy levels, giving strong emission at frequencies $\omega^p_{12} = \omega_{12} \pm \hbar\Omega_{12}$ as seen in the inset of (b), while a strong control tone will mask the transition completely as seen in the inset of (c).

QED ☐

A.2.7 Decay in system due to phase noise

Under assumption that the phase noise ($\delta\varphi(t)$) has a Gaussian distribution caused by temporal fluctuations of a qubit's energy ($\langle\delta E(t)\rangle = 0$)

$$\delta\varphi(t) = \int_0^t d\tau[\delta E(t)/\hbar],$$

multiple independent evolutions of the system $U(t) = \exp\left[i\hbar\left(\frac{1}{2}\omega_q\sigma_z + \delta\omega(t)\sigma_z\right)\right] = U_0(t)e^{i\delta\varphi(t)}$ will produce a decay

$$\left\langle e^{i\delta\varphi(t)}\right\rangle = \exp\left(-\frac{S_{EE}(\omega=0)}{2\hbar^2}t^2\right),$$

determined by the spectral density of the energy fluctuations $S_{EE}(\omega) = \int dt\,\langle\delta E(t)\delta E(0)\rangle\, e^{-i\omega t}$ at low frequencies.

Proof

1. The phase noise ($\delta\varphi(t)$), which is a random variable of t, is expanded through a moment generating function

$$M = \left\langle e^{i\delta\varphi(t)}\right\rangle = 1 + t\,\langle(i\delta\varphi)\rangle + \frac{t^2}{2!}\left\langle\frac{(i\delta\varphi)^2}{2}\right\rangle + \cdots = \sum_{m=0}\frac{t^m}{m!}\mu_m, \tag{A.2.18}$$

where $\mu_m = i^m\langle\delta\varphi^m\rangle$ is the m-th moment. As seen from (A.2.18), the moment generating function has the property that at $t=0$ its derivatives are equal to the moments of $i\delta\varphi$ i.e. $d^m M/d(i\partial\varphi)^m\Big|_{t=0} \equiv \mu_m$.

2. The cumulant is the natural log of (A.2.18)

$$K = \ln M = \sum_{n=1}\frac{t^n}{n!}k_n, \tag{A.2.19}$$

with cumulants $k_n = d^n K/dt^n$. Evaluating the first few cumulant terms at $t=0$:

$$\begin{aligned}
k_1 &= \frac{d}{dt}\ln M\Big|_{t=0} = \frac{1}{M}\frac{dM}{dt}\Big|_{t=0} = \frac{1}{1}\mu_1 = \mu_1 = i\langle\delta\varphi\rangle\\
k_2 &= -\frac{1}{M^2}\left(\frac{dM}{dt}\right)^2\Big|_{t=0} + \frac{1}{M}\frac{d^2M}{dt^2}\Big|_{t=0} = \mu_2 - \mu_1^2 = i^2\left(\left\langle\delta\varphi^2\right\rangle - \langle\delta\varphi\rangle^2\right)\\
k_3 &= \mu_3 - 3\mu_2\mu_1 + 2\mu_1^3 = \left\langle(\delta\varphi - \langle\delta\varphi\rangle)^3\right\rangle\\
&\cdots
\end{aligned} \tag{A.2.20}$$

3. For a Gaussian function the higher order cumulants $k_3 = k_4 = k_n = 0$, and symmetrically distributed phase is assumed $\langle\delta\varphi(t)\rangle = 0$, so re-evaluation of (A.2.19) with cumulants from (A.2.20)

$$M = \left\langle e^{i\delta\varphi(t)}\right\rangle = \exp\left(-\frac{1}{2}\left\langle\delta\varphi^2\right\rangle t^2\right). \tag{A.2.21}$$

4. As per (1.3.1), the accumulated phase will be the time integral of energy fluctuations,

which can be used to express $\langle \delta\varphi^2 \rangle$ through the spectral density of the energy fluctuations at zero frequency (refer to A.8.2)

$$\left\langle \delta\phi(t)^2 \right\rangle = \frac{1}{\hbar^2}\left(\int_0^t dt_2 \int_0^t dt_1 \left[\delta E(t_1)\delta E(t_2)\right]\right) \equiv \frac{1}{\hbar^2} S_{EE}(\omega = 0), \tag{A.2.22}$$

where $S_{EE}(\omega) = \int dt \, \langle \delta E(t)\delta E(0)\rangle \, e^{-i\omega t}$. Using (A.2.22) in (A.2.21)

$$\left\langle e^{i\delta\varphi(t)} \right\rangle = \exp\left(-\frac{S_{EE}(\omega = 0)}{2\hbar^2} t^2\right).$$

QED □

A.3 Microwave transmission lines

TLs connect the superconducting qubits to laboratory equipment that deliver power and track emission using propagating microwave modes. Ultimately, one can only control the input (V_{mw}) and monitor the scattered[6] (V_{sc}) waves from which all information about the qubit has to be derived.

This part of the appendix summarises the mathematical approach for treating classical voltages and currents in TLs (A.3.1), their quantisation (A.3.2) and noise from quantum fluctuations (A.3.4) which stimulates qubit emission into the TL (A.3.5), along with a specific scenario of a driven qubit emitting a dipole-like voltage into the TL (A.3.6).

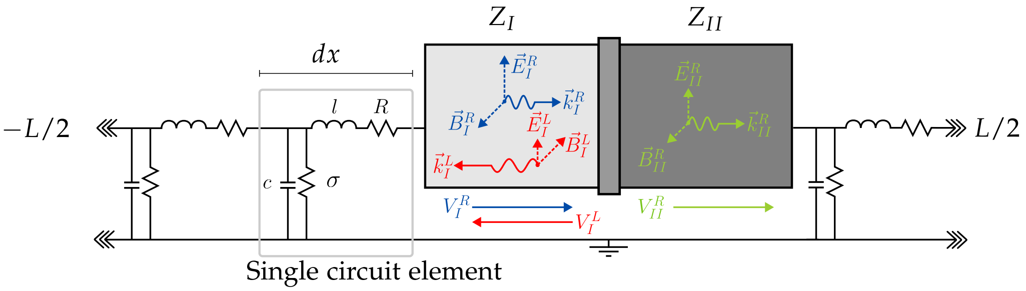

Figure A.7: Representation of a TL through unit cells of length dx with finite inductance (l) along the line and finite capacitance (c) between the central waveguide and ground. The microwave fields propagate in the $\overset{L}{\leftarrow}$ and $\overset{R}{\rightarrow}$ directions giving rise to voltage and current through the electric ($\vec{E}$) and magnetic ($\vec{B}$) components. At the interface between media with different impedances (Z_I, Z_{II}) the electric and magnetic field components must be continuous, which determines how an incoming wave (V_I^R, blue) is reflected (V_I^L, red) and transmitted (V_{II}^R, green).

A.3.1 Classical transmission line equations

A lossless TL with inductance l and capacitance c per unit length will support plane waves

$$V(x,t) = |V|e^{\pm ikx - i\omega t}, \qquad I(x,t) = |I|e^{\pm ikx - i\omega t}. \tag{A.3.1}$$

which are related to each other through the impedance of the medium

$$V(x,t) = Z\, I(x,t), \qquad Z = \sqrt{\frac{l}{c}},$$

---

[6] Scattering is more general than just the reflection of incoming waves - it is the total voltage emitted by the qubit in the $\overset{L}{\leftarrow}$ and $\overset{R}{\rightarrow}$ directions.

and have wave propagation speed

$$v = \frac{\omega}{k} = \frac{1}{\sqrt{lc}}.$$

Proof

1. To realise a TL one needs two conductors - the central waveguide and the ground plane. This line is split into unit length elements (see Fig. A.7): the proximity of the two conductors gives rise to a capacitance per unit length $c \approx \varepsilon_0$; the long lengths of the lines mean that current flowing through them will generate a magnetic field that opposes further current changes, giving a finite inductance $l \approx \mu_0$ per unit length. Assuming a losses TL with $R = 0$ along the lines and conductance per unit length $\sigma = 0$ across to the ground, the telegrapher equations determining the voltages and currents are

$$\begin{cases} \text{Faraday's law of induction} & V = -\partial_t \Phi = -L\partial_t I, \\ \text{Charge conservation} & I = -\partial_t Q = -C\partial_t V, \end{cases}$$

and written per unit length

$$\begin{cases} \text{Faraday's law of induction} & \partial_x V = -l\partial_t I, \\ \text{Charge conservation} & \partial_x I = -c\partial_t V. \end{cases} \tag{A.3.2}$$

2. Differentiation of (A.3.2) leads to a wave equations for voltage and current

$$\begin{aligned} \partial_{xx} V(x,t) &= -l\partial_t \left[\partial_x I\right] = -l(-c\partial_{tt} V) \\ &= \frac{1}{v^2}\partial_{tt} V(x,t), \\ \partial_{xx} I(x,t) &= \frac{1}{v^2}\partial_{tt} I(x,t) \end{aligned} \tag{A.3.3}$$

with $v = 1/\sqrt{lc}$ the wave propagation speed defined by the properties of the TL.

3. The solution to the wave equation (A.3.3) are plane waves

$$V(x,t) = |V|e^{\pm ikx - i\omega t}, \qquad I(x,t) = |I|e^{\pm ikx - i\omega t}, \tag{A.3.4}$$

with $v = \omega/k$ that travel in the $\overset{\text{L}}{\leftarrow}$ or $\overset{\text{R}}{\rightarrow}$ directions depending on the $\pm ikx - i\omega t$

factor. Substitution of the plane wave solution (A.3.4) into (A.3.2)

$$\begin{cases} ikV = i\omega l I \\ -i\omega I = -ickV \end{cases} \Rightarrow \begin{cases} \dfrac{V}{I} = \dfrac{\omega l}{k} \\ \dfrac{V}{I} = \dfrac{k}{\omega c} \end{cases}$$

connects voltages and currents in the TL through an impedance

$$Z = \frac{\omega l}{k} = \frac{l}{v} = \sqrt{\frac{l}{c}}, \tag{A.3.5}$$

meaning that the fields in region I and II of Fig. A.7 with impedances Z_I and Z_{II} respectively, have voltage-current relations

$$\frac{V_I^R}{I_I^R} = Z_I, \qquad \frac{V_I^L}{I_I^L} = Z_I, \qquad \frac{V_{II}^R}{I_{II}^R} = Z_{II}. \tag{A.3.6}$$

QED ☐

A.3.2 Quantised transmission line equations

In order to treat interaction between the qubit and TL, the latter needs to be quantised from its classical expressions seen in A.3.1. The voltage field in a TL of length $L \to \infty$ is shown to be

$$\hat{V}(x,t) = \sum_m \left[\underbrace{\hat{V}_m e^{i(kx+\omega_m t)} + \hat{V}_m^\dagger e^{-i(kx-\omega_m t)}}_{\overset{\mathrm{R}}{\rightarrow}} - \underbrace{\hat{V}_m e^{i(kx+\omega_m t)} - \hat{V}_m^\dagger e^{-i(kx+\omega_m t)}}_{\overset{\mathrm{L}}{\leftarrow}} \right],$$

representing modes indexed by the wavevector m propagating in the $\overset{\mathrm{L}}{\leftarrow}$ and $\overset{\mathrm{R}}{\rightarrow}$ directions, with an amplitude operator

$$\hat{V}_m = -i\sqrt{\frac{\hbar\omega_m}{2cL}}a_m,$$

containing the creation ($a_m^\dagger$) and annihilation (a_m) operators that are shown in Step 14 to operate on the photon number of the m-th mode.

Proof

The discussion follows the quantisation process proposed in [104, 164, 254] in reference to a TL broken down into circuit elements of length dx as shown in Fig. A.7.

1. The first step in circuit quantisation is to define a node charge[7]

$$Q(x,t) = \int_{-\infty}^{t} d\tau \, I(x,\tau), \tag{A.3.7}$$

which defines the local current $I(x,t) = \partial_t Q(x,t)$ in the TL at position x and time t. This charge also defines the voltage in the TL - each circuit element of length dx with capacitance cdx has a charge $-dx\partial_x Q(x,t)$ and thus

$$\begin{cases} I(x,t) = \partial_t Q(x,t), \\ V(x,t) = \dfrac{Q_{\text{element}}}{C_{\text{element}}} = \dfrac{-dx\,\partial_x Q(x,t)}{cdx} = -\dfrac{1}{c}\partial_x Q(x,t). \end{cases} \tag{A.3.8}$$

2. The Lagrangian $\mathcal{L}(\Phi, \partial_t\Phi, t) = T - U$ for a single circuit element consisting of an inductor capacitively coupled to the ground (see Fig. A.7), has a kinetic term which depends on the time derivative of the generalised coordinate (A.3.7)

$$T(\partial_t Q) = \frac{L_{\text{element}} I^2_{\text{element}}}{2} = \frac{(ldx)\, I^2}{2} = dx\frac{l}{2}\left(\partial_t Q\right)^2,$$

and corresponds to the current flowing through the inductor (with inductance per unit length l). The potential term depends on the coordinate itself

$$U(\partial_x Q) = \frac{Q^2_{\text{element}}}{2C_{\text{element}}} = \frac{(dx\partial_x Q)^2}{2cdx} = dx\frac{1}{2c}\left(\partial_x Q\right)^2,$$

and corresponds to the voltage (A.3.8) on the capacitor (with capacitance per unit length c).

3. The full Lagrangian is an integral of $T - U$ over the whole TL from $-L/2$ to $L/2$

$$\begin{aligned} \mathcal{L} &= \int_{-L/2}^{L/2} [T - U] \\ &= \int_{-L/2}^{L/2} dx \left[\frac{l}{2}(\partial_t Q)^2 - \frac{1}{2c}(\partial_x Q)^2\right] \end{aligned} \tag{A.3.9}$$

4. Solving the Euler-Lagrange equation[8] for (A.3.9) that depends on multiple derivatives

---

[7] Another equivalent approach is to define node flux $\Phi(x,t) = \int_{-\infty}^{t} d\tau\, V(x,\tau)$. The current and voltage are correspondingly $I(x,t) = -\partial_t\Phi(x,t)/l, V(x,t) = -\partial_t\Phi(x,t)$.

[8] The Euler-Lagrange equation comes from the principle of stationary action that minimises the action of the Lagrangian $S = \int_{t_1}^{t_1} dt\mathcal{L}(x,t,\theta,\partial_t\theta,\partial_x\theta)$. A partial motivation for this minimisation can be found in one of Feynman's lectures [255], where the trajectory of the system evolution in x,t space is associated with a complex number $e^{iS/\hbar}$. Summing over all possible trajectories that the system can evolve through, it is found that only trajectories near the stationary value of S reinforce each other without cancellation, and hence they determine the evolution of the system.

$(\partial_t Q, \partial_x Q, \cdots, \partial_q Q)$ of the generalised coordinate $Q(x,t)$

$$\begin{aligned} \frac{\partial \mathcal{L}}{\partial Q} &= \sum_{q=x,t} \frac{d}{dq}\frac{\partial \mathcal{L}}{\partial(\partial_q Q)} = \frac{d}{dt}\frac{\partial \mathcal{L}}{\partial(\partial_t Q)} + \frac{d}{dx}\frac{\partial \mathcal{L}}{\partial(\partial_x Q)} \\ \Rightarrow \qquad 0 &= \frac{d}{dt}\left[l\partial_t Q\right] - \frac{d}{dx}\left[\frac{1}{c}\partial_x Q\right] \\ \Rightarrow \quad \partial_{xx} Q(x,t) &= \frac{1}{v^2}\partial_{tt} Q(x,t) \end{aligned} \tag{A.3.10}$$

which unsurprisingly is identical to the wave equation (A.3.3).

5. A trial solution $Q(x,t) = Q(t)Q(x)$ for (A.3.10) yields two ordinary differential equations[9]

$$\begin{cases} \partial_{tt} Q_k(t) = -\omega_k^2 Q_k(t) \\ \partial_{xx} Q_k(x) = -\dfrac{\omega_k^2}{v^2} Q_k(x) \end{cases} \Rightarrow \begin{cases} Q_k(t) = e^{\pm i\omega_k t} \\ Q_k(x) = Ce^{\pm ikx} \end{cases} \tag{A.3.11}$$

where $k = \omega_k / v$ is a free constant that indexes the solutions.

6. The general solution is a weighted sum of (A.3.11) combinations for the different modes indexed by k[10]

$$Q(x,t) = \sum_{k>0} \left[\underbrace{C_1 e^{i(kx-\omega_m t)} + C_2 e^{-i(kx-\omega_m t)}}_{\overset{\mathrm{R}}{\rightarrow}} + \underbrace{C_1 e^{i(kx+\omega_m t)} + C_2 e^{-i(kx+\omega_m t)}}_{\overset{\mathrm{L}}{\leftarrow}} \right], \tag{A.3.12}$$

which describes a charge density of $\overset{\mathrm{R}}{\rightarrow}$ and $\overset{\mathrm{L}}{\leftarrow}$ moving solutions of an arbitrary shape. As this charge density is real valued, $C_1 = C_2^*$[11] and thus for the $\overset{\mathrm{R}}{\rightarrow}$ moving modes

$$Q_k(x) = \left(\alpha \cos(kx) + \beta \sin(kx)\right), \quad \alpha = 2\mathrm{Re}\left[C_1\right], \quad \beta = 2\mathrm{Im}\left[C_1\right]. \tag{A.3.13}$$

7. (A.3.13) is chosen to obey periodic Boundary conditions (BCs) on the TL of length L[12], taken for simplicity to be the charge neutrality on the ends of the TL $Q_k(-L/2,t) = Q_k(L/2,t) = 0$, which result in odd and even mode solutions for the spatial parts

---

[9] Separation of variables gives $v^2(\partial_{xx}Q(x))/Q(x) = (\partial_{tt}Q(t))/Q(t)$ and since the two sides depend on different variables x and t, for a general equality they need to be equal to a constant $-\omega^2$ (which is later seen to correspond to the oscillation frequency).

[10] The $k > 0$ in the summation allows both e^{ikx} and e^{-ikx} to be included to clearly identify the $\overset{\mathrm{R}}{\rightarrow}$ and $\overset{\mathrm{L}}{\leftarrow}$ propagating modes.

[11] Writing $C_1 = A + iB$ and $C_2 = C + iD$ in (A.3.12) results in $(A+C)\cos(kx) + (D-B)\sin(kx) + i(A-C)\sin(kx) + i(B+D)\sin(kx)$, which is real valued when $A = C, B = -D$ and hence $C_1 = C_2^*$.

[12] This is a standard and necessary step to limit the modes that exist in the TL.

(A.3.11)

$$Q_k(x) \to Q_m(x) = \begin{bmatrix} \sqrt{\frac{2}{L}} \cos{(k_m x)}, & m \text{ odd}, \\ \sqrt{\frac{2}{L}} \sin{(k_m x)}, & m \text{ even}, \end{bmatrix} \tag{A.3.14}$$

with $k \to k_m$ now becoming discretised

$$k_m = \frac{m\pi}{L}, \qquad m \in \mathbb{Z}. \tag{A.3.15}$$

The normalisation factor $\sqrt{2/L}$ ensures that

$$\int_{-L/2}^{L/2} dx\, |Q_m(x)|^2 = \frac{2}{L}\int_{-L/2}^{L/2} dx \left[\frac{1 \pm \cos(2k_m x)}{2}\right] \equiv 1, \tag{A.3.16}$$

for future integration purposes.

8. An alternative form to (A.3.12) that keeps the discretisation (A.3.15) and normalisation (A.3.16) conditions

$$Q(x,t) = \sum_m Q_m(x)\big(Q_{+m}(t) + Q^*_{-m}(t)\big), \tag{A.3.17}$$

will be defined for future steps. This form keeps the spatial component defined by (A.3.14) but *hides* the explicit time evolution inside $Q_m(t) = Q_{+m}(t) + Q_{-m}(t)$ for future association with a time-evolving quantum operator in the interaction picture.

9. Substituting (A.3.17) for each individual mode m into the Lagrangian (A.3.9)

$$\mathcal{L}_m = \frac{l}{2}(\partial_t Q_m(t))^2 \underbrace{\int_{-L/2}^{L/2} dx\, |Q_m(x)|^2}_{1 \text{ see (A.3.16)}} - \frac{1}{2c} Q_m(t)^2 \underbrace{\int_{-L/2}^{L/2} dx \left[\frac{2}{L}k_m^2 \left(\frac{1 \pm \cos{(2k_m x)}}{2}\right)\right]}_{k^2 \text{ see (A.3.16)}}$$

and thus for all modes the Lagrangian reads

$$\mathcal{L} = \sum_m \left[\frac{l}{2}(\partial_t Q_m(t))^2 - \frac{1}{2c}k_m^2 Q_m(t)^2\right],$$

expanded in terms of the modes $k_m = m\pi/L, m \in \mathbb{Z}$ that the TL supports.

10. Following Hamiltonian-Lagrangian formalism, the conjugate variable to $Q(t)$ is found by taking the partial derivative of (A.3.9)

$$\frac{\partial \mathcal{L}}{\partial(\partial_t Q)} = l\partial_t Q = lI(x,t) \equiv \Phi(x,t),$$

which is recognised to be the node flux. The Hamiltonian

$$\begin{aligned} H &= \int_{-L/2}^{L/2} dx\,[(\partial_t Q)\Phi] - \mathcal{L} \\ &= \int_{-L/2}^{L/2} dx\left[\frac{1}{2l}\Phi(x,t)^2 + \frac{1}{2c}(\partial_x Q(x,t))^2\right] \\ &= \sum_m \int_{-L/2}^{L/2} dx\left[\frac{l}{2}(\partial_t Q_m(t))^2 + \frac{1}{2c}k^2 Q_m(t)^2\right], \end{aligned} \tag{A.3.18}$$

represents the sum of energies stored in each element of the TL (see Fig. A.7) in the electric and magnetic fields of the circuit[13].

Table A.2: Equivalence of $\hat{\Phi}, \hat{Q}$ and $\hat{V}, \hat{I}$ operators in superconducting circuits to $\hat{x}, \hat{p}$ by comparing the classical expressions of electrical and mechanical harmonic oscillators.

	Q and Φ	Mechanical	V and I
Coordinate	Q	x	V
Momentum	$\Phi = l\partial_t Q$	$p = \partial_t x$	$I = C\partial_t V$
Mass	L	m	$1/L$
Stiffness	$\frac{1}{C}$	$k = m\omega^2$	C
H	$\frac{1}{2L}\Phi^2 + \frac{1}{2C}Q^2$	$\frac{1}{2m}p^2 + \frac{1}{2}m\omega^2 x^2$	$\frac{L}{2}I^2 + \frac{C}{2}V^2$
Commutator	$[\hat{Q}, \hat{\Phi}] = i\hbar$	$[\hat{x}, \hat{p}] = i\hbar$	$[\hat{\Phi}, \hat{Q}] = [CV, LI] = i\hbar$
Position operator	$\hat{Q}$	$\hat{x}$	$\hat{V}$
Momentum operator	$\hat{\Phi} = -i\hbar\frac{\partial}{\partial Q}$	$\hat{p} = -i\hbar\frac{\partial}{\partial x}$	$\hat{I} = -i\frac{\hbar}{LC}\frac{\partial}{\partial V}$
Creation operator	$a^\dagger = \frac{1}{\sqrt{2}}\left(\frac{\hat{Q}}{Q_0} - i\frac{\hat{\Phi}}{\Phi_0}\right)$	$a^\dagger = \frac{1}{\sqrt{2}}\left(\frac{\hat{x}}{x_0} - i\frac{\hat{p}}{p_0}\right)$	$a^\dagger = \frac{1}{\sqrt{2}}\left(\frac{\hat{V}}{V_0} - i\frac{\hat{I}}{I_0}\right)$

11. Quantisation is done by promoting the classical variables in (A.3.18) to quantum operators

$$\begin{aligned} Q_m(t) &\to \hat{Q}_m(t), \\ l\partial_t Q_m(t) &\to \hat{\Phi}_m(t), \end{aligned} \tag{A.3.19}$$

and demanding a commutation relation that corresponds to their classical Poisson brackets (refer to Sec. A.7.5). Because Hamiltonian (A.3.18) describes a collection of simple harmonic oscillators, the commutator between $\hat{Q}$ and $\hat{\Phi}$ will be equivalent to the one between $\hat{x}$ and $\hat{p}$ of the mechanical oscillator (see Tab. A.2)

$$[\hat{Q}, \hat{\Phi}] = i\hbar. \tag{A.3.20}$$

---

[13] Contrary to common belief, it is not the electrons that transfer energy in a circuit - it would actually invalidate the discussion of using constructive and destructive interference of incident waves with those scattered from the atom in Sec. 1.2.4 which requires the presence of propagating microwaves. Furthermore these fields exist in the dielectric between the TL and ground plane, making the topic of impedance matching (refer to A.3.3) very important to avoid dissipation of this energy into the chip.

12. It convenient to separate out the operators in (A.3.19) into operators $a_m(t), a_m^\dagger(t)$ by again following the quantisation analogy of a mechanical oscillator (see Tab. A.2)

$$\begin{cases} \hat{Q}_m(t) = \dfrac{1}{\gamma}\sqrt{\dfrac{\hbar}{2}}\left(a_m(t) + a_m^\dagger(t)\right), \\ \hat{\Phi}_m(t) = -i\gamma\sqrt{\dfrac{\hbar}{2}}\left(a_m(t) - a_m^\dagger(t)\right), \end{cases} \tag{A.3.21}$$

which are in turn defined by

$$\begin{cases} a_m = \dfrac{1}{\sqrt{2\hbar}}\left(\gamma\hat{Q}_k(t) + \dfrac{i}{\gamma}\hat{\Phi}_m(t)\right), \\ a_m^\dagger = \dfrac{1}{\sqrt{2\hbar}}\left(\gamma\hat{Q}_k(t) - \dfrac{i}{\gamma}\hat{\Phi}_m(t)\right), \end{cases} \tag{A.3.22}$$

and have a commutation relation

$$\begin{aligned} \left[a_m, a_{m'}^\dagger\right] &= \frac{1}{2\hbar}\gamma^2 \underbrace{\left[\hat{Q}_m, \hat{Q}_{m'}\right]}_{0} + \frac{1}{2\hbar}\frac{1}{\gamma^2}\underbrace{\left[i\hat{\Phi}_m, -i\hat{\Phi}_{m'}\right]}_{0} + \frac{1}{2\hbar}\left[\gamma\hat{Q}_m, -\frac{i}{\gamma}\hat{\Phi}_{m'}\right] + \frac{1}{2\hbar}\left[\frac{i}{\gamma}\hat{\Phi}_m, \gamma\hat{Q}_{m'}\right] \\ &= -\frac{i}{\hbar}\underbrace{\left[\hat{Q}_m, \hat{\Phi}_{m'}\right]}_{i\hbar\delta_{mm'}\text{ see (A.3.20)}} = \delta_{mm'}, \end{aligned} \tag{A.3.23}$$

where the different modes m of the TL are assumed to not interact with one another.

13. Hamiltonian (A.3.18) can be written out in terms of the newly-defined operators (A.3.22)

$$\begin{aligned} H &= \sum_m \int_{-L/2}^{L/2} dx \left[\frac{1}{2l}\hat{\Phi}_m^2 + \frac{1}{2c}k_m^2\hat{Q}_m^2\right] \\ &= \sum_m \int_{-L/2}^{L/2} dx \left[\frac{1}{2l}\gamma^2\frac{\hbar}{2}\left(a_m^\dagger a_m + a_m a_m^\dagger - a_m^2 - (a_m^\dagger)^2\right)\right. \\ &\qquad\qquad \left. + \frac{1}{2c}k_m^2\frac{1}{\gamma^2}\frac{\hbar}{2}\left(a_m^\dagger a_m + a_m a_m^\dagger + a_m^2 + (a_m^\dagger)^2\right)\right], \end{aligned}$$

and by choosing $\gamma = \sqrt{\omega_m l} = \sqrt{k_m Z}$[14] and $a_m a_m^\dagger = a_m^\dagger a_m + 1$ from (A.3.23) the expression can be simplified

$$\begin{aligned} H &= \sum_m \int_{-L/2}^{L/2} dx \left[\frac{\hbar\omega_m}{2}\left(a_m^\dagger a_m + a_m a_m^\dagger\right)\right] \\ &= \sum_m \int_{-L/2}^{L/2} dx \left[\hbar\omega_m\left(a_m^\dagger a_m + \frac{1}{2}\right)\right], \end{aligned} \tag{A.3.24}$$

---

[14] To eliminate non-mixed terms ($a_m a_m$ and $a_m^\dagger a_m^\dagger$) set $\hbar\gamma^2/4l = \hbar k_m^2/4c\gamma^2 \Rightarrow \gamma^2 = k_m\sqrt{l/c} = \omega_m\sqrt{l/c}/v = \omega_m l = k_m Z$.

with (A.3.21) and (A.3.22) becoming

$$\begin{cases} \hat{Q}_m(t) = \sqrt{\dfrac{\hbar}{2\omega_m l}}\left(a_m(t)+a_m^\dagger(t)\right) = \sqrt{\dfrac{\hbar}{2k_m Z}}\left(a_m(t)+a_m^\dagger(t)\right), \\ \hat{\Phi}_m(t) = -i\sqrt{\dfrac{\hbar k_m Z}{2}}\left(a_m(t)-a_m^\dagger(t)\right), \\ a_m(t) = \dfrac{1}{\sqrt{2\hbar}}\left(\sqrt{\omega_m l}\hat{Q}_m(t)+\dfrac{i}{\sqrt{\omega_m l}}\hat{\Phi}_m(t)\right), \\ a_m^\dagger(t) = \dfrac{1}{\sqrt{2\hbar}}\left(\sqrt{\omega_m l}\hat{Q}_m(t)-\dfrac{i}{\sqrt{\omega_m l}}\hat{\Phi}_m(t)\right). \end{cases} \tag{A.3.25}$$

14. At this point it is instructive to understand what operators $a_m^\dagger, a_m$ defined in (A.3.25) correspond to. Writing (A.3.24) for a single mode and dropping the m index

$$H = \hbar\omega\left(\hat{N}+\frac{1}{2}\right), \tag{A.3.26}$$

where number operator $\hat{N} = a^\dagger a$ is defined, which count the number of photons in the TL in mode m with energy $\hbar\omega_m$ each. The eigenstates ($|n\rangle$) of (A.3.26) will also be the eigenstates of $\hat{N}$

$$\hat{N}|n\rangle = n\,|n\rangle\,. \tag{A.3.27}$$

Using commutation relations (A.3.23) and

$$\begin{cases} [\hat{N},a] = [(1-aa^\dagger),a] = (a[a^\dagger,a]+[a,a]a^\dagger) = -a, \\ [\hat{N},a^\dagger] = a^\dagger \end{cases}$$

one applies (A.3.27) to states $a|n\rangle$ and $a^\dagger\,|n\rangle$

$$\begin{cases} \hat{N}\,a|n\rangle = a\hat{N}\,|n\rangle + [\hat{N},a]\,|n\rangle = (n-1)\;a|n\rangle, \\ \hat{N}\,a^\dagger|n\rangle = (n+1)\,a^\dagger\,|n\rangle \end{cases}$$

and thus states $a^\dagger\,|n\rangle\,, a\,|n\rangle$ are also eigenvectors of $\hat{N}$ with eigenvalues $n+1$ and $n-1$ respectively. As a consequence, starting from $|n\rangle$ one can construct a chain of eigenvectors and eigenvalues

Eigenvectors	$a^q\,\lvert n\rangle$	$\cdots$	$a\lvert n\rangle$	n	$a^\dagger\lvert n\rangle$	$\cdots$	$(a^\dagger)^p\lvert n\rangle,$
Eigenvalues	$n-q$	$\cdots$	$n-1$	n	$n+1$	$\cdots$	$n+p.$

Because $\hat{N}$ is a positive operator

$$\langle\lambda|\,\hat{N}\,|\lambda\rangle = \langle\lambda|\,a^\dagger a\,|\lambda\rangle = ||a\,|\lambda\rangle\,||^2 \geq 0,$$

the chain must terminate in a way that $a^{q_0}|n\rangle = 0$ to keep the eigenvalues positive. $n \in \mathbb{N}^+ = \{0, 1, 2, 3, \cdots\}$.

What this shows is that:

- Hamiltonian (A.3.26) has eigenenergies $E = \hbar\omega(n + \frac{1}{2})$ corresponding to a photon number n in the TL;
- The creation ($a^\dagger$) and annihilation (a) operators describe the number of photons increasing or decreasing in the TL.

Furthermore using the evolution of operator A in the interaction picture (A.7.8) $\frac{d}{dt}A(t) = \frac{i}{\hbar}[H, A]$ with Hamiltonian (A.3.26) the time evolution of these operators

$$\begin{cases} \partial_t a(t) = \dfrac{i}{\hbar}\left[\hbar\omega a^\dagger a, a(t)\right] = i\omega[a^\dagger, a]a \overset{\text{(A.3.23)}}{=} -i\omega a(t) & \Rightarrow a(t) = ae^{-i\omega t} \\ \partial_t a^\dagger(t) = i\omega a(t) & \Rightarrow a^\dagger(t) = a^\dagger e^{i\omega t}. \end{cases} \tag{A.3.28}$$

15. Now that the charge and phase operators the m-th mode have been defined through their classical spatial component (A.3.13)[15] and quantum temporal component (A.3.25)

$$\begin{cases} \hat{Q}_m(x,t) = Q_m(t)Q_m(x) = \dfrac{1}{\sqrt{L}}\sqrt{\dfrac{\hbar}{2k_m Z}}\left(a_m(t) + a_m^\dagger(t)\right)(e^{ikx} + e^{-ikx}), \\ \hat{\Phi}_m(x,t) = \Phi_m(t)\Phi_m(x) = -\dfrac{1}{\sqrt{L}}\sqrt{\dfrac{\hbar k_m Z}{2}}i\left(a_m(t) - a_m^\dagger(t)\right)(e^{ikx} + e^{-ikx}). \end{cases} \tag{A.3.29}$$

---

[15] In the limit of an infinite TL $L \to \infty$, the modes indexed by $k = m\pi/L$ go from being discrete to a continuum, in which case it is no longer necessary to track the odd and even solutions and instead of (A.3.14) use the more general solution with complex exponentials (A.3.12).

16. Applying (A.3.8) to (A.3.29) defines the localised voltage in the TL

$$
\begin{aligned}
\hat{V}(x,t) &= \sum_m -\frac{1}{c}\partial_x \hat{Q}_m(x,t) \\
&= \sum_m \left[-i\frac{1}{c}\frac{1}{\sqrt{L}}\sqrt{\frac{\hbar k_m}{2Z}} e^{ik_m x}(a_m(t) + a_m^\dagger(t)) + \text{h.c.} \right] \\
&= \sum_m \sqrt{\frac{\hbar\omega_m}{2cL}} \left[-ie^{ik_m x}(a_m(t) + a_m^\dagger(t)) + ie^{-ik_m x}(a_m(t) + a_m^\dagger(t)) \right] \\
&= \sum_m \sqrt{\frac{\hbar\omega_m}{2cL}} \left[\left(-ie^{i(k_m x - \omega_m t)} a_m + ie^{-i(k_m x - \omega_m t)} a_m^\dagger \right) + \left(ie^{-i(k_m x + \omega_m t)} a_m - ie^{i(k_m x + \omega_m t)} a_m^\dagger \right) \right] \\
&= \sum_m \left[\underbrace{\hat{V}_m e^{i(k_m x - \omega_m t)} + \hat{V}_m^* e^{-i(k_m x - \omega_m t)}}_{\underset{\rightarrow}{\mathrm{R}}} - \underbrace{\hat{V}_m e^{-i(k_m x + \omega_m t)} - \hat{V}_m^* e^{i(k_m x + \omega_m t)}}_{\underset{\leftarrow}{\mathrm{L}}} \right],
\end{aligned}
\tag{A.3.30}
$$

where the time evolution of the creation and annihilation operators is given in (A.3.28) and the mode amplitude operator

$$
\hat{V}_m = -i\sqrt{\frac{\hbar\omega_m}{2cL}} a_m,
$$

is defined. The terms in (A.3.30) are grouped into right and left propagating modes depending on the exponential factor.

QED ☐

A.3.3 Reflection in transmission lines

At the interfaces between two media with impedances Z_I and Z_{II} (see Fig. A.7) the incoming wave from region I (V_I^R) will partially reflect (V_I^L) and partially transmit (V_{II}) into region II, with a reflection coefficient

$$
r = \frac{V_I^L}{V_I^R} = \frac{Z_{II} - Z_I}{Z_{II} + Z_I},
$$

and transmission coefficient

$$
t = \frac{V_{II}^R}{V_I^R} = 1 - r = \frac{2Z_I}{Z_I + Z_{II}}.
$$

A mismatch in impedances ($Z_I \neq Z_{II}$) will result in partial reflection of the input signal.

Proof

1. Assuming that there is no inbound field from the $\overset{L}{\leftarrow}$ in region II, the voltage in region II is the sum of incoming and reflected voltages from voltage continuity at the interface of the two media

   $$V_{II}^{R} = V_{I}^{R} + V_{I}^{L}, \tag{A.3.31}$$

   while the total current will be the net difference of incoming and reflected currents from charge conservation

   $$I_{II}^{R} = I_{I}^{R} - I_{I}^{L}. \tag{A.3.32}$$

2. The combination of (A.3.31), (A.3.32) results in

   $$\begin{aligned} V_{I}^{L} &= V_{II}^{R} - V_{I}^{R} = Z_{II} I_{II}^{R} - V_{I}^{R} \\ &= Z_{II}\left(I_{I}^{R} - I_{I}^{L}\right) - V_{I}^{R}, \end{aligned}$$

   and substituting in current relations from (A.3.6)

   $$V_{I}^{L}\left(1 + \frac{Z_{II}}{Z_{I}}\right) = V_{I}^{R}\left(\frac{Z_{II}}{Z_{I}} - 1\right). \tag{A.3.33}$$

3. The reflection coefficient is the ratio of the $\overset{R}{\rightarrow}$ and $\overset{L}{\leftarrow}$ modes in region I

   $$r = \frac{V_{I}^{L}}{V_{I}^{R}},$$

   which evaluated with (A.3.33) gives

   $$\begin{aligned} r = \frac{V_{I}^{L}}{V_{I}^{R}} &= \left(\frac{Z_{II}}{Z_{I}} - 1\right) / \left(1 + \frac{Z_{II}}{Z_{I}}\right) \\ &= \frac{Z_{II} - Z_{I}}{Z_{II} + Z_{I}}. \end{aligned}$$

QED ☐

A.3.4 Noise in transmission lines

Back in 1928 Nyquist's theorem [152], verified by Josephson [256], established that a resistor (R) develops a noise voltage ($V_N(t)$) across its ends, characterised by (refer to Sec. A.8.2)

$$\langle V_N(t) V_N(0) \rangle = \int_{-\infty}^{\infty} \frac{d\omega}{2\pi} \left[e^{-i\omega\tau} S_{VV}(\omega) \right],$$

with a white noise spectral density $S_{VV}(\omega) = Rk_bT/\pi$ that maintains the Boltzmann distribution of energies in the electric circuit. At higher frequencies the effect of energy quantisation leads to the Plank-like spectrum $S_{VV}(\omega) = R\hbar\omega/\pi(\exp(\hbar\omega/k_bT) - 1)$ introduce sharp cutoff at high frequencies $\hbar\omega \gg kT$ and giving white noise at low ones $\hbar\omega \ll k_bT$ [257].

But in 1951, the serious treatment by Callen and Welton [258] concluded that the noise spectrum contained another noise term arising from the zero point fluctuations of the harmonic oscillators used to model the TL (see A.3.2)

$$S_{VV}(\omega) = \frac{R}{\pi}\left(\underbrace{\frac{1}{2}\hbar\omega}_{\text{quantum}} + \underbrace{\frac{\hbar\omega}{\exp(\hbar\omega/k_bT) - 1}}_{\text{thermal}}\right), \tag{A.3.34}$$

that would rise linearly with frequency, which was experimentally confirmed [118]. This quantum noise does not depend on temperature and is dominant for the GHz frequencies in TLs.

This appendix walks through how the quantised voltage modes derived in A.3.2 have a power spectral density

$$S_{VV}(\omega) = \frac{2\hbar\omega Z}{1 - \exp[-\hbar\omega/k_bT]},$$

supporting (A.3.34) using motivation from [104, 254, 259].

Proof

1. Representing V_I^R by the $\xrightarrow{\text{R}}$ propagating modes in the TL (A.3.30)

$$V_I^R(x,t) \equiv \sum_m \left[\hat{V}_m e^{i(k_m x - \omega_m t)} + \hat{V}_m^* e^{-i(k_m x - \omega_m t)}\right], \qquad \hat{V}_m = -i\sqrt{\frac{\hbar\omega_m}{2cL}}a_m,$$

   and evaluating its correlation function

$$\left\langle V_I^R(t)V_I^R(0)\right\rangle = \frac{\hbar}{2cL}\sum_{k,k'}\sqrt{\omega_m\omega_{m'}}\Big(.\left\langle a_m a_{m'}\right\rangle e^{i((k_m+k_{m'})x-\omega_m t)} + \left\langle a_m^\dagger a_{m'}^\dagger\right\rangle e^{-i((k_m+k_{m'})x-\omega_m t)} + \left\langle a_m a_{m'}^\dagger\right\rangle e^{i((k_m-k_{m'})x-\omega_m t)} + \left\langle a_m^\dagger a_{m'}\right\rangle e^{-i((k_m-k_{m'})x-\omega_m t)}\Big). \tag{A.3.35}$$

2. The operator combination $a^\dagger a$ describes the number of photons in the TL (see Step 14), and assuming that the TL is thermalised, the expectation value will follow the boson

distribution ($n_B(\omega)$)

$$\begin{cases} \left\langle a^\dagger_m a_{m'} \right\rangle = \delta_{mm'} n_B(\omega_m), \\ \left\langle a_m a^\dagger_{m'} \right\rangle \underset{(A.3.25)}{=} \left\langle a^\dagger_{m'} a_m + 1 \right\rangle = \delta_{mm'} (n_B(\omega_m) + 1), \end{cases} \qquad n_B(\omega) = \frac{1}{e^{\hbar\omega/k_b T} - 1},$$

while operator combinations $aa, a^\dagger a^\dagger$ represent double photon creation or annihilation, and will be zero at low temperatures.

$$\lim_{T\to 0} \langle a_m a_{m'} \rangle = \lim_{T\to 0} \left\langle a^\dagger_m a^\dagger_{m'} \right\rangle = 0,$$

which simplifies (A.3.35) to

$$\left\langle V_I^R(t) V_I^R(0) \right\rangle = \frac{\hbar}{2cL} \sum_m \left[\omega_m \left(n_\mathrm{B}(\omega_m) + 1 \right) e^{-i\omega_m t} + n_\mathrm{B}(\omega_m) e^{i\omega_m t} \right].$$

3. Taking the limit $L \to \infty$ for an infinite TL turns wavevectors k from discrete values $k = m\pi/L, m \in \mathbb{Z}$ into continuous steps $dk/2\pi$[16] and hence $\frac{1}{L}\sum_m \to \frac{1}{2\pi}\int_{-\infty}^{\infty} dk$. Then a change of variables $dk \to \delta\omega/v$ arrives at

$$\left\langle V_I^R(t) V_I^R(0) \right\rangle = \int_{-\infty}^{\infty} \frac{d\omega}{2\pi} \frac{2\hbar\omega}{cv} \left[\left(n_\mathrm{B}(\omega) + 1 \right) e^{-i\omega t} + n_\mathrm{B}(\omega) e^{i\omega t} \right].$$

4. Recalling the relation between spectral density and the correlation function (A.8.2) $\langle V(t)V(0) \rangle = \int_{-\infty}^{\infty} \frac{d\omega}{2\pi} e^{-i\omega t} S_{VV}(\omega)$ one can *read* of the power spectral densities

$$\left\langle V_I^R(t) V_I^R(0) \right\rangle = \int_{-\infty}^{\infty} \frac{d\omega}{2\pi} \left[\underbrace{\frac{\hbar\omega}{2cv} \left(n_\mathrm{B}(\omega) + 1 \right)}_{S^R_{VV}(\omega_+)} e^{-i\omega t} + \underbrace{\frac{\hbar\omega}{2cv} n_\mathrm{B}(\omega)}_{S^R_{VV}(\omega_-)} e^{i\omega t} \right],$$

associated with the positive (ω_+) and negative (ω_-) frequency components depending on the sign of the exponential in reference to (A.8.2). Taking this into account

$$\begin{cases} S^R_{VV}(\omega) = S^R_{VV}(\omega_+) + S^R_{VV}(\omega_-), \\ S^R_{VV}(\omega_+) = \dfrac{\hbar\omega Z}{2} \left(n_\mathrm{B}(\omega) + 1 \right) \Theta(\omega), \\ S^R_{VV}(\omega_-) = \dfrac{\hbar\omega Z}{2} n_\mathrm{B}(\omega) \Theta(-\omega). \end{cases}$$

where Θ is the step function. At low temperatures, the $S^R_{VV}(\omega_-)$ contribution becomes insignificant and there is no noise at negative frequencies.

---

[16] The factor $1/2\pi$ accounts for the radian units that are now being used.

5. With reference to Fig. A.8, this wave mode travels from a semi-infinite TL with impedance Z_I into another semi-infinite TL with impedance Z_{II}:

   - In the case of an open end ($Z_2 = \infty$), the $\overset{R}{\rightarrow}$ propagating voltage completely reflects (refer to A.3.3), and in region I the total noise from the forward and reflected components is $S_{VV}(\omega) = S^R_{VV}(1+r) = S^R_{VV}(1+\frac{\infty+Z_I}{\infty-Z_I})^2 = 4S^R_{VV}$;
   - In the case of the qubit shorting to ground ($Z_2 = 0$), the transmission coefficient from region I into region II is $t = 2Z_I/(Z_I+0)$, connecting the noise spectral densities in the two regions $S_{VV}(\omega) = \langle |V^R_{II}|^2 \rangle = |t|^2 S^R_{VV} = 4S^R_{VV}$.

   In both cases, the voltage spectral density in the region studied reads

$$\lim_{T\to 0} S_{VV}(\omega) = 2Z\left(\hbar\omega + \frac{\hbar\omega}{\exp(\hbar\omega/k_bT)-1}\right) = \frac{2\hbar\omega Z}{1-e^{-\hbar\omega/k_bT}}. \tag{A.3.36}$$

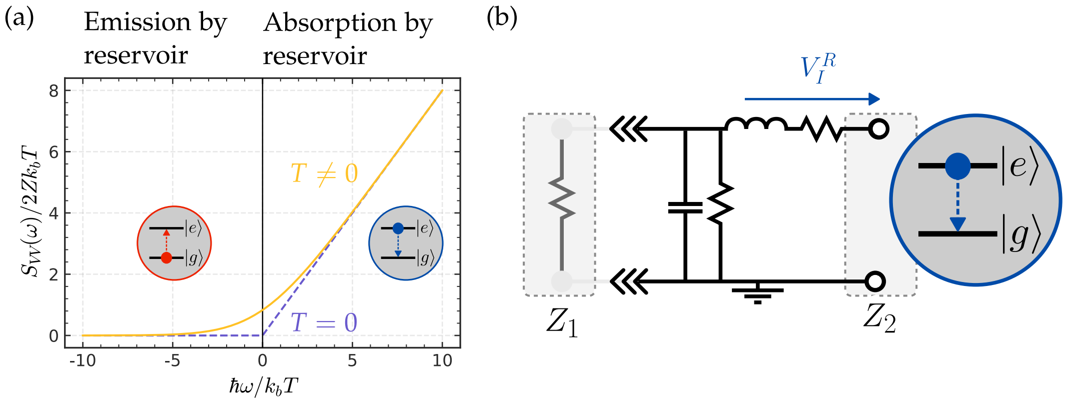

Figure A.8: **(a)** Spectral density of quantum noise in the TL at $T = 0$ (purple) and finite temperatures (yellow). Negative frequencies are associated with TL emissions, which can excite the qubit. Positive frequencies are associated with absorption by the TL. **(b)** Interface connecting two semi-infinite TL with impedances Z_1, Z_2. Voltage noise can either be considered by terminating with $Z_2 = \infty$ and looking at the voltage power in the LHS circuit under total reflection, or by setting $Z_2 = 0$ (the qubit *drawing* the voltage field upon itself) and looking at the power that is dissipated on it.

6. Some general comments can be made on (A.3.36) that put it in agreement with (A.3.34):

   - In the high temperature limit ($\hbar\omega \ll k_bT$), the expression reduces to the familiar Josephson noise $S_{VV}(\omega) = 2Zk_bT$;
   - The positive frequency part of the spectral density ($S_{VV}(\omega_+)$) is a measure of the ability of the noise to absorb energy, while the negative frequency part ($S(\omega_-)$) is a measure of its ability to emit energy. The freezing out of ($S(\omega_-)$) at low temperatures corresponds to the noise process not being able to release

energy, as energy cannot be extracted from zero point motion. The effect of this is shown in Fig. A.8 (a);

◎ In the low temperature limit ($|\hbar\omega| \gg k_b T$) it reduces to the vacuum quantum noise $S_{VV}(\omega) = 2Z_0\hbar\omega\Theta(\omega)$ - the step function indicates the ability of the noise source to only absorb energy at $T = 0$.

QED ☐

A.3.5 Emission rate into transmission lines

A number of noise processes can give rise to qubit depolarisation, such as dissipation through TLS, quasiparticle tunnelling and electron hopping (refer to Sec. 1.3.3). But the strongest effect in the strong coupling regime achieved with superconducting circuits [68] will come from the voltage noise (S_{VV} evaluated in A.3.4) of the vacuum fields in the TL.

The proof below demonstrates that the relaxation rate $|e\rangle \to |g\rangle$ caused by this quantum noise in the TL

$$\Gamma_1 = \frac{\vartheta^2}{\hbar^2} S_{VV}(\omega_q) = \frac{\vartheta^2 \omega_q Z_0}{\hbar}, \tag{A.3.37}$$

is determined by the impedance (Z_0) of the TL and coupling strength characterised by the dipole moment (ϑ).

Proof

1. The noise source giving rise to qubit transitions $|e\rangle \leftrightarrow |g\rangle$ is taken to be a dipole (A.2.7), albeit with the driving field (V_{mw}) replaced with the noise source amplitude ($V(t)$)

   $$\hat{V}_{\mathrm{noise}} = \vartheta V(t)\sigma_x,$$

   where ϑ is the coupling constant between the qubit and voltage in the TL (refer to A.2.3) and σ_x encodes the state transition. This perturbative term is added to the system's Hamiltonian

   $$H = H_{\mathrm{q}} + \hat{V}_{\mathrm{noise}}. \tag{A.3.38}$$

2. Under the assumption that the noise term $\hat{V}_{\mathrm{noise}}$ in (A.3.38) is small relative to the qubit Hamiltonian (H_{q}), first order perturbation theory is used (refer to A.7.4) to

approximate the state of the system at time t initially prepared in the excited state ($|e\rangle$)

$$\begin{aligned}|\psi(t)\rangle &= |e\rangle - \frac{i}{\hbar}\int_0^t d\tau\Big[\left(\langle e|\,\vartheta V(\tau)\sigma_x\,|e\rangle\right)|e\rangle + \Big(e^{i\omega_q\tau}\langle e|\,\vartheta V(\tau)\sigma_x\,|g\rangle\Big)|g\rangle\Big]\\ &= |e\rangle - \left(i\frac{\vartheta}{\hbar}\int_0^t d\tau e^{i\omega_q\tau}V(\tau)\right)|g\rangle\,.\end{aligned}$$

3. Therefore the probability of finding the atom collapsing to the ground state

$$|\langle g|\,|\psi(t)\rangle|^2 = \left|-\frac{i\vartheta}{\hbar}\int_0^t d\tau\Big[e^{i\omega_q\tau}\hat{V}(\tau)\Big]\right|^2 = \frac{\vartheta^2}{\hbar^2}\int_0^t\int_0^t d\tau_1\,d\tau_2\Big[e^{-i\omega_q(\tau_1-\tau_2)}V(\tau_1)V(\tau_2)\Big].$$

4. The probability of transition is found by averaging over the ensembles

$$P_{|e\rangle\to|g\rangle} = \frac{\vartheta^2}{\hbar^2}\int_0^t d\tau_1\,\underbrace{\int_0^t d\tau_2\Big[e^{i\omega_q(\tau_1-\tau_2)}\langle V(\tau_1)V(\tau_2)\rangle\Big]}_{✥},$$

and applying the Wiener-Khinchin theorem (refer to A.8.2) that connects the Fourier transform (FT) of the autocorrelation function ✥ to the spectral density of the noise source $S_{VV}(\omega_q)$

$$P_{|e\rangle\to|g\rangle} = t\frac{\vartheta^2}{\hbar^2}S_{VV}(\omega_q), \tag{A.3.39}$$

and therefore the probability of ground state occupation increases linearly with time.

5. With the probability of a transition defined in (A.3.39), the actual relaxation rate to the ground state is the time derivative

$$\Gamma_1 = \partial_t P_{|e\rangle\to|g\rangle} = \frac{\vartheta^2}{\hbar^2}S_{VV}(\omega_q), \tag{A.3.40}$$

and is determined by the spectral density of the noise coupling to the qubit.

6. A.3.4 derived that the voltage spectral density arising from zero point fluctuations in a TL with impedance Z_0 is $S_{VV}(\omega) = 2\hbar\omega Z$. Since there are two channels ($\overset{L}{\leftarrow}$ and $\overset{R}{\rightarrow}$ see Fig. 1.6) for emissions to occur into the effective impedance of the line is thus $Z = Z_0/2$ meaning that (A.3.40) can also be written as [260, 261]

$$\Gamma_1 = \frac{\vartheta^2\omega_q Z_0}{\hbar}.$$

QED □

A.3.6 Dipole source voltage scattering

The 1D wave equation for voltage in a TL with propagation speed $v = 1/\sqrt{lc}$ in presence of a dipole source located at $x = 0$

$$\partial_{xx}V(x,t) - \frac{1}{v^2}\partial_{tt}V(x,t) = V_{\text{source}}(x,t), \qquad V_{\text{source}} = l\partial_{tt}\left\langle \hat{\vartheta}(t)\right\rangle \delta(x), \tag{A.3.41}$$

has solution

$$\begin{cases} V(x,t) = V_{\text{mw}}(x,t) + V_{\text{sc}}(x,t), & \\ V_{\text{mw}}(x,t) = V_{\text{mw}}e^{ikx-i\omega t} & \text{Homogenous solution,} \\ V_{\text{sc}}(x,t) = il\dfrac{\omega^2\vartheta}{k}\left\langle \sigma_-\right\rangle e^{ik|x|-\omega t} & \text{Particular solution.} \end{cases}$$

Proof

1. The homogenous solution is found from the wave equation without the source term

$$\partial_{xx}V_{\text{mw}}(x,t) - \frac{1}{v^2}\partial_{tt}V_{\text{mw}}(x,t) = 0, \tag{A.3.42}$$

for which, using separation of variables, a factorised solution is proposed

$$V_{\text{mw}}(x,t) = X(x)T(t). \tag{A.3.43}$$

2. Substituting in (A.3.43) into (A.3.42) results in

$$\frac{\partial_{tt}T(t)}{T(t)} = v^2\frac{\partial_{xx}X(x)}{X(x)}. \tag{A.3.44}$$

3. Since the LHS in (A.3.44) is independent of x the RHS must be independent of x as well. Likewise for t, meaning the two sides have to be equal to a constant labelled $-\omega^2$

$$\begin{cases} \dfrac{\partial_{tt}T(t)}{T(t)} = -\omega^2 & \Rightarrow T(t) = T(0)e^{\pm i\omega t}, \\ v^2\dfrac{\partial_{xx}X(x)}{X(x)} = -\omega^2 & \Rightarrow X(x) = X(0)e^{i(\omega/v)t} = X(0)e^{\pm ikx}. \end{cases} \tag{A.3.45}$$

4. The full homogenous solution is a linear combination of (A.3.45)

$$V_{\text{mw}}(x,t) = \sum_k \left[\underbrace{Ae^{i(kx-\omega t)} + Be^{-i(kx-\omega t)}}_{\underset{\rightarrow}{\text{R}}} + \underbrace{Ce^{i(kx+\omega t)} + De^{-i(kx+\omega t)}}_{\underset{\leftarrow}{\text{L}}}\right], \tag{A.3.46}$$

for the different wavevectors $k = \omega/v$, and represent rightward ($\overset{\text{R}}{\rightarrow}$) and leftward ($\overset{\text{L}}{\leftarrow}$) propagating waves.

5. Matching (A.3.46) to experimental conditions where the driving field of amplitude V_{mw} from the laboratory equipment is propagating in the $\overset{\text{R}}{\rightarrow}$ direction:

    - $C = D = 0$ due to absence of leftward propagating waves;
    - $A = V_{\text{mw}}$ to match the amplitude of the drive;
    - $B = 0$ for simplicity;
    - Summation only needs to be done for a single k - the wavevector associated with the drive frequency,

    which results in a travelling wave solution

$$V_{\text{mw}}(x,t) = V_{\text{mw}} e^{i(kx-\omega t)}. \tag{A.3.47}$$

6. The particular solution is labelled as a scattering voltage $V_{\text{sc}}(x,t)$ as appears only in the presence of the dipole-like qubit source. Integrating (A.3.41) wrt dx, writing $V_{\text{sc}}(x,t) = V_{\text{sc}}(t)e^{ik|x|}$ to represent symmetric scattering about $x = 0$ (see Fig. 1.6 and (A.3.49)), and using (1.2.3) for the dipole operator ($\hat{\vartheta}(t) = \vartheta e^{-i\omega t}\sigma_x$)

$$\begin{aligned} \int dx \left[\partial_{xx} V_{\text{sc}}(x,t) - \frac{1}{v^2}\partial_{tt} V_{\text{sc}}(x,t)\right] &= \int dx \left[l\partial_{tt}\left\langle\hat{\vartheta}\right\rangle \delta(x)\right] \\ \partial_x V_{\text{sc}}(x,t) - \frac{1}{v^2}\partial_{tt} V_{\text{sc}}(t) \underbrace{\int dx \left[e^{ikx}\right]}_{2\pi\delta(k)\text{ see (A.8.2)}} &= -l\omega^2\vartheta e^{-i\omega t}\left\langle\sigma_x\right\rangle. \end{aligned} \tag{A.3.48}$$

7. The following can be said about (A.3.48):

    - In general $k \neq 0$, as it would correspond to a zero frequency ($\omega = 0$), so the term with $\delta(k)$ will be zero[17];
    - Since the scattered voltage comes about from the relaxation of the qubit (and not the other way around) relaxation operator σ_- is selected from σ_x on the RHS;
    - The scattered voltage will be a travelling wave of the form (A.3.47) except it propagates symmetrically from $x = 0$ in both directions

$$V_{\text{sc}}(x,t) = V_{\text{sc}}(x=0,t)e^{i(k|x|-\omega t)}, \tag{A.3.49}$$

---

[17] More rigorously, Cauchy's principal value of PV $\left[\int dx e^{iax}\right] = 0$

where the scattering amplitude at the dipole position $V_{\mathrm{sc}}(x=0,t)$ is defined.

Collectively this results in

$$ikV_{\mathrm{sc}}(x=0,t)e^{i(k|x|-\omega t)} = -l\omega^2\vartheta e^{-i\omega t}\langle\sigma_-\rangle\,. \tag{A.3.50}$$

8. Evaluating (A.3.50) at $x=0$ to find the initial scattering amplitude $V_{\mathrm{sc}}(x=0,t)$

$$V_{\mathrm{sc}}(x=0,t) = il\frac{\omega^2\vartheta}{k}\langle\sigma_-\rangle\,,$$

which has no time dependence.

9. The particular solution derived from (A.3.49) thus reads

$$V_{\mathrm{sc}}(x,t) = \left(il\frac{\omega^2\vartheta}{k}\langle\sigma_-\rangle\right)e^{i(kx-\omega t)}, \tag{A.3.51}$$

in which, unlike the homogenous solution (A.3.47), the amplitude of the wave is not free and is strictly determined by the:

- Frequency of the driving field through ω, k;
- Properties of the TL through l;
- Properties of the qubit through ϑ, $\langle\sigma_-\rangle$.

10. The full solution is a linear combination of homogenous (A.3.47) and particular (A.3.51) solutions:

$$\begin{cases} V(x,t) = V_{\mathrm{mw}}(x,t) + V_{\mathrm{sc}}(x,t), & \\ V_{\mathrm{mw}}(x,t) = V_{\mathrm{mw}}e^{ikx-i\omega t} & \text{Homogenous solution,} \\ V_{\mathrm{sc}}(x,t) = il\dfrac{\omega^2\vartheta}{k}\langle\sigma_-\rangle e^{ik|x|-\omega t} & \text{Particular solution.} \end{cases}$$

QED ☐

A.3.7 Dipole source power spectrum

The emission spectrum of dipole-scattered voltage (1.2.9) into a transmission like decomposes into coherent and incoherent components

$$S(\omega) = S_{\mathrm{coh}}(\omega) + S_{\mathrm{inc}}(\omega)$$

where the coherent component occurs exactly at the driving field frequency (ω_{01}) and incoherent is spread over a frequency range (Γ_1), using the procedure described in [95].

Furthermore the incoherent spectrum ($S_{\text{inc}}(\omega)$) is shown to have the shape of 3 superposed Lorentzians spaced by the strength of the drive (Ω) in what is known as the Mollow triplet.

Proof

1. Starting with the power spectral density expression (A.8.7) for the scattered voltage (1.2.9)
$$\begin{aligned} S(\omega) &= \frac{1}{2Z_0}\int_{-\infty}^{\infty} d\tau \left[\langle V_{\text{sc}}(\tau)V_{\text{sc}}^*(0)\rangle\, e^{-i\omega\tau}\right] \\ &= \frac{\hbar\omega\Gamma_1}{2}\int_{-\infty}^{\infty} d\tau \left[\langle \sigma_-(\tau)\,\sigma_+(0)\rangle\, e^{-i\omega\tau}\right], \end{aligned} \tag{A.3.52}$$
separate out $\langle \sigma_-(\tau)\,\sigma_+(0)\rangle$ into a steady state component that the driven system will eventually assume (see for example the steady solution in Fig. A.4) and fluctuations away from this value
$$\begin{cases} \langle \sigma_-\rangle_{ss} = \lim\limits_{\tau\to\infty} \langle \sigma_-(\tau)\rangle\,, \\ \Delta\sigma_-(\tau) = \sigma_-(\tau) - \langle \sigma_-\rangle_{ss}\,. \end{cases} \tag{A.3.53}$$
Substituting (A.3.53) into (A.3.52) and cancelling out the cross-terms such as $\langle \langle \sigma_-\rangle_{ss}\,\Delta\sigma_+(0)\rangle$[18] one separates the emitted power into two constituents
$$\begin{cases} S(\omega) = S_{\text{inc}}(\omega) + S_{\text{coh}}(\omega), \\ S_{\text{inc}}(\omega) = \dfrac{\hbar\omega\Gamma_1}{2}\displaystyle\int_{-\infty}^{\infty} d\tau \left[\langle \Delta\sigma_-(\tau)\Delta\sigma_+(0)\rangle_{ss}\, e^{-i\omega\tau}\right], \\ S_{\text{coh}}(\omega) = \dfrac{\hbar\omega\Gamma_1}{2}\displaystyle\int_{-\infty}^{\infty} d\tau \left[\langle \sigma_-\rangle_{ss}\,\langle \sigma_+\rangle_{ss}\, e^{-i\omega\tau}\right]. \end{cases} \tag{A.3.54}$$

2. Solutions of the Bloch equations (A.2.5) for an atom in initial state $\vec{\sigma}_0 = \{0,0,1\}$
$$\begin{aligned} \langle \sigma_\mp\rangle_{ss} &= \pm\frac{ie^{\mp i\varphi}}{2}\frac{\Gamma_1\Gamma_2\Omega}{\Gamma_1\Gamma_2^2+\Gamma_2\Omega^2} \\ \langle \sigma_z\rangle_{ss} &= -\frac{\Gamma_1\Gamma_2}{\Gamma_1\Gamma_2+\Omega^2}. \end{aligned} \tag{A.3.55}$$

---

[18] This is a product of a constant and a time varying quantity, so there is no correlation

result in a coherent part of the spectrum (A.3.54)

$$\begin{aligned} S_{\text{coh}}(\omega) &= \hbar\omega\Gamma_1 \int_{-\infty}^{\infty} d\tau \left[\langle \sigma_- \rangle_{ss} \langle \sigma_+ \rangle_{ss} e^{-i\omega\tau} \right] \\ &= \hbar\omega\Gamma_1 \frac{1}{4} \left(\frac{\Gamma_1\Gamma_2\Omega}{\Gamma_1\Gamma_2^2 + \Gamma_2\Omega^2} \right)^2 2\pi\delta(\omega - \omega_{01}), \end{aligned}$$

where an artificial shift $\delta(\omega) \to \delta(\omega - \omega_{01})$ is made to account for the fact that solutions (A.3.55) occurs at $\omega = \omega_{01}$.

3. The remaining part of the spectrum involving $\langle \Delta\sigma_-(\tau)\Delta\sigma_+(\tau) \rangle$ is solved using the quantum regression theorem [262], which states that Bloch equations that describe the motion of expectation values $\langle \sigma_i \rangle$ (one-time averages)

$$\partial_t \vec{\sigma}(t) = \mathbf{B}\vec{\sigma}(t)$$

are also the equations of motion for correlation functions (two-time averages) such as $s = \Delta\sigma_-(\tau)\Delta\sigma_+(t)$

$$\partial_\tau \vec{s}(\tau) = \mathbf{B}\vec{s}(\tau),$$

with the matrix **B** defined in (A.2.11).

4. Simplification for weak pumping leads to expression of spontaneous emission:

$$S_{\text{inc}}(\omega) \approx \frac{\rho_{22}\hbar\omega_{12}\Gamma_1}{2\pi} \frac{\Gamma_2}{\Gamma_2^2 + \delta\omega^2}.$$

QED □

A.3.7.1 Incoherent emission spectrum

The shape of the incoherent emission spectrum $S(\omega)$ is found by evaluating the Fourier transform for each component of $S_{\text{inc}}(\omega)$ in (A.3.54)

$$\begin{aligned} S_{\text{inc}}(\omega) &= \hbar\omega\Gamma_1 \int_{-\infty}^{\infty} d\tau e^{i(\omega-\omega_q)\tau} \langle \Delta\sigma_-(\tau)\Delta\sigma_+(0) \rangle_{ss} \\ &= \hbar\omega\Gamma_1 \int_{-\infty}^{\infty} d\tau e^{i(\omega-\omega_q)\tau} \\ &\qquad (A)\frac{1}{4}\frac{Y^2}{1+Y^2} e^{-\Gamma_1\tau/2} \\ &\qquad (B) - \frac{1}{8}\frac{Y^2}{(1+Y^2)^2}\left[1 - Y^2 + (1-5Y^2)\frac{\Gamma_1/4}{\delta}\right] e^{-(\frac{3\Gamma_1}{4}-\delta)\tau} \\ &\qquad (C) - \frac{1}{8}\frac{Y^2}{(1+Y^2)^2}\left[1 - Y^2 + (1-5Y^2)\frac{\Gamma_1/4}{\delta}\right] e^{-(\frac{3\Gamma_1}{4}+\delta)\tau}, \end{aligned}$$

using the result of A.8.4:

- ◎ (A) Identify $\omega - \omega_q = \delta\omega$ and $\Gamma = \Gamma/2$ to get

$$S(\omega) = \hbar\omega\Gamma_1 \frac{1}{4}\frac{\Upsilon^2}{1+\Upsilon^2}\frac{\Gamma/2}{(\Gamma/2)^2 + \delta\omega^2};$$

- ◎ (B-C) Here consider the case of $\delta^2 > 0$ (weak drive), in which case identify $\omega - \omega_q = \delta\omega$ and $\tilde{\Gamma} = \frac{3\Gamma_1}{4} \mp |\delta|$

$$S(\omega) = \hbar\omega\Gamma_1 \frac{1}{8}\frac{\Upsilon^2}{(1+\Upsilon^2)^2}\left[1 - \Upsilon^2 \pm (1-5\Upsilon^2)\frac{\Gamma_1/4}{|\delta|}\right]\frac{\tilde{\Gamma}/2}{(\tilde{\Gamma}/2)^2 + \delta\omega^2};$$

- ◎ (B-C) Here the case of $\delta^2 < 0$ (strong drive) is considered, in which case identify $\omega - (\omega_q \pm |\Omega|) = \delta\omega$ and $\tilde{\Gamma} = \frac{3\Gamma_1}{4}$ and ignore the imaginary component.

$$S(\omega) = \hbar\omega\Gamma_1 \frac{1}{8}\frac{\Upsilon^2}{(1+\Upsilon^2)^2}\left[1 - \Upsilon^2\right]\frac{\tilde{\Gamma}/2}{(\tilde{\Gamma}/2)^2 + (\delta\omega \pm \Omega)^2}.$$

A.4 Resonator

The model for the resonator can be adapted directly from the TL one in A.3, with the difference that while the transmission line was considered lossless and dissipationless, for a resonator of length (L) the conductance ($G = \sigma L$) must take on a finite value - if it were not the case, then the field reflecting off the capacitors terminating the resonator would build up indefinitely under a drive. As will be seen, conductance defines losses in the resonator and hence determines the resonator linewidth $\Delta\omega \sim G/C_r$.

A.4.1 Classical resonator equations

The m-th mode of a classical resonator of length (L) has a voltage field

$$V_m(x,t) = \begin{bmatrix} V_R \cos{(k_m x)} e^{-i\omega t}, & m \text{ even}, \\ V_R \sin{(k_m x)} e^{-i\omega t}, & m \text{ odd}. \end{bmatrix} \tag{A.4.1}$$

with discrete wavevectors and frequencies

$$k_m = \frac{m\pi}{L}, \qquad \omega_m = v k_m, \qquad v = \frac{1}{\sqrt{lc}},$$

and impedance

$$Z_r = Z_1 + iZ_2, \quad Z_1 = \frac{\omega k_m l}{\alpha^2 + k_m^2}, \quad Z_2 = \frac{\omega l \alpha}{\alpha^2 + k^2}$$

$$\lim_{\sigma \to 0} Z_r = l\frac{\omega}{k_m} = lv = \sqrt{\frac{l}{c}} \equiv \sqrt{\frac{L_r}{C_r}},$$

where $L_r = l \times L$ and $C_r = c \times L$ are the resonator's total inductance and capacitance and σ its conductance per unit length.

Proof

1. The current term in the telegrapher equations (A.3.2) is modified to take into account loss through short circuits giving finite conductance (σ) between the central waveguide and ground plane (see Fig. A.7)

$$\begin{cases} \partial_x V = -l\partial_t I, \\ \partial_x I = -c\partial_t V - \sigma V. \end{cases} \tag{A.4.2}$$

which results in a source term being added to the wave equation (A.3.3)

$$\partial_{xx}V(x,t) - \frac{1}{v^2}\partial_{tt}V(x,t) = \frac{\sigma}{c}\frac{1}{v^2}\partial_t V(x,t). \tag{A.4.3}$$

2. Using trial solutions similar to the plane waves of the TL (A.3.1)

$$\begin{cases} V(x,t) = V(x)e^{ikx-i\omega t}, \\ I(x,t) = I(x)e^{ikx-i\omega t}, \end{cases} \tag{A.4.4}$$

albeit with a spatially varying amplitude to account for dissipation, the wave equation (A.4.3) reads

$$\begin{aligned} & e^{-i\omega t}\left(\partial_{xx}V(x) - \frac{\omega^2}{v^2}V(x) - \frac{1}{v^2}\frac{\sigma}{c}i\omega V(x)\right) = 0 \\ \Rightarrow \qquad & \partial_{xx}V(x) - \gamma^2 V(x) = 0, \qquad \gamma = \sqrt{i\omega l(\sigma + i\omega c)} = \alpha + ik, \end{aligned} \tag{A.4.5}$$

which has solutions

$$V(x) = V_R e^{-\gamma x} + V_L e^{\gamma x}. \tag{A.4.6}$$

3. In the case of moderate losses $\sigma \ll \omega c$, the γ factor defined in (A.4.5) can be approximated

$$\begin{aligned} \gamma &= \sqrt{i\omega l\omega c\left(i + \frac{\sigma}{\omega c}\right)} = i\frac{\omega}{v}\sqrt{1 - i\frac{\sigma}{\omega c}} \\ &\approx i\frac{\omega}{v}\left(1 - i\frac{\sigma}{2\omega c}\right) \\ &= a + ik, \quad \alpha \approx \frac{\sigma}{2}\sqrt{\frac{l}{c}} =, \quad k = \frac{\omega}{v}. \end{aligned} \tag{A.4.7}$$

The exact solution done in `Mathematica`

```
In[2]:=    Simplify[ComplexExpand[Re[Sqrt[I ωl(σ+I ω c)]]]]
           Simplify[ComplexExpand[Im[Sqrt[I ωl(σ+I ω c)]]]]
```

Out[2]= $(\mathtt{l}^2\ \omega^2(\sigma^2\mathtt{+c}^2\ \omega^2))^{1/4}\mathtt{Cos}[\frac{1}{2}\ \mathtt{Arg[i\ l}\ \omega\ (\sigma\mathtt{+i\ c}\ \omega)]]$

Out[3]= $(\mathtt{l}^2\ \omega^2(\sigma^2\mathtt{+c}^2\ \omega^2))^{1/4}\mathtt{Sin}[\frac{1}{2}\ \mathtt{Arg[i\ l}\ \omega\ (\sigma\mathtt{+i\ c}\ \omega)]]$

identifies the sign of the real and imaginary components

$$\begin{cases} \alpha = \left(l^2\omega^2(\sigma^2 + c^2\omega^2)\right)^{1/4}\cos\left(\frac{1}{2}\phi\right), & \alpha < 0 \\ k = \left(l^2\omega^2(\sigma^2 + c^2\omega^2)\right)^{1/4}\sin\left(\frac{1}{2}\phi\right), & k > 0 \end{cases} \tag{A.4.8}$$

where $\phi = \arg(-cl\omega^2 + i\sigma l\omega)$ is the argument of a point necessarily located in the 2nd quadrant of the complex plane[19] i.e. $\phi \in [\pi/2, \pi]$, justifying the inequalities on the right side of (A.4.8).

4. Currents are defined through the combination of

$$\begin{cases} \text{(A.4.2)} \quad \partial_x V(x,t) & = -l\partial_t I(x,t) \\ \text{(A.4.4)} \quad I(x,t) & = I(x)e^{ikx-i\omega t} \end{cases} \Rightarrow I(x) = \frac{1}{-i\omega l}\partial_x V(x),$$

which applied to (A.4.6)

$$I(x) = \frac{V_R}{i\omega l/\gamma}e^{-\gamma x} - \frac{V_L}{i\omega l/\gamma}e^{\gamma x}, \tag{A.4.9}$$

implying a resonator impedance

$$Z_r = \frac{i\omega l}{\gamma} = Z_1 + iZ_2, \quad Z_1 = \frac{\omega l k}{\alpha^2 + k^2}, \quad Z_2 = \frac{\omega l \alpha}{\alpha^2 + k^2}.$$

5. Applying BCs of no current flow at the ends of the resonator ($I(-L/2) = I(L/2) = 0$) to solution (A.4.9) in the approximating case of $\sigma = 0$ for which $\gamma = ik$

$$\begin{cases} I(-L/2) = \frac{V_R}{Z}e^{ikL/2} - \frac{V_L}{Z}e^{-ikL/2} = 0 \\ I(L/2) = \frac{V_R}{Z}e^{-ikL/2} - \frac{V_L}{Z}e^{ikL/2} = 0 \end{cases} \Rightarrow \begin{cases} V_R e^{ikL} = V_L \\ V_R e^{-ikL} = V_L \end{cases} \Rightarrow \begin{cases} k_m = \frac{m\pi}{L}, m \in \mathbb{Z}, \\ V_R = -V_L, \quad m_{\text{odd}}, \\ V_R = V_L, \quad m_{\text{even}}, \end{cases}$$

results in the same mode quantisation as in (A.3.2), with current

$$I_m(x) = \frac{V_R}{Z}(e^{-ik_m x} - (-1)^m e^{ik_m x}),$$

and voltage

$$V_m(x) = V_R\left(e^{-ik_m x} + (-1)^m e^{ik_m x}\right) = \begin{bmatrix} V_R \cos(k_m x), & m \text{ even}, \\ V_R \sin(k_m x), & m \text{ odd}. \end{bmatrix}$$

6. The full voltage in the resonator (A.4.4) is thus one of the standing wave modes indexed by $k_m = m\pi/L, m \in \mathbb{Z}$

$$V_m(x,t) = \begin{bmatrix} V_R \cos(k_m x)e^{-i\omega t}, & m \text{ even}, \\ V_R \sin(k_m x)e^{-i\omega t}, & m \text{ odd}. \end{bmatrix}$$

QED □

---

[19] Because all quantities are real and greater than 0 so Re $[\phi] \leq 0$ and Im $[\phi] \geq 0$.

A.4.2 Quality factor of resonator

A resonator's m-th mode quality factor

$$Q_m = \frac{\omega_m}{\kappa_m},$$

is the ratio of its resonance frequency ($\omega_m = 2\pi m f_r$) and linewidth ($\Delta\omega \sim \kappa_m$) characterised by the decay rate out of the resonator. The decay rate in turn is determined by the coupling capacitors on the ends of the $\lambda/2$ resonator

$$\kappa_m \approx \frac{4(\omega_m Z_r C_{\text{r-t}})^2 \omega_m}{\pi m}.$$

A.4.1 studied the ideal resonator case - no loss and strict BCs, which is suitable for approximating the resonator voltage (A.4.1), but will lack the detail that gives the resonator a finite linewidth. The finite linewidth will be a result of resonator voltage *leaking* out into the external circuit, through the two coupling capacitors ($C_{\text{r-t}}$) at $x = \pm L/2$ linking the $\lambda/2$ resonator to the TL (see Fig. 3.11).

Proof

1. The TL-resonator system is split into 3 regions

$$\begin{cases} \text{Region I} & x < -L/2, & V_1 = V_I^R + V_I^L, \\ \text{Region II} & -L/2 < x < L/2, & V_2 = V_{II}^R + V_{II}^L, \\ \text{Region III} & L/2 < x, & V_3 = V_{III}^R, \end{cases} \tag{A.4.10}$$

   and an input field (V_I^R) is defined as propagating in the $\overset{\text{R}}{\to}$ direction in region I. It will be assumed that the system is not driven in the $\overset{\text{L}}{\leftarrow}$ direction in region III. The goal is to find the ratio of the output field (V_{III}^R) to this input field,

$$t = \frac{V_{III}^R}{V_I^R},$$

   which will define transmission through the $\lambda/2$ resonator.

2. The 3 regions will have BCs to ensure charge conservation

$$\begin{cases} I_1(-L/2) = I_2(-L/2), \\ I_2(L/2) = I_3(L/2), \end{cases} \tag{A.4.11}$$

and voltage continuity

$$\begin{cases} V_1(-L/2) = V_2(-L/2) + \underbrace{I_2(-L/2)\dfrac{1}{i\omega C_{\text{r-t}}}}_{✥}, \\ V_2(L/2) = V_3(L/2) + \underbrace{I_3(L/2)\dfrac{1}{i\omega C_{\text{r-t}}}}_{✥}, \end{cases} \tag{A.4.12}$$

where ✥ is the voltage across capacitor $C_{\text{r-t}}$ with impedance $1/i\omega C_{\text{r-t}}$ that drives the corresponding displacement current across the gap.

3. TLs in region I and III are assumed to be lossless and have the same impedance as the resonator $Z_r = \sqrt{l/c}$. The voltage generated in region III will drive a current $I_3(L/2) = V_3(L/2)/Z_r$, which is used to rearrange the last expression in (A.4.12)

$$\begin{aligned} &i\omega C_{\text{r-t}} Z_r V_2(L/2) = i\omega C_{\text{r-t}} Z_r V_3(L/2) + V_3(L/2) \\ &\qquad\qquad \Rightarrow V_3(L/2) = V_2(L/2)\frac{i\theta}{1+i\theta}, \qquad \theta = \omega C_{\text{r-t}} Z_r. \end{aligned} \tag{A.4.13}$$

(A.4.13) relates the field in the resonator to the voltage in the output line.

4. The system of BCs (A.4.11), (A.4.12), (A.4.13) for the voltages in (A.4.10) is applied to the solution from (A.4.6) and solved with `Mathematica`

```
In[-28]:=   Voltage = VR*Exp[-γ(x-x0)] +    VL*Exp[γ(x-x0)];

            Current = VR/Z * Exp[-γ(x-x0)] -  VL/Z* Exp[γ(x-x0)];

            V₁=Voltage/.{VR→V1R,VL→V1L,x0 → -L/2}
            I₁=Current/.{VR→V1R,VL→V1L,x0 → -L/2}
            V₂=Voltage/.{VR→V2R,VL→V2L,x0 → 0}
            I₂=Current/.{VR→V2R,VL→V2L,x0 → 0}
            V₃=Voltage/.{VR→V3R,VL→0,x0→L/2}
            I₃=Current/.{VR→V3R,VL→0,x0→L/2}
```

Out[-26]= $e^{(\frac{L}{2}+x)\,\gamma}\ V1L+e^{-(\frac{L}{2}+x)\,\gamma}\ V1R$

Out[-25]= $-\dfrac{e^{(\frac{L}{2}+x)\,\gamma}\ V1L}{Z}+\dfrac{e^{-(\frac{L}{2}+x)\,\gamma}\ V1R}{Z}$

Out[-24]= $e^{x\,\gamma}\ V2L+e^{-x\,\gamma}\ V2R$

Out[-23]= $-\dfrac{e^{x\,\gamma}\ V2L}{Z}+\dfrac{e^{-x\,\gamma}\ V2R}{Z}$

Out[-22]= $e^{-(-\frac{L}{2}+x)\,\gamma}\ V3R$

Out[-21]= $\dfrac{e^{-(-\frac{L}{2}+x)\,\gamma}\ V3R}{Z}$

In[-13]:=

$$\texttt{(}V_3\texttt{/.\{x}\to\texttt{L/2\})==}V_2\,\frac{\texttt{I}\quad\theta}{\texttt{1+I}\ \theta}\texttt{/.\{x}\to\texttt{L/2\}}$$

Out[-13]=

$$\texttt{V3R==}\frac{\texttt{i (}e^{\frac{L\gamma}{2}}\ \texttt{V2L+}e^{-\frac{L\gamma}{2}}\ \texttt{V2R)}\ \theta}{\texttt{1+i}\ \theta}$$

In[-19]:=

```
Simplify[Solve[{
  (*BC for current at x=-L/2 *)
  (I₁/.x→-L/2)==(I₂/.x→-L/2),
  (*BC for current at x=L/2*)
  (I₂/.x→ L/2) == (I₃/.x→L/2),
  (*BC for voltage at x=-L/2*)
```

$$\texttt{(}V_1\texttt{/.x}\to\texttt{-L/2)==}\quad\texttt{(}V_2\ \texttt{+}\ \frac{I_2 Z}{\texttt{I}\ \theta}\texttt{/.x}\to\texttt{-L/2)}$$

```
  },
{V2R,V2L,V1L}] ]
```

Out[-19]=

$$\texttt{\{\{V2R}\to\frac{e^{\frac{L\gamma}{2}}\ \texttt{(i V3R+2}\ e^{L\gamma}\ \texttt{V1R}\ \theta\texttt{)}}{\texttt{i+}e^{2L\gamma}\ \texttt{(-i+2}\ \theta\texttt{)}}\texttt{,V2L}\to\frac{e^{\frac{L\gamma}{2}}\ \texttt{(2 V1R}\ \theta\texttt{-}e^{L\gamma}\ \texttt{V3R (-i+2}\ \theta\texttt{))}}{\texttt{i+}e^{2L\gamma}\ \texttt{(-i+2}\ \theta\texttt{)}}\texttt{,V1L}\to\frac{\texttt{V1R (-1+}e^{2L\gamma}\texttt{+2 i}\ \theta\texttt{)-2 i}\ e^{L\gamma}\ \texttt{V3R}\ \theta}{\texttt{-1+}e^{2L\gamma}\ \texttt{(1+2 i}\ \theta\texttt{)}}\texttt{\}\}}$$

In[1]:=

$$\begin{aligned}&\texttt{Solve[\{}\\&\quad\texttt{V3R==}\frac{\texttt{i (}e^{\frac{L\gamma}{2}}\ \texttt{V2L+}e^{-\frac{L\gamma}{2}}\ \texttt{V2R)}\ \theta}{\texttt{1+i}\ \theta}\texttt{/.\{}\\&\qquad\texttt{V2R}\to\frac{e^{\frac{L\gamma}{2}}\ \texttt{(i V3R+2}\ e^{L\gamma}\ \texttt{V1R}\ \theta\texttt{)}}{\texttt{i+}e^{2L\gamma}\ \texttt{(-i+2}\ \theta\texttt{)}}\texttt{,}\\&\qquad\texttt{V2L}\to\frac{e^{\frac{L\gamma}{2}}\ \texttt{(2 V1R}\ \theta\texttt{-}e^{L\gamma}\ \texttt{V3R (-i+2}\ \theta\texttt{))}}{\texttt{i+}e^{2L\gamma}\ \texttt{(-i+2}\ \theta\texttt{)}}\\&\quad\texttt{\} \},}\\&\quad\texttt{\{V3R\}}\\&\texttt{]}\end{aligned}$$

Out[1]=

$$\texttt{\{\{V3R}\to\frac{\texttt{4}\ e^{L\gamma}\ \texttt{V1R}\ \theta^2}{\texttt{1-}e^{2L\gamma}\texttt{-4 i}\ e^{2L\gamma}\ \theta\texttt{+4}\ e^{2L\gamma}\ \theta^2}\texttt{\}\}}$$

5. Taking the ratio using the `Mathematica` output from the previous step determines the transmission coefficient through the resonator

$$t = \frac{V^R_{III}}{V^R_I} = \frac{4\theta^2 e^{-\gamma L}}{4\theta^2 - i4\theta - 1 + e^{-2\gamma L}}. \tag{A.4.14}$$

6. (A.4.14) can be expressed in compact form under the condition that:

   - ($\sigma \ll 1 \Leftrightarrow \alpha \ll ik$): There is low intrinsic losses in the resonator (see (A.4.7));
   - ($\theta \ll 1$): There is weak coupling to the TL (see (A.4.23)).

   In that case it is instructive to expand the wavevector around the m-th resonator mode (see A.4.4 for derivation of k'_m)

$$k \approx k'_m + \delta k = k'_m(1 + \frac{\delta\omega}{\omega_m}) = (\frac{\pi m}{L} - \frac{2\theta_m}{L})(1 + \frac{\delta\omega}{\omega_m})$$

where $\delta k = \delta\omega k/\omega_m$ was used. Expanding the complex part of the exponential in the denominator of (A.4.14)

$$-i2kL \approx i2\left(\frac{\pi m}{L} - \frac{2\theta_m}{L}\right)\left(1+\frac{\delta\omega}{\omega_m}\right)L = -i2\left(\pi m + \pi m\frac{\delta\omega}{\omega_m} - 2\theta_m - \underbrace{2\theta_m\frac{\delta\omega}{\omega_m}}_{\text{✥}\approx 0}\right)$$
$$\approx -i2\pi m - i2\pi m\frac{\delta\omega}{\omega_m} + i4\theta_m,$$

where ✥ was dropped since it is the product of two small values. The full complex exponential can then be written out and expanded to first order

$$\begin{aligned}\exp\left[-2\gamma L\right] &= \exp\left[-i2kL\right]\exp\left[-2\alpha L\right]\\ &\approx \underbrace{\exp\left[-i2\pi m\right]}_{=1}\exp\left[-i2\pi m\frac{\delta\omega}{\omega_m} + i4\theta_m\right]\exp\left[-2\alpha L\right]\\ &\approx \left(1 - i2\pi m\frac{\delta\omega}{\omega_m} + i4\theta_m\right)\left(1-2\alpha L\right)\\ &= 1 - i2\pi m\frac{\delta\omega}{\omega_m} + i4\theta_m - 2\alpha L - \underbrace{i8\alpha\theta_m L + i4\pi m\alpha\frac{\delta\omega}{\omega_m}L}_{\text{✥}\approx 0},\end{aligned}$$

where once again terms ✥ that are a product of two small parameters ($\alpha\theta$ and $\delta\omega\alpha$) are dropped. The factor $e^{-\gamma L}$ in the numerator will similarly evaluate to $1 - i\pi m\delta\omega/\omega_m + i2\theta_m - \alpha L \approx 1$. (A.4.8) has shown that $\alpha < 0$ and thus $-2\alpha L = 2|\alpha|L$, giving a complex transmission around the m-th mode

$$\begin{aligned}t_m &= \frac{4\theta_m^2}{4\theta_m^2 - i4\theta_m - 1 + \left(1 - i2\pi m\frac{\delta\omega}{\omega_m} + i4\theta_m + 2|\alpha|L\right)}\\ &= \frac{4\theta_m^2}{4\theta_m^2 + 2|\alpha|L - i2\pi m\frac{\delta\omega}{\omega_m}}\\ &= \frac{\kappa_{\text{ext}}/\kappa_{\text{total}}}{1 - i\frac{2\delta\omega}{\kappa_{\text{total}}}},\end{aligned} \tag{A.4.15}$$

that depends on the photon decay $\kappa_{\text{total}} = \kappa_{\text{ext}} + \kappa_{\text{int}}$ through external loss to the TL through the coupling capacitors

$$\kappa_{\text{ext}} = \frac{4\theta_m^2\omega_m}{\pi},$$

and the internal photon decay rate

$$\kappa_{\text{int}} = \frac{2|\alpha|L\omega_m}{\pi}.$$

7. In case of a lossless resonator with $\sigma = 0 \Leftrightarrow \alpha = 0$, (A.4.15) simplifies to give an absolute transmission amplitude

$$|t_m| = \left|\frac{V^R_{III}}{V^R_I}\right| = \frac{1}{\sqrt{1+\left(\frac{2\delta\omega}{\Delta\omega}\right)^2}}, \qquad \Delta\omega = \kappa_{ext} = \frac{4\theta_m^2\omega_m}{\pi}, \tag{A.4.16}$$

which can be recognised to be Lorentzian like (see A.8.3) with a width $\Delta\omega$. (A.4.16) is plotted for a range of coupling capacitor $C_{\text{r-t}}$ values in Fig. A.9.

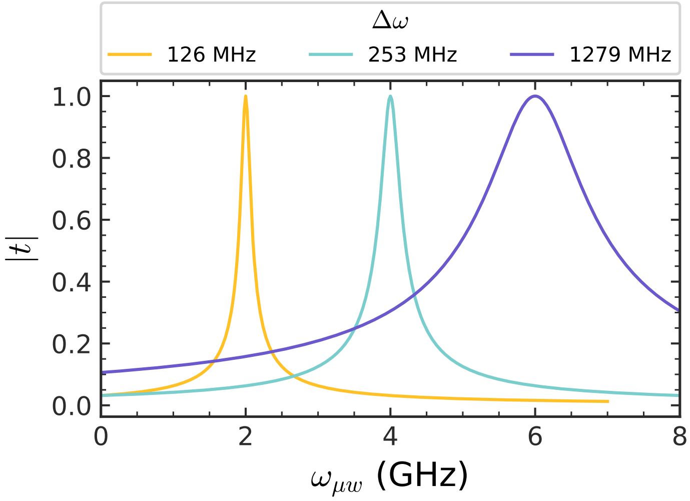

Figure A.9: Resonator transmission as a function of the detuning from resonance. Common parameters $f_1 = 2, 4, 8\,\text{GHz}, Z_r = 5000\,\Omega$ and **(Yellow)** $C_r = 100\,\text{fF}, C_{\text{r-t}} = 2\,\text{fF}$; **(Sky)** $C_r = 200\,\text{fF}, C_{\text{r-t}} = 2\,\text{fF}$; **(Yellow)** $C_r = 200\,\text{fF}, C_{\text{r-t}} = 3\,\text{fF}$ custom parameters, similar to the values of real resonators where used. Notice how stronger output coupling can drastically increase the linewidth of the resonator.

8. The quality factor of the m-th mode of the resonator is defined by the ratio

$$Q_m = \frac{\omega_m}{\Delta\omega} = \frac{\omega_m}{\kappa_m},$$

and is determined by the photon decay rate out of the resonator and into the TL which can be expressed as

$$\kappa_m = \frac{4\theta_m^2\omega_m}{\pi} = \frac{4(\omega_m Z_r C_{\text{r-t}})^2\omega_m}{\pi m} = 4Z_r\omega_m^2 C_{\text{r-t}}^2 \frac{\sqrt{l/c}k_m v}{\pi m} \sim \frac{4Z_r\omega_m^2 C_{\text{r-t}}^2}{mC_r},$$

which is consistent with the definitions given in [199, 237, 263].

QED □

A.4.3 Quantisation of fields in the resonator

The quantised voltage field of the m-th mode of a $\lambda/2$ resonator spanning $-L/2 \leq x \leq L/2$ is given by

$$\hat{V}_m(x,t) = V_m(x)(ia(t) - ia(t)^\dagger) = V_m(x)(iae^{-i\omega t} - ia^\dagger e^{i\omega t}), \tag{A.4.17}$$

with amplitude

$$V_m(x) = \begin{bmatrix} V_{r0}\sqrt{m}\cos{(k_m x)}, & m \text{ odd}, \\ V_{r0}\sqrt{m}\sin{(k_m x)}, & m \text{ even}, \end{bmatrix} \qquad V_{r0} = \sqrt{\frac{\hbar\omega_r}{C_r}}. \tag{A.4.18}$$

where $\omega = m\omega_r = k_m v$ and $k_m = m\pi/L, m \in \mathbb{Z}$. An alternative format sometimes encountered

$$\hat{V}_m(x,t) = V_m(x)(a(t) + a^\dagger(t)) = V_m(x)(ae^{-i\omega t} + a^\dagger e^{i\omega t}),$$

is completely equivalent. Similarly the current modes are defined, which will have opposite nodes to voltage

$$I_m(x) = \begin{bmatrix} \sqrt{m}I_{r0}\cos{(k_m x)}, & m \text{ even}, \\ \sqrt{m}I_{r0}\sin{(k_m x)}, & m \text{ odd}. \end{bmatrix}, \qquad I_{r0} = \sqrt{\frac{\hbar\omega_r}{L_r}}. \tag{A.4.19}$$

Proof

1. Quantisation of the classical expression (A.4.1) follows the exact same steps as in A.3.2, with the exception that

   - Different normalisation factor is used;
   - The limit $L \to \infty$ is not made since the resonator has a finite length;
   - Because of the discrete mode supported by the resonator, summation over the possible modes k_m is dropped and each mode m is worked on independently $a_m \to a, a_m^\dagger \to a^\dagger$;

   Working through the maths with spatial component defined by (A.4.1), one will arrive at the equivalent of (A.3.29) (shown here for m odd)

$$\hat{Q}_m(x,t) = \sqrt{\frac{2}{L}}\sqrt{\frac{\hbar}{2k_m Z_r}}\left(a(t) + a^\dagger(t)\right)\cos(k_m x),$$

2. With voltage defined by $V = -\partial_x Q/c$ (see (A.3.8)) and creation an annihilation operators having the time evolution in (A.3.28)

$$\begin{aligned}\hat{V}_m(x,t) &= -i\sqrt{\frac{\hbar k_m Z_r}{L}}\left(\partial_t a(t) - \partial_t a^\dagger(t)\right)\cos(k_m x)\\ &= -i\sqrt{\frac{\hbar k_m Z_r}{L}}\left(-i\omega_m a(t) - i\omega_m a^\dagger(t)\right)\cos(k_m x)\\ &= \sqrt{\frac{\hbar\omega_m}{cL}}\cos(k_m x)\left(a(t) + a^\dagger(t)\right).\\ &= \underbrace{\sqrt{m}V_{r0}\cos(k_m x)}_{V_m(x)}\left(a(t) + a^\dagger(t)\right), \qquad V_{r0} = \sqrt{\frac{\hbar\omega_r}{C_r}}.\end{aligned} \tag{A.4.20}$$

3. The alternative format $V_m(x)(ia(t) - ia^\dagger(t))$ that is sometimes presented is completely equivalent to (A.4.20)

$$\begin{aligned}V_m = V_m\left(ia(t) - a^\dagger(t)\right) &= V_m(a(0)e^{-i\omega t + i\pi/2} + a^\dagger(0)e^{i\omega t - i\pi/2})\\ &= V_m(a(0)e^{-i(\omega t - i\pi/2)} + a^\dagger(0)e^{i(\omega t - i\pi/2)})\\ &= V_m(a(0)e^{-i\omega t'} + a^\dagger(0)e^{i\omega t'})\\ &= V_m\left(a(t') + a^\dagger(t')\right),\end{aligned}$$

differing only by a time shift $t' - t = \pi/2\omega_r$. Likewise it can be shown that

$$\begin{aligned}\sigma_y = i(\sigma_-(t) - \sigma_+(t)) &= i\left(\sigma_-(0)e^{-i\omega_q t + i\pi/2} + \sigma_+(0)e^{i\omega_q t - i\pi/2}\right)\\ &= \sigma_-(t') + \sigma_+(t') = \sigma_x.\end{aligned}$$

4. Currents are defined by $I = d_t Q$ one uses (A.3.29) (shown here for m odd)

$$\begin{aligned}\hat{I}_m(x,t) &= \frac{2}{\sqrt{L}}\sqrt{\frac{\hbar}{2k_m Z_r}}\left(\partial_t a(t) + \partial_t a^\dagger(t)\right)\sin(k_m x)\\ &= -i\sqrt{\frac{\hbar\omega_m v}{LZ_r}}\sin(k_m x)\left(a(t) - a^\dagger(t)\right)\\ &= -i\sqrt{\frac{\hbar\omega_m}{Ll}}\sin(k_m x)\left(a(t) - a^\dagger(t)\right)\\ &= -i\underbrace{\sqrt{m}\sqrt{\frac{\hbar\omega_r}{L_r}}\sin(k_m x)}_{I_m(x)}\left(a(t) - a^\dagger(t)\right), \qquad I_{r0} = \sqrt{\frac{\hbar\omega_r}{L_r}}.\end{aligned}$$

A time shift like in (A.4.20) arrives at another form

$$\hat{I}_m(x,t) = I_m(x)\left(a(t) + a^\dagger(t)\right).$$

QED □

A.4.4 Resonator mode shift due to coupling

A $\lambda/2$ resonator that is coupled to outside lines via coupling capacitors $C_{\text{r-t}}$ (see Fig. 3.11) will have a shifted wavevector

$$k'_m = k_m - \frac{2\theta_m}{L},$$

and frequency

$$\omega'_m = \omega_m(1 - \frac{2\theta_m}{m\pi}),$$

of its m-th mode compared to its non coupled values $k_m = m\pi/L$. This shift is quantified by the small parameter

$$\theta_m = \omega C_{\text{r-t}} Z_r = m\pi \frac{C_{\text{r-t}}}{C_r} \ll 1,$$

that expresses the ratio of the coupling capacitors to the full resonator capacitance.

Proof

1. In the realistic scenario where the resonator has external coupling capacitors $C_{\text{r-t}}$ on its ends (see Fig. 3.11), the BC will be modified from $I(\pm L/2) = 0$ to

$$I_r(\pm L/2) = \partial_t Q(\pm L/2) = \partial_t (C_{\text{r-t}} V_r(\pm L/2)). \tag{A.4.21}$$

2. Concentrating on the $m = 1$ mode for brevity, the wavevectors of the resonator experience a shift $k_1 \to k_1 + dk$ that can be found by satisfying the new BC (A.4.21) using the current and voltage operators from A.4.3

$$I_{r0}(a + a^\dagger)\cos\left(\pm(k_1 + dk)\frac{L}{2}\right) = V_{r0} C_{\text{r-t}} \sin\left(\pm(k_1 + dk)\frac{L}{2}\right)(i\partial_t a - i\partial_t a^\dagger).$$

3. Expanding the trigonometric terms, recalling that $\sin(k_1 L/2) = \pm 1, \cos(k_1 L/2) = 0$, and using the time evolution of the photon operators $a(t) = ae^{-i\omega t}$ shown in (A.3.28)

$$I_{r0}(a + a^\dagger)\left(0 \mp \sin\left(\frac{dkL}{2}\right)\right) = V_{r0} C_{\text{r-t}}(\omega_1 a + \omega_1 a^\dagger)\left(\pm\cos\left(\frac{dkL}{2}\right)\right).$$

4. Using the small angle approximations $\sin(dkL/2) \approx dkL/2, \cos(dkL/2) \approx 1$

$$dk = -\omega_1 C_{\text{r-t}} \frac{2}{L}\frac{V_{r0}}{I_{r0}} = -\frac{2\omega_1 C_{\text{r-t}} Z_r}{L},$$

and generalising for an arbitrary modes, the shifted wavevectors

$$k'_m = k_m + dk = k_m - \frac{2\theta_m}{L}, \qquad \theta_m = \omega C_{\text{r-t}} Z_r. \tag{A.4.22}$$

5. The resonant frequency associated with the shifted wavevectors (A.4.22)

$$\omega'_m = k'_m v = \omega_m (1 - \frac{2\theta}{L}\frac{v}{v\underbrace{k_m}_{m\pi/L}}) = \omega_m(1 - \frac{2\theta}{m\pi}),$$

   is slightly lower than for ideal standing modes.

6. θ_m can be interpreted through its re-expression

$$\theta_m = v k_m C_{\text{r-t}} Z_r = C_{\text{r-t}} \frac{m\pi}{L}\frac{1}{\sqrt{lc}}\sqrt{\frac{l}{c}} = C_{\text{r-t}}\frac{m\pi}{cL} = m\pi\frac{C_{\text{r-t}}}{C_r} \tag{A.4.23}$$

   as the ratio of the coupling capacitors to the total resonator capacitance.

QED □

A.5 Twin qubit

A.5.1 Phase operator for the twin qubit

The operator $\cos(\hat{\varphi}_2 - \hat{\varphi}_1 - \varphi_{\text{ext}})$ can be expressed in the CP number basis $\{N_1, N_2, N_3\}$ using (A.1.6)

$$\begin{aligned}\cos(\hat{\varphi}_2 - \hat{\varphi}_1 - \varphi_{\text{ext}}) &= \frac{1}{2}\left(e^{i\hat{\varphi}_2}e^{-i\hat{\varphi}_1}e^{-i\varphi_{\text{ext}}} + \text{h.c.}\right) \\ &= \frac{1}{2}\Bigg(\left[\sum_{N_2} |N_2+1\rangle\langle N_2|\right] \\ &\quad \otimes \left[\sum_{N_1} |N_1-1\rangle\langle N_1|\right] \\ &\quad \otimes \mathbb{I}^{(3)}\Bigg) e^{-i\varphi_{\text{ext}}} + \text{h.c.} \\ &\quad = \frac{1}{2}e^{-i\varphi_{\text{ext}}} \sum_{N_{1,2,3}} |N_1-1, N_2+1, N_3\rangle\langle N_1, N_2, N_3| + \text{h.c.}\end{aligned}$$

Physically the term

$$\frac{1}{2}e^{-i\varphi_{\text{ext}}} |-1,1,0\rangle\langle 0,0,0| + \text{h.c.}.$$

corresponds to a CP exchange between island 1 and island 2, which would be a pair of symmetrical off-diagonal elements in the matrix of Fig. 2.4.

A.5.2 Potential energy

The values assumed by the phases across the JJs that would minimise the potential energy of the system are

$$\begin{aligned}\varphi_{01} = \varphi_{12} &= \frac{\varphi_{02} - \varphi_L}{2} + \pi F_L \\ \varphi_{03} = \varphi_{32} &= \frac{\varphi_{02} + \varphi_R}{2} - \pi F_R \\ \varphi_{02} &\approx \frac{\varphi_L - \varphi_R - 2\pi(F_L - F_R)}{2(1+\alpha)},\end{aligned}$$

with $F_L, F_R \in \mathbb{Z}$. The minimised potential is

$$\begin{aligned}U_{\text{min}}(F_L, F_R) = E_{J0}\Big(4 + \alpha &- 2(-1)^{F_L}\cos\left(\frac{\varphi_{02} - \varphi_L}{2}\right) \\ &- 2(-1)^{F_R}\cos\left(\frac{\varphi_{02} + \varphi_R}{2}\right) - \alpha\cos\varphi_{02}\Big),\end{aligned}$$

and the approximated potential, accurate for small deviations $\delta_L = \varphi_L - 2\pi F_L$ and $\delta_R = \varphi_L + 2\pi F_R$ from the center of cell $\{F_L, F_R\}$

$$\begin{cases} U_{\min}(F_L, F_R) \approx E_{J0}\left(\left(\frac{\varphi_{02} - \delta_L}{2}\right)^2 + \left(\frac{\varphi_{02} + \delta_R}{2}\right)^2 + \frac{\alpha}{2}\varphi_{02}^2 \right), \\ \qquad\qquad \frac{\varphi_{02}}{2} \approx \frac{\delta_L - \delta_R}{4(1+\alpha)}. \end{cases}$$

A.5.2.1 Exact evaluation for φ_{01} and φ_{03}

Proof

1. Performing minimisation of (2.1.4) with respect to φ_{01}

$$\frac{\partial U}{\partial \varphi_{01}} = \sin(\varphi_{01}) - \sin(\varphi_{02} - \varphi_{01} - \varphi_L) = 0 \tag{A.5.1}$$

results in a degree of freedom ($F_L \in \mathbb{Z}$), where we choose the $+2\pi F_L$, as opposed to $-2\pi F_L$, for convenience

$$\begin{aligned} \varphi_{01} &= \varphi_{02} - \varphi_{01} - \varphi_L + 2\pi F_L \\ &= \frac{\varphi_{02} - \varphi_L}{2} + \pi F_L, \qquad F_L \in \mathbb{Z}, \end{aligned} \tag{A.5.2}$$

and in a similar fashion for φ_{03}

$$\varphi_{03} = \frac{\varphi_{02} + \varphi_R}{2} - \pi F_R, \qquad F_R \in \mathbb{Z}. \tag{A.5.3}$$

2. Substitution back into (2.1.4) gives

$$\begin{aligned} U_{\min}(F_L, F_R) = E_{J0}\Big(4 + \alpha &- 2\cos\left(\frac{\varphi_{02} - \varphi_L + 2\pi F_L}{2}\right) \\ &- 2\cos\left(\frac{\varphi_{02} + \varphi_R - 2\pi F_R}{2}\right) - \alpha\cos\varphi_{02}\Big), \end{aligned} \tag{A.5.4}$$

or alternatively

$$\begin{aligned} U_{\min}(F_L, F_R) = E_{J0}\Big(4 + \alpha &- 2(-1)^{F_L}\cos\left(\frac{\varphi_{02} - \varphi_L}{2}\right) \\ &- 2(-1)^{F_R}\cos\left(\frac{\varphi_{02} + \varphi_R}{2}\right) - \alpha\cos\varphi_{02}\Big). \end{aligned} \tag{A.5.5}$$

QED □

A.5.2.2 First-order approximation for evaluating φ_{02}

Proof

1. Starting with (A.5.4) and minimising with respect to φ_{02}

$$\frac{\partial U_{\min}}{\partial \varphi_{02}} = \sin\left(\frac{\varphi_{02} - \varphi_L + 2\pi F_L}{2}\right) + \sin\left(\frac{\varphi_{02} + \varphi_R - 2\pi F_R}{2}\right) + \alpha \sin(\varphi_{02}) = 0.$$

2. The series expansion of the Right hand side (RHS) to first-order reads

$$\left(\frac{\varphi_{02} - \varphi_L + 2\pi F_L}{2}\right) + \left(\frac{\varphi_{02} + \varphi_R - 2\pi F_R}{2}\right) + \alpha\varphi_{02} \approx 0,$$

   resulting in

$$\varphi_{02} \approx \frac{\varphi_L - \varphi_R - 2\pi(F_L - F_R)}{2(1+\alpha)}.$$

QED □

A.5.2.3 Second-order approximation of $U_{\min}$

Proof

Expansion about the center of cell $\{F_L, F_R\}$ is valid when φ_L and φ_R deviate by δ_L and δ_R respectively

$$\begin{cases} \varphi_L = 2\pi F_L + \delta_L, & F_L \in \mathbb{Z}, \\ \varphi_R = 2\pi F_R + \delta_R, & F_R \in \mathbb{Z} \end{cases} \Rightarrow \begin{cases} \dfrac{-\varphi_L + 2\pi F_L}{2} = -\dfrac{\delta_L}{2}, \\ \dfrac{\varphi_R - 2\pi F_R}{2} = \dfrac{\delta_R}{2}, \\ \dfrac{\varphi_{02}}{2} \approx \dfrac{\delta_L - \delta_R}{4(1+\alpha)} \end{cases}$$

meaning that (A.5.4) can now read

$$\begin{aligned} U_{\min}(F_L, F_R) = E_{J0}\Big(4 + \alpha - 2\cos\left(\frac{\varphi_{02}}{2} - \frac{\delta_L}{2}\right) \\ - 2\cos\left(\frac{\varphi_{02}}{2} + \frac{\delta_R}{2}\right) - \alpha\cos\varphi_{02}\Big). \end{aligned}$$

The cosine terms, by nature of having small δ_L, δ_R, and correspondingly small φ_{02}, are valid for second-order expansion:

$$U_{\min}(F_L, F_R) \approx E_{J0}\left(\left(\frac{\varphi_{02} - \delta_L}{2}\right)^2 + \left(\frac{\varphi_{02} + \delta_R}{2}\right)^2 + \frac{\alpha}{2}\varphi_{02}^2\right).$$

QED □

A.5.3 Triple point

Derivation that the potential energy degeneracy point for the 3 cells $\{0,0\}, \{0,1\}, \{1,0\}$ occurs along the line $\varphi_L = \varphi_R = \varphi_T$ at

$$\varphi_T = 2\arccos\left(\sqrt{\alpha^2+1} - \alpha\right).$$

Proof

Table A.3: Minimisation of potential in different $\{L, R\}$ cells.

Cell	$\frac{U_{\min}}{E_{J0}}$ (A.5.5)
$\{0,0\}$	$4 - 4\cos\left(\frac{\varphi_T}{2}\right)$
$\{0,1\}$	$4 - \frac{2}{\alpha}\sin^2\left(\frac{\varphi_T}{2}\right)$
$\{1,0\}$	$4 - \frac{2}{\alpha}\sin^2\left(\frac{\varphi_T}{2}\right)$

Let us evaluate (A.5.1) and (A.5.5) along the line $\varphi_- = (\varphi_L - \varphi_R)/2 = 0$ where $\varphi_L = \varphi_R = \varphi_T$ for different $\{F_L, F_R\}$ cells (results are summarised in Table A.3)

- $\{F_L = 0, F_R = 0\}$

$$\begin{aligned}
(\text{A.5.1}) \Longrightarrow & \sin\left(\frac{\varphi_{02}-\varphi_T}{2}\right) + \sin\left(\frac{\varphi_{02}+\varphi_T}{2}\right) + \alpha\sin\varphi_{02} \\
&= \sin\left(\frac{\varphi_{02}}{2}\right)\left(\cos\left(\frac{\varphi_T}{2}\right) + \alpha\cos\left(\frac{\varphi_{02}}{2}\right)\right) = 0 \\
&\Longrightarrow \varphi_{02} = 0 \\
(\text{A.5.5}) \Longrightarrow \frac{U_{\min}}{E_{J0}} &= 4 + \alpha - 2\cos\left(-\frac{\varphi_T}{2}\right) - 2\cos\left(\frac{\varphi_T}{2}\right) - \alpha \\
&= 4 - 4\cos\left(\frac{\varphi_T}{2}\right)
\end{aligned}$$

- $\{F_L = 0, F_R = 1\}$

$$\begin{aligned}
(\text{A.5.1}) \Longrightarrow & \sin\left(\frac{\varphi_{02}-\varphi_T}{2}\right) - \sin\left(\frac{\varphi_{02}+\varphi_T}{2}\right) + \alpha\sin\varphi_{02} = 0 \\
&\Longrightarrow \sin\left(\frac{\varphi_{02}}{2}\right) = \frac{1}{\alpha}\sin\left(\frac{\varphi_T}{2}\right)
\end{aligned}$$

$$\begin{aligned}
(\text{A.5.5}) \Longrightarrow \frac{U_{\min}}{E_{J0}} &= 4 + \alpha - 2\cos\left(\frac{\varphi_{02}}{2} - \frac{\varphi_T}{2}\right) + 2\cos\left(\frac{\varphi_{02}}{2} + \frac{\varphi_T}{2}\right) - \alpha\cos(\varphi_{02}) \\
&= 4 - \frac{2}{\alpha}\sin^2\left(\frac{\varphi_T}{2}\right)
\end{aligned}$$

- $\{F_L = 1, F_R = 0\}$ is done is the similar fashion to $\{F_L = 0, F_R = 1\}$

$$\begin{aligned}(\text{A.5.1}) &\implies \sin\left(\frac{\varphi_{02}}{2}\right) = -\frac{1}{\alpha}\sin\left(\frac{\varphi_T}{2}\right)\\ (\text{A.5.5}) &\implies \frac{U_{\min}}{E_{J0}} = 4 - \frac{2}{\alpha}\sin^2\left(\frac{\varphi_T}{2}\right).\end{aligned}$$

Solving for the degenerate case when $U_{\min}(0,0) = U_{\min}(0,1) = U_{\min}(1,0)$ using Table A.3:

$$\begin{aligned}&\frac{1}{\alpha}\left(1 - \cos^2\left(\frac{\varphi_T}{2}\right)\right) - 2\cos\left(\frac{\varphi_T}{2}\right) = 0\\ &\cos^2\left(\frac{\varphi_T}{2}\right) + 2\alpha\cos\left(\frac{\varphi_T}{2}\right) - 1 = 0\\ &\implies \cos\left(\frac{\varphi_T}{2}\right) = \frac{-2\alpha \pm \sqrt{4\alpha^2 + 4}}{2}\\ &\implies \varphi_T = 2\arccos\left(\sqrt{\alpha^2+1} - \alpha\right).\end{aligned}$$

QED ☐

A.5.4 Degeneracy point

At the symmetric point ($\varphi_L = \pi, \varphi_R = \pi$) located on the boundary of the $\{F_L = 0, F_R = 1\}$ and $\{F_L = 1, F_R = 0\}$ cells, minimisation of (A.5.2) and (A.5.3) gives

$$\begin{aligned}&\{F_L = 0, F_R = 1\} \qquad \varphi_{01} = \frac{\varphi_{02} - \pi}{2}, \quad \varphi_{03} = \frac{\varphi_{02} - \pi}{2},\\ &\{F_L = 1, F_R = 0\} \qquad \varphi_{01} = \frac{\varphi_{02} + \pi}{2}, \quad \varphi_{03} = \frac{\varphi_{02} + \pi}{2}.\end{aligned}$$

When substituted into (2.1.4)

$$\begin{aligned}&\{F_L = 0, F_R = 1\} \qquad \min_{\varphi_{01},\varphi_{03}}(U) = E_{J0}\left(4 + \alpha - \alpha\cos(\varphi_{02}) - 4\sin\left(\frac{\varphi_{02}}{2}\right)\right),\\ &\{F_L = 1, F_R = 0\} \qquad \min_{\varphi_{01},\varphi_{03}}(U) = E_{J0}\left(4 + \alpha - \alpha\cos(\varphi_{02}) + 4\sin\left(\frac{\varphi_{02}}{2}\right)\right).\end{aligned}$$

Note, that movement from $\{0,1\} \to \{1,0\}$ is accompanied with φ_{02} moving from $\pi_{-0} \to \pi_{+0}$, to minimise the potential, that flips $\sin(\varphi_{02}/2)$ and accounts for the minus sign.

A.5.5 Transition matrix elements

It is shown that the twin qubit has voltage matrix elements

$$d_{ij} = \langle i|\hat{V}_2|j\rangle \equiv \frac{2E_C}{e(1+\alpha)}\langle i|\left[\hat{N}_1 + 2\hat{N}_2 + \hat{N}_3\right]|j\rangle.$$

arising from its capacitance network.

Proof

1. Microwaves in the TL, with voltage $V_{\text{mw}} = |V_{\text{mw}}|\cos(\omega_{21}t)$ are coupled via the coupling capacitor ($C_{\text{q-t}}$) to the qubit. Transitions $|1\rangle \leftrightarrow |2\rangle$ stimulated by this driving generate a qubit voltage of $V_2 = \langle 1|\,\hat{V}_2\,|2\rangle$.

2. Expressing the voltage on the different islands using capacitance matrix (2.1.2):

$$\begin{pmatrix} V_1 \\ V_2 \\ V_3 \end{pmatrix} = \vec{V} = C^{-1}\vec{Q} = C^{-1}2e\vec{N} = \frac{2e}{|C|}\begin{pmatrix} 2 & -1 & 0 \\ -1 & 2+\alpha & -1 \\ 0 & -1 & 2 \end{pmatrix}^{-1}\begin{pmatrix} N_1 \\ N_2 \\ N_3 \end{pmatrix}$$
$$= \frac{2e}{|C|}\frac{1}{4+4\alpha}\begin{pmatrix} 3+2\alpha & 2 & 1 \\ 2 & 4 & 2 \\ 1 & 2 & 3+2\alpha \end{pmatrix}\begin{pmatrix} N_1 \\ N_2 \\ N_3 \end{pmatrix}$$

one can read off

$$V_2 = \frac{e}{C(1+\alpha)}\left(N_1 + 2N_2 + N_3\right)$$
$$\Rightarrow \qquad \hat{V}_2 = \frac{e}{C(1+\alpha)}\left(\hat{N}_1 \otimes \mathbb{I}_{2,3} + 2\hat{N}_2 \otimes \mathbb{I}_{1,3} + \hat{N}_3 \otimes \mathbb{I}_{1,2}\right),$$

Equivalently, this operator can be evaluated through $\hat{V}_2 = (2e)^{-1}\partial H/\partial N_2$, using H from (2.1.1).

3. In the basis $\{|N_1\rangle, |N_2\rangle, |N_3\rangle\}$ the operator will take the form

$$\hat{V}_{20} \equiv \begin{pmatrix} \langle 000|\,\hat{V}_{20}\,|000\rangle & \langle 000|\,\hat{V}_{20}\,|001\rangle & \cdots \\ \langle 001|\,\hat{V}_{20}\,|000\rangle & \langle 001|\,\hat{V}_{20}\,|001\rangle & \cdots \\ \vdots & \vdots & \ddots \end{pmatrix},$$

with matrix elements

$$d_{ij} = \langle i|\,\hat{V}_2\,|j\rangle \equiv \frac{2E_C}{e(1+\alpha)}\langle i|\left[\hat{N}_1 + 2\hat{N}_2 + \hat{N}_3\right]|j\rangle\,.$$

QED □

A.6 Coherent quantum phase slip qubit

A.6.1 Qubit-resonator system

The Jaynes-Cummings Hamiltonian describing a qubit-resonator system

$$\frac{1}{\hbar}H_{\text{q-r}} = -\frac{\omega_q}{2}\sigma_z + \omega_r(a^\dagger a + \frac{1}{2}) + g(\sigma_+ a + \sigma_- a^\dagger), \tag{A.6.1}$$

in the basis of qubit-resonator states $\{|e,n\rangle, |g,n\rangle\}$ can be solved analytically, and shown to have eigenenergies

$$E_{\pm,n\geq 1} = \frac{\hbar}{2}\left((2n+1)\omega_r + \omega_q \pm \Omega_n\right), \qquad E_{g,n=0} = -\frac{\hbar\delta_{q-r}}{2},$$

for the n-th excitation manifold (n is number of resonator photons + ground (0) or excited (1) state of the atom), where

- $\delta_{q-r} = \omega_q - \omega_r$ is the detuning between resonator and qubit;
- $\Omega_n = \sqrt{\delta_{q-r}^2 + 4ng^2}$ is interaction term between the qubit and resonator.

The corresponding eigenstates are

$$\begin{cases} \quad |-,n\rangle = U_y(\theta_n/2)\,|g,n\rangle & = \cos(\theta_n/2)\,|g,n\rangle - \sin(\theta_n/2)\,|e,n-1\rangle, \\ \quad |+,n\rangle = U_y(\theta_n/2)\,|e,n-1\rangle & = \sin(\theta_n/2)\,|g,n\rangle + \cos(\theta_n/2)\,|e,n-1\rangle, \\ |g,n=0\rangle, & \end{cases}$$

with $\tan(\theta_n) = 2g\sqrt{n}/\delta_{q-r}$.

Proof

1. Hamiltonian (A.6.1) is shifted by $\omega_q/2 - \omega_r/2$ and the qubit frequency is written as a detuning from the resonator $\omega_q = \omega_r + \delta_{q-r}$

$$\frac{1}{\hbar}H'_{\text{q-r}} = \frac{1}{2}\left(\omega_r + \delta_{q-r}\right)(\mathbb{I} - \sigma_z) + \omega_r a^\dagger a + g(\sigma_+ a + \sigma_- a^\dagger).$$

2. Expressed in the qubit-resonator basis, where operators take the form $\sigma_z = |g\rangle\langle g| - |e\rangle\langle e|$, $\sigma^+ = |e\rangle\langle g|$, $\sigma^- = |g\rangle\langle e|$, $a = \sqrt{n+1}\,|n\rangle\langle n+1|$, $a^\dagger = \sqrt{n+1}\,|n+1\rangle\langle n|$, $a^\dagger a\,|n\rangle =$

$n\,|n\rangle$:

$$\frac{1}{\hbar}H_{\text{q-r}} = \begin{array}{c|ccccc|} & |g,0\rangle & |g,1\rangle \quad |e,1\rangle & |g,2\rangle \quad |e,1\rangle & \cdots & |g,n\rangle \quad |e,n-1\rangle \\ \hline \langle g,0| & \underbrace{0}_{\oplus} & & & & \\ \begin{matrix}\langle g,1| \\ \langle e,0|\end{matrix} & & \underset{n=1}{\boxed{\begin{matrix}\omega_r & g \\ g & (\omega_r+\delta_{q-r})\end{matrix}}} & & & \\ \begin{matrix}\langle g,2| \\ \langle e,1|\end{matrix} & & & \underset{n=2}{\boxed{\begin{matrix}2\omega_r & g\sqrt{2} \\ g\sqrt{2} & \omega_r+(\omega_r+\delta_{q-r})\end{matrix}}} & & \\ \vdots & & & & \ddots & \\ \begin{matrix}\langle g,n| \\ \langle e,n-1|\end{matrix} & & & & & \underset{n=n}{\boxed{\begin{matrix}n\omega_r & g\sqrt{n} \\ g\sqrt{n} & (n-1)\omega_r+(\omega_r+\delta_{q-r})\end{matrix}}} \end{array}, \tag{A.6.2}$$

where n tracks the number of *excitations* in the system (number of resonator photons + excited or ground state atom), and all elements that are not shown being 0.

3. Each of the submatrices of (A.6.2) can be diagonalised independently[20]. To begin, the submatrix is factorised

$$\begin{aligned} &\begin{array}{c|cc|} & |g,n\rangle & |e,n-1\rangle \\ \hline \langle g,n| & n\omega_r & g\sqrt{n} \\ \langle e,n-1| & g\sqrt{n} & n\omega_r+\delta_{q-r} \end{array} = n\omega_r\mathbb{I} + \frac{\delta_{q-r}}{2}(1-\sigma_z) + g\sqrt{n}\sigma_x \\ &= n\omega_r\mathbb{I} + \frac{1}{2}\sqrt{\delta_{q-r}^2+4ng^2}\left(\frac{\delta_{q-r}/2}{\sqrt{\delta_{q-r}^2+4ng^2}/2}(1-\sigma_z) + \frac{g\sqrt{n}}{\sqrt{\delta_{q-r}^2+4ng^2}/2}\sigma_x\right) \\ &= n\omega_r\mathbb{I} + \frac{1}{2}\Omega_n(\cos(\theta_n)(1-\sigma_z) + \sin(\theta_n)\sigma_x), \end{aligned} \tag{A.6.3}$$

where $\Omega_n = \sqrt{\delta_{q-r}^2+4ng^2}$ and $\tan(\theta_n) = 2g\sqrt{n}/\delta_{q-r}$.

4. A rotation $U_y(\theta_n/2) = \exp(i\theta_n/2\sigma_y)$ (applied exactly as in A.2.2) diagonalises (A.6.3) into

$$\begin{array}{c|cc|} & |-,n\rangle & |+,n\rangle \\ \hline \langle -,n| & n\omega_r - \frac{1}{2}\Omega_n & 0 \\ \langle +,n| & 0 & n\omega_r + \frac{1}{2}\Omega_n \end{array} - \frac{1}{2}\omega_q\mathbb{I} + \frac{1}{2}\omega_r\mathbb{I},$$

where the shift made in Step 1 (which is not affected by the unitary transformation) is reintroduced. The n-th excitation manifold has eigenenergies

$$E_{\pm,n\geq 1} = \frac{\hbar}{2}\left((2n+1)\omega_r - \omega_q \pm \Omega_n\right)$$

---

[20] In practise this means setting all eigenvector elements outside this subspace to 0.

and eigenvectors[21]

$$\begin{cases} |-,n\rangle = U_y(\theta_n/2)\,|g,n\rangle & = \cos(\theta_n/2)\,|g,n\rangle - \sin(\theta_n/2)\,|e,n-1\rangle\,, \\ |+,n\rangle = U_y(\theta_n/2)\,|e,n-1\rangle & = \sin(\theta_n/2)\,|g,n\rangle + \cos(\theta_n/2)\,|e,n-1\rangle\,. \end{cases}$$

The degeneracy of the original system eigenstates $|g,n\rangle$ $|e,n-1\rangle$ in this n-th excitation manifold at $\delta_{q-r} = 0 \Leftrightarrow \omega_q = \omega_r$ is lifted by the qubit resonator interaction.

5. The ground term ✥ in (A.6.2) is treated individually, and can easily be seen to have eigenenergy and eigenstate

$$E_{g,n=0} = 0 - -\frac{1}{2}\omega_q + \frac{1}{2}\omega_r = -\frac{\hbar\delta_{q-r}}{2}, \qquad |g,n=0\rangle\,.$$

QED ☐

A.6.2 Unitary transformation of a qubit-resonator system

Proof

1. The qubit-resonator system with Hamiltonian

$$H_{\text{q-r}} = \underbrace{-\frac{\hbar\omega_q}{2}\sigma_z + \hbar\omega_r(a^\dagger a + \frac{1}{2})}_{H_0} - \underbrace{\hbar g\sigma_y(ia - ia^\dagger)}_{H_{\text{int}}} \tag{A.6.4}$$

is separated out into the H_0 is the bare system Hamiltonian and H_{int} describing the coupling between qubit and resonator.

2. A unitary transformation

$$U(t) = \exp\left[i\frac{H_0 t}{\hbar}\right] = \exp\left[-i\frac{\omega_q t}{2}\sigma_z + \omega_r\left(a^\dagger a + \frac{1}{2}\right)\right], \tag{A.6.5}$$

moves the Hamiltonian into the interaction picture (see A.7.2.1),

$$\begin{aligned} H'_{\text{q-r}} = UH_{\text{int}}U^\dagger &= -\hbar g U\left[\sigma_+ a + \sigma_- a^\dagger - \sigma_+ a^\dagger - \sigma_- a\right]U^\dagger \\ &= -\hbar g\left(\sigma_+ a e^{i(\omega_q-\omega_r)t} + \sigma_- a^\dagger e^{-i(\omega_q-\omega_r)t} - \underbrace{\sigma_+ a^\dagger e^{-i(\omega_q+\omega_r)} - \sigma_- a e^{-i(\omega_q+\omega_r)}}_{\text{✥}}\right), \end{aligned} \tag{A.6.6}$$

where identities $e^{iH_0 t/\hbar}[\sigma_-]e^{-iH_0 t/\hbar} = e^{-i\omega_q t/2\sigma_z}[\sigma_-]e^{+i\omega_q t/2\sigma_z} = \sigma_- e^{-i\omega_q t}$ and $e^{iH_0 t/\hbar}[a]e^{-iH_0 t/\hbar} = e^{a^\dagger a\omega_r}[a]e^{-a^\dagger a\omega_r} = ae^{-i\omega_r t}$ from (A.7.5) are used.

---

[21] Recall from (A.7.2) that $U_y(\alpha) = \cos(\alpha)\mathbb{I} + i\sin(\alpha)\sigma_y = \begin{pmatrix} \cos\alpha & \sin\alpha \\ -\sin\alpha & \cos\alpha \end{pmatrix}$.

3. The fast rotating terms ✥ in (A.6.6) are ignored in the RWA, since they correspond to energy non-conserving processes and the fast time scale on which they occur means that they average out and do not contribute to dynamics, leaving the following terms

$$\frac{1}{\hbar}H'_{\text{q-r}} = -\hbar g\left(\sigma_+ a + \sigma_- a^\dagger\right).$$

4. Thus, in the original Hamiltonian (A.6.4) the $\sigma_+ a^\dagger$ and $\sigma_- a$ terms (corresponding to atom excitation-photon creation or atom relaxation photon-annihilation events) can be dropped, leaving the Jaynes-Cummings Hamiltonian form

$$\frac{1}{\hbar}H_{\text{q-r}} = -\frac{\omega_q}{2}\sigma_z + \omega_r(a^\dagger a + \frac{1}{2}) - g(\sigma_+ a + \sigma_- a^\dagger).$$

QED □

A.6.3 Unitary transformation of driven qubit-resonator system

Proof

1. The driven system Hamiltonian consists of the qubit resonator Hamiltonian $H_{\text{q-r}}$ (3.1.19) and the driving term H_{mw} (3.1.28)

$$\begin{aligned}\frac{1}{\hbar}H &= \frac{1}{\hbar}H_{\text{q-r}} + \frac{1}{\hbar}H_{\text{mw}} \\ &= -\frac{\omega}{2}\sigma_z + \omega a^\dagger a - g(a\sigma_+ + a^\dagger\sigma_-) + \Omega\left(ia - ia^\dagger\right)\left(e^{-i\omega t} + e^{i\omega t}\right).\end{aligned} \tag{A.6.7}$$

2. A unitary transformation is applied to (A.6.7)

$$U = \exp\left[-i\frac{\omega t}{2}\sigma_z + i\omega t a^\dagger a\right],$$

which is similar to (A.6.5), except that the driving field frequency (ω) is used, rather than the qubit (ω_q) and resonator (ω_r) frequencies. This operator commutes with the resonator and qubit parts of the Hamiltonian ($[U, \sigma_z] = \left[U, a^\dagger a\right] = 0$), simplifying the evaluation of terms in (A.7.4)

$$\begin{aligned}\frac{1}{\hbar}H' &= \frac{1}{\hbar}UHU^\dagger - iU\partial_t U^\dagger, \\ \frac{1}{\hbar}UHU^\dagger &= -\frac{\omega_q}{2}\sigma_z + \omega_r a^\dagger a \\ &\quad - gU\left[(a\sigma_+ + a^\dagger\sigma_-)\right]U^\dagger \\ &\quad - \frac{\hbar\Omega}{2}U\left[iae^{i\omega t} + iae^{-i\omega t} - ia^\dagger e^{i\omega t} - ia^\dagger e^{-i\omega t}\right]U^\dagger, \\ iU\partial_t U^\dagger &= -\frac{\omega}{2}\sigma_z + \omega a^\dagger a\end{aligned} \tag{A.6.8}$$

3. Evaluation of the multiple cross terms in (A.6.8) is shown in (A.7.5) and summarised here

$$\begin{aligned} a &\to U(H_r)aU^\dagger(H_r) = e^{i\omega_r t a^\dagger a}\,[a]\,e^{-i\omega_r t a^\dagger a} = e^{-i\omega_r t}a, \\ a^\dagger &\to U(H_r)a^\dagger U^\dagger(H_r) = e^{i\omega_r t}a^\dagger, \\ \sigma_- &\to U(H_\mathrm{q})\sigma_- U^\dagger(H_\mathrm{q}) = e^{i\omega_q t\sigma_z/2}\,[\sigma_-]\,e^{-i\omega_q t\sigma_z/2} = e^{-i\omega t}\sigma_-, \\ \sigma_+ &\to U(H_\mathrm{q})\sigma_+ U^\dagger(H_\mathrm{q}) = e^{i\omega t}\sigma_+. \end{aligned} \tag{A.6.9}$$

4. Substituting (A.6.9) into (A.6.8)

$$\begin{aligned} &UHU^\dagger - i\hbar U\partial_t U^\dagger \\ &\quad = -\frac{\hbar\delta_q}{2}\sigma_z + \hbar\delta_r a^\dagger a \\ &\quad - g\left[a\sigma_+ + a^\dagger\sigma_-\right] \\ &\quad - \frac{\hbar\Omega}{2}\left[ia + \underbrace{iae^{-2i\omega t} - ia^\dagger e^{2i\omega t}}_{\text{✥}} - ia^\dagger\right]. \end{aligned} \tag{A.6.10}$$

where $\delta_q = \omega_q - \omega, \delta_r = \omega_r - \omega$.

5. Fast rotating terms ✥ in (A.6.10) that do not influence transient dynamics can be ignored like in Sec. A.6.2, resulting in

$$\frac{1}{\hbar}H' = -\frac{\delta_q}{2}\sigma_z + \delta_r a^\dagger a - g\left(a\sigma_+ + a^\dagger\sigma_-\right) - \frac{\hbar\Omega}{2}\left(ia - ia^\dagger\right). \tag{A.6.11}$$

QED □

A.6.4 Solving qubit-resonator master equation

The master equation of the rotated Hamiltonian (A.6.11) with the Linbland dissipation term (A.7.29)

$$\begin{aligned}
\partial_t \rho &= -\frac{i}{\hbar}\left[H_{\text{total}}, \rho\right] + \mathcal{L}\left[\rho\right] \\
&= i\frac{\delta_q}{2}\left[\sigma_z\rho - \rho\sigma_z\right] - i\delta_r\left[a^\dagger a\rho - \rho a^\dagger a\right] \\
&+ ig\left[a\sigma_+\rho - \rho a\sigma_+ + a^\dagger\sigma_-\rho - \rho a^\dagger\sigma_-\right] \\
&+ i\frac{i\Omega}{2}\left[a\rho - \rho a - a^\dagger\rho + \rho a^\dagger\right] \\
&+ \frac{\kappa}{2}\left[2a\rho a^\dagger - a^\dagger a\rho - \rho a^\dagger a\right] \\
&+ \frac{\Gamma_1}{2}\left[2\sigma_-\rho\sigma_+ - \sigma_+\sigma_-\rho - \rho\sigma_+\sigma_-\right] \\
&+ \frac{\Gamma_\phi}{2}\left[\sigma_z\rho\sigma_z - \rho\right],
\end{aligned} \tag{A.6.12}$$

is solved in the qubit-resonator basis $\{|e,n\rangle, |e,n+1\rangle, |g,n\rangle, |g,n+1\rangle\}$ in the case of low photon number in the resonator ($n = 0$ and $n = 1$) in which operators are defined as:

$$\sigma_z = \begin{pmatrix} 1 & . & . & . \\ . & 1 & . & . \\ . & . & -1 & . \\ . & . & . & -1 \end{pmatrix} \qquad \sigma_+ = \begin{pmatrix} . & . & . & . \\ . & . & . & . \\ 1 & . & . & . \\ . & 1 & . & . \end{pmatrix} \qquad \sigma_- = \begin{pmatrix} . & . & 1 & . \\ . & . & . & 1 \\ . & . & . & . \\ . & . & . & . \end{pmatrix}$$

$$a = \begin{pmatrix} . & \sqrt{n+1} & . & . \\ . & . & . & . \\ . & . & . & \sqrt{n+1} \\ . & . & . & . \end{pmatrix} \qquad a^\dagger = \begin{pmatrix} . & . & . & . \\ \sqrt{n+1} & . & . & . \\ . & . & . & . \\ . & . & \sqrt{n+1} & . \end{pmatrix}$$

and the density matrix as

$$\rho = \begin{pmatrix} 1-\rho_{11}-\rho_{22}-\rho_{33} & \rho_{01} & \rho_{02} & \rho_{03} \\ \rho_{10} & \rho_{11} & \rho_{12} & \rho_{13} \\ \rho_{20} & \rho_{21} & \rho_{22} & \rho_{23} \\ \rho_{30} & \rho_{31} & \rho_{32} & \rho_{33} \end{pmatrix}.$$

An analytical solution is found by evaluating for the stationary state ($\partial_t\rho = 0$) and using the low drive limit ($\Omega \ll 1$ and therefore $\mathcal{O}(\Omega^2) \rightarrow 0$) with the aid of `Mathematica` that supports symbolic execution. Starting with the matrix representation of (A.6.12) the following tricks are used (see full notebook in [264]):

- The density matrix is Hermitian, and therefore $\rho_{ji} = \rho_{ij}^*$ so only one half of the matrix needs to be solved for. Furthermore the elements are decomposed into real and imaginary components $\rho_{ij} = A_{ij} + iB_{ij}$, where $A = \mathrm{Re}[\rho_{ij}]$ and $B = \mathrm{Im}[\rho_{ij}]$, which reveals symmetry in the 10 simultaneous equations (see Fig. A.10);

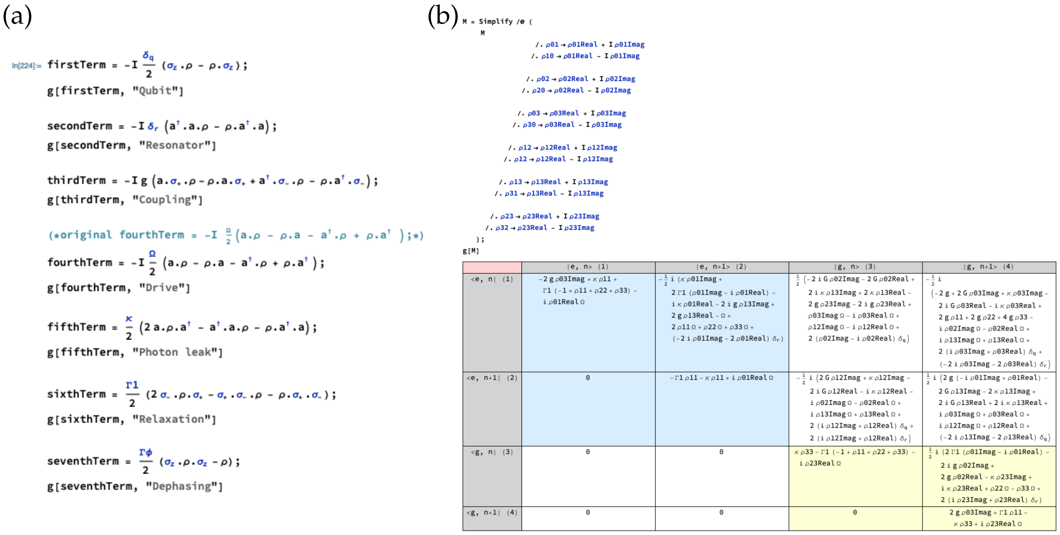

(a)

```
In[224]:= firstTerm = -I δq/2 (σz.ρ - ρ.σz);
          g[firstTerm, "Qubit"]

          secondTerm = -I δr (a†.a.ρ - ρ.a†.a);
          g[secondTerm, "Resonator"]

          thirdTerm = -I g (a.σ+.ρ - ρ.a.σ+ + a†.σ-.ρ - ρ.a†.σ-);
          g[thirdTerm, "Coupling"]

          (*original fourthTerm = -I Ω/2 (a.ρ - ρ.a - a†.ρ + ρ.a† );*)
          fourthTerm = -I Ω/2 (a.ρ - ρ.a - a†.ρ + ρ.a† );
          g[fourthTerm, "Drive"]

          fifthTerm = κ/2 (2 a.ρ.a† - a†.a.ρ - ρ.a†.a);
          g[fifthTerm, "Photon leak"]

          sixthTerm = Γ1/2 (2 σ-.ρ.σ+ - σ+.σ-.ρ - ρ.σ+.σ-);
          g[sixthTerm, "Relaxation"]

          seventhTerm = Γϕ/2 (σz.ρ.σz - ρ);
          g[seventhTerm, "Dephasing"]
```

(b)

```
M = Simplify /@ (
    M
          /. ρ01 → ρ01Real + I ρ01Imag
         /. ρ10 → ρ01Real - I ρ01Imag

        /. ρ02 → ρ02Real + I ρ02Imag
       /. ρ20 → ρ02Real - I ρ02Imag

      /. ρ03 → ρ03Real + I ρ03Imag
     /. ρ30 → ρ03Real - I ρ03Imag

    /. ρ12 → ρ12Real + I ρ12Imag
   /. ρ12 → ρ12Real - I ρ12Imag

   /. ρ13 → ρ13Real + I ρ13Imag
  /. ρ31 → ρ13Real - I ρ13Imag

  /. ρ23 → ρ23Real + I ρ23Imag
 /. ρ32 → ρ23Real - I ρ23Imag
 );
g[M]
```

	|e, n> (1)	|e, n+1> (2)	|g, n> (3)	|g, n+1> (4)
<e, n| (1)	-2 g ρ03Imag + κ ρ11 + Γ1 (-1 + ρ11 + ρ22 + ρ33) - i ρ01Real Ω	-1/2 i (κ ρ01Imag + 2 Γ1 (ρ01Imag - i ρ01Real) - i κ ρ01Real - 2 i g ρ13Imag + 2 g ρ13Real - Ω + 2 ρ11 Ω + ρ22 Ω + ρ33 Ω + (-2 i ρ01Imag - 2 ρ01Real) δr)	1/2 (-2 i G ρ02Imag - 2 G ρ02Real + 2 i κ ρ13Imag + 2 κ ρ13Real - 2 g ρ23Imag - 2 i g ρ23Real + ρ03Imag Ω - i ρ03Real Ω + ρ12Imag Ω - i ρ12Real Ω + 2 (ρ02Imag - i ρ02Real) δq)	-1/2 i (-2 g + 2 G ρ03Imag + κ ρ03Imag - 2 i G ρ03Real - i κ ρ03Real + 2 g ρ11 + 2 g ρ22 + 4 g ρ33 - i ρ02Imag Ω - ρ02Real Ω + i ρ13Imag Ω + ρ13Real Ω + 2 (i ρ03Imag + ρ03Real) δq + (-2 i ρ03Imag - 2 ρ03Real) δr)
<e, n+1| (2)	0	-Γ1 ρ11 - κ ρ11 + i ρ01Real Ω	-1/2 i (2 G ρ12Imag + κ ρ12Imag - 2 i G ρ12Real - i κ ρ12Real - i ρ02Imag Ω - ρ02Real Ω + i ρ13Imag Ω + ρ13Real Ω + 2 (i ρ12Imag + ρ12Real) δq + 2 (i ρ12Imag + ρ12Real) δr)	1/2 i (2 g (-i ρ01Imag + ρ01Real) - 2 G ρ13Imag - 2 κ ρ13Imag + 2 i G ρ13Real + 2 i κ ρ13Real + i ρ03Imag Ω + ρ03Real Ω + i ρ12Imag Ω + ρ12Real Ω + (-2 i ρ13Imag - 2 ρ13Real) δq)
<g, n| (3)	0	0	κ ρ33 - Γ1 (-1 + ρ11 + ρ22 + ρ33) - i ρ23Real Ω	1/2 i (2 Γ1 (ρ01Imag - i ρ01Real) - 2 i g ρ02Imag + 2 g ρ02Real - κ ρ23Imag + i κ ρ23Real + ρ22 Ω - ρ33 Ω + 2 (i ρ23Imag + ρ23Real) δr)
<g, n+1| (4)	0	0	0	2 g ρ03Imag + Γ1 ρ11 - κ ρ33 + i ρ23Real Ω

Figure A.10: **(a)** Writing out the master equation, which is solved for $\partial_t \rho = 0$; **(b)** Splitting entries into real and imaginary components and removing the diagonal terms since they will be complex conjugates.

- Each of the cells in Fig. A.10 (b) is equated to zero, using the `Solve` and `Simplify` functions to iteratively solve for all the ρ_{ij} components. Some screenshots of evaluation at different stages is shown in Fig. A.11;

Once a solution for ρ is found, expectation values can be evaluated using the traces:

$$\begin{aligned}\left\langle a^{\dagger}\right\rangle &= \mathrm{Tr}\left\{a\rho\right\} = \rho_{10} + \rho_{32} \\ &= \frac{-i\Omega/2}{\frac{g^2}{\delta_q + i\left(\frac{\Gamma_1}{2} + \Gamma_\phi\right)} - \left(\delta_r + i\frac{\kappa}{2}\right)}.\end{aligned}$$

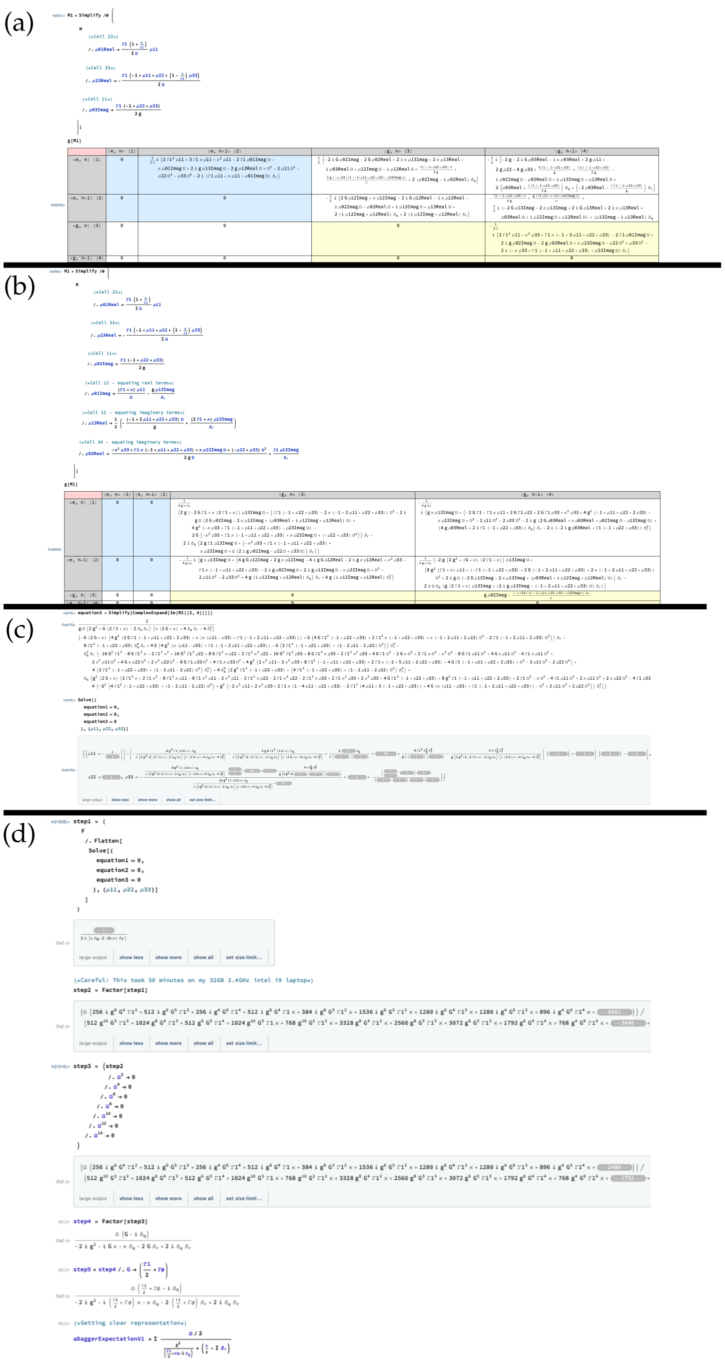

(a)

```
In[331]:= M1 = Simplify /@ (
      M
        (*Cell 22*)
        /. ρ01Real → (Γ1 (1 + κ/Γ1))/(I Ω) ρ11

        (*Cell 33*)
        /. ρ23Real → -(Γ1 (-1 + ρ11 + ρ22 + (1 - κ/Γ1) ρ33))/(I Ω)

        (*Cell 11*)
        /. ρ03Imag → (Γ1 (-1 + ρ22 + ρ33))/(2 g)
      );
g[M1]
```

(b)

```
In[403]:= M1 = Simplify /@ (
      M
        (*Cell 22*)
        /. ρ01Real → (Γ1 (1 + κ/Γ1))/(I Ω) ρ11

        (*Cell 33*)
        /. ρ23Real → -(Γ1 (-1 + ρ11 + ρ22 + (1 - κ/Γ1) ρ33))/(I Ω)

        (*Cell 11*)
        /. ρ03Imag → (Γ1 (-1 + ρ22 + ρ33))/(2 g)

        (*Cell 12 - equating real terms*)
        /. ρ01Imag → ((Γ1 + κ) ρ11)/Ω - (g ρ13Imag)/δr

        (*Cell 12 - equating imaginary terms*)
        /. ρ13Real → 1/2 (-((-1 + 2 ρ11 + ρ22 + ρ33) Ω)/g + ((2 Γ1 + κ) ρ13Imag)/δr)

        (*Cell 34 - equating imaginary terms*)
        /. ρ02Real → (-κ^2 ρ33 + Γ1 κ (-1 + ρ11 + ρ22 + ρ33) + κ ρ23Imag Ω + (-ρ22 + ρ33) Ω^2)/(2 g Ω) + (Γ1 ρ13Imag)/δr
      );
g[M1]
```

(c)

```
In[475]:= equation3 = Simplify[ComplexExpand[Im[M2[[2, 4]]]]]
```

```
In[476]:= Solve[{
    equation1 == 0,
    equation2 == 0,
    equation3 == 0
   }, {ρ11, ρ22, ρ33}]
```

(d)

```
In[1303]:= step1 = (
   F
    /. Flatten[
     Solve[{
        equation1 == 0,
        equation2 == 0,
        equation3 == 0
       }, {ρ11, ρ22, ρ33}]
     ]
   )
```

```
(*Careful! This took 30 minutes on my 32GB 2.4GHz intel i9 laptop*)
step2 = Factor[step1]
```

```
In[1314]:= step3 = (step2
          /. Ω^2 → 0
         /. Ω^4 → 0
        /. Ω^6 → 0
       /. Ω^8 → 0
      /. Ω^10 → 0
     /. Ω^12 → 0
    /. Ω^14 → 0
   )
```

```
step4 = Factor[step3]
Out= (Ω (G - i δq))/(-2 i g^2 - i G κ - κ δq - 2 G δr + 2 i δq δr)
```

```
step5 = step4 /. G → (Γ1/2 + Γϕ)
Out= (Ω (Γ1/2 + Γϕ - i δq))/(-2 i g^2 - i (Γ1/2 + Γϕ) κ - κ δq - 2 (Γ1/2 + Γϕ) δr + 2 i δq δr)
```

```
(*Getting clear representation*)
aDaggerExpectationV1 = I (Ω/2)/(g^2/(Γ1/2 + Γϕ - I δq) + (κ/2 - I δr))
```

Figure A.11: Screenshots of progressively working through system, by evaluating Re$[\rho_{ij}]$ and Im$[\rho_{ij}]$ that would satisfy the stationary state solution of (A.6.12) $\partial_t \rho = 0$ using the `Solve` function. As terms are eliminated, the leftover combination gets ever more complex: **(a)** Start of evaluation; **(b)** Middle of evaluation; **(c)** Increasing complexity of terms in the system; **(d)** Last 3 equations for $\rho_{11}, \rho_{22}, \rho_{33}$ are solved simultaneously, after which the approximation $\mathcal{O}(\Omega^2) \to 0$ is made. Evaluation of such kind takes 30 minutes on a laptop.

A.6.5 Inductive coupling to resonator

Inductive coupling between a Coherent quantum phase slip (CQPS) qubit and resonator has a coupling strength

$$\hbar g_I \propto M I_p I_r E_s / \Delta E,$$

that depends on the energy of the qubit ΔE in additional the mutual inductance (M), qubit's persistent current (I_p), resonator current (I_r) and CQPS energy (E_s).

Proof

1. By direct analogy to (3.1.13), the coupling energy between the qubit and resonator

$$H_{\text{int}} = \hat{I}_r M \hat{I}_q, \tag{A.6.13}$$

depends on the mutual inductance between the qubit and resonator (M), as well as the current operators in the resonator ($\hat{I}_r$) and qubit ($\hat{I}_q$).

2. Defining the qubit current operator as the derivative of the CQPS Hamiltonian (3.1.5) wrt flux (analogous to the differentiation step in (3.1.15))

$$\begin{aligned} \hat{I}_q &= \frac{1}{\Phi_0}\frac{\partial H_{\text{q}}}{\partial \hat{F}} \\ &= \frac{1}{\Phi_0}\frac{\partial}{\partial \hat{F}}\left(\frac{E_L}{2}(\hat{F} - f_{ext})^2 - E_S\cos(\hat{N})\right) \\ &= \frac{E_L}{\Phi_0}(\hat{F} - f_{ext}) = I_p(\hat{F} - f_{ext}). \end{aligned} \tag{A.6.14}$$

3. In the 2-level basis $\{|F\rangle, |F+1\rangle\}$ (A.6.14) becomes

$$\hat{I}_p = I_p(\sigma_z - f_{\text{ext}}), \tag{A.6.15}$$

which directly describes the state of the current in the qubit in relation to its quantum state.

4. The second term in (A.6.15) is a constant and so is not important when considering the qubit-resonator interaction. Thus by combining (A.6.13),(A.6.15) inductive coupling between the qubit and resonator is described by [199, 265]

$$H_{\text{int}} = \hat{I}_r M I_p \sigma_z, \tag{A.6.16}$$

where in contrast to traverse coupling through a capacitor ($\propto \sigma_y$, see (3.1.17)) that promotes a flux state exchange, inductive coupling is longitudinal ($\propto \sigma_z$) and modifies the persistent current of the qubit directly.

5. Diagonalising the CQPS qubit Hamiltonian using the same $U_y(\theta/2)$ rotation as in A.2.2, will transform the interaction term (A.6.16) into a representation in the new $\{|e\rangle, |g\rangle\}$ basis

$$\begin{aligned} H'_{\text{int}} &= \hat{I}_r M I_p U_y^\dagger(\theta/2)\sigma_z U_y(\theta/2) = \hat{I}_r M I_p \sigma_z U_y(\theta) \\ &= \hat{I}_r M I_p \begin{pmatrix} 1 & 0 \\ 0 & -1 \end{pmatrix} \begin{pmatrix} \cos\theta & \sin\theta \\ -\sin\theta & \cos\theta \end{pmatrix} \\ &= \hat{I}_r M I_p \left(\cos(\theta)\sigma_z + \sin(\theta)\sigma_x\right) \\ &= -\hat{I}_r M I_p \left(\frac{\varepsilon}{\Delta E}\sigma_z + \frac{\Delta}{\Delta E}\sigma_x\right), \end{aligned}$$

where the definitions $\Delta E = \hbar\omega_q = \sqrt{\varepsilon^2 + \Delta^2}, \varepsilon = 2I_p\delta\Phi, \Delta = E_S$ come from (3.1.7).

6. Substituting in expression (A.4.19) for the current in a resonator for the odd modes at $x = 0$[22] $\hat{I}_r = I_m(a + a^\dagger)\cos(k_m x), I_m = \sqrt{\hbar m \omega_r / 2L_r}$

$$\begin{aligned} H'_{\text{int}} &= -I_m M I_p (a + a^\dagger)\left(\frac{\varepsilon}{\Delta E}\sigma_z + \frac{\Delta}{\Delta E}\sigma_x\right) \\ &= -\hbar g_I (a + a^\dagger)\left(\frac{\varepsilon}{\Delta}\sigma_z + \sigma_x\right), \end{aligned} \tag{A.6.17}$$

where the coupling strength

$$\hbar g_I = I_m M I_p \frac{\Delta}{\Delta E} \tag{A.6.18}$$

is identified.

7. Finally, transforming (A.6.17) into a form that resembles the Jaynes-Cumming Hamiltonian by moving into the interaction picture (refer to A.6.2) using rotation $U = \exp[iH_0 t/\hbar]$

$$\begin{aligned} UH'_{\text{int}}U^\dagger = &-\hbar g_I U \left[\left(a^\dagger\sigma_- + a^\dagger\sigma_+ + a\sigma_0 + a\sigma_+\right) + \left(a + a^\dagger\right)\frac{\varepsilon}{\Delta}\sigma_z\right] U^\dagger \\ = &-\hbar g_I \left(a\sigma_+ e^{i(\omega_q - \omega_r)t} + \text{h.c.}\right) \\ &-\hbar g_I \underbrace{\left(a\sigma_- e^{-i(\omega_q + \omega_r)t} + a^\dagger\sigma_+ e^{+i(\omega_q + \omega_r)t}\text{h.c.}\right)} \\ &-\hbar g_I \frac{\varepsilon}{\Delta}\sigma_z (a e^{-i\omega_r t} + a^\dagger e^{i\omega_r t}). \end{aligned} \tag{A.6.19}$$

---

[22] Even modes $\propto \sin(k_m x)$ have a node at $x = 0$ and thus don't contribute.

8. The last term in (A.6.19) will be a modification to the qubit energy, while the ⌖ term is ignored in the RWA when $\omega_q \sim \omega_r$, leaving

$$-\hbar g_I \left(a\sigma_+ + a^\dagger \sigma_- \right)$$

as the term describing inductive interaction between the qubit and resonator.

9. As seen from (A.6.18), the coupling strength depends on the energy (ΔE), or effectively the bias magnetic field ($\delta\Phi$), which is not present in capacitive coupling (see (3.1.18)). A comparison of the two effects is shown in Fig. 3.6, where over a single period the coupling strength will vary for inductive coupling, but not for capacitive coupling.

QED □

A.7 Generic quantum formalism

A.7.1 Pauli matrices

Pauli matrices are useful definitions when working with 2-level systems

$$\sigma_x = \begin{pmatrix} 0 & 1 \\ 1 & 0 \end{pmatrix} \qquad \sigma_y = \begin{pmatrix} 0 & -i \\ i & 0 \end{pmatrix} \qquad \sigma_z = \begin{pmatrix} 1 & 0 \\ 0 & -1 \end{pmatrix}.$$

They have the following interrelations

$$\sigma_i \sigma_j = -\sigma_j \sigma_i, \qquad i, j \in \{x, y, z\}. \tag{A.7.1}$$

A.7.1.1 Pauli matrix rotations

Pauli matrices are commonly used in unitary transformation (refer to A.7.2) to rotate the state of a 2-levels system by an angle 2α about the jth axis of the Bloch sphere $j \in \{x, y, z\}$

$$\begin{aligned} U_j(\alpha) &= \exp\left[i\alpha\sigma_j\right] = \sum_k \frac{(i\alpha)^k}{k!}\sigma_j^k \\ &= \sum_{k=0} \frac{\alpha^{2k}(-1)^k}{2k}\mathbb{I} + i\sum_{k=0} \frac{\alpha^{2k+1}(-1)^k}{2k+1}\sigma_j \Rightarrow \\ &= \cos(\alpha)\mathbb{I} + i\sin(\alpha)\sigma_j, \end{aligned} \left[\begin{aligned} U_x(\alpha) &= \begin{pmatrix} \cos\alpha & i\sin\alpha \\ i\sin\alpha & \cos\alpha \end{pmatrix}, \\ U_y(\alpha) &= \begin{pmatrix} \cos\alpha & \sin\alpha \\ -\sin\alpha & \cos\alpha \end{pmatrix}, \\ U_z(\alpha) &= \begin{pmatrix} e^{i\alpha} & 0 \\ 0 & e^{-i\alpha} \end{pmatrix}. \end{aligned} \right. \tag{A.7.2}$$

Using the RHS procedure of (A.7.2) and useful identities from (A.7.1) one can show that

$$\begin{cases} U_y\sigma_z = \Big(\cos(\alpha)\mathbb{I} + i\sin(\alpha)\sigma_y\Big)\sigma_z = \sigma_z\Big(\cos(\alpha)\mathbb{I} - i\sin(\alpha)\sigma_y\Big) = \sigma_z U_y^\dagger, \\ U_y\sigma_x = \sigma_x U_y^\dagger, \\ U_y\sigma_y = \sigma_y U_y, \\ U_y^\dagger(\alpha)U_y^\dagger(\alpha) = U_y(\alpha)U_y(\alpha) = U_y(2\alpha). \end{cases} \tag{A.7.3}$$

A.7.2 Unitary transformations

A unitary quantum mechanical operator U, is one that satisfies the relationship $U^\dagger U = \mathbb{I}$. It can be useful for representing a Hamiltonian in a rotated eigenbasis $|\psi'\rangle = U|\psi\rangle$

$$\begin{aligned} i\hbar\partial_t |\psi\rangle &= H|\psi\rangle \\ i\hbar\partial_t \left[U^\dagger |\psi'\rangle\right] &= H\left[U^\dagger |\psi'\rangle\right] \\ i\hbar U^\dagger\partial_t |\psi'\rangle + i\hbar\partial_t U^\dagger |\psi'\rangle &= HU^\dagger |\psi'\rangle \\ i\hbar\partial_t |\psi'\rangle &= \left[UHU^\dagger - i\hbar U\partial_t U^\dagger\right] |\psi'\rangle , \end{aligned} \tag{A.7.4}$$

and hence in this rotated eigenbasis the Hamiltonian reads

$$H' = UHU^\dagger - i\hbar U\partial_t U^\dagger.$$

Importantly, expectation values of operators, which are also transformed $A \to UAU^\dagger$, are conserved under such transformations

$$\begin{aligned} \langle\psi| A |\psi\rangle &\equiv \left(\langle\psi| U^\dagger\right) UAU^\dagger \left(U|\psi\rangle\right) \\ &\equiv \langle\psi'| A' |\psi'\rangle , \end{aligned}$$

and there are cases in which symmetry allows for simpler evaluation with the transformed Hamiltonian where one can identify negligible interactions and gauge physical meaning.

A.7.2.1 Interaction picture transformation

When treating a Hamiltonian of the form

$$H = H_0 + V$$

where H_0 is the bare system Hamiltonian and V is *perturbation*, a unitary transformation $U_0(t) = \exp[iH_0 t/\hbar]$ will modify the operators

$$V' = U_0 V U_0^\dagger,$$

in the rotated basis. Some useful identifies for qubit ($H_0 = H_\mathrm{q} = -\hbar\omega_q/2\sigma_z$) and resonator ($H_0 = H_r = \hbar\omega_r(a^\dagger a + 1)$) interaction picture operators:

$$
\begin{aligned}
a &\to U_0 a U_0^\dagger = e^{i\omega_r t a^\dagger a}\,[a]\,e^{-i\omega_r t a^\dagger a} = e^{-i\omega_r t} a,\\
a^\dagger &\to U_0 a^\dagger U_0^\dagger = e^{i\omega_r t} a^\dagger,\\
\sigma_- &\to U_0 \sigma_- U_0^\dagger = e^{i\omega_q t \sigma_z/2}\,[\sigma_-]\,e^{-i\omega_q t \sigma_z/2} = e^{-i\omega t}\sigma_-,\\
\sigma_+ &\to U_0 \sigma_+ U_0^\dagger = e^{i\omega t}\sigma_+.
\end{aligned}
\tag{A.7.5}
$$

A unitary transformation

$$U_0(t) = e^{iH_0 t/\hbar}, \tag{A.7.6}$$

applied to $H = H_0 + V$ using (A.7.4) simplifies the system by taking care of the *internal* dynamics (ones described by H_0) of the system

$$
\begin{aligned}
H' &= U_0 H U_0^\dagger - i\hbar U_0 \partial_t U_0{}^\dagger = U_0 H_0 U_0^\dagger + U_0 V U_0^\dagger - i\hbar U_0 \left(-i\frac{H_0}{\hbar} U_0^\dagger\right)\\
&= H_0 U_0 U_0^\dagger + U_0 V U_0^\dagger - H_0 U_0 U_0^\dagger\\
&= U_0 V U_0^\dagger.
\end{aligned}
\tag{A.7.7}
$$

The effect of this transformation is to transfer the time evolution from the original states $|\psi\rangle$ that would evolve uniteraly under the Schrödinger equation $H_0 |\psi(t)\rangle = i\hbar\partial_t |\psi(t)\rangle$ as

$$\frac{\partial_t |\psi(t)\rangle}{|\psi(t)\rangle} = \frac{-i}{\hbar} H_0 \qquad \Rightarrow \qquad |\psi(t)\rangle = |\psi(0)\rangle\, e^{-iH_0 t/\hbar} = U_0^\dagger |\psi(0)\rangle$$

into states that have no time dependence

$$|\psi'(t)\rangle = U_0 |\psi(t)\rangle = U_0^\dagger U_0 |\psi(0)\rangle = |\psi(0)\rangle$$

but whose operators now evolve as defined in (A.7.7)

$$
\begin{aligned}
\frac{d}{dt} V'(t) &= \partial_t[U_0] V U_0^\dagger + U_0 \partial_t[V] U_0^\dagger + U_0 V \partial_t[U_0^\dagger]\\
&= \frac{i}{\hbar} U (H_0 V - V H_0) U_0^\dagger + U_0 \partial_t[V] U_0^\dagger\\
&= U_0 \left[\frac{i}{\hbar}[H_0, V] + (\partial_t V)\right] U_0^\dagger.
\end{aligned}
\tag{A.7.8}
$$

A useful example is the time evolution of the creation and annihilation operators of the resonator with Hamiltonian $H_0 = \hbar\omega_r(a^\dagger a + 1)$. Applying unitary operator (A.7.6) translates one to the interaction picture, where the time evolution of operators a and $a^\dagger$ is evaluated using (A.7.7) and exponential matrices[23]

$$
\begin{aligned}
U_0 a U_0^\dagger &= e^{i\omega t a^\dagger a}\,[a]\,e^{-i\omega t a^\dagger a} \\
&= e^{i\omega t a^\dagger a}\left[\sum_n \sqrt{n}\,|n-1\rangle\,\langle n|\right]e^{-i\omega t a^\dagger a} \\
&= \sum_n \left[\sqrt{n}e^{i\omega t(n-1)}\,|n-1\rangle\,\langle n|\,e^{-i\omega t(n)}\right] \\
&= e^{-i\omega t}\sum_n \sqrt{n}\,|n-1\rangle\,\langle n| \\
&= e^{-i\omega t}a, \\
U_0 a^\dagger U_0^\dagger &= e^{i\omega t}a^\dagger.
\end{aligned}
$$

Likewise it can be done for qubit operators under a qubit Hamiltonian $H_0 = -\hbar\omega_q/2\sigma_z$

$$
\begin{aligned}
U_0\sigma_+U_0^\dagger &= e^{-i\frac{\omega t}{2}\sigma_z}\,[\sigma_+]\,e^{i\frac{\omega t}{2}\sigma_z} \\
&= \left(\cos\left(\frac{\omega t}{2}\right)\mathbb{I} - i\sin\left(\frac{\omega t}{2}\right)\sigma_z\right)\sigma_+\left(\cos\left(\frac{\omega t}{2}\right)\mathbb{I} + i\sin\left(\frac{\omega t}{2}\right)\sigma_z\right) \\
&= \begin{pmatrix} e^{-i\frac{\omega t}{2}} & 0 \\ 0 & e^{i\frac{\omega t}{2}} \end{pmatrix}\begin{pmatrix} 0 & 0 \\ 1 & 0 \end{pmatrix}\begin{pmatrix} e^{\frac{i\omega t}{2}} & 0 \\ 0 & e^{-i\frac{\omega t}{2}} \end{pmatrix} \\
&= e^{i\omega t}\sigma_+, \\
U_0\sigma_-U_0^\dagger &= e^{-i\frac{\omega t}{2}\sigma_z}\,[\sigma_-]\,e^{i\frac{\omega t}{2}\sigma_z} = e^{-i\omega t}\sigma_-.
\end{aligned}
$$

A.7.3 The master equation

The Schrödinger equation will not accurately describe a system's evolution under the presence of decoherence and requires a more general treatment. For this purpose the state of a 2-level system is represented with a density matrix

$$
\rho = \begin{pmatrix} \rho_{00} & \rho_{01} \\ \rho_{10} & \rho_{11} \end{pmatrix},
$$

which can be constructed from, but is not limited to, a pure quantum state $|\psi\rangle = \alpha|0\rangle + \beta|1\rangle$

$$
\rho = |\psi\rangle\,\langle\psi| = \begin{pmatrix} \alpha \\ \beta \end{pmatrix}\begin{pmatrix} \alpha^* & \beta^* \end{pmatrix} = \begin{pmatrix} |\alpha|^2 & \alpha\beta^* \\ \alpha^*\beta & |\beta|^2 \end{pmatrix},
$$

and can represent statistical state mixtures that appear in experimental conditions.

---

[23] See (A.7.2) for the σ_z exponential. For the number operator $e^{i\omega t a^\dagger a}\,|n\rangle = \sum_m[\frac{1}{m!}(i\omega t)^m(a^\dagger a)^m]\,|n\rangle = \sum_m[\frac{1}{m!}(i\omega t)^m(n)^m]\,|n\rangle = e^{i\omega t n}\,|n\rangle$.

The off-diagonal elements represent quantum coherence, while the diagonal elements (ρ_{ii}) represent the probability of finding the system in state $|i\rangle$. In order to describe a physical state the density matrix must satisfy

$$\begin{cases} \mathrm{Tr}\{\rho\} = 1, \\ \rho = \rho^\dagger. \end{cases}$$

Expectation values for an operator $\hat{A}$ are found by taking the trace $\mathrm{Tr}\left\{\rho\hat{A}\right\}$:

$$\begin{cases} \langle\sigma_z\rangle & = \mathrm{Tr}\left\{\begin{pmatrix} \rho_{00} & \rho_{01} \\ \rho_{10} & \rho_{11} \end{pmatrix} \begin{pmatrix} 1 & 0 \\ 0 & -1 \end{pmatrix}\right\} = \rho_{00} - \rho_{11}, \\ \langle\sigma_x\rangle & = \rho_{01} + \rho_{10}, \qquad \langle\sigma_y\rangle = i\rho_{01} - i\rho_{10}, \\ \langle\sigma_+\rangle & = \frac{\langle\sigma_x\rangle + i\langle\sigma_y\rangle}{2} = \rho_{10}, \qquad \langle\sigma_-\rangle = \frac{\langle\sigma_x\rangle - i\langle\sigma_y\rangle}{2} = \rho_{01}. \end{cases} \tag{A.7.9}$$

Evolution of the quantum state (ρ) under a Hamiltonian H is governed by the master equation

$$\partial_t\rho = -\frac{i}{\hbar}\Big[H, \rho\Big] + \mathcal{L}[\rho], \tag{A.7.10}$$

where

$$\mathcal{L}[\rho] = \begin{pmatrix} \Gamma_1\rho_{11} & -\Gamma_2\rho_{01} \\ -\Gamma_2\rho_{10} & -\Gamma_1\rho_{11} \end{pmatrix},$$

is the Linbland term that incorporates the dissipation elements of evolution, related to the relaxation $|1\rangle \to |0\rangle$ at a rate Γ_1 and decoherence of the off-diagonal elements at a rate Γ_2 (refer to Sec. 1.3).

A.7.3.1 Density matrix

The density matrix for a statistical ensemble of states $|\psi_j\rangle$ prepared with probabilities p_j is defined as

$$\rho = \sum_j p_j |\psi_j\rangle\langle\psi_j|, \tag{A.7.11}$$

and is able to describe the physical state of a system as a mixture of states that evolve ($p_j(0) \to p_j(t)$) over the course of an experiments due classical randomness and decoherence.

- ◎ From the form of (A.7.11) the hermiticity property of the density matrix can easily be seen

$$\rho = \rho^\dagger;$$

- The density matrix can be expressed in an orthornormal basis $\{|n\rangle\}$ as[24]

  $$\rho = \sum_{n,m} \rho_{nm} |n\rangle \langle m| , \qquad \rho_{nm} = \langle n| \rho |m\rangle,$$

  useful when dealing with matrix equations;

- Evolving under a Hamiltonian H, each of the states in (A.7.11) will undergo unitary transformation to $U(t) = \exp[-iHt/\hbar]$[25] and hence

  $$\begin{aligned} \rho(t) &= \sum_j p_j U(t) |\psi_j\rangle \langle \psi_j| U^\dagger \\ &= U(t)\rho(0)U^\dagger(t), \end{aligned} \tag{A.7.12}$$

  which defines the time evolution of the operator from initial state $\rho(0)$ much like in (A.7.7)

  $$\begin{aligned} \partial_t \rho(t) &= \partial_t (U^\dagger(t)\rho(0)U^\dagger(t) + U_0(t)\rho(0)\partial_t(U^\dagger(t)) \\ &= -\frac{i}{\hbar} \underbrace{HU(t)\rho(0)U^\dagger(t)}_{\rho(t) \text{ from (A.7.12)}} + \frac{i}{\hbar} HU(t)\rho(0)U^\dagger(t) \\ &= -\frac{i}{\hbar} [H, \rho(t)] , \end{aligned} \tag{A.7.13}$$

  and is called the von Neumann equation. A.7.3.4 will show how to generalise (A.7.13) to also involve decoherence in the system.

A.7.3.2 Getting expectation values from density matrix

Proof

For a system in a *pure* state $|\psi\rangle$ the expectation value of operator $\hat{A}$ is $\langle \hat{A} \rangle = \langle \psi| \hat{A} |\psi\rangle$. By taking the trace of $\hat{A}\rho$, with ρ defined in (A.7.11) and using its cyclic invariance property

$$\begin{aligned} \text{Tr}\left\{\hat{A}\rho\right\} &= \text{Tr}\left\{\sum_j p_j |\psi_j\rangle \langle \psi_j| \hat{A}\right\} \\ &= \sum_n \sum_j p_j |n\rangle |\psi_j\rangle \langle \psi_j| \hat{A} |n\rangle \\ &= \sum_j \langle \psi_j| \hat{A} \underbrace{\sum_n |n\rangle \langle n|}_{\mathbb{I}} |\psi_i\rangle \\ &= \sum_j p_j \langle \psi_j| \hat{A} |\psi_j\rangle , \end{aligned} \tag{A.7.14}$$

---

[24] Note that the basis does not need to coincide with states $|\psi_j\rangle$ in (A.7.11) - in fact they themselves can be represented in this basis $|\psi_j\rangle = \sum_n c_n |n\rangle$.

[25] This is the solution to the Schrödinger equation $H|\psi\rangle = i\hbar\partial_t |\psi\rangle \Rightarrow |\psi\rangle = |\psi(t=0)\rangle e^{-iHt/\hbar}$.

which is exactly the weighted sum of expectation values for each of the state *contributions* to the density matrix. QED ☐

A.7.3.3 Constrain on the trace

Proof

1. A measurement on the system can be represented by a collection of positive operators P_m which are associated with outcomes m and that satisfy the completeness relation

   $$\sum_m P_m = \mathbb{I},$$

   which ensures representation of every measurement outcome is accounted for, in direct analogy for how a basis of vectors $\sum_m |m\rangle\langle m| = \mathbb{I}$ allows the representation of every quantum state.

2. The probability of outcome m is given by (A.7.14)

   $$p_m = \mathrm{Tr}\{P_m\rho\}. \tag{A.7.15}$$

3. Summing up (A.7.15) should give unity

   $$\begin{aligned} 1 = \sum_m p_m &= \sum_m \mathrm{Tr}\{P_m\rho\} \\ &= \mathrm{Tr}\left\{ \underbrace{\sum_m P_m}_{\mathbb{I}} \rho \right\} = \mathrm{Tr}\{\rho\}. \end{aligned} \tag{A.7.16}$$

4. (A.7.16) ensures that the probabilities of all measurement outcomes sum up to 1 and can be used to eliminate a diagonal component when solving for the state of the system e.g. $\rho_{00} = 1 - \rho_{11}$.

QED ☐

A.7.3.4 Deriving the master equation

The following is one of the simpler ways to arrive at the master equation based on an algebraic argument presented in [266].

Proof

1. In parallel with the way that an operator maps one vector to another $|\psi'\rangle = \hat{O}\,|\psi\rangle$ a superoperator (S) maps one density matrix onto another

$$\rho' = S\big[\rho\big], \qquad S\big[\rho\big] = \sum_j K_j \rho K_j^\dagger, \qquad \sum_j K_j^\dagger K_j = \mathbb{I}, \tag{A.7.17}$$

where Kraus operators K_j are defined[26].

2. The task is to derive an evolution that returns the rate of change of the density matrix $\partial_t \rho(t)$ in analogy to the Schrödinger equation $i\hbar\partial_t\,|\psi\rangle = H|\psi\rangle$, under the Markovian assumption that evolution only depends on the immediate state of the system and has no *memory*.

   This can be expressed through the change over a small time interval δt

$$\rho(\delta t) = S\big[\rho(0)\big] = \sum_j K_j(\delta t)\rho(0)K_j^\dagger(\delta t), \tag{A.7.18}$$

which takes $\rho(0) \to \rho(\delta t)$ using only information on the current system state, and

$$\partial_t \rho(\delta t) = \lim_{\delta t \to 0} \frac{\rho(\delta t) - \rho(0)}{\delta t} \quad \Rightarrow \quad \rho(\delta t) = \rho(0) + \partial_t \rho(0)\delta t. \tag{A.7.19}$$

3. Expanding (A.7.18) with Kraus operators

$$K_j = \begin{cases} K_0 & = \mathbb{I} + \delta t A, \\ K_j & = \sqrt{\delta t} L_j, \end{cases}$$

where A and L_j are linear operators

$$\begin{aligned} \rho(\delta t) &= K_0 \rho(0) K_0^\dagger + \sum_{j=1}^{\infty} K_j(\delta t)\rho(0)K_j^\dagger(\delta t) \\ &= \big(\mathbb{I} + \delta t A\big)\rho(0)\big(\mathbb{I} + \delta t A^\dagger\big) + \delta t \sum_{j=1}^{\infty} L_j \rho(0) L_j^\dagger \\ &= \rho(0) + \delta t A\rho(0) + \delta t \rho(0) A^\dagger + \underbrace{\mathcal{O}(\delta t^2)}_{\approx 0} + \delta t \sum_{j=1}^{\infty} L_j \rho(0) L_j^\dagger \\ &= \rho(0) + \delta t \bigg(A\rho(0) + \rho(0)A^\dagger + \sum_{j=1}^{\infty} L_j \rho(0) L_j^\dagger \bigg). \end{aligned} \tag{A.7.20}$$

---

[26] For example, the probabilistic distribution of unitary evolutions seen in (A.7.12) $\rho(t) = \sum_j p_j U_j \rho(0) U_j^\dagger$ will have Kraus operators $K_j = \sqrt{p_j} U_j(t)$.

4. Equating (A.7.19) to (A.7.20)

$$\partial_t \rho(0) = A\rho(0) + \rho(0)A^\dagger + \sum_{j=1}^{\infty} L_j \rho(0) L_j^\dagger,$$

and because evolution is Markovian there is time transnational invariance

$$\partial_t \rho(t) = A\rho(t) + \rho(t)A^\dagger + \sum_{j=1}^{\infty} L_j \rho(t) L_j^\dagger.$$

5. Expressing linear operator A as a sum of Hermitian operators $H = H^\dagger, M = M^\dagger$

$$A = -\frac{i}{\hbar}H + M \qquad \Rightarrow \qquad K_0 = \mathbb{I} + \delta t\big(-\frac{i}{\hbar}H + M\big), \tag{A.7.21}$$

and requiring $\sum_j K_j^\dagger K_j = \mathbb{I}$ from (A.7.17)

$$\begin{aligned}
\mathbb{I} &= \sum_j K_j^\dagger K_j = \Big(\mathbb{I} + \delta t\big(+\frac{i}{\hbar}H + M\big)\Big)\Big(\mathbb{I} + \delta t\big(-\frac{i}{\hbar}H + M\big)\Big) + \sum_{j=1}^{\infty} \sqrt{\delta t} L_j^\dagger \sqrt{\delta t} L_j \\
&= \mathbb{I} + \delta t\big(+\frac{i}{\hbar}H + M\big) + \delta t\big(-\frac{i}{\hbar}H + M\big) + \underbrace{\mathcal{O}(\delta t^2)}_{\approx 0} + \delta t \sum_{j=1}^{\infty} L_j^\dagger L_j \\
&= \mathbb{I} + 2\delta t M + \delta t \sum_{j=1}^{\infty} L_j^\dagger L_j \\
\Rightarrow \qquad M &= -\frac{1}{2}\sum_{j=1}^{\infty} L_j^\dagger L_j.
\end{aligned} \tag{A.7.22}$$

6. Tying the results of (A.7.20), (A.7.21) and (A.7.22)

$$\begin{cases}
\partial_t \rho(t) = \Big(-\frac{i}{\hbar}H + M\Big)\rho(t) + \rho(t)\Big(+\frac{i}{\hbar}H + M\Big) + \sum_{j=1}^{\infty} L_j \rho(t) L_j^\dagger \\
\qquad\quad = -\frac{i}{\hbar}\,[H, \rho] + \mathcal{L}[\rho], \\
\mathcal{L}[\rho] = \sum_{j=1}^{\infty} \Big[L_j \rho L_j^\dagger - \frac{1}{2}\rho L_j^\dagger L_j - \frac{1}{2} L_j^\dagger L_j \rho\Big]
\end{cases} \tag{A.7.23}$$

which is the general form of the master equation, which is a modification of von Neumann's equation (A.7.13) by the Linbland term ($\mathcal{L}[\rho]$) that section A.7.3.5 connects to irreversible dynamics from environmental coupling.

The whole premise of the proof comes from a heuristic constraints that evolution is Markovian, which necessitates the additional trailing terms to *mask* the system's history. A more complex but physical argument based on interaction of the system with a dissipative environment is given in [257].

QED □

A.7.3.5 Adding decoherence dynamics to master equation

With operators L_j of the Linbland term in (A.7.23) already fulfilling the Markovian condition Step 2, one has the liberty of defining them in a way that would represent the expected decoherence dynamics introduced Sec. 1.3.2 - they are thus called *jump* operators.

- **Depolarisation** from the excited to ground state is associated with $\sigma_- = |g\rangle\langle e|$ with characteristic rate Γ_1, motivating the jump operator definition $L = \sqrt{\Gamma}\sigma_-$. Substituting into ✥ of (A.7.23) for a two level system this leads to a dissipation term

  $$\mathcal{L}[\rho] = \begin{array}{c c} & \begin{array}{cc} |g\rangle & |e\rangle \end{array} \\ \begin{array}{c} \langle g| \\ \langle g| \end{array} & \begin{bmatrix} \Gamma_1\rho_{11} & -\frac{\Gamma_1}{2}\rho_{01} \\ -\frac{\Gamma_1}{2}\rho_{10} & -\Gamma_1\rho_{11} \end{bmatrix} \end{array}, \tag{A.7.24}$$

  which describes the gradual relaxation dynamic $|e\rangle \to |g\rangle$ but also the decay of the off-diagonal elements, the effect of which is shown clearly in Fig. A.5 (b) as the system loses phase information;

- **Photon relaxation** is defined in the same way as depolarisation with $L = \sqrt{\kappa}a$ leading to a dissipation term

  $$\mathcal{L}[\rho] = \kappa\left(a\rho a^\dagger - \frac{1}{2}a^\dagger a\rho - \frac{1}{2}\rho a^\dagger a\right). \tag{A.7.25}$$

- **Pure dephasing** is a result of fluctuations in the transition energy ($\delta E = \hbar\delta\omega(t)$) that leads to a randomised phase accumulation during unitary evolution of the system

  $$U(t) = U_0(t)e^{i\delta\varphi(t)}, \quad \delta\varphi(t) = \int_0^t d\tau\delta\omega(\tau),$$

  and which on average produces a decay (refer to Sec. 1.3.2 and A.2.7) with characteristic rate Γ_φ

  $$\left\langle e^{i\delta\varphi(t)}\right\rangle = e^{-\Gamma_\varphi^2 t^2} \sim e^{-\Gamma_\varphi t}.$$

  Thus a 2-level system prepared in superposition state $(|g\rangle + |e\rangle)/\sqrt{2}$ evolving with

$U_0 = \exp[-i\omega_q t\sigma_z]$ (see (A.7.2) for expansion)

$$\begin{aligned}|\psi(t)\rangle &= U(t)\left(\frac{|g\rangle + |e\rangle}{\sqrt{2}}\right)\\ &= \frac{1}{\sqrt{2}}e^{-\Gamma_\varphi t}\begin{pmatrix} e^{-i\omega_q t} & 0 \\ 0 & e^{i\omega_q t}\end{pmatrix}\begin{pmatrix}1\\1\end{pmatrix}\\ &= \frac{1}{\sqrt{2}}e^{-\Gamma_\varphi t}\left(e^{-i\omega_q t}|g\rangle + e^{i\omega_q t}|e\rangle\right),\end{aligned}$$

which is simply the damped oscillations between states $|e\rangle$ and $|g\rangle$. The density matrix

$$\rho(t) = |\psi(t)\rangle\langle\psi(t)| = \frac{1}{2}e^{-2\Gamma_\varphi t}\begin{array}{c} \\ \langle g| \\ \langle e| \end{array}\begin{array}{c}\begin{array}{cc} |g\rangle & |e\rangle \end{array}\\ \left[\begin{array}{cc} 1 & e^{-2i\omega_q(t)} \\ e^{2i\omega_q(t)} & 1 \end{array}\right]\end{array}, \tag{A.7.26}$$

is constrained to the Tr $\{\rho\} = 1$ condition from A.7.3.3. Therefore applying the decay only on the off-diagonal terms in (A.7.26)

$$\rho(t) = \frac{1}{2}\begin{array}{c} \\ \langle g| \\ \langle e| \end{array}\begin{array}{c}\begin{array}{cc} |g\rangle & |e\rangle \end{array}\\ \left[\begin{array}{cc} 1 & e^{-2\Gamma_\varphi t}e^{-2i\omega_q(t)} \\ e^{-2\Gamma_\varphi t}e^{2i\omega_q(t)} & 1 \end{array}\right]\end{array}. \tag{A.7.27}$$

A Linbland operator creating the decay dynamics in (A.7.27), is related to energy fluctuations $L = \sqrt{\Gamma_\varphi/2}\sigma_z$. which leads to a dissipation term

$$\mathcal{L}[\rho] = \begin{array}{c} \\ \langle g| \\ \langle g| \end{array}\begin{array}{c}\begin{array}{cc} |g\rangle & |e\rangle \end{array}\\ \left[\begin{array}{cc} 0 & -\Gamma_\varphi\rho_{01} \\ -\Gamma_\varphi\rho_{10} & 0 \end{array}\right]\end{array}, \tag{A.7.28}$$

that recovers the decaying off diagonal dynamics $\partial_t\rho_{10}(t) = -\Gamma_\varphi\rho_{10}(t)$ in (A.7.27).

A.7.3.6 Decoherence in specific systems

◎ For the qubit, combining (A.7.28), (A.7.24) results in a decoherence term

$$\mathcal{L}_q[\rho] = \begin{pmatrix} \Gamma_1\rho_{11} & -\Gamma_2\rho_{01} \\ -\Gamma_2\rho_{10} & -\Gamma_1\rho_{11}\end{pmatrix}, \qquad \Gamma_2 = \Gamma_\varphi + \frac{\Gamma_1}{2},$$

where the decay of the diagonal terms from depolarisation and dephasing is labelled Γ_2 (introduced this time more mathematically than in (1.3.4));

◎ For a qubit-resonator system, combining (A.7.28), (A.7.25), (A.7.24) one gets the decoherence term

$$\begin{aligned} L_{q-r}[\rho] = {} & \kappa\left(a\rho a^{\dagger} - \frac{1}{2}a^{\dagger}a\rho - \frac{1}{2}\rho a^{\dagger}a\right) \\ & + \Gamma_1\left(\sigma^{-}\rho\sigma^{+} - \frac{1}{2}\sigma^{+}\sigma^{-}\rho - \frac{1}{2}\rho\sigma^{+}\sigma^{-}\right) \\ & + \frac{\Gamma_{\varphi}}{2}\left(\sigma_z\rho\sigma_z - \rho\right). \end{aligned} \tag{A.7.29}$$

A.7.4 Perturbation theory

A small time dependent perturbation $\hat{v} = \lambda\hat{V}, \lambda \ll 1$ applied to system with Hamiltonian H_0

$$H(t) = H_0 + \lambda\hat{V}(t).$$

leads to an evolution of an initial state

$$|i\rangle \quad \rightarrow \quad |i\rangle + \sum_n c_n^{(1)}(t)\,|n\rangle$$

which is expanded in the eigenstate basis $\{|n\rangle\}$ of H_0 and where the coefficients are

$$c_i^{(1)}(t) = \frac{1}{i\hbar}\int_0^t dt\;\hat{V}_{ii}(\tau), \qquad c_n^{(1)}(t) = \frac{1}{i\hbar}\int_0^t d\tau\;\left[\hat{V}_{ni}(\tau)e^{i\omega_{ni}\tau}\right], \qquad \hat{V}_{ni} = \langle n|\,\hat{V}\,|n\rangle\,.$$

Proof

1. The state at an arbitrary time is expanded out in the basis of the eigenstate of H_0

$$\begin{aligned} |\psi(t)\rangle_I &= \sum_n c_n(t)\,|n\rangle && \text{interaction picture - operator evolves,} \\ |\psi(t)\rangle_S &= \sum_n c_n(t)\exp\left[\frac{-iE_n\hbar}{t}\right]|n\rangle && \text{Schrodinger picture - state evolves.} \end{aligned} \tag{A.7.30}$$

2. Solving the Schrödinger equation in the interaction picture (refer to Sec. A.7.2.1)

$$i\hbar\partial_t\,|\psi(t)\rangle_I = \left(U_0\lambda\hat{V}(t)U_0^{\dagger}\right)|\psi(t)\rangle_I\,,$$

and substituting in (A.7.30)

$$i\hbar\partial_t\left[\sum_n c_n(t)\,|n\rangle\right] = \left(U_0^{\dagger}\lambda\hat{V}(t)U_0\right)\left[\sum_k c_k(t)\,|k\rangle\right]. \tag{A.7.31}$$

3. Taking out the time dependent terms in (A.7.31) and separating out an arbitrary state component $|m\rangle$

$$\begin{aligned}\sum_j \partial_t c_m(t)\,\langle m|n\rangle &= \frac{\lambda}{i\hbar}\sum_k \left(\langle m|\,U_0\right)\hat{V}(t)c_k(t)\left(U_0^\dagger\,|k\rangle\right)\\ \Rightarrow \qquad \sum_j \partial_t c_m(t)\;\delta_{mj} &= \frac{\lambda}{i\hbar}\sum_k \left(\langle m|\,e^{iE_m t/\hbar}\right)\hat{V}(t)c_k(t)\left(e^{-iE_k t/\hbar}\,|k\rangle\right),\end{aligned} \tag{A.7.32}$$

where the application of unitary operator U_0 to one of the basis state is used

$$U_0\,|m\rangle = e^{iH_0 t/\hbar}\,|m\rangle = \sum_n \frac{1}{n!}\left(\frac{iH_0 t}{\hbar}\right)^n |m\rangle = \sum_n \frac{1}{n!}\left(\frac{iE_m t}{\hbar}\right) b^n\,|m\rangle = e^{iE_m t/\hbar}\,|m\rangle\,.$$

4. Simplifying (A.7.32) further

$$\begin{aligned}\partial_t c_m(t) &= \frac{\lambda}{i\hbar}\sum_k c_k(t)e^{i(E_m-E_k)t/\hbar}\,\langle m|\,\hat{V}(t)\,|k\rangle\\ &= \frac{\lambda}{i\hbar}\sum_k c_k(t)e^{i(E_m-E_k)t/\hbar}\,\left\langle \hat{V}(t)\right\rangle_{mk}.\end{aligned} \tag{A.7.33}$$

5. Expanding the $c_m(t)$ as a power series of the small parameter λ quantifying the perturbation:

$$c_m(t) = c_m^{(0)}(t) + \lambda c_m^{(1)}(t) + \mathcal{O}(\lambda^2), \tag{A.7.34}$$

and comparing (A.7.33) with (A.7.34) for equal powers of λ:

(a)

$$\lambda^0 \qquad \rightarrow \qquad \partial_t c_m^{(0)}(t) = 0,$$

and so $c_m^{(0)}$ doesn't change - the system remains in the state $|i\rangle$ before any perturbation ($\lambda = 0$) was applied

$$c_m^{(0)}(t) = \text{ constant } = \langle m|i\rangle = \delta_{m,i}. \tag{A.7.35}$$

(b)

$$\begin{aligned}\lambda^1 \qquad \rightarrow \qquad \partial_t c_m^{(1)}(t) &= \frac{1}{i\hbar}\sum_k c_k^{(0)}(t)e^{i\omega_{mk}t}\left\langle \hat{V}(t)\right\rangle_{mk}\\ &= \frac{1}{i\hbar}\sum_k \delta_{k,i}e^{i\omega_{mk}t}\left\langle \hat{V}(t)\right\rangle_{mk}\\ &= \frac{1}{i\hbar}e^{i\omega_{mi}t}\left\langle \hat{V}(t)\right\rangle_{mi},\end{aligned}$$

which upon integration gives

$$\begin{aligned} c_i^{(1)}(t) &= \frac{1}{i\hbar}\int_0^t d\tau\ \hat{V}_{ii}(\tau) \\ c_m^{(1)}(t) &= \frac{1}{i\hbar}\int_0^\tau d\tau\left[\hat{V}_{mi}(\tau)e^{i\omega_{mi}\tau}\right]. \end{aligned} \tag{A.7.36}$$

6. Collecting up (A.7.35),(A.7.36) in (A.7.34) and (A.7.30) gives the state of the system at time t after the perturbation is introduced to first order in λ

$$\begin{aligned} |\psi(t)\rangle_I &= \sum_n c_n(t)\,|n\rangle \\ &= \sum_n \left[\delta_{n,i} + c_n^{(1)}(t)\right]|n\rangle \\ &= |i\rangle + \sum_n c_n^{(1)}(t)\,|n\rangle\,. \end{aligned}$$

QED □

A.7.5 Comment on Poisson brackets

In classical mechanics, the Poisson bracket of two function $F(q,p), G(q,p)$ under generalised coordinates q, p is defined to be

$$\{F,G\}_{qp} = \frac{\partial F}{\partial q}\frac{\partial G}{\partial p} - \frac{\partial F}{\partial p}\frac{\partial G}{\partial q} \tag{A.7.37}$$

and describes how a quantity F changes under a transformation generated by quantity G - the trajectory parameter. This can be seen by differentiating the quantity $F(q,p,t)$ with respect to time and using the equations of motion $\partial_t q = \partial H/\partial p, \partial_t p = -\partial H/\partial q$ from the system's Hamiltonian $H(q,p)$

$$\begin{aligned} \frac{d}{dt}F(q,p,t) &= \frac{\partial F}{\partial q}\partial_t q(t) + \frac{\partial F}{\partial p}\partial_t p(t) + \partial_t F \\ &= \{F,H\}_{qp} + \partial_t F. \end{aligned} \tag{A.7.38}$$

Some instructive examples:

◎ In the case that $F = q$ evaluation of (A.7.38) gives

$$\frac{dq}{dt} = \{q,H\}_{qp},$$

describing how the Hamiltonian results in an translation of the generalised coordinate q - time t being the trajectory parameter.

- In the case that $F = x, G = p$ evaluation of (A.7.37) gives

  $$\{x, p\} = \frac{\partial x}{\partial x}\frac{\partial p}{\partial p} - 0 = 1, \tag{A.7.39}$$

  describing how p generates a translation in x. In quantum mechanics the equivalent relation between $\hat{x}$ and $\hat{p} = -i\frac{\partial}{\partial x}$ is

  $$[\hat{x}, \hat{p}] = i\hbar, \tag{A.7.40}$$

  and Dirac [267] extended the analogy between (A.7.39) and (A.7.40)[27] to state that any classical variables can be quantised with their Poisson brackets defining the quantum commutation relation

  $$\{A, B\} \to -i\hbar[\hat{A}, \hat{B}]. \tag{A.7.41}$$

  (A.7.41) is used to quantise the classical charge (Q) and flux (Φ) with Poisson brackets $\{Q, \Phi\} = 1$ (refer to A.3.2) under the constraint that they occur on the same coordinate

  $$[\hat{Q}(x), \hat{\Phi}(x)] = i\hbar\partial(x - x\prime).$$

- In quantum mechanics, the equivalent to the time evolution in (A.7.38) is the time evolution of an operator already seen in (A.7.8)

  $$\frac{d\hat{f}}{dt} = -\frac{i}{\hbar}\left[\hat{f}, H\right] + \partial_t \hat{f}.$$

---

[27] This was later shown to be non-general.

A.8 Generic maths formalism

A.8.1 Fourier transform definition

The following definition is used for FTs in this thesis

$$\begin{cases} f(\omega) = \mathcal{F}[f(t)] = \displaystyle\int_{-\infty}^{\infty} dt \Big[f(t) \times e^{-i\omega t} \Big], \\ f(t) = \mathcal{F}_{\text{inv}}[f(\omega)] = \displaystyle\int_{-\infty}^{\infty} \frac{d\omega}{2\pi} \Big[f(\omega) e^{i\omega t} \Big], \end{cases} \tag{A.8.1}$$

and the FT of the delta function

$$2\pi\delta(\omega - \omega') = \int_{-\infty}^{\infty} dt\, e^{-i(\omega-\omega')t}, \qquad 2\pi\delta(t - t') = \int_{-\infty}^{\infty} d\omega\, e^{-i\omega(t-t')}. \tag{A.8.2}$$

A.8.1.1 Regular Fourier transform (FT)

Forward ($\mathcal{F}$) and inverse ($\mathcal{F}_{\text{inv}}$) FTs between the frequency-time pair (f, t) are defined as

$$f(f) = \mathcal{F}[f(t)] = \int_{-\infty}^{\infty} dt \Big[f(t) e^{-i2\pi f t} \Big], \qquad f(t) = \mathcal{F}_{\text{inv}}[f(f)] = \int_{-\infty}^{\infty} df \left[f(f) e^{i2\pi f t} \right], \tag{A.8.3}$$

(analogous expressions exist for the $(x, 1/\lambda)$ pair). If the 2π factor in the exponential is *absorbed* into $\omega = 2\pi f$ or $k = 2\pi/\lambda$ this changes the units of the transformation domains - if f was measured in inverse seconds it now becomes the angular frequency. This necessitates a change of variables $df = d\omega/2\pi$ which modifies the inverse transform of (A.8.3)

$$f(\omega) = \mathcal{F}[f(t)] = \int_{-\infty}^{\infty} dt \Big[f(t) e^{-i\omega t} \Big], \qquad f(t) = \mathcal{F}_{\text{inv}}[f(\omega)] = \frac{1}{2\pi} \int_{-\infty}^{\infty} df \left[f(f) e^{i2\omega t} \right], \tag{A.8.4}$$

which has an alternative symmetrical definition

$$\begin{aligned} f(\omega) = \mathcal{F}[f(t)] &= \frac{1}{\sqrt{2\pi}} \int_{-\infty}^{\infty} dt \Big[f(t) \times e^{-i\omega t} \Big], \\ f(t) = \mathcal{F}_{\text{inv}}[f(\omega)] &= \frac{1}{\sqrt{2\pi}} \int_{-\infty}^{\infty} d\omega \Big[f(\omega) e^{i\omega t} \Big], \end{aligned}$$

that saves one having to figure out whether the forward or inverse transform is being executed.

A.8.1.2 Delta function Fourier transform (FT)

Proof

1. The delta function is characterised by the following properties

$$\int_{-\infty}^{\infty} dx\,\delta(x-y) = 1, \qquad \int_{-\infty}^{\infty} dx\,f(x)\delta(x-y) = f(y). \tag{A.8.5}$$

2. To define its FT, combine the forward and inverse FTs of (A.8.4)

$$\begin{aligned} f(\omega') &= \mathcal{F}\left[\mathcal{F}_{\text{inv}}[f(\omega')]\right] \\ &= \frac{1}{2\pi}\int_{-\infty}^{\infty} dt \int_{-\infty}^{\infty} d\omega \left[f(\omega)e^{i\omega t}e^{-i\omega' t}\right] \\ &= \frac{1}{2\pi}\int_{-\infty}^{\infty} d\omega\, f(\omega)\int_{-\infty}^{\infty} dt\, e^{i(\omega-\omega')t}. \end{aligned} \tag{A.8.6}$$

3. Comparing the definition of the delta function (A.8.5) to (A.8.6)

$$\begin{cases} f(\omega') = \dfrac{1}{2\pi}\displaystyle\int_{-\infty}^{\infty} d\omega\, f(\omega)\int_{-\infty}^{\infty} dt\, e^{i(\omega-\omega')t} \\ f(\omega') = \displaystyle\int_{-\infty}^{\infty} d\omega\, \left[f(\omega)\delta(\omega-\omega')\right] \end{cases} \Rightarrow \delta(\omega-\omega') = \frac{1}{2\pi}\int_{-\infty}^{\infty} dt\, e^{-i(\omega-\omega')t},$$

and similarly

$$\delta(t-t') = \frac{1}{2\pi}\int_{-\infty}^{\infty} d\omega\, e^{-i\omega(t-t')}.$$

QED ☐

A.8.2 Wiener-Khinchin theorem for evaluating power spectral density

The Wiener-Khinchin theorem relates power spectral density of a voltage signal ($V(t)$) in an environment with impedance Z [268, 269]

$$S(\omega) = \frac{1}{Z}\int_{-\infty}^{\infty} dt\left[\langle V(t)V^*(0)\rangle\, e^{-i\omega t}\right] \equiv \frac{1}{Z}\mathcal{F}[\langle V(t)V^*(0)\rangle]. \tag{A.8.7}$$

to the FT of the autocorrelation function of the signal $\langle V(t)V^*(0)\rangle$. A signal with a very short correlation $\langle V(t)V^*(0)\rangle \sim \delta(t)$ produces white noise at all frequencies, while correlated (more periodic) signals will have a more concentrated power spectrum.

The inverse relation is

$$\frac{1}{Z}\langle V(t)V^*(0)\rangle = \mathcal{F}_{\text{inv}}[S(\omega)] = \int_{-\infty}^{\infty} \frac{d\omega}{2\pi}\left[S(\omega)e^{i\omega t}\right].$$

Proof

1. Begin by taking a windowed FT of the signal (refer to (A.8.1))

$$X(\omega) = \int_{-T/2}^{T/2} d\tau \Big[V(\tau) e^{-i\omega\tau} \Big],$$

where one limits the observation time (T) to avoid convergence issues. Correspondingly the instantaneous power V^2/Z, where Z is the impedance of the environment, will be

$$\frac{1}{Z}|X(\omega)|^2 = \frac{1}{T}\frac{1}{Z}\int_{-T/2}^{T/2}\int_{-T/2}^{T/2} d\tau_1\, d\tau_2 \left[V(\tau_1)V^*(\tau_2)e^{-i\omega(\tau_1-\tau_2)} \right], \tag{A.8.8}$$

normalised over the time period (T).

2. Taking the expectation value of (A.8.8) to find the expected power

$$S(\omega) = \frac{1}{Z}\langle XX^*\rangle = \frac{1}{T}\frac{1}{Z}\int_{-T/2}^{T/2}\int_{-T/2}^{T/2} d\tau_1\, d\tau_2 \left[\langle V(\tau_1)V^*(\tau_2)\rangle\, e^{-i\omega(\tau_1-\tau_2)} \right],$$

and performing a change of variables $t = \tau_1 - \tau_2$ and $\tau = \tau_1 + \tau_2$ (refer to Sec. A.8.6)

$$S(\omega) = \frac{1}{T}\frac{1}{Z}\frac{1}{2}\int_{-T}^{T} dt \left[\underbrace{\left\langle V(\frac{\tau+t}{2})V^*(\frac{\tau-t}{2})\right\rangle}_{\text{✥}} e^{-i\omega t}\,(2T - 2|t|) \right], \tag{A.8.9}$$

3. Under assumptions:

   - That the signal has a correlation function that is time-translation invariant (stationary), allowing to shift the arguments in ✥ (A.8.9) to only depend on the time difference $(\tau+t)/2 - (\tau-t)/2 = t$;
   - Take the long time limit $T \to \infty$ to produce a more representative spectrum,

   (A.8.9) can be simplified to relate $S(\omega)$ directly to the correlation function through a FT defined in (A.8.1)

$$\lim_{T\to\infty} S(\omega) = \frac{1}{Z}\int_{-\infty}^{\infty} dt \Big[\langle V(t)V^*(0)\rangle\, e^{-i\omega t} \Big] \equiv \frac{1}{Z}\mathcal{F}[\langle V(t)V^*(0)\rangle].$$

4. This can be repeated in the other direction by taking an inverse FT

$$\frac{1}{Z}\langle V(t)V^*(0)\rangle = \mathcal{F}_{\text{inv}}[S(\omega)] = \int_{-\infty}^{\infty}\frac{d\omega}{2\pi}\Big[S(\omega)e^{i\omega t} \Big].$$

QED □

A.8.3 Lorentzian fit

A Lorentzian is a fit to a function of the form

$$L(x) = L_0 \frac{1}{\pi} \frac{(\frac{1}{2}\Delta)^2}{\left(\frac{1}{2}\Delta\right)^2 + (x - x_0)^2} = \frac{2L_0}{\pi\Delta} \frac{1}{1 + (\frac{2dx}{\Delta})^2}, \tag{A.8.10}$$

with an amplitude

$$V_{\max} = \frac{2}{\pi\Delta} L_0 = \frac{2L_0T}{\pi},$$

and Full width at half maximum (FWHM)

$$\begin{aligned} \text{FWHM} &= \Delta \qquad \text{(x-scale)} \\ &= \frac{2\pi}{T} \qquad (\omega\text{-scale}). \end{aligned}$$

A.8.4 Fourier transform of exponential decay

The FT of a complex decay

$$V(t) = V_0 e^{i\omega_q t} e^{-|t|/\Gamma},$$

where an exponential decay at rate Γ *envelopes* a fast oscillating signal ω_q is

$$V(\omega) = V_0 \frac{\Gamma}{\Gamma^2 + (\omega - \omega_q)^2},$$

which is a Lorentzian (see (A.8.10)) with a FWHM $\Delta = 2\Gamma$. This is a trivial, yet useful result, as software such as `Mathematica` does not always perform symbolic transforms correctly without additional constraints.

Proof

1. The standard FT from (A.8.1) is applied

$$\begin{aligned} V(\omega) &= \mathcal{F}\Big[V(t)\Big] \\ &= \int_{-\infty}^{\infty} dt \Big[V_0 e^{i\omega_q t} e^{-|t|\Gamma} e^{-i\omega t}\Big] \\ &= V_0 \int_0^{\infty} dt \bigg[e^{-t\Gamma}\bigg(\cos((\omega - \omega_q)t) - i\sin((\omega - \omega_q)t)\bigg)\bigg] \\ &+ \int_{-\infty}^{0} dt \bigg[e^{-t\Gamma}\bigg(\cos((\omega - \omega_q)t) - i\sin((\omega - \omega_q)t)\bigg)\bigg]. \end{aligned}$$

2. Performing a change of variables $t = -y$ so that $dt = -dy$ in second integral

$$\begin{aligned}
V(\omega) = V_0 \int_0^\infty e^{-t\Gamma} \Big[\cos((\omega-\omega_q)t) - i\sin((\omega-\omega_q)t) \Big] dt \\
- \int_\infty^0 e^{-y\Gamma} \Big[\cos((\omega-\omega_q)y) + i\sin((\omega-\omega_q)y) \Big] dy \\
= V_0 \int_0^\infty e^{-t\Gamma} \Big[\cos((\omega-\omega_q)t) - i\sin((\omega-\omega_q)t) \Big] dt \\
+ \int_0^\infty e^{-t\Gamma} \Big[\cos((\omega-\omega_q)t) + i\sin((\omega-\omega_q)t) \Big] dt \\
= V_0 \int_0^\infty \cos((\omega-\omega_q)t) e^{-t\Gamma} dt.
\end{aligned}$$

3. This is a standard integral, with solution

$$\begin{aligned}
\mathcal{I} &= \int_0^\infty \cos(ax) e^{-bx} dx \\
&= \frac{1}{a}\sin(ax)e^{-bx}|_0^\infty + \frac{b}{a}\int_0^\infty \sin(ax)e^{-bx}dx \\
&= \frac{b}{a}\left[\frac{-\cos(ax)}{a} e^{-bx}|_0^\infty - \frac{b}{a}\mathcal{I} \right] = \frac{b}{a^2} - \frac{b^2}{a^2}\mathcal{I} \\
&\Rightarrow \mathcal{I} = \frac{b}{a^2+b^2},
\end{aligned}$$

resulting in

$$V(\omega) = V_0 \frac{\Gamma}{\Gamma^2 + (\omega-\omega_q)^2}.$$

QED □

A.8.5 Distortion of exponential decay by VNA

The Vector Network Analyser (VNA) does not measure instantaneous voltage

$$V(t) = Ae^{-t\Gamma}\cos(\omega t),$$

of a decaying signal, but instead evaluates the mean signal accumulated in a window of width T

$$\begin{aligned}
V_{\text{VNA}}(t)\frac{1}{T}\int_{t-T/2}^{t+T/2} d\tau V(\tau) &= \int_{t-T/2}^{t+T/2} Ae^{-t\Gamma}\cos(\omega t) \\
&= \frac{A}{T}\frac{e^{-\tau\Gamma}(\omega\sin(\tau\omega) - \Gamma\cos(\tau\omega))}{\Gamma^2+\omega^2}\Bigg|_{t-T/2}^{t+T/2}.
\end{aligned}$$

The raw decay signal and *windowed* signal are plotted in Fig. A.12 - the shape and characteristic time of decay remains the same, with the *windowed* signal only adding a phase shift and an amplitude boost proportional to its length T.

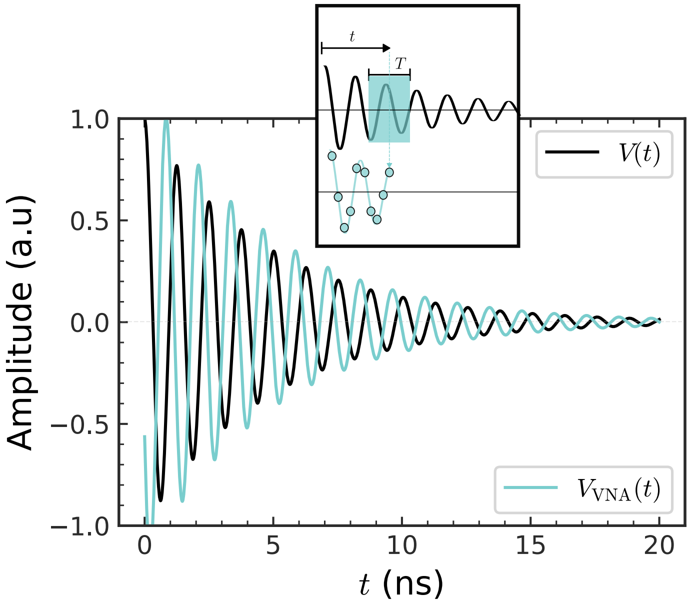

Figure A.12: Raw decay signal from a qubit (black) and the windowed signal that is measured experimentally on the VNA (blue). The plots are performed with $\Gamma/2\pi = 1/30\,\mathrm{ns}$, $\omega = 5\,\mathrm{GHz}$ and readout window $T = 40\,\mathrm{ns}$. The decay measured by the VNA will mirror the profile of the real signal that it average over. Inset shows how the readout window of width T is swept across the qubit signal - the average value at each position (t) is mapped to a single $V_{\mathrm{VNA}}(t)$ point.

A.8.6 Change of integration limits

Proof

1. The two dimensional integral

$$I = \int_{-T/2}^{T/2}\int_{-T/2}^{T/2} d\tau_1\, d\tau_2 \left[\langle V(\tau_1)V(\tau_2)\rangle\, e^{-i\omega(\tau_1-\tau_2)}\right], \tag{A.8.11}$$

has a domain of integration is depicted in Fig. A.13 (a).

2. Because the integrand is constant along the contours $\tau_1 - \tau_2$ (see the dotted line) a convenient change of variables is performed

$$\begin{cases} t = \tau_1 - \tau_2, \\ \tau = \tau_1 + \tau_2, \end{cases} \Rightarrow \begin{pmatrix} t \\ \tau \end{pmatrix} = \begin{pmatrix} 1 & -1 \\ 1 & 1 \end{pmatrix} = \begin{pmatrix} \tau_1 \\ \tau_2 \end{pmatrix}. \tag{A.8.12}$$

3. Transformation (A.8.12) is a rotation that moves points A, B, C, D and changes the domain of integration as shown in Fig. A.13. The Jacobian factor responsible for the

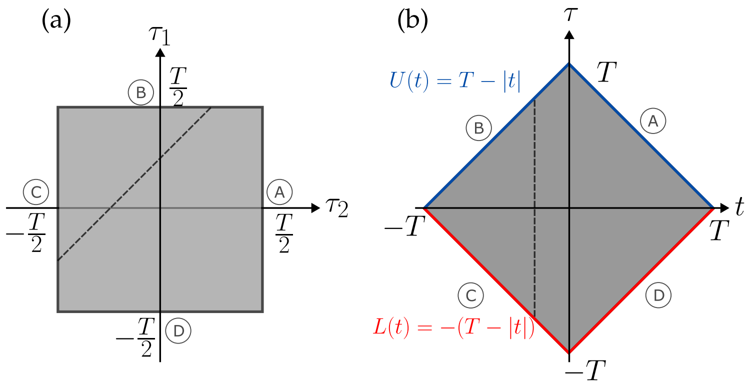

Figure A.13: Domains of integration: **(a)** Original domain; **(b)** Under new coordinate system, showing the upper ($U(t)$) and lower ($L(t)$) integration limits.

change of area occurring during the transformation is

$$J = \begin{bmatrix} \partial\tau_1/\partial t & \partial\tau_1/\partial\tau \\ \partial\tau_2/\partial t & \partial\tau_2/\partial\tau \end{bmatrix} = 2.$$

4. Therefore integral (A.8.11) is rewritten

$$\begin{aligned} I &= \frac{1}{J}\int_{L(\tau)}^{U(\tau)} d\tau \int_{-T}^{T} dt \left[\left\langle V\left(\frac{\tau+t}{2}\right) V^*\left(\frac{\tau-t}{2}\right)\right\rangle e^{-i\omega t}\right] \\ &= \frac{1}{2}\int_{-T}^{T} dt \left[\left\langle V\left(\frac{\tau+t}{2}\right) V^*\left(\frac{\tau-t}{2}\right)\right\rangle e^{-i\omega t}\left(\int_{L(t)}^{U(t)} d\tau\right)\right] \\ &= \frac{1}{2}\int_{-T}^{T} dt \left[\left\langle V\left(\frac{\tau+t}{2}\right) V^*\left(\frac{\tau-t}{2}\right)\right\rangle e^{-i\omega t}\left(2T - 2|t|\right)\right]. \end{aligned}$$

QED □

Appendix B

Appendix fabrication

B.1 Lithography basics

All sample fabrication is performed in clean room facilities at Royal Holloway University of London. We use processes to pattern the surface of a wafer, and etch or deposit material through the pattern to define a layer of the structure. Multiple repetitions of this build up the device on a Silicon (Si) wafer, in a procedure known as lithography.

Recipes B.4, B.5, B.6 that describe the fabrication of the qubits studied in this thesis make reference to common lithographical terms and procedures which are summarised in this appendix with reference to Fig. B.1.

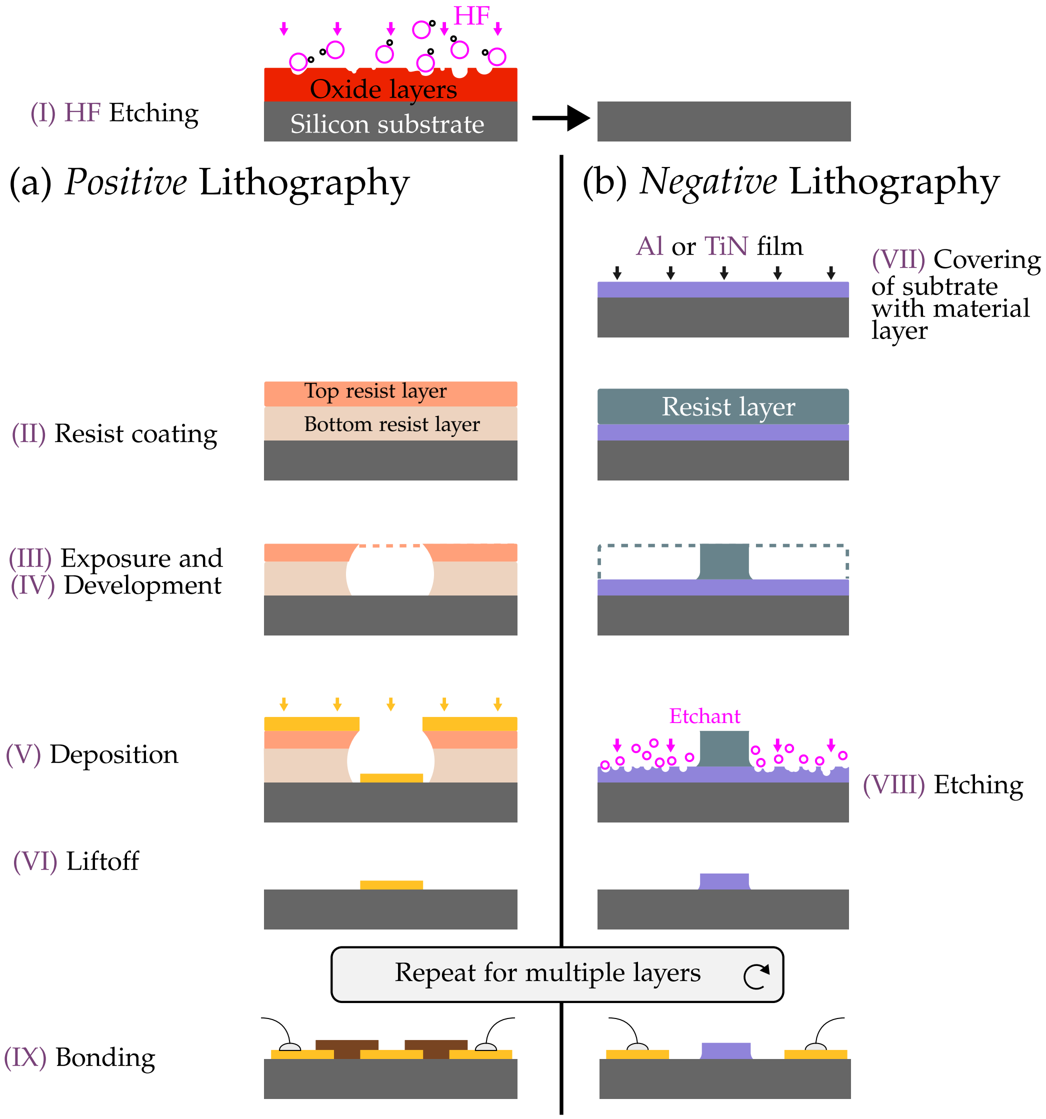
HF
(I) HF Etching
Oxide layers
Silicon substrate
(a) *Positive* Lithography
(b) *Negative* Lithography
Al or TiN film
(VII) Covering of subtrate with material layer
(II) Resist coating
Top resist layer
Bottom resist layer
Resist layer
(III) Exposure and
(IV) Development
(V) Deposition
Etchant
(VIII) Etching
(VI) Liftoff
Repeat for multiple layers
(IX) Bonding

Figure B.1: Summary of possible procedures for the fabrication of multi-layered structures on Si wafers, with equivalent steps using **(a)** positive and **(b)** negative lithography shown side by side.

B.1.1 Hydrogen fluoride (HF) etching: (I) in Fig. B.1

A big contributor to decoherence are oxides residing on the surface of the Si wafers (see Sec. 1.3.3) with a thickness of a few nanometers. It has been taken as a rule that every fabrication begins with a wafer cleaning step using HF, which etches uniformly into the wafer to remove this oxide layer.

This process should be performed with extra caution and in a well ventilated chamber as HF vapours are carcinogenic. Immediately after etching, the wafer should be covered with resist or loaded into a deposition system and pumped to vacuum, to avoid the re-oxidation of the exposed surface.

B.1.2 Resist coating: (II) in Fig. B.1

Every new fabrication layer begins by coating the wafer with a layer of resist. This polymer resist will have a pattern carved into it, serving as a mask for material deposition (refer to B.1.5) or etching (refer to B.1.8). It is vital to control the composition and thickness of the resist to accurately perform these steps.

Start by placing some resist solution, consisting of a polymer dissolved in a solvent, onto the Si wafer. The wafer is rotated in a spinner, letting centripetal acceleration spread the resist over the surface. The resist dries and thins out, eventually passing a point where the increase of its viscosity (due to the evaporation of the solvent) balances out the centripetal shear force, and the thickness stabilises. Typically

$$\text{thickness} \propto \frac{1}{\sqrt{\omega}}, \tag{B.1.1}$$

where ω is the angular rotation speed of the wafer [270]. Resist companies supply calibrated process trend charts that quantify (B.1.1) by summarising the film thickness at different spinning speeds.

Baking the resist evaporates the remaining solvent, leaving a polymer film on the wafer. A second layer of resist may be deposited on top of the first, depending on whether *positive* or *negative* lithography is being performed.

B.1.3 Exposure: (III) in Fig. B.1

The exposure step transfers the desired pattern onto the resist, and can be done with photo or electron beam lithography depending on the desired accuracy and size of the structures.

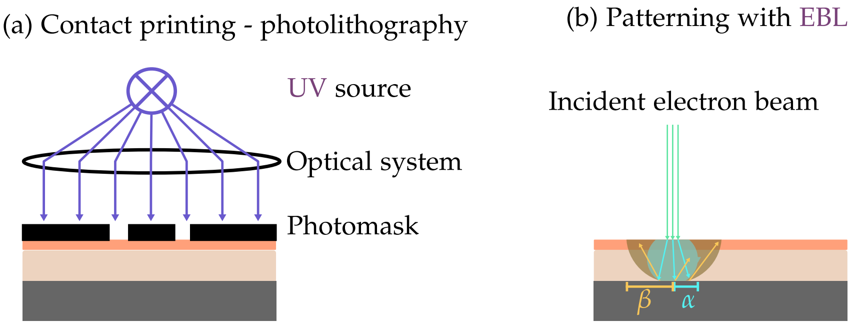

Figure B.2: Tracing out desired patterns in the resist: **(a)** Transferring the pattern of the photomask onto the resist using contact printing. Resolution is limited by the wavelength of the light $\sim 400\,\mathrm{nm}$; **(b)** Lithography with EBL, transferring a digitised pattern by moving an electron beam. The electron beam accelerated with 30 kV will have a spot size $\alpha \sim 2\,\mathrm{nm}$ (blue) and a backscattering region $\beta > 50\,\mathrm{nm}$ (yellow), which limits maximal resolution to $\sim$ 10-20 nm (although this heavily depends on the resist and substrate used). The backscattered region may lead to resist exposure far outside the desired pattern.

B.1.3.1 Photolithography

When working with large structures where low accuracy is permissible, such as ground planes and coplanar lines that connect the device to laboratory microwave circuitry (see for example Fig. 2.14), the pattern can be exposed using Ultra violet (UV) radiation. The resist on the wafer has to be a photoresist, whose internal bonds will be broken under exposure to UV light, softening it for the development process in B.1.4.

Fig. B.2 (a) shows the principle of contact printing photolithography. A photomask is placed on top of the resist-covered wafer, whose pattern defines what sections will receive a dose once the UV source is turned on. Contact printing increases the chances of scratching the resist or adding dirt. The resolution such an exposure is limited by the wavelength of the UV light ($\lambda \sim 400\,\mathrm{nm}$) and typically takes a 3-5 minutes.

B.1.3.2 Electron beam lithography

When working with fine structures on the order of $\sim 100\,\mathrm{nm}$, patterning has to be performed with an electron beam, for which the limiting resolution is the de-Broglie wavelength of the $\sim 30\,\mathrm{kV}$ electrons accelerated by an electron gun $\lambda = h/\sqrt{2m_eE} \sim 0.01\,\mathrm{nm}$. An appropriate electron beam resist is spun on in B.1.2 to be softened (or hardened) by the incident electrons.

Pattern preparation The designs in `Autocad` are converted to a file readable by an Electron beam lithographer (EBL) using `Beamer` [271]. This software outputs instruction of shots that the lithographer needs to fire to deliver the minimum dose

$$\text{Dose} = \frac{I \times t}{A},$$

to soften (harden) the resist, where I is the current in the beam and t is the dwell time over an area A.

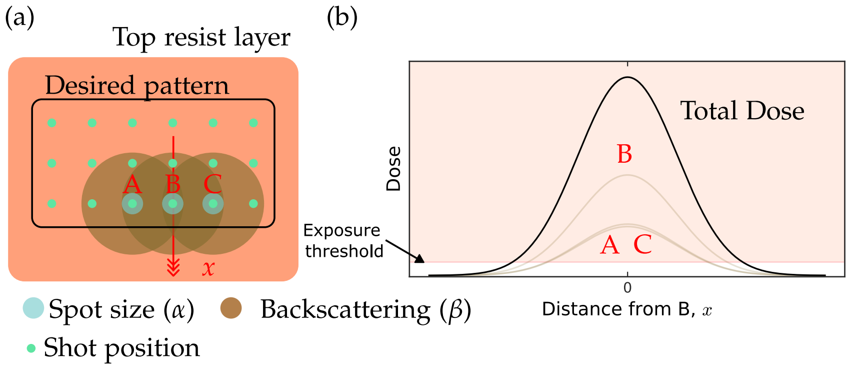

Figure B.3: **(a)** Desired pattern has a shot array applied to it. Each of the shots will have a spot size and a backscattering size; **(b)** Tracking the dose delivered along the x-axis from superposed shots A, B and C. Any area that receive a dose above the exposure threshold will be exposed. The diagram shows just how big of an area would be exposed around point B if proximity correction is not applied.

The software is also capable of performing proximity correction, to account for the forward and backscattering of electrons shown in Fig. B.2 (b). The forward scattering size (also called spot size) $\alpha \sim 2\,\text{nm}$ is two magnitudes greater than the de-Broglie wavelength of the electrons, and is limited by the focusing capabilities of the EBL and acceleration voltage. The backscattering size denoted by β results from large angle collision of electrons with the substrate, and their ionisation of the resist and substrate releasing a cascade of secondary electrons. Backscattering will expose the resist several microns away from the initial target. The two effects combined, give an energy density profile

$$\frac{1}{1+\eta}\left(\frac{1}{\pi\alpha^2}e^{\frac{-r^2}{\alpha^2}} + \frac{\eta}{\pi\beta^2}e^{\frac{-r^2}{\beta^2}}\right), \tag{B.1.2}$$

that expresses the relative dose that regions at a distance r away from an illuminated point will receive in terms of α, β and the energy ratio between the incident and backscattered electrons η [272].

The effect of the broad profile (B.1.2), is that a shot array meant to trace out a desired pattern will additionally expose resist in the surrounding regions (see Fig. B.3). In a device with a mix of thin and bulk features, this unaccounted-for profile could result in undesired exposure. To compensate for this effect, a proximity correction is done by using table of

α, β, η values for different resist-substrate combinations, to numerically evaluate the dose correction that needs to be applied to each shot, in order for the correct pattern to be exposed.

In principle all the patterning can be done with the EBL. However, as this method requires a far more expensive machine when compared to the UV lamp for photolithography (see B.1.3.1) and also takes hours instead of minutes, it is preferable to only use it for very small features without compromising the final quality of the device.

EBL preparation The resist-covered wafer is loaded onto a cassette and into a `JEOL 8100` [273] machine. The EBL is corrected for astigmatism and focused before each exposure. Depending on the machine, this operation would be automated or manual. For manual focusing, one would make a physical scratch on the device and focus on it, since it would be in the same plane as the resist being exposed. Alignment with previous layers is performed by using markers - crosses or squares located in known design coordinates. Locating two of these markers is enough for the EBL to correct its field and align itself with the previous layer.

B.1.4 Development: (IV) in Fig. B.1

A developer solution is used to develop the softer areas of the resist which have shorter polymer chains. The exact time of removal varies depending on the resist used, size of exposed features, base dose applied by the EBL, and is determined by performing calibration runs. This opens up *windows* in the resist matching the pattern of the photolithography mask or `Autocad` design.

The exposed wafer is cleaned with Oxygen (O_2) plasma in a `Oxford Plasmalab` Reactive ion etching (RIE) [274] which removes residual resist on the wafer through chemical reaction with radicals in the plasma.

B.1.5 Deposition: (V) in Fig. B.1

Material (Gold (Au), Al) is deposited through the *windows* and onto the wafer in an evaporator:

- `Plassys Electron Beam Evaporator MEB550S` [275] for high purity 99.9999% Al;
- `Edwards A500 FI500 Beam evaporator` for all other materials.

The thickness is monitored with a quartz crystal, whose frequency depends on the mass of the crystal, which increases during the deposition process [276]. Evaporation is stopped once a required thickness is reached. Evaporation should occur at a good vacuum and under a steady evaporation rate.

B.1.6 Liftoff: (VI) in Fig. B.1

At this stage, the sample will resemble the first structure in Fig. B.4 (a), and soaking it in a remover solution would remove all resist and the material deposited on top of it. For successful lift-off, the lower resist layer must be developed more than the top one (called an undercut) and the thickness of the lower resist must be three times that of the deposited material. Otherwise one can have the situation of Fig. B.4 (b,c), with a continuous sheet of material covering the whole sample, which is anchored to the wafer making liftoff harder.

Difficult liftoff can be assisted by placing the sample in Isopropanol (IPA) and gently moving it over an ultrasound bath filled with water, taking care not to damage existing structures.

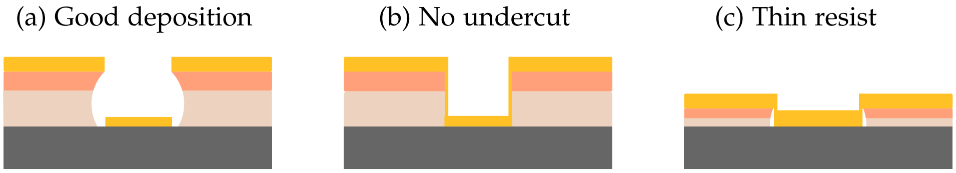

Figure B.4: Incorrect engineering of the resist layers may lead a continuous film covering both the resist and the wafer following deposition which affects the quality of lift-off: **(a)** Good resist structure with undercut to isolate the deposited pattern; **(b)** Lower resist does not have an undercut - potential for the pattern to form a continuous film with the material deposited on top of resist; **(c)** Resists are too thin, making the material deposited on top of resist overlap with the pattern, again creating a continuous film.

B.1.7 Covering of substrate with material layer: (VII) in Fig. B.1

When performing *negative lithography*, instead of depositing a material through a pattern as done in Sec. B.1.5, the material is first deposited to cover the whole wafer, and then a resist defines the regions to protect during the etching process.

When the material is Al or Au, the deposition is done at Royal Holloway facilities and does not have any complications. However when working with materials such as Titanium Nitride (TiN), Niobium Nitride (NbN), they are ordered from a 3rd party institution that specialises in Atomic layer deposition (ALD).

B.1.8 Etching: (VIII) in Fig. B.1

Following photo or electron beam lithography and development (refer to B.1.3 and Sec. B.1.4), the patterned mask covers up the regions of the material that one does not want to remove during etching. The rate of etching is calibrated for different materials, and is done either with:

- RIE in `Oxford Plasmalab` [274]. The resist defining the protected regions will also be inevitably etched away, and needs to be made thick enough to protect the underlying structure throughout the whole process. It is likely that following this step, resist will harden and it cannot be removed with usual removers. Figure B.5 shows the colour before and after etching of Al;
- Wet etching is done by putting the wafer in a etching solution. The resist can be hardened with post-development baking. During etching the sample should be inspected in an optical microscope, and progress assessed by the observed colour change (see Fig. B.5). Extra time can be added if patches remain, but this should be kept to a minimum as the resist gets less stable with each attempt.

  Care must be taken to wash the etcher off the sample at the end, by thoroughly rinsing with IPA.

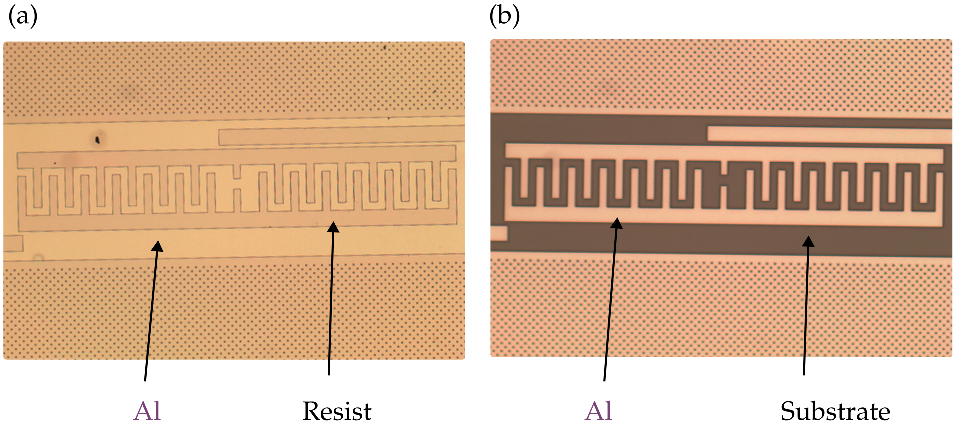

Figure B.5: **(a)** An Al-covered wafer following development of the resist. The resist is seen as the bleak pattern, and will protect the Al underneath during etching; **(b)** Same wafer following wet etching, showing how the resist pattern protected the interdigitated capacitors and ground planes in a transmon chip.

B.1.9 Bonding: (IX) in Fig. B.1

As the final step, the contacts samples are bonded with 25 μm Al wires using a `7KE West Bond machine` [141] to the corresponding elements on the Printed circuit board (PCB).

B.2 Josephson junction fabrication

B.2.1 Tilting deposition of JJs

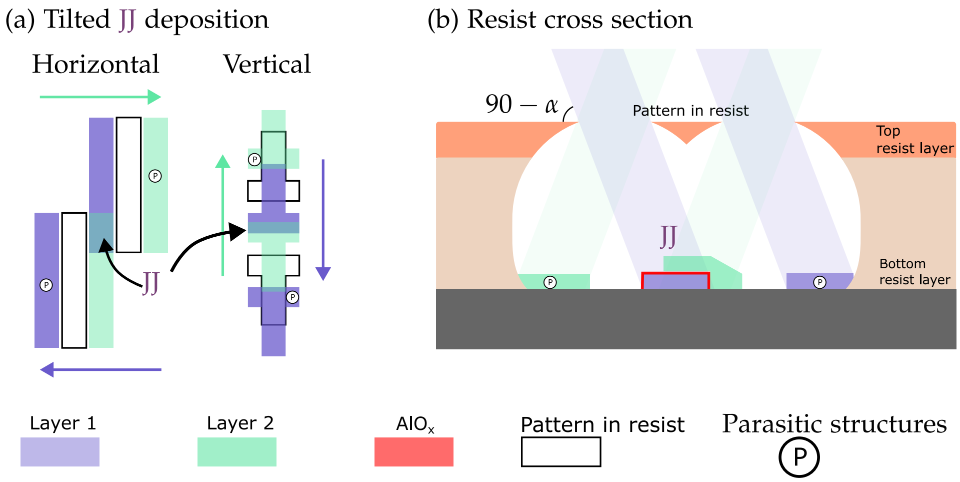
(a) Tilted JJ deposition

(b) Resist cross section

Figure B.6: JJs made using horizontal and vertical tilting; **(a)** Pattern in resist and tilting directions resulting in the overlap of layer 1 and layer 2; **(b)** Resist cross section, showing deposition angle and overlap of the two Al layers in the common undercut of the pattern windows creating the Superconductor-insulator-superconductor (SIS) junction. Parasitic structures are inevitably deposited next the the JJ.

The standard fabrication of JJ involves patterning of parallel windows in the resist (see Fig. B.6 (a)) and angled evaporation in the `Plassys` (refer to B.1.5). Evaporation of Al is first performed at one angle α, after which a 10 minute controlled oxidation is run to create the insulating AlO_x layer of the SIS junction. Pressure is either selected to be static ~ 0.25 mBar or dynamic, in which case O_2 is passed through a mass flow controller ~ 20 sccm. The oxidation is a diffusive process and the thickness of the oxide has a logarithmic increase over time. A longer oxidation time at lower pressures is preferred to minimise the effects of varying bleed rate[1]. It was found that flushing the O_2 line before this process was important to remove contaminants that affect JJ yield.

Following this, a second evaporation is performed at angle $-\alpha$ by tilting the sample either in the horizontal or vertical axis. This creates the SIS overlap in the middle of the two *windows*, with some additional parasitic structures. These structures have the potential to distort electric fields next to the JJs and host Two level systems (TLS) (refer to Sec. 1.3.3).

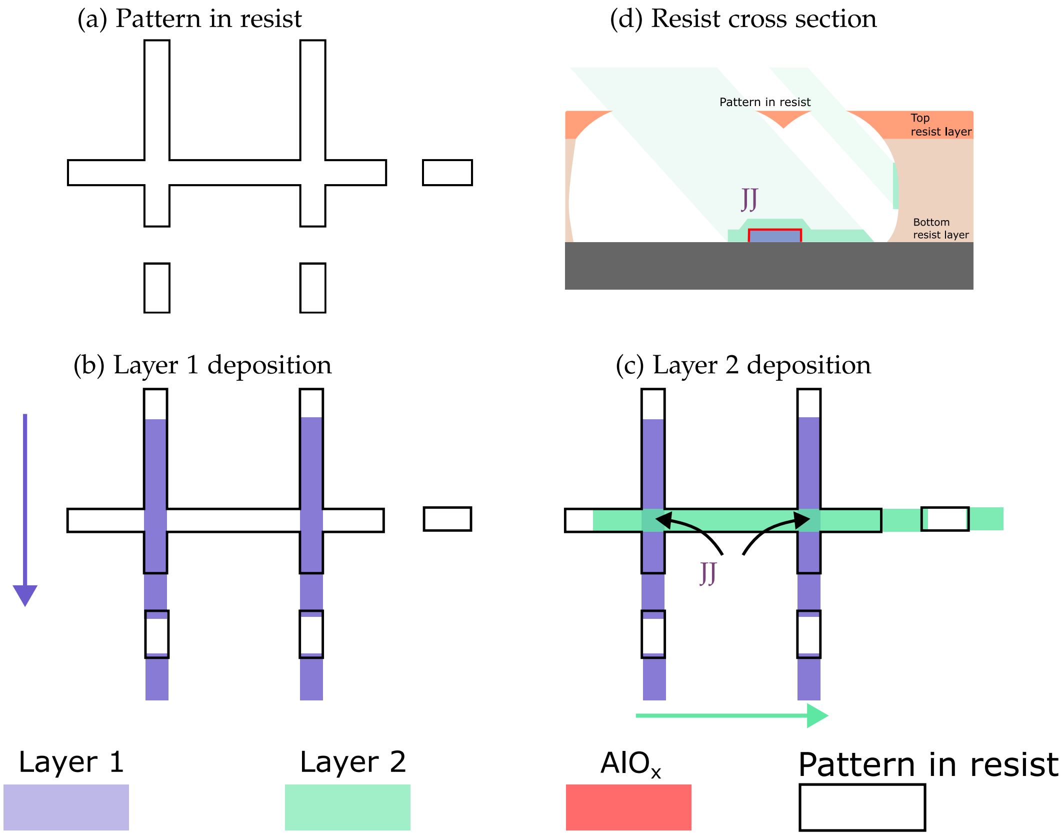
(a) Pattern in resist
(d) Resist cross section
Pattern in resist
Top resist layer
JJ
Bottom resist layer
(b) Layer 1 deposition
(c) Layer 2 deposition
JJ
Layer 1
Layer 2
AlO$_x$
Pattern in resist

Figure B.7: Deposition using the Manhattan approach, which has the advantage of more reliably creating the overlap with the crossing of the two fingers and creating less parasitic structures. The holes ensure that there are no *cliffs* at the end of the strips that could impact fabrication quality.

B.2.2 Manhattan deposition of JJs

In the Manhattan deposition, tilting is replaced by rotation of the sample by 90° between the two evaporation steps of horizontal and vertical strips (see Fig. B.7 (a-c)). The angle of evaporation is much sharper than with tilted deposition, which ensures that the perpendicular strips are only deposited a single time.

The mask needs to be designed with small rectangular squares on the end of vertical and horizontal strips, so that there is a big enough undercut for the strips deposited with the sharp angle to extend into. The thickness of resist is chosen so that material evaporated through these small rectangles lands on the wall of the resist leaving no parasitic structures on the substrate (see Fig. B.7 (d)).

Manhattan deposition has demonstrated better uniformity of the JJs [188] and also avoids the artifact structures that are formed under tilted deposition (see Fig. B.6).

---

[1] The flow rate of O_2 into the chamber where oxidation is occurring.

B.3 Coplanar capacitance heuristic

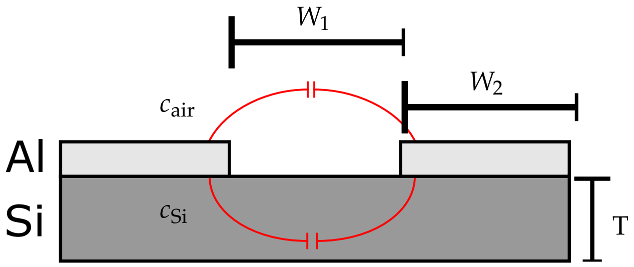

Figure B.8: Capacitance network of two coplanar structures sitting on a common substrate, where capacitances are given per unit length.

The capacitance per unit length between two coplanar structures with dimensions shown in Fig. B.8, will be the sum of the parallel capacitances through the air and substrate. The logarithmic dependence on the thickness of substrate ($T \sim 1\,\text{mm}$), size of gap ($W_1 \sim 2\,\mu\text{m}$) and size of structures ($W_2 \sim 10\,\mu\text{m}$) [277]

$$\begin{aligned} c &= c_{\text{air}} + c_{\text{Si}}, \\ c_{\text{air}} &\approx \varepsilon_0 \frac{2}{\pi}\left(4\frac{W_2}{W_1}\right), \\ c_{\text{Si}} &\approx \varepsilon_0(\varepsilon_r - 1)\frac{1}{\pi}\ln\left(16\frac{T}{\pi W_1}\right), \end{aligned} \tag{B.3.1}$$

means that it is an order of magnitude calculation, and will depend primarily on the capacitance through the substrate of relative permittivity $\varepsilon_r = 11.7$ for Si. Approximate evaluation of (B.3.1) using aforementioned parameters gives $c \sim 2 \times 10^{-10}\,\text{F/m}$. Heuristically our group has found that we have better agreement when assuming a coplanar capacitance per unit length

$$c \approx 0.85 \times 10^{-10}\,\text{F/m}.$$

B.4 Transmon photon source fabrication

Fabrication is performed on an undoped Si 100 wafer.

B.4.1 Wafer cleaning and Al layer

This procedure etches away the top layer of Si and covers it with Al.

1. Clean wafer in `Nanostrip 5%` for 3 min at 60° C followed by a double 30 s rinse in Water (H_2O) and blow dry with Nitrogen (N_2);
2. Remove oxides and radicals in `HF 2%` for 5 min followed by a double 30 s rinse in H_2O and blow dry with N_2;
3. Immediately load sample into `Plassys` and begin pumping;
4. Anneal sample at 300° C once base pressure is reached - heating will change the structure of the top Si layer for better adhesion of the subsequent Al evaporation.
5. Perform deposition of 100 nm of Al at a constant 0.5 nm/s evaporation rate;
6. Incubate the sample at 10 mBar for 10 min to create a controlled Aluminum Oxide (AlO_x) layer.
7. Protect structure in `ARP 6200` resist.

B.4.2 Layer 1: Coplanar waveguides

This step will *carve* out the TL and qubit structures from the Al film.

1. Cut off required chip size from wafer and remove the protective resist layer with `Ar 600-71` for 20 min at 60° C. Clean with IPA and blow dry;
2. Spin `ARP6200 9%` resist at 2000 rpm and bake for 3 min at 160° C. Repeat again for a combined thickness 250+150 = 400 nm;
3. EBL using 360 μC/cm^2 dose and 100 nA current. At this current, spot size will be 250-2000 nm, so structures smaller than 2 μm will not be stable in the resist;
4. Develop in `ARP 600-546` for 30 sec and rinse with IPA;
5. Clean and harden the resist with plasma etching in O_2 for 15 sec at 100 W power (`Oxford Plasmalab 80`). At a rate of 200 nm per minute, 60 nm of resist will be removed in the process;

6. Perform a postbake for 5 min at 160° C to harden the resist even more;

7. Wet etch the exposed Al in `MF319`, with a recommended starting time of 60 sec and progress based on assessment in optical microscope. Rinse thoroughly in IPA. This should leave a sample with defined TL, ground planes and capacitor (see Fig. B.5);

8. (Optional) Remove remaining resist with `AR-600-71` Remover for 10 min at 65° C, rinsing with IPA.

B.4.3 Layer 2: JJ

This step will deposit JJ in close proximity to the shunting capacitor, but not connected to it.

1. Wafer is split into chip sizes 2 cm×2 cm on which 4-8 samples can be fit;

2. Spin `Copolymer 13%` resist at 4500 rpm and bake for 3 min at 160° C for a thickness of 700 nm;

3. Spin `ARP6200 9%` resist at 2000 rpm and bake for 3 min at 160° C for a thickness of 70 nm;

4. EBL with dose 330 μC/cm^2 and current of 2 nA;

5. Develop top layer in `ARP 600-546` for 35 sec and rinse in IPA;

6. Develop bottom layer in `H20:IPA 1:9` for 6 min and rinse in IPA;

7. Clean the resist with plasma etching in O_2 for 20 sec at 40 W power;

8. Load into `Plassys` evaporator and pump overnight for a base pressure of 10^{-8} mBar;

9. Argon (Ar) etch the sample in the `Plassys` for 3 min to prepare surface for JJ;

10. Proceed to perform Manhattan evaporation of JJ as described in Sec. B.2.2. Oxidation can be chosen to be dynamic or static as desired. One must remember to flush the O_2 line before starting the program. 0.1 mBar was used for the photon source in the thesis;

11. Liftoff in `Ar 600-71` for 20 min at 65° C and rinse in IPA. What should be left, are disconnected JJ and shunt capacitor structures (see Fig. B.9).

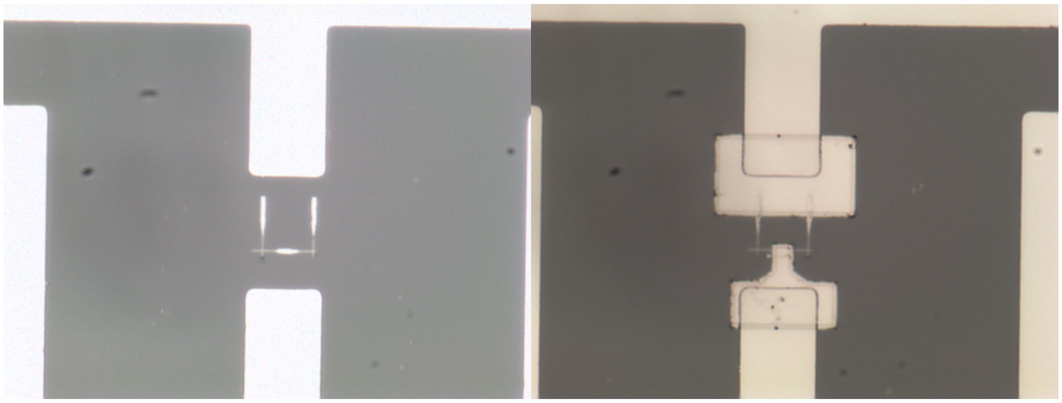

Figure B.9: Optical images showing the connection of capacitor and a *floating* JJ made in B.4.3 using galvanic patch. **(Left)** Before; **(Right)** After patch has been deposited.

B.4.4 Layer 3: Patches

In this final layer, a connection between the JJ and rest of qubit is made (see Fig. B.9). The AlO_x on the surface of both structure will need to be etched away before the patch is applied.

1. Spin `Copolymer 13%` resist at 4500 rpm and bake for 3 min at 160° C for a thickness of 700 nm;
2. Spin `ARP6200 9%` resist at 2000 rpm and bake for 3 min at 160° C for a thickness of 70 nm;
3. EBL with dose 360 $\mu C/cm^2$ and current of 2 nA;
4. Develop top layer in `ARP 600-546` for 30 sec and rinse in IPA;
5. Develop bottom layer in `H20:IPA 1:9` for 6 min and rinse in IPA;
6. Load into `Plassys` evaporator - at this stage the goal is to etch away the AlO_x in developed holes, prior to depositing the patches themselves;
7. Perform 400 V, 20 mA Ar etching of the exposed windows, and follow up with deposition of 150 nm of Al, under a tilt of 20° and continuous rotation. The latter ensures that the patch fully envelops the contacts and does not suffer breakages;
8. Cap the structures with a 10 mBar oxidation for 5 minutes at the end of recipe.

B.5 Twin qubit fabrication

B.5.1 Wafer cleaning

This step removes organics on the wafer and cleans it from physical debris.

1. Clean wafer in `acetone` for 20 min at 55° C rinse in H_2O and blow dry with N_2;
2. Clean organics with plasma etching in O_2 for 5 min at 100 W power.

B.5.2 Layer 1: Coplanar waveguides

This step deposits an array of ground planes and TLs defined by a pre-fabricated photo mask. These default chips would serve as the starting point for many different fabrications. This is a photolithography, and therefore work must be performed in a yellow room absent from stray UV light, that would otherwise expose the resits.

1. Spin `LOR5B` photoresist at 4500 rpm and bake for 5 min at 160° C for a thickness of 400 nm;
2. Spin `S1813` photoresist at 4500 rpm and bake for 3 min at 110° C for a thickness of 1200 nm;
3. Press the mask against the wafer, ensuring good contact is made to avoid diffraction effects. Slide into the UV lamp box and expose for 4 min;
4. Develop in `MF140` for 30 sec and rinse with H_2O;
5. Deposit 10 nm of Nickel (Ni) followed by 80 nm of Au. Ni improves adhesion of Au to the Si wafer;
6. Liftoff in `MF 1165` for 30 min at 65° C, rinsing in IPA. An ultrasound bath may be used to shake off flakes if required.

B.5.3 Layer 2: JJ

JJ are fabricated according to recipe in Sec. B.4.3 with the following changes:

1. EBL was performed on an older machine, using a current of 15 pA and lower dose `200µC/cm2`;
2. Instead of Manhattan deposition, tilted deposition of 20 nm and 30 nm of Al at angles ±12° is performed;

3. Because the ground planes and TLs are made out of Au, there is no oxide layer on their surface and therefore the JJ can be connected directly, without needing a separate patch layer (see Sec. B.4.4).

B.6 CQPS qubit fabrication

Fabrication of CQPS qubits was done on a Si substrate covered in a film of TiN. There is no wafer cleaning process to avoid accidentally damaging or changing properties of the TiN film.

B.6.1 Layer 1: Coplanar waveguides

Au coplanar waveguides and ground planes are patterned with an EBL, because at the time of fabrication there was no suitable photo mask to repeat the photolithography recipe from Sec. B.5.2.

1. Spin `Copolymer 6%` resist at 3000 rpm and bake for 3 min at 160° C;
2. Spin `ARP6200 9%` resist at 2000 rpm and bake for 3 min at 160° C;
3. EBL with dose 360 μC/cm^2 and current of 2 nA;
4. Develop top layer in `ARP 600-546` for 30 sec and rinse in IPA;
5. Develop bottom layer in `H20:IPA 1:9` for 6 min and rinse in IPA;
6. Deposit 10 nm of Ni followed by 80 nm of Au at a rate of 0.5 nm/s;
7. Liftoff in `ARP Remover` for 30 min at 65° C, rinsing in IPA.

B.6.2 Layer 2: Constrictions

The resonator or TL etched out from TiN along with the CQPS qubits are aligned with the coplanar waveguides from Sec. B.6.1. Negative EBL lithography is performed, with the beam tracing out the contour of the CQPS loops and constrictions and hardening the resist in those locations. After development, TiN under resist will be protected from etching, while the rest of the TiN will be removed.

1. Spin a `Ma-N2410` negative photoresist;
2. EBL with high resolution, using a 200 pA current. This is required to limit the spot size for the patterning of the narrow constrictions;
3. Develop with `Ma-D-525`, removing all but the hardened areas of the resist;
4. Strengthen the resist with a postbake for 2 min at 110° C;

5. Plasma etch with Ar:CF_4 1:10;
6. Resist is not removed after etching, as it acts as a good protector of the TiN film underneath it.

Appendix C

Appendix experiment

C.1 Dilution refrigerator

Cooling is performed with a `BlueFors` dilution refrigerator [278], achieving a base temperature of 13 mK, whose main components and cooldown profile are summarised in Fig. C.1. Once cooled the system operates in a closed cycle for an indefinite period of time, in contrast to standard dewars filled with Helium 4 (He^4) that experience a continuous boil-off.

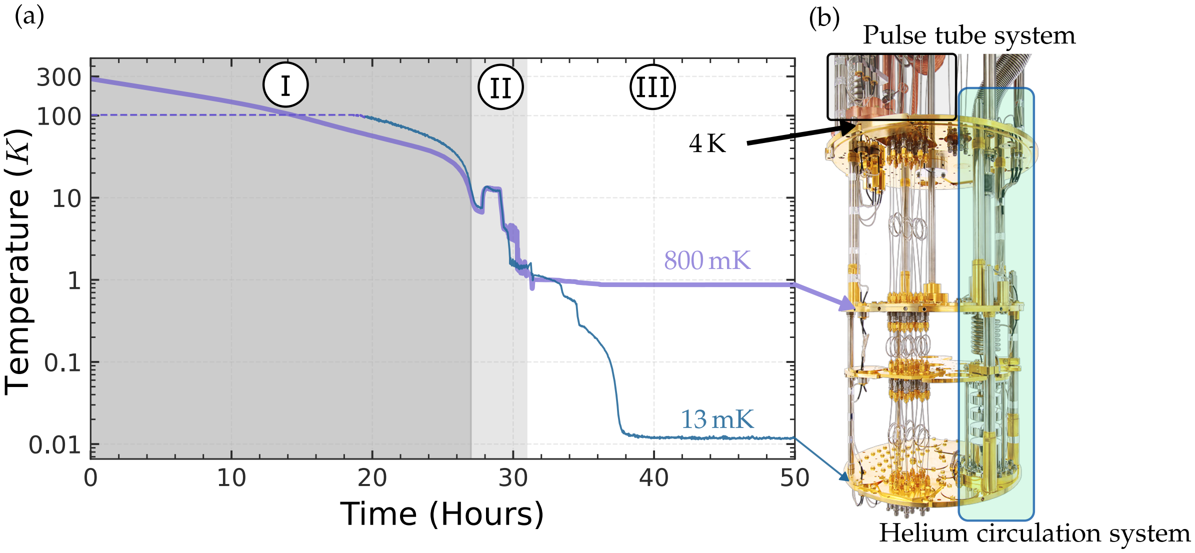

Figure C.1: **(a)** Steps of the cooldown process tracking the temperature of the 800 mK and 13 mK fridge stages: (I) Pulse tube operation performing initial cooling from Room temperature (RT) to 4 K; (II) Condensing of He^3-He^4 mixture; (III) He^3-He^4 mixture circulation; **(b)** Disassembled view of a dilution refrigerator, showing the pulse tube and He^3-He^4 system used for the different cooldown steps (image adapted from [278]).

The steps for achieving base temperature are as follows:

1. The fridge is closed with an air-tight can that is evacuated with a vacuum system to 10^{-6} mBar, to remove any vapour that could cause condensation once temperatures begin to drop;

2. **Initial pre-cool to 4 K is done using a pulse tube** (see Fig. C.1 (I) and Fig. C.2 (a)), which uses periodic expansion of pre-cooled Helium 3 (He^3) to transport heat against a temperature gradient. The benefit of the pulse tube, is the lack of moving parts at its cold end, reducing vibration in the experimental system and increasing operation lifetime.

   In stage (I) the gas is compressed adiabatically, with the work done in moving the piston causing a rise in gas temperature at the hot end of the pulse tube, which is

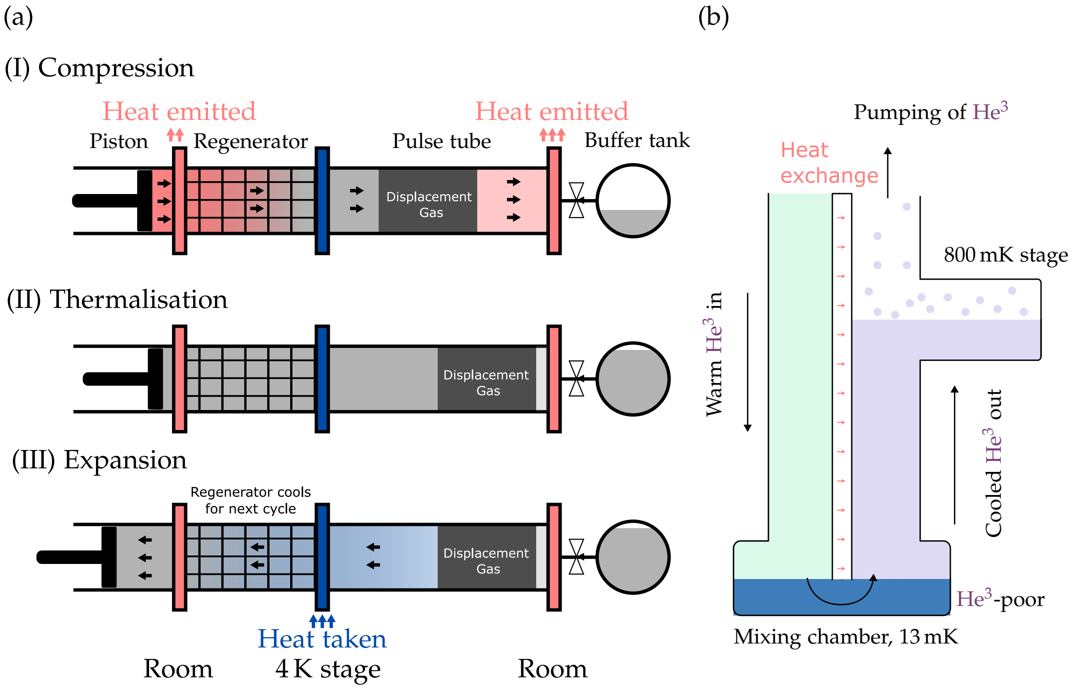
(a)
(b)
(I) Compression
Heat emitted
Piston
Regenerator
Pulse tube
Heat emitted
Buffer tank
Displacement Gas
(II) Thermalisation
Displacement Gas
(III) Expansion
Regenerator cools for next cycle
Displacement Gas
Heat taken
Room
4 K stage
Room
Pumping of He3
Heat exchange
800 mK stage
Warm He3 in
Cooled He3 out
He3-poor
Mixing chamber, 13 mK

Figure C.2: Principle of operation of the two cooling systems labelled in Fig. C.1 (b). **(a)** Pulse tube system steps: (I) Compression of He^3 gas raising its temperature on the hot end of the pulse tube, which is dumped to the hot heat exchanger; (II) Thermalisation brings the gases to ambient temperature. At this stage the buffer tank is filled up through the needle valve - its effect is to introduce a phase delay between the movement of the piston and movement of the displacement gas; (III) During expansion, a drop in the gas pressure at the cold end of the pulse tube causes a drop in temperature resulting in cooling. The regenerator mesh also cools in the process, and will precool the gas further during the next compression step; **(b)** Helium circulation system at the low temperature stages. The pumping of He^3 through He^4 in the mixing chamber requires energy that is taken from the surrounding environment. The He^3 is collected on the 800 mK stage, where continuous pumping creates a concentration gradient for continuous circulation to occur.

dissipated to a suitable RT heat sink. A displacement gas keeps the hot and cold ends of the pulse tube (connected to the RT and 4 K stages respectively) separate during operation.

In stage (II) the gas undergoes thermalisation to the ambient temperature of the pulse tube and in stage (III) the piston begins to move in the opposite direction. The delayed response of the displacement gas, facilitated by the buffer tank connected through the needle valve, causes a rapid pressure drop at the cold end of the pulse tube, and a corresponding temperature drop[1], creating a cooling effect on the 4 K stage.

In the next cycle, the regenerator, which has cooled as the result of gas expansion in stage (III), precools the incoming gas in step (I), which progressively cools the pulse tube with each cycle. For this purpose, the regenerator has a high surface area and heat capacity, to *trap* the *cooling power* in between cycles [279];

---

[1] Recall the ideal gas law $PV = nRT$

3. **Condensation of He^3-He^4** (see Fig. C.1 (II)). At this point the 4 K stage is mechanically decoupled from the lower temperature stages to reduce thermal heating. This is done using heat switches that are filled with an inert gas and a poorly-conducting steel connector. Upon reaching specific temperature criteria, activated carbon inside the switch adsorbs the inert gas, stopping heat conduction across the switch.

   The He^3-He^4 mixture is injected into the circulation system and liquefied by a combination of:

   - Compressing the mixture and firing it through an expansion valve to achieve Joule-Thompson cooling;
   - Once the He^4 (boiling point 4.2 K) and He^3 (boiling point 3.2 K) begin to liquefy at the low temperature stages shown in Fig. C.2 (b), pumping on the mixture on the 800 mK stage causes evaporative cooling dropping temperature down to 800 mK - this is the steady state seen in Fig. C.1 (II-III).

   This process is sped up in **BlueFors** cryostats by using a precooling sequence to cool down the *hot spots* left after pulse tube cooling in Step 2. The helium mixture is repeatedly admitted and pumped out of the system to *erase* these regions, allowing condensation of the helium mixture to happen quicker;

4. **Cooling from 800 mK to 13 mK using dilution pumping** (see Fig. C.1 (III) and Fig. C.2 (b)). At a certain point the diminishing vapour pressure on the 800 mK stage reduces the cooling effect from pumping He^3 in Step 3.

   But by this point the He^4 is a superfluid (occurs at 2.7 K), and the mixture separates out into a He^3-rich and He^3-poor (He^4-rich) phases which coexist in separate layers in the mixing chamber [280].

   The enthalpy of He^3 in the He^3-poor phase is larger than in the He^3-rich phase[2]. Hence energy is required to move He^3 atoms into the He^4-rich phase, which takes energy from the mixing chamber, achieving cooling. By continuously pumping He^3 collecting on the 800 mK stage, a concentration gradient is maintained that causes osmotic pressure to pull He^3 through the mixing chamber continuing the cooling effect.

---

[2] Enthalpy describes the energy change between two states during a phase transition. For a He^3 atom to move into the He^3-poor phase, it needs to break the strong bonds in the He^4-rich phase and create weaker ones.

The heat exchanger shown in Fig. C.2 (b) will pre-cool the incoming He^3 from RT to the mK environment of the mixing chamber, improving the efficiency of the cycle;

5. In the steady state it is only the He^3 being cycled, delivering a cooling power that can maintain a temperature of 13 mK. Any contaminants that leak into the line (gases other than He^3 and He^4) are *frozen* out from circulation by a N_2 trap at 70 K and cold trap at 50 K on the helium circulation system (not shown in diagrams).

C.2 Data acquisition program

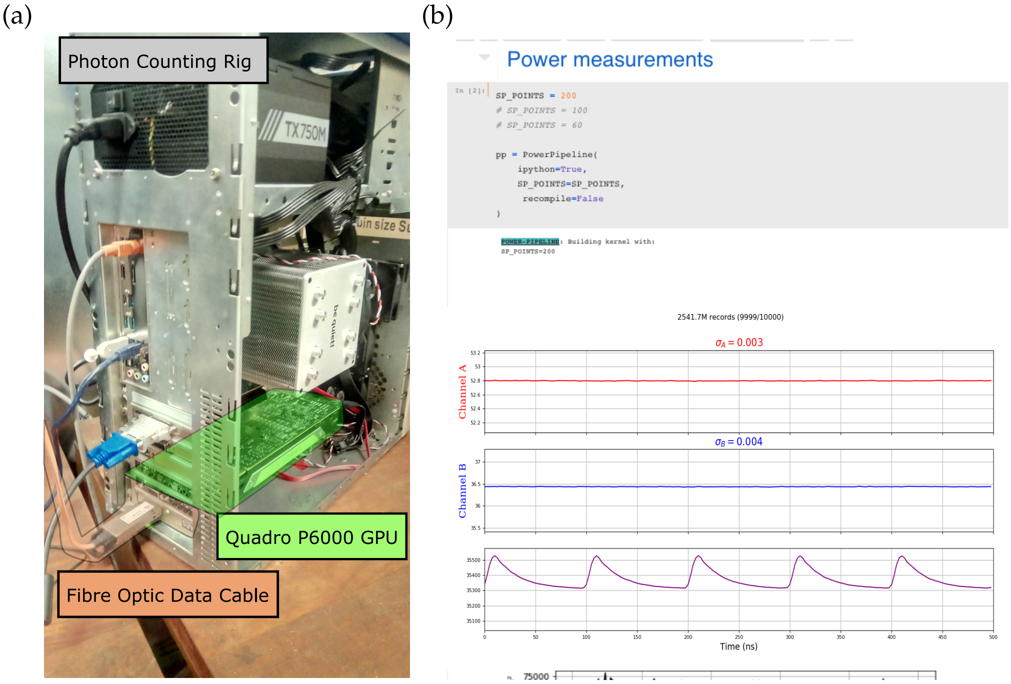
(a)
Photon Counting Rig
Quadro P6000 GPU
Fibre Optic Data Cable
(b)
Power measurements
2541.7M records (9999/10000)
$\sigma_A = 0.003$
Channel A
53.2
53
52.8
52.6
52.4
52.2
$\sigma_B = 0.004$
Channel B
37
36.5
36
35.5
35500
35400
35300
35200
35100
0
50
100
150
200
250
300
350
400
450
500
Time (ns)
75000

```
In [2]: SP_POINTS = 200
        # SP_POINTS = 100
        # SP_POINTS = 60

        pp = PowerPipeline(
            ipython=True,
            SP_POINTS=SP_POINTS,
             recompile=False
        )
```

```
POWER-PIPELINE: Building kernel with:
SP_POINTS=200
```

Figure C.3: **(a)** Experimental computer equipped with fibre-optic data line and `Quadro P6000` Graphical processing unit (GPU); **(b)** Program frontend through a `Jupyter Notebook (Python)`. Setup of digitiser and devices involved in measurements can all be done here. Experiments could be run remotely through the web interface and from `LabView`, with a live update of results.

A software library was developed for running time-resolved power and correlation measurements, the source code can be found on the Github Repository. It will be colloquially called the Photon source library (PSL), and it provides:

- An interface to a `ADQ214 SP Devices` digitiser [143] for setup and readout;
- Evaluation of the instantaneous power of a complex voltage $\xi(t) = I(t) + iQ(t)$ in the TL

$$P(t) = \frac{1}{Z}\left\langle \xi(t)\xi^*(t)\right\rangle \underset{\text{discrete}}{=} \frac{1}{Z}\left(\frac{1}{N_{\text{repetitions}}}\sum_{i=0}^{N_{\text{repetitions}}} I_i^2(t) + Q_i^2(t)\right), \tag{C.2.1}$$

  given two quadrature signals $I_i(t), Q_i(t)$ on two inputs of a digitiser;
- Evaluation of autocorrelation function

$$g^{(1)}(\tau) = \frac{1}{T}\int_0^T dt[\xi_1(t)\xi_2^*(t+\tau)] \underset{\text{discrete}}{=} \sum_{i=0}^{N}\left[\frac{\xi_1(t_i)\xi_2^*(t_i+\tau)}{t_N - \tau}\right],$$

given two voltage signals ξ_1, ξ_2 reconstructed from the quadratures on each of the two digitisers. This evaluation has a more efficient evaluation through a Fast Fourier transform (FFT) using the Wiener-Khinchin theorem that relates the autocorrelation function to the spectral density of the cross signal (see A.8.2)

$$g^{(1)}(\tau) \equiv \langle \xi_1(t)\xi_2(0) \rangle = \mathcal{F}_{\text{inv}}\left[S_{12}(\omega)\right], \tag{C.2.2}$$

with discrete FT defined similarly to (A.8.1)

$$\begin{cases} \text{Forward,} & \mathcal{F}: Y_k = \dfrac{1}{\sqrt{N}} \displaystyle\sum_{j=0}^{N-1} X_j e^{-i2\pi jk/N}, \\ \text{Backward,} & \mathcal{F}_{\text{inv}}: Y_k = \dfrac{1}{\sqrt{N}} \displaystyle\sum_{j=0}^{N-1} X_j e^{i2\pi jk/N}. \end{cases}$$

C.2.1 Program structure

The library combined the best functionalities of 3 different environments:

- The interactivity of `Python` was used for all plotting and user interaction, as it was intuitive and, via `Jupyter Notebook`, could be performed remotely through a web browser. The library's support for other devices (VNA, Spectrum analyser (SPA), Pulse generator (PG)) allows for synchronisation of measurements and setup through a single access point;
- Thread parallelisation of `C++` and native code of the digitiser being exposed as a `C` library. The main logic handler, readout from digitiser and pre and post processing of data was written in `C++`;
- Ultra-parallelisation of simple multiplication and addition operations on large arrays on a GPU. The kernels for evaluating (C.2.1) and (C.2.2) are written in `CUDA` - the `nVidia` proprietary language for writing software for GPUs.

The library should be compiled as a dynamically linked library and loaded into a `Python` environment to invoke its functions as if they came from a standard library. Figure C.4 demonstrates the workflow of the program, with a user launching measurement from a Python environment, and the parallel thread processes launched in the `C++/CUDA` environment. Real time data could be visualised in `Python` by using *log-like* rotation of the files with the latest accumulated data. Parallel processes allow one to overcome bottlenecks in certain blocks such as readout.

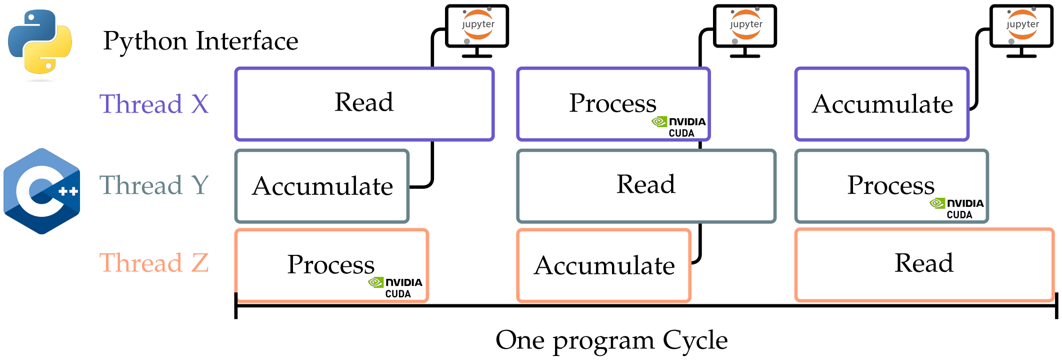

Figure C.4: Program flow using a `Python` entry point and the `C++` library processes that that are spun up. Three parallel threads execute readout, processing and storage of data from the digitiser sequentially, to make the digitiser readout time the main bottleneck for measurement acquisition. The accumulation thread dumps data into a raw text file, that the `Python` layer monitors to update graphs in real time.

C.2.2 Performance

Tab. C.1 demonstrates the benchmarked speeds of the different PSL blocks, demonstrating the order of magnitude difference between `Python`, `C++` and `CUDA` implementations. It is also evident that the readout speed from the digitiser was the main bottleneck in the program, arising from the $\sim 1\,\text{MHz}$ repetition frequency ($1000\,\text{ns}$) of the experiment. The repetition frequency was kept low so that the transmon had time to relax to its ground state in between the pulses.

Table C.1: Benchmarking individual blocks of the library, evaluated with the `Celero` library [281].

Group	Block	ms/Iteration	Iterations/sec
Power	Reading `C++` (400 samples × 0.128 M times)	917	1.09
	Reading `Python`	1400	0.7
	`C++` kernel	2314	0.43
	`CUDA` kernel	65	15.2
	Total time (using `CUDA` kernel)	995	1.0
$g^{(1)}$	Reading `C++` (64 M samples)	4.4	229
	`Python` kernel	7400	0.13
	`C++` kernel	137	7.3
	`C++` kernel using FFT	14	73
	`CUDA` kernel using FFT	0.9	1034
	`CUDA` kernel preprocessor	0.24	4230
	Total time (using `CUDA` kernel)	5.7	175

The library is supported with:

- Benchmarking framework, in order to guide optimisation of its processing block speeds (see examples in Tab. C.1);

- Unit testing framework, to test the functionality of each block with pre-generated data and expected results. This also allowed the safe optimisation of components while maintaining the program integrity (see Fig. C.5 (a));
- Automated documentation generation based of doc comments, to help with navigation in this extended library (see Fig. C.5 (b)).

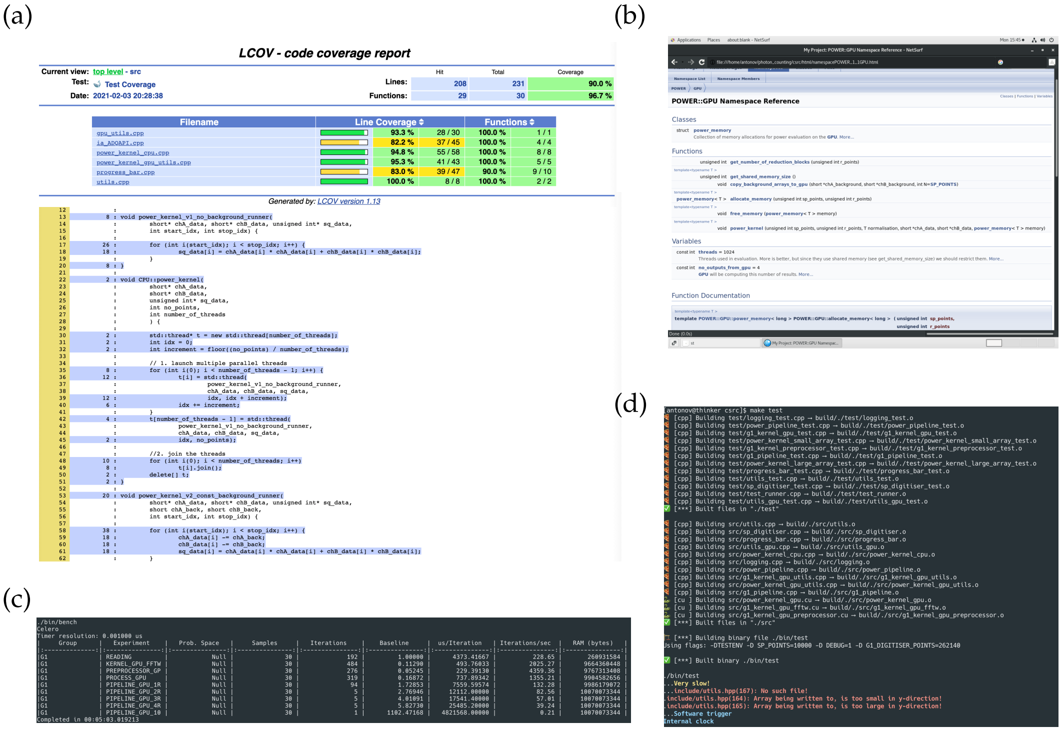
(a)
(b)
(c)
(d)
Applications
Places
about:blank - NetSurf
Mon 15:45
My Project: POWER::GPU Namespace Reference - NetSurf
file:///home/antonov/photon_counting/csrc/html/namespacePOWER_1_1GPU.html
Namespace List
Namespace Members
POWER
GPU
Classes | Functions | Variables
Done (0.0s)
st
My Project: POWER::GPU Namespac...

LCOV - code coverage report

Current view: top level - src
Test: Test Coverage
Date: 2021-02-03 20:28:38

	Hit	Total	Coverage
Lines:	208	231	90.0 %
Functions:	29	30	96.7 %

Filename	Line Coverage		Functions	
gpu_utils.cpp	93.3 %	28 / 30	100.0 %	1 / 1
ia_ADQAPI.cpp	82.2 %	37 / 45	100.0 %	4 / 4
power_kernel_cpu.cpp	94.8 %	55 / 58	100.0 %	8 / 8
power_kernel_gpu_utils.cpp	95.3 %	41 / 43	100.0 %	5 / 5
progress_bar.cpp	83.0 %	39 / 47	90.0 %	9 / 10
utils.cpp	100.0 %	8 / 8	100.0 %	2 / 2

Generated by: LCOV version 1.13

```
     :
   8 : void power_kernel_v1_no_background_runner(
     :         short* chA_data, short* chB_data, unsigned int* sq_data,
     :         int start_idx, int stop_idx) {
     :
  26 :         for (int i(start_idx); i < stop_idx; i++) {
  18 :                 sq_data[i] = chA_data[i] * chA_data[i] + chB_data[i] * chB_data[i];
     :         }
   8 : }
     :
   2 : void CPU::power_kernel(
     :         short* chA_data,
     :         short* chB_data,
     :         unsigned int* sq_data,
     :         int no_points,
     :         int number_of_threads
     :         ) {
     :
   2 :         std::thread* t = new std::thread[number_of_threads];
   2 :         int idx = 0;
   2 :         int increment = floor((no_points) / number_of_threads);
     :
     :         // 1. launch multiple parallel threads
   8 :         for (int i(0); i < number_of_threads - 1; i++) {
  12 :                 t[i] = std::thread(
     :                         power_kernel_v1_no_background_runner,
     :                         chA_data, chB_data, sq_data,
  12 :                         idx, idx + increment);
   6 :                 idx += increment;
     :         }
   4 :         t[number_of_threads - 1] = std::thread(
     :                 power_kernel_v1_no_background_runner,
     :                 chA_data, chB_data, sq_data,
   2 :                 idx, no_points);
     :
     :         //2. join the threads
  10 :         for (int i(0); i < number_of_threads; i++)
   8 :                 t[i].join();
   2 :         delete[] t;
   2 : }
     :
  20 : void power_kernel_v2_const_background_runner(
     :         short* chA_data, short* chB_data, unsigned int* sq_data,
     :         short chA_back, short chB_back,
     :         int start_idx, int stop_idx) {
     :
  38 :         for (int i(start_idx); i < stop_idx; i++) {
  18 :                 chA_data[i] -= chA_back;
  18 :                 chB_data[i] -= chB_back;
  18 :                 sq_data[i] = chA_data[i] * chA_data[i] + chB_data[i] * chB_data[i];
     :         }
```

POWER::GPU Namespace Reference

Classes

struct power_memory
Collection of memory allocations for power evaluation on the GPU. More...

Functions

unsigned int get_number_of_reduction_blocks (unsigned int r_points)
template<typename T >
unsigned int get_shared_memory_size ()
void copy_background_arrays_to_gpu (short *chA_background, short *chB_background, int N=SP_POINTS)
template<typename T >
power_memory< T > allocate_memory (unsigned int sp_points, unsigned int r_points)
template<typename T >
void free_memory (power_memory< T > memory)
template<typename T >
void power_kernel (unsigned int sp_points, unsigned int r_points, T normalisation, short *chA_data, short *chB_data, power_memory< T > memory)

Variables

const int threads = 1024
Threads used in evaluation. More is better, but since they use shared memory (see get_shared_memory_size) we should restrict them. More...
const int no_outputs_from_gpu = 4
GPU will be computing this number of results. More...

Function Documentation

template<typename T >
template POWER::GPU::power_memory< long > POWER::GPU::allocate_memory< long > (unsigned int sp_points,
unsigned int r_points

```
./bin/bench
Celero
Timer resolution: 0.001000 us
|     Group      |   Experiment    |   Prob. Space   |     Samples     |   Iterations    |    Baseline     |  us/Iteration   | Iterations/sec  |   RAM (bytes)   |
|:--------------:|:---------------:|:---------------:|:---------------:|:---------------:|:---------------:|:---------------:|:---------------:|:---------------:|
|G1              | READING         |            Null |              30 |             192 |         1.00000 |      4373.41667 |          228.65 |       260931584 |
|G1              | KERNEL_GPU_FFTW |            Null |              30 |             484 |         0.11290 |       493.76033 |         2025.27 |      9664360448 |
|G1              | PREPROCESSOR_GP |            Null |              30 |             276 |         0.05245 |       229.39130 |         4359.36 |      9767313408 |
|G1              | PROCESS_GPU     |            Null |              30 |             319 |         0.16872 |       737.89342 |         1355.21 |      9904582656 |
|G1              | PIPELINE_GPU_1R |            Null |              30 |              94 |         1.72853 |      7559.59574 |          132.28 |      9986179072 |
|G1              | PIPELINE_GPU_2R |            Null |              30 |               5 |         2.76946 |     12112.00000 |           82.56 |     10070073344 |
|G1              | PIPELINE_GPU_3R |            Null |              30 |               5 |         4.01091 |     17541.40000 |           57.01 |     10070073344 |
|G1              | PIPELINE_GPU_4R |            Null |              30 |               5 |         5.82730 |     25485.20000 |           39.24 |     10070073344 |
|G1              | PIPELINE_GPU_10 |            Null |              30 |               1 |      1102.47168 |   4821568.00000 |            0.21 |     10070073344 |
Completed in 00:05:03.019213
```

```
[antonov@thinker csrc]$ make test
🍕 [cpp] Building test/logging_test.cpp → build/./test/logging_test.o
🍕 [cpp] Building test/power_pipeline_test.cpp → build/./test/power_pipeline_test.o
🍕 [cpp] Building test/g1_kernel_gpu_test.cpp → build/./test/g1_kernel_gpu_test.o
🍕 [cpp] Building test/power_kernel_small_array_test.cpp → build/./test/power_kernel_small_array_test.o
🍕 [cpp] Building test/g1_kernel_preprocessor_test.cpp → build/./test/g1_kernel_preprocessor_test.o
🍕 [cpp] Building test/g1_pipeline_test.cpp → build/./test/g1_pipeline_test.o
🍕 [cpp] Building test/power_kernel_large_array_test.cpp → build/./test/power_kernel_large_array_test.o
🍕 [cpp] Building test/progress_bar_test.cpp → build/./test/progress_bar_test.o
🍕 [cpp] Building test/utils_test.cpp → build/./test/utils_test.o
🍕 [cpp] Building test/sp_digitiser_test.cpp → build/./test/sp_digitiser_test.o
🍕 [cpp] Building test/test_runner.cpp → build/./test/test_runner.o
🍕 [cpp] Building test/utils_gpu_test.cpp → build/./test/utils_gpu_test.o
✅ [***] Built files in "./test"

🍕 [cpp] Building src/utils.cpp → build/./src/utils.o
🍕 [cpp] Building src/sp_digitiser.cpp → build/./src/sp_digitiser.o
🍕 [cpp] Building src/progress_bar.cpp → build/./src/progress_bar.o
🍕 [cpp] Building src/utils_gpu.cpp → build/./src/utils_gpu.o
🍕 [cpp] Building src/power_kernel_cpu.cpp → build/./src/power_kernel_cpu.o
🍕 [cpp] Building src/logging.cpp → build/./src/logging.o
🍕 [cpp] Building src/power_pipeline.cpp → build/./src/power_pipeline.o
🍕 [cpp] Building src/g1_kernel_gpu_utils.cpp → build/./src/g1_kernel_gpu_utils.o
🍕 [cpp] Building src/power_kernel_gpu_utils.cpp → build/./src/power_kernel_gpu_utils.o
🍕 [cpp] Building src/g1_pipeline.cpp → build/./src/g1_pipeline.o
🐍 [cu ] Building src/power_kernel_gpu.cu → build/./src/power_kernel_gpu.o
🐍 [cu ] Building src/g1_kernel_gpu_fftw.cu → build/./src/g1_kernel_gpu_fftw.o
🐍 [cu ] Building src/g1_kernel_gpu_preprocessor.cu → build/./src/g1_kernel_gpu_preprocessor.o
✅ [***] Built files in "./src"

🏗 [***] Building binary file ./bin/test
Using flags: -DTESTENV -D SP_POINTS=10000 -D DEBUG=1 -D G1_DIGITISER_POINTS=262140

✅ [***] Built binary ./bin/test

./bin/test
...Very slow!
...include/utils.hpp(167): No such file!
.include/utils.hpp(164): Array being written to, is too small in y-direction!
.include/utils.hpp(165): Array being written to, is too large in y-direction!
...Software trigger
Internal clock
```

Figure C.5: **(a)** Unit testing and code coverage reports, identified areas of the code that were cross checked against validated inputs and outputs and ensured the integrity of library during development; **(b)** Documentation automatically generated based on comments in files; **(c)** Benchmarking of the program modules is used to identify bottlenecks; **(d)** Compilation processing that links `C++` and `CUDA` code into one dynamic library.

Appendix D

Glossary

Acronyms

ADC	Analogue to digital converter
Al	Aluminum
Al-AlO_x-Al	Al-AlO_x-Al
ALD	Atomic layer deposition
AlO_x	Aluminum Oxide
Ar	Argon
Au	Gold
BC	Boundary condition
BCS	Bardeen-Cooper-Schrieffer theory
CP	Cooper pair
CPB	Cooper pair box
CPW	Coplanar waveguide
CQPS	Coherent quantum phase slip
CQUID	Coherent quantum interference device
DC	Direct current

EBL	Electron beam lithographer
FFT	Fast Fourier transform
FIB	Focused ion beam
FT	Fourier transform
FWHM	Full width at half maximum
GPU	Graphical processing unit
H_2O	Water
He^3	Helium 3
He^4	Helium 4
HF	Hydrogen fluoride
InO_x	Indium Oxide
IPA	Isopropanol
JJ	Josephson junction
LHS	Left hand side
MOSFET	Metal–oxide–semiconductor field-effect transistor
N_2	Nitrogen
Nb	Niobium
NbN	Niobium Nitride
NbTi	Niobium Titanium
Ni	Nickel
O_2	Oxygen
PCB	Printed circuit board
PEC	Proximity effect correction
PG	Pulse generator
PSL	Photon source library

QPS	Quantum phase slip
QPSJ	Quantum phase slip junction
RBW	Radio bandwidth
RF	Radio frequency
RHS	Right hand side
RIE	Reactive ion etching
RT	Room temperature
RWA	Rotating wave approximation
SEM	Scanning electron microscope
Si	Silicon
SIS	Superconductor-insulator-superconductor
SIT	Superconductor-insulator transition
SMA	SubMiniature version A
SMP	SubMiniature push-on
SNR	Signal to noise ratio
SPA	Spectrum analyser
SQUID	Superconducting interference device
TAPS	Thermally activated phase slips
Ti	Titanium
TiN	Titanium Nitride
TL	Transmission line
TLS	Two level systems
UV	Ultra violet
VBW	Video band width
VNA	Vector Network Analyser
wrt	with respect to

Constants

Constant	**Description**	**Value**
R_q	Resistance quantum	$h/4e^2 = 6.484\,\mathrm{k\Omega}$
Z_0	Standard impedance	$50\,\Omega$
Φ_0	Flux quantum	$h/2e = 2.067 \times 10^{-15}\,\mathrm{Wb}$
$\hbar$	Reduced Planck's constant	$h/2\pi$
μ_0	Vacuum permeability	$1.257 \times 10^{-6}\,\mathrm{N/A^2}$
ε_0	Vacuum permittivity	$8.8541 \times 10^{-12}\,\mathrm{F/m}$
e	Electron charge	$1.602 \times 10^{-19}\,\mathrm{As}$
h	Planck's constant	$6.6260 \times 10^{-34}\,\mathrm{Js}$
k_b	Boltzmann's constant	$1.3806 \times 10^{-23}\,\mathrm{J/K}$
m_e	Electron mass	$9.109 \times 10^{-31}\,\mathrm{kg}$

Symbols

Symbol	Description
$a, a^\dagger$	Photon annihilation/creation operators (hats are dropped)
α	Dimensional asymmetry of a Josephson junction relative to neighbours
α, β, η	Forward scattering (spot), backscattering size of an electron beam, energy ratio of the forward and backscattered electrons
A	Area
B_{ext}	External magnetic field applied to loop of area A linking a flux $\Phi = B_{\text{ext}}A$
c	Capacitance per unit length. Unless indicated is has a constant value $c = 0.85 \times 10^{-10}\,\text{F/m}$
C_Σ	Total capacitance
$C_{\text{s}}, C_{J0}, C_r$	Shunting, junction, resonator capacitance
$C_{\text{q-t(e/c)/q-r/r-t}}$	Capacitive coupling between: qubit and transmission line (emission side or control side), qubit and resonator, resonator and transmission line
$\Delta(T, B)$	Superconducting energy gap
Δf	Measurement or filter bandwidth
Δ	Off-diagonal term of a 2-level system, describing coupling energy between the two states
δ, δ_{q-r}	Frequency detuning from a determined value, detuning between qubit and resonator $\delta_{q-r} = \omega_q - \omega_r$
$\Delta\omega$	Full width at half maximum of a peak
Δ, Ψ	Superconducting energy gap (also the Cooper pair condensation energy), superconducting order parameter wavefunction $\Psi(\vec{r}) = \sqrt{n_{\text{CP}}}e^{i\varphi(\vec{r})}$
$\partial_t, \partial_{tt}$	First and second partial derivatives wrt time
$\partial_x, \partial_{xx}$	First and second partial derivatives wrt position
$\vartheta, \hat{\vartheta}$	Dipole moment of qubit, corresponding operator
d_{ij}	Dipole matrix element describing transition amplitude between two states $\|i\rangle \leftrightarrow \|j\rangle$
$\vec{E}, \vec{B}$	Electric and magnetic field components of a propagating wave
E, E_{ij}	Energy, energy of a $\|i\rangle \leftrightarrow \|j\rangle$ transition
E_c	Charging energy $e^2/2C$
$E_e, \|e\rangle$	Excited state energy and eigenstate of a 2-level system

Symbol	**Description**
E_F	Fermi energy
$E_g, \|g\rangle$	Ground state energy and eigenstate of a 2-level system
E_c	Inductance energy $\Phi_0^2/2L$
E_{J0}, E_J	Josephson energy, equivalent Josephson junction energy of SQUID loop
E_s, E_{ss}, E_{sc}	Phase slip energy, across the side junction to environment, across the central junction
ε_r	Relative permittivity of material
ε	Diagonal term of a 2-level system, describing energy asymmetry between the two states
f_r, f_m, κ, Q, L	Resonator's fundamental mode, m-th harmonic $m \in Z_{\geq 1}$, decay rate, quality factor $Q = f_r/(\kappa/2\pi)$, length
$\Phi, \hat{\Phi}$	Flux, corresponding operator
$F, \hat{F}$	Flux number, corresponding operator. F_L, F_R are operators for the left and right loops respectively
$\Delta\varphi, \Phi_{\text{element}}$	Phase across an element, flux across the same element, related to each other by $\Delta\varphi = 2\pi\Phi_{\text{element}}/\Phi_0$
$\Delta\varphi, \varphi, \hat{\varphi}$	Phase difference, phase across a Josephson junction, corresponding operator
$\varphi_{ij}, \hat{\varphi}_{ij}$	Phase difference across a Josephson junction between islands i and j
$\mathcal{F}, \mathcal{F}_{\text{inv}}$	Forward and inverse Fourier transforms
$g^{(1)}(\tau)$	1st order correlation function of a signal $\int dt\, V(\tau+t)V^*(t)$
$g^{(2)}(\tau)$	2nd order correlation function of a signal $\int dt\, V(\tau+t)V(t)V^*(\tau+t)V^*(t)$
G, F	Gain, noise figure of a microwave component
G, σ	Conductance, conductance per unit length quantifying the short circuit between transmission line and ground plane
H	Hamiltonian equation of motion for classical and quantum systems
$H_0, H_q, H_r, H_{\text{q-r}}, H_{\text{int}}, H_{\text{mw}}$	Unperturbed, qubit, resonator, qubit-resonator with interaction, generic interaction, driving Hamiltonians
I	Current
I_c	Josephson critical current
I_p	Persistent current in a loop

Symbol	**Description**
$I_{r0}, \hat{I}_r$	Zero-point root mean square current $I_{r0} = \sqrt{\frac{\hbar\omega_r}{L_r}}$, resonator's current operator
$I_{\text{solenoid}}, I_{\Phi_0}$	Current in the magnet biasing the qubit setups, period of current in solendoid corresponding to a flux change of Φ_0
$K_j, S[\rho]$	Kraus operator that defines the superoperator $\rho' = S[\rho]$, which acts on a density state to produce a new density state
l	Inductance per unit length of transmission line
$L_{\square}, L_k, L_{\text{geometric}}$	Total inductance, sheet inductance, kinetic inductance (material dependent), geometric inductance (topology dependent), resonator's inductance
L_J, L_r	Josephson junction's inductance, resonator's inductance
$\mathcal{L}$	Lagrangian equation of motion for classical systems
$\mathcal{L}[\rho]$	Linbland operator describing dissipation dynamics
$\hat{\lambda}$	Noise operator
λ_L	London penetration depth, giving the scale of external magnetic field penetration into the bulk of a superconductor and the thickness of the circulating current layer that ensure zero magnetic field in the bulk
M	Mutual inductance between qubit and transmission line or resonator
m	Mass, collision time of charge carriers in a material
μ	Magnetic permeability of material
$N, \hat{N}$	Cooper pair number, corresponding operator
$N_{\text{ext}}, \varphi_{\text{ext}}, \Phi_{\text{ext}}, f_{\text{ext}}$	Externally induced charge, phase, flux, flux number $f_{\text{ext}} = \Phi_{\text{ext}}/\Phi_0$
$n, \hat{n}, \bar{n}, \Delta n$	Photon number, corresponding operator, average photon number and photon number variation in the field
n_B	Bose occupation factor $n_B(\omega) = (\exp[\hbar\omega/k_bT] - 1)^{-1}$
n_{CP}	Cooper pair concentration
η	Non-radiative emission of qubit into a transmission line
$\omega, \omega_q, \omega_{ij}$	Microwave frequency (radians), corresponding to first qubit transition $\omega_q = \omega_{01}$, corresponding to transition $\|i\rangle \leftrightarrow \|j\rangle$
ω_r, ω_m	Resonator's fundamental frequency, resonator's mth harmonic frequency $m \in Z_{\geq 1}$
$\omega, \omega^c, \omega^p$	Driving microwave field, control field (first tone) in two tone measurements, probe field (second field) in two tone measurements

Symbol	**Description**
Ω, θ	Rabi frequency corresponding to an external drive, qubit rotation angle $\theta = \Omega t$ as a result of the drive
$\sigma_{x,y,z}$	Pauli matrix operators for a 2-level system (hats are dropped)
$\sigma_{-,+}$	Atom relaxation and excitation operators (hats are dropped)
$P(t)$	Power emitted by system
$Q, \hat{Q}$	Charge, corresponding operator
r, t	Reflection and transmission of microwaves in transmission line
$R, R_\square, R_n, R_\xi$	Resistance, sheet resistance, normal resistance, resistance of segment of length ξ
ρ, ρ_{ij}	Density matrix and density matrix element
$S(\omega)$	Power spectral density - the signal power at different frequencies
$\sigma, \sigma_1, \sigma_2, \sigma_N$	Conductivity of a material, real part, imaginary, at room temperature
$T, \Delta t, \Delta t_\pi$	Repetition interval, pulse length, π-pulse length
T_1, Γ_1	Relaxation time and relaxation (depolarisation) rate of system
$T_2, T_2^*, T_{2R}, T_{2E}, \Gamma_2$	Dephasing time of system, quantified by Ramsay interferometry, Rabi oscillation, spin echo measurements, decoherence rate (sometimes labelled γ for clearer differentiation with the relaxation rate)
Γ_φ	Pure dephasing rate of system
T, T_c	Temperature, superconducting transition temperature
$U(t)$	Unitary evolution operator
v	Speed of a propagating wave determined by transmission line properties $v = 1/\sqrt{lc}$
$V(t), \xi(t), I(t), Q(t)$	Voltage, envelope of a high frequency voltage signal $V(t) = \xi(t)e^{-i\omega t}$, quadratures of a voltage signal $V(t) = I(t) + iQ(t)$
$V_{\mathrm{mw}}, V_{\mathrm{sc}}, V_{\mathrm{source}}$	Drive, scattering, dipole source voltages in transmission line
$V_{r0}, V_m, \hat{V}_r$	Zero-point root mean square voltage $V_{r0} = \sqrt{\frac{\hbar\omega_r}{C_r}}$, voltage of the m-th mode $V_m = \sqrt{\frac{\hbar m\omega_r}{C_r}}$, resonator's voltage operator
$\Xi, \mathcal{N}$	Power of signal $\Xi \propto \xi^2$, noise power coming in with the signal
V_s	Phase slip voltage $V_s = 2\pi E_s/2e$
V_g	External gate voltage applied to a system
$W, L, T, N_x, N_{\mathrm{sq}}$	Dimensions: width, length, thickness, number of element x, number of squares of an element

Symbol	**Description**
ξ_0, ξ	Coherence length of superconducting wavefunction (also the approximate size of Cooper pairs), coherence length scale $\xi = \sqrt{W\xi_0}$ for a wire of width W
$\hat{x}, \hat{y}, \hat{z}$	Unit vectors in x, y and z directions
Z, Z_r	Complex impedance of circuit or circuit element, impedance of resonator

Bibliography

[1] J. Bardeen and W. H. Brattain. "The Transistor, A Semi-Conductor Triode". In: *Phys. Rev.* 74 (2 July 1948), pp. 230–231.

[2] A. L. Schawlow and C. H. Townes. "Infrared and Optical Masers". In: *Phys. Rev.* 112 (6 Dec. 1958), pp. 1940–1949.

[3] B.D. Josephson. "Possible new effects in superconductive tunnelling". In: *Physics Letters* 1.7 (July 1962), pp. 251–253.

[4] L. Essen and J. V. L. Parry. "An Atomic Standard of Frequency and Time Interval: A Cæsium Resonator". In: *Nature* 176.4476 (Aug. 1955), pp. 280–282.

[5] Alain Aspect, Philippe Grangier, and Gérard Roger. "Experimental Realization of Einstein-Podolsky-Rosen-Bohm Gedankenexperiment: A New Violation of Bell's Inequalities". In: *Phys. Rev. Lett.* 49 (2 July 1982), pp. 91–94.

[6] Richard P. Feynman. "Simulating physics with computers". In: *International Journal of Theoretical Physics* 21.6–7 (June 1982), pp. 467–488.

[7] Ashley Montanaro. "Quantum algorithms: an overview". In: *npj Quantum Information* 2.1 (Jan. 2016).

[8] D. Coppersmith. *An approximate Fourier transform useful in quantum factoring*. 2002.

[9] Ye Cao et al. "Quantum Fourier Transform and Phase Estimation in Qudit System". In: *Communications in Theoretical Physics* 55.5 (May 2011), pp. 790–794.

[10] Peter W. Shor. "Polynomial-Time Algorithms for Prime Factorization and Discrete Logarithms on a Quantum Computer". In: *SIAM Journal on Computing* 26.5 (Oct. 1997), pp. 1484–1509.

[11] Lov K. Grover. "Quantum Computers Can Search Rapidly by Using Almost Any Transformation". In: *Physical Review Letters* 80.19 (May 1998), pp. 4329–4332.

[12] Siddhant Garg and Goutham Ramakrishnan. *Advances in Quantum Deep Learning: An Overview*. 2020.

[13] Nathan Wiebe, Ashish Kapoor, and Krysta M. Svore. *Quantum Deep Learning*. 2014.

[14] Seth Lloyd. "Universal Quantum Simulators". In: *Science* 273.5278 (1996), pp. 1073–1078.

[15] J. Randall et al. "Many-body&#x2013;localized discrete time crystal with a programmable spin-based quantum simulator". In: *Science* 374.6574 (2021), pp. 1474–1478.

[16] V. A. Vozhakov et al. "State control in superconducting quantum processors". In: *Phys. Usp.* 65.5 (2022), pp. 421–439.

[17] J. Ignacio Cirac and Peter Zoller. "Goals and opportunities in quantum simulation". In: *Nature Physics* 8.4 (Apr. 2012), pp. 264–266.

[18] I. M. Georgescu, S. Ashhab, and Franco Nori. "Quantum simulation". In: *Reviews of Modern Physics* 86.1 (Mar. 2014), pp. 153–185.

[19] Katherine L. Brown, William J. Munro, and Vivien M. Kendon. "Using Quantum Computers for Quantum Simulation". In: *Entropy* 12.11 (Nov. 2010), pp. 2268–2307.

[20] Matthew Reagor et al. "Quantum memory with millisecond coherence in circuit QED". In: *Phys. Rev. B* 94 (1 July 2016), p. 014506.

[21] Kasra Sardashti et al. "Voltage-Tunable Superconducting Resonators: A Platform for Random Access Quantum Memory". In: *IEEE Transactions on Quantum Engineering* 1 (2020), pp. 1–7.

[22] Mathieu Pierre et al. "Storage and on-demand release of microwaves using superconducting resonators with tunable coupling". In: *Applied Physics Letters* 104 (2014), p. 232604.

[23] Max Hofheinz et al. "Synthesizing arbitrary quantum states in a superconducting resonator". In: *Nature* 459.7246 (May 2009), pp. 546–549.

[24] N. Leung et al. "Deterministic bidirectional communication and remote entanglement generation between superconducting qubits". In: *npj Quantum Information* 5.1 (Feb. 2019).

[25] Io-Chun Hoi et al. "Demonstration of a Single-Photon Router in the Microwave Regime". In: *Phys. Rev. Lett.* 107 (7 Aug. 2011), p. 073601.

[26] Charles H. Bennett et al. "Teleporting an unknown quantum state via dual classical and Einstein-Podolsky-Rosen channels". In: *Phys. Rev. Lett.* 70 (13 Mar. 1993), pp. 1895–1899.

[27] S. J. van Enk, J. I. Cirac, and P. Zoller. "Photonic Channels for Quantum Communication". In: *Science* 279.5348 (1998), pp. 205–208.

[28] Valerio Scarani et al. "The security of practical quantum key distribution". In: *Reviews of Modern Physics* 81.3 (Sept. 2009), pp. 1301–1350.

[29] Charles H. Bennett and Gilles Brassard. "Quantum cryptography: Public key distribution and coin tossing". In: *Theoretical Computer Science* 560 (Dec. 2014), pp. 7–11.

[30] Artur K. Ekert. "Quantum cryptography based on Bell's theorem". In: *Phys. Rev. Lett.* 67 (6 Aug. 1991), pp. 661–663.

[31] Nicolas Gisin and Rob Thew. "Quantum communication". In: *Nature Photonics* 1.3 (Mar. 2007), pp. 165–171.

[32] Daniel J. Bernstein and Tanja Lange. "Post-quantum cryptography". In: *Nature* 549.7671 (Sept. 2017), pp. 188–194.

[33] H. J. Kimble. "The quantum internet". In: *Nature* 453.7198 (June 2008), pp. 1023–1030.

[34] R. J. Schoelkopf et al. "The Radio-Frequency Single-Electron Transistor (RF-SET): A Fast and Ultrasensitive Electrometer". In: *Science* 280.5367 (1998), pp. 1238–1242.

[35] M. Brownnutt et al. "Ion-trap measurements of electric-field noise near surfaces". In: *Rev. Mod. Phys.* 87 (4 Dec. 2015), pp. 1419–1482.

[36] Haoquan Fan et al. "Atom based RF electric field sensing". In: *Journal of Physics B: Atomic, Molecular and Optical Physics* 48.20 (Sept. 2015), p. 202001.

[37] R. C. Jaklevic et al. "Macroscopic Quantum Interference in Superconductors". In: *Phys. Rev.* 140 (5A Nov. 1965), A1628–A1637.

[38] J.E. Lenz. "A review of magnetic sensors". In: *Proceedings of the IEEE* 78.6 (1990), pp. 973–989.

[39] M. Simmonds, W. Fertig, and R. Giffard. "Performance of a resonant input SQUID amplifier system". In: *IEEE Transactions on Magnetics* 15.1 (1979), pp. 478–481.

[40] Mete Atatüre et al. "Observation of Faraday rotation from a single confined spin". In: *Nature Physics* 3.2 (Jan. 2007), pp. 101–106.

[41] Miro Kroutvar et al. "Optically programmable electron spin memory using semiconductor quantum dots." eng. In: *Nature* 432.7013 (Nov. 4, 2004), pp. 81–84.

[42] Lan Shi et al. "Quantum effect-based flexible and transparent pressure sensors with ultrahigh sensitivity and sensing density". In: *Nature Communications* 11.1 (July 2020).

[43] Chung-Jui Yu et al. "A Molecular Approach to Quantum Sensing". In: *ACS Central Science* 7.5 (Apr. 2021), pp. 712–723.

[44] "A gravitational wave observatory operating beyond the quantum shot-noise limit". In: *Nature Physics* 7.12 (Sept. 2011), pp. 962–965.

[45] C. L. Degen, F. Reinhard, and P. Cappellaro. "Quantum sensing". In: *Reviews of Modern Physics* 89.3 (July 2017).

[46] R. Hanbury Brown and R. Q. Twiss. "A Test of a New Type of Stellar Interferometer on Sirius". In: *Nature* 178.4541 (Nov. 1956), pp. 1046–1048.

[47] Osip Schwartz et al. "Superresolution Microscopy with Quantum Emitters". In: *Nano Letters* 13.12 (Nov. 2013), pp. 5832–5836.

[48] Seth Lloyd. "Enhanced Sensitivity of Photodetection via Quantum Illumination". In: *Science* 321.5895 (2008), pp. 1463–1465.

[49] E. D. Lopaeva et al. "Experimental Realization of Quantum Illumination". In: *Phys. Rev. Lett.* 110 (15 Apr. 2013), p. 153603.

[50] Mingnan Le et al. "Underwater computational ghost imaging". In: *Opt. Express* 25.19 (Sept. 2017), pp. 22859–22868.

[51] Bin Bai et al. "Imaging around corners with single-pixel detector by computational ghost imaging". In: *Optik* 147 (Oct. 2017), pp. 136–142.

[52] Cristoforo Abbattista et al. "Towards Quantum 3D Imaging Devices". In: *Applied Sciences* 11.14 (2021).

[53] Marta Gilaberte Basset et al. "Perspectives for Applications of Quantum Imaging". In: *Laser & Photonics Reviews* 13.10 (2019), p. 1900097.

[54] C. Monroe et al. "Demonstration of a Fundamental Quantum Logic Gate". In: *Physical Review Letters* 75.25 (Dec. 1995), pp. 4714–4717.

[55] J. F. Poyatos, J. I. Cirac, and P. Zoller. "Schemes of Quantum Computations with Trapped Ions". In: *Scalable Quantum Computers* (Jan. 2005), pp. 15–29.

[56] Daniel Loss and David P. DiVincenzo. "Quantum computation with quantum dots". In: *Phys. Rev. A* 57 (1 Jan. 1998), pp. 120–126.

[57] Xin Zhang et al. "Qubits based on semiconductor quantum dots". In: *Chinese Physics B* 27.2 (Feb. 2018), p. 020305.

[58] Warren S. Warren. "The Usefulness of NMR Quantum Computing". In: *Science* 277.5332 (Sept. 1997), pp. 1688–1690.

[59] Neil A. Gershenfeld and Isaac L. Chuang. "Bulk Spin-Resonance Quantum Computation". In: *Science* 275.5298 (1997), pp. 350–356.

[60] T. F. Havel et al. "Principles and Demonstrations of Quantum Information Processing by NMR Spectroscopy". In: *Applicable Algebra in Engineering, Communication and Computing* 10.4-5 (May 2000), pp. 339–374.

[61] Ivan H. Deutsch, Gavin K. Brennen, and Poul S. Jessen. "Quantum Computing with Neutral Atoms in An Optical Lattice". In: *Scalable Quantum Computers*. John Wiley and Sons, Ltd, 2000. Chap. 10, pp. 155–173.

[62] E. Knill, R. Laflamme, and G. J. Milburn. "A scheme for efficient quantum computation with linear optics". In: *Nature* 409.6816 (Jan. 2001), pp. 46–52.

[63] Y. Nakamura, Yu. A. Pashkin, and J. S. Tsai. "Coherent control of macroscopic quantum states in a single-Cooper-pair box". In: *Nature* 398.6730 (Apr. 1999), pp. 786–788.

[64] I. Chiorescu. "Coherent Quantum Dynamics of a Superconducting Flux Qubit". In: *Science* 299.5614 (Feb. 2003), pp. 1869–1871.

[65] M. Büttiker. "Zero-current persistent potential drop across small-capacitance Josephson junctions". In: *Physical Review B* 36.7 (Sept. 1987), pp. 3548–3555.

[66] T.P. Orlando et al. "A Superconducting Persistent Current Qubit". In: *Science* 285 (1999), p. 1036.

[67] M W Johnson et al. "A scalable control system for a superconducting adiabatic quantum optimization processor". In: *Superconductor Science and Technology* 23.6 (Apr. 2010), p. 065004.

[68] O. Astafiev et al. "Resonance Fluorescence of a Single Artificial Atom". In: *Science* 327.5967 (2010), pp. 840–843.

[69] A. A. Abdumalikov et al. "Electromagnetically Induced Transparency on a Single Artificial Atom". In: *Phys. Rev. Lett.* 104 (19 May 2010), p. 193601.

[70] T. Hönigl-Decrinis et al. "Mixing of coherent waves in a single three-level artificial atom". In: *Physical Review A* 98.4 (Oct. 2018).

[71] Jung-Tsung Shen and Shanhui Fan. "Coherent Single Photon Transport in a One-Dimensional Waveguide Coupled with Superconducting Quantum Bits". In: *Physical Review Letters* 95.21 (Nov. 2005), p. 213001.

[72] O. V. Astafiev et al. "Ultimate On-Chip Quantum Amplifier". In: *Physical Review Letters* 104.18 (May 2010), p. 183603.

[73] Anton Frisk Kockum et al. "Ultrastrong coupling between light and matter". In: *Nature Reviews Physics* 1.1 (Jan. 2019), pp. 19–40.

[74] P. Forn-Díaz et al. "Ultrastrong coupling of a single artificial atom to an electromagnetic continuum in the nonperturbative regime". In: *Nature Physics* 13.1 (Oct. 2016), pp. 39–43.

[75] Z. H. Peng et al. "Tuneable on-demand single-photon source in the microwave range". In: *Nature Communications* 7.1 (Aug. 2016).

[76] A. Yu. Dmitriev et al. "Quantum wave mixing and visualisation of coherent and superposed photonic states in a waveguide". In: *Nature Communications* 8.1 (Nov. 2017).

[77] J. Kim et al. "A single-photon turnstile device". In: *Nature* 397.6719 (Feb. 1999), pp. 500–503.

[78] B. Lounis and W. E. Moerner. "Single photons on demand from a single molecule at room temperature". In: *Nature* 407.6803 (Sept. 2000), pp. 491–493.

[79] Xing Ding et al. "On-Demand Single Photons with High Extraction Efficiency and Near-Unity Indistinguishability from a Resonantly Driven Quantum Dot in a Micropillar". In: *Physical Review Letters* 116.2 (Jan. 2016).

[80] A. A. Houck et al. "Controlling the Spontaneous Emission of a Superconducting Transmon Qubit". In: *Physical Review Letters* 101.8 (Aug. 2008).

[81] D. Bozyigit et al. "Antibunching of microwave-frequency photons observed in correlation measurements using linear detectors". In: *Nature Physics* 7.2 (Dec. 2010), pp. 154–158.

[82] C. Lang et al. "Correlations, indistinguishability and entanglement in Hong–Ou–Mandel experiments at microwave frequencies". In: *Nature Physics* 9.6 (May 2013), pp. 345–348.

[83] A. A. Houck et al. "Generating single microwave photons in a circuit". In: *Nature* 449.7160 (Sept. 2007), pp. 328–331.

[84] Yu Zhou et al. "Tunable Microwave Single-Photon Source Based on Transmon Qubit with High Efficiency". In: *Physical Review Applied* 13.3 (Mar. 2020).

[85] I. Gerhardt et al. "Strong Extinction of a Laser Beam by a Single Molecule". In: *Physical Review Letters* 98.3 (Jan. 2007).

[86] G. Wrigge et al. "Efficient coupling of photons to a single molecule and the observation of its resonance fluorescence". In: *Nature Physics* 4.1 (Dec. 2007), pp. 60–66.

[87] Meng Khoon Tey et al. "Strong interaction between light and a single trapped atom without the need for a cavity". In: *Nature Physics* 4.12 (Oct. 2008), pp. 924–927.

[88] Marlan O. Scully and M. Suhail Zubairy. "Quantum Optics". In: (Sept. 1997), pp. 292–319.

[89] Y.-F. Chen et al. "Microwave Photon Counter Based on Josephson Junctions". In: *Physical Review Letters* 107.21 (Nov. 2011).

[90] Roy J. Glauber. "Photon Correlations". In: *Physical Review Letters* 10.3 (Feb. 1963), pp. 84–86.

[91] Marcus P. da Silva et al. "Schemes for the observation of photon correlation functions in circuit QED with linear detectors". In: *Physical Review A* 82.4 (Oct. 2010).

[92] Jens Koch et al. "Charge-insensitive qubit design derived from the Cooper pair box". In: *Physical Review A* 76.4 (Oct. 2007).

[93] J. A. Schreier et al. "Suppressing charge noise decoherence in superconducting charge qubits". In: *Physical Review B* 77.18 (May 2008).

[94] K. W. Lehnert et al. "Measurement of the Excited-State Lifetime of a Microelectronic Circuit". In: *Phys. Rev. Lett.* 90 (2 Jan. 2003), p. 027002.

[95] Howard Carmichael. "An Open Systems Approach to Quantum Optics". In: *Lecture Notes in Physics Monographs* (1993).

[96] B. R. Mollow. "Power Spectrum of Light Scattered by Two-Level Systems". In: *Physical Review* 188.5 (Dec. 1969), pp. 1969–1975.

[97] J.R. Johansson, P.D. Nation, and Franco Nori. "QuTiP 2: A Python framework for the dynamics of open quantum systems". In: *Computer Physics Communications* 184.4 (2013), pp. 1234–1240.

[98] G. Ithier et al. "Decoherence in a superconducting quantum bit circuit". In: *Physical Review B* 72.13 (Oct. 2005).

[99] D. J. Van Harlingen et al. "Decoherence in Josephson-junction qubits due to critical-current fluctuations". In: *Phys. Rev. B* 70 (6 Aug. 2004), p. 064517.

[100] Rogerio de Sousa. "Dangling-bond spin relaxation and magnetic 1/f noise from the amorphous-semiconductor/oxide interface: Theory". In: *Physical Review B* 76.24 (Dec. 2007).

[101] E. Paladino et al. "1/f noise: Implications for solid-state quantum information". In: *Rev. Mod. Phys.* 86 (2 Apr. 2014), pp. 361–418.

[102] P. Dutta and P. M. Horn. "Low-frequency fluctuations in solids: $\frac{1}{f}$ noise". In: *Rev. Mod. Phys.* 53 (3 July 1981), pp. 497–516.

[103] P. Kumar et al. "Origin and Reduction of $1/f$ Magnetic Flux Noise in Superconducting Devices". In: *Phys. Rev. Applied* 6 (4 Oct. 2016), p. 041001.

[104] A. A. Clerk et al. "Introduction to quantum noise, measurement, and amplification". In: *Reviews of Modern Physics* 82.2 (Apr. 2010), pp. 1155–1208.

[105] Leonid V. Abdurakhimov et al. "A long-lived capacitively shunted flux qubit embedded in a 3D cavity". In: *Applied Physics Letters* 115.26 (Dec. 2019), p. 262601.

[106] U. Weiss. *Quantum Dissipative Systems*. Series in modern condensed matter physics. World Scientific, 1999.

[107] D. Vion et al. "Manipulating the Quantum State of an Electrical Circuit". In: *Science* 296.5569 (May 2002), pp. 886–889.

[108] Charles P. Slichter. *Principles of Magnetic Resonance*. Springer Berlin Heidelberg, 1978.

[109] Alexander Shnirman et al. "Low- and High-Frequency Noise from Coherent Two-Level Systems". In: *Phys. Rev. Lett.* 94 (12 Apr. 2005), p. 127002.

[110] I. Martin, L. Bulaevskii, and A. Shnirman. "Tunneling Spectroscopy of Two-Level Systems Inside a Josephson Junction". In: *Physical Review Letters* 95.12 (Sept. 2005).

[111] John M. Martinis et al. "Decoherence in Josephson Qubits from Dielectric Loss". In: *Phys. Rev. Lett.* 95 (21 Nov. 2005), p. 210503.

[112] R. Barends et al. "Coherent Josephson Qubit Suitable for Scalable Quantum Integrated Circuits". In: *Physical Review Letters* 111.8 (Aug. 2013).

[113] O. Astafiev et al. "Quantum Noise in the Josephson Charge Qubit". In: *Phys. Rev. Lett.* 93 (26 Dec. 2004), p. 267007.

[114] P. Krantz et al. "A quantum engineer extquotesingles guide to superconducting qubits". In: *Applied Physics Reviews* 6.2 (June 2019), p. 021318.

[115] J. Pettersson et al. "Extending the high-frequency limit of a single-electron transistor by on-chip impedance transformation". In: *Phys. Rev. B* 53 (20 May 1996), R13272–R13274.

[116] David P. Pappas et al. "Two Level System Loss in Superconducting Microwave Resonators". In: *IEEE Transactions on Applied Superconductivity* 21.3 (2011), pp. 871–874.

[117] Jonas Bylander et al. "Noise spectroscopy through dynamical decoupling with a superconducting flux qubit". In: *Nature Physics* 7.7 (May 2011), pp. 565–570.

[118] Roger H. Koch, D. J. Van Harlingen, and John Clarke. "Measurements of quantum noise in resistively shunted Josephson junctions". In: *Physical Review B* 26.1 (July 1982), pp. 74–87.

[119] M. Gurvitch, M. A. Washington, and H. A. Huggins. "High quality refractory Josephson tunnel junctions utilizing thin aluminum layers". In: *Applied Physics Letters* 42.5 (Mar. 1983), pp. 472–474.

[120] William D. Oliver and Paul B. Welander. "Materials in superconducting quantum bits". In: *MRS Bulletin* 38.10 (Oct. 2013), pp. 816–825.

[121] C. Wang et al. "Surface participation and dielectric loss in superconducting qubits". In: *Applied Physics Letters* 107.16 (Oct. 2015), p. 162601.

[122] R. W. Simmonds et al. "Decoherence in Josephson Phase Qubits from Junction Resonators". In: *Phys. Rev. Lett.* 93 (7 Aug. 2004), p. 077003.

[123] Li-Chung Ku and Clare C. Yu. "Decoherence of a Josephson qubit due to coupling to two-level systems". In: *Phys. Rev. B* 72 (2 July 2005), p. 024526.

[124] Stefan Fritz et al. "TEM investigations of Al/AlOx/Al Josephson junctions". In: *European Microscopy Congress 2016: Proceedings*. John Wiley and Sons, Ltd, 2016, pp. 996–997.

[125] Leonid V. Abdurakhimov et al. *Identification of different types of high-frequency defects in superconducting qubits*. 2021.

[126] Sh. Kogan. *Electronic Noise and Fluctuations in Solids*. Cambridge University Press, Aug. 1996.

[127] A. Yu. Dmitriev and O. V. Astafiev. "A perspective on superconducting flux qubits". In: *Applied Physics Letters* 119.8 (Aug. 2021), p. 080501.

[128] F. Yoshihara et al. "Decoherence of Flux Qubits due to1/fFlux Noise". In: *Physical Review Letters* 97.16 (Oct. 2006).

[129] G. Zimmerli et al. "Noise in the Coulomb blockade electrometer". In: *Applied Physics Letters* 61.2 (July 1992), pp. 237–239.

[130] Fei Yan et al. "The flux qubit revisited to enhance coherence and reproducibility". In: *Nature Communications* 7.1 (Nov. 2016).

[131] R. Barends et al. "Minimizing quasiparticle generation from stray infrared light in superconducting quantum circuits". In: *Applied Physics Letters* 99.11 (2011), p. 113507.

[132] R.-P. Riwar et al. "Normal-metal quasiparticle traps for superconducting qubits". In: *Phys. Rev. B* 94 (10 Sept. 2016), p. 104516.

[133] Vinay Ambegaokar and Alexis Baratoff. "Tunneling Between Superconductors". In: *Physical Review Letters* 10.11 (June 1963), pp. 486–489.

[134] *Coplanar waveguide with ground characteristic impedance calculator*. (Visited on 10/08/2021).

[135] Brian C. Wadell. *Transmission Line Design Handbook*. Oct. 1991.

[136] W. Meissner and R. Ochsenfeld. "Ein neuer Effekt bei Eintritt der Supraleitfhigkeit". In: *Die Naturwissenschaften* 21.44 (Nov. 1933), pp. 787–788.

[137] A. C. Rose-Innes, E. H. Rhoderick, and A. M. Goldman. "Introduction to Superconductivity". In: *American Journal of Physics* 38.8 (Aug. 1970), pp. 1048–1049.

[138] Jürgen Lisenfeld et al. "Decoherence spectroscopy with individual two-level tunneling defects". In: *Scientific Reports* 6.1 (Mar. 2016).

[139] *Zeiss Orion Nanofab focused ion beam microscope*. (Visited on 10/29/2021).

[140] Nima Arjmandi. "Resist Homogeneity". In: *Updates in Advanced Lithography*. Ed. by Sumio Hosaka. Rijeka: IntechOpen, 2013. Chap. 6.

[141] *West Bond wire bonder*. (Visited on 10/28/2021).

[142] *Anritsu MS2830*. (Visited on 10/29/2021).

[143] *ADQ214 Low Noise 14-bit digitiser*. (Visited on 10/03/2021).

[144] *National Instruments PXIe-1075 Crate*. (Visited on 10/03/2021).

[145] *National Instruments PCIe-8375 fibe optic cable*. (Visited on 10/03/2021).

[146] *Nvidia Quadro P6000 GPU*. (Visited on 10/03/2021).

[147] *Marki Microwave IQ Mixer*. (Visited on 10/04/2021).

[148] *Quinstar Cryogenic Circulators*. (Visited on 10/04/2021).

[149] *LNF-LNC1-12A Cryogenic Low Noise Amplifier*. (Visited on 10/04/2021).

[150] *ZVA-183G+ Wideband Amplifier*. (Visited on 10/04/2021).

[151] *Atlantic Wide Band Amplifiers*. (Visited on 10/04/2021).

[152] H. Nyquist. "Thermal Agitation of Electric Charge in Conductors". In: *Physical Review* 32.1 (July 1928), pp. 110–113.

[153] David P. DiVincenzo. "The Physical Implementation of Quantum Computation". In: *Fortschritte der Physik* 48.9-11 (Sept. 2000), pp. 771–783.

[154] Yuriy Makhlin, Gerd Schön, and Alexander Shnirman. "Quantum-state engineering with Josephson-junction devices". In: *Reviews of Modern Physics* 73.2 (May 2001), pp. 357–400.

[155] Alexander P. M. Place et al. "New material platform for superconducting transmon qubits with coherence times exceeding 0.3 milliseconds". In: *Nature Communications* 12.1 (Mar. 2021).

[156] Pengfei Wang et al. "Single ion qubit with estimated coherence time exceeding one hour". In: *Nature Communications* 12.1 (Jan. 2021).

[157] J. E. Mooij et al. "Josephson Persistent-Current Qubit". In: *Science* 285.5430 (Aug. 1999), p. 1036.

[158] F. Yoshihara et al. "Decoherence of Flux Qubits due to 1/f Flux Noise". In: *Physical Review Letters* 97.16 (Oct. 2006).

[159] Alexander P. M. Place et al. "New material platform for superconducting transmon qubits with coherence times exceeding 0.3 milliseconds". In: *Nature Communications* 12.1 (Mar. 2021).

[160] M. R. Vissers et al. "Low loss superconducting titanium nitride coplanar waveguide resonators". In: *Applied Physics Letters* 97.23 (Dec. 2010), p. 232509.

[161] R. Esteban Goetz et al. "Quantum optimal control of photoelectron spectra and angular distributions". In: *Physical Review A* 93.1 (Jan. 2016).

[162] I. M. Pop et al. "Experimental demonstration of Aharonov-Casher interference in a Josephson junction circuit". In: *Physical Review B* 85.9 (Mar. 2012).

[163] Josephine B. Chang et al. "Improved superconducting qubit coherence using titanium nitride". In: *Applied Physics Letters* 103.1 (July 2013), p. 012602.

[164] Alexandre Blais et al. "Cavity quantum electrodynamics for superconducting electrical circuits: An architecture for quantum computation". In: *Phys. Rev. A* 69 (6 June 2004), p. 062320.

[165] Hanhee Paik et al. "Observation of High Coherence in Josephson Junction Qubits Measured in a Three-Dimensional Circuit QED Architecture". In: *Physical Review Letters* 107.24 (Dec. 2011).

[166] Chad Rigetti et al. "Superconducting qubit in a waveguide cavity with a coherence time approaching 0.1 ms". In: *Physical Review B* 86.10 (Sept. 2012).

[167] Seongshik Oh et al. "Elimination of two level fluctuators in superconducting quantum bits by an epitaxial tunnel barrier". In: *Physical Review B* 74.10 (Sept. 2006).

[168] H. Wang et al. "Improving the coherence time of superconducting coplanar resonators". In: *Applied Physics Letters* 95.23 (Dec. 2009), p. 233508.

[169] L. Sun et al. "Measurements of Quasiparticle Tunneling Dynamics in a Band-Gap-Engineered Transmon Qubit". In: *Physical Review Letters* 108.23 (June 2012).

[170] M. H. Devoret and R. J. Schoelkopf. "Superconducting Circuits for Quantum Information: An Outlook". In: *Science* 339.6124 (Mar. 2013), pp. 1169–1174.

[171] Erik Lucero et al. "Computing prime factors with a Josephson phase qubit quantum processor". In: *Nature Physics* 8.10 (Aug. 2012), pp. 719–723.

[172] L. Casparis et al. "Gatemon Benchmarking and Two-Qubit Operations". In: *Physical Review Letters* 116.15 (Apr. 2016).

[173] J. Q. You et al. "Low-decoherence flux qubit". In: *Physical Review B* 75.14 (Apr. 2007).

[174] Jiansong Gao et al. "Experimental evidence for a surface distribution of two-level systems in superconducting lithographed microwave resonators". In: *Applied Physics Letters* 92.15 (Apr. 2008), p. 152505.

[175] J. Wenner et al. "Surface loss simulations of superconducting coplanar waveguide resonators". In: *Applied Physics Letters* 99.11 (Sept. 2011), p. 113513.

[176] Yueyin Qiu et al. "Four-junction superconducting circuit". In: *Scientific Reports* 6.1 (June 2016), p. 28622.

[177] Vladimir E. Manucharyan et al. "Evidence for coherent quantum phase slips across a Josephson junction array". In: *Physical Review B* 85.2 (Jan. 2012).

[178] Ioan M. Pop et al. "Coherent suppression of electromagnetic dissipation due to superconducting quasiparticles". In: *Nature* 508.7496 (Apr. 2014), pp. 369–372.

[179] K. V. Shulga et al. "Magnetically induced transparency of a quantum metamaterial composed of twin flux qubits". In: *Nature Communications* 9.1 (2018), p. 150.

[180] A. Kou et al. "Fluxonium-Based Artificial Molecule with a Tunable Magnetic Moment". In: *Phys. Rev. X* 7 (3 Aug. 2017), p. 031037.

[181] K. V. Shulga et al. "Magnetically induced transparency of a quantum metamaterial composed of twin flux qubits". In: *Nature Communications* 9.1 (Jan. 2018), p. 150.

[182] M. Stern et al. "Flux Qubits with Long Coherence Times for Hybrid Quantum Circuits". In: *Physical Review Letters* 113.12 (Sept. 2014).

[183] Simon Gustavsson et al. "Dynamical Decoupling and Dephasing in Interacting Two-Level Systems". In: *Physical Review Letters* 109.1 (July 2012).

[184] J.E. Mooij and Yu.V. Nazarov. "Quantum phase slip junctions". In: ().

[185] Y. Aharonov and D. Bohm. "Significance of Electromagnetic Potentials in the Quantum Theory". In: *Physical Review* 115.3 (Aug. 1959), pp. 485–491.

[186] Y. Aharonov and A. Casher. "Topological Quantum Effects for Neutral Particles". In: *Physical Review Letters* 53.4 (July 1984), pp. 319–321.

[187] R. Barends et al. "Superconducting quantum circuits at the surface code threshold for fault tolerance". In: *Nature* 508.7497 (Apr. 2014), pp. 500–503.

[188] J M Kreikebaum et al. "Improving wafer-scale Josephson junction resistance variation in superconducting quantum coherent circuits". In: *Superconductor Science and Technology* 33.6 (May 2020), 06LT02.

[189] J. Verjauw et al. "Path toward manufacturable superconducting qubits with relaxation times exceeding 0.1 ms". In: *npj Quantum Information* 8.1 (Aug. 2022).

[190] N M van Esbroeck et al. "Quantum device fine-tuning using unsupervised embedding learning". In: *New Journal of Physics* 22.9 (Sept. 2020), p. 095003.

[191] Rais S. Shaikhaidarov et al. "Quantized current steps due to the a.c. coherent quantum phase-slip effect". In: *Nature* 608.7921 (Aug. 2022), pp. 45–49.

[192] Sidney Shapiro. "Josephson Currents in Superconducting Tunneling: The Effect of Microwaves and Other Observations". In: *Physical Review Letters* 11.2 (July 1963), pp. 80–82.

[193] Johannes Kohlmann, Ralf Behr, and Torsten Funck. "Josephson voltage standards". In: *Measurement Science and Technology* 14.8 (July 2003), pp. 1216–1228.

[194] S. E. de Graaf et al. "Charge quantum interference device". In: *Nature Physics* 14.6 (Apr. 2018), pp. 590–594.

[195] T. T. Hongisto and A. B. Zorin. "Single-Charge Transistor Based on the Charge-Phase Duality of a Superconducting Nanowire Circuit". In: *Physical Review Letters* 108.9 (Feb. 2012).

[196] Zeng-Zhao Li et al. "Collective quantum phase slips in multiple nanowire junctions". In: *Phys. Rev. A* 99 (1 Jan. 2019), p. 012309.

[197] J. T. Peltonen et al. "Hybrid rf SQUID qubit based on high kinetic inductance". In: *Scientific Reports* 8.1 (July 2018).

[198] J. E. Mooij and Yu. V. Nazarov. "Superconducting nanowires as quantum phase-slip junctions". In: *Nature Physics* 2.3 (Feb. 2006), pp. 169–172.

[199] O. V. Astafiev et al. "Coherent quantum phase slip". In: *Nature* 484.7394 (Apr. 2012), pp. 355–358.

[200] J. T. Peltonen et al. "Coherent flux tunneling through NbN nanowires". In: *Physical Review B* 88.22 (Dec. 2013).

[201] J. T. Peltonen et al. "Coherent dynamics and decoherence in a superconducting weak link". In: *Physical Review B* 94.18 (Nov. 2016).

[202] M. Bell et al. "One-dimensional resistive states in quasi-two-dimensional superconductors: Experiment and theory". In: *Physical Review B* 76.9 (Sept. 2007).

[203] Kazi Rafsanjani Amin et al. "Loss mechanisms in TiN high impedance superconducting microwave circuits". In: *Applied Physics Letters* 120.16 (2022), p. 164001.

[204] C. N. Lau et al. "Quantum Phase Slips in Superconducting Nanowires". In: *Physical Review Letters* 87.21 (Nov. 2001).

[205] Michael Tinkham. *Introduction to superconductivity*. Courier Corporation, 2004.

[206] J. S. Langer and Vinay Ambegaokar. "Intrinsic Resistive Transition in Narrow Superconducting Channels". In: *Physical Review* 164.2 (Dec. 1967), pp. 498–510.

[207] D. E. McCumber and B. I. Halperin. "Time Scale of Intrinsic Resistive Fluctuations in Thin Superconducting Wires". In: *Physical Review B* 1.3 (Feb. 1970), pp. 1054–1070.

[208] R. S. Newbower, M. R. Beasley, and M. Tinkham. "Fluctuation Effects on the Superconducting Transition of Tin Whisker Crystals". In: *Physical Review B* 5.3 (Feb. 1972), pp. 864–868.

[209] N. Giordano. "Evidence for Macroscopic Quantum Tunneling in One-Dimensional Superconductors". In: *Physical Review Letters* 61.18 (Oct. 1988), pp. 2137–2140.

[210] Dmitri S. Golubev and Andrei D. Zaikin. *Quantum tunneling of the order parameter in superconducting nanowires*. June 2001.

[211] A. Bezryadin, C. N. Lau, and M. Tinkham. "Quantum suppression of superconductivity in ultrathin nanowires". In: *Nature* 404.6781 (Apr. 2000), pp. 971–974.

[212] I. Schneider et al. "Magnetic field-tuned superconductor/insulator transition in TiN nanostrips". In: *arXiv* (2018).

[213] J E Mooij et al. "Superconductor extendashinsulator transition in nanowires and nanowire arrays". In: *New Journal of Physics* 17.3 (Mar. 2015), p. 033006.

[214] K.Yu. Arutyunov, D.S. Golubev, and A.D. Zaikin. "Superconductivity in one dimension". In: *Physics Reports* 464.1-2 (July 2008), pp. 1–70.

[215] Mihajlo Vanević and Yuli V. Nazarov. "Quantum Phase Slips in Superconducting Wires with Weak Inhomogeneities". In: 108.18 (May 2012).

[216] J E Mooij and C J P M Harmans. "Phase-slip flux qubits". In: *New Journal of Physics* 7 (Oct. 2005), pp. 219–219.

[217] B Peropadre et al. "Scattering of coherent states on a single artificial atom". In: *New Journal of Physics* 15.3 (Mar. 2013), p. 035009.

[218] C. J. Hood et al. "The Atom-Cavity Microscope: Single Atoms Bound in Orbit by Single Photons". In: *Science* 287.5457 (Feb. 2000), pp. 1447–1453.

[219] E. M. Purcell, H. C. Torrey, and R. V. Pound. "Resonance Absorption by Nuclear Magnetic Moments in a Solid". In: *Physical Review* 69.1-2 (Jan. 1946), pp. 37–38.

[220] P. Goy et al. "Observation of Cavity-Enhanced Single-Atom Spontaneous Emission". In: *Phys. Rev. Lett.* 50 (24 June 1983), pp. 1903–1906.

[221] Daniel Kleppner. "Inhibited Spontaneous Emission". In: *Phys. Rev. Lett.* 47 (4 July 1981), pp. 233–236.

[222] David Isaac Schuster. "Circuit quantum electrodynamics". PhD thesis. Yale University, Connecticut, Jan. 2007.

[223] Randall G. Hulet, Eric S. Hilfer, and Daniel Kleppner. "Inhibited Spontaneous Emission by a Rydberg Atom". In: *Phys. Rev. Lett.* 55 (20 Nov. 1985), pp. 2137–2140.

[224] M. Brune et al. "Manipulation of photons in a cavity by dispersive atom-field coupling: Quantum-nondemolition measurements and generation of "Schrödinger cat" states". In: *Phys. Rev. A* 45 (7 Apr. 1992), pp. 5193–5214.

[225] J. M. Raimond, M. Brune, and S. Haroche. "Manipulating quantum entanglement with atoms and photons in a cavity". In: *Rev. Mod. Phys.* 73 (3 Aug. 2001), pp. 565–582.

[226] A. Wallraff et al. "Approaching Unit Visibility for Control of a Superconducting Qubit with Dispersive Readout". In: *Phys. Rev. Lett.* 95 (6 Aug. 2005), p. 060501.

[227] Serge Haroche. "Quantum Engineering with Atoms and Photons in a Cavity". In: *Epistemological and Experimental Perspectives on Quantum Physics*. Ed. by Daniel Greenberger, Wolfgang L. Reiter, and Anton Zeilinger. Dordrecht: Springer Netherlands, 1999, pp. 155–166.

[228] Jay Gambetta et al. "Qubit-photon interactions in a cavity: Measurement-induced dephasing and number splitting". In: *Phys. Rev. A* 74 (4 Oct. 2006), p. 042318.

[229] C.P. Wen. "Coplanar Waveguide: A Surface Strip Transmission Line Suitable for Nonreciprocal Gyromagnetic Device Applications". In: *IEEE Transactions on Microwave Theory and Techniques* 17.12 (1969), pp. 1087–1090.

[230] Yulin Wu et al. "An efficient and compact switch for quantum circuits". In: *npj Quantum Information* 4.1 (Oct. 2018).

[231] C. G. L. Bøttcher et al. "Parametric longitudinal coupling between a high-impedance superconducting resonator and a semiconductor quantum dot singlet-triplet spin qubit". In: *Nature Communications* 13.1 (Aug. 2022).

[232] Benjamin A. Mazin et al. "Superconducting kinetic inductance photon detectors". In: *Highly Innovative Space Telescope Concepts*. Ed. by Howard A. MacEwen. Vol. 4849. International Society for Optics and Photonics. SPIE, 2002, pp. 283–293.

[233] J. M. Fink et al. "Dressed Collective Qubit States and the Tavis-Cummings Model in Circuit QED". In: *Physical Review Letters* 103.8 (Aug. 2009).

[234] S. E. de Graaf et al. "Charge control of blockade of Cooper pair tunneling in highly disordered TiN nanowires in an inductive environment". In: *Physical Review B* 99.20 (May 2019).

[235] S Linzen et al. "Structural and electrical properties of ultrathin niobium nitride films grown by atomic layer deposition". In: *Superconductor Science and Technology* 30.3 (Jan. 2017), p. 035010.

[236] *Micro Resist Technology: ma-N 2400 resist*. (Visited on 10/08/2021).

[237] G. Oelsner et al. “Weak continuous monitoring of a flux qubit using coplanar waveguide resonator”. In: *Physical Review B* 81.17 (May 2010).

[238] A. M. Hriscu and Yu. V. Nazarov. “Coulomb blockade due to quantum phase slips illustrated with devices”. In: *Physical Review B* 83.17 (May 2011).

[239] I. V. Antonov et al. “Superconducting “twin” qubit”. In: *Physical Review B* 102.11 (Sept. 2020).

[240] T J B M Janssen et al. “Operation of graphene quantum Hall resistance standard in a cryogen-free table-top system”. In: *2D Materials* 2.3 (Aug. 2015), p. 035015.

[241] M. Hegedüs et al. “Detection of black body radiation using a compact terahertz imager”. In: *Applied Physics Letters* 117.23 (Dec. 2020), p. 231106.

[242] V. F. Weisskopf. *The formation of Cooper pairs and the nature of superconducting currents*. Tech. rep. CERN–79-12. European Organization for Nuclear Research (CERN), 1979, p. 29.

[243] H. Kamerlingh Onnes. “Further experiments with Liquid Helium. G. On the Electrical Resistance of Pure Metals, etc. VI. On the Sudden Change in the Rate at which the Resistance of Mercury Disappears.” In: *Boston Studies in the Philosophy of Science* (1991), pp. 267–272.

[244] J. Bardeen, L. N. Cooper, and J. R. Schrieffer. “Theory of Superconductivity”. In: *Physical Review* 108.5 (Dec. 1957), pp. 1175–1204.

[245] John M. Martinis and Kevin Osborne. *Superconducting Qubits and the Physics of Josephson Junctions*. 2004.

[246] Lev Davidovich Landau and V L Ginzburg. “On the theory of superconductivity”. In: *Zh. Eksp. Teor. Fiz.* 20 (1950), p. 1064.

[247] *Feynman’s seminar on superconductivity*. (Visited on 10/30/2021).

[248] Lei Yu et al. “Fabrication of niobium titanium nitride thin films with high superconducting transition temperatures and short penetration lengths”. In: *IEEE Transactions on Applied Superconductivity* 15.1 (2005), pp. 44–48.

[249] Anand Kamlapure et al. “Measurement of magnetic penetration depth and superconducting energy gap in very thin epitaxial NbN films”. In: *Applied Physics Letters* 96.7 (Feb. 2010), p. 072509.

[250] A. Johansson et al. "Nanowire Acting as a Superconducting Quantum Interference Device". In: *Physical Review Letters* 95.11 (Sept. 2005).

[251] *The Schrödinger Equation in a Classical Context: A Seminar on Superconductivity*. (Visited on 01/04/2023).

[252] John M. Martinis and Kevin Osborne. *Superconducting Qubits and the Physics of Josephson Junctions*. 2004.

[253] B.H. Bransden. *Quantum Mechanics*. Pearson Education, 2000.

[254] M. H. Devoret. *Quantum fluctuations in electrical circuits*. France: Edition de Physique, 1997.

[255] *The Principle of Least Action*. (Visited on 01/04/2022).

[256] J. B. Johnson. "Thermal Agitation of Electricity in Conductors". In: *Phys. Rev.* 32 (1 July 1928), pp. 97–109.

[257] Crispin W Gardiner and Peter Zoller. *Quantum noise*. en. Springer Series in Synergetics. Berlin, Germany: Springer, Dec. 2010.

[258] Herbert B. Callen and Theodore A. Welton. "Irreversibility and Generalized Noise". In: *Physical Review* 83.1 (July 1951), pp. 34–40.

[259] Ephraim Shahmoon. "Casimir forces in transmission-line circuits: QED and fluctuation-dissipation formalisms". In: *Physical Review A* 95.6 (June 2017).

[260] R. J. Schoelkopf et al. "Qubits as Spectrometers of Quantum Noise". In: *Quantum Noise in Mesoscopic Physics* (2003), pp. 175–203.

[261] Carlton M. Caves et al. "On the measurement of a weak classical force coupled to a quantum-mechanical oscillator. I. Issues of principle". In: *Reviews of Modern Physics* 52.2 (Apr. 1980), pp. 341–392.

[262] Melvin Lax. "Formal Theory of Quantum Fluctuations from a Driven State". In: *Physical Review* 129.5 (Mar. 1963), pp. 2342–2348.

[263] A. N. Omelyanchouk et al. "Quantum behaviour of a flux qubit coupled to a resonator". In: (2010).

[264] *Qubit Simulation*. (Visited on 10/01/2021).

[265] Sebastian T. Skacel. "Development of superconducting devices employing coherent Quantum Phase Slip". PhD thesis. Karlsruher Institut für Technologie (KIT), 2018.

[266] H. Nakazato et al. "Solution of the Lindblad equation in the Kraus representation". In: *Physical Review A* 74.6 (Dec. 2006).

[267] Paul Adrien Maurice Dirac. *The Principles of Quantum Mechanics*. Clarendon Press, 1930.

[268] D. C. Champeney. "A Handbook of Fourier Theorems". In: (Aug. 1987).

[269] B. Cowan. *Topics in Statistical Mechanics*. Imperial College Press Advanced Physics Texts. World Scientific Publishing Company, 2005.

[270] *Sping Coating: Complete Guide to Theory and Techniques*. (Visited on 10/07/2021).

[271] *Beamer Lithgraphy Software*. (Visited on 10/03/2021).

[272] L. I. Aparshina. "Energy dependence of proximity parameters investigated by fitting before measurement tests". In: *Journal of Vacuum Science and Technology B: Microelectronics and Nanometer Structures* 15.6 (Nov. 1997), p. 2298.

[273] *JEOL 8100*. (Visited on 10/03/2021).

[274] *Oxford Instruments PlasmaPro 80 RIE*. (Visited on 10/30/2021).

[275] *Plassys Electron Beam Evaporator MEB550S*. (Visited on 10/30/2021).

[276] *Midwest Tungsten Servce: Quartz Thickness Monitors*. (Visited on 10/07/2021).

[277] O. G. Vendik, S. P. Zubko, and M. A. Nikol'skii. "Modeling and calculation of the capacitance of a planar capacitor containing a ferroelectric thin film". In: *Technical Physics* 44.4 (Apr. 1999), pp. 349–355.

[278] *BlueFors DL Refrigirator*. (Visited on 10/03/2021).

[279] Ray Radebaugh et al. "Development of the pulse tube refrigerator as an efficient and reliable cryocooler". In: *Proc. Institute of Refrigeration (London)* 1999 (2000), p. 00.

[280] Guy K White and Philip Meeson. *Experimental techniques in low-temperature physics*. en. Monographs on the Physics and Chemistry of Materials. London, England: Oxford University Press, July 2001.

[281] *C++ Benchmarking Library*.